

**Molekulare Simulation als  
effizientes Werkzeug  
zur Bestimmung thermodynamischer Stoffdaten**

zur Erlangung des akademischen Grades  
DOKTOR DER INGENIEURWISSENSCHAFTEN (Dr.-Ing.)  
der Fakultät für Maschinenbau  
der Universität Paderborn

genehmigte  
DISSERTATION

von  
Andreas Köster, M.Sc.  
aus Bielefeld, Deutschland

Tag des Kolloquiums:	24.11.2017
Referent:	Prof. Dr.-Ing. habil. Jadran Vrabec
Korreferent:	Prof. Dr. habil. rer. nat. Sabine Enders



# Vorwort

Die vorliegende Arbeit ist im Rahmen meiner Tätigkeit als wissenschaftlicher Mitarbeiter am Lehrstuhl für Thermodynamik und Energietechnik der Universität Paderborn entstanden. Da eine wissenschaftliche Arbeit längst nicht ausschließlich das Werk einer einzelnen Person ist, möchte ich hiermit die Gelegenheit nutzen mich bei allen Menschen, die mir in dieser Zeit zur Seite standen, zu bedanken.

Ganz besonderer Dank gilt zuallererst meinem Doktorvater Prof. Dr.-Ing. habil. Jadran Vrabec der mich stets bei meinem Promotionsvorhaben unterstützte, zu jeder Uhrzeit erreichbar war und mir half mich persönlich weiterzuentwickeln. Seine Begeisterung für das vorliegende Arbeitsgebiet gab mir häufig neuen Mut.

Frau Prof. Dr. habil. rer. nat. Sabine Enders möchte ich für die freundliche Übernahme des Korreferats danken.

Für die fortwährende fachliche und freundschaftliche Unterstützung möchte ich auch Dr. Gábor Rutkai und Dr. Monika Thol danken. Prof. Dr. Peter Mausbach, Dr. Colin W. Glass, Michael Schappals, Prof. Dr. Rolf Lustig, Prof. Dr. Roland Span und Prof. Dr. Thomas D. Kühne gilt mein Dank für die ausgezeichnete wissenschaftliche Zusammenarbeit in den letzten Jahren.

Auch meinen Kollegen, mit denen mich nach all den Jahren wesentlich mehr verbindet als nur der gemeinsame Arbeitgeber, bin ich zu Dank verpflichtet. Nennen möchte ich in diesem Zusammenhang stellvertretend Matthias Linnemann, Stefan Eckelsbach, Gerrit Sonnenrein, Matthias Heinen, Dr. Yonny M. Muñoz-Muñoz, René S. Chatwell, Tatjana Janzen, Andreas Paul, Robin Fingerhut, Denis Šarić, Elmar Baumhögger, Dr. Gerhard Herres, Dr. Thorsten Windmann und Dr. Svetlana Miroshnichenko.

Abschließend gilt mein herzlicher Dank meiner Partnerin Annalena, die in den letzten Jahren meine Klagen ertragen hat und mir immer ein großer Rückhalt war.

Paderborn, im November 2017

Andreas Köster





## Zusammenfassung

Thermodynamische Stoffdaten sind für die Auslegung und Optimierung von verfahrenstechnischen Prozessen entscheidend. In der chemischen Industrie werden solche Daten üblicherweise experimentell erhoben und anschließend in Form von Zustandsgleichungen weiterverwendet. Dieser Ansatz ist teuer, zeitintensiv und bei sicherheitsrelevanten Stoffen oft nur schwer durchführbar. Die molekulare Modellierung und Simulation ist eine attraktive Alternative zur Generierung dieser Daten, welche jedoch aufgrund des Fehlens vielseitiger und einfach zu bedienender Werkzeuge häufig nur von Experten genutzt wird. Im Rahmen dieser Arbeit wird ein effizientes Simulationswerkzeug zur Bestimmung aller zeitunabhängiger Zustandsgrößen während eines Simulationslaufs beschrieben und auf verschiedene Problemstellungen angewandt. Dazu gehören u.a.: Die systematische Auswertung komplexer Zustandsgrößen, die Erstellung von hybriden empirischen Zustandsgleichungen und die vollautomatische Anpassung simulationsdatenbasierter Zustandsgleichungen für reale Fluide.

## Abstract

Thermodynamic data are essential for the design and optimization of chemical engineering processes. Typically, the chemical industry is relying on experimental investigations along with empirical equations of state to generate and utilize such data. This approach is expensive, time-consuming and in the case of hazardous substances difficult to conduct. Molecular modeling and simulation is an attractive alternative method to generate such data, which is typically only used by experts because of the lack of versatile and easy-to-use tools. In this work, an efficient simulation tool for the determination of all time-independent thermodynamic properties during a single molecular simulation run is described and applied to various problems, including the systematic assessment of complex thermodynamic properties, the creation of hybrid empirical equations of state and the fully automatized parameterization based on molecular simulation data for real fluids.



# Inhaltsverzeichnis

<b>Vorwort</b>	<b>III</b>
<b>Zusammenfassung</b>	<b>V</b>
<b>1 Inhalt der Arbeit</b>	<b>1</b>
<b>2 Literaturverzeichnis</b>	<b>30</b>
<b>3 Wissenschaftliche Publikationen</b>	<b>31</b>
3.1 Molecular Models for the Hydrogen Age: Hydrogen, Nitrogen, Oxygen, Argon and Water . . . . .	34
3.2 <i>ms2</i> : A molecular simulation tool for thermodynamic properties, new version release . . . . .	51
3.3 <i>ms2</i> : A molecular simulation tool for thermodynamic properties, release 3.0 . .	57
3.4 Molecular models for cyclic alkanes and ethyl acetate as well as surface tension data from molecular simulation . . . . .	67
3.5 Assessing the accuracy of improved force-matched water models derived from <i>ab initio</i> molecular dynamics simulations . . . . .	84
3.6 Comparative study of the Grüneisen parameter for 28 pure fluids . . . . .	96
3.7 Equation of State for the Lennard-Jones Fluid . . . . .	108
3.8 Fundamental equation of state for ethylene oxide based on a hybrid dataset . .	145
3.9 Equation of state for 1,2-dichloroethane based on a hybrid data set . . . . .	159
3.10 Fundamental equation of state correlation for hexamethyldisiloxane based on experimental and molecular simulation data . . . . .	180
3.11 Thermodynamic Properties of Octamethylcyclotetrasiloxane . . . . .	200
3.12 Automatized determination of fundamental equations of state based on molecular simulations in the cloud . . . . .	217
3.13 Premelting, solid-fluid equilibria, and thermodynamic properties in the high density region based on the Lennard-Jones potential . . . . .	227
3.14 Round Robin Study: Molecular Simulation of Thermodynamic Properties from Models with Internal Degrees of Freedom . . . . .	238
<b>4 Beiträge zu wissenschaftlichen Konferenzen</b>	<b>251</b>



# 1 Inhalt der Arbeit

Die vorliegende Schrift ist eine kumulative Dissertation, die die Forschungsarbeit des Autors am Lehrstuhl für Thermodynamik und Energietechnik der Universität Paderborn zusammenfasst. Im nachfolgenden Text wird zunächst ein Überblick über den Inhalt dieser Arbeit gegeben, um den Publikationen einen Rahmen zu setzen. Daran anschließend werden die einzelnen Publikationen mit einer kurzen Zusammenfassung und einer Erklärung über den jeweiligen Beitrag des Autors präsentiert.<sup>1</sup>

## Stand der Forschung

Zu den Grundvoraussetzungen für das Verständnis von natur- und ingenieurwissenschaftlichen Prozessen zählt das detaillierte Wissen über die relevanten Eigenschaften der beteiligten Stoffe. Beispiele hierfür sind u.a. der Zusammenhang zwischen der Konzentration von Kohlendioxid in der Atmosphäre und der Klimaerwärmung oder auch die Festigkeit von Stahl in Verbindung mit dessen Versagen. Sollen verfahrenstechnische Prozesse ausgelegt werden, bilden die thermodynamischen Stoffdaten der involvierten Substanzen diese Grundlage. Die Genauigkeitsanforderungen an solche Daten hängen dabei primär von der Art der Anwendung ab. Im Allgemeinen gilt jedoch: Je genauer und umfassender eine zugrundeliegende Datenbasis ist, desto besser können verfahrenstechnische Prozesse im Hinblick auf ihre Ressourcen- und Energieeffizienz ausgelegt werden. Vor dem Hintergrund, dass der Primärenergieverbrauch für

---

<sup>1</sup>Literaturquellen die durch eine Kombination von Buchstaben und Jahreszahlen gekennzeichnet sind, beziehen sich auf fremde Arbeiten, wohingegen die Arbeiten des Autors mit Zahlen gekennzeichnet wurden.

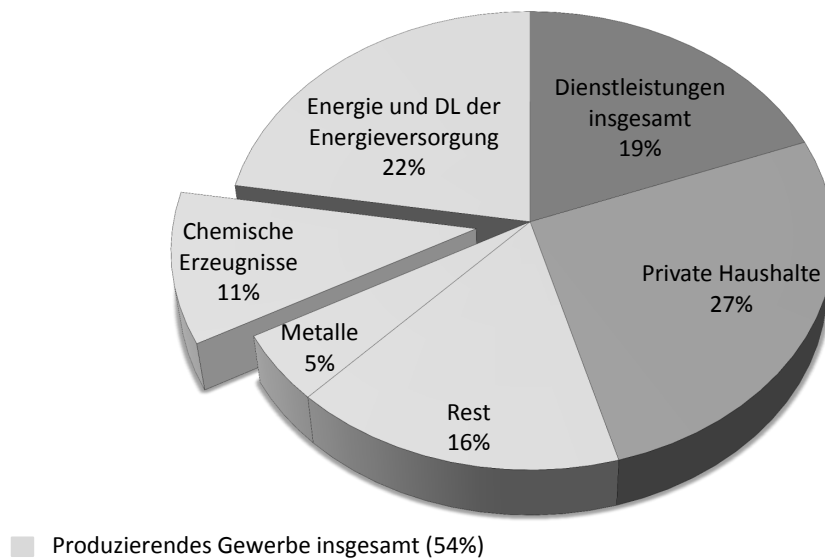


**Abbildung 1:** Primärenergieverbrauch in Deutschland im Jahre 2014 [Bun15]

chemische Erzeugnisse im Jahre 2014 in Deutschland ungefähr  $1,42 \cdot 10^{18}$  J betrug und damit einen Anteil von ca. 11 % des gesamten Primärenergieverbrauchs ausmachte [Bun15], scheint das Einsparpotential von optimierten Prozessen signifikant zu sein, siehe Abbildung 1.

Seit mehr als einem Jahrhundert ist es üblich und allgemein anerkannt thermodynamische Stoffdaten durch Experimente zu erheben. Von Vorteil ist dabei, dass bei einer sorgfältigen Planung und Ausführung von Messungen davon ausgegangen werden kann, dass die Ergebnisse der Realität entsprechen. Gleichzeitig haben experimentelle Untersuchungen, insbesondere bei schwierigen Bedingungen wie z.B. bei extremen Temperaturen oder im Fall von sicherheitsrelevanten Substanzen, den Nachteil zeitaufwändig und teuer zu sein. In einer Arbeit die vor der vorliegenden Dissertation veröffentlicht wurde [16], hat der Autor das Dampf-Flüssigkeits-Gleichgewicht der Mischung Ethylen und Perfluorbutan sowohl experimentell als auch mit molekularen Simulationen untersucht. Für die experimentelle Vermessung von 56 Mischungsdampfdrücken und Gleichgewichtszusammensetzungen benötigte er mit Hilfe einer bereits vorliegenden und gut arbeitenden Messapparatur ungefähr drei Monate. Die Modellierung der molekularen Wech-

selwirkungen von Perfluorbutan, die Simulation seiner Reinstoffeigenschaften sowie die anschließende Modellierung und Simulation der zu untersuchenden Mischung benötigte hingegen nur rund einen Monat. Es kann davon ausgegangen werden, dass die gleichen Simulationen ohne eine erneute Anpassung des Wechselwirkungsmodells für Perfluorbutan aufgrund von leistungsfähigeren Computern heute nur etwa zwei Tage dauern würden.

Die molekulare Modellierung und Simulation ist daher eine attraktive Alternative zur Ermittlung von thermodynamischen Stoffdaten und das Kernthema dieser Dissertation. Stark an Bedeutung gewonnen hat diese Methode in den letzten Jahrzehnten, auch weil die Verfügbarkeit von Rechenleistung weiterhin exponentiell wächst. Bei der molekularen Simulation wird auf der Basis der statistischen Mechanik vom mikroskopischen Verhalten von Atomen und Molekülen auf makroskopische thermodynamische Zustandsgrößen geschlossen. Die statistische Genauigkeit dieser makroskopischen Größen hängt dabei hauptsächlich von der Anzahl und Qualität der aufgezeichneten mikroskopischen Konfigurationen ab. Es gibt im Wesentlichen zwei grundsätzlich verschiedene molekulare Simulationsmethoden, die dazu genutzt werden können solche repräsentativen Konfigurationen zu erzeugen: Die Molekulardynamik und die Monte-Carlo Technik.

Mit der Molekulardynamik werden die Newtonschen Bewegungsgleichungen der untersuchten Teilchen numerisch gelöst. Es wird also die sich aufgrund von Wechselwirkungskräften ergebende zeitliche Veränderung ihrer Position, Geschwindigkeit und Beschleunigung betrachtet und ausgewertet. Mit der Monte-Carlo Technik werden hingegen stochastisch Konfigurationen erzeugt, die vorgegebenen Randbedingungen genügen. Obwohl diese beiden Methoden sehr unterschiedlichen Ansätzen folgen, führen sie bei gleichen Randbedingungen zu statistisch übereinstimmenden Ergebnissen. Zu den genannten Randbedingungen gehören in der molekularen Simulation hauptsächlich die vorgegebenen Zustandsgrößen die einen Systemzustand determinieren. Hierzu zählen beispielsweise die Anzahl der Teilchen  $N$ , die Temperatur  $T$ , das Volumen  $V$ ,

der Druck  $p$ , die innere Energie  $E$ , die Enthalpie  $H$  oder das chemische Potential  $\mu$ , wobei eine Kombination von drei dieser Größen Ensemble genannt wird. Eine molekulare Simulation im kanonischen  $NVT$  Ensemble findet also bei einer vorgegebenen Anzahl von Teilchen in einem festen Volumen bei konstanter Temperatur statt.

Um die Anzahl der Teilchen und damit gleichzeitig den Rechen- und Speicheraufwand einer molekularen Simulation zu begrenzen, werden normalerweise nur Volumenausschnitte einer homogenen Phase des Fluids betrachtet. Für die Ermittlung von thermodynamischen Stoffdaten beinhalten diese Kontrollvolumina in der Regel zwischen 500 und 5000 Teilchen. Eine zentrale Problemstellung ist die Modellierung von Kraftfeldern für die molekularen Wechselwirkungen dieser Teilchen. Im Rahmen der vorliegenden Dissertation wurden die Repulsions- (Abstoßung) und Dispersions-Wechselwirkungen (Anziehung) durch das häufig verwendete Lennard-Jones Potential beschrieben, wohingegen elektrostatische Wechselwirkungen durch Punktladungen, Punktdipole oder Punktquadrupole modelliert wurden. Die Auswahl der Art und Anzahl von Wechselwirkungszentren sowie deren Parametrierung ist eine herausfordernde Aufgabe und erfordert eine genaue Kenntnis über den Aufbau zu untersuchender Moleküle. Der Kern einer jeden molekularen Simulation besteht schließlich daraus, die Wechselwirkungen zwischen den betrachteten Teilchen auszuwerten. In dieser Zusammenfassung soll nicht näher auf die zugrundeliegenden Potentiale und Simulationsdetails eingegangen werden, diese können in den in Kapitel 3 gezeigten Veröffentlichungen und den darin enthaltenen Referenzen nachvollzogen werden.

Zur Verdeutlichung der Vorhersagefähigkeit der molekularen Simulation wurde im Rahmen dieser Dissertation eine systematische und umfassende Studie über das Mischungsverhalten von Wasserstoff, Stickstoff, Sauerstoff, Argon und Wasser angefertigt [1]. Die Ergebnisse der Studie wurden diskutiert auf der Basis von Dampf-Flüssigkeits-Gleichgewichten, homogenen Dichten und Löslichkeiten für binäre, ternäre und quaternäre Mischungen und verdeutlichen



die breite Einsetzbarkeit und die hohe Qualität von molekularen Simulationsdaten. Es zeigte sich, dass die Verfügbarkeit von experimentellen Daten auch für dieses sehr elementare System überraschend lückenhaft ist, da nur lediglich zwei von zehn ternären und eine von fünf quaternären Mischungen vermessen wurden. Das molekulare Modell aus dieser Arbeit kann für jede mögliche Mischung dieser fünf Komponenten genutzt werden und hat eine hohe Vorhersagekraft. Eine weitere wichtige Erkenntnis aus dieser Arbeit war, dass die Gaslöslichkeit in der Form der Henry-Konstanten sehr viel besser mit molekularen Simulationen als z.B. mit empirischen oder physikalisch fundierten Zustandsgleichungen abgebildet werden können.

Es zeigt sich, dass die molekulare Modellierung und Simulation gegenüber experimentellen Untersuchungen den Vorteil hat, dass sobald ein hochwertiges Kraftfeld verfügbar ist, viele verschiedene thermodynamische Größen für eine große Anzahl an Zustandspunkten in kürzester Zeit bestimmt werden können. Während in einem Experiment in der Regel nur ein Fluid gleichzeitig untersucht werden kann, besteht bei der molekularen Simulation zusätzlich die Möglichkeit der parallelen Untersuchung unterschiedlicher Fluide. Dabei ist es vollkommen unerheblich, ob diese Fluide sicherheitsrelevant sind oder Zustandspunkte bei extremen Bedingungen untersucht werden sollen. Aus diesen Gründen und weil zudem auf teure Messapparaturen verzichtet werden kann, ist eine Untersuchung mit Hilfe der molekularen Simulation sehr viel kostengünstiger und schneller als eine vergleichbare Reihe von Experimenten. Da molekulare Simulationen Informationen auf der mikroskopischen Ebene liefern, tragen sie außerdem dazu bei, das Verständnis der zugrundeliegenden thermophysikalischen Phänomene zu verbessern [MMHV17].

Leider wird das vorhandene Potential der molekularen Modellierung und Simulation noch nicht in ausreichendem Maße ausgeschöpft, insbesondere industrielle Nutzer scheuen häufig vor der Verwendung solcher Methoden zurück. Dies liegt vor allem daran, dass die vorhandenen Werkzeuge komplex sind und oft nur von Experten, sowohl im Hinblick auf die zugrundeliegenden Theorien als auch auf die zumeist Kommandozeilen-basierte Bedienung, verstanden werden.

Ein weiterer Grund ist das Fehlen von vielseitigen Werkzeugen, die eine effiziente Berechnung verschiedenster Zustandsgrößen ermöglichen.

## ***ms2*: Ein Werkzeug für die molekulare Simulation**

Um diesen Herausforderungen entgegenzutreten wurde in den letzten Jahren durch eine Kooperation der Lehrstühle für Thermodynamik aus Kaiserslautern und Paderborn sowie des Höchstleistungsrechenzentrums Stuttgart die Entwicklung des molekularen Simulationsprogramms *ms2* [DES<sup>+</sup>11,2,3] vorangetrieben. Dieses vereint eine Vielzahl möglicher Funktionalitäten:

- Molekulardynamik und Monte-Carlo Simulationen
- Diverse Ensembles
- Berechnung zeitunabhängiger Größen
- Berechnung dynamischer Größen
- Berechnung entropischer Größen
- Kraftfelder für die molekularen Wechselwirkungen zahlreicher Fluide
- Konsistente Vektorisierung und Parallelisierung
- Werkzeuge zur Vorbereitung und Auswertung von Simulationen
- Werkzeuge zur Visualisierung von Simulationen

Im Zusammenhang mit der Forschung des Autors dieser Dissertation wurden zwei neue Programmversionen von *ms2* veröffentlicht [2,3], die sich vorwiegend mit einem Formalismus zur simultanen Ermittlung aller zeitunabhängiger Zustandsgrößen befassen. Dieser sogenannte Lustig-Formalismus [Lus11, Lus12] soll im Folgenden kurz beschrieben werden. Darüber hinaus

**Tabelle 1:** Vergleich der in *ms2* implementierten Ensembles für Fluormethan [VSH01] in Bezug auf Temperatur  $T$ , Dichte  $\rho$ , Druck  $p$  und potentielle Energie  $u$ . Die Zahlen in den Klammern stehen für die statistische Unsicherheit in der letzten Stelle, die mit der Blockmittelwertmethode von Flyvbjerg und Petersen [FP89] berechnet wurde.

		$T$ K	$\rho$ mol/l	$p$ MPa	$u$ kJ/mol
MD	<i>NVT</i>	300	1	2,090(2)	-1048(3)
	<i>NpT</i>	300	1,0015(7)	2,090	-1051(3)
	<i>NVE</i>	300,0(1)	1	2,088(1)	-1048(3)
	<i>NpH</i>	300,0(1)	1,0003(2)	2,090	-1048(2)
MC	<i>NVT</i>	300	1	2,0880(2)	-1051,6(2)
	<i>NpT</i>	300	1,0019(2)	2,0880	-1053,6(3)
	<i>NVE</i>	299,99(1)	1	2,0882(2)	-1051,3(2)
	<i>NpH</i>	300,06(2)	1,0010(1)	2,0880	-1051,7(2)

werden auch weitere Änderungen vorgestellt, die die Funktionalität von *ms2* im Allgemeinen verbessern.

Eine solche allgemeine Verbesserung wurde durch die Einführung zweier weiterer klassischer Ensembles erreicht, dem mikrokanonischen (*NVE*) und dem isobar-isenthalpen (*NpH*) Ensemble. Neben den bereits zuvor verfügbaren Ensembles, d.h. dem kanonischen (*NVT*), dem isobar-isothermen (*NpT*) und dem großkanonischen ( $\mu VT$ ) Ensemble, stehen damit in *ms2* nunmehr insgesamt fünf Ensembles zur Verfügung. Ein Vergleich aller geschlossenen Ensembles (d.h.  $N=\text{const.}$ ) ist in Tabelle 1 zu finden. Es zeigt sich, dass sowohl zwischen den Simulationsmethoden als auch zwischen den verschiedenen geschlossenen Ensembles eine exzellente Übereinstimmung erreicht wird. Die Erhebung solcher Daten ist ein wichtiges Instrument zu Validierung von neuen Implementationen in das Simulationswerkzeug.

Die Berechnung von Dampf-Flüssigkeits-Gleichgewichten spielt eine große Rolle in verfahrenstechnischen Prozessen, wie z.B. der Destillation, und kann in *ms2* mit Hilfe der Grand Equilibrium Methode [VH02] durchgeführt werden, wofür das chemische Potential der Flüssig-

keitsphase benötigt wird. Dieses kann mit der weit verbreiteten Testteilchenmethode von Widom [Wid63] berechnet werden, bei der die Wechselwirkungsenergie eines zusätzlich eingesetzten Testteilchens ausgewertet wird. Durch die Schwierigkeit der Teilcheneinsetzung bei hohen Dichten müssen jedoch auch andere Methoden in Betracht gezogen werden. Zu diesem Zweck bestand seit der ersten Version von *ms2* die Möglichkeit die graduelle Einsetzung [NK91, VKH02] zu verwenden. Da diese Methode jedoch komplex ist und eine Vielzahl von Eingabeparametern benötigt, konnte damit nicht in allen Fällen eine effiziente Berechnung des chemischen Potentials durchgeführt werden. Mit der dritten und neuesten Version von *ms2* [3] wurde deshalb zusätzlich die thermodynamische Integration [FS02] implementiert. Bei dieser Methode werden im Prinzip zwei Systeme miteinander gekoppelt: 1. Das komplexe zu untersuchende System und 2. ein vereinfachtes System, bei dem eine Testteilcheneinsetzung nach Widom unproblematisch ist. Die Kopplung dieser beiden Systeme kann z.B. durch Funktionen der Form  $U_i(\lambda) = \lambda^d U_i$  mit einem Skalierungsparameter  $\lambda_{\min} \leq \lambda \leq 1 = \lambda_{\max}$  erreicht werden, wobei  $U_i$  die potentielle Energie des zusätzlichen Partikels  $i$  und  $d$  einen beliebigen Exponenten darstellt. Für die Berechnung des chemischen Potentials  $\mu$  gilt schließlich

$$\mu_{1,i} - \mu_{2,i} = \int_{2(\lambda_{\min})}^{1(\lambda_{\max})} \left\langle \frac{\partial U_i(\lambda)}{\partial \lambda} \right\rangle d\lambda, \quad (1)$$

wobei die Klammern  $\langle \rangle$  einen Ensemblemittelwert darstellen. Die Wahl der Funktion  $U_i(\lambda)$  ist in diesem Zusammenhang unerheblich, weil das chemische Potential eine Zustandsgröße und damit wegunabhängig ist [FS02].

Von zentraler Bedeutung für die vorliegende Dissertation war jedoch die Implementation des Lustig-Formalismus [Lus11, Lus12] für das kanonische ( $NVT$ ) und das mikrokanonische ( $NVE$ ) Ensemble [2,3]. Dieser Formalismus ermöglicht prinzipiell die Berechnung einer beliebigen Anzahl von partiellen Ableitungen der Helmholtzenergie im Laufe einer einzelnen molekularen Simulation. Da es sich bei der Helmholtzenergie  $a$  als Funktion von Temperatur  $T$  und Volu-

men  $V$  um ein thermodynamisches Potential handelt, kann jede beliebige thermodynamische Zustandsgröße durch eine Kombination ihrer partiellen Ableitungen

$$A_{mn} = (1/T)^m \rho^n \frac{\partial^{m+n} a / (RT)}{\partial (1/T)^m \partial \rho^n}, \quad (2)$$

berechnet werden. Dabei stellt  $\rho$  die Dichte,  $R$  die Idealgaskonstante und  $m$  und  $n$  die Ordnung der Ableitung nach der inversen Temperatur bzw. der Dichte dar. In Gleichung (2) ist außerdem zu erkennen, dass die Helmholtzenergie  $a$  durch den Faktor  $1/(RT)$  in eine dimensionslose Form überführt wird. Die Helmholtzenergie und auch ihre Ableitungen können als Summe eines Ideal- ( $a^o$  bzw.  $A_{mn}^o$ ) und eines Residualanteils ( $a^r$  bzw.  $A_{mn}^r$ ) dargestellt werden, wobei sich der Residualanteil direkt aus den Wechselwirkungen zwischen den Molekülen ergibt und damit in molekularen Vielteilchensimulationen zu berechnen ist. Für den Idealanteil der Ableitungen der Helmholtzenergie gilt [Spa00]

- $A_{mn}^o(T, \rho) = 0$ , für  $m > 0$  und  $n > 0$ ,
- $A_{mn}^o(T, \rho) = A_{mn}^o(T) + 0$ , für  $m > 0$  und  $n = 0$ ,
- $A_{mn}^o(T, \rho) = 0 + (-1)^{1+n}$ , für  $m = 0$  und  $n > 0$ ,

wobei  $A_{mn}^o(T)$  nicht durch molekulare Simulationen, sondern durch *ab initio* Berechnungen oder spektroskopische Messungen ermittelt werden kann. In *ms2* wurden lediglich Ableitungen bis zur dritten Ordnung der inversen Temperatur ( $m = 3$ ) und zur zweiten Ordnung der Dichte ( $n = 2$ ) implementiert, womit es bereits möglich ist alle gängigen thermodynamischen Zustandsgrößen zu berechnen, siehe Tabelle 2. Der große Vorteil dieser Methode ist, dass während einer Simulation im  $NVT$  oder  $NVE$  Ensemble alle Zustandsgrößen gleichzeitig ermittelt werden können und nicht verschiedene Ensembles bzw. Simulationstechniken für verschiedene Zustandsgrößen benötigt werden. So ist es gängige Praxis in molekularen Simulationsstudien aus der Literatur für Größen wie die isobare Wärmekapazität  $c_p = (\partial h / \partial T)_p$  das  $NpT$  Ensemble zu verwenden [UNDR<sup>+</sup>07],

weil diese Größe damit am einfachsten auszuwerten ist. Aus den gleichen Gründen wird zumeist das  $NVT$  Ensemble für die isochore Wärmekapazität  $c_v = (\partial u / \partial T)_v$  [UNDR<sup>+</sup>07] oder das  $NpH$  Ensemble für den Joule-Thomson Koeffizient  $\mu_{JT} = (\partial T / \partial p)_h$  verwendet [LSA03]. Der Lustig-Formalismus nutzt den Umstand, dass jede dieser Zustandsgrößen durch andere Potentiale oder partielle Ableitungen dargestellt werden kann [Lus11].

**Tabelle 2:** Berechnung von thermodynamischen Zustandsgrößen aus den partiellen Ableitungen der Helmholtzenergie.

Zustandsgröße	Funktion der partiellen Ableitungen der Helmholtzenergie
Druck $p = -(\partial a / \partial v)_T$	$\frac{p}{\rho RT} = 1 + A_{01}^r$
Innere Energie $u = a - T(\partial a / \partial T)_v$	$\frac{u}{RT} = A_{10}^o + A_{10}^r$
Enthalpie $h = u + pv$	$\frac{h}{RT} = 1 + A_{01}^r + A_{10}^o + A_{10}^r$
Entropie $s = -(\partial a / \partial T)_v$	$\frac{s}{R} = A_{10}^o + A_{10}^r - A_{00}^o - A_{00}^r$
Isochore Wärmekapazität $c_v = (\partial u / \partial T)_v$	$\frac{c_v}{R} = -A_{20}^o - A_{20}^r$
Isobare Wärmekapazität $c_p = (\partial h / \partial T)_p$	$\frac{c_p}{R} = -A_{20}^o - A_{20}^r + \frac{(1 + A_{01}^r - A_{11}^r)^2}{1 + 2A_{01}^r + A_{02}^r}$
Wärmeausdehnungskoeffizient $\alpha = \frac{(\partial p / \partial T)_\rho}{\rho(\partial p / \partial \rho)_T}$	$\alpha T = \frac{1 + A_{01}^r - A_{11}^r}{1 + 2A_{01}^r + A_{02}^r}$
Isotherme Kompressibilität $\beta_T = (\rho(\partial p / \partial \rho)_T)^{-1}$	$\beta_T \rho RT = \frac{1}{1 + 2A_{01}^r + A_{02}^r}$
Thermischer Druckkoeffizient $\gamma_v = (\partial p / \partial T)_\rho$	$\frac{\gamma_v}{\rho R} = 1 + A_{01}^r - A_{11}^r$
Dichteskalierungsexponent $\gamma = (\partial \ln T / \partial \ln \rho)_{s^r}$	$\gamma = -\frac{A_{01}^r - A_{11}^r}{A_{20}^r}$
Grüneisen-Parameter $\gamma_G = (\partial \ln T / \partial \ln \rho)_s$	$\gamma_G = -\frac{1 + A_{01}^r - A_{11}^r}{A_{20}^o + A_{20}^r}$
Schallgeschwindigkeit $w = ((\partial p / \partial \rho)_s)^{1/2}$	$\frac{Mw^2}{RT} = 1 + 2A_{01}^r + A_{02}^r - \frac{(1 + A_{01}^r - A_{11}^r)^2}{A_{20}^o + A_{20}^r}$
Joule-Thomson-Koeffizient $\mu_{JT} = (\partial T / \partial p)_h$	$\mu_{JT} \rho R = \frac{-(A_{01}^r + A_{02}^r + A_{11}^r)}{(1 + A_{01}^r - A_{11}^r)^2 - (A_{20}^o + A_{20}^r)(1 + 2A_{01}^r + A_{02}^r)}$

Aufgrund einer Vermutung von Lustig [Lus14], dass die Berechnung der partiellen Ableitungen der Helmholtzenergie im  $NVE$  Ensemble statistisch genauer seien müsste als im  $NVT$  Ensemble, wurde im Rahmen dieser Dissertation eine Studie zur Vergleichbarkeit der Ergebnisse dieser beiden Ensembles angefertigt [4]. Diese Vermutung beruhte auf der Tatsache, dass das  $NVE$  Ensemble energiekonservierend und weniger anfällig für Schwankungen ist, weil alle drei Vorgabegrößen extensiv sind. So muss beispielsweise im Vergleich zum  $NVT$  Ensemble in der Molekulardynamik die Temperatur nicht über einen Thermostat geregelt werden. Es stellte sich jedoch heraus, dass die Ergebnisse für beide Ensembles von vergleichbarer statistischer Qualität waren. Da die Vorgabegrößen für das  $NVT$  Ensemble näher an der experimentellen Realität angelehnt sind ( $V$  und  $T$  sind im Gegensatz zu  $E$  messbar) spielt dieses Ensemble natürlich ohnehin eine größere Rolle. Dennoch konnte durch diese Studie [4] die Richtigkeit der Implementation in *ms2* bestätigt werden.

Um den Standards moderner Großrechner zu genügen, wurde bei der Weiterentwicklung von *ms2* durchgängig auf die Parallelisierung geachtet. Das Message Passing Interface (MPI) stellt seit der ersten Programmversion von *ms2* die Grundlage für parallele Rechnungen auf Mehrkernsystemen dar. Darin rechnen mehrere, untereinander kommunizierende Prozesse an einem gemeinsamen Problem. Die zweite Programmversion [2] wurde schließlich durch den Open Multi-Processing (OpenMP) Standard ergänzt, der eine weitere Parallelisierung von Unterschleifen im Quellcode ermöglicht [DM98]. Eine weitere Ebene der Parallelisierung wurde in der dritten und aktuellen Programmversion von *ms2* [3] realisiert, die ausnutzt, dass beliebig viele Zustandspunkte unabhängig voneinander sind und deshalb parallel mit einer Programmausführung berechnet werden können.

Durch die oben beschriebenen Erweiterungen wurde der Funktionsumfang von *ms2* erheblich verbessert. Neben der vereinfachten Berechnung von chemischen Potentialen für Dampf-Flüssigkeits-Gleichgewichte wurde eine effiziente Methode zur Ermittlung aller zeitunabhängi-

gen Zustandsgrößen implementiert. Die neue Parallelisierung in Verbindung mit dem Lustig-Formalismus bietet die Möglichkeit, alle in Tabelle 2 genannten Zustandsgrößen in einem beliebig großen Zustandsbereich für ein zu untersuchendes Fluid mit einer einzigen Programmausführung von *ms2* zu berechnen. *ms2* kommt damit der Nachfrage nach universell einsetzbaren molekularen Simulationswerkzeugen einen weiteren Schritt näher.

## Bestimmung thermodynamischer Stoffdaten für reale Fluide

Für die Anwendung des nun in *ms2* verfügbaren Lustig-Formalismus [Lus11, Lus12] gibt es eine Vielzahl denkbarer Szenarien. Dieser kann im Prinzip überall dort eingesetzt werden, wo eine effiziente Berechnung verschiedenster Zustandsgrößen über weite Teile des jeweiligen Zustandsgebiets gefragt ist. Für eine solche Anwendung wird auch heute noch oft auf große Tabellenwerke, wie z.B. den „VDI-Wärmeatlas“ [e.V13], den „Landolt-Börnstein“ [Lan99] oder das „CRC Handbook of Chemistry and Physics“ [Wea76], zurückgegriffen, siehe Abbildung 2. Zwei solcher Szenarien die im Rahmen der vorliegenden Dissertation bearbeitet wurden, sollen nachfolgend besprochen werden. Beide Arbeiten sind eher theoretischer Natur und dienen vor allem der Demonstration der Leistungsfähigkeit des Lustig-Formalismus [Lus11, Lus12].

Dieser wurde in Publikation [5] verwendet, um die Qualität verschiedener molekularer Kraftfelder für Wasser zu untersuchen. Zu diesem Zweck wurden 24 Zustandspunkte in einem großen Temperatur- und Dichtebereich ausgewählt, die partiellen Ableitungen der Helmholtzenergie simuliert und daraus Zustandsgrößen berechnet, siehe Tabelle 2. Obwohl die Eigenschaften von Wasser in der Literatur ausführlich untersucht wurden, eine Tatsache die sich in der Verfügbarkeit einer hochgenauen Referenzzustandsgleichung [WP02] widerspiegelt, fehlt es immer noch an einem fundierten Verständnis der zugrundeliegenden mikroskopischen Mechanismen dieses besonders schwierigen Stoffs [Bal08]. Daher wurden in dieser Studie auch zwei neue Kraftfelder,



**SPECIFIC HEAT OF WATER**

**Heat Capacity of Air-free Water 0°-100°C at 1 Atmosphere Pressure**

The heat capacity of air-free water is given in international steam table calories per gram and in absolute joules per gram. (1 absolute joule = 0.238846 I.T. Cal.).

The enthalpy or heat content is given for air-free water in I.T. Cal. per gram and in absolute joules per gram.

From Osborne, Stimson and Ginnings; B. of S. Jour. Res. 23, 233, 1939.

Temp. °C.	Thermal Capacity		Enthalpy		Temp. °C	Thermal Capacity		Enthalpy	
	Cal./g/°C	Joules/g/°C	Cal./g	Joules/g		Cal./g/°C	Joules/g/°C	Cal./g	Joules/g
0	1.00738	4.2177	0.0245	0.1026	50	.99854	4.1807	50.0079	209.3729
1	1.00652	4.2141	1.0314	4.3184	51	.99862	4.1810	51.0065	213.5538
2	1.00571	4.2107	2.0376	8.5308	52	.99871	4.1814	52.0051	217.7350
3	1.00499	4.2077	3.0429	12.7400	53	.99878	4.1817	53.0039	221.9166
4	1.00430	4.2048	4.0475	16.9462	54	.99885	4.1820	54.0027	226.0984
5	1.00368	4.2022	5.0515	21.1498	55	.99895	4.1824	55.0016	230.2806
6	1.00313	4.1999	6.0549	25.3508	56	.99905	4.1828	56.0006	234.4632
7	1.00260	4.1977	7.0578	29.5496	57	.99914	4.1832	56.9997	238.6462
8	1.00213	4.1957	8.0602	33.7463	58	.99924	4.1836	57.9989	242.8296
9	1.00170	4.1939	9.0621	37.9410	59	.99933	4.1840	58.9982	247.0134
10	1.00129	4.1922	10.0636	42.1341	60	.99943	4.1844	59.9975	251.1976
11	1.00093	4.1907	11.0647	46.3255	61	.99955	4.1849	60.9970	255.3822
12	1.00060	4.1893	12.0654	50.5155	62	.99964	4.1853	61.9966	259.5673
13	1.00029	4.1880	13.0659	54.7041	63	.99976	4.1858	62.9963	263.7529
14	1.00002	4.1869	14.0660	58.8916	64	.99988	4.1863	63.9962	267.9390
15	.99976	4.1858	15.0659	63.0779	65	1.00000	4.1868	64.9961	272.1256
16	.99955	4.1849	16.0655	67.2632	66	1.00014	4.1874	65.9962	276.3127
17	.99933	4.1840	17.0650	71.4476	67	1.00026	4.1879	66.9964	280.5003
18	.99914	4.1832	18.0642	75.6312	68	1.00041	4.1885	67.9967	284.6885
19	.99897	4.1825	19.0633	79.8141	69	1.00053	4.1890	68.9972	288.8772
20	.99883	4.1819	20.0622	83.9963	70	1.00067	4.1896	69.9977	293.0665
21	.99869	4.1813	21.0609	88.1778	71	1.00081	4.1902	70.9985	297.2564
22	.99857	4.1808	22.0596	92.3589	72	1.00096	4.1908	71.9994	301.4469
23	.99847	4.1804	23.0581	96.5395	73	1.00112	4.1915	73.0004	305.6381
24	.99838	4.1800	24.0565	100.7196	74	1.00127	4.1921	74.0016	309.8299

**Abbildung 2:** Ausschnitt aus dem Tabellenwerk „CRC Handbook of Chemistry and Physics“ [Wea76] für die Wärmekapazität und Enthalpie im homogenen Zustandsgebiet.

die auf Basis von *ab initio* Molekulardynamiksimulationen erstellt worden waren, untersucht und mit empirischen Kraftfeldern verglichen. Diese *ab initio* Kraftfelder haben den Vorteil, dass keine experimentellen Daten in ihre Erstellung einfließen. Neben zeitunabhängigen Zustandsgrößen im homogenen Zustandsgebiet waren auch Dampf-Flüssigkeits-Gleichgewichte sowie Struktur- und Transporteigenschaften Gegenstand der Studie. Es zeigte sich, dass *ab initio* Kraftfelder konkurrenzfähig und insbesondere bei strukturellen Eigenschaften bessere Ergebnisse als rein empirische Kraftfelder zeigen können.

Auch die systematische Auswertung komplexer Zustandsgrößen für verschiedene Fluide kann mit Hilfe des Lustig-Formalismus durchgeführt werden. So befasste sich eine weitere Studie im Rahmen dieser Dissertation mit der umfassenden Simulation von partiellen Ableitungen der

Helmholtzenergie für 28 verschiedene Reinstoffe. Diese Daten wurden anschließend verwendet um den relativ unbekannten Grüneisen-Parameter zu analysieren [6], eine Zustandsgröße die beispielsweise in der Fluidodynamik eine Rolle spielt [APC84]. Auch für die Untersuchung des qualitativ korrekten Verlaufs von Zustandsgleichungen kann der Grüneisen-Parameter genutzt werden, weil er ein Verhältnis aus kalorischen ( $c_v$ ) und thermischen Zustandsgrößen ( $\gamma_v$ ) darstellt, siehe Tabelle 2. Verschiedene Literaturstudien [TRS<sup>+</sup>15, AZL15] zeigten weiterhin, dass mit der Sicherstellung eines qualitativ korrekten Verlaufs des Grüneisen-Parameters auch die isochore und isobare Wärmekapazität sowie die Schallgeschwindigkeit qualitativ richtig sind. Zu den Ergebnissen der Studie aus der vorliegenden Dissertation zählte die Identifikation eines allgemeinen Trends für den Verlauf des Grüneisen-Parameters, dem alle untersuchten Fluide bis auf Wasser folgen. Ein Vergleich der Simulationsdaten mit den genauesten verfügbaren Zustandsgleichungen aus der Literatur ergab, dass vier von 28 untersuchten Zustandsgleichungen, die vom „National Institute of Standards and Technology“ empfohlen werden, ein inkonsistentes Verhalten zeigten.

## **Zustandsgleichungen auf Basis molekularer Simulationen**

Im Gegensatz zur molekularen Modellierung und Simulation sind Zustandsgleichungen ein gängiges Werkzeug in der verfahrenstechnischen Industrie, nicht zuletzt weil hierfür leistungsfähige und einfach zu verwendende Software zur Verfügung steht [LHM13, SEH<sup>+</sup>16, BWQL14]. Empirische Zustandsgleichungen bestechen dadurch, dass sie eine Fülle von zugrundeliegenden Datenpunkten in einer komprimierten Form darstellen können und sich für die Interpolation zwischen diesen Datenpunkten eignen. Viele moderne empirische Zustandsgleichungen können zusätzlich auch zu Extrapolationszwecken genutzt werden, weil in der Anpassung der Gleichungen auf diese Eigenschaft vermehrt Wert gelegt wird. Ein großer Nachteil empirischer Zustandsgleichungen ist, dass diese überhaupt erst erstellt werden können wenn ein Fluid

hinlänglich vermessen wurde.

Aufgrund der zuvor angesprochenen Einschränkungen von Experimenten, erscheint die Nutzung von Daten aus der molekularen Simulation für die Anpassung von Zustandsgleichungen sinnvoll. Insbesondere die effiziente Generierung einer Vielzahl von Zustandsgrößen mit Hilfe des in *ms2* implementierten Lustig-Formalismus [Lus11, Lus12] ist wie für diesen Zweck geschaffen.

Moderne empirische Zustandsgleichungen sind in aller Regel auf Basis der Helmholtzenergie formuliert, die wie oben beschrieben in einen Ideal- ( $a^o$ ) und einen Residualanteil ( $a^r$ ) aufgeteilt werden kann

$$\frac{a(T, \rho)}{RT} = \frac{a^o(T, \rho) + a^r(T, \rho)}{RT} = \alpha^o(\tau, \delta) + \alpha^r(\tau, \delta), \quad (3)$$

mit den auf die kritischen Daten bezogenen Parametern  $\tau = T_c/T$  und  $\delta = \rho/\rho_c$  [Spa00]. Während der Idealanteil praktisch nur von  $\tau$  abhängt und durch einen verhältnismäßig einfachen Zusammenhang beschrieben werden kann, ist die Anpassung von empirischen Zustandsgleichungen für den Residualanteil komplex, weil dieser sich durch eine nicht-triviale Abhängigkeit von  $\tau$  und  $\delta$  auszeichnet. Bei seiner Anpassung werden üblicherweise verschiedene empirische Terme genutzt [Spa00], dazu zählen im Wesentlichen Polynomial- (P), Exponential- (E) und Gaußterme (G)

$$\begin{aligned} \alpha^r(\tau, \delta) &= \alpha_P^r(\tau, \delta) + \alpha_E^r(\tau, \delta) + \alpha_G^r(\tau, \delta) \\ &= \sum_{i=1}^{N_P} n_i \tau^{t_i} \delta^{d_i} \\ &\quad + \sum_{i=N_P+1}^{N_E+N_P} n_i \tau^{t_i} \delta^{d_i} \exp(-\delta^{l_i}) \\ &\quad + \sum_{i=N_E+N_P+1}^{N_E+N_P+N_G} n_i \tau^{t_i} \delta^{d_i} \exp(-\eta_i(\delta - \epsilon_i)^2 - \beta_i(\tau - \gamma_i)^2), \end{aligned} \quad (4)$$

wobei es sich sowohl bei den Koeffizienten  $n_i$  als auch den Exponenten  $t_i$ ,  $d_i$ ,  $l_i$ ,  $\eta_i$ ,  $\epsilon_i$ ,  $\beta_i$  und  $\gamma_i$  um anpassbare Parameter handelt. Zusätzlich ist auch die Anzahl der jeweils genutzten Terme  $N_P$ ,  $N_E$  und  $N_G$  variabel. Für die hochgenaue Zustandsgleichung von Stickstoff wurden beispielsweise sechs Polynomial-, 26 Exponential- und vier Gaußterme an ungefähr 5650 experimentelle Datenpunkte angepasst [SLJ<sup>+</sup>00]. Einige Zustandsgleichungen beinhalten auch nicht-analytische Terme, auf die hier nicht weiter eingegangen werden soll. Diese Fülle von Parametern ist nur durch eine nicht-lineare Anpassung an eine große Menge qualitativ hochwertiger thermodynamischer Stoffdaten zu bestimmen [Spa00]. Zu diesem Zweck werden in aller Regel experimentelle Daten aus der Literatur identifiziert und ausführlich auf ihre Qualität hin bewertet. Gegebenenfalls werden daraufhin auch eigene Messreihen durchgeführt. Die Erstellung genauer und strukturoptmierter Zustandsgleichungen zeichnet sich also durch ein hohes Maß an manuellem Arbeitsaufwand aus.

Die durch molekulare Simulationen ermittelten partiellen Ableitungen der Helmholtzenergie können sehr gut in den Anpassungsprozess von Zustandsgleichungen eingebunden werden, weil sie genaue Informationen über die Beschaffenheit der zugrundeliegenden Helmholtzenergieoberfläche beinhalten [RTL<sup>+</sup>13]. Dafür gibt es verschiedene Ansätze, die sich in den Publikationen im Rahmen dieser Dissertation widerspiegeln:

1. Die Nutzung von Daten aus molekularen Simulationen für die Erstellung von Zustandsgleichungen für Modellfluide [7].
2. Die gleichzeitige Nutzung von Daten aus Experimenten und molekularen Simulationen für die Erstellung von Zustandsgleichungen realer Fluide („Hybridansatz“) [8-11].
3. Die Nutzung von Daten aus molekularen Simulationen für automatisch erstellte Zustandsgleichungen realer Fluide [12].

Die eindeutigste Methode zur Kombination von Daten aus molekularen Simulationen und Zu-

standsgleichungen ist selbstverständlich die Erstellung einer Zustandsgleichung für ein Fluid welches nur *in silico* existiert, weil hierfür keine experimentellen Daten vorliegen können. So wurde im Rahmen dieser Dissertation an einer neuen Zustandsgleichung für das bekannte Lennard-Jones Fluid mitgearbeitet [7], welches eines der wichtigsten Potentiale in der molekularen Thermodynamik ist und für die Beschreibung von einfachen Molekülen, wie den Edelgasen oder Methan, verwendet werden kann. Im Vergleich zu älteren Zustandsgleichungen aus der Literatur zeichnet sich diese neue Gleichung dadurch aus, dass ausschließlich partielle Ableitungen der Helmholtzenergie und zweite Virialkoeffizienten als Grundlage für die Korrelation genutzt werden konnten. Phasengleichgewichtsdaten wurden nicht in die Parametrierung aufgenommen, die Übereinstimmung mit Referenzdaten aus der Literatur ist dennoch exzellent. Während des Anpassungsprozesses wurde insbesondere auf ein physikalisch korrektes Extrapolationsverhalten geachtet. Neben einem großen Gültigkeitsbereich ( $0.5 < T/T_c < 7$ ,  $p/p_c < 500$ ) verfügt diese neue Zustandsgleichung über eine hohe Genauigkeit und stellt insgesamt eine Verbesserung im Vergleich zu den Literaturgleichungen dar. Die Qualität der Gleichung spiegelt sich auch dadurch wider, dass sie im renommierten „Journal of Physical and Chemical Reference Data“ für Referenzdaten in der Chemie und Physik abgedruckt werden konnte.

Der zweite der oben gezeigten Ansätze beinhaltet die gleichzeitige Nutzung von Daten aus der molekularen Simulation und aus Experimenten, wodurch eine im Prinzip neue Art von Zustandsgleichung entstanden ist, die sogenannten „hybriden Zustandsgleichungen“ [8-11]. Hybride Zustandsgleichungen sind sinnvoll, wenn Fluide beschrieben werden sollen, deren experimentelle Datenbasis sehr lückenhaft ist. Dies kann sich z.B. auf Lücken in der Vermessung des Zustandsgebiets oder auch auf die fehlende Vermessung einzelner Zustandsgrößen beziehen. In solchen Fällen kann der Lustig-Formalismus dazu genutzt werden, diese Lücken zu schließen. Auch für eine generelle Erweiterung des Gültigkeitsbereichs einer Zustandsgleichung sind molekulare Simulationsdaten geeignet, da diese ein physikalisch adäquates Extrapolationsverhalten

haben und sich so sehr viel besser für die Untersuchung von extremen Bedingungen eignen. Eine wichtige Grundvoraussetzung für qualitativ hochwertige hybride Zustandsgleichungen ist jedoch, dass für das untersuchte Fluid ein sehr gutes molekulares Modell vorliegen muss.

Als ein geeigneter Kandidat für eine hybride Zustandsgleichung stellte sich deshalb Ethylenoxid ( $\text{C}_2\text{H}_4\text{O}$ ) heraus [8]. Obwohl dieser Stoff ein wichtiges Zwischenprodukt in der Herstellung verschiedener Chemikalien ist, sind zu wenige experimentelle Daten vorhanden, um eine hochwertige empirische Zustandsgleichung daran anzupassen. Dieser Umstand ergibt sich aus den für den Menschen ungünstigen Eigenschaften von Ethylenoxid, das extrem giftig, krebserregend und leicht entzündlich ist. Gleichzeitig wurde für diesen Stoff ein sehr gutes molekulares Modell erstellt [EVH08], welches im Jahre 2007 die „Fourth Industrial Fluid Properties Simulation Challenge“ [CBC<sup>+</sup>08] gewinnen konnte. Eine gründliche Erfassung und Bewertung aller vorhandener experimenteller Daten ergab, dass lediglich die Gasphase sowie das Dampf-Flüssigkeits-Gleichgewicht von Ethylenoxid vermessen wurden. Dementsprechend dienten die molekularen Simulationen hauptsächlich als Ergänzung für das Gebiet der homogenen Flüssigkeit und im überkritischen Zustandsgebiet. Weiterhin konnte der Gültigkeitsbereich der Zustandsgleichung durch die Nutzung der partiellen Ableitungen der Helmholtzenergie aus dem Lustig-Formalismus bezogen auf die Temperatur verdoppelt und bezogen auf den Druck versiebzigfacht werden. Eine Extrapolation der hybriden Zustandsgleichung auch über diese Grenzen hinaus stellt kein Problem dar, weil besonderes Augenmerk auf eine physikalisch korrekte Extrapolationsfähigkeit gelegt wurde.

Ähnliche Voraussetzungen wie für Ethylenoxid galten auch für die Substanz 1,2-Dichlorethan ( $\text{C}_2\text{H}_4\text{Cl}_2$ ) [9], die aufgrund ihrer sicherheitsrelevanten Eigenschaften schwer im Labor zu handhaben ist. 1,2-Dichlorethan ist u.a. leichtentzündlich, krebserregend und mutagen, wird aber trotzdem in großen Mengen, beispielsweise als Zwischenprodukt in der Herstellung von Polyvinylchlorid (PVC), benötigt. Experimentelle Daten für diesen Stoff sind deshalb nur in

einem sehr begrenzten Temperatur- und Druckbereich verfügbar. Für die gesättigte Dampfdichte konnte sogar nur ein einziger Datenpunkt in der Literatur gefunden werden. Alle genannten Faktoren führten dazu, dass keine hochgenaue Zustandsgleichung für 1,2-Dichlorethan in der Literatur verfügbar war. Um den Lustig-Formalismus verwenden zu können, wurde daraufhin ein molekulares Modell für 1,2-Dichlorethan erstellt, welches aus vier Lennard-Jones Wechselwirkungszentren und einem Punktquadrupol besteht. Daraufhin konnten 83 Simulationen in einem großen Temperatur- ( $T_{\max} = 1000$  K) und Druckbereich ( $p_{\max} = 1200$  MPa) des homogenen Zustandsgebiets von 1,2-Dichlorethan durchgeführt und eine qualitativ hochwertige hybride Zustandsgleichung erstellt werden.

Auch Hexamethyldisiloxan (MM,  $C_6H_{18}OSi_2$ ) [10] und Octamethylcyclotetrasiloxan (D4,  $C_8H_{24}O_4Si_4$ ) [11] wurden im Rahmen der vorliegenden Dissertation untersucht. Neben der Verwendung in Kosmetika eignen sich Siloxane hervorragend als Arbeitsmedien in „Organic Rankine Cycles“, einer Unterkategorie des in Kraftwerken standardmäßig mit Wasser betriebenen Rankine-Prozesses. Ein großer Vorteil der organischen Rankine-Prozesse ist, dass die für die Verdampfung des Arbeitsmediums benötigte Wärme bei niedrigeren Temperaturen bereitgestellt werden kann. Damit eignen sie sich z.B. für die Nutzung von Abwärme aus Industrieanlagen. Im Jahre 2006 veröffentlichten Colonna et al. [CNGL06] bereits einige Zustandsgleichungen für verschiedene Siloxane, darunter auch MM und D4. Bei genauerer Untersuchung dieser Gleichungen ergaben sich jedoch größere Abweichungen gegenüber neueren experimentell gemessenen Daten zur Schallgeschwindigkeit und Dichte. Es lag daher die Vermutung nahe, dass die Zustandsgleichungen von Colonna et al. [CNGL06] zu wenige und/oder qualitativ schlechte experimentelle Daten zugrundelagen. Da es für die Auslegung von Organic Rankine Cycles von großer Wichtigkeit ist, eine genaue Kenntnis der thermodynamischen Stoffeigenschaften zu haben, wurde im Rahmen dieser Dissertation an hybriden Zustandsgleichungen gearbeitet [10,11].

Eine umfangreiche Literaturrecherche führte zu dem Ergebnis, dass dazu sowohl für MM als auch für D4 zusätzliche Schallgeschwindigkeitsmessungen und molekulare Simulationen der partiellen Ableitungen der Helmholtzenergie notwendig waren. Aus diesem Grund mussten neue molekulare Kraftfelder für beide Fluide entwickelt werden. MM besteht im Kern aus einer Silizium-Sauerstoff-Silizium Verbindung, wobei an den Siliziumatomen jeweils drei Methylgruppen angelagert sind. Für seine Modellierung wurde daher jeweils ein Lennard-Jones Wechselwirkungszentrum für die Siliziumatome, das Sauerstoffatom und die sechs Methylgruppen verwendet. Zusätzlich wurden zur Berücksichtigung der elektrostatischen Wechselwirkungen drei Punktladungen entlang der inneren Si-O-Si Bindung genutzt. D4 ist ein zyklischer und signifikant größerer Vertreter der Siloxane und besteht aus einem alternierenden Ring von vier Silizium- und vier Sauerstoffatomen, wobei jeweils zwei Methylgruppen an den Siliziumatomen angelagert sind. Bei Molekülen dieser Größe stoßen die hier verwendeten Modellierungsmethoden annähernd an ihre Grenzen. Es konnte jedoch trotzdem ein adäquates molekulares Kraftfeld erstellt werden, weil D4 aufgrund seiner zyklischen Form eine kompakte Geometrie hat. Dieses Modell besteht aus 16 Lennard-Jones Wechselwirkungszentren (4 Si, 4 O, 8 CH<sub>3</sub>) und acht Punktladungen (4 Si, 4 O). Beide molekularen Modelle konnten für die Simulation der partiellen Ableitungen der Helmholtzenergie in einem großen Zustandsbereich genutzt werden und trugen dazu bei, dass der Gültigkeitsbereich im Vergleich zu rein experimentellen Zustandsgleichungen im Hinblick auf die Temperatur verdoppelt und im Hinblick auf den Druck verdrei- bzw. vervierfacht wurde. Die neuen hybriden Zustandsgleichung übertreffen die Qualität der Zustandsgleichungen von Colonna et al. [CNGL06] erheblich und verfügen durch die Verwendung von molekularen Simulationsdaten über ein physikalisch adäquates Extrapolationsverhalten.

Mit Hilfe der zuvor beschriebenen Ansätze [7-11] konnte gezeigt werden, dass eine Verbindung von empirischen Zustandsgleichungen und molekularen Simulationen ein leistungsfähiges Instrument zur Bereitstellung von Daten für Modellfluide und reale Substanzen auf einem aggregierten



Niveau ist. Leider benötigt die Erstellung solcher hochwertiger Gleichungen sowohl Know-How als auch Zeit für die Auslese der Daten und die manuelle Strukturoptimierung. In Fällen in denen die Zeit ein kritischer Faktor ist und die Vorhersagequalität eines molekularen Modells in Verbindung mit einer einfacheren Zustandsgleichung ausreicht, wenn also beispielsweise ein neuer verfahrenstechnischer Prozess zunächst grob ausgelegt werden soll, könnte ein rein simulationsbasiertes und automatisiertes Verfahren sinnvoll sein.

Ein solcher Ansatz wurde im Rahmen der vorliegenden Dissertation in Publikation [12] vorgestellt. Zu diesem Zweck wurden alle Schritte vom Erstellen der molekularen Simulationen bis zur fertigen Zustandsgleichung ausgewertet und auf ihre Komplexität hin untersucht. Dabei wurden Zwischenschritte die viel Expertise und/oder Zeit benötigten identifiziert und, wenn möglich, vereinfacht. Aus dieser Untersuchung entstand schließlich ein Cloud-basierter Workflow mit einfachen grafischen Nutzeroberflächen, der über jeden gängigen Internetbrowser aufrufbar ist und auch von Nutzern mit wenig Know-How verwendet werden kann, siehe Abbildung 3. Mit Hilfe dieses Workflows kann durch einige wenige Mausklicks der zu untersuchende Zustandsbereich eines Fluids festgelegt und beliebig viele Zustandspunkte ausgewählt werden. Im Hintergrund werden daraufhin automatisch Simulationen der partiellen Ableitungen der Helmholtzenergie auf in der Cloud verfügbaren Rechenressourcen gestartet. Der Nutzer hat dabei durchgängig die Möglichkeit den Status der Simulationen abzufragen. Nachdem die Simulationsergebnisse zur Verfügung stehen, kann daran automatisch eine Zustandsgleichung angepasst werden. Es besteht zusätzlich die Möglichkeit, alte Simulationsergebnisse oder Zustandsgleichungen in der Cloud zu speichern.

Zu den hierfür notwendigen Vereinfachungen zählten hauptsächlich die automatische Nutzung von geeigneten Standardeinstellungen für die Simulationen und die Verwendung von verallgemeinerten Zustandsgleichungen. Diese zeichnen sich dadurch aus, dass lediglich Polynomial- und Exponentialterme genutzt werden, deren Exponenten  $t_i$ ,  $d_i$  und  $l_i$  feststehen, siehe Gleichung

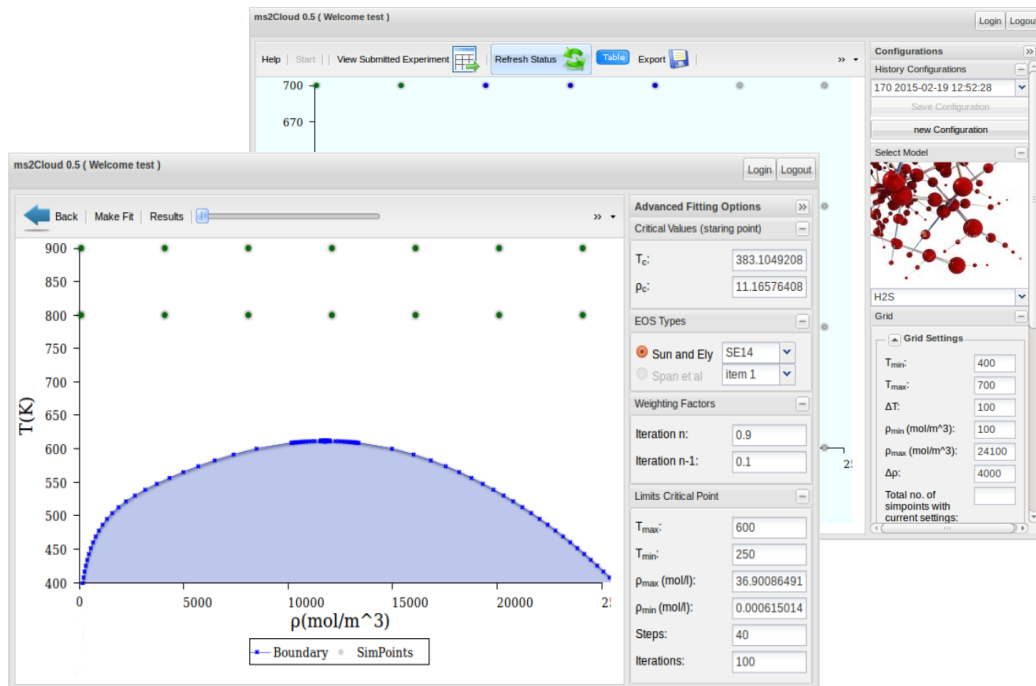


**Abbildung 3:** Grafische Benutzeroberflächen eines Cloud-basierten Werkzeugs zur automatischen Erstellung von Zustandsgleichungen [12].

(4). Die Anpassung der Gleichung kann damit auf die lineare Anpassung der Koeffizienten  $n_i$  reduziert werden. Beispiele für verallgemeinerte Zustandsgleichungen von Span und Wagner mit 12 Termen [SW03], von Sun und Ely mit 14 Termen [SE05] oder von Jacobson und Stewart mit 40 Termen [JS73] (überführt in die Helmholtzenergie) können in der Literatur gefunden werden. Dabei führt die Verwendung einer größeren Anzahl von Termen üblicherweise zu einer besseren Repräsentation der zugrundeliegenden Daten, weil die Flexibilität einer Gleichung mit steigender Anzahl an Termen zunimmt. Um die Qualität dieses Ansatzes zu überprüfen, wurde eine automatisch erstellte 40-Terme Zustandsgleichung für Ethylenoxid mit der zuvor beschriebenen, nicht-linear angepassten und strukturoptimierten hybriden Zustandsgleichung [8] dieses Stoffs verglichen. Wie erwartet wurden bei diesem Vergleich Abweichungen der automatischen Zustandsgleichung von der Referenzgleichung identifiziert. Da diese Abweichungen jedoch fast durchgehend unter 5% lagen und die Gleichung innerhalb weniger Tage

erstellt wurde, kann die Umsetzung dieses Ansatzes als Erfolg gewertet werden. Der Autor der vorliegenden Dissertation hofft, dass durch die einfache Verwendbarkeit dieses Workflows molekulare Simulationsmethoden mehr in den Fokus von bisher unerfahrenen Nutzern rücken.

## Aktuelle Forschung und Ausblick

In diesem abschließenden Kapitel über die Forschungsarbeit des Autors soll zunächst die Anwendung der vorgestellten Werkzeuge auf laufende Fragestellungen thematisiert werden, um daran anschließend einen Ausblick auf die zukünftige Verwendung zu geben. In einer kürzlich eingereichten Studie [13] wurde *ms2* dafür genutzt, alle zeitunabhängigen thermodynamischen Stoffdaten des Lennard-Jones Potentials bei sehr hohen Dichten im fluiden und im Feststoffbereich ( $\rho_{\text{Tripel}} < \rho < 3 \rho_{\text{Tripel}}$ ) zu bestimmen. Neben der Bereitstellung von Daten in diesem generell schlecht vermessenen Zustandsgebiet wurde zusätzlich ein interessantes Phänomen in der Nähe der Schmelzlinie betrachtet, das sogenannte „Premelting“. Dieses zeichnet sich aus durch die starke Änderung (Zu- oder Abnahme) einiger Zustandsgrößen vor Erreichen der Schmelzlinie. Eine Erklärung hierfür könnten lokale Fehlstellen in der Kristallgitterstruktur sein, die schon vor dem eigentlichen Schmelzprozess auftreten [GGD<sup>+</sup>05]. Die Ergebnisse der Studie wurden im fluiden Zustandsbereich mit der Lennard-Jones Zustandsgleichung aus dieser Dissertation [7] und im Feststoffbereich u.a. mit einer neuen Zustandsgleichung auf Basis der Lennard-Jones und Devonshire Zelltheorie verglichen [Lus17] und zeigten innerhalb der jeweiligen Gültigkeitsbereiche eine gute Übereinstimmung in beiden Phasen. Die identifizierten „Premelting“ Effekte konnten mit der Zelltheorie nur unzureichend vorhergesagt werden, so dass hier noch weitere Nachforschungen nötig sind. Eine weitere wichtige Erkenntnis aus dieser Studie ist, dass das Simulationswerkzeug *ms2* mit dem Lustig-Formalismus [Lus11, Lus12] nicht nur auf fluide Zustände beschränkt ist.

In einem zeitgleich laufenden Dissertationsprojekt des Lehrstuhls für Thermodynamik der Universität Kaiserslautern wird an einer neuen Version von *ms2* gearbeitet, die die Modellierung der inneren molekularen Freiheitsgrade erlaubt. Mit dieser Funktion wird das Spektrum der Moleküle, für die realistische Kraftfelder erzeugt werden können, stark erweitert. Dies gilt im Besonderen für große Moleküle, deren intramolekulare Wechselwirkungen üblicherweise einen signifikanten Beitrag haben. Die Komplexität und die Rechenzeit einer Simulation werden mit dieser Änderung selbstverständlich zunehmen, dennoch ist dieser Schritt, auch vor dem Hintergrund steigender verfügbarer Rechenleistung, notwendig um weiterhin ein zukunftsfähiges Werkzeug bereit stellen zu können. Erste Ergebnisse dieser neuen Version wurden in einer aktuellen Veröffentlichung [14] mit anderen Simulationsprogrammen in Rahmen eines Ringversuchs verglichen. Dabei stand neben der Validierung der Ergebnisse auch die Fragestellung im Raum, ob verschiedene Arbeitsgruppen mit verschiedenen Simulationswerkzeugen für denselben Simulationsauftrag zu einem im Rahmen der statistischen Unsicherheit konsistenten Ergebnis kommen. Es zeigte sich, dass systematische Abweichungen zwischen verschiedenen Arbeitsgruppen und Werkzeugen bei der hohen zugrundeliegenden Komplexität kaum vermeidbar sind.

Zu den in der Zukunft geplanten Verbesserungen von *ms2* gehört die Substitution des für die Repulsion und Dispersion genutzten (12-6) Lennard-Jones Potentials durch das verallgemeinerte (m-n) Mie-Potential [Mie03]. Bei diesem Potential sind die Exponenten, die die intermolekulare Anziehung und Abstoßung beschreiben, frei vorgebar, wodurch sich neue Modellierungsmöglichkeiten ergeben. Auch diese Erweiterung wird mit einer Erhöhung des Rechenaufwands einhergehen, der sich jedoch durch die Verfügbarkeit genauerer molekularer Modelle lohnen wird.

Schließlich sollen die in dieser Dissertation vorgestellten effizienten Methoden zur Berechnung zeitunabhängiger Zustandsgrößen auf ihre Anwendbarkeit auf Mischungen hin untersucht werden. Mischungen spielen in der Verfahrenstechnik zweifellos eine größere Rolle als Reinstoffe,

gleichzeitig ist die verfügbare experimentelle Datenbasis viel lückenhafter. Das liegt hauptsächlich daran, dass dabei die Kombinatorik durch die Komponenten sowie der zusätzliche Zusammensetzungsvektor berücksichtigt werden müssen. Dementsprechend gibt es auch nur für sehr wenige Mischungen hochgenaue empirische Zustandsgleichungen [KW12, GS16]. Der in *ms2* implementierte Lustig-Formalismus zur Berechnung der partiellen Ableitungen der Helmholtzenergie ist jedoch prinzipiell nicht auf Reinstoffe limitiert. Es können also ohne weiteres auch große Zustandsbereiche von Mischungen beliebiger Ordnung untersucht und Zustandsgrößen systematisch ausgewertet werden. Natürlich würde auch für diese Systeme die Möglichkeit bestehen hybride Zustandsgleichungen anzupassen. Auch eine Erweiterung des in Publikation [12] vorgestellten automatischen Workflows zur Anpassung generalisierter Zustandsgleichungen ist geplant. Dazu müssen jedoch zunächst geeignete Gleichungsformen identifiziert werden.



# Literaturverzeichnis

- [APC84] V. Arp, J. M. Persichetti und G.-B. Chen. The Grüneisen Parameter in Fluids. *J. Fluids Eng.* 106:193–200, 1984.
- [AT89] M. P. Allen und D. J. Tildesley. *Computer simulation of liquids*. Oxford University Press, Oxford, 1989.
- [AZL15] R. Akasaka, Y. Zhou und E. W. Lemmon. A fundamental equation of state for 1,1,1,3,3-Pentafluoropropane (R-245fa). *J. Phys. Chem. Ref. Data.* 44:013104, 2015.
- [Bal08] P. Ball. Water - an enduring mystery. *Nature.* 452:291–292, 2008.
- [Bun15] Statistisches Bundesamt. *Daten zum Primärenergieverbrauch.* 2015. In [www.destatis.de](http://www.destatis.de) (Thematische Recherche: Zahlen & Fakten - Gesamtwirtschaft & Umwelt - Umwelt - Umweltökonomische Gesamtrechnungen - Material- & Energieflüsse - Dokumentart: Tabelle). Abrufdatum: 08.08.2017.
- [BWQL14] I. H. Bell, J. Wronski, S. Quoilin und V. Lemort. Pure and pseudo-pure fluid thermophysical property evaluation and the open-source thermophysical property library CoolProp. *Ind. Eng. Chem. Res.* 53:2498–2508, 2014.
- [CBC<sup>+</sup>08] F. H. Case, J. Brennan, A. Chaka, K. D. Dobbs, D. G. Friend, P. A. Gordon, J. D. Moore, R. D. Mountain, J. D. Olson, R. B. Ross, M. Schiller, V. K. Shen und E. A. Stahlberg. The fourth industrial fluid properties simulation challenge. *Fluid Phase Equilib.* 274:2–9, 2008.
- [CNGL06] P. Colonna, N. R. Nannan, A. Guardone und E. W. Lemmon. Multiparameter equations of state for selected siloxanes. *Fluid Phase Equilib.* 244:193–211, 2006.
- [DES<sup>+</sup>11] S. Deublein, B. Eckl, J. Stoll, S. V. Lishchuk, G. Guevara-Carrion, C. W. Glass, T. Merker, M. Bernreuther, H. Hasse und J. Vrabec. ms2: A molecular simulation

- tool for thermodynamic properties. *Comput. Phys. Commun.* 182:2350–2367, 2011.
- [DM98] L. Dagum und R. Menon. OpenMP: an industry standard API for shared-memory programming. *IEEE Comput. Sci. Eng.* 5:46–55, 1998.
- [e.V13] VDI e.V. *VDI-Wärmeatlas*. Springer Vieweg, Berlin, 2013.
- [EVH08] B. Eckl, J. Vrabec und H. Hasse. On the application of force fields for predicting a wide variety of properties: Ethylene oxide as an example. *Fluid Phase Equilib.* 274:16–26, 2008.
- [FP89] H. Flyvbjerg und H. G. Petersen. Error estimates on averages of correlated data. *J. Chem. Phys.* 91:461–466, 1989.
- [FS02] D. Frenkel und B. Smit. *Understanding Molecular Simulation: From Algorithms to Applications*. Academic Press, San Diego, 2002.
- [GGD<sup>+</sup>05] L. Gómez, C. Gazza, H. Dacharry, L. Peñaranda und A. Dobry. Pressure dependence of the melting mechanism at the limit of overheating in Lennard-Jones crystals. *Phys. Rev. B.* 71:134106, 2005.
- [GS16] J. Gernert und R. Span. EOS–CG: A Helmholtz energy mixture model for humid gases and CCS mixtures. *J. Chem. Thermodyn.* 93:274–293, 2016.
- [JS73] R. T. Jacobsen und R. B. Stewart. Thermodynamic properties of nitrogen including liquid and vapor phases from 63K to 2000K with pressures to 10,000 bar. *Phys. Chem. Ref. Data.* 2:757–922, 1973.
- [KW12] O. Kunz und W. Wagner. The GERG-2008 wide-range equation of state for natural gases and other mixtures: an expansion of GERG-2004. *J. Chem. Eng. Data.* 57:3032–3091, 2012.
- [Lan99] Landolt-Börnstein: Thermodynamic Properties of Inorganic Materials, Group IV - Physical Chemistry, Volume 19, Springer-Verlag Berlin Heidelberg, 1999.
- [LHM13] E. W. Lemmon, M. L. Huber und M. O. McLinden. NIST Standard Reference Database 23: Reference Fluid Thermodynamic and Transport Properties–REFPROP Version 9.1, 2013.



- [LSA03] M. Lísal, W. R. Smith und K. Aim. Direct molecular-level Monte Carlo simulation of Joule-Thomson processes. *Mol. Phys.* 101:2875–2884, 2003.
- [Lus11] R. Lustig. Direct molecular NVT simulation of the isobaric heat capacity, speed of sound and Joule–Thomson coefficient. *Mol. Simulat.* 37:457–465, 2011.
- [Lus12] R. Lustig. Statistical analogues for fundamental equation of state derivatives. *Mol. Phys.* 110:3041–3052, 2012.
- [Lus14] R. Lustig. Private Mitteilung, 2014.
- [Lus17] R. Lustig. On the Lennard-Jones and Devonshire theory for solid state thermodynamics. *Mol. Phys.* 115:1362–1377, 2017.
- [Mie03] G. Mie. Zur kinetischen Theorie der einatomigen Körper. *Ann. Phys.* 316:657–697, 1903.
- [MMHV17] Y. M. Muñoz-Muñoz, C.-M. Hsieh und J. Vrabec. Understanding the Differing Fluid Phase Behavior of Cyclohexane+ Benzene and Their Hydroxylated or Aminated Forms. *J. Phys. Chem. B.* 2017.
- [NK91] I. Nezbeda und J. Kolafa. A new version of the insertion particle method for determining the chemical potential by Monte Carlo simulation. *Mol. Simulat.* 5:391–403, 1991.
- [RTL<sup>+</sup>13] G. Rutkai, M. Thol, R. Lustig, R. Span und J. Vrabec. Communication: Fundamental equation of state correlation with hybrid data sets. *J. Chem. Phys.* 139:041102, 2013.
- [SE05] L. Sun und J. F. Ely. A corresponding states model for generalized engineering equations of state. *Int. J. Thermophys.* 26:705–728, 2005.
- [SEH<sup>+</sup>16] R. Span, T. Eckermann, S. Herrig, S. Hielscher, A. Jäger und M. Thol. TREND. Thermodynamic Reference and Engineering Data 3.0. Lehrstuhl für Thermodynamik, Ruhr-Universität Bochum, 2016.
- [SLJ<sup>+</sup>00] R. Span, E. W. Lemmon, R. T. Jacobsen, W. Wagner und A. Yokozeki. A reference equation of state for the thermodynamic properties of nitrogen for temperatures from 63.151 to 1000 K and pressures to 2200 MPa. *J. Phys. Chem. Ref. Data.* 29:1361–1433, 2000.

- [Spa00] R. Span. *Multiparameter Equations of State: An Accurate Source of Thermodynamic Property Data*. Springer Verlag, Berlin, 2000.
- [SW03] R. Span und W. Wagner. Equations of state for technical applications. I. Simultaneously optimized functional forms for nonpolar and polar fluids. *Int. J. Thermophys.* 24:1–39, 2003.
- [TRS<sup>+</sup>15] M. Thol, G. Rutkai, R. Span, J. Vrabec und R. Lustig. Equation of State for the Lennard-Jones Truncated and Shifted Model Fluid. *Int. J. Thermophys.* 36:25–43, 2015.
- [UNDR<sup>+</sup>07] P. Ungerer, C. Nieto-Draghi, B. Rousseau, G. Ahunbay und V. Lachet. Molecular simulation of the thermophysical properties of fluids: From understanding toward quantitative predictions. *J. Mol. Liq.* 134:71–89, 2007.
- [VH02] J. Vrabec und H. Hasse. Grand equilibrium: vapour-liquid equilibria by a new molecular simulation method. *Mol. Phys.* 100:3375–3383, 2002.
- [VKH02] J. Vrabec, M. Kettler und H. Hasse. Chemical potential of quadrupolar two-centre lennard-jones fluids by gradual insertion. *Chem. Phys. Lett.* 356:431–436, 2002.
- [VSH01] J. Vrabec, J. Stoll und H. Hasse. A Set of Molecular Models for Symmetric Quadrupolar Fluids. *J. Phys. Chem. B.* 105:12126–12133, 2001.
- [Wea76] R. C. Weast, editor. *CRC Handbook of Chemistry and Physics, 57th Edition*. CRC Press, Cleveland, 1976.
- [Wid63] B. Widom. Some Topics in the Theory of Fluids. *J. Chem. Phys.* 39:2808–2812, 1963.
- [WP02] W. Wagner und A. Pruß. The IAPWS formulation 1995 for the thermodynamic properties of ordinary water substance for general and scientific use. *J. Phys. Chem. Ref. Data.* 31:387–535, 2002.

### 3 Wissenschaftliche Publikationen

In Zusammenhang mit der vorliegenden Dissertation, in thematischer Anordnung:

1. **A. Köster**, M. Thol, J. Vrabec, Molecular Models for the Hydrogen Age: Hydrogen, Nitrogen, Oxygen, Argon and Water, *Journal of Chemical & Engineering Data*, im Druck, DOI: 10.1021/acs.jced.7b00706, 2018.
2. C. W. Glass, S. Reiser, G. Rutkai, S. Deublein, **A. Köster**, G. Guevara-Carrion, A. Wafai, M. Horsch, M. Bernreuther, T. Windmann, H. Hasse, J. Vrabec, *ms2: A molecular simulation tool for thermodynamic properties, new version release*, *Computer Physics Communications* 185:3302-3306, 2014.
3. G. Rutkai, **A. Köster**, G. Guevara-Carrion, T. Janzen, M. Schappals, C. W. Glass, M. Bernreuther, A. Wafai, S. Stephan, M. Kohns, S. Reiser, S. Deublein, M. Horsch, H. Hasse, J. Vrabec, *ms2: A molecular simulation tool for thermodynamic properties, release 3.0*, *Computer Physics Communications* 221:343-351, 2017.
4. S. Eckelsbach, T. Janzen, **A. Köster**, S. Miroshnichenko, Y. M. Muñoz-Muñoz, J. Vrabec, Molecular models for cyclic alkanes and ethyl acetate as well as surface tension data from molecular simulation, *High Performance Computing in Science and Engineering'14*, Springer, Berlin, 645-659, 2015.
5. **A. Köster**, T. Spura, G. Rutkai, J. Kessler, H. Wiebeler, J. Vrabec, T. D. Kühne, Assessing the accuracy of improved force-matched water models derived from Ab initio molecular dynamics simulations, *Journal of Computational Chemistry* 37:1828-1838, 2016.
6. P. Mausbach, **A. Köster**, G. Rutkai, M. Thol, J. Vrabec, Comparative study of the Grüneisen parameter for 28 pure fluids, *The Journal of Chemical Physics* 144:244505, 2016.
7. M. Thol, G. Rutkai, **A. Köster**, R. Lustig, R. Span, J. Vrabec, Equation of state for the Lennard-Jones fluid, *Journal of Physical and Chemical Reference Data* 45:023101, 2016.

8. M. Thol, G. Rutkai, **A. Köster**, M. Kortmann, R. Span, J. Vrabec, Fundamental equation of state for ethylene oxide based on a hybrid dataset, *Chemical Engineering Science* 121:87-99, 2015 und 134:887-890, 2015.
9. M. Thol, G. Rutkai, **A. Köster**, S. Miroshnichenko, W. Wagner, J. Vrabec, R. Span, Equation of state for 1,2-dichloroethane based on a hybrid data set, *Molecular Physics* 115:1166-1185, 2017.
10. M. Thol, F. H. Dubberke, G. Rutkai, T. Windmann, **A. Köster**, R. Span, J. Vrabec, Fundamental equation of state correlation for hexamethyldisiloxane based on experimental and molecular simulation data, *Fluid Phase Equilibria* 418:133-151, 2016.
11. M. Thol, G. Rutkai, **A. Köster**, F. H. Dubberke, T. Windmann, R. Span, J. Vrabec, Thermodynamic Properties of Octamethylcyclotetrasiloxane, *Journal of Chemical & Engineering Data* 61:2580-2595, 2016.
12. **A. Köster**, T. Jiang, G. Rutkai, C. W. Glass, J. Vrabec, Automatized determination of fundamental equations of state based on molecular simulations in the cloud, *Fluid Phase Equilibria* 425:84-92, 2016.
13. **A. Köster**, P. Mausbach, J. Vrabec, Premelting, solid-fluid equilibria, and thermodynamic properties in the high density region based on the Lennard-Jones potential, *The Journal of Chemical Physics* 147:144502, 2017.
14. M. Schappals, A. Mecklenfeld, L. Kröger, V. Botan, **A. Köster**, S. Stephan, E. J. Garcia, G. Rutkai, G. Raabe, P. Klein, K. Leonhard, C. W. Glass, J. Lenhard, J. Vrabec, H. Hasse, Round Robin Study: Molecular Simulation of Thermodynamic Properties from Models with Internal Degrees of Freedom, *Journal of Chemical Theory and Computation* 13:4270-4280, 2017.

Weitere Veröffentlichungen ohne direkten Bezug zur vorliegenden Dissertation oder noch in Bearbeitung:

15. T. Windmann, **A. Köster**, J. Vrabec, Vapor Liquid Equilibrium Measurements of the Binary Mixtures Nitrogen + Acetone and Oxygen + Acetone, *Journal of Chemical & Engineering Data* 57:1672-1677, 2012.

16. **A. Köster**, P. Nandi, T. Windmann, D. Ramjugernath, J. Vrabec, Vapor-liquid equilibria of ethylene ( $C_2H_4$ ) + decafluorobutane ( $C_4F_{10}$ ) at 268-298 K from experiment, molecular simulation and the Peng-Robinson equation of state, *Fluid Phase Equilibria* 336:104-112, 2012.
17. J. Vrabec, M. Bernreuther, H.-J. Bungartz, W.-L. Chen, W. Cordes, R. Fingerhut, C. W. Glass, J. Gmehling, R. Hamburger, M. Heilig, M. Heinen, M. T. Horsch, C.-M. Hsieh, M. Hülsmann, P. Jäger, P. Klein, S. Knauer, T. Köddermann, **A. Köster**, K. Langenbach, S.-T. Lin, P. Neumann, J. Rarey, D. Reith, G. Rutkai, M. Schappals, M. Schenk, A. Schedemann, M. Schönherr, S. Seckler, S. Stephan, K. Stübener, N. Tchipev, A. Wafai, S. Werth, H. Hasse, SkaSim - Skalierbare HPC-Software für molekulare Simulationen in der chemischen Industrie, *Chemie Ingenieur Technik*, im Druck, 2018.

### 3.1 Molecular Models for the Hydrogen Age: Hydrogen, Nitrogen, Oxygen, Argon and Water

A. Köster, M. Thol, J. Vrabec, *Journal of Chemical & Engineering Data*, im Druck, 2018.

DOI: 10.1021/acs.jced.7b00706

Nachgedruckt mit Erlaubnis der American Chemical Society (Copyright 2018).

In dieser umfassenden Studie wurden verschiedene Modellierungsansätze genutzt, um das Mischungsverhalten von Wasserstoff, Stickstoff, Sauerstoff, Argon und Wasser zu beschreiben. Es zeigte sich, dass die Verfügbarkeit von experimentellen Daten auch für dieses sehr elementare System überraschend lückenhaft ist, da nur lediglich zwei von zehn ternären und eine von fünf quaternären Mischungen vermessen wurden. Zu den genutzten Modellen zählten atomistische molekulare Simulationen, die PC-SAFT Zustandsgleichung sowie komplexe empirische Zustandsgleichungen. Die Ergebnisse der Studie wurden diskutiert auf der Basis von Dampf-Flüssigkeits-Gleichgewichten, homogenen Dichten und Löslichkeiten für binäre, ternäre und quaternäre Mischungen und verdeutlichen die gute Vorhersagekraft und breite Einsetzbarkeit von molekularen Simulationen.

Arbeiten an dieser Publikation wurden koordiniert vom Autor der vorliegenden Dissertation, der gleichzeitig das Manuskript verfasst, die molekularen Simulationen durchgeführt und alle verwendeten Zustandsgleichungen korreliert hat. Dr. Monika Thol hat die Anpassung des neuen Wasserstoff Kraftfeldes an homogene Dichten und Schallgeschwindigkeiten übernommen. Die Überarbeitung des Manuskripts wurde unter Mithilfe von Prof. Jadran Vrabec und Dr. Monika Thol durchgeführt. Der Autor wurde während des gesamten Prozesses von Prof. Jadran Vrabec betreut.

# Molecular Models for the Hydrogen Age: Hydrogen, Nitrogen, Oxygen, Argon, and Water

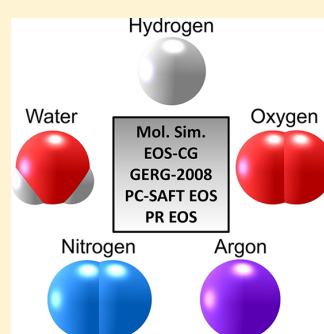
Andreas Köster,<sup>†</sup> Monika Thol,<sup>‡,✉</sup> and Jadran Vrabec<sup>\*,†,✉</sup>

<sup>†</sup>Lehrstuhl für Thermodynamik und Energietechnik, Universität Paderborn, 33098 Paderborn, Germany

<sup>‡</sup>Lehrstuhl für Thermodynamik, Ruhr-Universität Bochum, 44801 Bochum, Germany

## Supporting Information

**ABSTRACT:** Thermodynamic properties including the phase behavior of all mixtures containing hydrogen, the main air components nitrogen, oxygen, and argon, as well as water are of particular interest for the upcoming postcarbon age. Molecular modeling and simulation, the PC-SAFT equation of state, and sophisticated empirical equations of state are employed to study the mixture behavior of these five substances. For this purpose, a new force field for hydrogen is developed. All relevant subsystems, that is, binary, ternary, and quaternary mixtures, are considered. The quality of the results is assessed by comparing to available experimental literature data, showing an excellent agreement in many cases. Molecular simulation, which is the most versatile approach in general, also provides the best overall agreement. Consequently, this contribution aims at an improved availability of thermodynamic data that are required for the hydrogen age.



## 1. INTRODUCTION

Even in the international political arena, it is now globally accepted that human civilization must switch from fossil to renewable energy sources because atmospheric pollution threatens our climate.<sup>1</sup> Much less attention is being paid in these discussions to the fact that fossil fuel resources were always also a potent driver of conflict basically from the onset of industrialization.<sup>2,3</sup> An attractive alternative energy carrier that has major advantages over carbon-based fuels is hydrogen ( $H_2$ ). It can be used in all kinds of combustion processes and can reduce harmful carbon dioxide ( $CO_2$ ) emissions to a minimum. An approach with an even wider impact, avoiding thermal energy that is associated with the Carnot limit, is the use of fuel cells to directly convert chemical energy from  $H_2$  with ambient air into electric energy and water. One kilogram of  $H_2$  contains 33.3 kWh of chemical energy, if the lower heating value of  $H_2$  is employed. Modern electrolyzers require an electricity input of 52 kWh/kg on average, which corresponds to an electrical efficiency of 64%.<sup>4</sup> Since renewable energy sources, such as wind or solar energy, are fluctuating in nature and need to be balanced, their excess power may be employed for hydrogen production.<sup>5</sup>

The NASA space shuttles<sup>6</sup> were very prominent devices using  $H_2$  as a fuel both for combustion and for fuel cells. However, the whole classical transportation sector could in general profit from fuel cells as Momirlan and Veziroglu<sup>6</sup> point out. In 2016, over 100 fuel cell buses for public transportation were in use worldwide.<sup>7</sup> More recently, first test runs with a new fuel cell passenger train were performed.<sup>8</sup> There are, however, numerous other meaningful approaches for the use of  $H_2$ .<sup>9</sup> For example, it may be processed together with  $CO_2$  in a power to gas approach and subsequently stored in the form of

methane in widely available storage facilities.<sup>10</sup> All of these techniques have in common the need for accurate thermodynamic data for their design and optimization.

Since experimental measurements alone do not keep up with the demand for thermodynamic information, data must be also obtained by other methods, which is the goal of this study. Accordingly, the mixture behavior of five substances related to the hydrogen age, that is,  $H_2$ , nitrogen ( $N_2$ ), oxygen ( $O_2$ ), argon (Ar), and water ( $H_2O$ ), is tackled with molecular modeling and simulation, the PC-SAFT equation of state (EOS), and sophisticated empirical EOS and compared to experimental data, where available. All relevant subsystems are described. Several literature studies already dealt with some of these subsystems. Stoll et al.<sup>11</sup> and Vrabec et al.<sup>12</sup> performed molecular simulation studies on binary mixtures related to dry air ( $N_2 + O_2$ ,  $N_2 + Ar$ , and  $Ar + O_2$ ), which were then used to predict cryogenic vapor–liquid equilibria (VLE) of dry air ( $N_2 + O_2 + Ar$ ).<sup>13,14</sup> Furthermore, humid air ( $N_2 + O_2 + Ar + H_2O$ ) was examined by Eckl et al.<sup>14</sup> Related studies with a different objective, that is,  $CO_2$  mixtures for carbon capture and sequestration (CCS) and the like, were conducted by means of molecular modeling and simulation by Vrabec et al.<sup>15</sup> ( $N_2 + O_2 + CO_2$ ), Tenorio et al.<sup>16</sup> ( $H_2 + CO_2$ ), and Cresswell et al.<sup>17</sup> (binary mixtures of  $CO_2$  with  $H_2$ ,  $N_2$ , Ar, and  $O_2$ ). Moreover, several studies employed the statistical associating fluid theory (SAFT) in its various forms or cubic EOS to study mixtures containing  $CO_2$ .<sup>18,19</sup> Solubilities of binary aqueous systems ( $N_2 + H_2O$  and  $H_2 + H_2O$ ) were examined by Sun et

Received: August 2, 2017

Accepted: December 15, 2017



Table 1. Parameters of the Present Molecular Interaction Force Fields

interaction site	$x$ Å	$y$ Å	$\sigma$ Å	$\epsilon/k_B$ K	$q$ e	$Q$ DÅ
hydrogen A						
H <sub>2</sub>	0	0	3.0366	25.84		
hydrogen B <sup>36</sup>						
H <sub>2</sub>	0	0	2.9580	36.7		0.6369
nitrogen <sup>24</sup>						
N	0	−0.5232	3.3211	34.897		
N	0	0.5232	3.3211	34.897		
quadrupole oxygen <sup>24</sup>	0	0				−1.4397 <sup>a</sup>
O	0	−0.4850	3.1062	43.183		
O	0	0.4850	3.1062	43.183		
quadrupole argon <sup>24</sup>	0	0				−0.8081 <sup>a</sup>
Ar	0	0	3.3952	116.79		
water <sup>29</sup>						
O	0	0	3.1589	93.2		
H	0.5859	0.7570			0.5564	
H	0.5859	−0.7570			0.5564	
M (midpoint)	0.1546	0			−1.1128	

<sup>a</sup>The quadrupole is oriented along the molecular axis.

al.<sup>20</sup> with the SAFT–Lennard-Jones EOS. Finally, empirical multiparameter EOS formulated in terms of the Helmholtz energy are available, namely the GERG-2008<sup>21</sup> and a recently developed model for combustion gases (EOS-CG).<sup>22</sup> These EOS are typically very accurate in reproducing experimental data. However, the EOS-CG unfortunately does not cover H<sub>2</sub>, and the GERG-2008 EOS does not aim at cryogenic conditions. Consequently, a comprehensive study focusing on carbon-free mixtures containing H<sub>2</sub> is a necessity.

Different thermodynamic properties were considered in this work to describe a substantial number of mixtures. Apart from VLE properties, such as vapor pressure, saturated densities or residual enthalpy of vaporization, homogeneous density and solubility were also studied. Solubility, that is, Henry's law constant, is typically relevant for mixtures in which one component is only little soluble in the other, as it is the case for aqueous systems that are considered in the present work. In the following sections, the employed models are described before the results of this study are presented and discussed. Finally, a summary of the present work is given.

## 2. METHODOLOGY

**2.1. Modeling of Pure Fluids and Mixtures.** In this study, nonpolarizable force fields were employed for the intermolecular interactions. Because of the small size of all considered molecules, the internal degrees of freedom were neglected throughout. Dispersive and repulsive interactions were described with the widely known Lennard-Jones (LJ) 12–6 potential, whereas electrostatic interactions, if present, were modeled with point charges or point quadrupoles. Under these assumptions, the total intermolecular potential writes as

$$\begin{aligned}
 U = & \sum_{i=1}^{N-1} \sum_{j=i+1}^N \left\{ \sum_{a=1}^{S_i^{\text{LJ}}} \sum_{b=1}^{S_j^{\text{LJ}}} 4\epsilon_{ijab} \left[ \left( \frac{\sigma_{ijab}}{r_{ijab}} \right)^{12} - \left( \frac{\sigma_{ijab}}{r_{ijab}} \right)^6 \right] \right. \\
 & + \sum_{c=1}^{S_i^e} \sum_{d=1}^{S_j^e} \frac{1}{4\pi\epsilon_0} \left[ \frac{q_{ic}q_{jd}}{r_{ijcd}} + \frac{q_{ic}Q_{jd} + Q_{ic}q_{jd}}{r_{ijcd}^3} f_1(\omega_i, \omega_j) \right. \\
 & \left. \left. + \frac{Q_{ic}Q_{jd}}{r_{ijcd}^5} f_2(\omega_i, \omega_j) \right] \right\} \quad (1)
 \end{aligned}$$

Therein, the pairwise interaction between LJ site  $a$  on molecule  $i$  and LJ site  $b$  on molecule  $j$  with a mutual distance  $r_{ijab}$  is specified by the LJ energy parameter  $\epsilon_{ijab}$  and the LJ size parameter  $\sigma_{ijab}$ .  $q_{ic}$ ,  $Q_{ic}$ ,  $q_{jd}$  and  $Q_{jd}$  represent the point charge magnitudes and quadrupolar moments of electrostatic interaction site  $c$  on molecule  $i$  and interaction site  $d$  on molecule  $j$ , respectively, while  $\epsilon_0$  denotes the permittivity of the vacuum. The orientational dependence of the electrostatic interactions is considered through the trigonometric expressions  $f_x(\omega_i, \omega_j)$ .<sup>23</sup> Finally, the summation limits  $N$ ,  $S_i^{\text{LJ}}$ , and  $S_i^e$  denote the number of molecules, the number of LJ sites, and the number of electrostatic sites, respectively.

The force fields for Ar, N<sub>2</sub>, and O<sub>2</sub> were taken from the work of Vrabec et al.<sup>24</sup> These force fields were adjusted to experimental VLE data and it was shown that they are an adequate choice for numerous fluid mixtures.<sup>17,25–28</sup> For H<sub>2</sub>O, the widely appreciated TIP4P/2005 force field,<sup>29</sup> which performs well for a large variety of thermodynamic properties,<sup>30–32</sup> was employed.

The description of molecular hydrogen with semiempirical force fields or other common thermodynamic models, such as EOS, is challenging. Because of hydrogen's small mass, quantum effects have to be taken into account. These effects have a strong influence on macroscopic thermodynamic properties, especially at low temperatures.<sup>33</sup> Therefore, a force field that was adjusted to the VLE properties of hydrogen



at low temperatures will lead to poor results using classical atomistic simulations at higher temperatures. Furthermore, molecular hydrogen is anisotropic because of its two nuclei and its nonspherical charge distribution and typically consists of ortho and para hydrogen with different quantum spin states.<sup>34</sup> Several authors have been working on modeling H<sub>2</sub> in the last decades, describing the intermolecular interactions with a single LJ 12–6 site,<sup>35</sup> a LJ 12–6 site with an additional point quadrupole for the anisotropic interactions,<sup>36–38</sup> or more complex force fields, which also account for many-body polarization.<sup>39</sup> In this work, both a single site LJ force field, initially taken from Hirschfelder et al.<sup>35</sup> and subsequently adjusted to the speed of sound and thermal (*pVT*) properties of H<sub>2</sub> at temperatures from 50 to 250 K, and one with an additional point quadrupole from Marx and Nielaba<sup>36</sup> were considered. All force field parameters are listed in Table 1. It should be noted that point quadrupoles can easily be represented with a set of three point charges if required.<sup>40</sup>

When describing mixtures, interactions between unlike molecules have to be taken into account. The unlike dispersive and repulsive interactions between LJ site *a* of molecule *i* and LJ site *b* of molecule *j* were specified with the modified Lorentz–Berthelot combination rule

$$\sigma_{ijab} = \frac{\sigma_{iaa} + \sigma_{jbb}}{2} \quad (2)$$

and

$$\varepsilon_{ijab} = \xi(\varepsilon_{iaa}\varepsilon_{jbb})^{1/2} \quad (3)$$

The temperature independent binary interaction parameter  $\xi$  was adjusted to achieve a better representation of experimental mixture data. This adjustment can most favorably be done on the basis of one experimental data point of the vapor pressure at an equimolar composition because the binary interaction parameter  $\xi$  has the strongest influence under these conditions.<sup>41</sup> If a binary interaction parameter is available, mixtures with more than two components do not require further optimization because of pairwise additivity. The unlike electrostatic interactions were treated straightforwardly according to the laws of electrostatics and do not require any binary interaction parameters.

**2.2. Simulation Details.** Throughout, Monte Carlo (MC) sampling<sup>42</sup> with release 3.0 of the molecular simulation program *ms2*<sup>43–45</sup> was used to generate the thermodynamic data presented here. A cutoff radius of 15 Å was employed. The LJ long-range corrections, considering the interactions beyond the cutoff radius, were calculated with the angle-averaging method of Lustig,<sup>46</sup> whereas long-range electrostatic interactions were considered by means of the reaction field method.<sup>23</sup> Statistical uncertainties of the simulation data were estimated by averaging over a sufficiently large number of uncorrelated blocks consisting of 5000 MC cycles each.<sup>47</sup> Three different molecular simulation workflows were employed:

1. VLE calculations were carried out with the grand equilibrium method.<sup>48</sup> This approach consists of two independent and subsequent simulation runs for the two phases in equilibrium. For the liquid phase, 864 particles were sufficiently equilibrated and then sampled for 10<sup>6</sup> production cycles in the isobaric–isothermal (*NpT*) ensemble. One such cycle consists of  $M/3 \times 864$  translational and rotational as well as one volume move

attempt, where *M* is the number of molecular degrees of freedom. The chemical potential of every component in the liquid phase was sampled with Widom's test particle insertion.<sup>49</sup> From the results of this run, the chemical potential as a function of pressure  $\mu_i(p)$  at constant temperature and liquid composition was approximated by a Taylor series expansion. This function was used in the subsequent pseudogrand canonical ( $\mu VT$ ) ensemble simulation of the vapor phase to sample the vapor pressure. For this run 1000 particles were used, which were thoroughly equilibrated in advance. The production phase was  $2 \times 10^5$  MC cycles, which consisted of  $M/3 \times 1000$  particle displacements as well as three insertion and three deletion attempts. More details on the grand equilibrium method can be found elsewhere.<sup>48</sup>

2. The Henry's law constant  $H_i$  was sampled in the *NpT* ensemble in the saturated liquid state of the solvent, that is, H<sub>2</sub>O, using 1000 particles.  $H_i$  is closely related to the chemical potential at infinite dilution  $\mu_i^\infty$ <sup>50</sup>

$$H_i = \rho_s k_B T \exp(\mu_i^\infty / (k_B T)) \quad (4)$$

wherein  $\rho_s$  is the saturated liquid density of the solvent, *T* is the temperature, and  $k_B$  is Boltzmann's constant. The chemical potential at infinite dilution was obtained with Widom's test particle insertion.<sup>49</sup> For this purpose, the mole fraction of the solute was set to zero such that only test particles were inserted into the pure solvent. The simulation runs consisted of  $3 \times 10^6$  MC cycles, that is,  $2 \times 10^5$  equilibration and  $2.8 \times 10^6$  production cycles.

3. *pVT* calculations for homogeneous bulk phases were carried out in the *NpT* ensemble using 864 particles. After a thorough equilibration, the density  $\rho$  was sampled over 10<sup>6</sup> production cycles. Again, one cycle consisted of  $M/3 \times 864$  translational and rotational as well as one volume move attempt.

**2.3. PC-SAFT Equation of State.** In addition to atomistic molecular simulation, the perturbed-chain statistical associating fluid theory (PC-SAFT) EOS was employed. It is also based on theoretical considerations (i.e., intermolecular interactions) and can therefore, like atomistic molecular simulation, be used in cases where only few experimental data are available. Since Gross and Sadowski developed the PC-SAFT EOS in 2001,<sup>51</sup> several improvements were implemented. Having only three pure component parameters in its initial form, Gross and Sadowski added a term to account for association in 2002 that requires two additional parameters.<sup>52</sup> Further developments involved for example, Helmholtz energy contributions of polar interactions<sup>53–55</sup> or cross associations.<sup>56</sup> Numerous studies showed that the PC-SAFT EOS is a powerful predictive approach to mixture behavior.<sup>19,57,58</sup>

Since pairwise additivity is assumed, modeling mixtures in the PC-SAFT framework is reduced to the description of unlike chain interactions. This was done here with the modified Lorentz–Berthelot combination rule, see eqs 2 and 3, with a slightly different expression for the unlike energy parameter

$$\varepsilon_{ij} = (1 - k_{ij})(\varepsilon_i \varepsilon_j)^{1/2} \quad (5)$$

wherein  $k_{ij}$  is a temperature independent binary parameter.

The pure component parameters of the PC-SAFT EOS were taken from the literature,<sup>18,51,59,60</sup> (Table 2). It has to be noted

Table 2. Pure Component Parameters of the PC-SAFT EOS

component	$M$ g/mol	$m$	$\sigma$ Å	$\varepsilon/k_B$ K	$\kappa^{A,B_i}$	$\varepsilon^{A,B_i}/k_B$ K
hydrogen <sup>59</sup>	2.016	1	2.9150	37.00		
nitrogen <sup>51</sup>	28.010	1.2053	3.3130	90.96		
oxygen <sup>18</sup>	32.050	1.1217	3.2100	114.96		
argon <sup>51</sup>	39.948	0.9285	3.4784	122.23		
water <sup>60</sup>	18.015	2.5472	2.1054	138.63	0.2912	1718.2

that H<sub>2</sub> is modeled as a spherical molecule having similar parameters as the force field developed in this work. VLE properties and homogeneous densities can be calculated straightforwardly with the PC-SAFT EOS. Solubility data, that is, the Henry's law constant, can be obtained with the PC-SAFT EOS through the fugacity coefficient of a solute at infinite dilution. This approach was, for example, utilized by Vinš and Hruby<sup>61</sup> for the solubility of N<sub>2</sub> in refrigerants. Note that these systems exhibit solubilities which are orders of magnitude larger than those of the present aqueous systems.

The solubility of H<sub>2</sub>, N<sub>2</sub>, O<sub>2</sub>, and Ar in H<sub>2</sub>O could not be reproduced satisfactorily with the PC-SAFT EOS, even with the application of more complex methods. Various H<sub>2</sub>O models with several association schemes (2B, 4C), permanent polarities for both H<sub>2</sub>O and the solutes, as well as induced association as described by Kleiner and Sadowski<sup>56</sup> led only to little improvement. Therefore, modeling the solubility of the present aqueous mixtures with the PC-SAFT EOS was omitted in the main body of this study. However, some solubility results from the PC-SAFT EOS are shown in the [Supporting Information](#).

**2.4. Peng–Robinson Equation of State.** Empirical EOS are typically used to correlate thermodynamic data from experiment, offering inter- and extrapolation capabilities between and beyond these data. Being simple and often considered to be accurate enough to cover a wide range of thermodynamic properties, the Peng–Robinson EOS<sup>62</sup> is one of the most widely used cubic EOS.<sup>63</sup> It is given by

$$p = \frac{RT}{v - b} - \frac{a(T)}{v(v + b) + b(v - b)} \quad (6)$$

with pressure  $p$ , universal gas constant  $R$ , molar volume  $v$ , and two substance-specific parameters

$$a(T) = 0.45724 \frac{(RT_c)^2}{p_c} \alpha(T) \quad (7)$$

and

$$b = 0.07780 \frac{RT_c}{p_c} \quad (8)$$

Therein,  $T_c$  and  $p_c$  are the critical temperature and pressure. Numerous alpha functions  $\alpha(T)$  were proposed in the literature, for example, by Soave,<sup>64</sup> Peng and Robinson,<sup>62</sup> Mathias and Copeman<sup>65</sup> or Stryjek and Vera.<sup>66</sup> However, the best overall results for the present fluid mixtures were achieved here with the alpha function of Twu et al.<sup>67</sup>

$$\alpha(T) = (T/T_c)^{N(M-1)} \exp(L(1 - (T/T_c)^{NM})) \quad (9)$$

wherein  $L$ ,  $M$ , and  $N$  are substance-specific parameters, which are usually fitted to pure component vapor pressure data. [Table](#)

[3](#) lists the numerical values for  $L$ ,  $M$ , and  $N$  for the pure substances considered in the present work.<sup>68</sup>

Table 3. Pure Component Parameters of the Twu–Bluck–Cunningham–Coon Alpha Function According to the Dortmund Data Base<sup>68</sup>

component	$T_c/K$	$p_c/\text{MPa}$	$L$	$M$	$N$
hydrogen	33.2	1.297	0.926823	5.127460	0.084639
nitrogen	126.2	3.394	0.329500	0.882750	1.052080
oxygen	154.6	5.046	0.550161	0.933432	0.693063
argon	150.8	4.874	0.557990	0.998454	0.669817
water	647.3	22.048	0.44132	0.87340	1.75990

Mixtures can be represented by applying mixing rules to EOS. A standard approach, which is commonly used in conjunction with the Peng–Robinson EOS, is the quadratic van der Waals one-fluid mixing rule.<sup>67</sup> Following this rule, the two substance-specific parameters are replaced by

$$a_m = \sum_i \sum_j x_i x_j a_{ij} \quad (10)$$

and

$$b_m = \sum_i x_i b_i \quad (11)$$

wherein

$$a_{ij} = (1 - k_{ij})(a_i a_j)^{1/2} \quad (12)$$

In this work, the Peng–Robinson EOS was not only used to determine vapor pressure and composition of the coexisting phases, but also homogeneous density and residual enthalpy of vaporization data. For details on these calculations in the context of cubic EOS, the reader is referred to the standard literature.<sup>69</sup> In analogy to the approach described for the PC-SAFT EOS, it was attempted to calculate fugacity coefficients in order to obtain the Henry's law constant. Unfortunately, it was not possible to achieve even qualitative agreement with the experimental data. Therefore, solubility of the aqueous systems was not described with the Peng–Robinson EOS in the main body of this study. However, some solubility results from the Peng–Robinson EOS are shown in the [Supporting Information](#).

**2.5. Multiparameter Helmholtz Energy Equations of State.** It is widely known that empirical multiparameter EOS, which are most often explicit in terms of the Helmholtz energy, are among the most accurate models for thermodynamic properties, if the underlying experimental database is of high quality and sufficiently large. These requirements are met for several pure substances, such as H<sub>2</sub>O<sup>70</sup> or CO<sub>2</sub>,<sup>71</sup> where the uncertainty of the resulting empirical EOS is comparable to the error of the underlying experiments. Unfortunately, very few

pure substances were measured that thoroughly. When considering mixtures, the necessary size of an experimental database is even larger, since the mixture composition appears as an additional independent variable.

To date, only few empirical Helmholtz energy EOS are available for mixtures; among the most popular ones are the GERG-2008 EOS<sup>21</sup> and the EOS-CG.<sup>22</sup> Both of these EOS were adjusted to experimental binary mixture data and are able to predict the mixture behavior of higher order mixtures assuming pairwise additivity. The GERG-2008 EOS was mainly developed for the thermodynamic properties of natural gases<sup>21</sup> and covers 21 components, including the five present ones. Although the EOS-CG covers only six components, CO<sub>2</sub>, H<sub>2</sub>O, N<sub>2</sub>, O<sub>2</sub>, Ar, and CO, it is also highly relevant here because it aims at humid combustion gases and humid or compressed air.<sup>22</sup> Consequently, the EOS-CG serves in this work as a reference for binary mixtures without H<sub>2</sub>, whereas the GERG-2008 EOS was seen as a reference for systems containing H<sub>2</sub>.

### 3. RESULTS AND DISCUSSION

The VLE behavior of all employed models was evaluated on the basis of vapor pressure, saturated densities, and residual enthalpy of vaporization

$$\Delta h_{\text{vap}}^{\text{res}} = h_{\text{liq}}^{\text{res}} - h_{\text{gas}}^{\text{res}} = (h_{\text{liq}} - h_{\text{liq}}^{\text{ideal}}) - (h_{\text{gas}} - h_{\text{gas}}^{\text{ideal}}) \quad (13)$$

Additionally, homogeneous density and Henry's law constant data are presented. Binary, ternary, and quaternary mixtures are discussed under conditions in which experimental data are available for assessment. Typically, three experimental isotherms from the literature were taken to study the VLE behavior of binary mixtures. Attention was paid to selecting more than one experimental data source to assess the validity of any single measurement series. Along with a large temperature range, it was also aimed at a large composition range. Experimental  $p$  $v$  $T$  data were selected to allow for an extrapolation of the employed models to extreme conditions. An equimolar composition was preferred for binary  $p$  $v$  $T$  data because this implies that unlike interactions have the strongest influence. If possible, supercritical "liquid-like" (at high density) and supercritical "gas-like" (at low density) states were taken into account. Deviations were evaluated using the mean absolute percentage error (MAPE) to a reference value (experimental or multiparameter EOS)

$$\text{MAPE} = \frac{100}{n} \sum_{i=1}^n \left| \frac{X_{\text{model},i} - X_{\text{ref},i}}{X_{\text{ref},i}} \right| \quad (14)$$

where  $n$  is the number of data points and  $X$  is a given thermodynamic property.

In cases where binary mixture models had to be adjusted to experimental data, only a single temperature independent parameter was allowed (section 2). For molecular simulation, the binary interaction parameter  $\xi$  was either adjusted to one experimental vapor pressure data point at some intermediate temperature close to equimolar composition or, in the case of the aqueous systems, to reproduce experimental Henry's law constant data at  $T \approx 320$  K because numerous measurements are available around this temperature. The adjustment of  $k_{ij}$  for the Peng–Robinson and the PC-SAFT EOS was carried out with the least-squares method using the available experimental vapor pressure data.

Some of the binary mixtures presented here, namely N<sub>2</sub> + O<sub>2</sub>, N<sub>2</sub> + Ar, and Ar + O<sub>2</sub>, were already studied by our group. Therefore, the binary interaction parameter  $\xi$  for these mixtures was taken from that preceding work.<sup>11,12</sup> All binary parameters are listed in Table 4. Higher order mixture data

**Table 4.** Binary Parameters for Molecular Models  $\xi$ , Peng–Robinson EOS  $k_{ij}$ , and PC-SAFT EOS  $k_{ij}$

mixture	$\xi$	ref	$k_{ij}$ (PR EOS)	$k_{ij}$ (PC-SAFT EOS)
hydrogen A/B + nitrogen	1.08/0.88		−0.0878	0.1248
hydrogen A/B + oxygen <sup>a</sup>	1/1		0	0
hydrogen A/B + argon	1.06/0.895		−0.1996	0.0962
hydrogen A/B + water	1.52/1.05		−1.4125	0.0500
nitrogen + oxygen	1.007	11	−0.0115	−0.0030
nitrogen + argon	1.008	12	−0.0037	−0.0065
nitrogen + water	1.07		−0.0501	0.1198
oxygen + water	1			
argon + oxygen	0.988	12	0.0139	0.0086
argon + water	1.05			

<sup>a</sup>Data for this binary mixture were predicted without assessment and are thus presented in the Supporting Information only.

were not considered for adjustment because all of the present models assume pairwise additivity. The numerical molecular simulation data and the associated statistical uncertainties can be found in the Supporting Information. It has to be noted that statistical uncertainties are only shown in the figures below if they exceed symbol size.

**3.1. Binary Vapor–Liquid Equilibria.** The fluid phase behavior of H<sub>2</sub> + N<sub>2</sub> is shown in Figure 1 for three isotherms. For better visibility, the diagram was separated, showing mixture data from molecular simulation obtained with the present H<sub>2</sub> force field (top) and the literature force field<sup>136</sup> (center), respectively. Additionally, the relative volatility

$$\alpha = \frac{y_i/x_i}{y_j/x_j} \quad (15)$$

is depicted (bottom). Sufficient experimental data are available to validate the performance of the models. This mixture shows a two-phase region that is typical if one of the components is supercritical. Among the EOS correlations, the Peng–Robinson EOS exhibits the best agreement with the experimental data, both in the saturated liquid and vapor, which also leads to a good agreement for the relative volatility. The PC-SAFT EOS overestimates the critical point and also shows an inadequate slope for the saturated liquid line at 83.15 K. None of the two empirical multiparameter EOS are shown in Figure 1 because (a) H<sub>2</sub> is not implemented in the EOS-CG and (b) the GERG-2008 EOS yields a false liquid–liquid equilibrium phase separation at 83.15 K and strongly overestimates the pressure for  $T > 83.15$  K. However, cryogenic H<sub>2</sub> mixtures were not the main focus during the development of the GERG-2008 EOS, and its normal range of validity in temperature is specified as 90 to 450 K,<sup>21</sup> which means that the lowest isotherm is an extrapolation. More details on the performance of GERG-2008 EOS in the case of H<sub>2</sub> mixtures are shown in the Supporting Information. Comparing the two H<sub>2</sub> force fields, the present one shows a better agreement (see Figure 1 (bottom)). Especially at  $T =$

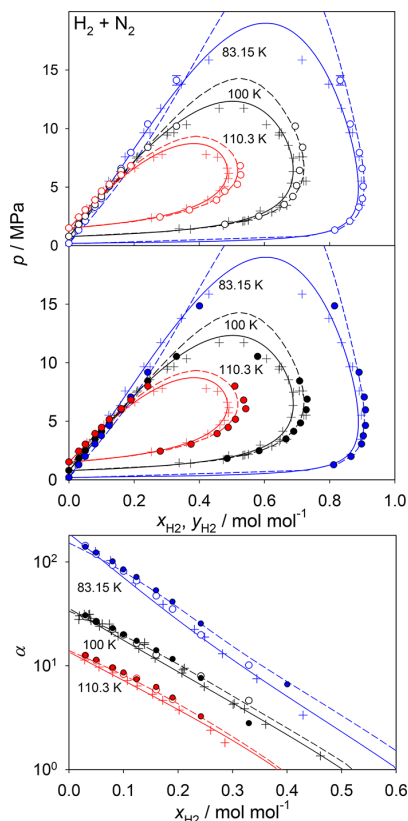


**Figure 1.** Isothermal fluid phase diagrams (top and center) and relative volatility  $\alpha$  (bottom) of the binary mixture  $\text{H}_2 + \text{N}_2$ : (○) molecular simulation results obtained with the present  $\text{H}_2$  force field or (●) with the  $\text{H}_2$  force field of Marx and Nielaba,<sup>36</sup> (—) Peng–Robinson EOS, (---) PC-SAFT EOS, and (+) experimental literature data.<sup>72–75</sup> Statistical uncertainties of the molecular simulation data are only shown if they exceed symbol size.

83.15 K on the saturated liquid line, the use of the force field of Marx and Nielaba<sup>36</sup> leads to an underestimation of the vapor pressure by about 9% when compared to the Peng–Robinson EOS.

Figure 2 shows saturated densities (top) and residual enthalpy of vaporization (bottom) for  $\text{H}_2 + \text{N}_2$  for the same isotherms. Typically, there are no experimental mixture data available for these properties. For the reasons discussed above, no empirical multiparameter EOS results are shown. Cubic EOS, especially in their simple forms, often tend to yield a poor representation of the saturated liquid density,<sup>63</sup> which can also be observed for this system. The saturated liquid density at 83.15 K of pure  $\text{N}_2$  was overestimated by about 3.5 mol/L, which corresponds to a deviation of 13% when compared to the other models and the reference EOS for pure  $\text{N}_2$ .<sup>76</sup> For both properties, the two  $\text{H}_2$  force fields lead to quite similar results.

VLE properties of  $\text{H}_2 + \text{Ar}$  are depicted in Figure 3. The separation of these diagrams into subdiagrams was done in analogy to  $\text{H}_2 + \text{N}_2$ . When compared to  $\text{H}_2 + \text{N}_2$ , this system shows a similar shape of the phase envelope, but the vapor pressure is higher by about a factor of 2 at the same temperature and  $\text{H}_2$  mole fraction. The solubility of  $\text{H}_2$  in

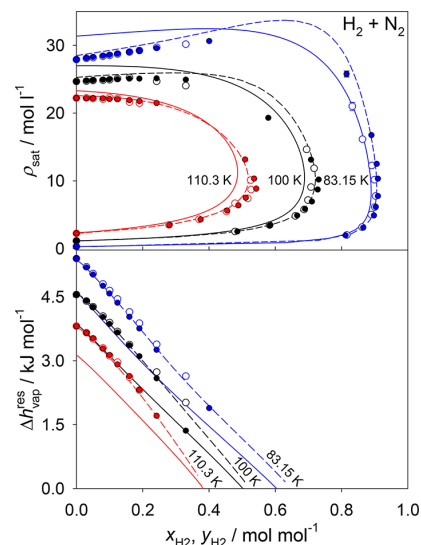


**Figure 2.** Isothermal saturated densities  $\rho_{\text{sat}}$  (top) and residual enthalpy of vaporization  $\Delta h_{\text{vap}}^{\text{res}}$  (bottom) of the binary mixture  $\text{H}_2 + \text{N}_2$ : (○) molecular simulation results obtained with the present  $\text{H}_2$  force field or (●) with the  $\text{H}_2$  force field of Marx and Nielaba,<sup>36</sup> (—) Peng–Robinson EOS, and (---) PC-SAFT EOS. Statistical uncertainties of the molecular simulation data are only shown if they exceed symbol size.

liquid Ar is thus lower than in liquid  $\text{N}_2$ . The agreement between the Peng–Robinson EOS, the molecular simulation data on the basis of the present  $\text{H}_2$  force field and the experimental data is very satisfactory for the saturated liquid line. On the saturated vapor line, especially for lower temperatures, deviations of all employed models to the experimental data can be observed. This finding is validated by the relative volatility representation (see Figure 3 (bottom)). The PC-SAFT EOS is again characterized by an inadequate slope of the saturated liquid line and yields a critical line which is higher than expected. At lower temperatures, the molecular simulations with the literature force field for  $\text{H}_2$  show a similar behavior (see Figure 3 (center)). For the same reasons as discussed before, the GERG-2008 EOS is not shown here. Saturated densities and residual enthalpy of vaporization data for  $\text{H}_2 + \text{Ar}$  are not discussed in detail because they are quite similar to  $\text{H}_2 + \text{N}_2$ . The reader is referred to the Supporting Information for more details.

The vapor pressure of  $\text{H}_2 + \text{H}_2\text{O}$  is shown in Figure 4 for two isotherms. This system is characterized by a low solubility of  $\text{H}_2$  in liquid  $\text{H}_2\text{O}$ . It has to be noted that a scale break on the horizontal axis had to be applied to make the results for the saturated liquid line of this mixture discernible. Experimental data to assess the quality of the present models are scarce and relatively old. The agreement of the molecular simulation results from both force fields with the experimental data is satisfactory along the saturated liquid line, whereas deviations are larger for the saturated vapor. As opposed to this, all employed EOS perform well on the saturated vapor line. As before, the GERG-2008 EOS predicts a liquid–liquid equilibrium for this mixture. The saturated liquid line from the PC-SAFT EOS is similar to the results obtained by molecular simulation. No relative volatility data are presented here for the VLE of aqueous systems because no composition



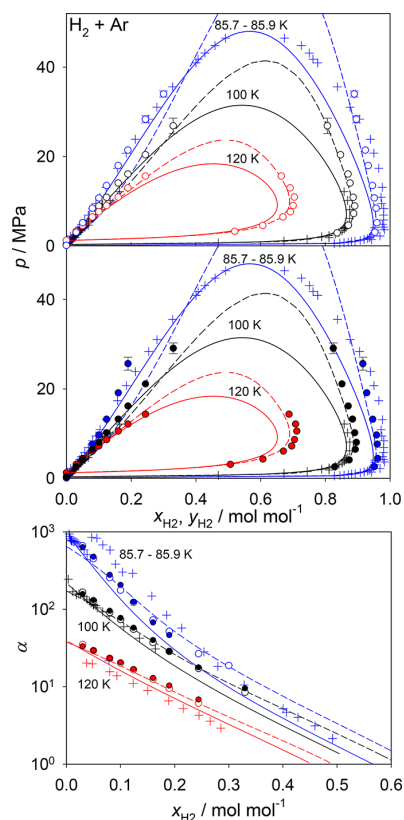


**Figure 3.** Isothermal fluid phase diagrams (top and center) and relative volatility  $\alpha$  (bottom) of the binary mixture  $\text{H}_2 + \text{Ar}$ : (○) molecular simulation results obtained with the present  $\text{H}_2$  force field or (●) with the  $\text{H}_2$  force field of Marx and Nielaba,<sup>36</sup> (—) Peng–Robinson EOS, (---) PC-SAFT EOS, and (+) experimental literature data.<sup>75,77–80</sup> Statistical uncertainties of the molecular simulation data are only shown if they exceed symbol size.

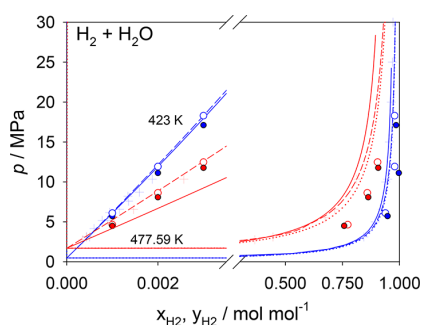


**Figure 4.** Isothermal fluid phase diagram of the binary mixture  $\text{H}_2 + \text{H}_2\text{O}$ : (○) Molecular simulation results obtained with the present  $\text{H}_2$  force field or (●) with the  $\text{H}_2$  force field of Marx and Nielaba,<sup>36</sup> (—) Peng–Robinson EOS, (---) PC-SAFT EOS, (···) GERG-2008 EOS and (+) experimental literature data.<sup>81–85</sup>

data for the saturated liquid and vapor were available at the same vapor pressure.

$\text{N}_2$  and  $\text{O}_2$  are the main components of air; therefore, the VLE properties of this mixture are of central importance, for instance, for air liquefaction. A molecular simulation study on

this system was conducted by Stoll et al.,<sup>11</sup> using the same pure component force fields. Their results agree extraordinarily well with experimental vapor pressure data from the literature (Figure 5 (top)). The bottom panel of Figure 5 allows for a

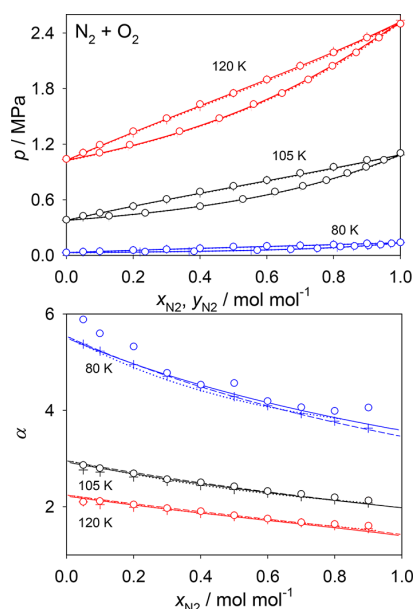


**Figure 5.** Isothermal fluid phase diagram (top) and relative volatility  $\alpha$  (bottom) of the binary mixture  $\text{N}_2 + \text{O}_2$ : (○) molecular simulation results, (—) Peng–Robinson EOS, (---) PC-SAFT EOS, (···) EOS-CG, and (+) experimental literature data.<sup>86,87</sup>

more precise examination of this binary mixture. It can be seen that the molecular simulation data exhibit noticeable deviations at  $T = 80 \text{ K}$  for both small concentrations of  $\text{N}_2$  and small concentrations of  $\text{O}_2$ . Around equimolar composition, the agreement is excellent. It has to be noted that this system is rather simple (both components are similar, subcritical, and the mixture is zeotropic) such that all other employed modeling approaches perform very well.

The saturated densities and the residual enthalpy of vaporization of  $\text{N}_2 + \text{O}_2$  are shown in Figure 6. It has to be noted that there is a scale break on the vertical axis of the top diagram, dividing it into saturated liquid density (above the break) and saturated vapor density (below the break). For this system, the EOS-CG can be used as a reference. It is striking that the saturated liquid density from molecular simulation agrees exceptionally well with the EOS-CG, exhibiting a MAPE value of 0.2%. The PC-SAFT EOS performs also quite well, that is, the MAPE is 1.0%, and is even preferable to the molecular simulation data for the saturated vapor at  $T = 120 \text{ K}$  (0.4% versus 2.4% MAPE). Again, the Peng–Robinson EOS leads to an overestimation of the saturated liquid density, which becomes increasingly severe with increasing density. The residual enthalpy of vaporization was reproduced satisfactorily by all present models. At  $T = 120 \text{ K}$  and larger mole fractions of  $\text{N}_2$ , the PC-SAFT EOS is superior to both molecular simulation and the Peng–Robinson EOS.

$\text{N}_2 + \text{H}_2\text{O}$  is presented in a similar manner as  $\text{H}_2 + \text{H}_2\text{O}$  in Figure 7. Two isotherms were used to assess the quality of the present models. There is, however, a discrepancy between the

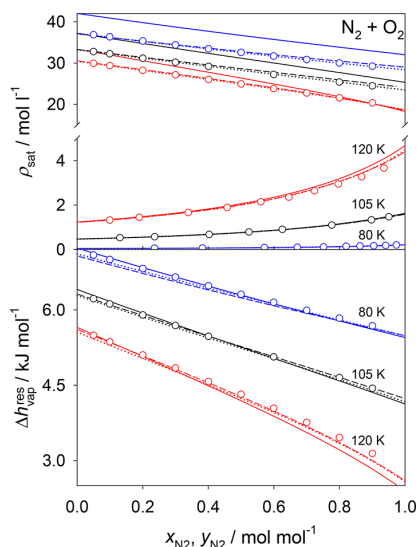


**Figure 6.** Isothermal saturated densities  $\rho_{\text{sat}}$  (top) and residual enthalpy of vaporization  $\Delta h_{\text{vap}}^{\text{res}}$  (bottom) of the binary mixture  $\text{N}_2 + \text{O}_2$ : (○) molecular simulation results, (—) Peng–Robinson EOS, (---) PC-SAFT EOS, and (···) EOS-CG.

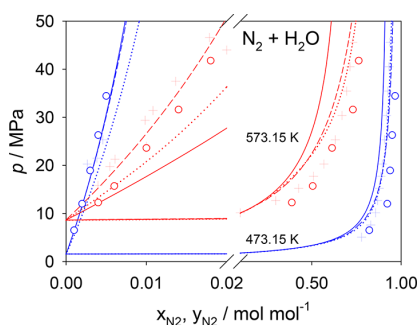


**Figure 7.** Isothermal fluid phase diagram of the binary mixture  $\text{N}_2 + \text{H}_2\text{O}$ : (○) molecular simulation results, (—) Peng–Robinson EOS, (---) PC-SAFT EOS, (···) EOS-CG, and (+) experimental literature data.<sup>88–91</sup>

different experimental data sources on the saturated liquid line for both isotherms. Therefore, a precise evaluation is difficult. Nonetheless, both molecular simulation and the PC-SAFT EOS show reliable results for the saturated liquid, whereas EOS-CG and the Peng–Robinson EOS deviate, especially at  $T = 573.15$  K. The agreement of molecular simulation with experimental data on the saturated vapor line is good. All employed EOS perform better at  $T = 473.15$  K than at  $T = 573.15$  K along the saturated vapor line.

The remaining two binary mixtures for which classical VLE properties were investigated are  $\text{N}_2 + \text{Ar}$  and  $\text{Ar} + \text{O}_2$ . Both of these systems were in the focus of our group before so that the binary interaction parameter  $\xi$  was already adjusted to experimental data in ref 12 and was simply adopted here. The performance of these molecular models was evaluated in a work of Vrabec et al.<sup>28</sup> for the vapor pressure along a single isotherm. Therefore, the present work complements this study by providing results for a larger temperature range and additional mixture properties.

The vapor pressure of  $\text{N}_2 + \text{Ar}$  is depicted in Figure 8 (top), showing a similar mixture behavior to that of  $\text{N}_2 + \text{O}_2$ . The

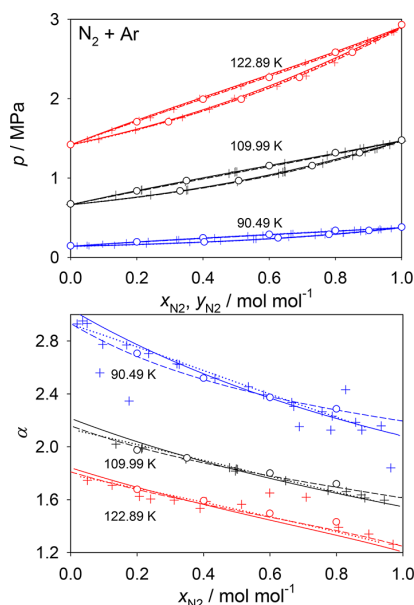


**Figure 8.** Isothermal fluid phase diagram (top) and relative volatility  $\alpha$  (bottom) of the binary mixture  $\text{N}_2 + \text{Ar}$ : (○) molecular simulation results, (—) Peng–Robinson EOS, (---) PC-SAFT EOS, (···) EOS-CG, and (+) experimental literature data.<sup>92,93</sup>

agreement of molecular simulation, the PC-SAFT, and the Peng–Robinson EOS in comparison to EOS-CG is excellent for the vapor pressure, that is, MAPE values of 0.8%, 0.6%, and 0.4% were achieved. A more precise evaluation of the performance of all models is possible by looking at the relative volatility in Figure 8 (bottom). In this magnified view, it can be seen that the experimental uncertainties are significant. All models lie within that scatter. Saturated densities and residual enthalpy of vaporization of this system are depicted in the Supporting Information.

Ar and  $\text{O}_2$  are substances with very similar macroscopic properties, for example their critical point differs only by 4 K in temperature and 0.2 MPa in pressure. Mixing these substances leads to a very narrow two-phase region and an essentially ideal mixing behavior, which was reproduced almost perfectly by all present models (Figure 9 (top)). When compared to the EOS-CG, MAPE values of 0.2% for the Peng–Robinson EOS, 0.2% for the PC-SAFT EOS, and 0.9% for molecular simulation data were achieved for the vapor pressure. All considered EOS show a similar behavior with respect to the relative volatility (Figure 9 (bottom)), and deviate from experimental data only at the lowest isotherm, whereas molecular simulation data show some deviation. Due to the similarity of the two components, the saturated mixture densities are almost constant over the whole composition range (Figure 10 (top)). Both molecular based models, atomistic simulations and the PC-SAFT EOS, predict this behavior equally well, whereas the Peng–Robinson EOS deviates by a constant offset of 5 mol/L in terms of the saturated liquid density. Some discrepancies between all models were observed for the residual enthalpy of vaporization, which is shown in Figure 10 (bottom). For this property, the EOS-CG shows a somewhat more convex shape than

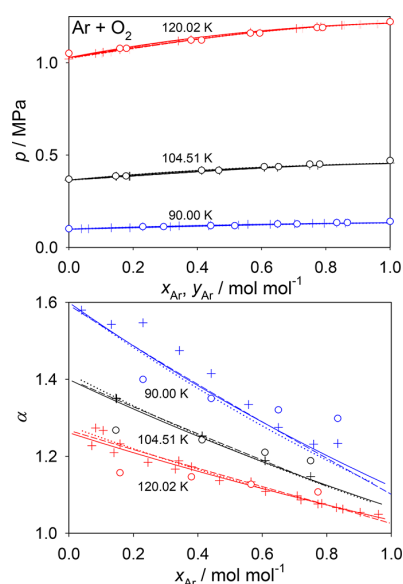


**Figure 9.** Isothermal fluid phase diagram (top) and relative volatility  $\alpha$  (bottom) of the binary mixture Ar + O<sub>2</sub>: (O) Molecular simulation results, (—) Peng–Robinson EOS, (---) PC-SAFT EOS, (···) EOS-CG, and (+) experimental literature data.<sup>94–96</sup>

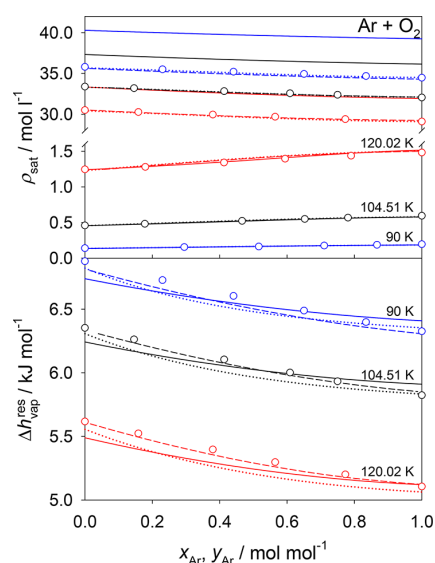


**Figure 10.** Isothermal saturated densities  $\rho_{\text{sat}}$  (top) and residual enthalpy of vaporization  $\Delta h_{\text{vap}}^{\text{res}}$  (bottom) of the binary mixture Ar + O<sub>2</sub>: (O) molecular simulation results, (—) Peng–Robinson EOS, (---) PC-SAFT EOS, and (···) EOS-CG.

molecular simulation, the PC-SAFT, and the Peng–Robinson EOS.

Binary VLE data for the mixtures H<sub>2</sub> + O<sub>2</sub>, O<sub>2</sub> + H<sub>2</sub>O, and Ar + H<sub>2</sub>O are not presented due to the lack of sufficient high quality experimental data. The aqueous systems were, however, investigated on the basis of Henry's law constant.

**3.2. Binary Homogeneous  $pVT$  Data.** Beyond VLE properties, there is also interest in homogeneous  $pVT$  data, which are discussed for binary mixtures in this section. An

equimolar composition was chosen because a maximal occurrence of unlike molecular interactions was targeted. Figure 11 presents the homogeneous density for H<sub>2</sub> + N<sub>2</sub> (top)

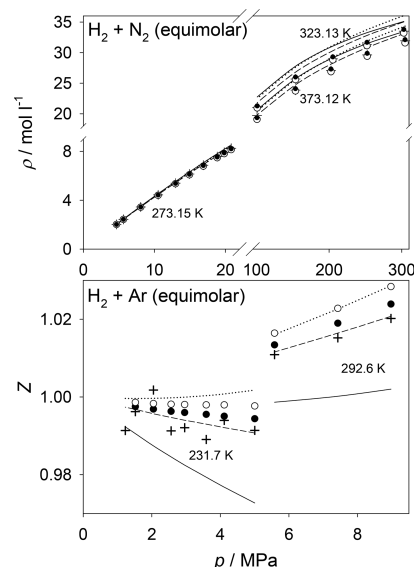


**Figure 11.** Homogeneous density  $\rho$  of the binary mixture H<sub>2</sub> + N<sub>2</sub> (top) and the compressibility factor  $Z$  of the binary mixture H<sub>2</sub> + Ar (bottom) at equimolar composition along isotherms: (O) molecular simulation results obtained with the present H<sub>2</sub> force field or (●) with the H<sub>2</sub> force field of Marx and Nielaba,<sup>36</sup> (—) Peng–Robinson EOS, (---) PC-SAFT EOS, (···) GERG-2008 EOS, and (+) experimental literature data.<sup>97–99</sup>

and the compressibility factor  $Z$  for H<sub>2</sub> + Ar (bottom), both properties were evaluated at given pressure and composition along isotherms.  $Z$  was chosen for the latter mixture, because the considered experimental data are dominated by ideal gas behavior. Unfortunately, no experimental data at higher densities were available in the vicinity of equimolar composition. In contrast to the saturated densities of the systems containing H<sub>2</sub> as discussed in Figure 2, the GERG-2008 EOS is applicable under these conditions. Therefore, a better assessment of the models with respect to the density is feasible.

For H<sub>2</sub> + N<sub>2</sub>, a large pressure and density range was covered by experimental studies (Figure 11 (top)). Both the horizontal and the vertical axes have a scale break, showing a supercritical “gas-like” isotherm at  $T = 273.15$  K and supercritical “liquid-like” isotherms at  $T = 323.13$  and  $373.12$  K. All models perform very well at  $T = 273.15$  K and exhibit a MAPE of  $\leq 1\%$ . For elevated pressure and density, however, the discrepancies become larger. This applies in particular to all EOS, which tend to overestimate the density. The atomistic molecular simulations, both with the present (MAPE 0.7%) and the H<sub>2</sub> force field from the literature<sup>36</sup> (MAPE 0.9%) perform very well.

The experimental database for the mixture H<sub>2</sub> + Ar is smaller; measurements are available up to pressures of 9 MPa (Figure 11 (bottom)). Over the whole pressure range, the atomistic molecular simulations, the PC-SAFT, and the GERG-2008 EOS perform well, whereas the Peng–Robinson EOS deviates qualitatively. Accordingly, MAPE values of 0.3%,

1.0%, 0.5%, 0.4%, and 0.7% were found for the PC-SAFT EOS, the Peng–Robinson EOS, molecular simulation with the present force field, molecular simulation with the literature force field, and the GERG-2008 EOS at  $T = 231.7$  K, respectively.

The homogeneous  $pVT$  behavior of three binary mixtures without  $H_2$ , i.e.  $N_2 + O_2$ ,  $N_2 + Ar$ , and  $Ar + O_2$ , is illustrated in Figure 12. Experimental data and the EOS-CG were used to assess the quality of the molecular simulation data, the PC-SAFT, and the Peng–Robinson EOS.

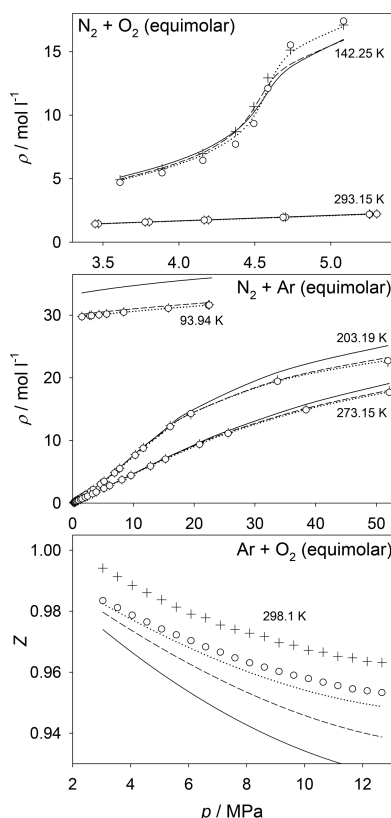


**Figure 12.** Homogeneous density  $\rho$  of the binary mixtures  $N_2 + O_2$  (top),  $N_2 + Ar$  (center), and the compressibility factor  $Z$  of the binary mixture  $Ar + O_2$  (bottom) at equimolar composition along isotherms: (O) molecular simulation results, (—) Peng–Robinson EOS, (---) PC-SAFT EOS, (···) EOS-CG, and (+) experimental literature data.<sup>100–103</sup>

For the system  $N_2 + O_2$ , two isotherms at intermediate pressures are presented (Figure 12 (top)). At 293.15 K and low density, hardly any difference between the employed models and the experimental data can be observed. Peng–Robinson EOS, PC-SAFT EOS, EOS-CG, and molecular simulation have MAPE values of 1.1%, 0.5%, 0.1%, and 0.3%, respectively. The isotherm at  $T = 142.25$  K is below the critical temperature of  $O_2$  ( $T_{c,O_2} = 154.6$  K); therefore, a VLE of the mixture is conceivable. Consequently, the EOS-CG predicts the critical point of  $N_2 + O_2$  at  $p = 4.44$  MPa and  $x_{N_2} = 0.454$  mol·mol<sup>−1</sup> at this temperature. The shape of this isotherm can therefore be explained by a close passing of the critical line of this mixture, starting from a “gas-like” state and ending in a

“liquid-like” state. It can be seen that the EOS-CG shows the best agreement with the experimental data. Close to the mixtures’ critical line, molecular simulation data show the largest deviations, which may be caused by finite size effects. State points that are not in the vicinity of the critical line agree satisfactorily with the experimental data. The PC-SAFT and Peng–Robinson EOS agree well with each other, but fail to reproduce the reference data in the “liquid-like” region.

Figure 12 (center) shows three isotherms for  $N_2 + Ar$ . The results are comparable and indicate a tendency that has been observed before. Namely, a good agreement to the reference data at low density was achieved by all employed models, whereas deviations become increasingly severe for the Peng–Robinson EOS and, to a limited extent, also for the PC-SAFT EOS at higher density. Results from molecular simulation agree excellently with both the experimental data and the EOS-CG, exhibiting a MAPE value of 0.4%. For  $Ar + O_2$  only one isotherm at low densities could be examined, which was done here in terms of the compressibility factor (Figure 12 (bottom)). The best agreement to both experimental data and the EOS-CG was found for the molecular simulation data, whereas the Peng–Robinson and PC-SAFT EOS deviate more or less thoroughly.

**3.3. Henry’s Law Constant.** Henry’s law constant data were used in the present work to assess aqueous systems, that is,  $H_2$ ,  $N_2$ ,  $O_2$ , or  $Ar$  in  $H_2O$ . This property is typically employed in cases where a solute is only little soluble in a solvent. Various definitions of the Henry’s law constant are established in the literature. The present work considers the purely temperature dependent Henry’s law constant, which requires that the solvent is in its saturated liquid state. Consequently, Henry’s law constant data are presented from the triple point temperature to the critical temperature of  $H_2O$ . To validate the results of the present work, both experimental data and the official IAPWS correlation<sup>104,105</sup> of these data were used.

All considered aqueous systems exhibit a qualitatively similar, strongly nonmonotonic behavior (Figure 13). A pronounced maximum of the Henry’s law constant is passed between 330 and 370 K. Note that large values of the Henry’s law constant correspond to a low solubility; therefore, the solubility decreases with increasing temperature, passes through a minimum and then increases again. However, quantitative differences between the solutes are present. Close to the triple point temperature,  $H_2$  and  $N_2$  are almost equally soluble in  $H_2O$  ( $H_{H_2} \approx H_{N_2} \approx 6$  GPa), but roughly three times less soluble than  $O_2$  and  $Ar$  ( $H_{O_2} \approx H_{Ar} \approx 2$  GPa). Furthermore, the maximum values of the Henry’s law constant differ significantly.

The results from molecular simulation are satisfactory; the region of increasing Henry’s law constant at low temperature was reproduced almost perfectly for all four solutes, whereas deviations are present at intermediate temperatures for  $N_2$ ,  $O_2$ , and  $Ar$ . For  $H_2$ , the agreement to the reference data is satisfying throughout for both employed force fields. Nonetheless, a disadvantage of the present force field for  $H_2$  becomes apparent here. To compensate the missing electrostatic interactions of  $H_2$ , which are obviously very important when  $H_2O$  is involved, the unlike LJ interaction energy had to be increased. This fact is reflected by a rather unphysically large value of  $\xi = 1.52$ .

The EOS-CG fails to reproduce the solubility data for  $Ar$  even qualitatively and predicts a monotonically decreasing



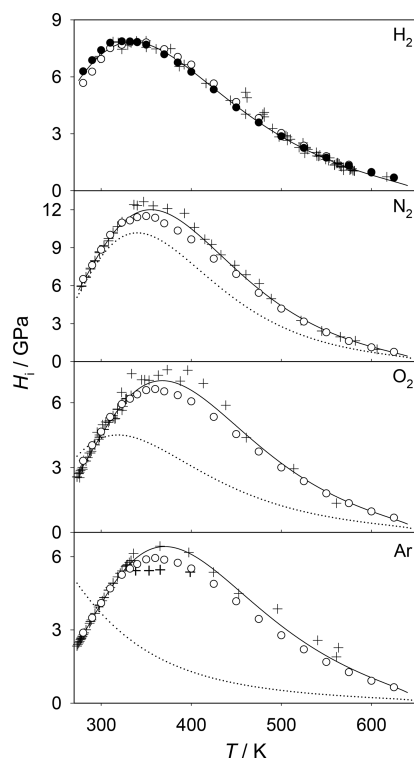


**Figure 13.** Henry's law constant of  $\text{H}_2$ ,  $\text{N}_2$ ,  $\text{O}_2$ , and Ar in  $\text{H}_2\text{O}$  (from top to bottom): (○●) molecular simulation results ( $\text{H}_2$ : (○) present force field, (●) force field of Marx and Nielaba<sup>36</sup>), (—) official IAPWS guideline,<sup>104,105</sup> (···) EOS-CG, and (+) experimental literature data ( $\text{H}_2$ ,<sup>106,107</sup>  $\text{N}_2$ ,<sup>107–110</sup>  $\text{O}_2$ ,<sup>111–114</sup> Ar<sup>115–118</sup>).

Henry's law constant for increasing temperature. For  $\text{N}_2$  and  $\text{O}_2$ , that behavior is predicted in a qualitatively correct way, but deviates quantitatively from the IAPWS reference. An application of the Henry's law constant to the fitting algorithms for empirical Helmholtz energy EOS should therefore be considered in the future.

**3.4. Ternary Vapor–Liquid Equilibria.** For higher order mixtures smaller experimental databases can be found in the literature. Consequently, only for 2 of the 10 possible ternary systems are experimental VLE data available for comparison, that is,  $\text{N}_2 + \text{O}_2 + \text{Ar}$  and  $\text{H}_2 + \text{N}_2 + \text{Ar}$ . Since all models applied in this study are based on pairwise additivity and neglect higher order interactions, the presented results are considered as predictive. This also applies to the EOS-CG and the GERG-2008 EOS; therefore, mainly experimental data were used as a reference for higher order mixtures. The following ternary VLE diagrams show the saturated mixture compositions at constant temperature and pressure.

Figure 14 depicts the VLE for  $\text{N}_2 + \text{O}_2 + \text{Ar}$  (dry air) which was already examined in molecular simulation studies of our group.<sup>13,14</sup> This system is characterized by a comparably narrow two-phase region. At  $T = 83.6$  K and pressures of about  $p = 0.13$  MPa, the experimental data seem to scatter considerably, but this is rather caused by their small temperature and pressure variations (Figure 14). Molecular simulations were specified to reproduce the experimental data on the saturated liquid line and therefore seemingly scatter as well. Nonetheless, the agreement of all employed models is

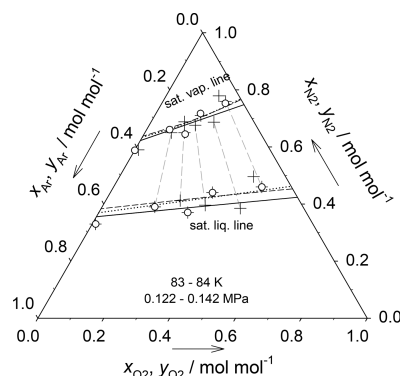


**Figure 14.** Fluid phase diagram of the ternary mixture  $\text{N}_2 + \text{O}_2 + \text{Ar}$  at 83 to 84 K and 0.122 to 0.142 MPa: (○) molecular simulation results, (—) Peng–Robinson EOS, (---) PC-SAFT EOS, (···) EOS-CG, and (+) experimental literature data.<sup>119</sup>

satisfactory. Especially the PC-SAFT EOS and the EOS-CG agree quite well.

A VLE phase diagram of  $\text{H}_2 + \text{N}_2 + \text{Ar}$  is presented in Figure 15. This system exhibits a large two-phase region due to the

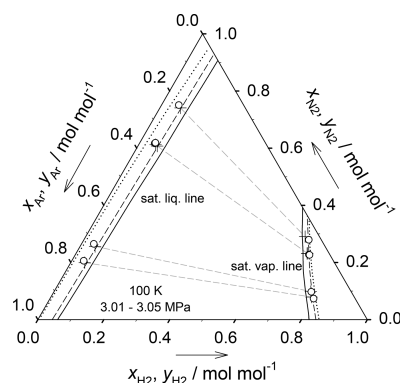


**Figure 15.** Fluid phase diagram of the ternary mixture  $\text{H}_2 + \text{N}_2 + \text{Ar}$  at 100 K and 3.01 to 3.05 MPa: (○) molecular simulation results, (—) Peng–Robinson EOS, (---) PC-SAFT EOS, (···) GERG-2008 EOS, and (+) experimental literature data.<sup>75</sup>

presence of  $\text{H}_2$ . An excellent agreement between the molecular simulation data, the PC-SAFT EOS, and the experimental data on the saturated liquid and vapor line was observed. The GERG-2008 EOS predicts the saturated vapor line satisfactorily, but deviates from the experiments when the saturated liquid line is considered, whereas the Peng–Robinson EOS predicts a two-phase region that is slightly too narrow. Additional ternary VLE data for both of these mixtures can be found in the [Supporting Information](#).

**3.5. Higher Order Homogeneous  $pVT$  Data.** Although any higher order mixture could be targeted with the considered modeling approaches, the present study is limited by experimental data availability. Therefore, homogeneous  $pVT$  data are only presented for one ternary and one quaternary system:  $\text{N}_2 + \text{O}_2 + \text{Ar}$  (dry air) and  $\text{N}_2 + \text{O}_2 + \text{Ar} + \text{H}_2\text{O}$  (humid air), respectively. For both mixtures, large temperature and pressure ranges were studied.

The homogeneous  $pVT$  behavior along four isotherms for  $\text{N}_2 + \text{O}_2 + \text{Ar}$  is shown in Figure 16. Experimental data are

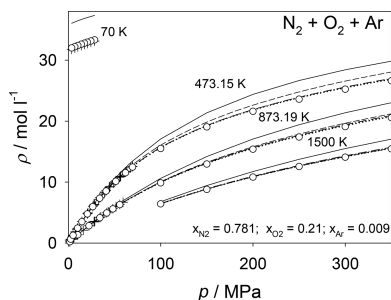


**Figure 16.** Homogeneous density  $\rho$  of the ternary mixture  $\text{N}_2 + \text{O}_2 + \text{Ar}$  at a composition which represents dry air along four isotherms: (O) molecular simulation results, (—) Peng–Robinson EOS, (---) PC-SAFT EOS, (···) EOS-CG, (---) dry air EOS by Lemmon et al.,<sup>120</sup> and (+) experimental literature data.<sup>121–123</sup>

available at  $T \leq 873.19 \text{ K}$  and  $p \leq 70 \text{ MPa}$ . In this case, a high quality Helmholtz energy explicit EOS for standard dry air by Lemmon et al.<sup>120</sup> was used as a reference. The experimental data were predicted well by molecular simulation, the EOS-CG, and the PC-SAFT EOS with MAPE values of 0.6%, 0.2%, and 1.1%, respectively. At  $T = 70 \text{ K}$ , where dry air is in its liquid state, the Peng–Robinson EOS shows large deviations. It can be seen that the EOS-CG and the molecular simulation data agree well to the dry air EOS by Lemmon et al.<sup>120</sup> for pressures above 70 MPa in the gaseous phase, whereas the Peng–Robinson and the PC-SAFT EOS deviate more or less thoroughly. In the liquid state, molecular simulation data, and the PC-SAFT EOS overestimate the density on average by 0.6% and 1.8% (MAPE), respectively.

Two different compositions are discussed for the quaternary system  $\text{N}_2 + \text{O}_2 + \text{Ar} + \text{H}_2\text{O}$ , the first corresponding to humid air (Figure 17 (top)) and the second corresponding to supercritical  $\text{H}_2\text{O}$  containing a substantial amount of solved gases (Figure 17 (bottom)). Since no adjustment of the PC-SAFT and the Peng–Robinson EOS could be carried out for the subsystems  $\text{O}_2 + \text{H}_2\text{O}$  and  $\text{Ar} + \text{H}_2\text{O}$  due to the lack of experimental data, their binary interaction parameter was set to  $k_{ij} = 0$  for these calculations. Although plenty of experimental measurements were conducted for humid air, only one experimental data point is shown here due to varying temperatures and compositions in the experiment series. Over the whole range of temperature and pressure, the agreement between the EOS-CG and the present molecular simulations is excellent; a MAPE of 0.8% was found. The PC-SAFT and the Peng–Robinson EOS differ more or less strongly from the EOS-CG and yield MAPE values of 1.5% and 5.4%, respectively. The bottom panel of Figure 17 shows a “water-like” composition of the four discussed substances. It is interesting that the EOS-CG reproduces the experimental data very well at lower pressures, whereas molecular simulation is superior at higher pressures. One cause for the deviation of the molecular simulation results at lower pressures could be the close proximity to the critical point of this mixture; water as the main component has critical properties of  $T_c = 647.1 \text{ K}$ ,  $p_c = 22 \text{ MPa}$ , and  $\rho_c = 17.87 \text{ mol/L}$ . The best agreement for this mixture was found for the PC-SAFT EOS, whereas the Peng–Robinson EOS deviates strongly from the experimental data at high pressures.

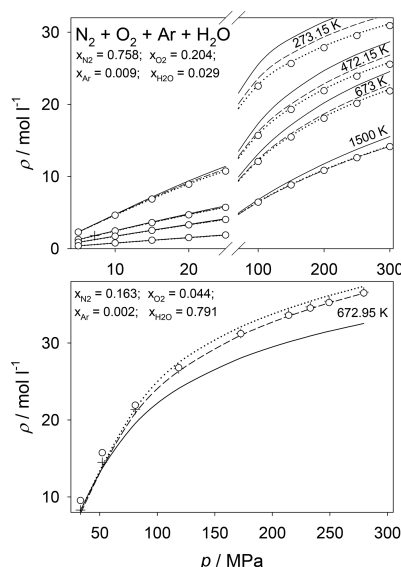


**Figure 17.** Homogeneous density  $\rho$  of the quaternary mixture  $\text{N}_2 + \text{O}_2 + \text{Ar} + \text{H}_2\text{O}$  along four isotherms at a composition which represents humid air (top) and supercritical  $\text{H}_2\text{O}$  containing  $\approx 0.2 \text{ mol}\cdot\text{mol}^{-1}$  of air components (bottom): (O) molecular simulation results, (—) Peng–Robinson EOS, (---) PC-SAFT EOS, (···) EOS-CG, and (+) experimental literature data.<sup>124,125</sup>

#### 4. CONCLUSION

Several models were applied to describe the mixture behavior of five substances that are relevant for hydrogen technology. In a first step, available pure component force fields were complemented by a new force field for  $\text{H}_2$  and subsequently adjusted to reproduce the fluid phase behavior of all involved binary mixtures. This was done by fitting a single temperature independent parameter to experimental vapor pressure data of binary mixtures or, in the case of the aqueous systems, to one experimental Henry's law constant data point. The primary focus was on molecular simulation; however, also a molecular based EOS (PC-SAFT EOS) and empirical EOS of different complexity (Peng–Robinson EOS, GERG-2008 EOS, and EOS-CG) were studied. In addition to VLE properties, such as vapor pressure, saturated densities, and residual enthalpy of vaporization, also the  $pVT$  behavior and solubility were considered. Furthermore, the thermodynamic properties of higher order mixtures were predicted assuming pairwise additivity throughout.

Not all of the employed models could be used for every system or thermodynamic property under the constraints of this study (one temperature independent parameter to describe a given binary mixture pair). The Henry's law constant of aqueous systems, for example, is satisfactorily represented only by molecular simulation, whereas the cryogenic VLE of  $\text{H}_2$  mixtures could not be calculated with the GERG-2008 EOS. In this regard, it would be desirable that  $\text{H}_2$  mixtures receive more attention in empirical multi-parameter EOS development. As expected, results from the Peng–Robinson EOS for the saturated liquid density deviate considerably. In summary, molecular modeling and simulation yields the best overall agreement with experimental data and, at the same time, is most versatile with respect to different thermodynamic properties and state points.

With the present molecular mixture model, a contribution to improving the availability of thermodynamic data for the upcoming hydrogen age was made. In principle, this model can be used to predict thermodynamic properties of this quinary mixture and its 25 subsystems due to pairwise additivity.

## ■ ASSOCIATED CONTENT

### 5 Supporting Information

The Supporting Information is available free of charge on the ACS Publications website at DOI: [10.1021/acs.jced.7b00706](https://doi.org/10.1021/acs.jced.7b00706).

Predictive mixture data for  $H_2 + O_2$ ; additional VLE data; VLE results for  $H_2$  mixtures from the GERG-2008 EOS; results from the PC-SAFT and the Peng–Robinson EOS for the Henry's law constant; numerical molecular simulation data (PDF)

## ■ AUTHOR INFORMATION

### Corresponding Author

\*E-mail: [jadran.vrabec@upb.de](mailto:jadran.vrabec@upb.de). Tel.: +49-5251 60-2421. Fax: +49 5251 60-3522.

### ORCID

Monika Thol: [0000-0002-3250-0515](https://orcid.org/0000-0002-3250-0515)

Jadran Vrabec: [0000-0002-7947-4051](https://orcid.org/0000-0002-7947-4051)

### Funding

The authors gratefully acknowledge the Paderborn Center for Parallel Computing (PC<sup>2</sup>) for the generous allocation of computer time on the OCuLUS cluster and computational support by the High Performance Computing Center Stuttgart (HLRS) under Grant MMHBF2. The present research was conducted under the auspices of the Boltzmann-Zuse Society of Computational Molecular Engineering (BZS).

### Notes

The authors declare no competing financial interest.

## ■ ACKNOWLEDGMENTS

The authors wish to thank Denis Šarić for helping with the molecular simulations and Dr.-Ing. Christoph Held for his assistance during the PC-SAFT EOS calculations.

## ■ REFERENCES

- (1) United Nations Framework Convention on Climate Change, *The Paris Agreement*. 2015; [http://unfccc.int/files/essential\\_background/convention/application/pdf/english\\_paris\\_agreement.pdf](http://unfccc.int/files/essential_background/convention/application/pdf/english_paris_agreement.pdf) (accessed July 7, 2017).
- (2) Klare, M. *Resource Wars: The New Landscape of Global Conflict*; Henry Holt and Company: New York, 2002.
- (3) Bannon, I.; Collier, P. *Natural Resources and Violent Conflict: Options and Actions*; World Bank Publications: WA, 2003.
- (4) Bertuccioli, L.; Chan, A.; Hart, D.; Lehner, F.; Madden, B.; Standen, E. *Final report in fuel cells and hydrogen joint undertaking: Study on development of water electrolysis in the EU*; E4tech Sarl; Element Energy Ltd., 2014.
- (5) Edwards, P. P.; Kuznetsov, V. L.; David, W. I. F.; Brandon, N. P. Hydrogen and fuel cells: towards a sustainable energy future. *Energy Policy* **2008**, 36, 4356–4362.
- (6) Momirlan, M.; Veziroglu, T. N. The properties of hydrogen as fuel tomorrow in sustainable energy system for a cleaner planet. *Int. J. Hydrogen Energy* **2005**, 30, 795–802.
- (7) Center for Transportation and the Environment, *International Fuel Cell Bus Workshop Report*. 2016; <http://www.cte.tv/wp-content/uploads/2016/12/FCBW-Report.pdf> (accessed July 7, 2017).
- (8) Alstom Holding, *Alstom's hydrogen train Coradia iLint first successful run at 80 km/h*. 2017; [http://www.alstom.com/press-](http://www.alstom.com/press-centre/2017/03/alstoms-hydrogen-train-coradia-ilint-first-successful-run-at-80-kmh)

[centre/2017/03/alstoms-hydrogen-train-coradia-ilint-first-successful-run-at-80-kmh](http://www.alstom.com/press-centre/2017/03/alstoms-hydrogen-train-coradia-ilint-first-successful-run-at-80-kmh) (accessed July 7, 2017).

(9) Dunn, S. Hydrogen futures: toward a sustainable energy system. *Int. J. Hydrogen Energy* **2002**, 27, 235–264.

(10) Götz, M.; Lefebvre, J.; Mörs, F.; Koch, A. M.; Graf, F.; Bajohr, S.; Reimert, R.; Kolb, T. Renewable Power-to-Gas: A technological and economic review. *Renewable Energy* **2016**, 85, 1371–1390.

(11) Stoll, J.; Vrabec, J.; Hasse, H. Vapor-liquid equilibria of mixtures containing nitrogen, oxygen, carbon dioxide, and ethane. *AIChE J.* **2003**, 49, 2187–2198.

(12) Vrabec, J.; Stoll, J.; Hasse, H. Molecular models of unlike interactions in fluid mixtures. *Mol. Simul.* **2005**, 31, 215–221.

(13) Huang, Y.-L.; Vrabec, J.; Hasse, H. Prediction of ternary vapor-liquid equilibria for 33 systems by molecular simulation. *Fluid Phase Equilib.* **2009**, 287, 62–69.

(14) Eckl, B.; Schnabel, T.; Vrabec, J.; Wendland, M.; Hasse, H. Thermophysical properties of dry and humid air by molecular simulation including dew point calculations with the Mollier ensemble. *Ind. Eng. Chem. Res.* **2009**, 48, 10110–10119.

(15) Vrabec, J.; Kedia, G. K.; Buchhauser, U.; Meyer-Pittroff, R.; Hasse, H. Thermodynamic models for vapor-liquid equilibria of nitrogen+ oxygen+ carbon dioxide at low temperatures. *Cryogenics* **2009**, 49, 72–79.

(16) Tenorio, M.-J.; Parrott, A. J.; Calladine, J. A.; Sanchez-Vicente, Y.; Cresswell, A. J.; Graham, R. S.; Drage, T. C.; Poliakoff, M.; Ke, J.; George, M. W. Measurement of the vapour-liquid equilibrium of binary and ternary mixtures of CO<sub>2</sub>, N<sub>2</sub> and H<sub>2</sub>, systems which are of relevance to CCS technology. *Int. J. Greenhouse Gas Control* **2015**, 41, 68–81.

(17) Cresswell, A. J.; Wheatley, R. J.; Wilkinson, R. D.; Graham, R. S. Molecular simulation of the thermophysical properties and phase behaviour of impure CO<sub>2</sub> relevant to CCS. *Faraday Discuss.* **2016**, 192, 415–436.

(18) Diamantonis, N. I.; Economou, I. G. Evaluation of statistical associating fluid theory (SAFT) and perturbed chain-SAFT equations of state for the calculation of thermodynamic derivative properties of fluids related to carbon capture and sequestration. *Energy Fuels* **2011**, 25, 3334–3343.

(19) Diamantonis, N. I.; Boulougouris, G. C.; Mansoor, E.; Tsangaris, D. M.; Economou, I. G. Evaluation of cubic, SAFT, and PC-SAFT equations of state for the vapor-liquid equilibrium modeling of CO<sub>2</sub> mixtures with other gases. *Ind. Eng. Chem. Res.* **2013**, 52, 3933–3942.

(20) Sun, R.; Lai, S.; Dubessy, J. Calculations of vapor-liquid equilibria of the H<sub>2</sub>O–N<sub>2</sub> and H<sub>2</sub>O–H<sub>2</sub> systems with improved SAFT-LJ EOS. *Fluid Phase Equilib.* **2015**, 390, 23–33.

(21) Kunz, O.; Wagner, W. The GERG-2008 wide-range equation of state for natural gases and other mixtures: an expansion of GERG-2004. *J. Chem. Eng. Data* **2012**, 57, 3032–3091.

(22) Gernert, J.; Span, R. EOS-CG: A Helmholtz energy mixture model for humid gases and CCS mixtures. *J. Chem. Thermodyn.* **2016**, 93, 274–293.

(23) Allen, M. P.; Tildesley, D. J. *Computer Simulation of Liquids*; Oxford University Press: Oxford, 1989.

(24) Vrabec, J.; Stoll, J.; Hasse, H. A set of molecular models for symmetric quadrupolar fluids. *J. Phys. Chem. B* **2001**, 105, 12126–12133.

(25) Windmann, T.; Linnemann, M.; Vrabec, J. Fluid Phase Behavior of Nitrogen, Acetone and Oxygen. Acetone by Molecular Simulation, Experiment and the Peng–Robinson Equation of State. *J. Chem. Eng. Data* **2014**, 59, 28–38.

(26) Elts, E.; Windmann, T.; Staak, D.; Vrabec, J. Fluid phase behavior from molecular simulation: Hydrazine, Monomethylhydrazine, Dimethylhydrazine and binary mixtures containing these compounds. *Fluid Phase Equilib.* **2012**, 322, 79–91.

(27) Huang, Y.-L.; Miroshnichenko, S.; Hasse, H.; Vrabec, J. Henry's law constant from molecular simulation: a systematic study of 95 systems. *Int. J. Thermophys.* **2009**, 30, 1791–1810.

- (28) Vrabec, J.; Huang, Y.-L.; Hasse, H. Molecular models for 267 binary mixtures validated by vapor-liquid equilibria: A systematic approach. *Fluid Phase Equilib.* **2009**, *279*, 120–135.
- (29) Abascal, J. L. F.; Vega, C. A general purpose model for the condensed phases of water: TIP4P/2005. *J. Chem. Phys.* **2005**, *123*, 234505.
- (30) Vega, C.; Abascal, J. L. F. Simulating water with rigid non-polarizable models: a general perspective. *Phys. Chem. Chem. Phys.* **2011**, *13*, 19663–19688.
- (31) Shvab, I.; Sadus, R. J. Atomistic water models: Aqueous thermodynamic properties from ambient to supercritical conditions. *Fluid Phase Equilib.* **2016**, *407*, 7–30.
- (32) Köster, A.; Spura, T.; Rutkai, G.; Kessler, J.; Wiebeler, H.; Vrabec, J.; Kühne, T. D. Assessing the accuracy of improved force-matched water models derived from Ab initio molecular dynamics simulations. *J. Comput. Chem.* **2016**, *37*, 1828–1838.
- (33) Nagashima, H.; Tsuda, S.; Tsuboi, N.; Koshi, M.; Hayashi, K.; Tokumasu, T. An analysis of quantum effects on the thermodynamic properties of cryogenic hydrogen using the path integral method. *J. Chem. Phys.* **2014**, *140*, 134506.
- (34) Leachman, J. W.; Jacobsen, R. T.; Penoncello, S. G.; Lemmon, E. W. Fundamental equations of state for parahydrogen, normal hydrogen, and orthohydrogen. *J. Phys. Chem. Ref. Data* **2009**, *38*, 721–748.
- (35) Hirschfelder, J.; Curtiss, C. F.; Bird, R. B. *Molecular Theory of Gases and Liquids*; John Wiley & Sons: New York, 1964.
- (36) Marx, D.; Nielaba, P. Path-integral Monte Carlo techniques for rotational motion in two dimensions: Quenched, annealed, and no-spin quantum-statistical averages. *Phys. Rev. A: At., Mol., Opt. Phys.* **1992**, *45*, 8968–8971.
- (37) Buch, V. Path integral simulations of mixed *para*-D<sub>2</sub> and *ortho*-D<sub>2</sub> clusters: The orientational effects. *J. Chem. Phys.* **1994**, *100*, 7610–7629.
- (38) Darkrim, F.; Levesque, D. Monte Carlo simulations of hydrogen adsorption in single-walled carbon nanotubes. *J. Chem. Phys.* **1998**, *109*, 4981–4984.
- (39) Belof, J. L.; Stern, A. C.; Space, B. An accurate and transferable intermolecular diatomic hydrogen potential for condensed phase simulation. *J. Chem. Theory Comput.* **2008**, *4*, 1332–1337.
- (40) Engin, C.; Vrabec, J.; Hasse, H. On the difference between a point multipole and an equivalent linear arrangement of point charges in force field models for vapour-liquid equilibria; partial charge based models for 59 real fluids. *Mol. Phys.* **2011**, *109*, 1975–1982.
- (41) Schnabel, T.; Vrabec, J.; Hasse, H. Unlike Lennard-Jones parameters for vapor-liquid equilibria. *J. Mol. Liq.* **2007**, *135*, 170–178.
- (42) Frenkel, D.; Smit, B. *Understanding Molecular Simulation: From Algorithms to Applications*; Academic Press: San Diego, 2002.
- (43) Deublein, S.; Eckl, B.; Stoll, J.; Lishchuk, S. V.; Guevara-Carrion, G.; Glass, C. W.; Merker, T.; Bernreuther, M.; Hasse, H.; Vrabec, J. *ms2*: A molecular simulation tool for thermodynamic properties. *Comput. Phys. Commun.* **2011**, *182*, 2350–2367.
- (44) Glass, C. W.; Reiser, S.; Rutkai, G.; Deublein, S.; Köster, A.; Guevara-Carrion, G.; Wafai, A.; Horsch, M.; Bernreuther, M.; Windmann, T.; Hasse, H.; Vrabec, J. *ms2*: A molecular simulation tool for thermodynamic properties, new version release. *Comput. Phys. Commun.* **2014**, *185*, 3302–3306.
- (45) Rutkai, G.; Köster, A.; Guevara-Carrion, G.; Janzen, T.; Schappals, M.; Glass, C. W.; Bernreuther, M.; Wafai, A.; Stephan, S.; Kohns, M.; Reiser, S.; Deublein, S.; Horsch, M.; Hasse, H.; Vrabec, J. *ms2*: A molecular simulation tool for thermodynamic properties, release 3.0. *Comput. Phys. Commun.* **2017**, *221*, 343–351.
- (46) Lustig, R. Angle-average for the powers of the distance between two separated vectors. *Mol. Phys.* **1988**, *65*, 175–179.
- (47) Flyvbjerg, H.; Petersen, H. G. Error estimates on averages of correlated data. *J. Chem. Phys.* **1989**, *91*, 461–466.
- (48) Vrabec, J.; Hasse, H. Grand Equilibrium: vapour-liquid equilibria by a new molecular simulation method. *Mol. Phys.* **2002**, *100*, 3375–3383.
- (49) Widom, B. Some topics in the theory of fluids. *J. Chem. Phys.* **1963**, *39*, 2808–2812.
- (50) Shing, K. S.; Gubbins, K. E.; Lucas, K. Henry constants in non-ideal fluid mixtures: computer simulation and theory. *Mol. Phys.* **1988**, *65*, 1235–1252.
- (51) Gross, J.; Sadowski, G. Perturbed-chain SAFT: An equation of state based on a perturbation theory for chain molecules. *Ind. Eng. Chem. Res.* **2001**, *40*, 1244–1260.
- (52) Gross, J.; Sadowski, G. Application of the perturbed-chain SAFT equation of state to associating systems. *Ind. Eng. Chem. Res.* **2002**, *41*, 5510–5515.
- (53) Gross, J.; Vrabec, J. An equation-of-state contribution for polar components: Dipolar molecules. *AIChE J.* **2006**, *52*, 1194–1204.
- (54) Gross, J. An equation-of-state contribution for polar components: Quadrupolar molecules. *AIChE J.* **2005**, *51*, 2556–2568.
- (55) Vrabec, J.; Gross, J. Vapor-liquid equilibria simulation and an equation of state contribution for dipole-quadrupole interactions. *J. Phys. Chem. B* **2008**, *112*, 51–60.
- (56) Kleiner, M.; Sadowski, G. Modeling of polar systems using PCP-SAFT: an approach to account for induced-association interactions. *J. Phys. Chem. C* **2007**, *111*, 15544–15553.
- (57) Tumakaka, F.; Gross, J.; Sadowski, G. Thermodynamic modeling of complex systems using PC-SAFT. *Fluid Phase Equilib.* **2005**, *228*, 89–98.
- (58) Aasen, A.; Hammer, M.; Skaugen, G.; Jakobsen, J. P.; Wilhelmsen, Ø. Thermodynamic models to accurately describe the PVT<sub>xy</sub>-behavior of water/carbon dioxide mixtures. *Fluid Phase Equilib.* **2017**, *442*, 125–139.
- (59) Stavrou, M.; Lampe, M.; Bardow, A.; Gross, J. Continuous molecular targeting-computer-aided molecular design (CoMT-CAMD) for simultaneous process and solvent design for CO<sub>2</sub> capture. *Ind. Eng. Chem. Res.* **2014**, *53*, 18029–18041.
- (60) Kiesow, K.; Tumakaka, F.; Sadowski, G. Experimental investigation and prediction of oiling out during crystallization process. *J. Cryst. Growth* **2008**, *310*, 4163–4168.
- (61) Vinš, V.; Hrubý, J. Solubility of nitrogen in one-component refrigerants: Prediction by PC-SAFT EoS and a correlation of Henry's law constants. *Int. J. Refrig.* **2011**, *34*, 2109–2117.
- (62) Peng, D.-Y.; Robinson, D. B. A new two-constant equation of state. *Ind. Eng. Chem. Fundam.* **1976**, *15*, 59–64.
- (63) Lopez-Echeverry, J. S.; Reif-Acherman, S.; Araujo-Lopez, E. Peng-Robinson equation of state: 40 years through cubics. *Fluid Phase Equilib.* **2017**, *447*, 39–71.
- (64) Soave, G. Equilibrium constants from a modified Redlich-Kwong equation of state. *Chem. Eng. Sci.* **1972**, *27*, 1197–1203.
- (65) Mathias, P. M.; Copeman, T. W. Extension of the Peng-Robinson equation of state to complex mixtures: evaluation of the various forms of the local composition concept. *Fluid Phase Equilib.* **1983**, *13*, 91–108.
- (66) Stryjek, R.; Vera, J. H. PRSV: An improved Peng-Robinson equation of state for pure compounds and mixtures. *Can. J. Chem. Eng.* **1986**, *64*, 323–333.
- (67) Twu, C. H.; Coon, J. E.; Cunningham, J. R. A new generalized alpha function for a cubic equation of state Part 1. Peng-Robinson equation. *Fluid Phase Equilib.* **1995**, *105*, 49–59.
- (68) *Dortmund Data Base*, version 7.3.0.459; Dortmund Data Bank, 2015.
- (69) Sandler, S. I. *Chemical, Biochemical, And Engineering Thermodynamics*; John Wiley & Sons: Hoboken, 2006.
- (70) Wagner, W.; Prüss, A. The IAPWS formulation 1995 for the thermodynamic properties of ordinary water substance for general and scientific use. *J. Phys. Chem. Ref. Data* **2002**, *31*, 387–535.
- (71) Span, R.; Wagner, W. A new equation of state for carbon dioxide covering the fluid region from the triple-point temperature to 1100 K at pressures up to 800 MPa. *J. Phys. Chem. Ref. Data* **1996**, *25*, 1509–1596.
- (72) Eubanks, L. S. Vapor-liquid equilibria in the system hydrogen-nitrogen-carbon monoxide. Ph.D. Thesis, Rice University, 1957.



- (73) Akers, W. W.; Eubanks, L. S. Vapor-Liquid Equilibria in the System Hydrogen-Nitrogen-Carbon Monoxide. *Adv. Cryog. Eng.* **1960**, *3*, 275–293.
- (74) Streett, W. B.; Calado, J. C. G. Liquid-vapour equilibrium for hydrogen + nitrogen at temperatures from 63 to 110 K and pressures to 57 MPa. *J. Chem. Thermodyn.* **1978**, *10*, 1089–1100.
- (75) Xiao, J.; Liu, K. Measurement and correlation of vapor - liquid equilibrium data in H<sub>2</sub> - N<sub>2</sub> - Ar system. *J. Chem. Eng. (China)* **1990**, *8*, 8–12.
- (76) Span, R.; Lemmon, E. W.; Jacobsen, R. T.; Wagner, W.; Yokozeki, A. A reference equation of state for the thermodynamic properties of nitrogen for temperatures from 63.151 to 1000 K and pressures to 2200 MPa. *J. Phys. Chem. Ref. Data* **2000**, *29*, 1361–1433.
- (77) Calado, J. C. G.; Streett, W. B. Liquid-vapor equilibrium in the system H<sub>2</sub> + Ar at temperatures from 83 to 141 K and pressures to 52 MPa. *Fluid Phase Equilib.* **1979**, *2*, 275–282.
- (78) Ostronov, M. G.; Shatskaya, L. V.; Finyagina, R. A.; Brodskaya, L. F.; Zhirnova, N. A. Gas-Liquid Phase Equilibrium in the Argon-Hydrogen System at Intermediate Pressures. *Russ. J. Phys. Chem.* **1977**, *51*, 1407–1409.
- (79) Volk, H.; Halsey, G. D., Jr. Solubility of hydrogen and deuterium in liquid argon. *J. Chem. Phys.* **1960**, *33*, 1132–1139.
- (80) Mullins, J. C.; Ziegler, W. T. Phase equilibria in the argon-helium and argon-hydrogen systems from 68 to 108 K and pressures to 120 atm. *Adv. Cryog. Eng.* **1965**, *10*, 171–181.
- (81) DeVaney, W.; Berryman, J. M.; Kao, P.-L.; Eakin, B. *High temperature VLE measurements for substitute gas components*; GPA Research Report RR-30; Gas Processors Association, 1978.
- (82) Gillespie, P. C.; Wilson, G. M. *Vapor-Liquid Equilibrium Data on Water-Substitute Gas Components: N<sub>2</sub>-H<sub>2</sub>O, H<sub>2</sub>-H<sub>2</sub>O, CO-H<sub>2</sub>O, H<sub>2</sub>-CO-H<sub>2</sub>O, and H<sub>2</sub>S-H<sub>2</sub>O*. GPA Research Report RR-48; Gas Processors Association, 1982.
- (83) Ipat'ev, V. V.; Teodorovich, V. P. Solubility of hydrogen in water under pressure at elevated temperatures. *Zhur. Obsh. Khim* **1934**, *4*, 395–397.
- (84) Kling, G.; Maurer, G. The solubility of hydrogen in water and in 2-aminoethanol at temperatures between 323 and 423 K and pressures up to 16 MPa. *J. Chem. Thermodyn.* **1991**, *23*, 531–541.
- (85) Maslennikova, V. Y.; Goryunova, N. P.; Subbotina, L. A.; Tsiklis, D. S. The solubility of water in compressed hydrogen. *Russ. J. Phys. Chem.* **1976**, *50*, 240–243.
- (86) Dodge, B. F. Isotherms and isobars for air separation studies. *Chem. Metall. Eng.* **1928**, *35*, 622.
- (87) Baidakov, V. G.; Kaverin, A. M.; Andbaeva, V. N. The liquid-gas interface of oxygen-nitrogen solutions: 1. Surface tension. *Fluid Phase Equilib.* **2008**, *270*, 116–120.
- (88) Maslennikova, V. Y.; Vdovina, N. A.; Tsiklis, D. S. The solubility of water in compressed nitrogen. *Russ. J. Phys. Chem.* **1971**, *45*, 1354.
- (89) Maslennikova, V. Y. The solubility of nitrogen in water. *Trudy GIAP, Moscow* **1971**, *12*, 82–87.
- (90) Saddington, A. W.; Krause, N. W. Vapor-Liquid Equilibria in the System Nitrogen-Water. *J. Am. Chem. Soc.* **1934**, *56*, 353–361.
- (91) Japas, M. L.; Franck, E. U. High Pressure Phase Equilibria and PVT-Data. of the Water-Nitrogen System to 673 K and 250 MPa. *Ber. Bunsenges. Phys. Chem.* **1985**, *89*, 793–800.
- (92) Narinskii, G. B. Liquid-vapor equilibrium in argon-nitrogen system. I. Experimental data and their verification. *Russ. J. Phys. Chem.* **1966**, *40*, 1093–1096.
- (93) Liu, K.; Wang, W. VLE Measurement and Correlation of N<sub>2</sub>-Ar-CH<sub>4</sub> System at 122.89 K. *J. Chem. Eng. (China)* **1988**, *16*, 58–63.
- (94) Bourbo, P.; Ischkin, I. Study of the vapor-liquid equilibrium of the system argon-oxygen. *Phys. Z. Sowjetunion* **1936**, *10*, 271–291.
- (95) Baba-Ahmed, A. Appareillage pour l'étude des équilibre liquide-vapeur dans le domaine cryogénique conception et développement. (Equipment for the study of equilibrium liquid-vapor in the cryogenic field design and development.) Ph.D. Thesis, Ecole des Mines de Paris, 1999.
- (96) Narinskii, G. B. Investigation of the liquid-vapor equilibrium in the oxygen-argon system. *Kislород* **1957**, *10*, 9–16.
- (97) Bennett, C. O.; Dodge, B. F. Compressibilities of mixtures of hydrogen and nitrogen above 1000 atm. *Ind. Eng. Chem.* **1952**, *44*, 180–185.
- (98) Verschoyle, T. T. H. Isotherms of Hydrogen, of Nitrogen, and of Hydrogen-Nitrogen Mixtures, at 0° and 20° C., up to a Pressure of 200 atm. *Proc. R. Soc. London, Ser. A* **1926**, *111*, 552–576.
- (99) Zandbergen, P.; Beenakker, J. J. M. Experimental determination of the volume change on mixing for gaseous N<sub>2</sub>-H<sub>2</sub>, Ar-H<sub>2</sub> and Ar-N<sub>2</sub> between 170 and 292° K up to 100 ATM. *Physica* **1967**, *33*, 343–365.
- (100) Kuenen, J. P.; Verschoyle, T.; van Urk, A. T. Isotherms of Diatomic Substances and their Binary Mixtures. XX. The Critical Curve of Oxygen - Nitrogen Mixtures, the Critical Phenomena and some Isotherms of Two Mixtures of 50% and 75% by Volume of Oxygen in the Neighborhood of the Critical Region. *Proc. R. Acad.* **1922**, *22*, 49–64.
- (101) Palavra, A. M. Effect of pressure and temperature on excess properties in the system argon–nitrogen. M.Sc. Thesis, Universidade Tecnica De Lisboa, 1979.
- (102) Crain, R. W., Jr; Sonntag, R. E. *Advances in Cryogenic Engineering*; Springer, New York, 1966; pp 379–391.
- (103) Masson, I.; Dolley, L. G. F. The Pressures of Gaseous Mixtures. *Proc. R. Soc. London, Ser. A* **1923**, *103*, 524–538.
- (104) Fernández-Prini, R.; Alvarez, J. L.; Harvey, A. H. Henry's constants and vapor-liquid distribution constants for gaseous solutes in H<sub>2</sub>O and D<sub>2</sub>O at high temperatures. *J. Phys. Chem. Ref. Data* **2003**, *32*, 903–916.
- (105) *Guideline on the Henry's Constant and Vapor-Liquid Distribution Constant for Gases in H<sub>2</sub>O and D<sub>2</sub>O at High Temperatures*; International Association for the Properties of Water and Steam, 2004.
- (106) Morris, D. R.; Yang, L.; Giraudeau, F.; Sun, X.; Steward, F. R. Henry's law constant for hydrogen in natural water and deuterium in heavy water. *Phys. Chem. Chem. Phys.* **2001**, *3*, 1043–1046.
- (107) Alvarez, J.; Fernández-Prini, R. A semiempirical procedure to describe the thermodynamics of dissolution of non-polar gases in water. *Fluid Phase Equilib.* **1991**, *66*, 309–326.
- (108) Rettich, T. R.; Battino, R.; Wilhelm, E. Solubility of gases in liquids. XVI. Henry's law coefficients for nitrogen in water at 5 to 50° C. *J. Solution Chem.* **1984**, *13*, 335–348.
- (109) Cosgrove, B. A.; Walkley, J. Solubilities of gases in H<sub>2</sub>O and <sup>2</sup>H<sub>2</sub>O. *J. Chromatogr. A* **1981**, *216*, 161–167.
- (110) Alvarez, J.; Crovetto, R.; Fernández-Prini, R. The dissolution of N<sub>2</sub> and of H<sub>2</sub> in water from room temperature to 640 K. *Ber. Bunsenges. Phys. Chem.* **1988**, *92*, 935–940.
- (111) Rettich, T. R.; Battino, R.; Wilhelm, E. Solubility of gases in liquids. 22. High-precision determination of Henry's law constants of oxygen in liquid water from T= 274 K to T= 328 K. *J. Chem. Thermodyn.* **2000**, *32*, 1145–1156.
- (112) Benson, B. B.; Krause, D.; Peterson, M. A. The solubility and isotopic fractionation of gases in dilute aqueous solution. I. Oxygen. *J. Solution Chem.* **1979**, *8*, 655–690.
- (113) Rettich, T. R.; Handa, Y. P.; Battino, R.; Wilhelm, E. Solubility of gases in liquids. 13. High-precision determination of Henry's constants for methane and ethane in liquid water at 275 to 328 K. *J. Phys. Chem.* **1981**, *85*, 3230–3237.
- (114) Cramer, S. D. The solubility of oxygen in brines from 0 to 300° C. *Ind. Eng. Chem. Process Des. Dev.* **1980**, *19*, 300–305.
- (115) Rettich, T. R.; Battino, R.; Wilhelm, E. Solubility of gases in liquids. 18. High-precision determination of Henry fugacities for argon in liquid water at 2 to 40° C. *J. Solution Chem.* **1992**, *21*, 987–1004.
- (116) Krause, D.; Benson, B. B. The solubility and isotopic fractionation of gases in dilute aqueous solution. IIa. Solubilities of the noble gases. *J. Solution Chem.* **1989**, *18*, 823–873.
- (117) Potter, R. W.; Clynnne, M. A. The solubility of the noble gases He, Ne, Ar, Kr, and Xe in water up to the critical point. *J. Solution Chem.* **1978**, *7*, 837–844.

- (118) Crovetto, R.; Fernández-Prini, R.; Japas, M. L. Solubilities of inert gases and methane in H<sub>2</sub>O and in D<sub>2</sub>O in the temperature range of 300 to 600 K. *J. Chem. Phys.* **1982**, *76*, 1077–1086.
- (119) Fastovskii, V. G.; Petrovskii, Y. V. A study of the vapor-liquid equilibrium in the system oxygen-argon-nitrogen. *Zh. Fiz. Khim.* **1957**, *31*, 836–841.
- (120) Lemmon, E. W.; Jacobsen, R. T.; Penoncello, S. G.; Friend, D. G. Thermodynamic properties of air and mixtures of nitrogen, argon, and oxygen from 60 to 2000 K at pressures to 2000 MPa. *J. Phys. Chem. Ref. Data* **2000**, *29*, 331–385.
- (121) Holborn, L.; Schultze, H. Über die Druckwage und die Isothermen von Luft, Argon und Helium zwischen 0 und 200° C. *Ann. Phys.* **1915**, *352*, 1089–1111.
- (122) Kozlov, A. Experimental investigation of the specific volumes of air in the 20–600 °C temperature range and 20–700 bar pressure range. Ph.D. Thesis, Moscow, 1968.
- (123) Diller, D. E.; Aragon, A. S.; Laesecke, A. Measurements of the viscosity of compressed liquid air at temperatures between 70 and 130 K. *Cryogenics* **1991**, *31*, 1070–1072.
- (124) Japas, M. L.; Franck, E. U. High Pressure Phase Equilibria and PVT-Data of the Water-Oxygen System Including Water-Air to 673 K and 250 MPa. *Ber. Bunsenges. Phys. Chem.* **1985**, *89*, 1268–1275.
- (125) Ulbig, P.; Trusler, M.; Wendland, M.; Wöll, O.; Nieto de Castro, C. A. *Summary report on experimental results for thermodynamic and transport properties, AA-CAES, Deliverable Report D4.1.* 2005.

### 3.2 *ms2*: A molecular simulation tool for thermodynamic properties, new version release

C. W. Glass, S. Reiser, G. Rutkai, S. Deublein, A. Köster, G. Guevara-Carrion, A. Wafai, M. Horsch, M. Bernreuther, T. Windmann, H. Hasse, J. Vrabec, *Computer Physics Communications* 185:3302-3306, 2014.

DOI: [doi.org/10.1016/j.cpc.2014.07.012](https://doi.org/10.1016/j.cpc.2014.07.012)

Nachgedruckt mit Erlaubnis von Elsevier (Copyright 2014).

In dieser Veröffentlichung wurde die erste Weiterentwicklung des Simulationsprogramms *ms2* beschrieben. Wichtige Funktionen, wie z.B. der Lustig-Formalismus zur Berechnung der partiellen Ableitungen der Helmholtzenergie im kanonischen (*NVT*) Ensemble [Lus11, Lus12], die Ewald-Summation für die langreichweitigen Wechselwirkungen von Ionen [AT89, FS02] oder die radiale Paarverteilungsfunktion, wurden implementiert. Durch die Zusammenarbeit mit dem Höchstleistungsrechenzentrum Stuttgart konnte die hybride Parallelisierung eingeführt und damit die Skalierbarkeit des Programms verbessert werden.

Der Autor der vorliegenden Dissertation hat umfassende Funktionstests des Simulationsprogramms *ms2* im Hinblick auf die Simulation der partiellen Ableitungen der Helmholtzenergie, die Parallelisierung, die Vektorisierung und weitere Funktionen durchgeführt. Er assistierte Dr. Gábor Rutkai bei der Implementierung der partiellen Ableitungen der Helmholtzenergie in *NVT* Ensemble Simulationen. Er wurde während des gesamten Prozesses von Prof. Jadran Vrabec betreut.



Contents lists available at ScienceDirect

## Computer Physics Communications

journal homepage: [www.elsevier.com/locate/cpc](http://www.elsevier.com/locate/cpc)

## ms2: A molecular simulation tool for thermodynamic properties, new version release<sup>☆</sup>



Colin W. Glass<sup>a</sup>, Steffen Reiser<sup>b</sup>, Gábor Rutkai<sup>c</sup>, Stephan Deublein<sup>b</sup>, Andreas Köster<sup>c</sup>, Gabriela Guevara-Carrion<sup>c</sup>, Amer Wafai<sup>a</sup>, Martin Horsch<sup>b</sup>, Martin Bernreuther<sup>a</sup>, Thorsten Windmann<sup>c</sup>, Hans Hasse<sup>b</sup>, Jadran Vrabec<sup>c,\*</sup>

<sup>a</sup> Höchstleistungsrechenzentrum Universität Stuttgart (HLRS), 70550 Stuttgart, Germany

<sup>b</sup> Lehrstuhl für Thermodynamik, Universität Kaiserslautern, 67653 Kaiserslautern, Germany

<sup>c</sup> Lehrstuhl für Thermodynamik und Energietechnik, Universität Paderborn, 33098 Paderborn, Germany

### ARTICLE INFO

#### Article history:

Received 6 January 2014

Received in revised form

10 June 2014

Accepted 14 July 2014

Available online 30 July 2014

#### Keywords:

Molecular simulation

Molecular dynamics

Monte Carlo

Vapor–liquid equilibrium

Transport properties

Massieu potential derivatives

### ABSTRACT

A new version release (2.0) of the molecular simulation tool *ms2* [S. Deublein et al., Comput. Phys. Commun. 182 (2011) 2350] is presented. Version 2.0 of *ms2* features a hybrid parallelization based on MPI and OpenMP for molecular dynamics simulation to achieve higher scalability. Furthermore, the formalism by Lustig [R. Lustig, Mol. Phys. 110 (2012) 3041] is implemented, allowing for a systematic sampling of Massieu potential derivatives in a single simulation run. Moreover, the Green–Kubo formalism is extended for the sampling of the electric conductivity and the residence time. To remove the restriction of the preceding version to electro-neutral molecules, Ewald summation is implemented to consider ionic long range interactions. Finally, the sampling of the radial distribution function is added.

#### Program summary

Program title: *ms2*

Catalogue identifier: AEJF\_v2\_0

Program summary URL: [http://cpc.cs.qub.ac.uk/summaries/AEJF\\_v2\\_0.html](http://cpc.cs.qub.ac.uk/summaries/AEJF_v2_0.html)

Program obtainable from: CPC Program Library, Queen's University, Belfast, N. Ireland

Licensing provisions: Standard CPC licence, <http://cpc.cs.qub.ac.uk/licence/licence.html>

No. of lines in distributed program, including test data, etc.: 50375

No. of bytes in distributed program, including test data, etc.: 345786

Distribution format: tar.gz

Programming language: Fortran90.

Computer: The simulation program *ms2* is usable on a wide variety of platforms, from single processor machines to modern supercomputers.

Operating system: Unix/Linux.

Has the code been vectorized or parallelized?: Yes: Message Passing Interface (MPI) protocol and OpenMP Scalability is up to 2000 cores.

RAM: *ms2* runs on single cores with 512 MB RAM. The memory demand rises with increasing number of cores used per node and increasing number of molecules.

Classification: 7.7, 7.9, 12.

External routines: Message Passing Interface (MPI)

<sup>☆</sup> This paper and its associated computer program are available via the Computer Physics Communication homepage on ScienceDirect (<http://www.sciencedirect.com/science/journal/00104655>).

\* Correspondence to: Warburger Str. 100, 33098 Paderborn, Germany. Tel.: +49 5251 60 2421; fax: +49 5251 60 3522.

E-mail address: [jadran.vrabec@upb.de](mailto:jadran.vrabec@upb.de) (J. Vrabec).

<http://dx.doi.org/10.1016/j.cpc.2014.07.012>

0010-4655/© 2014 Elsevier B.V. All rights reserved.



*Catalogue identifier of previous version:* AEJF\_v1\_0

*Journal reference of previous version:* Comput. Phys. Comm. 182 (2011) 2350

*Does the new version supersede the previous version?:* Yes.

*Nature of problem:* Calculation of application oriented thermodynamic properties for fluids consisting of rigid molecules: vapor–liquid equilibria of pure fluids and multi-component mixtures, thermal and caloric data as well as transport properties.

*Solution method:* Molecular dynamics, Monte Carlo, various classical ensembles, grand equilibrium method, Green–Kubo formalism, Lustig formalism

*Reasons for new version:* The source code was extended to introduce new features.

*Summary of revisions:* The new features of Version 2.0 include: Hybrid parallelization based on MPI and OpenMP for molecular dynamics simulation; Ewald summation for long range interactions; sampling of Massieu potential derivatives; extended Green–Kubo formalism for the sampling of the electric conductivity and the residence time; radial distribution function.

*Restrictions:* None. The system size is user-defined. Typical problems addressed by *ms2* can be solved by simulating systems containing typically 1000–4000 molecules.

*Unusual features:* Auxiliary feature tools are available for creating input files, analyzing simulation results and visualizing molecular trajectories.

*Additional comments:* Sample makefiles for multiple operation platforms are provided. Documentation is provided with the installation package and is available at <http://www.ms-2.de>.

*Running time:* The running time of *ms2* depends on the specified problem, the system size and the number of processes used in the simulation. E.g. running four processes on a “Nehalem” processor, simulations calculating vapor–liquid equilibrium data take between two and 12 hours, calculating transport properties between six and 24 hours. Note that the examples given above stand for the total running time as there is no post-processing of any kind involved in property calculations.

© 2014 Elsevier B.V. All rights reserved.

## 1. Introduction

Molecular modeling and simulation is a technology central to many areas of research in academia and industry. With the advance of computing power, the scope of application scenarios for molecular simulation is widening, both in terms of complexity of a given simulation and in terms of high throughput. Nowadays, e.g. the predictive simulation of entire phase equilibrium diagrams has become feasible. However, in order to rely on simulation results, the methodology needs to be sound and the implementation must be thoroughly verified. In its first release [1], we have introduced the molecular simulation tool *ms2*. Results from *ms2* have been verified and the implementation was found to be robust and efficient.

As described in Section 2, in Version 2.0 of the simulation tool *ms2* the existing molecular dynamics (MD) MPI parallelization was hybridized with OpenMP, leading to an improved performance on multi-core processors. Furthermore, the new release offers a wider scope of accessible properties. In particular, *ms2* was extended to calculate Massieu potential derivatives in a systematic manner, cf. Section 3. This augments the range of sampled properties significantly and, as was demonstrated in [2], it allows to straightforwardly develop competitive fundamental equations of state from a combination of experimental VLE data and molecular simulation results. Lastly, besides being now capable of simulating ionic substances, the time and memory demand for calculating transport properties was reduced significantly (Section 4).

*ms2* is freely available as an open source code for academic users at [www.ms-2.de](http://www.ms-2.de).

## 2. Hybrid MPI & OpenMP parallelization

The molecular simulation tool *ms2* focuses on thermodynamic properties of homogeneous fluids. Therefore, systems investigated with *ms2* typically contain on the order of  $10^3$  molecules. While

for Monte Carlo simulations a perfect scaling behavior up to large numbers of cores can be trivially achieved, MD domain decomposition – the de facto standard for highly scalable MD – is not feasible for such system sizes, because the cut-off radius is in the same range as half the edge length of the simulation volume. This excludes domain decomposition and limits the scalability of the MPI parallelization. The present release of *ms2* features an OpenMP parallelization, which was hybridized with MPI. At the point where MPI communication becomes a bottleneck, a single process still has enough load to distribute to multiple threads, improving scalability.

Three parts of *ms2* were parallelized with OpenMP: the interaction partner search, the energy and the force calculations. All OpenMP parallel regions rely on loop parallelism, as the compute intensive parts of the algorithm all feature a loop over the molecules. In the force calculation, race conditions need to be considered, because every calculated force is written to both interacting molecules. Introducing atomic updates or critical sections leads to massive overheads. Instead, it is more efficient to assign forces from individual interactions to the elements of a list (or an array) which is subsequently summed up. The same holds true for torques.

In Fig. 1 the speed-up of hybrid MPI/OpenMP vs. pure MPI is plotted for 2048 cores, varying the number of threads per MPI process and the number of molecules in the simulation volume. As can be seen, using 2 to 4 threads per MPI process delivers a speed-up of around 20% for 2048 cores. The evaluation of the hybrid parallelization algorithm was performed on a CRAY XE6 Supercomputer at the High Performance Computing Center in Stuttgart, which has an overall peak performance of one PFLOPS. It consists of 3552 nodes, each equipped with two AMD Opteron 6276 (Interlagos) processors. Each processor has 16 cores, sharing eight FPUs (Floating Point Units). Nodes are equipped with 32 GB RAM and are interconnected by a high-speed CRAY Gemini network. Additional

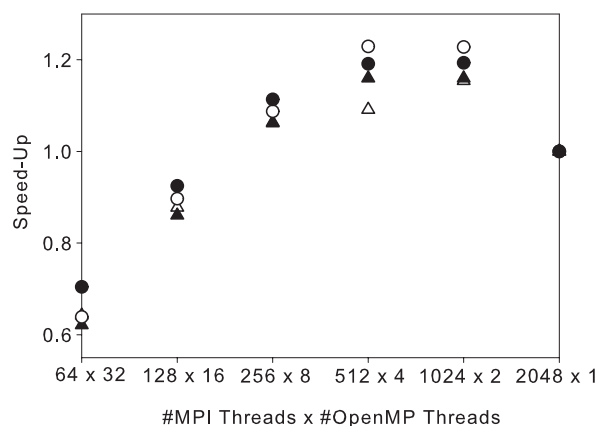


**Fig. 1.** Speed-up of hybrid MPI/OpenMP vs. pure MPI for 2048 cores, varying number of threads per MPI process and 8192 molecules (solid circles), 4096 molecules (empty circles), 2048 molecules (solid triangles), 1024 molecules (empty triangles).

**Table 1**

Runtime performance results with *ms2* version 2.0 and *gromacs* v4.6.5 [3] for MD simulations with pure water at 298.15 K and  $55.345 \text{ mol} \cdot \text{dm}^{-3}$ . The number of time steps was 100 000 for every simulation, the cut-off radius was identical for simulations with the same number of particles. All simulations were performed on the same computer cluster.

Cores	Threads	<i>N</i>	Gromacs / s	<i>ms2</i> (RF) / s	<i>ms2</i> (EW) / s
8	8 MPI	500	164	416	785
8	8 MPI	1000	299	874	1607
8	8 MPI	2000	1284	4461	6777
16	16 MPI	500	95	233	415
16	16 MPI	1000	166	477	848
16	16 MPI	2000	678	2298	3506
32	32 MPI	500	62	152	245
32	32 MPI	1000	106	296	487
32	32 MPI	2000	361	1286	1898
64	64 MPI	500	40	119	166
64	64 MPI	1000	65	228	324
64	64 MPI	2000	220	814	1261
128	128 MPI	500	38	105	131
128	128 MPI	1000	51	197	247
128	128 MPI	2000	147	557	727
8	1 MPI, 8 OMP/MPI	500	167	483	
8	1 MPI, 8 OMP/MPI	1000	323	975	
8	1 MPI, 8 OMP/MPI	2000	1416	4831	
16	2 MPI, 8 OMP/MPI	500	105	253	
16	2 MPI, 8 OMP/MPI	1000	186	517	
16	2 MPI, 8 OMP/MPI	2000	763	2514	
32	4 MPI, 8 OMP/MPI	500	75	167	
32	4 MPI, 8 OMP/MPI	1000	121	316	
32	4 MPI, 8 OMP/MPI	2000	418	1362	
64	8 MPI, 8 OMP/MPI	500	60	119	
64	8 MPI, 8 OMP/MPI	1000	92	217	
64	8 MPI, 8 OMP/MPI	2000	261	785	
128	16 MPI, 8 OMP/MPI	500	49	101	
128	16 MPI, 8 OMP/MPI	1000	74	172	
128	16 MPI, 8 OMP/MPI	2000	170	496	

(*N*) number of water molecules

(RF) simulations with reaction field correction

(EW) simulations with Ewald summation

runtime performance comparisons with the simulation tool *gromacs* [3] are listed in Table 1.

### 3. Massieu potential derivatives

*ms2* version 2.0 features evaluating free energy derivatives in a systematic manner, thus greatly extending the thermodynamic property types that can be sampled in single simulation runs. The approach is based on the fact that the fundamental equation of state contains the complete thermodynamic information about

a system, which can be expressed in terms of various thermodynamic potentials [4], e.g. internal energy  $E(N, V, S)$ , enthalpy  $H(N, p, S)$ , Helmholtz free energy  $F(N, V, T)$  or Gibbs free energy  $G(N, p, T)$ , with number of particles  $N$ , volume  $V$ , pressure  $p$ , temperature  $T$  and entropy  $S$ . These representations are equivalent in the sense that any other thermodynamic property is essentially a combination of derivatives of the chosen form with respect to its independent variables. The form  $F/T(N, V, 1/T)$ , known as the Massieu potential, is preferred in molecular simulations due to practical reasons [5,6]. The statistical mechanical formalism of

Lustig allows for the simultaneous sampling of any  $A_{mn}^r$  in a single NVT ensemble simulation for a given state point [5–8]

$$\frac{\partial^{m+n}(F/(RT))}{\partial \beta^m \partial \rho^n} \beta^m \rho^n \equiv A_{mn} = A_{mn}^i + A_{mn}^r, \quad (1)$$

where  $R$  is the gas constant,  $\beta \equiv 1/T$  and  $\rho \equiv N/V$ .  $A_{mn}$  can be separated into an ideal part  $A_{mn}^i$  and a residual part  $A_{mn}^r$  [9]. The calculation of the residual part is the target of molecular simulation and the derivatives  $A_{10}^r, A_{01}^r, A_{20}^r, A_{02}^r, A_{11}^r, A_{30}^r, A_{21}^r$  and  $A_{12}^r$  were implemented in *ms2* for NVT ensemble simulations. The ideal part can be obtained by independent methods, e.g. from spectroscopic data or ab initio calculations. However, it can be shown that for any  $A_{mn} = A_{mn}^i + A_{mn}^r$ , where  $n > 0$ , the ideal part is either zero or depends exclusively on the density, thus it is known by default [6]. Note that the calculation of  $A_{00}^r$  still requires additional concepts such as thermodynamic integration or particle insertion methods. From the first five derivatives  $A_{10}, A_{01}, A_{20}, A_{11}, A_{02}$  every measurable thermodynamic property can be expressed (see the supplementary material for a list of properties, [Appendix A](#)) with the exception of phase equilibria. A detailed description of the implementation is in the supplementary material, here, only an overview is provided.

The calculation of the derivatives up to the order of  $n = 2$  requires the explicit mathematical expression of  $\partial U/\partial V$  and  $\partial^2 U/\partial V^2$  with respect to the applied molecular interaction pair potential and has to be determined analytically beforehand [5,6]. The general formula for  $\partial^n U/\partial V^n$  can be found in Ref. [8]. For common molecular interaction pair potentials, like the Lennard-Jones (LJ) potential [10,11], describing repulsive and dispersive interactions, or Coulomb's law, describing electrostatic interactions between point charges, the analytical formulas for  $\partial U/\partial V$  and  $\partial^2 U/\partial V^2$  can be obtained straightforwardly.

As molecular simulation is currently limited to operate with considerably fewer particles than real systems, the effect of the small system size thus has to be counter-balanced with a contribution to  $U$  and  $\partial^n U/\partial V^n$  called long range correction (LRC) [10,11]. The mathematical form of the LRC depends on the molecular interaction potential and the cut-off method (site-site or center-of-mass cut-off mode) applied. For the LJ potential, the LRC scheme was well described in the literature for both the site-site [5,12] and the center-of-mass cut-off mode [8,13]. The reaction field method [14] was the default choice in the preceding version of *ms2* for the LRC of electrostatic interactions modeled by considering charge distributions on molecules. The usual implementation of the reaction field method combines the explicit and the LRC part in a single pair potential [14,15] from which  $\partial^n U/\partial V^n$  (including the LRC contribution) is directly obtainable. However, practical applications show that the electrostatic LRC of  $\partial U/\partial V$  and  $\partial^2 U/\partial V^2$  can be neglected in case of systems for which the reaction field method is an appropriate choice. E.g., the contribution of the electrostatic LRC for a liquid system ( $T = 298$  K and  $\rho = 45.86$  mol/l) consisting of only 200 water and 50 methanol molecules with a very short cut-off radius of 20% of the edge length of the simulation volume is still  $\ll 1\%$  for both  $\partial U/\partial V$  and  $\partial^2 U/\partial V^2$ . The supplementary material contains detailed elaborations on the LRC for the LJ potential (see [Appendix A](#)).

#### 4. Algorithmic developments

##### Transport property calculations

In *ms2*, transport properties are determined via equilibrium MD simulations by means of the Green–Kubo formalism [16]. This formalism offers a direct relationship between transport coefficients and the time integral of the autocorrelation function of the corresponding fluxes. An extended time step was defined

for the calculation of the fluxes, the autocorrelation functions and their integrals. The extended time step is  $n$  times longer than the specified MD time step, where  $n$  is a user defined variable. The autocorrelation functions are hence evaluated in every  $n$ th MD time step. As a consequence, the memory demand for the autocorrelation functions was reduced and the restart files, which contain the current state of the autocorrelation functions and time integrals, become accordingly smaller. In addition, the overall computing time of the associated MD simulation was reduced significantly.

##### Ewald summation

Ewald summation [10,11] was implemented for the calculation of electrostatic interactions between point charges. It extends the applicability of *ms2* to thermodynamic properties of e.g. ions in solutions. In Ewald summation, the electrostatic interactions according to Coulomb's law are divided into two contributions: short-range and long-range. The short-range term includes all charge–charge interactions at distances smaller than the cut-off radius. The remaining contribution is calculated in Fourier space and only the final value is transformed back into real space. This allows for an efficient calculation of the long-range interactions between the charges. The algorithm is well described in literature. Currently, some of the new features, the calculation of Massieu potential derivatives and Hybrid MPI & OpenMP Parallelization for MD, are not available together with Ewald summation.

#### 5. Property calculations

##### Radial distribution function

The radial distribution function (RDF)  $g(r)$  is a measure for the microscopic structure of matter. It is defined by the local number density around a given position within a molecule  $\rho^L(r)$  in relation to the overall number density  $\rho = N/V$

$$g(r) = \frac{\rho^L(r)}{\rho} = \frac{1}{\rho} \frac{dN(r)}{dV} = \frac{1}{4\pi r^2 \rho} \frac{dN(r)}{dr}. \quad (2)$$

Therein,  $dN(r)$  is the differential number of molecules in a spherical shell volume element  $dV$ , which has the width  $dr$  and is located at the distance  $r$  from the regarded position.  $g(r)$  can be evaluated for every molecule of a given species.

In the present release of *ms2*, RDF can be calculated during MD simulation runs for pure components and mixtures on the fly. RDF are sampled between all LJ sites. In order to evaluate RDF for arbitrary positions, say point charge sites, superimposed dummy LJ sites with the parameters  $\sigma = \epsilon = 0$  have to be introduced in the potential model file by the user.

##### Electric conductivity

The evaluation of the electric conductivity  $\sigma$  was implemented in *ms2* version 2.0, being a measure for the flow of ions in solution. The Green–Kubo formalism [16] offers a direct relationship between  $\sigma$  and the time-autocorrelation function of the electric current flux  $\mathbf{j}_e(t)$  [17]

$$\sigma = \frac{1}{3Vk_B T} \int_0^\infty \langle \mathbf{j}_e(t) \cdot \mathbf{j}_e(0) \rangle dt, \quad (3)$$

where  $k_B$  is Boltzmann's constant. The electric current flux is defined by the charge  $q_k$  of ion  $k$  and its velocity vector  $\mathbf{v}_k$  according to

$$\mathbf{j}_e(t) = \sum_{k=1}^{N_j} q_k \cdot \mathbf{v}_k(t), \quad (4)$$

where  $N_j$  is the number of molecules of component  $j$  in solution. Note that only the ions in the solution have to be considered, not the electro-neutral molecules. For better statistics,  $\sigma$  is sampled over all independent spatial elements of  $\mathbf{j}_e(t)$ .

#### Thermal conductivity of mixtures

In the previous version of *ms2* the determination of the thermal conductivity by means of the Green–Kubo formalism was implemented for pure substances only. In the present release, the calculation of the thermal conductivity was extended to multi-component mixtures. The thermal conductivity  $\lambda$  is given by the autocorrelation function of the elements of the microscopic heat flow  $J_q^x$

$$\lambda = \frac{1}{V k_B T^2} \int_0^\infty \langle J_q^x(t) \cdot J_q^x(0) \rangle dt. \quad (5)$$

In mixtures, energy transport and diffusion occur in a coupled manner, thus, the heat flow for a mixture of  $n$  components is given by [18]

$$\begin{aligned} \mathbf{J}_q = & \frac{1}{2} \sum_{i=1}^n \sum_{k=1}^{N_i} \left[ m_i^k (v_i^k)^2 + \mathbf{w}_i^k \mathbf{I}_i^k \mathbf{w}_i^k + \sum_{j=1}^n \sum_{l \neq k}^{N_j} u(r_{ij}^{kl}) \right] \cdot \mathbf{v}_i^k \\ & - \frac{1}{2} \sum_{i=1}^n \sum_{j=1}^n \sum_{k=1}^{N_i} \sum_{l \neq k}^{N_j} \mathbf{r}_{ij}^{kl} \cdot \left( \mathbf{v}_i^k \cdot \frac{\partial u(r_{ij}^{kl})}{\partial \mathbf{r}_{ij}^{kl}} + \mathbf{w}_i^k \mathbf{I}_i^{kl} \right) \\ & - \sum_{i=1}^n h_i \sum_{k=1}^{N_i} \mathbf{v}_i^k, \end{aligned} \quad (6)$$

where  $\mathbf{w}_i^k$  is the angular velocity vector of molecule  $k$  of component  $i$  and  $\mathbf{I}_i^k$  its matrix of angular momentum of inertia.  $u(r_{ij}^{kl})$  is the intermolecular potential energy and  $\mathbf{I}_{ij}^{kl}$  is the torque due to the interaction of molecules  $k$  and  $l$ . The indices  $i$  and  $j$  denote the components of the mixture.  $h_i$  is the partial molar enthalpy. It has to be specified as an input in the *ms2* parameter file and can be calculated from  $NpT$  simulations.

#### Residence time

The residence time  $\tau_j$  defines the average time span that a molecule of component  $j$  remains within a given distance  $r_{ij}$  around a specific molecule  $i$ . It is given by the autocorrelation function

$$\tau_j = \int_0^\infty \left\langle \frac{1}{n_{ij}(0)} \sum_{k=1}^{n_{ij}(0)} \Theta_k(t) \Theta_k(0) \right\rangle dt, \quad (7)$$

where  $t$  is the time,  $n_{ij}(0)$  the solvation number around molecule  $i$  at  $t = 0$  and  $\Theta$  is the Heaviside function, which yields unity, if the

two molecules are within the given distance, and zero otherwise. Following the proposal of Impey et al. [19], the residence time explicitly allows for short time periods during which the distance between the two molecules exceeds  $r_{ij}$ . Also, the solvation number  $n_{ij}$  can be evaluated on the fly

$$n_{ij} = 4\pi \rho_j \int_0^{r_{\min}} r^2 g_{ij}(r) dr, \quad (8)$$

where  $\rho_j$  is the number density of component  $j$  and  $r_{\min}$  is the distance up to which the solvation number is calculated.

#### Acknowledgments

The authors gratefully acknowledge financial support by BMBF under the grant “01IH13005A SkaSim: Skalierbare HPC-Software für molekulare Simulationen in der chemischen Industrie” and computational support by the High Performance Computing Center Stuttgart (HLRS) under the grant MMHBF2. The present research was conducted under the auspices of the Boltzmann-Zuse Society of Computational Molecular Engineering (BZS).

#### Appendix A. Supplementary data

Supplementary material related to this article can be found online at <http://dx.doi.org/10.1016/j.cpc.2014.07.012>.

#### References

- [1] S. Deublein, B. Eckl, J. Stoll, S.V. Lishchuk, G. Guevara-Carrion, C.W. Glass, T. Merker, M. Bernreuther, H. Hasse, J. Vrabec, *Comp. Phys. Comm.* 182 (2011) 2350–2367.
- [2] G. Rutkai, M. Thol, R. Lustig, R. Span, J. Vrabec, *J. Chem. Phys.* 139 (2013) 041102.
- [3] Gromacs molecular dynamics simulation package, <http://www.gromacs.org>.
- [4] A. Münster, *Classical Thermodynamics*, Wiley and Sons, Bristol, 1970.
- [5] R. Lustig, *Mol. Sim.* 37 (2011) 457–465.
- [6] R. Lustig, *Mol. Phys.* 110 (2012) 3041–3052.
- [7] R. Lustig, *J. Chem. Phys.* 100 (1994) 3048–3059.
- [8] R. Lustig, *J. Chem. Phys.* 100 (1994) 3060–3067.
- [9] J.S. Rowlinson, F.L. Swinton, *Liquids and Liquid Mixtures*, third ed., Butterworths, London, 1982.
- [10] M. Allen, D. Tildesley, *Computer Simulation of Liquids*, Clarendon Press, Oxford, 1987.
- [11] D. Frenkel, B. Smith, *Understanding Molecular Simulation*, Academic Press, San Diego, 1993.
- [12] K. Meier, S. Kabelac, *J. Chem. Phys.* 124 (2006) 064104.
- [13] R. Lustig, *Mol. Phys.* 65 (1988) 175–179.
- [14] J.A. Barker, R.O. Watts, *Mol. Phys.* 26 (1973) 789–792.
- [15] I.P. Omelyan, *Phys. Lett. A* 223 (1996) 295–302.
- [16] K. Gubbins, *Statistical Mechanics*, Burlington House, London, 1972.
- [17] J.P. Hansen, I.R. McDonald, *Theory of Simple Liquids*, Academic, New York, 1986.
- [18] D.J. Evans, W.B. Streett, *Mol. Phys.* 36 (1978) 161–176.
- [19] R. Impey, M. Madden, I. McDonald, *J. Phys. Chem.* 87 (1983) 5071.

### 3.3 *ms2*: A molecular simulation tool for thermodynamic properties, release 3.0

G. Rutkai, **A. Köster**, G. Guevara-Carrion, T. Janzen, M. Schappals, C. W. Glass, M. Bernreuther, A. Wafai, S. Stephan, M. Kohns, S. Reiser, S. Deublein, M. Horsch, H. Hasse, J. Vrabec, *Computer Physics Communications* 221:343-351, 2017.

DOI: [doi.org/10.1016/j.cpc.2017.07.025](https://doi.org/10.1016/j.cpc.2017.07.025)

Nachgedruckt mit Erlaubnis von Elsevier (Copyright 2017).

In dieser Arbeit wurden weitere neue Funktionen des Simulationsprogramms *ms2* präsentiert. Durch diese besteht die Möglichkeit sowohl für Molekulardynamik als auch für Monte Carlo Simulationen das mikrokanonische (*NVE*) Ensemble, das isobar-isenthalpe (*NpH*) Ensemble und die thermodynamische Integration zur Berechnung des chemischen Potentials zu nutzen. Weitere wichtige Implementationen umfassten u.a. den Lustig-Formalismus zur Berechnung der partiellen Ableitungen der Helmholtzenergie im *NVE* Ensemble [Lus11, Lus12], die Berechnung des osmotischen Drucks und die Auswertung von Wasserstoffbrückenbindungen. Um den Anforderungen neuer Hochleistungsrechner an große Simulationen zu genügen, wurde für die Molekulardynamik eine Funktion eingeführt, die die gleichzeitige Simulation einer beliebigen Anzahl von Zustandspunkten durch eine Programmausführung erlaubt.

Der Autor der vorliegenden Dissertation hat umfassende Funktionstests des Simulationsprogramms *ms2* im Hinblick auf die Simulationen im *NVE* und *NpH* Ensemble durchgeführt. Er assistierte Dr. Gábor Rutkai bei der Implementierung der partiellen Ableitungen der Helmholtzenergie für *NVE* Ensemble Simulationen, sowie bei der Implementierung der thermodynamischen Integration. Weiterhin führte der Autor die Implementierung des *NpH* Ensembles durch. Er konsolidierte das Manuskript und wurde während des gesamten Prozesses von Prof. Jadran Vrabec betreut.



Contents lists available at ScienceDirect

## Computer Physics Communications

journal homepage: [www.elsevier.com/locate/cpc](http://www.elsevier.com/locate/cpc)

## ms2: A molecular simulation tool for thermodynamic properties, release 3.0<sup>☆</sup>



Gábor Rutkai<sup>a</sup>, Andreas Köster<sup>a</sup>, Gabriela Guevara-Carrion<sup>a</sup>, Tatjana Janzen<sup>a</sup>, Michael Schappals<sup>b</sup>, Colin W. Glass<sup>c</sup>, Martin Bernreuther<sup>c</sup>, Amer Wafai<sup>c</sup>, Simon Stephan<sup>b</sup>, Maximilian Kohns<sup>b</sup>, Steffen Reiser<sup>b</sup>, Stephan Deublein<sup>b</sup>, Martin Horsch<sup>b</sup>, Hans Hasse<sup>b</sup>, Jadran Vrabec<sup>a,\*</sup>

<sup>a</sup> Lehrstuhl für Thermodynamik und Energietechnik, Universität Paderborn, 33098 Paderborn, Germany

<sup>b</sup> Lehrstuhl für Thermodynamik, Universität Kaiserslautern, 67653 Kaiserslautern, Germany

<sup>c</sup> Höchstleistungsrechenzentrum Universität Stuttgart (HLRS), 70550 Stuttgart, Germany

## ARTICLE INFO

## Article history:

Received 1 February 2017

Received in revised form 28 July 2017

Accepted 31 July 2017

Available online 16 August 2017

## Keywords:

Molecular simulation

Molecular dynamics

Monte Carlo

## ABSTRACT

A new version release (3.0) of the molecular simulation tool *ms2* (Deublein et al., 2011; Glass et al. 2014) is presented. Version 3.0 of *ms2* features two additional ensembles, i.e. microcanonical (*NVE*) and isobaric–isoenthalpic (*NpH*), various Helmholtz energy derivatives in the *NVE* ensemble, thermodynamic integration as a method for calculating the chemical potential, the osmotic pressure for calculating the activity of solvents, the six Maxwell–Stefan diffusion coefficients of quaternary mixtures, statistics for sampling hydrogen bonds, smooth-particle mesh Ewald summation as well as the ability to carry out molecular dynamics runs for an arbitrary number of state points in a single program execution.

## New version program summary

Program Title: *ms2*

Program Files doi: <http://dx.doi.org/10.17632/9rcrykvkyh.1>

Licensing provisions: CC by NC 3.0

Programming language: Fortran95

Supplementary material: A detailed description of the parameter setup for thermodynamic integration and hydrogen bonding is given in the supplementary material. Furthermore, all molecular force field models developed by our group are provided

Journal reference of previous versions: Deublein et al., Comput. Phys. Commun. 182 (2011) 2350 and Glass et al., Comput. Phys. Commun. 185 (2014) 3302

Does the new version supersede the previous version?: Yes

Reasons for the new version: Introduction of new features as well as enhancement of computational efficiency

Summary of revisions: Two new ensembles (*NVE* and *NpH*), new properties (Helmholtz energy derivatives, chemical potential via thermodynamic integration, activity coefficients via osmotic pressure, Maxwell–Stefan diffusion coefficients of quaternary mixtures), new functionalities (detection and statistics of hydrogen bonding, smooth-particle mesh Ewald summation, ability to carry out molecular dynamics runs for an arbitrary number of state points in a single program execution).

Nature of problem: Calculation of application oriented thermodynamic properties: vapor–liquid equilibria of pure fluids and multi-component mixtures, thermal, caloric and entropic data as well as transport properties and data on microscopic structure

Solution method: Molecular dynamics, Monte Carlo, various ensembles, Grand Equilibrium method, Green–Kubo formalism, Lustig formalism, OPAS method, smooth-particle mesh Ewald summation

<sup>☆</sup> This paper and its associated computer program are available via the Computer Physics Communication homepage on ScienceDirect (<http://www.sciencedirect.com/science/journal/00104655>).

\* Correspondence to: Warburger Str. 100, 33098 Paderborn, Germany.

E-mail address: [jadran.vrabec@upb.de](mailto:jadran.vrabec@upb.de) (J. Vrabec).



*Restrictions:* Typical problems addressed by *ms2* are solved by simulating systems containing 1000 to 5000 molecules that are modeled as rigid bodies.

*Additional comments:* Documentation is available at <http://www.ms-2.de>

© 2017 Elsevier B.V. All rights reserved.

## 1. Introduction

Due to the continuous increase in computing power, the range of possible applications of molecular modeling and simulation has become broader over time, proceeding from qualitative basic research in soft matter physics to quantitative applications in chemical engineering. Reaching agreement with the available experimental data and predicting properties where experimental data are rare or absent, molecular methods transform engineering data science [1,2]. This progress is driven by massively-parallel high performance computing with scalable codes [3] and by the concurrent execution of large numbers of simulations [4] or of simulations which can be decomposed into a large number of concurrent tasks [5–7].

The program *ms2* (molecular simulation 2) was designed to compute thermodynamic properties of pure fluids and mixtures by Monte Carlo (MC) and molecular dynamics (MD) simulation. Licenses are available without cost for all purposes which concern academic research and teaching [8]. The previous two major releases of *ms2* [9,10] facilitate the simulation of vapor–liquid equilibria (VLE) by Grand Equilibrium simulation and the computation of many thermodynamic bulk properties, including linear transport coefficients, for molecular models consisting of Lennard-Jones interaction sites, point charges and point multipoles. It has been shown that such models can reach a high accuracy for a wide variety of thermodynamic properties for many molecular fluids [11–16], leading to an increasing popularity of molecular methods in the engineering sciences [17–21].

Similar molecular simulation programs, which address multiple academic communities, include CHARMM [22], DL\_POLY [23], ESPResSo [24], GIBBS [25], GROMACS [26], IMD [27], LAMMPS [28], *ls1* mardyn [29], NAMD [30], TINKER [31] and Towhee [32]. In comparison with these codes, the aim of *ms2* is to focus on applications of molecular modeling and simulation in fluid process engineering, both industrial and academic. Hence, a high accuracy, short response times and the suitability for coupling with equations of state [4,33] and rigorous model optimization approaches [34–36] have been priorities in developing both the code base as well as the toolset which is provided jointly with it. In contrast to other molecular simulation programs, *ms2* excels in its variety of properties that are all sampled on the fly. The present work discusses the third major release of *ms2* and its most important innovations, which are presented in detail in the following sections.

## 2. Microcanonical and isobaric–isoenthalpic ensembles

An ensemble is the set of all theoretically possible microscopic configurations on the molecular level under specific macroscopic constraints. The microcanonical (*NVE*) ensemble is the set of all configurations that fulfill the condition of having the same number of particles  $N$ , volume  $V$  and energy  $E$ , whereas the isobaric–isoenthalpic (*NpH*) ensemble represents a system at constant number of particles  $N$ , pressure  $p$  and enthalpy  $H$ . Molecular dynamics (MD) mimics the time evolution of a mechanical system by numerically solving Newton's equations of motion for all considered molecules. Because of the nature of this solution, the progress of time is discretized and the method yields microscopic configurations at discrete and consecutive time steps. The Monte Carlo

(MC) method is the application of statistical mechanics to describe molecular systems. With this approach, microscopic configurations are generated by random numbers that are potentially accepted such that only relevant and physically meaningful configurations are sampled [37]. The generation and acceptance of these configurations is governed by specific probabilities that are ensemble-dependent and described in the literature for essentially every relevant ensemble. For MC simulations, the *NVE* and *NpH* ensembles were implemented in *ms2* release 3.0 according to Refs. [38,39]. For MD simulations, the pressure is kept constant with Andersen's barostat [40] in case of the *NpH* ensemble. Because the solution of Newton's equations of motion is approximate, the total energy of the system  $E = K + U$ , which consists of a kinetic  $K$  (exclusively molecular momentum dependent) and potential  $U$  (exclusively molecular position dependent) energy contribution, is not rigorously conserved in a standard MD run mainly for numerical reasons. Therefore, the translational and rotational momentum of every molecule is rescaled such that the total kinetic energy  $K$  fulfills  $K = E - U$ , where the total energy  $E$  is specified and the potential energy  $U$  is calculated from the current microscopic configuration. For a *NpH* ensemble run, the solution is analogous: Momenta are rescaled such that the current kinetic energy  $K$  fulfills  $K = H - U - pV$ , where  $H$  and  $p$  are specified, while  $U$  and  $V$  are dependent on the current microscopic configuration. This extends the ensembles available in *ms2* to five: *NVT*, *NVE*, *NpT*, *NpH* and  $\mu VT$ , where  $\mu$  is the chemical potential.

For verification purposes, Table 1 contains numerical results for methyl fluoride modeled by a dipolar two-center Lennard-Jones potential [41] at  $T = 300$  K and  $\rho = 1$  mol/l. Fig. 1 shows the running averages of the calculated properties in Table 1 at the same state point.

## 3. Helmholtz energy derivatives in the microcanonical ensemble

The generalized calculation of the Helmholtz energy derivatives

$$A_{nm}^r = (1/T)^n \rho^m \frac{\partial^{n+m} f^r(T, \rho)/(RT)}{\partial (1/T)^n \partial \rho^m}, \quad (1)$$

with molar residual Helmholtz energy  $f^r$ , temperature  $T$ , density  $\rho$  and molar gas constant  $R$  was introduced in *ms2* also for the *NVE* ensemble up to the order  $n = 3$  and  $m = 2$ . The total reduced Helmholtz energy  $f/(RT)$  can be additively separated into an ideal  $f^0/(RT)$  and a residual contribution  $f^r/(RT)$ . The ideal contribution by definition corresponds to the value of  $f/(RT)$  when no intermolecular interactions are at work [43].  $f^0/(RT)$  consists of an exclusively temperature and an exclusively density dependent part. The latter is the trivial term  $\ln(\rho/\rho_{\text{ref}})$ , whereas the former is non-trivial. A formalism that allows for the calculation of all residual Helmholtz derivatives on the fly from a single simulation run per state point was published by Lustig [44,45] and was already introduced for the *NVT* ensemble in the preceding program version. *ms2* release 3.0 now yields these derivatives also for the *NVE* ensemble. However, in contrast to *NVT* simulations, there are two numerical results for each calculated derivative  $A_{nm}$  due to the two possible entropy definitions in statistical mechanics [45]. In any case, these two different sets of results must be identical in the thermodynamic limit ( $N \rightarrow \infty$ ). In practice, they already agree within their statistical uncertainty for a simulation based on

**Table 1**

Comparison of the ensembles implemented in *ms2* for methyl fluoride [41] in terms of temperature  $T$ , density  $\rho$ , pressure  $p$  and potential energy  $u$ . Numbers in parentheses denote statistical uncertainties in the last digit that were estimated with the block averaging method of Flyvbjerg and Petersen [42].

		$T$ K	$\rho$ mol/l	$p$ MPa	$u$ J/mol
MD	NVT	300	1	2.090(2)	−1048(3)
	NpT	300	1.0015(7)	2.090	−1051(3)
	NVE	300.0(1)	1	2.088(1)	−1048(3)
	NpH	300.0(1)	1.0003(2)	2.090	−1048(2)
MC	NVT	300	1	2.0880(2)	−1051.6(2)
	NpT	300	1.0019(2)	2.0880	−1053.6(3)
	NVE	299.99(1)	1	2.0882(2)	−1051.3(2)
	NpH	300.06(2)	1.0010(1)	2.0880	−1051.7(2)

around a thousand molecules. For verification purposes, Table 2 contains numerical results for methyl fluoride [41]. A detailed description of the calculation of these derivatives can be found in Ref. [45]. Their conversion into common thermodynamic properties is provided in the supplementary material of release 2.0 of *ms2* [10] and in Ref. [43].

#### 4. Thermodynamic integration

The previously described method of Lustig does not allow for the direct sampling of the chemical potential and other entropic properties like  $A_{00}$ . Such an effort requires techniques based on free energy calculation, such as particle insertion and/or thermodynamic integration [37]. Widom's particle insertion method [46] is a conceptually straightforward approach to calculate the chemical potential at low computational cost, both for pure substances and mixtures. The total chemical potential  $\mu_i$  of species  $i$  can be separated into an ideal (o) and a residual (r) contribution in the same way as the Helmholtz energy is decomposed, cf. Section 2:  $\mu_i(T, \rho, \mathbf{x}) = \mu_i^o(T) + RT \ln(N_i/(V\rho_{\text{ref}})) + \mu_i^r(T, \rho, \mathbf{x})$ , where  $\mathbf{x}$  is the mole fraction vector,  $N_i$  is the number of molecules of species  $i$ ,  $\rho = N/V$  and  $\rho_{\text{ref}}$  is an arbitrary reference density. The expression  $\mu_i - \mu_i^o(T)$  is often referred to as the configurational chemical potential  $\mu_i^{\text{conf}}$ . Widom's method requires the frequent insertion of an additional ( $i = N + 1$ ) test particle into the simulation volume at a random position with a random orientation. At constant temperature and constant pressure or volume, the potential energy  $U_i$  of this test particle, i.e. the interaction energy with all other “real”  $N$  molecules, yields the configurational chemical potential according to

$$\mu_i^{\text{conf}} = \mu_i - \mu_i^o(T) = -k_B T \ln \frac{\langle V \exp(-U_i/k_B T) \rangle}{\langle N_i \rangle}, \quad (2)$$

where  $k_B$  is Boltzmann's constant. The test particle is discarded immediately after the calculation of its potential energy  $U_i$  such that it does not influence the real molecules in the system in any way. In contrast to the usual convention, the brackets  $\langle \rangle$  have a dual meaning here: They stand for either NVT or NpT ensemble averages as well as an integral over all possible positions and orientations of the test particles added to the system. The density of the system

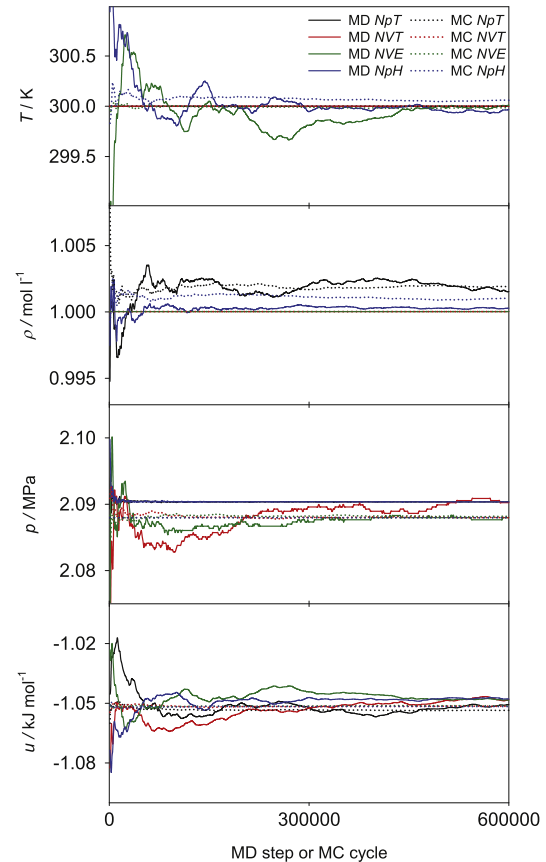


**Fig. 1.** Comparison of the ensembles implemented in *ms2* for methyl fluoride [41] in terms of running averages for temperature  $T$ , density  $\rho$ , pressure  $p$  and potential energy  $u$ .

has a significant influence on the accuracy of this method. For state points with a very high density, test particles almost always overlap with real molecules, which leads to a potential energy  $U_i \rightarrow \infty$  and thus to a vanishing contribution to Eq. (2), resulting in poor statistics and often even to complete failure of sampling.

Thermodynamic integration is one solution to overcome the limitations of Widom's particle insertion method. The idea behind calculating the chemical potential by thermodynamic integration is to avoid insertion of test particles in a challenging system  $A$ , but rather perform it in system  $B$  for which this can be done without sampling problems. Because the chemical potential is a state property, its difference  $\mu_{A,i} - \mu_{B,i}$  can be calculated along any path between states  $A$  and  $B$ , which is represented by the scalar parameter  $\lambda$ . It can be shown [37] that the relation between  $\lambda$  and

**Table 2**

Comparison of the residual Helmholtz energy derivatives  $A_{nm}^r$  of methyl fluoride [41] at  $T = 300$  K and  $\rho = 1$  mol/l. Numbers in brackets denote statistical uncertainties in the last digit that were estimated with the block averaging method of Flyvbjerg and Petersen [42]. Superscripts (1) and (2) indicate the two different entropy definitions [45].

		$A_{10}^r$	$A_{01}^r$	$A_{20}^r$	$A_{11}^r$	$A_{02}^r$
MD	NVT	−0.420(1)	−0.1620(6)	−0.54(4)	−0.40(2)	0.03(3)
	NVE <sup>1</sup>	−0.418(1)	−0.1622(4)	−0.55(3)	−0.37(1)	0.05(3)
	NVE <sup>2</sup>	−0.418(1)	−0.1621(4)	−0.55(3)	−0.37(1)	0.05(3)
MC	NVT	−0.42158(8)	−0.16290(8)	−0.562(2)	−0.391(2)	0.011(6)
	NVE <sup>1</sup>	−0.42149(5)	−0.16280(8)	−0.560(2)	−0.385(3)	0.024(6)
	NVE <sup>2</sup>	−0.42133(5)	−0.16274(8)	−0.560(2)	−0.385(3)	0.024(6)



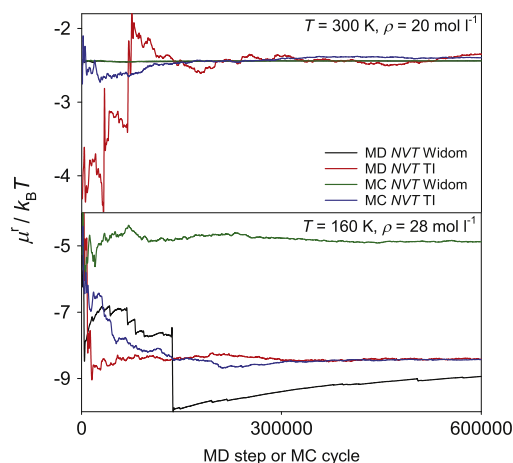


**Fig. 2.** Comparison of the residual chemical potential  $\mu^f$  of methyl fluoride [41] at two different state points calculated by *ms2* using either Widom's particle insertion or thermodynamic integration (TI).

$\mu_{A,i} - \mu_{B,i}$  is

$$\mu_{A,i} - \mu_{B,i} = \int_{B(\lambda_{\min})}^{A(\lambda_{\max})} \left\langle \frac{\partial U_i(\lambda)}{\partial \lambda} \right\rangle d\lambda. \quad (3)$$

The brackets  $\langle \rangle$  in this equation denote *NVT* or *NpT* ensemble averages and  $U_i$  is the potential energy of particle  $i$  that must be a part of the system in the same way as the other molecules are. The only difference between particle  $i$  and all other molecules is that its interaction energy  $U_i(\lambda)$  is scaled between states  $A(\lambda_{\max})$  and  $B(\lambda_{\min})$  with  $\lambda$ . As long as  $\partial U_i(\lambda)/\partial \lambda$  can be calculated analytically and sampled during simulation, the actual way of scaling  $U_i(\lambda)$  with  $\lambda$  can be chosen arbitrarily because  $\mu_i$  is a state property. The integration with respect to  $\lambda$  is carried out numerically. Assuming that  $\mu_{B,i}$  is practically zero or at least can successfully be calculated by Widom's particle insertion method for state  $B$  using Eq. (2),  $\mu_{A,i}$  yields the configurational contribution to the total chemical potential. The non-linear scaling  $U_i(\lambda) = \lambda^d U_i$  for  $\lambda_{\min} \leq \lambda \leq 1 = \lambda_{\max}$  with an adaptive sampling technique [47] was implemented for MC simulations with  $d$  and  $\lambda_{\min}$  being input parameters. This adaptive technique allows for the sampling of the entire range of  $\lambda_{\min} \leq \lambda \leq 1$  in a single MC run with an arbitrary resolution for numerical integration. In addition to the standard *NVT* and *NpT* ensemble MC moves, the simulation includes changes of  $\lambda$  controlled by a proper MC acceptance criterion, ensuring visits at each discrete  $\lambda$  value in the range  $\lambda_{\min} \leq \lambda \leq 1$ . For MD simulations, changes of  $\lambda$  are also carried out on the fly in a single simulation, but without any acceptance criterion. A common problem related to the thermodynamic integration is the so called "end-point catastrophe", i.e. the occurrence of singularities at  $\lambda = 0$  or  $1$  [48–50]. Such effects can be circumvented by the variable and non-linear scaling described above, where the exponent  $d$  of  $\lambda$  and  $\lambda_{\min}$  are input parameters. Furthermore, sampling at  $\lambda \rightarrow 1$  is improved by scaling the fluctuating particle dynamically back and forth during simulation. A detailed description of the parameter setup is given in the supplementary material.

Fig. 2 shows the running averages for the residual chemical potential of methyl fluoride at two different state points calculated by either Widom's particle insertion or thermodynamic integration. For high temperatures and low densities, the agreement between Widom's particle insertion and thermodynamic integration is satisfactory. Widom fails, however, for dense and strongly interacting fluids.

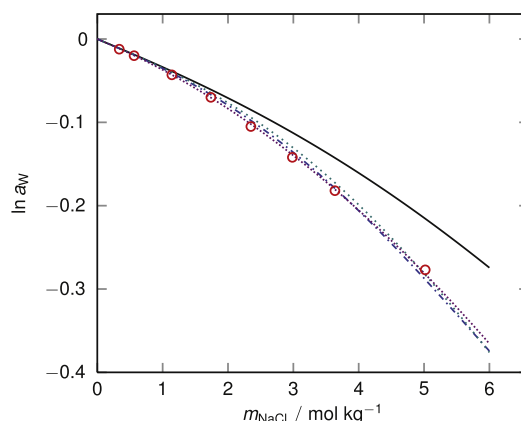


**Fig. 3.** Water activity over the salt molality for aqueous NaCl solutions at  $T = 298.15$  K and  $p = 1$  bar. The red open circles are simulation results obtained with the OPAS method as implemented in *ms2* [54]. The colored lines represent correlations to simulation results by different groups: Free energy calculations by Benavides et al. [56] (violet densely-dotted line), gradual insertion of ion pairs by Mester and Panagiotopoulos [52] (blue dashed-dotted line) and osmotic ensemble Monte Carlo simulations by Moučka et al. [53] (green dotted line). All simulation results were obtained using the SPC/E + Joung–Cheatham [55] model combination. The black solid line shows the correlation to experimental data by Hamer and Wu [57].

## 5. OPAS method

The OPAS (osmotic pressure for the activity of the solvent) method was implemented in *ms2*. It is an alternative to e.g. Widom's particle insertion [46] or thermodynamic integration [51–53] for calculating the chemical potential of the liquid phase by MD simulations. It is particularly well-suited for studying the solvent activity of electrolyte solutions, but can in principle also be used for mixtures of molecular species. Details and a thorough assessment of the method are presented in Ref. [54], the method is only briefly outlined in the following.

The basic idea is a direct simulation of the osmotic equilibrium between a pure solvent phase and a solution phase by introducing semi-permeable membranes into the simulation volume. These are realized by an external force field that acts only on the solute molecules to keep them in the solution phase. By sampling the total net membrane force per membrane area, the pressure difference between the two phases, i.e. the osmotic pressure  $\Pi$ , is sampled. Assuming an incompressible solvent, the solvent activity  $a_s$  is related to this osmotic pressure by

$$\ln a_s = -\frac{\Pi v_s}{RT}, \quad (4)$$

where  $v_s$  is the molar volume of the pure solvent at the temperature  $T$ , which is straightforwardly available from separate, standard molecular simulation runs. If an electrolyte solution is considered, the activity coefficient of the salt can be obtained by performing OPAS simulations at various salt molalities and applying the Gibbs–Duhem equation to the results for the solvent activity.

Fig. 3 shows molecular simulation results for the water activity in aqueous NaCl solutions at  $T = 298.15$  K and  $p = 1$  bar. Therein, results obtained by different groups, employing different computational approaches, are presented. Throughout, the molecular models by Joung and Cheatham [55] for  $\text{Na}^+$  and  $\text{Cl}^-$  ions together with the SPC/E water model were used. It can be seen that all simulation results, including those obtained with OPAS simulations carried out with *ms2*, are in mutual agreement.

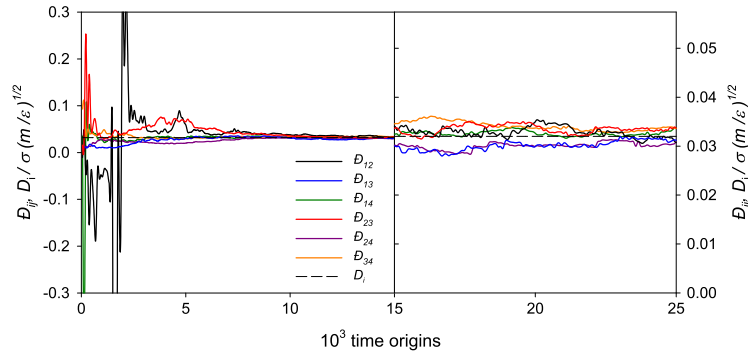


**Fig. 4.** Maxwell–Stefan diffusion coefficients  $D_{ij}$  and self-diffusion coefficient  $D_i$  as a function of time origins of a quaternary pseudo-mixture ( $\epsilon = \epsilon_1 = \epsilon_2 = \epsilon_3 = \epsilon_4$  and  $\sigma = \sigma_1 = \sigma_2 = \sigma_3 = \sigma_4$ ) at  $k_B T / \epsilon = 0.728$  and  $\rho \sigma^3 = 0.8442$ .

## 6. Quaternary Maxwell–Stefan diffusion coefficients

*ms2* employs the Green–Kubo formalism based on the net velocity correlation function to obtain  $n \times n$  phenomenological coefficients [58]

$$L_{ij} = \frac{1}{3N} \int_0^\infty \left\langle \sum_{k=1}^{N_i} \mathbf{v}_{i,k}(0) \cdot \sum_{l=1}^{N_j} \mathbf{v}_{j,l}(t) \right\rangle dt, \quad (5)$$

in a mixture of  $n$  components. Here,  $N$  is the total number of molecules,  $N_i$  is the number of molecules of species  $i$  and  $\mathbf{v}_{i,k}(t)$  denotes the center of mass velocity vector of the  $k$ th molecule of species  $i$  at time  $t$ . Note that the phenomenological coefficients given in Eq. (5) are constrained by [58]

$$\sum_i M_i L_{ij} = 0, \quad (6)$$

where  $M_i$  is the molar mass of component  $i$ .

Starting from the phenomenological coefficients  $L_{ij}$ , the elements of a  $(n-1) \times (n-1)$  matrix  $\Delta$  can be defined as [58]

$$\Delta_{ij} = (1 - x_i) \left( \frac{L_{ij}}{x_j} - \frac{L_{in}}{x_n} \right) - x_i \sum_{k=1 \neq i}^n \left( \frac{L_{kj}}{x_j} - \frac{L_{kn}}{x_n} \right), \quad (7)$$

so that its inverse matrix  $\mathbf{B} = \Delta^{-1}$  is related to the Maxwell–Stefan diffusion coefficients  $D_{ij}$ . In the case of a quaternary mixture, the six Maxwell–Stefan diffusion coefficients are then given by [58]

$$D_{14} = \frac{1}{B_{11} + (x_2/x_1)B_{12} + (x_3/x_1)B_{13}}, \quad (8)$$

$$D_{24} = \frac{1}{B_{22} + (x_1/x_2)B_{21} + (x_3/x_2)B_{23}}, \quad (9)$$

$$D_{34} = \frac{1}{B_{33} + (x_1/x_3)B_{31} + (x_2/x_3)B_{32}}, \quad (10)$$

$$D_{12} = \frac{1}{1/D_{24} - B_{21}/x_2}, \quad (11)$$

$$D_{13} = \frac{1}{1/D_{14} - B_{13}/x_1}, \quad (12)$$

$$D_{23} = \frac{1}{1/D_{24} - B_{23}/x_2}. \quad (13)$$

MD simulation runs for Lennard–Jones fluids were performed in order to test the validity of the quaternary Maxwell–Stefan diffusion coefficients implementation in *ms2*. For this purpose, a quaternary Lennard–Jones pseudo-mixture was created by giving different labels to otherwise identical molecules, dividing them

into four mole fractions ( $x_1 = 0.1$ ,  $x_2 = 0.2$ ,  $x_3 = 0.3$  and  $x_4 = 0.4$  mol mol<sup>-1</sup>). A system containing 800 molecules was simulated in the dense liquid state and the resulting Maxwell–Stefan diffusion coefficients were compared with the corresponding self-diffusion coefficient that all have to be identical in the present case.

Fig. 4 shows the development of the calculated values of the six Maxwell–Stefan diffusion coefficients with the number of sampled time origins. As can be seen, the resulting values become independent after around  $10^4$  time origins and then oscillate around their mean value. The higher statistical uncertainties of  $D_{12}$  and  $D_{13}$  are due to the small number of species 1 molecules compared with the number of molecules of the other species.

## 7. Hydrogen bonding

There is no definitive characterization of a hydrogen bond between two molecules [59–61]. Rather, the hydrogen (H) bond ‘is a structural motif and involves at least three atoms’ [62]. The International Union of Pure and Applied Chemistry (IUPAC) defines the hydrogen bond as ‘an attractive interaction between a hydrogen atom from a molecule or molecular fragment X–H in which X is more electronegative than H, and an atom or a group of atoms in the same or a different molecule, in which there is evidence of bond formation’ [61].

Energetic [59], geometric [63] and topological [60] hydrogen bonding criteria have been proposed in the literature. Geometric criteria, which are not overly complex, are often based on the following assumptions [64]:

- The interaction between two hydrogen bonded sites is highly directional and short ranged.
- A donor interacts at most with a single acceptor, an acceptor may interact with multiple donors.

Accordingly, a class of geometric criteria for the evaluation of hydrogen bonding networks in fluids was implemented in *ms2*. Thereby, the triangle between three charge sites, being part of two different molecules, is evaluated to determine whether two sites constitute a hydrogen bond or not. A molecule acts as a donor to another molecule, i.e. the acceptor, if the following conditions hold [63–66], cf. Fig. 5:

- The distance between the donor and the acceptor is smaller than a threshold distance, i.e.  $\ell_{AD}$  or  $\ell_{DA}$ .
- The distance between the acceptor sites of the acceptor and donor molecules is smaller than a threshold distance, i.e.  $\ell_{AA}$ .
- The angle between the acceptor–donor axis and the acceptor–acceptor axis is smaller than a threshold angle, i.e.  $\varphi_{DAA}$  or  $\varphi_{AAD}$ .

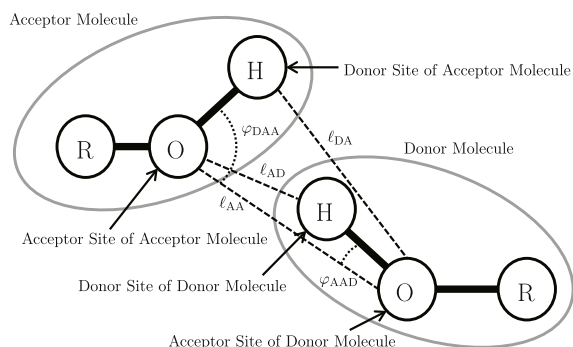


Fig. 5. Hydrogen bonding criteria implemented in the present release version of *ms2*.

Therein,  $\ell_{AD}$ ,  $\ell_{DA}$ ,  $\ell_{AA}$ ,  $\varphi_{DAA}$  and  $\varphi_{AAD}$  are parameters of the implemented class of hydrogen bonding criteria. For methanol, e.g. Haughney et al. [63] proposed  $\ell_{AD} = \ell_{DA} = 2.6$  Å,  $\ell_{AA} = 3.5$  Å and  $\varphi_{AAD} = \varphi_{DAA} = 30^\circ$ . Such geometric criteria have been applied to a variety of fluids, in particular to water [65–67], methanol–water mixtures [68,69] or ethanol [64,70,71]. Hydrogen bonds in sorbate–sorbent interactions can be treated analogously [72]. E.g., for hydrogen fluoride, a simpler distance-based criterion can be used [73], which is also covered by the present implementation. Hydrogen bonding statistics are calculated by *ms2* on the fly during a standard simulation run which avoids post-processing and evaluation of trajectory files. A detailed description of the parameter setup is given in the supplementary material.

To test the capabilities of the hydrogen bonding statistics implemented in *ms2*, a MD simulation run of the ternary mixture water (w) + methanol (m) + ethanol (e) ( $x_w = 0.33$ ,  $x_m = 0.33$ ,  $x_e = 0.34$  mol mol<sup>−1</sup>) at  $T = 298.15$  K and  $p = 0.1$  MPa was carried out with 4000 molecules. All species of this mixture can form hydrogen bonds with each other because all three molecules contain hydroxyl groups. Thus the hydrogen atoms may act as donors and the oxygen atoms as acceptors to form hydrogen bonds. Throughout, between like and unlike molecules, the geometric criteria of Haughney et al. [63] were used. The results are listed in Table 3. The hydrogen bonding statistics in *ms2* not only indicates the amount of monomers (no bond), dimers (one bond), trimers (two bonds) and tetramers (three bonds), but also provides information about which molecule species are mutually bonded.

## 8. Electrostatic long range corrections

The applicability of *ms2* was extended to electrically charged molecules or ions. The long ranged intermolecular interactions are considered by two well established approaches, Ewald summation and smooth-particle mesh Ewald summation (SPME). Both are well known [37] and are thus introduced here only briefly.

In Ewald summation, the overall Coulombic potential acting in the simulation volume is determined by a sum of two terms, i.e. the short range Coulombic contribution  $u^{c,short}$  and the long range Coulombic contribution  $u^{c,long}$

$$u^c = u^{c,short} + u^{c,long}. \quad (14)$$

The separation into these terms is achieved by the introduction of a fictive charge density function  $\rho^{screen}(\mathbf{r})$ , which acts in the entire simulation volume.

Following the Ewald summation approach, for any configuration of molecules in the simulation volume, each point charge of magnitude  $q_i$  in the simulation volume is superimposed with one

Table 3

Hydrogen bonding statistics of the ternary mixture water (w) + methanol (m) + ethanol (e) ( $x_w = 0.33$ ,  $x_m = 0.33$ ,  $x_e = 0.34$  mol mol<sup>−1</sup>) at  $T = 298.15$  K and  $p = 0.1$  MPa in relative terms.

	Water	Methanol	Ethanol
Monomer	0.1%	0.9%	1.1%
Dimer bonded to	1.2%	10.6%	11.5%
(w)	0.8%	3.5%	4.1%
(m)	0.2%	3.3%	3.6%
(e)	0.2%	3.8%	3.8%
Trimer bonded to	7.8%	47.7%	42.6%
(w)(w)	2.8%	2.8%	2.8%
(w)(m)	1.9%	10.5%	8.9%
(w)(e)	2.0%	12.3%	10.2%
(m)(m)	0.3%	5.0%	4.9%
(m)(e)	0.4%	11.0%	10.3%
(e)(e)	0.4%	6.1%	5.5%
Tetramer bonded to	25.8%	35.9%	36.8%
(w)(w)(w)	3.9%	15.6%	12.7%
(w)(w)(m)	4.9%	7.6%	7.8%
(w)(w)(e)	5.1%	7.7%	7.6%
(w)(m)(m)	2.7%	0.7%	1.3%
(w)(m)(e)	3.8%	1.7%	2.8%
(w)(e)(e)	2.8%	0.9%	1.5%
(m)(m)(m)	0.6%	0.2%	0.4%
(m)(m)(e)	0.7%	0.6%	1.1%
(m)(e)(e)	0.6%	0.7%	1.2%
(e)(e)(e)	0.7%	0.2%	0.4%
Four or more bonds	65.1%	4.9%	8.0%

countercharge of magnitude  $-q_i$ . Due to the presence of this superimposed charge, the interaction potential decays to zero within a distance that is reasonably short for molecular simulation and can, hence, be explicitly considered by the short range contribution of the Ewald summation.

The second term in Eq. (14) determines the contribution that was subtracted due to the introduction of the fictive charge density function. This term cannot be determined explicitly by an evaluation of pairwise interactions, since the Coulombic potential at  $r_{lm} = V^{1/3}/2$ , i.e. the largest distance accessible in the molecular simulation volume  $V$ , constitutes still a substantial part of the potential energy of the system. In Ewald summation, this contribution is determined in Fourier space from the negative charge distribution function  $-\rho^{screen}(\mathbf{r})$ . Since  $\rho^{screen}(\mathbf{r})$  depends on the molecular positions  $\mathbf{r}$ , a Fourier transformation is performed for every configurational change in the simulation volume.

The SPME is widely considered as an improved Ewald summation method. In this approach, the concept of splitting the long range charge–charge interactions is fully employed. The difference between both methods lies only in the calculation of the long range contributions. In the SPME approach, the electrostatic field of ions in the simulation volume is described by a spline function with a given functional form. For this given spline equation, the Fourier transformation is known and has, hence, not to be determined in each simulation step. This accelerates the calculation of the long range contribution and reduces simulation effort and time. The accuracy of the SPME results is assumed to be equivalent to the Ewald approach. In *ms2* release 3.0, the SPME method was implemented in its original form, wherein the splines are evaluated for all particles at a time, making it particularly useful for MD simulations.

To validate the present implementation of the SPME method, otherwise identical MD simulations with either full Ewald summation or the SPME method were carried out. For both methods, the Debye length was set to  $\kappa = 5.6$ . In case of SPME, a grid with 35 points and a spline order of 6 were used. The simulations were equilibrated for  $0.5 \cdot 10^6$  time steps, before sampling was carried

**Table 4**

Comparison of simulation results obtained with Ewald summation and SPME, indicating the reduction of total computation time when using SPME instead of Ewald summation.

System	NpT ensemble			NVT ensemble		
	$\rho$ / mol l <sup>-1</sup>		Speedup	$u$ / kJ mol <sup>-1</sup>		Speedup
	Ewald	SPME		Ewald	SPME	
SPC/E water	55.44(2)	55.41(2)	22%	-46.67(3)	-46.72(3)	19%
NaCl solution	55.74(2)	55.73(2)	29%	-53.70(3)	-53.75(3)	16%

out over  $2.5 \cdot 10^6$  time steps of 1.2 fs. The electrostatic cutoff was the same as the Lennard-Jones cutoff of 15 Å. The studied systems were pure SPC/E water [74] (1000 molecules) and an aqueous NaCl solution (980 SPC/E molecules and 10 Na<sup>+</sup> and Cl<sup>-</sup> ions each [75]) at  $T = 300$  K. For a comparison of the density, simulations were carried out in the NpT ensemble at a pressure of 0.1 MPa. For a comparison of the internal energy, simulations were carried out in the NVT ensemble at a density of 55.44 mol l<sup>-1</sup>. The results can be found in Table 4, which shows that both simulation approaches are in mutual agreement for both studied systems. Furthermore, SPME was found to be about 15%–30% faster than full Ewald summation in the form as it is implemented in *ms2*.

## 9. Vectorization

For the vectorization of loops it is essential how accessed data are distributed in physical memory. Deducing this information automatically from the code can be very difficult for the compiler, especially if there is indirection. In *ms2*, many arrays are accessed via array pointers and the order of the underlying data is therefore obfuscated. The most relevant information is whether or not data are contiguous in physical memory. To provide this information to the compiler directly, array pointers can be given the attribute “contiguous”. The Fortran standard states: “The contiguous attribute specifies that [...] an array pointer can only be pointer associated with a contiguous target.” This means that the array elements of a contiguous array pointer are not separated by any other data, potentially enabling a higher degree of vectorization. In *ms2* release 3.0, array pointers associated with contiguous targets were given the contiguous attribute. The sequential performance gains and the resulting parallel performance gains achieved with this optimization depend on the specific simulation scenario, but are on average very significant. For MC and MD simulations, a suite of simulations was executed to evaluate the performance gains. The suite covered the NpT and NVT ensembles, thermodynamic integration, Widom test particle insertion, different thermostats, different pure fluids and mixtures. A total of 71 simulation runs was performed. For MC simulations, the observed average reduction of runtime was more than 7% and for MD simulations more than 20%.

## 10. Parallel ensemble calculations

*ms2* was already parallelized in its initial version for distributed memory architectures using the message passing interface (MPI) [9,10]. A typical MD simulation with  $N = 1000$  to 4000 particles usually scales up to 48 cores. The present release 3.0 adds an additional level of parallelization for MD simulations. Different ensembles are independent of each other in the sense that sampling different state points can be done concurrently. To achieve this, the processing elements (PE) were split in disjunct groups and each group computes the ensembles assigned to it. In principle, this allows for the sampling of an arbitrary number of state points in the whole relevant fluid region with a single program execution. The vast amount of data generated can then, e.g. be used for the development of an equation of state. To enable this feature, the *mpiEnsembleGroups* option was introduced in the input file. The default (if not set or set to 0) is to use a single ensemble group.

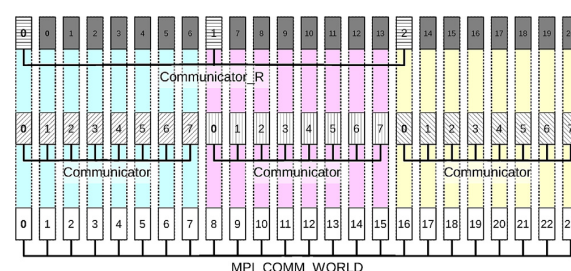


**Fig. 6.** MPI ranks for 24 PE in 3 MPI groups, indicating communicator hierarchy of *ms2*.

A value of 1 will enable the new feature and automatically set the number of ensemble groups to the minimum of the number of ensembles and the number of PE, i.e.  $mpiEnsembleGroups = \min(\text{ensembles}, \text{PE})$ . Otherwise, this option will set the number of ensemble groups according to the specified integer value. The “coloring”, i.e. the assignment of the PE to the ensemble groups, is done in contiguous blocks. This is advantageous, e.g. compared to a round robin fashion, if the processes have to be pinned to NUMA domains.

Another change applies to the restart capability of *ms2*. A checkpoint now consists of one restart (\*.rst) file for each ensemble group that can be restarted with the *ms2* -r (or -restart) option.

To illustrate the new feature, a MD program execution for three ensembles with 24 processes is exemplarily discussed: Without the *mpiEnsembleGroups* option (or with  $mpiEnsembleGroups = 0$ ) all 24 PE will in parallel calculate the first time step of the first ensemble, then the first time step of the second ensemble and finally the first time step of the third one, before the second time step is handled accordingly. Setting  $mpiEnsembleGroups = 1$  is equivalent to  $mpiEnsembleGroups = 3$  in this example and three groups of eight PE each will calculate one ensemble in parallel concurrently. The user may also directly specify the number of groups, but has to be aware that in this example with  $mpiEnsembleGroups = 2$  one group will have to process two ensembles, while the other one only processes a single one.

*ms2* creates a MPI communicator for each of the ensemble groups with the `MPI_Comm_Split` command, cf. Fig. 6. Another MPI communicator contains the root processes of all groups (Communicator\_R including subcommunicators rank 0 processes) to ease collective communication on a higher level among the groups.

Even if the computation of different ensembles is embarrassingly parallel, an interaction between the different ensemble groups through communicators remains, e.g. when the program receives a signal to write a checkpoint and terminate. This signal may be received from an arbitrary single PE (or non-isochronic from multiple PE). In the preceding releases of *ms2*, where ensembles were calculated consecutively with the single global communicator `MPI_COMM_WORLD`, a `MPI_Allreduce` spreads this information among all processes after every MD time step. This is still the case within the ensemble groups. A collective communication of all PE beyond ensemble group boundaries for every



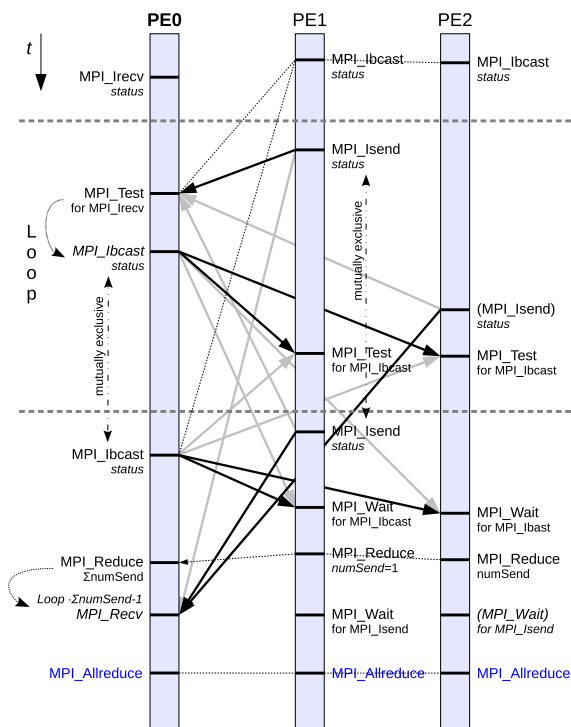


**Fig. 7.** Communication to distribute status information within a MD time step avoiding barriers. Thick solid arrows indicate communication among PE (gray arrows for alternative possible receiving points). Dotted lines between the PE indicate collective communication implicating a barrier. For mutually exclusive commands, the second one is only executed if the first one was not triggered.

MD time step would implicitly synchronize all ensemble computations. However, this is not satisfactory because computationally less intensive ensembles would be forced to wait for slower ones to conclude their time step. The present implementation uses non-blocking communication between the ensemble group roots through Communicator\_R to avoid this problem.

Before any MD time step iterations start, the root process executes a `MPI_Irecv` call to receive a potential terminate message, whereas all other processes execute a `MPI_ibcast` to obtain a potential terminate message from the root, cf. Fig. 7. During program execution, any process may trigger termination by sending a message to the root, which will then broadcast the information to notify all other processes. If no termination occurs during the iterations, the root will send a message to itself and broadcast a non-termination message to all other processes to satisfy the outstanding receive and broadcast (avoiding `MPI_Cancel`). To take care of several processes sending a termination message, a summation reduction determines the sum of all respective messages for the root process to receive all of them. This technique can also be used hierarchically, replacing the `MPI_Allreduce` call within each subcommunicator. After termination, every ensemble group writes its own restart (\*.rst) file.

## Acknowledgments

The authors gratefully acknowledge financial support by BMBF under the grant "01IH13005A SkaSim: Skalierbare HPC-Software für molekulare Simulationen in der chemischen Industrie" and computational support by the High Performance Computing Center Stuttgart (HLRS) under the grant MMHBF2. Furthermore, we

gratefully acknowledge the Paderborn Center for Parallel Computing (PC<sup>2</sup>) for the generous allocation of computer time on the OCuLUS cluster. The present research was conducted under the auspices of the Boltzmann-Zuse Society of Computational Molecular Engineering (BZS). H.H. and M.K. acknowledge support of this work by DFG under a Reinhart Koselleck grant (HA1993/15-1).

## Appendix A. Supplementary data

Supplementary material related to this article can be found online at <http://dx.doi.org/10.1016/j.cpc.2017.07.025>.

## References

- [1] P. Ungerer, C. Nieto-Draghi, B. Rousseau, G. Ahunbay, V. Lachet, J. Mol. Liq. 134 (2007) 71–89.
- [2] J.C. Palmer, P.G. Debenedetti, *AIChE J.* 61 (2015) 370–383.
- [3] A. Heinecke, W. Eckhardt, M. Horsch, H.-J. Bungartz, *Supercomputing for Molecular Dynamics Simulations*, Springer Verlag, Heidelberg, 2015.
- [4] A. Köster, T. Jiang, G. Rutkai, C.W. Glass, J. Vrabec, *Fluid Phase Equilib.* 425 (2016) 84–92.
- [5] C. Valeriani, R.J. Allen, M.J. Morelli, D. Frenkel, P.R. ten Wolde, *J. Chem. Phys.* 127 (2007) 114109.
- [6] D.R. Glowacki, E. Paci, D.V. Shalashilin, *J. Chem. Theory Comput.* 7 (2011) 1244–1252.
- [7] S.L. Meadley, F.A. Escobedo, *J. Chem. Phys.* 137 (2012) 074109.
- [8] URL <http://www.ms-2.de/>.
- [9] S. Deublein, B. Eckl, J. Stoll, S.V. Lishchuk, G. Guevara-Carrion, C.W. Glass, T. Merker, M. Bernreuther, H. Hasse, J. Vrabec, *Comput. Phys. Comm.* 182 (2011) 2350–2367.
- [10] C.W. Glass, S. Reiser, G. Rutkai, S. Deublein, A. Köster, G. Guevara-Carrion, A. Wafai, M. Horsch, M. Bernreuther, T. Windmann, H. Hasse, J. Vrabec, *Comput. Phys. Comm.* 185 (2014) 3302–3306.
- [11] C. Nieto-Draghi, P. Bonnaud, P. Ungerer, *J. Phys. Chem. C* 111 (2007) 15942–15951.
- [12] E. El Ahmar, B. Creton, A. Valtz, C. Coquelet, V. Lachet, D. Richon, P. Ungerer, *Fluid Phase Equilib.* 304 (2011) 21–34.
- [13] Y.-L. Huang, M. Heilig, H. Hasse, J. Vrabec, *AIChE J.* 57 (2011) 1043–1060.
- [14] M.H. Ketko, G. Kamath, J.J. Potoff, *J. Phys. Chem. B* 115 (2011) 4949–4954.
- [15] S. Reiser, M. Horsch, H. Hasse, *J. Chem. Eng. Data* 60 (2015) 1614–1628.
- [16] S. Werth, K. Stöbener, P. Klein, K.-H. Küfer, M. Horsch, H. Hasse, *Chem. Eng. Sci.* 121 (2015) 110–117.
- [17] R. Srivastava, H. Docherty, J.K. Singh, P.T. Cummings, *J. Phys. Chem. C* 115 (2011) 12448–12457.
- [18] L. Lu, S. Wang, E.A. Müller, W. Cao, Y. Zhu, X. Lu, G. Jackson, *Fluid Phase Equilib.* 362 (2014) 227–234.
- [19] A. Sharma, S. Namsani, J.K. Singh, *Mol. Sim.* 41 (2015) 414–422.
- [20] J.L. Kern, T.J. Flynn, Z. Wang, W.H. Thompson, B.B. Laird, *Fluid Phase Equilib.* 411 (2016) 81–87.
- [21] J. Muscatello, F. Jaeger, O.K. Matar, E.A. Müller, *Appl. Mater. Interf.* 8 (2016) 12330–12336.
- [22] B.R. Brooks, C.L. Brooks, A.D. Mackerell, L. Nilsson, R.J. Petrella, B. Roux, Y. Won, G. Archontis, C. Bartels, S. Boresch, A. Cafilisch, L. Caves, Q. Cui, A.R. Dinner, M. Feig, S. Fischer, J. Gao, M. Hodoscek, W. Im, K. Kuczera, T. Lazaridis, J. Ma, V. Ovchinnikov, E. Paci, R.W. Pastor, C.B. Post, J.Z. Pu, M. Schaefer, B. Tidor, R.M. Venable, H.L. Woodcock, X. Wu, W. Yang, D.M. York, M. Karplus, *J. Comput. Chem.* 30 (2009) 1545–1614.
- [23] I.T. Todorov, W. Smith, K. Trachenko, M.T. Dove, *J. Mater. Chem.* 16 (2006) 1911–1918.
- [24] H.-J. Limbach, A. Arnold, B.A. Mann, C. Holm, *Comput. Phys. Comm.* 174 (2006) 704–727.
- [25] M. Lagache, P. Ungerer, A. Boutin, A. Fuchs, *Phys. Chem. Chem. Phys.* 3 (2001) 4333–4339.
- [26] M.J. Abraham, M. Murtola, R. Schulz, S. Páll, J.C. Smith, B. Hess, E. Lindahl, *SoftwareX* 1 (2015) 19–25.
- [27] J. Roth, F. Gähler, H.-R. Trebin, *Internat. J. Modern Phys. C* 11 (2000) 317–322.
- [28] S. Plimpton, *J. Comput. Phys.* 117 (1995) 1–19.
- [29] C. Niethammer, S. Becker, M. Bernreuther, M. Buchholz, W. Eckhardt, A. Heinecke, S. Werth, H.-J. Bungartz, C.W. Glass, H. Hasse, J. Vrabec, M. Horsch, *J. Chem. Theory Comput.* 10 (2014) 4455–4464.
- [30] J.C. Phillips, R. Braun, W. Wang, J. Gumbart, E. Tajkhorshid, E. Villa, C. Chipot, R.D. Skeel, L. Kale, K. Schulten, *J. Comput. Chem.* 26 (2005) 1781–1802.
- [31] P. Ren, J.W. Ponder, *J. Phys. Chem. B* 107 (2003) 5933–5947.
- [32] M.G. Martin, *Mol. Sim.* 39 (2013) 1212–1222.
- [33] M. Thol, G. Rutkai, A. Köster, R. Lustig, R. Span, J. Vrabec, *J. Phys. Chem. Ref. Data* 45 (2016) 023101.

- [34] M. Hülsmann, T. Köddermann, J. Vrabec, D. Reith, *Comput. Phys. Comm.* 181 (2010) 499–513.
- [35] M. Hülsmann, J. Vrabec, A. Maaß, D. Reith, *Comput. Phys. Comm.* 181 (2010) 887–905.
- [36] K. Stöbener, P. Klein, S. Reiser, M. Horsch, K.-H. Küfer, H. Hasse, *Fluid Phase Equilib.* 373 (2014) 100–108.
- [37] D. Frenkel, B. Smit, *Understanding Molecular Simulation: From Algorithms to Applications*, Academic Press, Elsevier, San Diego, 2002.
- [38] R. Lustig, *J. Chem. Phys.* 109 (1998) 8816–8828.
- [39] T. Kristóf, G. Rutkai, L. Merényi, J. Liszi, *Mol. Phys.* 103 (2005) 537–545.
- [40] H.C. Andersen, *J. Chem. Phys.* 72 (1980) 2384–2393.
- [41] J. Stoll, J. Vrabec, H. Hasse, *J. Chem. Phys.* 119 (2003) 11396–11407.
- [42] H. Flyvbjerg, H.G. Petersen, *J. Chem. Phys.* 91 (1989) 461–466.
- [43] R. Span, *Multiparameter Equations of State: An Accurate Source of Thermodynamic Property Data*, Springer Verlag, Berlin, 2000.
- [44] R. Lustig, *Mol. Sim.* 37 (2011) 457–465.
- [45] R. Lustig, *Mol. Phys.* 110 (2012) 3041–3052.
- [46] B. Widom, *J. Chem. Phys.* 39 (1963) 2808–2812.
- [47] T. Kristóf, G. Rutkai, *Chem. Phys. Lett.* 445 (2007) 74–78.
- [48] M. Mezei, D.L. Beveridge, *Ann. New York Acad. Sci.* 482 (1986) 1–23.
- [49] S.H. Fleischman, D.A. Zichi, *J. Chem. Phys.* 88 (1991) 2617–2622.
- [50] T. Steinbrecher, D.L. Mobley, D.A. Case, *J. Chem. Phys.* 127 (2007) 214108.
- [51] F. Moučka, I. Nezbeda, W.R. Smith, *J. Chem. Phys.* 139 (2013) 124505.
- [52] Z. Mester, A.Z. Panagiotopoulos, *J. Chem. Phys.* 142 (2015) 044507.
- [53] F. Moučka, I. Nezbeda, W.R. Smith, *J. Chem. Theory Comput.* 11 (2015) 1756–1764.
- [54] M. Kohns, S. Reiser, M. Horsch, H. Hasse, *J. Chem. Phys.* 144 (2016) 084112.
- [55] I.S. Joung, T.E. Cheatham, *J. Phys. Chem. B* 112 (2008) 9020–9041.
- [56] A.L. Benavides, J.L. Aragones, C. Vega, *J. Chem. Phys.* 144 (2016) 124504.
- [57] W.J. Hamer, Y. Wu, *J. Phys. Chem. Ref. Data* 1 (1972) 1047–1100.
- [58] R. Krishna, J.M. van Baten, *Ind. Eng. Chem. Res.* 44 (2005) 6939–6947.
- [59] F.H. Stillinger, *Science* 209 (1980) 451–457.
- [60] R.H. Henchman, S.J. Irudayam, *J. Phys. Chem. B* 114 (2010) 16792–16810.
- [61] E. Arunan, G.R. Desiraju, R.A. Klein, J. Sadlej, S. Scheiner, I. Alkorta, D.C. Clary, R.H. Crabtree, J.J. Dannenberg, P. Hobza, H.G. Kjaergaard, A.C. Legon, B. Mennucci, D.J. Nesbitt, *Pure Appl. Chem.* 83 (2011) 1637–1641.
- [62] J. Thar, B. Kirchner, *J. Phys. Chem. A* 110 (2006) 4229–4237.
- [63] M. Haughney, M. Ferrario, I.R. McDonald, *J. Phys. Chem.* 91 (1987) 4934–4940.
- [64] S. Reiser, N. McCann, M. Horsch, H. Hasse, *Supercrit. Fluids* 68 (2012) 94–103.
- [65] A. Luzar, D. Chandler, *J. Chem. Phys.* 98 (1993) 8160–8173.
- [66] S. Chowdhuri, A. Chandra, *J. Phys. Chem. B* 110 (2006) 9674–9680.
- [67] A. Luzar, D. Chandler, *Nature* 379 (1996) 55–57.
- [68] J.R. Choudhuri, A. Chandra, *J. Chem. Phys.* 141 (2014) 134703.
- [69] G. Guevara-Carrion, C. Nieto-Draghi, J. Vrabec, H. Hasse, *J. Phys. Chem. B* 112 (2008) 16664–16674.
- [70] L. Saiz, J.A. Padró, E. Guàrdia, *J. Phys. Chem. B* 101 (1997) 78–86.
- [71] W. Xu, J. Yang, Y. Hu, *J. Phys. Chem. B* 113 (2009) 4781–4789.
- [72] D. Bhandary, S. Khan, J.K. Singh, *J. Phys. Chem. C* 118 (2014) 6809–6819.
- [73] M. Kreitmair, H. Bertagnolli, J.J. Mortensen, M. Parrinello, *J. Chem. Phys.* 118 (2003) 3639–3645.
- [74] H.J.C. Berendsen, J.R. Grigera, T.P. Straatsma, *J. Phys. Chem.* 91 (1987) 6269–6271.
- [75] S. Reiser, S. Deublein, J. Vrabec, H. Hasse, *J. Chem. Phys.* 140 (2014) 044504.

### 3.4 Molecular models for cyclic alkanes and ethyl acetate as well as surface tension data from molecular simulation

S. Eckelsbach, T. Janzen, **A. Köster**, S. Miroshnichenko, Y. M. Muñoz-Muñoz, J. Vrabec, *High Performance Computing in Science and Engineering'14*, Springer, Berlin, 645-659, 2015.

DOI: [doi.org/10.1007/978-3-319-10810-0\\_42](https://doi.org/10.1007/978-3-319-10810-0_42)

Nachgedruckt mit Erlaubnis von Springer Nature (Copyright 2015).

In dieser ausführlichen Arbeit wurden molekulare Kraftfelder für vier zyklische Alkane und Ethylacetat erstellt und erfolgreich an experimentelle Daten angepasst. Für binäre Mischungen eines Modelltreibstoffs aus Aceton und Stickstoff sowie Aceton und Sauerstoff wurden die Oberflächenspannung und Dichteprofile untersucht. Weiterhin wurden die partiellen Ableitungen der Helmholtzenergie aus *NVE* Ensemble Simulationen mit denen aus *NVT* Ensemble Simulationen für Ethylenoxid verglichen.

Der Autor der vorliegenden Dissertation hat im Rahmen dieser Publikation Simulationen für Ethylenoxid im *NVE* Ensemble durchgeführt und Ergebnisse für die partiellen Ableitungen der Helmholtzenergie ausgewertet. Die Überarbeitung des Manuskripts wurde unter Mithilfe von Prof. Jadran Vrabec durchgeführt. Der Autor wurde während des gesamten Prozesses von Prof. Jadran Vrabec betreut.

# Molecular models for cyclic alkanes and ethyl acetate as well as surface tension data from molecular simulation

Stefan Eckelsbach<sup>1</sup>, Tatjana Janzen<sup>1</sup>, Andreas Köster<sup>1</sup>, Svetlana Miroshnichenko<sup>1</sup>, Yonny Mauricio Muñoz-Muñoz<sup>1</sup>, and Jadran Vrabec<sup>1</sup>

## 1 Introduction

Thermodynamic data for most technically interesting systems are still scarce or even unavailable despite the large experimental effort that was invested over the last century into their measurement. This particularly applies to mixtures containing two or more components and systems under extreme conditions. In contrast to phenomenological methods, molecular modeling and simulation is based on a sound physical foundation and is therefore well suited for the prediction of such properties and processes.

In this work new molecular force field models, i.e. for four cyclic alkanes and ethyl acetate, are presented to widen the application area of molecular simulation.

In the second part of this work vapor-liquid interfaces were investigated, deepening the understanding of interfacial processes of a model fuel, consisting of acetone, nitrogen and oxygen, similar to the state of injected acetone droplets in a gaseous fluid in combustion chambers.

In the third part an efficient method for the generation of large simulation data sets is studied with respect to the stability and accuracy, using the microcanonical ensemble (*NVE*) instead of the canonic (*NVT*) ensemble.

## 2 Optimization of potential models for cyclic alkanes from cyclopropane to cyclohexane

Cyclic hydrocarbons are substances that are very common in the chemical industry, having one or more rings in their molecular structure. Cyclic alkanes with a single

<sup>1</sup> Lehrstuhl für Thermodynamik und Energietechnik (ThEt), Universität Paderborn, Warburger Str. 100, 33098 Paderborn · Author to whom correspondence should be addressed: J. Vrabec, e-mail: jadran.vrabec@upb.de.



ring are part of this class of compounds and can be represented with the general molecular formula  $C_nH_{2n}$ . These compounds, that are primarily found in crude oil, have single bonds between the carbon atoms, i.e. their carbon atoms are completely saturated.

In the petrochemical industry, for example, cyclohexane is produced from the hydrogenation of benzene, albeit the inverse reaction, i.e. the dehydrogenation of cyclohexane to yield benzene is more important. An improvement of the understanding of the nature of all involved physical forces of the cyclic alkanes may lead to various technical applications, including chemical equilibrium studies and vapor-liquid equilibrium (VLE) data extraction for both pure substances and mixtures. Furthermore, both temperature and pressure can be obtained using molecular simulations to study the development of hydrates, which is important since their formation e.g. causes obstructions of pipes.

Moreover, it is believed that with accurate potential models it will be possible to obtain hybrid models which might decrease experimental effort and costs. Scarce experimental data are available for cyclobutane, such that molecular simulation can be a source to provide pseudo experimental data and can contribute to extend existing models. Thus the motivation is to develop accurate molecular force field models for these substances, which constitutes the principal objective of this work.

The parameterization route introduced in prior work of our group [1] was adapted in this work, to obtain accurate intermolecular potential models from cyclopropane ( $C_3H_6$ ) to cyclohexane ( $C_6H_{12}$ ). To obtain such potential models, the cycloalkane molecules were assumed to be rigid, i.e. without internal degrees of freedom, formed by Lennard-Jones (LJ) sites bonded in a ring shaped structure with internal angles computed by quantum mechanical calculations.

The geometric structure of all molecules was obtained with the open source code for computational chemistry calculations GAMESS (US) [2], using the Hartree-Fock (HF) method with a relatively small (6-31 G) basis set. Thereby all atomic positions were determined for each hydrogen and carbon atom in the molecule. Cyclopropane is an essentially planar molecule, characterized only by bond angles and bond lengths. This is in contrast to cyclobutane, cyclopentane and cyclohexane, which require the specification of dihedral angles due to their three-dimensional structure.

A reduction of computational costs can be achieved by employing the united atoms approximation, whereby the methylene group is represented by a single methylene site. The LJ force centre for each methylene site was initially located at the position of the carbon atom, as determined by the HF method.

Subsequently, the methylene site-site distance was gradually modified while keeping the bond and dihedral angles invariant, molecular simulation runs were performed to compute VLE data for the pure substances using the *ms2* code [3] and the LJ parameters reported by [1]. The procedure was repeated for all molecules studied in this work.

The simulation results were compared to experimental data for the VLE properties, the critical point and second virial coefficient from the literature. Whenever reasonable results were obtained for VLE properties, such as saturated liquid den-

sity, vapor pressure and enthalpy of vaporization, the methylene site-site distances were fixed and the models were then subject to further optimization.

The LJ parameters were optimized using the reduced method by Merker et al. [4], which constitutes a computationally effective procedure, since no additional molecular simulation runs are necessary.

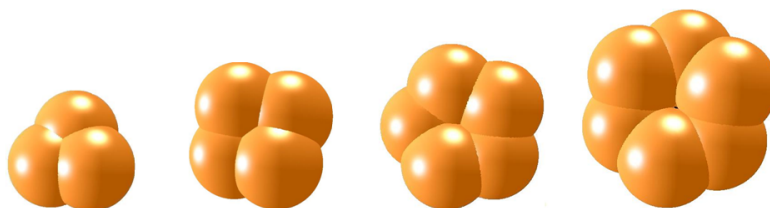


**Fig. 1** Snapshots of cyclopropane ( $C_3H_6$ ), cyclobutane ( $C_4H_8$ ), cyclopentane ( $C_5H_{10}$ ) and cyclohexane ( $C_6H_{12}$ ) obtained in this work (left to right)

Figure 1 shows a snapshot for each molecular structure obtained in this work. Every geometry contains the internal angles as computed by quantum mechanical calculations, but the site-site distances were enlarged. The cyclopropane structure was planar, while the cyclobutane and cyclopentane are three-dimensional structures. For the cyclohexane case, the chair configuration was chosen.

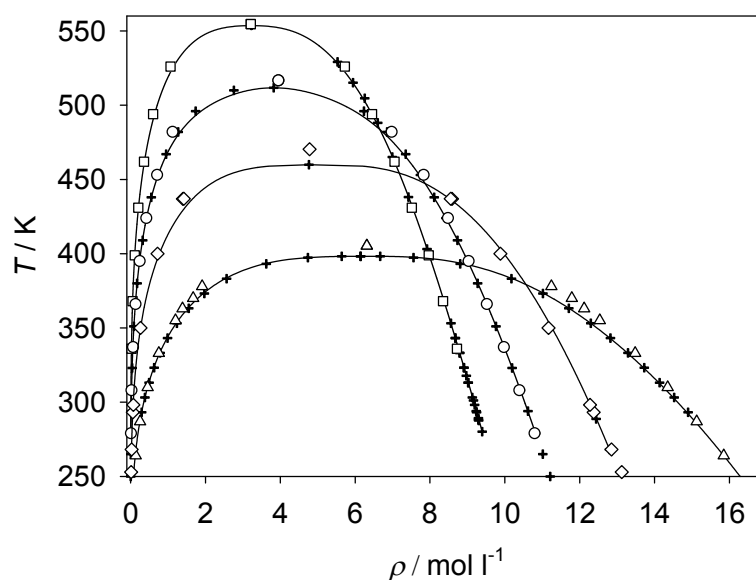


**Fig. 2** Vapor-liquid envelopes of the cycloalkanes studied in this work. Triangles represent  $C_3H_6$ , diamonds  $C_4H_8$ , circles  $C_5H_{10}$  and squares  $C_6H_{12}$ . The cross symbol corresponds to experimental data from the literature.

Figure 2 shows the molecular simulation results for the VLE for each fluid studied in this work, including the critical point. The continuous lines are the data from the best reference equations of state that are available for cyclopentane and cyclohexane. For the cyclopropane and cyclobutane cases, the continuous lines are data from typical correlations that are used in the literature. Moreover, experimental data are shown for each fluid. Note that for the cyclobutane case, the experimental data are very scarce, but molecular simulation results have similar performance as the DIPPR [5] correlations.

### 3 Ethyl acetate

Ethyl acetate is the organic compound with the formula  $\text{CH}_3 - \text{COO} - \text{CH}_2 - \text{CH}_3$ . It is produced by the esterification reaction of ethanol and acetic acid and is synthesized on a large scale for a use as a solvent. VLE data are necessary for the design and optimization of separation processes, therefore, a new molecular model for ethyl acetate is proposed here.

#### 3.1 Molecular model class

The present molecular model include three groups of potential parameters. These are the geometric parameters, specifying the positions of different interaction sites, the electrostatic parameters, defining the polar interactions in terms of point charges, dipoles or quadrupoles, and the dispersive and repulsive parameters, determining the attraction by London forces and the repulsion by electronic orbital overlaps. Here, the LJ 12-6 potential [6, 7] was used to describe the dispersive and repulsive interactions. The total intermolecular interaction energy thus writes as

$$U = \sum_{i=1}^{N-1} \sum_{j=i+1}^N \left\{ \sum_{a=1}^{S_i^{\text{LJ}}} \sum_{b=1}^{S_j^{\text{LJ}}} 4\epsilon_{ijab} \left[ \left( \frac{\sigma_{ijab}}{r_{ijab}} \right)^{12} - \left( \frac{\sigma_{ijab}}{r_{ijab}} \right)^6 \right] + \sum_{c=1}^{S_i^e} \sum_{d=1}^{S_j^e} \frac{1}{4\pi\epsilon_0} \left[ \frac{q_{ic}q_{jd}}{r_{ijcd}} + \frac{q_{ic}\mu_{jd} + \mu_{ic}q_{jd}}{r_{ijcd}^2} \cdot f_1(\mathbf{w}_i, \mathbf{w}_j) + \frac{q_{ic}Q_{jd} + Q_{ic}q_{jd}}{r_{ijcd}^3} \cdot f_2(\mathbf{w}_i, \mathbf{w}_j) + \frac{\mu_{ic}\mu_{jd}}{r_{ijcd}^3} \cdot f_3(\mathbf{w}_i, \mathbf{w}_j) + \frac{\mu_{ic}Q_{jd} + Q_{ic}\mu_{jd}}{r_{ijcd}^4} \cdot f_4(\mathbf{w}_i, \mathbf{w}_j) + \frac{Q_{ic}Q_{jd}}{r_{ijcd}^5} \cdot f_5(\mathbf{w}_i, \mathbf{w}_j) \right] \right\}, \quad (1)$$

where  $r_{ijab}$ ,  $\epsilon_{ijab}$ ,  $\sigma_{ijab}$  are the distance, the LJ energy parameter and the LJ size parameter, respectively, for the pair-wise interaction between LJ site  $a$  on molecule  $i$  and LJ site  $b$  on molecule  $j$ . The permittivity of the vacuum is  $\epsilon_0$ , whereas  $q_{ic}$ ,  $\mu_{ic}$  and  $Q_{ic}$  denote the point charge magnitude, the dipole moment and the quadrupole

moment of the electrostatic interaction site  $c$  on molecule  $i$  and so forth. The expressions  $f_x(\mathbf{\omega}_i, \mathbf{\omega}_j)$  stand for the dependence of the electrostatic interactions on the orientations  $\mathbf{\omega}_i$  and  $\mathbf{\omega}_j$  of the molecules  $i$  and  $j$  [8, 9]. Finally, the summation limits  $N$ ,  $S_x^{\text{LJ}}$  and  $S_x^{\text{e}}$  denote the number of molecules, the number of LJ sites and the number of electrostatic sites, respectively. The atomic charges were estimated here by the Mulliken method [10].

Lorentz-Berthelot combining rules are used to determine cross-parameters for Lennard-Jones interactions between sites of different type [11, 12]:

$$\sigma_{ijab} = \frac{\sigma_{iiaa} + \sigma_{jjbb}}{2}, \quad (2)$$

and

$$\epsilon_{ijab} = \sqrt{\epsilon_{iiaa}\epsilon_{jjbb}}. \quad (3)$$

### 3.2 Molecular model of ethyl acetate

A new molecular model was developed for ethyl acetate based on quantum chemical (QC) information on molecular geometry and electrostatics. In a first step, the geometric data of the molecules, i.e. bond lengths, angles and dihedrals, were determined by QC calculations. Therefore, a geometry optimization was performed via an energy minimization using the GAMESS(US) package [2]. The Hartree-Fock level of theory was applied with a relatively small (6-31 G) basis set. Intermolecular electrostatic interactions mainly occur due to the static polarity of single molecules that can well be obtained by QC. Here, the Møller-Plesset 2 level of theory was used that considers electron correlation in combination with the polarizable 6-31G basis set.

Figure 3 shows the devised molecular model.

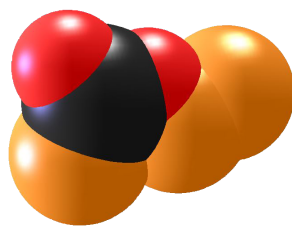


**Fig. 3** Snapshot of ethyl acetate

The new model of ethyl acetate is based on the work of Kamath et al. [13], which is improved by including geometry and electrostatics from QM calculations. The initial model adopted the LJ parameters by Kamath et al., which were then adjusted to experimental VLE data, i.e. saturated liquid density, vapor pressure, and enthalpy of vaporization, until a desired quality was reached.

The present ethyl acetate model consists of six LJ sites (one for the methylene bridge, one for each oxygen atom, and one for each methyl group). The electrostatic interactions were modeled by five point charges. The parameters of the LJ sites were adjusted to experimental saturated liquid density and vapor pressure. The full parameter set of the new ethyl acetate model is listed in Table 1.

**Table 1** Parameters of the molecular model for ethyl acetate developed in this work. Lennard-Jones interaction sites are denoted by the modeled atomic groups. Electrostatic interaction sites are denoted by point charge. Coordinates are given with respect to the center of mass in a principal axes system.

interaction site	$x$ Å	$y$ Å	$z$ Å	$\sigma$ Å	$\epsilon/k_B$ K	$q$ e
CH <sub>3</sub>	-2.273	1.172	0	3.7227	74.139	
CH <sub>2</sub>	-1.312	0.018	0	3.9212	34.800	
O	0.000	0.589	0	3.0278	59.765	
C	1.101	-0.203	0	3.8716	31.018	
O	2.188	0.321	0	2.7796	41.609	
CH <sub>3</sub>	0.897	-1.690	0	3.7227	74.139	
point charge (CH <sub>2</sub> )	-1.312	0.018	0			0.306
point charge (O)	0.000	0.589	0			-0.474
point charge (C)	1.101	-0.203	0			0.593
point charge (O)	2.188	0.321	0			-0.415
point charge (CH <sub>3</sub> )	0.897	-1.690	0			-0.010

The pure substance VLE simulation results are shown in figures 4 and 5, where they are compared to experimental data and the DIPPR correlations [14]. The new ethyl acetate model shows mean unsigned deviations to experimental data of 0.1 % for the saturated liquid density, 4.6 % for the vapor pressure and 4.3 % for the enthalpy of vaporization over the whole temperature range from the triple point to the critical point.

For pure ethyl acetate, predicted data on the second virial coefficient is available from DIPPR. Figure 5 shows the simulation results compared to correlation of predicted data taken from DIPPR [14]. The present second virial coefficient agrees well with the DIPPR correlation at high temperatures, however at low temperatures, some noticeable deviations are present yielding a mean error of about 0.5 l/mol.

### 3.3 Binary vapor-liquid equilibria

Based on the devised molecular model of ethyl acetate, VLE data were predicted for the binary system ethyl acetate + chloroform. The molecular model for chloroform was taken from Stoll et al. [16] and is of the two-center LJ plus point dipole type. The vapor-liquid phase behavior of the binary mixture was predicted by molecular simulation and compared to experimental data as well as the Peng-Robinson equation of state [17].

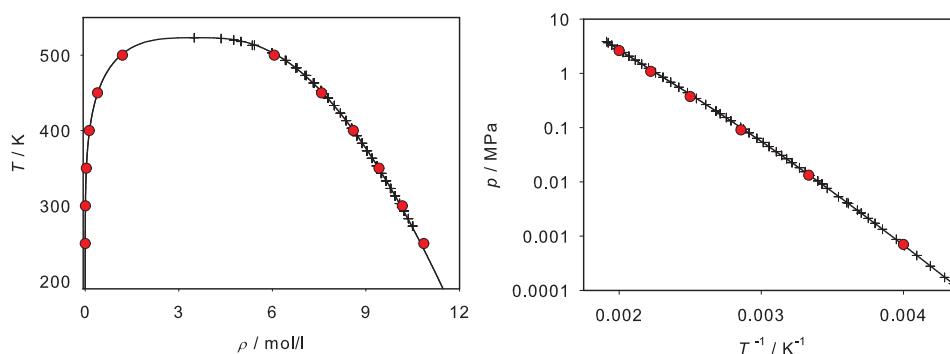


**Fig. 4** Simulation results (●), experimental data [15] (+) and DIPPR correlation of experimental data [14] (—) of ethyl acetate. Left: saturated densities, right: vapor pressure. The statistical uncertainties of the present simulation data are within symbol size.

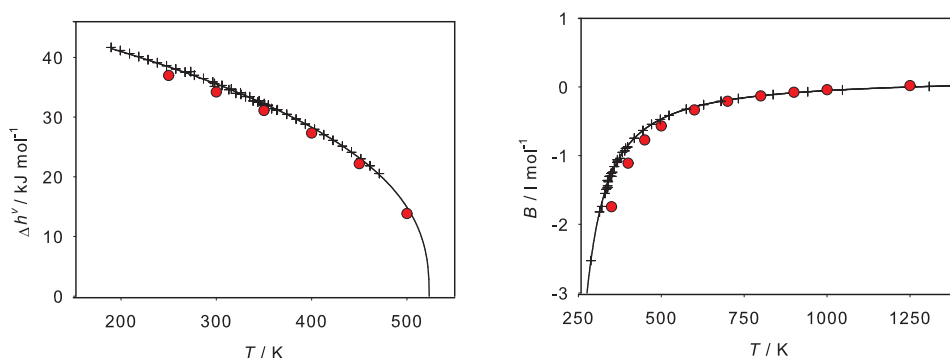


**Fig. 5** Simulation results (●), experimental data [15] (+) and DIPPR correlation of experimental data [15] (—) of ethyl acetate. Left: enthalpy of vaporisation, right: second virial coefficient. The statistical uncertainties of the present simulation data are within symbol size.

Figure 6 shows the isothermal VLE of ethyl acetate + chloroform at 323.15 K from experiment [18], simulation and Peng-Robinson equation of state. The experimental vapor pressure at a liquid mole fraction of  $x_{\text{chloroform}} = 0.5$  mol/mol was taken to adjust the binary parameter of the molecular model ( $\xi = 1.04$ ) and of the Peng-Robinson equation of state ( $k_{ij} = -0.085$ ). It can be seen that the results obtained by molecular simulation agree well with the experimental results and the Peng-Robinson equation of state.

## 4 Interfacial properties of binary mixtures

Interfacial properties are of interest for processes containing two or more phases, which is basically the default case for complex technical and natural systems, in-

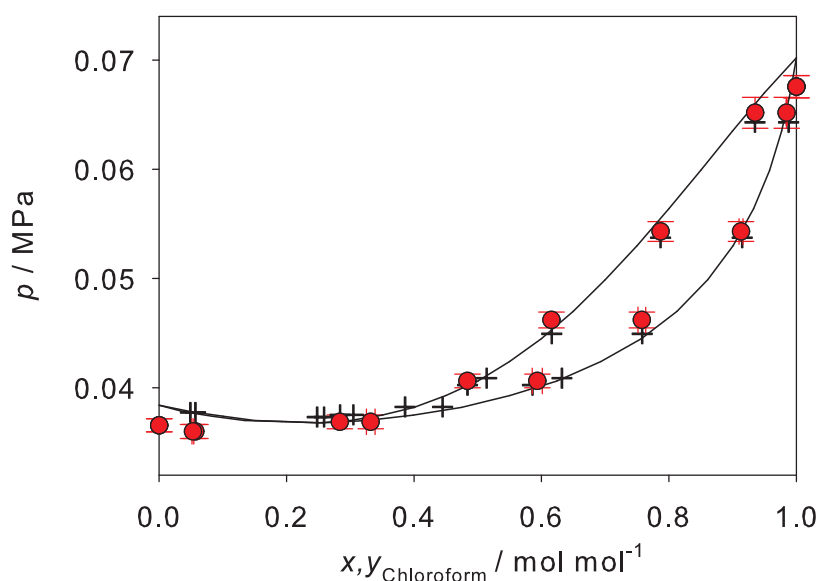


**Fig. 6** Isothermal vapor-liquid phase diagram of ethyl acetate + chloroform at 323.15 K: present simulation data with  $\xi = 1.04$  (●); experimental data by Ohta et al. [18] (+); Peng-Robinson equation of state with  $k_{ij} = -0.085$  (—).

cluding separation processes, boiling and any system containing droplets. Many of these processes occur under extreme conditions of temperature or pressure, e.g. in case of flash boiling in combustion chambers. Such processes are actively being used although striking gaps remain in their essential understanding. At the same time, thermodynamic data for most technically interesting systems are still scarce or even unavailable despite the large experimental effort that was invested into their measurement. This particularly applies to mixtures of two or more components and systems under extreme conditions.

In this work, interfacial properties of the binary mixtures nitrogen + oxygen and nitrogen + acetone were investigated. These mixtures serve as a model fuel, yielding interfacial data and deepen the general understanding of the interfacial processes for the injection of acetone droplets in a gaseous fluid, consisting of nitrogen and oxygen. For this purpose, direct simulations of vapor-liquid equilibria were carried out, with particular attention to the interface region.

First, density and composition data of the bulk phases were required to set up the simulations. These data were obtained from simulations using the molecular simulation tool *ms2* [3]. Molecular force field models, adjusted to the mixtures with an additional binary interaction parameter, from previous works of our group were used [19, 20]. They lead to very good agreement with reference data even for temperatures near the critical point, typically having only a 2 % deviation to the critical density  $\rho_c$  [20].

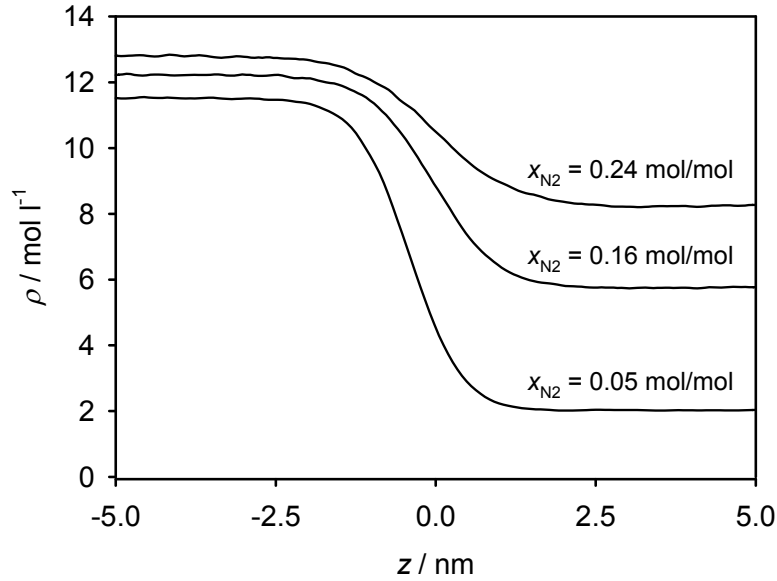


**Fig. 7** Profile of the total density over the length of the simulation volume. The temperature is constant at 400 K. Three mixtures containing nitrogen and acetone are shown for three different compositions: the liquid mole fractions are  $x_{N_2} = 0.05$  mol/mol,  $x_{N_2} = 0.16$  mol/mol, and  $x_{N_2} = 0.24$  mol/mol.

Further simulations were carried out with the highly parallel molecular dynamics code *ls1* [21]. Due to the inhomogeneity of the simulated systems, the long range correction of Janeček was used [22]. After an equilibration period, the interface region was formed, which gave the possibility for further investigation. The equilibrated states of the interface region are shown exemplarily in figure 7 for three different compositions at the constant temperature of 400 K.

The surface tension can be calculated following the Irving-Kirkwood approach [23]

$$\gamma = \frac{1}{2A} (2\Pi_{zz} - (\Pi_{xx} + \Pi_{yy})), \quad (4)$$

where  $A$  is the area of the interface and  $\Pi_{\alpha\beta}$  is an element of the virial tensor, which is defined as

$$\Pi_{\alpha\beta} = \left\langle \frac{1}{2} \sum_{i=1}^N \sum_{j=1}^N r_{ij}^{\alpha} f_{ij}^{\beta} \right\rangle. \quad (5)$$

The indices  $\alpha$  and  $\beta$  represent the  $x$ -,  $y$ - or  $z$ -directions of the distance vector  $\mathbf{r}_{ij}$  and the force vector  $\mathbf{f}_{ij}$ , in each case between molecules  $i$  and  $j$ . The virial tensor in normal ( $\Pi_N = \Pi_{zz}$ ) and tangential direction ( $\Pi_T = (\Pi_{xx} + \Pi_{yy})/2$ ) as well as the difference between these are exemplarily shown in figure 8 for one state point.

The simulated surface tension was compared to experimental data, which are relatively rare and only available for the pure substances. Thus the prediction of the



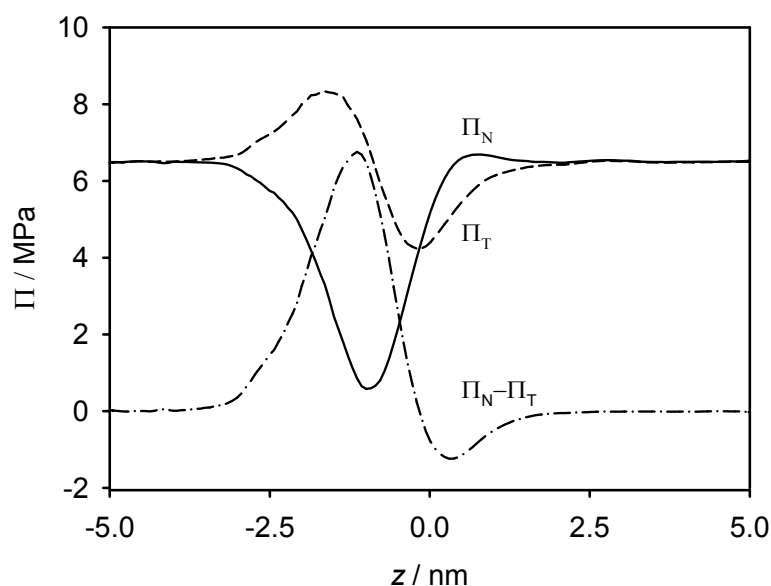


**Fig. 8** Profile of the virial tensor over the length of the simulation volume. The virial tensor in normal direction  $\Pi_N$ , in tangential direction  $\Pi_T$  and the difference of these are shown. The mixture consists of nitrogen and acetone with a liquid mole fraction of  $x_{N_2} = 0.05$  and a temperature of 400 K.

surface tension based on the parachor [29] was used for comparison with the results for the binary mixtures. In figure 9 the simulation results for the pure substances nitrogen and oxygen as well as their mixture are given. The mixture was set up in an equimolar state for the liquid phase. The simulation data for the pure substances are in good agreement with the surface tension correlation by Mulero et al. [25], which is based on experimental data, and the experimental data itself. In general, the direct simulations using the Monte Carlo scheme by Neyt et al. [24] show a slight overestimation in comparison with the reference data. The simulation results of the mixture nitrogen + oxygen also show a good agreement with the correlation [25]. The prediction following the parachor method is based on data calculated with the equations of state by Schmidt et al. [30] and Span et al. [31] and yields results, that are a little bit lower in the whole considered temperature range, but are relatively close to the reference.

In figure 10 the simulation results for the surface tension of the mixture nitrogen + acetone are plotted over the liquid mole fraction at 400 K and 450 K. For higher mole fractions near the critical point, the simulated data concur with the results of Klink and Gross (personal communication, 25 Feb 2014), determined by the density functional theory method. For smaller mole fractions, the simulation results are somewhat lower, until they match the correlation by Mulero et al. [25] for pure acetone within the estimated uncertainties of the present simulations. For this state the data by Klink and Gross overestimate the surface tension in comparison

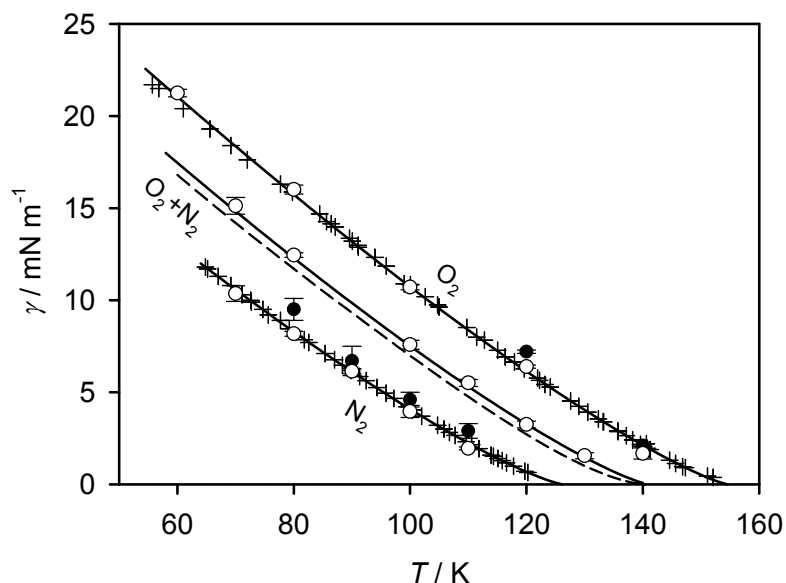


**Fig. 9** Surface tension over temperature for the pure substances nitrogen and oxygen and their equimolar (liquid phase) mixture. Simulations:  $\circ$  this work,  $\bullet$  Neyt et al. [24]; correlations: — Mulero et al. [25], --- parachor method; experimental data: + [26, 27, 28]. The statistical uncertainties of the simulation data indicate the standard error on a 95 % confidence interval.

to the correlation of experimental data. Here the parachor method was based on the Peng-Robinson equation of state with the Huron-Vidal mixing rule, published by Windmann et al. [20]. Its results underestimate the surface tension significantly for both investigated temperatures. The parachor method strongly depends on the input data and is thus susceptible to their quality, which, of course, is better for the highly accurate and more complex equations of state by Schmidt et al. [30] and Span et al. [31].

## 5 Thermodynamic data by molecular simulations in the microcanonical ensemble

The importance of a solid base of thermodynamic data for the design and optimization of technological processes is crucial [32]. It was shown that molecular force field models allow for the generation of large and widespread data sets in a very short amount of time, due to the use of the molecular simulation framework proposed by Lustig [33], which gives access to any  $A_{mn}^r$  ( $m, n > 0$ ) in the  $NVT$  ensemble for a specific state point through

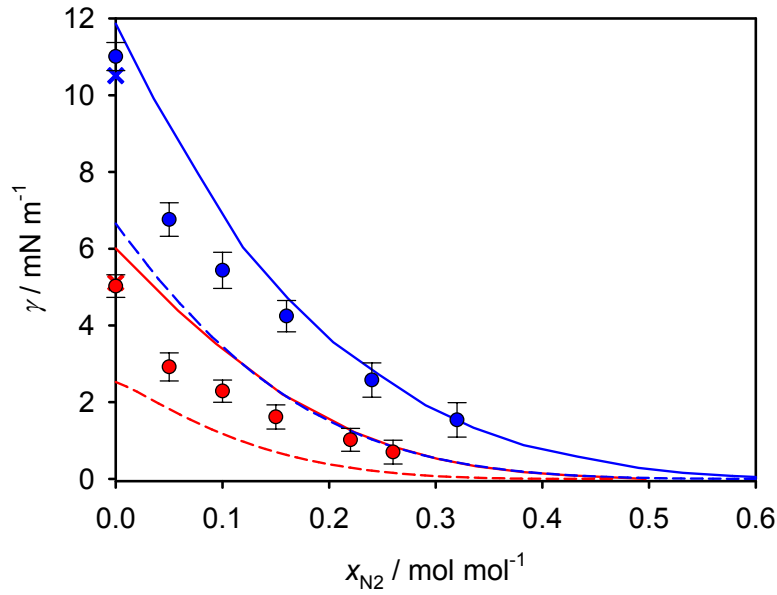


**Fig. 10** Surface tension over liquid mole fraction of nitrogen for the mixture nitrogen and acetone at 400 K (blue) and 450 K (red), respectively.  $\circ$  molecular dynamics, this work, — density functional theory, Klink and Gross (personal communication, 25 Feb 2014); correlations:  $\times$  Mulero et al. [25], --- parachor method. The statistical uncertainties of the simulation data indicate the standard error on a 95 % confidence interval.

$$\frac{\partial^{m+n} F / RT}{\partial^m (1/T) \partial^n (N/V)} \equiv A_{mn} = A_{mn}^i + A_{mn}^r, \quad (6)$$

wherein  $F$  is the Helmholtz energy,  $R$  the gas constant,  $T$  the temperature,  $N$  the number of particles and  $V$  the volume. The ideal part  $A_{mn}^i$ , which is needed to calculate any derivative of the Helmholtz energy, can be determined with other methods [33].

In order to extend this procedure, the present work deals with the usage of the microcanonical ensemble ( $NVE$ ) to generate such data sets. In the  $NVE$  ensemble, the number of particles  $N$ , the Volume  $V$  and the total energy  $E$  of the system are kept constant. Although  $E$  is not directly accessible through experimental study, there are some advantages to using the  $NVE$  ensemble. Compared to other statistical mechanical ensembles, it is isolated from its environment in terms of energy or particle exchange and can therefore be considered as more stable and less susceptible to fluctuations. This implies that there is no need to regulate temperature through an external thermostat ( $NVT$ ) and/or pressure through an external barostat ( $NpT$ ) in molecular dynamics simulations, because  $E$  is conserved naturally through Newton's equations of motion. Moreover, the  $NVE$  ensemble links mechanics and thermodynamics in a very direct way [34].

In order to validate the implementation of the *NVE* ensemble into the simulation tool *ms2* [3], tests were carried out for the substance ethylene oxide using the molecular force field model by Eckl et al. [35]. As can be seen in figure 11, several simulations in the homogeneous fluid region were carried out using the *NVT* and *NVE* ensemble, respectively. It should be noted, that *NVT* ensemble simulations using this framework were compared to highly accurate equations of state in preceding work yielding excellent results. The overall agreement between the different types can be considered as quite good. Only in the vicinity of the critical point and for higher order derivatives, some deviations of the *NVE* ensemble simulation data were found. Contrary to the expectation of more stable molecular simulations in the *NVE* ensemble, the statistical uncertainties indicated by the error bars are quite similar. Therefore, further investigation is required.

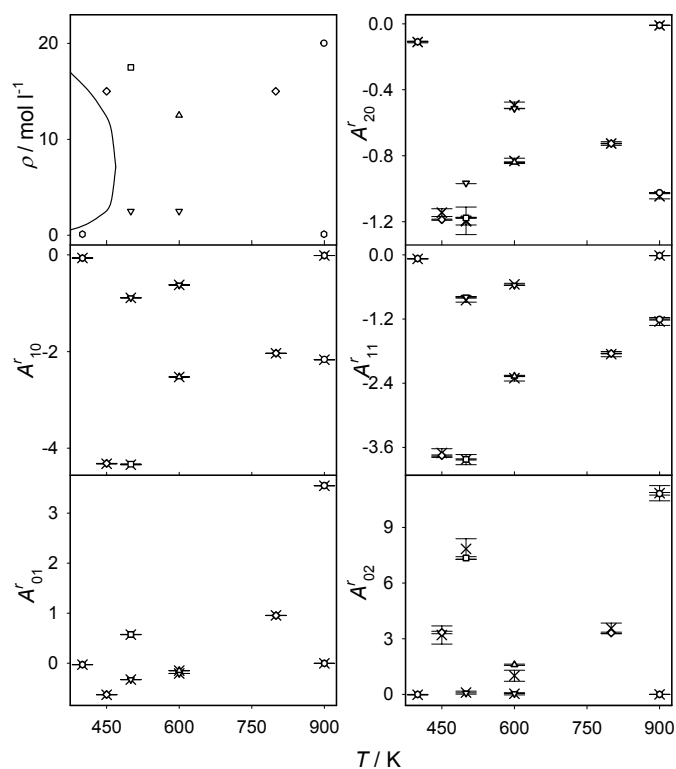


**Fig. 11** Top left: Sampled state points of ethylene oxide in the temperature vs. density plane. Remaining figures:  $A_{mn}^r$  values as a function of temperature from Monte Carlo molecular simulation for ethylene oxide [35]. The open symbols denote various isochores in the *NVT* ensemble. The cross symbols represent the simulations which were carried out in the *NVE* ensemble.

## 6 Conclusion

Five new molecular models were developed and optimized in this work. They were validated against experimental data for the VLE properties, the critical point and second virial coefficient, showing a good coincidence with the reference data.

Interfacial simulations of a model fuel were carried out, yielding the surface tension for two binary mixtures, which agree well with the experimental reference data, and fill gaps where such data were unavailable.

The expected accuracy gain by using the microcanonical ensemble was not observed in the present simulations using the molecular simulation framework proposed by Lustig [33]. Here, further investigations are required.

## 7 Acknowledgements

We gratefully acknowledge support by Deutsche Forschungsgemeinschaft. This work was carried out under the auspices of the Boltzmann-Zuse Society (BZS) of Computational Molecular Engineering. The simulations were performed on the Cray XE6 (Hermit) at the High Performance Computing Center Stuttgart (HLRS).

## References

- [1] B. Eckl, J. Vrabec, and H. Hasse. “Set of Molecular Models Based on Quantum Mechanical Ab Initio Calculations and Thermodynamic Data”. In: *J. Phys. Chem. B* 112 (2008), pp. 12710–12721.
- [2] M. W. Schmidt, K. K. Baldridge, J. A. Boatz, S. T. Elbert, M. S. Gordon, J. H. Jensen, S. Koseki, N. Matsunaga, K. A. Nguyen, S. Su, T. L. Windus, M. Dupuis, and J. A. Montgomery. “General atomic and molecular electronic structure system”. In: *J. Comput. Chem.* 14 (1993), pp. 1347–1363.
- [3] S. Deublein, B. Eckl, J. Stoll, S. V. Lishchuk, G. Guevara-Carrion, C. W. Glass, T. Merker, M. Bernreuther, H. Hasse, and J. Vrabec. “ms2: A molecular simulation tool for thermodynamic properties”. In: *Computer Physics Communications* 182 (2011), pp. 2350–2367.
- [4] T. Merker, J. Vrabec, and H. Hasse. “Engineering Molecular Models: Efficient Parameterization Procedure and Cyclohexanol as Case Study”. In: *Soft Mater.* 10 (2012), pp. 3–25.
- [5] R. L. Rowley, W. V. Wilding, J. L. Oscarson, Y. Yang, N. A. Zundel, T. E. Daubert, and R. P. Danner. *DIPPR data compilation of pure compound properties*. Design Institute for Physical Properties, AIChE. New York, 2006.
- [6] J. E. Jones. “On the Determination of Molecular Fields. I. From the Variation of the Viscosity of a Gas with Temperature”. In: *Proc. Roy. Soc.* 106A (1924), pp. 441–462.

## REFERENCES

15

- [7] J. E. Jones. “On the Determination of Molecular Fields. II. From the Equation of State of a Gas”. In: *Proc. Roy. Soc.* 106A (1924), pp. 463–477.
- [8] M. P. Allen and D. J. Tildesley. *Computer simulations of liquids*. Oxford: Oxford University Press, 1987.
- [9] C. G. Gray and K. E. Gubbins. *Theory of molecular fluids*. Vol. 1. Fundamentals. Oxford: Clarendon Press, 1984.
- [10] R. S. Mulliken. “Criteria for the Construction of Good Self-Consistent-Field Molecular Orbital Wave Functions, and the Significance of LCAO-MO Population Analysis”. In: *J. Chem. Phys.* 36 (2004), pp. 3428–3439.
- [11] H. A. Lorentz. “Über die Anwendung des Satzes vom Virial in der kinetischen Theorie der Gase”. In: *Ann. Phys.* 12 (1881), pp. 127–136.
- [12] D. Berthelot. “Sur le Mélange des Gaz”. In: *Compt. Rend. Ac. Sc.* 126 (1898), pp. 1703–1706.
- [13] G. Kamath, J. Robinson, and J. J. Potoff. “Application of TraPPE-UA force field for determination of vapor-liquid equilibria of carboxylate esters”. In: *Fluid Phase Equilibr.* 240 (2006), pp. 46–55.
- [14] R. L. Rowley, W. V. Wilding, J. L. Oscarson, Y. Yang, N. A. Zundel, T. E. Daubert, and R. P. Danner. *DIPPR Information and Data Evaluation Manager for the Design Institute for Physical Properties*. Design Institute for Physical Properties, AIChE. Version 5.0.2. New York, 2011.
- [15] *Dortmund Data Bank*. DDBST GmbH. Version 6.3.0.384. Oldenburg, 2010.
- [16] J. Stoll, J. Vrabec, and H. Hasse. “A set of molecular models for carbon monoxide and halogenated hydrocarbons”. In: *J. Chem. Phys.* 119 (2003), pp. 11396–11407.
- [17] D.-Y. Peng and D. B. Robinson. “A New Two-Constant Equation of State”. In: *Ind. Eng. Chem. Fund.* 15 (1976), pp. 59–64.
- [18] T. Ohta, H. Asano, and I. Nagata. “Thermodynamic Study of Complex-Formation in 4 Binary-Liquid Mixtures Containing Chloroform”. In: *Fluid Phase Equilibr.* 4 (1980), pp. 105–114.
- [19] J. Vrabec, J. Stoll, and H. Hasse. “A Set of Molecular Models for Symmetric Quadrupolar Fluids”. In: *J. Phys. Chem. B* 105 (2001), pp. 12126–12133.
- [20] T. Windmann, M. Linnemann, and J. Vrabec. “Fluid Phase Behavior of Nitrogen + Acetone and Oxygen + Acetone by Molecular Simulation, Experiment and the Peng–Robinson Equation of State”. In: *J. Chem. Eng. Data* 59 (2014), pp. 28–38.
- [21] C. Niethammer, M. Becker, M. Bernreuther, M. Buchholz, W. Eckhardt, A. Heinecke, S. Werth, H.-J. Bungartz, C. W. Glass, H. Hasse, J. Vrabec, and M. Horsch. “ls1 mardyn: The massively parallel molecular dynamics code for large systems”. In: *J. Chem. Theory Comput.* 10 (2014), pp. 4455–4464.
- [22] J. Janeček. “Long Range Corrections in Inhomogeneous Simulations”. In: *J. Phys. Chem. B* 110 (2006), pp. 6264–6269.
- [23] J. H. Irving and J. G. Kirkwood. “The Statistical Mechanical Theory of Transport Processes. IV. The Equations of Hydrodynamics”. In: *J. Chem. Phys.* 18 (1950), pp. 817–829.

- [24] J.-C. Neyt, A. Wender, V. Lachet, and P. Malfreyt. "Prediction of the Temperature Dependence of the Surface Tension Of SO<sub>2</sub>, N<sub>2</sub>, O<sub>2</sub>, and Ar by Monte Carlo Molecular Simulations". In: *J. Phys. Chem. B* 115 (2011), pp. 9421–9430.
- [25] A. Mulero, I. Cachadiña, and M. I. Parra. "Recommended Correlations for the Surface Tension of Common Fluids". In: *J. Phys. Chem. Ref. Data* 41 (2012), pp. 043105–1–043105–13.
- [26] Y. P. Blagoi, V. A. Kireev, M. P. Lobko, and V. V. Pashkov. "Surface Tension of Krypton, Methane, Deuteromethane and Oxygen". In: *Ukr. Fiz. Zh.* 15 (1970), pp. 427–432.
- [27] V. B. Ostromoukhov and M. G. Ostronov. "Surface Tension of Liquid Solutions O<sub>2</sub>–N<sub>2</sub> at 54–77 K". In: *Zh. Fiz. Khim.* 68 (1994), pp. 39–43.
- [28] V. G. Baidakov, K. V. Khvostov, and G. N. Muratov. "Surface-Tension of Nitrogen, Oxygen and Methane in a wide Temperature-Range". In: *Zh. Fiz. Khim.* 56 (1982), pp. 814–817.
- [29] Y. Sun and B. Y. Shekunov. "Surface tension of ethanol in supercritical CO<sub>2</sub>". In: *J. Supercrit. Fluid.* 27 (2003), pp. 73–83.
- [30] R. Schmidt and W. Wagner. "A new form of the equation of state for pure substances and its application to oxygen". In: *Fluid Phase Equilib.* 19 (1985), pp. 175–200.
- [31] R. Span, E. W. Lemmon, R. T. Jacobsen, W. Wagner, and A. Yokozeki. "A Reference Equation of State for the Thermodynamic Properties of Nitrogen for Temperatures from 63.151 to 1000 K and Pressures to 2200 MPa". In: *J. Phys. Chem. Ref. Data* 29 (2000), pp. 1361–1433.
- [32] S. Eckelsbach, S. Miroshnichenko, G. Rutkai, and J. Vrabec. "Surface tension, large scale thermodynamic data generation and vapor–liquid equilibria of real compounds". In: *High Performance Computing in Science and Engineering '13*. Ed. by W. E. Nagel, D. H. Kröner, and M. M. Resch. Berlin: Springer, 2013, pp. 635–646.
- [33] R. Lustig. "Statistical analogues for fundamental equation of state derivatives". In: *Mol. Phys.* 110 (2012), pp. 3041–3052.
- [34] R. Lustig. "Microcanonical Monte Carlo simulation of thermodynamic properties". In: *J. Chem. Phys.* 109 (1998), pp. 8816–8828.
- [35] B. Eckl, J. Vrabec, and H. Hasse. "On the application of force fields for predicting a wide variety of properties: Ethylene oxide as an example". In: *Fluid Phase Equilib.* 274 (2008), pp. 16–26.

### 3.5 Assessing the accuracy of improved force-matched water models derived from *ab initio* molecular dynamics simulations

A. Köster, T. Spura, G. Rutkai, J. Kessler, H. Wiebeler, J. Vrabec, T. D. Kühne, *Journal of Computational Chemistry* 37:1828-1838, 2016.

DOI: [doi.org/10.1002/jcc.24398](https://doi.org/10.1002/jcc.24398)

Nachgedruckt mit Erlaubnis von Wiley & Sons (Copyright 2016).

In dieser Studie wurde die Qualität verschiedener Typen von molekularen Kraftfeldern für Wasser untersucht. Hierzu gehörten zwei klassisch empirische Kraftfelder sowie zwei *ab initio* Kraftfelder aus dem sogenannten „Force-Matching“ Ansatz. Neben diversen zeitunabhängigen thermodynamischen Zustandsgrößen, wurden auch Transportgrößen und strukturelle Eigenschaften analysiert. Es zeigte sich dabei, dass *ab initio* Kraftfelder konkurrenzfähig und insbesondere bei strukturellen Eigenschaften bessere Ergebnisse zeigen können. Ein großer Vorteil dieser Kraftfelder ist, dass keine experimentellen Daten für ihre Erstellung notwendig sind und diese damit auch für extrem schlecht vermessene oder kaum vorhandene Substanzen erstellt werden können.

Arbeiten an dieser Publikation wurden koordiniert vom Autor der vorliegenden Dissertation unter Betreuung von Prof. Thomas D. Kühne und Prof. Jadran Vrabec. Der Autor hat die molekularen Simulationen und deren Auswertung und Diskussion durchgeführt. Prof. Thomas D. Kühne hat die Einordnung der verwendeten *ab initio* Kraftfelder und die Beschreibung des zugrundeliegenden „Force-Matching“ Ansatzes durchgeführt. Die Überarbeitung des Manuskripts wurde unter Mithilfe von Prof. Thomas D. Kühne und Prof. Jadran Vrabec durchgeführt. Der Autor wurde während des gesamten Prozesses von Prof. Jadran Vrabec betreut.



# Assessing the Accuracy of Improved Force-Matched Water Models Derived from *Ab Initio* Molecular Dynamics Simulations

Andreas Köster,<sup>[a]</sup> Thomas Spura,<sup>[b]</sup> Gábor Rutkai,<sup>[a]</sup> Jan Kessler,<sup>[b]</sup> Hendrik Wiebeler,<sup>[b]</sup> Jadran Vrabec,<sup>[a]</sup> and Thomas D. Kühne<sup>\*,[b]</sup>

The accuracy of water models derived from *ab initio* molecular dynamics simulations by means of an improved force-matching scheme is assessed for various thermodynamic, transport, and structural properties. It is found that although the resulting force-matched water models are typically less accurate than fully empirical force fields in predicting thermodynamic properties, they are nevertheless much more accurate than generally appreciated in reproducing the structure of liq-

uid water and in fact superseding most of the commonly used empirical water models. This development demonstrates the feasibility to routinely parametrize computationally efficient yet predictive potential energy functions based on accurate *ab initio* molecular dynamics simulations for a large variety of different systems. © 2016 Wiley Periodicals, Inc.

DOI: 10.1002/jcc.24398

## Introduction

Since the very first application of molecular dynamics (MD) to realistic systems,<sup>[1]</sup> liquid water has been one of the most thoroughly studied systems and is arguably the most important liquid because of its role in chemistry, physics, and biology.<sup>[2,3]</sup> In fact, the chemistry of living things crucially depends on the interplay of its unusual properties and anomalous behavior and it is hard to imagine life without it.<sup>[4]</sup> It is also a desirable “green” solvent that offers great economic, safety, and environmental benefits, since it is inexpensive, nonflammable, and nontoxic at the same time.<sup>[5]</sup> Yet, in synthetic organic chemistry, water is generally not a popular choice of solvent. On the one hand, because the oxygen atom of water molecules is rather reactive and may itself react with organic compounds. On the other hand, because most organic molecules are nonpolar and thus hydrophobic, the reactants are insoluble in liquid water. However, rather recently, the use of water as a solvent for organic synthesis was popularized by Sharpless and coworkers, who recognized that many important organic reactions exhibit greatly enhanced selectivity, improved yields, and dramatically reduced reaction time when floating “on-water.”<sup>[6–8]</sup> Therefore, the behavior and properties of liquid water have been the subject of extensive scientific investigation.<sup>[9–11]</sup> Nevertheless, a detailed understanding of liquid water is still lacking.<sup>[2,12,13]</sup> Studying liquid water *in silico* is rather challenging, which is due to the difficulties in accurately modeling the numerous physical phenomena that conspire to make water unique, such as the cooperativity of the hydrogen bond (HB) network,<sup>[14,15]</sup> strong permanent dipole moment, large polarizability effects, and sizeable nuclear quantum effects.<sup>[9]</sup>

*Ab initio* molecular dynamics (AIMD),<sup>[16–18]</sup> where the interatomic forces are calculated on-the-fly by accurate electronic structure calculations, has become widespread in computa-

tional studies of liquid water.<sup>[19–42]</sup> Despite constant advances in high-performance computing, the computational cost of AIMD has limited the attainable length- and timescales in defiance of substantial progress.<sup>[17,43]</sup> Therefore, great effort has been spent into developing empirical water potentials, which are fitted to reproduce experimental data, such as the structure factor, radial distribution function (RDF), heat of vaporization, vapor–liquid equilibria (VLE), and the density maximum of liquid water.<sup>[44–50]</sup> Despite the fact that these force fields are typically remarkably successful in reproducing the underlying experiments, the transferability to regions of the phase diagram that are different from those in which they have been fitted is restricted.

Nevertheless, it is possible to circumvent the latter by deriving water potentials from parameter-free electronic structure calculations.<sup>[51–57]</sup> Apart from the trivial finite difference scheme,<sup>[50]</sup> there are various different techniques to parametrize water models to match *ab initio* data such as inverse Monte Carlo,<sup>[58,59]</sup> iterative Boltzmann inversion,<sup>[60]</sup> or force-matching<sup>[61]</sup> approaches. In this work, we assess the general accuracy, with a specific emphasis on thermodynamic quantities, of force-matched water potentials derived from first-principles electronic structure calculations as obtained by the recently devised improved force-matching method of Spura et al.<sup>[62]</sup>

[a] A. Köster, G. Rutkai, J. Vrabec  
Thermodynamics and Energy Technology, Department of Mechanical Engineering, University of Paderborn, Warburger Str. 100, Paderborn D-33098, Germany

[b] T. Spura, J. Kessler, H. Wiebeler, T. D. Kühne  
Dynamics of Condensed Matter, Department of Chemistry, University of Paderborn, Warburger Str. 100, Paderborn D-33098, Germany  
E-mail: tdkuehne@mail.upb.de

© 2016 Wiley Periodicals, Inc.

The remainder of this paper is organized as follows. In Force Matching section, we revisit the force-matching scheme to derive the parameters of a rigid, nonpolarizable TIP4P-like water model. The computational details are described in Computational Details section, whereas in Results and Discussion section, the results as obtained by MD and Monte Carlo (MC) simulations are discussed. Conclusion section summarizes this work.

## Force Matching

The force-matching technique of Ercolessi and Adams,<sup>[61]</sup> where the interaction potential is derived so as to mimic the forces of accurate reference calculations, not only includes many-body environmental effects but also allows to employ a rather high level of theory since in general relatively few electronic structure calculations are required. At variance to parametrization schemes that rely on Henderson's theorem,<sup>[63]</sup> no computationally expensive generation of reference RDF from first-principle by means of AIMD is required.<sup>[19–42]</sup> Specifically, to determine the parameters of an arbitrary interaction potential based on first-principles force calculations for a set of given configurations, we minimize the normalized  $L_1$  force distance

$$\|\delta\mathbf{F}\|_1 = \frac{1}{3} \left\langle \sum_{i=1}^N \sum_{\alpha \in (x,y,z)} \left[ \frac{\mathbf{F}_{i,\alpha}^{\text{QM}} - \mathbf{F}_{i,\alpha}^{\text{FF}}}{\sigma_i} \right] \right\rangle, \quad (1)$$

where  $N$  is the number of atoms and  $\sigma_i$  stands for the standard deviation of the force distribution  $\mathbf{F}_{i,\alpha}$  of atom  $i$  in directions  $\alpha \in (x, y, z)$ , while  $\langle \dots \rangle$  implies the ensemble average of the selected configurations. The quantum mechanical reference forces are denoted as  $\mathbf{F}_{i,\alpha}^{\text{QM}}$ , while  $\mathbf{F}_{i,\alpha}^{\text{FF}}$  are the nuclear forces of the classical interaction potential, respectively.

However, the minimization of eq. (1) with respect to the variational parameters of  $\mathbf{F}_{i,\alpha}^{\text{FF}}$  represents an ill-posed problem, in particular when including atomic partial charges in the optimization procedure. As a consequence, the optimization may not be stable for small variations of the corresponding parameters. This is reflected in an error landscape with many saddle points and flat areas, where the Hessian matrix is nearly singular, which leads to numerical inaccuracies because of the limited precision of floating point arithmetic. Thus, an important problem of gradient-based minimization methods is the particular form of the objective function, whose derivative with respect to partial charges is often found to be ill-conditioned.

Although it is possible to ameliorate this difficulty by augmenting the penalty function with additional properties, such as the total force or torque with its respective weights,<sup>[64–66]</sup> this is circumvented here by means of the sequential least-squares quadratic programming method (SLSQP) together with physically sensible bound constraints.<sup>[67]</sup> The SLSQP scheme treats the original problem as a sequence of constrained least-squares problems, which is equivalent to a quadratic programming algorithm for nonlinearly-constrained gradient-based optimization, hence its name. More precisely, each SLSQP step involves solving a quadratic approximation of the original objective function, where the linear term is the

gradient and the quadratic term is an approximate Hessian, with first-order affine approximations of the nonlinear constraints. The approximate Hessian, which is initialized to the identity matrix, is continuously updated, while maintaining it positive definite, based on the gradients and function values at subsequent steps similar to the BFGS quasi-Newton scheme.<sup>[68]</sup> Therefore, like any quasi-Newton method, the true Hessian is only approached in the limit of many iterations close to the minimum. Because of the ill-posed nature of the problem, we search for the minimum along the direction of the modified quasi-Newton scheme by first bracketing the minimum and then using Brent's method.<sup>[69]</sup> Contrary to more elaborate techniques that exploit gradient information, the availability of the function's derivative is not required here. However, it should be noted that this procedure offers no guarantee about whether the global minimum of the optimization function is indeed found.

## Computational Details

For the purpose to generate first-principles-based water models from AIMD simulations that are as transferable as possible, we have extracted 1500 decorrelated snapshots from path-integral MD simulations<sup>[70]</sup> consisting of 125 water molecules in the isobaric-isothermal ( $NpT$ ) ensemble using the q-TIP4P/F water potential of Habershon et al.<sup>[71]</sup> More precisely, we have selected 125 different configurations at 1 bar pressure for each temperature over the whole liquid temperature range between 248 K to 358 K. Therefore, the resulting water model was not just parametrized to a single state point at ambient conditions, but over a wide range of state points from undercooled to nearly saturated liquid water.

Force matching, as alluded to above, was conducted using reference forces from density functional theory (DFT) calculations.<sup>[72,73]</sup> Specifically, the mixed Gaussian and plane wave approach,<sup>[74]</sup> as implemented in the CP2K/Quickstep code, was employed.<sup>[75]</sup> In this approach, the Kohn–Sham orbitals are represented by a TZV2P Gaussian basis set,<sup>[76]</sup> while the charge density is expanded by plane waves using a density cutoff of 320 Ry. The exchange and correlation (XC) energy was described by the Tao–Perdew–Staroverov–Scuseria (TPSS) meta-generalized gradient approximation,<sup>[77]</sup> and norm-conserving Goedecker–Teter–Hutter pseudopotentials were used to describe the interactions between the valence electrons and the ionic cores.<sup>[78,79]</sup> Van der Waals interactions, which are typically neglected by common local and semi-local XC functionals, were approximated by an additional, attractive pair-potential.<sup>[80,81]</sup> In its most recent and elaborate form, the latter is referred to as D3 correction.<sup>[82]</sup>

The parameters of the q-TIP4P/F-like water potentials were obtained by minimizing eq. (1) using the SLSQP algorithm of Kraft with a convergence tolerance of  $10^{-6}$  between the individual iterations.<sup>[67]</sup> Gradients with respect to the various variational parameters were computed using finite differences with a displacement of  $10^{-8}$ . The initial parameters were taken from the original q-TIP4P/F water model.<sup>[71]</sup> The resulting DFT-based water model is denoted as TIP4P/TPSS-D3 in the

Table 1. Parameters of the molecular interaction models for water.

Interaction model	$r_{OH}$ (Å)	$r_{OM}$ (Å)	$\theta_{HOH}$ (deg)	$\sigma$ (Å)	$\epsilon/k_B(K)$	$q_M$ (e)	$q_H$ (e)
TIP4P-TPSS <sup>[62]</sup>	0.9662	0.1654	107.21	3.2081	64.95	−1.0552	0.5276
TIP4P-TPSS-D3 <sup>[62]</sup>	0.9666	0.1547	107.38	3.1625	79.37	−1.0318	0.5159
TIP4P/2005 <sup>[48]</sup>	0.9572	0.1546	104.52	3.1589	93.20	−1.1128	0.5564
Huang et al. <sup>[87]</sup>	1.3338	0.2048	104.52	3.1183	208.08	−0.8391	0.4196

following.<sup>[62]</sup> The usage of the TPSS XC functional is due to the observation that, when combined with Grimme's D3 correction,<sup>[82]</sup> the resulting TPSS-D3 level of theory is remarkably accurate in reproducing the structure of liquid water.<sup>[62]</sup> In fact, as demonstrated in the present article, when comparing with the recently revised experimental x-ray and neutron measurements,<sup>[83,84]</sup> the present TIP4P/TPSS-D3 water model is even more accurate than most of the commonly used empirical water potentials. Nevertheless, we find it important to note that the present fixed point-charge water model is neither polarizable nor able to mimic cooperativity effects and chemical reactions that may take place in liquid water. Even though these many-body effects are explicitly taken into account by DFT, in this way it is generally only possible to simulate liquid water in qualitative, but not in quantitative agreement with experiment.<sup>[40,42,85,86]</sup>

For comparison, two empirical water potentials, that is, TIP4P/2005 by Abascal and Vega<sup>[48]</sup> and another one of Huang et al.,<sup>[87]</sup> were employed in this work. Being one of the most important "general purpose" water potentials, TIP4P/2005 is an obvious choice for this task and performs well for a large variety of different thermodynamic properties.<sup>[48,50]</sup> In contrast, the potential of Huang et al. was mainly optimized to reproduce the vapor–liquid equilibrium.<sup>[87]</sup> To that extent, the intramolecular OH distance is chosen to be 40% larger to yield a more localized hydrogen bond network. However, the magnitude of the point charges is significantly smaller than that of other TIP4P-like water models, while the attractive force is compensated by a relatively high Lennard-Jones energy parameter.

All water models used in the present work consist of two positive charge sites of magnitude  $q/2$  on the hydrogen atoms and a negative charge of magnitude  $q$  positioned at  $\mathbf{r}_M = \gamma \mathbf{r}_O + (1-\gamma)(\mathbf{r}_{H1} + \mathbf{r}_{H2})/2$  to ensure local charge neutrality of each water molecule. These so-called M-sites and the hydrogen atoms on different water molecules interact with each other through a simple Coulomb potential. Together with a Lennard-Jones potential between the oxygen atoms, this constitutes the following pairwise-additive intermolecular potential

$$V_{\text{inter}} = \sum_i \sum_{j>i} 4\epsilon \left[ \left( \frac{\sigma}{r_{ij}} \right)^{12} - \left( \frac{\sigma}{r_{ij}} \right)^6 \right] + \sum_{m \in i} \sum_{n \in j} \frac{q_m q_n}{r_{mn}},$$

where  $r_{ij}$  is the distance between the oxygen atoms and  $r_{mn}$  the distance between the partial charges in molecules  $i$  and  $j$ . All molecular interaction parameters are listed in Table 1.

All simulations in the present work were carried out with the molecular simulation tool *ms2*.<sup>[88]</sup> Except for the transport

property calculations with the Green–Kubo formalism,<sup>[89,90]</sup> where MD is mandatory,<sup>[91,92]</sup> all results were generated by MC sampling.<sup>[93,94]</sup> In the case of the latter, a cubic simulation volume consisting of 864 water molecules was considered. The Lennard-Jones interactions beyond a cut-off radius of 12.25 Å were corrected as proposed by Lustig,<sup>[95]</sup> while the long-range electrostatic interactions were taken into account by means of the reaction field method.<sup>[96]</sup> Each MC move in the  $NpT$  ensemble consisted of 864 displacement, 864 rotation and one volume move attempt. For the MD simulations to compute the transport properties, a simulation volume containing 3000 water molecules together with a Lennard-Jones cut-off of 17.5 Å was considered. The equations of motion were discretized by a timestep of 0.87 fs and solved numerically by employing a fifth-order Gear predictor-corrector integrator.<sup>[96]</sup> The temperature was kept constant by means of isokinetic rescaling of the velocities, while the pressure was controlled with the piston method of Andersen.<sup>[97]</sup>

## Results and Discussion

To validate the present results, they were compared to a highly accurate fundamental equation of state (EOS), to experimental data and a correlation thereof. In the case of time independent thermodynamic properties, the reference class<sup>[98]</sup> EOS of Wagner and Pruß<sup>[99]</sup> was used as recommended by the International Association for the Properties of Water and Steam (IAPWS). This equation was parameterized to around 6000 carefully selected experimental data points. The uncertainty for most properties is below 0.1% over a large temperature and pressure range. Uncertainties for the vapor pressure and the saturated liquid density are even below 0.0025%. The shear viscosity was compared to the correlation of Huber et al.<sup>[100]</sup> which has an uncertainty of 1% in the temperature range considered here. Relative deviations between the simulation results and the reference EOS were quantified by

$$\Delta X = 100 \left( \frac{X_{\text{SIM}} - X_{\text{EOS}}}{X_{\text{EOS}}} \right). \quad (2)$$

Based on this definition, the average absolute (unsigned) deviation (AAD) was defined as

$$\text{AAD} = \frac{1}{N} \sum_{i=1}^N |\Delta X_i|. \quad (3)$$

The corresponding results of the considered water models are listed in Table 2.

**Table 2.** Average absolute (unsigned) deviations (AAD) of four water potentials in comparison to the reference fundamental equation of state by Wagner and Pruß.<sup>[99]</sup>

Thermodynamic property	Molecular interaction model			
	TIP4P-TPSS <sup>[62]</sup>	TIP4P-TPSS-D3 <sup>[62]</sup>	TIP4P/2005 <sup>[48]</sup>	Huang et al. <sup>[87]</sup>
	AAD/%			
Vapor pressure $p_v$	234.8	162.6	55.4	12.3
Saturated liquid density $\rho'$	14.0	10.0	0.5	1.5
Saturated vapor density $\rho''$	309.0	205.8	54.2	11.9
Enthalpy of vaporization $\Delta h_v$	23.2	18.8	11.7	2.4
Res. isochoric heat capacity $c_v^{\text{res}}$	7.1	7.2	22.1	11.0
Res. isobaric heat capacity $c_p^{\text{res}}$	16.8	15.1	18.8	6.8
Pressure $p$	50.9	38.5	5.2	30.2
Isothermal compressibility $\beta_T$	16.4	15.6	7.3	26.0
Residual enthalpy $h^{\text{res}}$	19.7	15.5	24.0	11.4
Speed of sound $w$	7.0	6.1	2.6	19.7

Vapor–liquid equilibrium properties were evaluated between 300 K and 525 K.

### Second virial coefficient

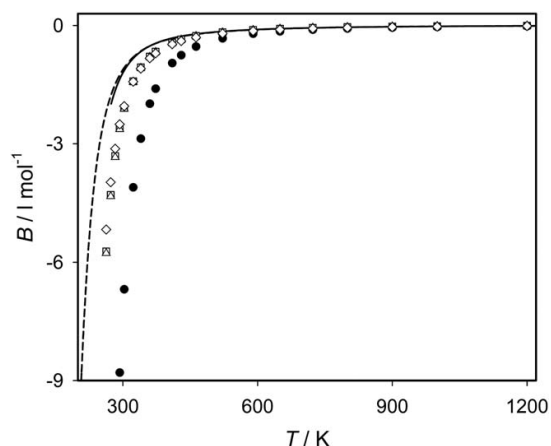
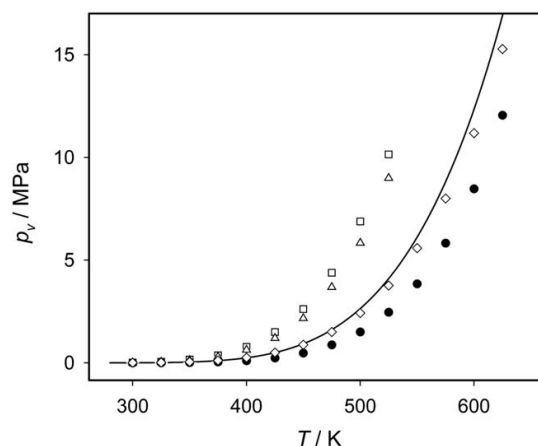
Over a temperature range from 263 K to 1200 K, the second virial coefficient  $B$  was calculated by evaluating Mayer's  $f$ -function as described, for example, by Eckl et al.<sup>[101]</sup> Results for the four water potentials are presented in Figure 1 and compared to the reference EOS,<sup>[99]</sup> as well as to a correlation of experimental data from the DIPPR database.<sup>[102]</sup> Above 600 K, the agreement between the reference data and the various potentials is very good, while for lower temperatures the second virial coefficient is generally underestimated. The latter is particularly true for the TIP4P/2005 force field, whereas the deviation is systematically smaller for the potential of Huang et al., as well as for the DFT-derived TIP4P-TPSS and TIP4P-TPSS-D3 water models, which are of comparable quality.

### Vapor–liquid equilibrium

VLE were determined with the grand equilibrium method.<sup>[103]</sup> In this two-step procedure, the coexisting phases are simu-

lated independently. First, at a specified temperature one molecular simulation run in the liquid phase is carried out in the  $NpT$  ensemble to obtain the chemical potential as a function of pressure. This was done here using the gradual insertion method.<sup>[104,105]</sup> The second step includes one pseudo-grand canonical ( $\mu VT$ ) ensemble simulation for the vapor phase and yields the saturated vapor state point. A detailed description of this method can be found elsewhere.<sup>[103]</sup>

In Figures 2 and 3, the representation of the vapor pressure as determined by the four considered water potentials is shown and compared to the reference EOS.<sup>[99]</sup> The TIP4P/2005 force field yields a vapor pressure that is throughout too low with decreasing deviations at higher temperatures resulting in an AAD of 55%, cf. Table 2. In contrast, the two DFT-derived water models TIP4P-TPSS and TIP4P-TPSS-D3 throughout overestimate the experimental data by at least 100%. The potential of Huang et al., however, overestimates the vapor pressure at low temperatures by about 30%, while underestimating it at 625 K by around 10%, which results in an AAD of only 12%.

**Figure 1.** Second virial coefficient of water: (—) Reference fundamental equation of state by Wagner and Pruß.<sup>[99]</sup> (---) DIPPR correlation of experimental data.<sup>[102]</sup> Computational data: (•) TIP4P/2005; (◇) Huang et al.; (□) TIP4P-TPSS; (△) TIP4P-TPSS-D3.**Figure 2.** Vapor pressure of water: (—) Reference fundamental equation of state by Wagner and Pruß.<sup>[99]</sup> Computational data: (•) TIP4P/2005; (◇) Huang et al.; (□) TIP4P-TPSS; (△) TIP4P-TPSS-D3. The statistical simulation uncertainties are within symbol size.

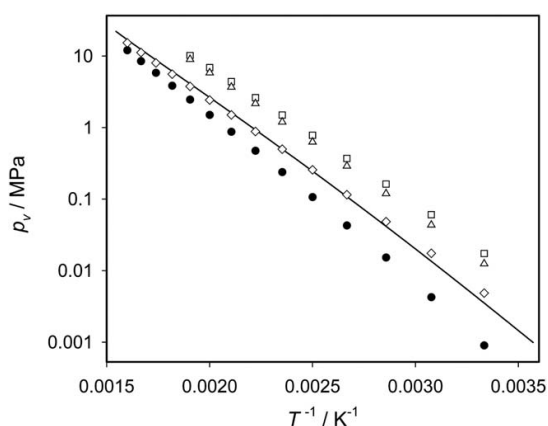


Figure 3. Vapor pressure of water: (—) Reference fundamental equation of state by Wagner and Pruß.<sup>[99]</sup> Computational data: (•) TIP4P/2005; (◊) Huang et al.; (◻) TIP4P-TPSS; (△) TIP4P-TPSS-D3. The statistical simulation uncertainties are within symbol size.

The coexisting liquid and vapor densities are presented in Figure 4. With an AAD of 0.5%, the TIP4P/2005 force field shows the best agreement with the reference EOS<sup>[99]</sup> on the liquid side, whereas the potential of Huang et al. yields a slope that is slightly too steep. Nonetheless, the AAD = 1.5% of the potential of Huang et al. is not much larger than that of the TIP4P/2005 force field. Both exhibit deviations of around 5% at 625 K, which is close to the critical point. However, the DFT-derived TIP4P-TPSS and TIP4P-TPSS-D3 water models, systematically underestimate the saturated liquid density, yielding AAD values of 14% and 10%, respectively. As a consequence, the critical temperature of both potentials is around 100 K below the experimental value.

Regarding the saturated vapor density, which is closely related to the vapor pressure, the TIP4P/2005 force field underestimates the reference by approximately 54%. The

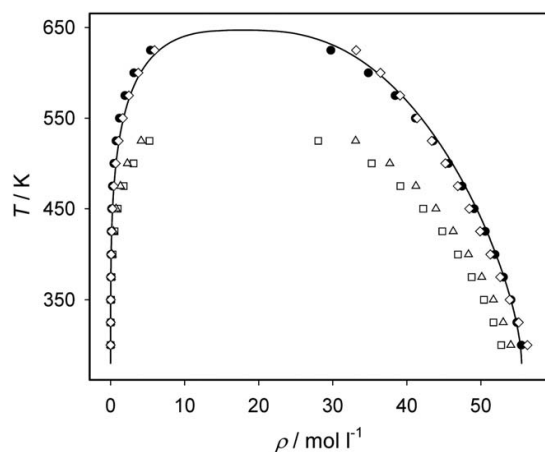


Figure 4. Saturated densities of water: (—) Reference fundamental equation of state by Wagner and Pruß.<sup>[99]</sup> Computational data: (•) TIP4P/2005; (◊) Huang et al.; (◻) TIP4P-TPSS; (△) TIP4P-TPSS-D3. The statistical simulation uncertainties are within symbol size.

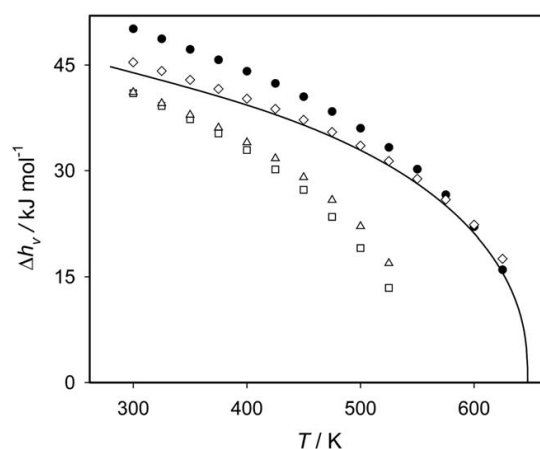


Figure 5. Enthalpy of vaporization of water: (—) Reference fundamental equation of state by Wagner and Pruß.<sup>[99]</sup> Computational data: (•) TIP4P/2005; (◊) Huang et al.; (◻) TIP4P-TPSS; (△) TIP4P-TPSS-D3. The statistical simulation uncertainties are within symbol size.

potential of Huang et al. exhibits the best agreement with the reference EOS,<sup>[99]</sup> that is, AAD = 12%, while the TIP4P-TPSS and TIP4P-TPSS-D3 water models overestimate this property on average by more than 200%.

Similar to the representation of the vapor pressure and saturated vapor density, the potential of Huang et al. also performs rather well in terms of the enthalpy of vaporization and yields AAD = 2.4%, cf. Figure 5. At temperatures above 575 K, in the extended critical region, the TIP4P/2005 force field also shows a very good agreement with the reference EOS.<sup>[99]</sup> At lower temperatures, however, the deviations increase up to 14%, which results in AAD = 12%. The two DFT-derived water models underestimate the enthalpy of vaporization throughout with deviations of around 6% for lower temperatures. Over the whole sampled temperature range the DFT-derived TIP4P-TPSS and TIP4P-TPSS-D3 water models yield an AAD of 23% and 19%, respectively.

#### Homogeneous properties

A wide range of different static properties in the homogeneous fluid region were generated using the formalism proposed by Lustig<sup>[106,107]</sup>: Residual isobaric heat capacity  $c_p^{\text{res}}$ , residual isochoric heat capacity  $c_v^{\text{res}}$ , residual enthalpy  $h^{\text{res}}$ , pressure  $p$ , speed of sound  $w$ , isothermal compressibility  $\beta_T$ , and Joule-Thomson coefficient  $\mu_{JT}$ . For a given state point, this formalism allows to calculate an arbitrary number of time-independent thermodynamic properties from a single simulation run within the canonical (NVT) ensemble. More precisely, the method was designed to directly yield the temperature and density derivatives

$$A_{mn} = (1/T)^m \rho^n \frac{\partial^{m+n}(a^0 + a^r)/(RT)}{\partial(1/T)^m \partial \rho^n}, \quad (4)$$

of the residual Helmholtz free energy  $a(T, \rho) = a^0(T, \rho) + a^r(T, \rho)$  for any  $m > 0$  or  $n > 0$ , where  $\rho$  is the molar density,  $R$  is the



molar gas constant, while the factor  $1/(RT)$  renders  $A_{mn}$  dimensionless. The molar Helmholtz free energy  $a$ , and thus the derivatives  $A_{mn}$ , can be additively separated into an ideal and residual contribution. The ideal contribution  $a^0(T, \rho) = a^0(T) + R T \ln(\rho/\rho_{\text{ref}})$  by definition corresponds to the value of  $a(T, \rho)$  when no intermolecular interactions are at work. The exclusively temperature-dependent part of the ideal contribution  $a^0(T)$  has a non-trivial temperature dependence and is directly related to the isochoric heat capacity of the ideal gas  $A_{20}^0(T) = -c_v^0/R$ . However, not every derivative  $A_{mn}$  requires the knowledge of  $a^0(T) = RTA_{00}^0(T)$ , namely

- $A_{mn}^0(T, \rho) = 0$ , for  $m > 0$  and  $n > 0$ ,
- $A_{mn}^0(T, \rho) = A_{mn}^0(T) + 0$ , for  $m > 0$  and  $n = 0$ ,
- $A_{mn}^0(T, \rho) = 0 + (-1)^{1+n}$ , for  $m = 0$  and  $n > 0$ .

The value of  $A_{00}^0(T) = a^0(T)/(RT)$  is often determined by spectroscopy or *ab initio* calculations, whereas the residual contribution is typically the target of molecular simulations.

Since  $a/(RT)$  is a thermodynamic potential, any other time-independent thermodynamic property is a combination of its derivatives with respect to its independent variables<sup>[106,107]</sup>. Numerous properties, such as the internal energy  $u$ , pressure  $p$ , enthalpy  $h$ , Gibbs energy  $g$ , and isochoric heat capacity  $c_v$ , are linear functions

$$\frac{u}{RT} = A_{10}^0(T) + A_{10}^r, \quad (5)$$

$$\frac{p}{\rho RT} = 1 + A_{01}^r, \quad (6)$$

$$\frac{1}{RT} \left( \frac{\partial p}{\partial \rho} \right)_T = 1 + 2A_{01}^r + A_{02}^r, \quad (7)$$

$$\frac{1}{\rho R} \left( \frac{\partial p}{\partial T} \right)_\rho = 1 + A_{01}^r - A_{11}^r, \quad (8)$$

$$\frac{h}{RT} = 1 + A_{01}^r + A_{10}^0(T) + A_{10}^r, \quad (9)$$

$$\frac{g}{RT} = 1 + A_{01}^r + A_{00}^0 + A_{00}^r, \quad (10)$$

$$\frac{c_v}{R} = -A_{20}^0(T) - A_{20}^r, \quad (11)$$

whereas the molar isobaric heat capacity  $c_p$ , speed of sound  $w$ , and Joule–Thomson coefficient  $\mu_{JT}$  are nonlinear combinations of derivatives

$$\frac{c_p}{R} = -A_{20}^0(T) - A_{20}^r + \frac{(1 + A_{01}^r - A_{11}^r)^2}{1 + 2A_{01}^r + A_{02}^r}, \quad (12)$$

$$\frac{Mw^2}{RT} = 1 + 2A_{01}^r + A_{02}^r - \frac{(1 + A_{01}^r - A_{11}^r)^2}{A_{20}^0(T) + A_{20}^r}, \quad (13)$$

$$\frac{\rho R}{\mu_{JT}} = \frac{(A_{20}^0(T) + A_{20}^r)(1 + 2A_{01}^r + A_{02}^r) - (1 + A_{01}^r - A_{11}^r)^2}{A_{01}^r + A_{02}^r + A_{11}^r}, \quad (14)$$

where  $M$  is the molar mass. For properties that cannot be additively separated into ideal and residual part, such as  $w$  and  $\mu_{JT}$ , the ideal contribution  $A_{20}^0(T) = -c_v^0/R$  was taken from

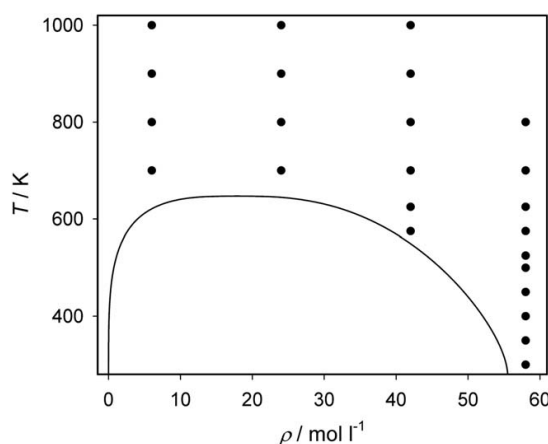


Figure 6. Studied state points in the homogeneous fluid region of water along four isochores. The solid line indicates saturated states according to the reference equation of state for water.<sup>[99]</sup>

the reference EOS<sup>[99]</sup> because it does not depend on the intermolecular interactions.

Properties in the homogeneous fluid region were compared to the reference EOS<sup>[99]</sup> along four isochores (i.e., 6, 24, 42, and 58 mol/l) up to temperatures of 1000 K. The corresponding state points are shown in Figure 6.

The results of the four investigated water potentials for the residual isochoric heat capacity (top) and the residual isobaric heat capacity (bottom) are shown in Figure 7 and compared to the reference EOS<sup>[99]</sup>. The residual isochoric heat capacity is throughout overestimated by the TIP4P/2005 force field, which performs particularly poorly at low densities, leading to an AAD of 22%. On the contrary, the potential of Huang et al. underestimates the isochoric heat capacity for densities above 6 mol/l by around 11%. With an AAD of around 7% over the entire temperature and density range, both the TIP4P-TPSS and TIP4P-TPSS-D3 water models perform quite well in comparison with the reference. However, regarding the residual isobaric heat capacity, the agreement between the TIP4P/2005 force field and the reference EOS<sup>[99]</sup> is better than for the residual isochoric heat capacity. Again, the largest deviations can be observed for lower densities, resulting in AAD = 19%. With AAD = 17% and 15%, respectively, the DFT-derived TIP4P-TPSS and TIP4P-TPSS-D3 water models are slightly superior. Nevertheless, both water models underestimate the residual isobaric heat capacity along the 24 mol/l isochore by more than 25%. The best agreement with the reference was observed for the potential of Huang et al. with AAD = 6.8%. But it has to be noted that the state point at 700 K and 24 mol/l is within the extended critical region, which leads to relatively large statistical uncertainties of the simulations.

The pressure and the isothermal compressibility in the homogeneous fluid region are shown in Figure 8. In comparison to the reference EOS, the two DFT-derived water models TIP4P-TPSS and TIP4P-TPSS-D3 yield a too high pressure. With AAD = 39%, the TIP4P-TPSS-D3 water model is somewhat better than the TIP4P-TPSS potential (AAD = 51%). The potential

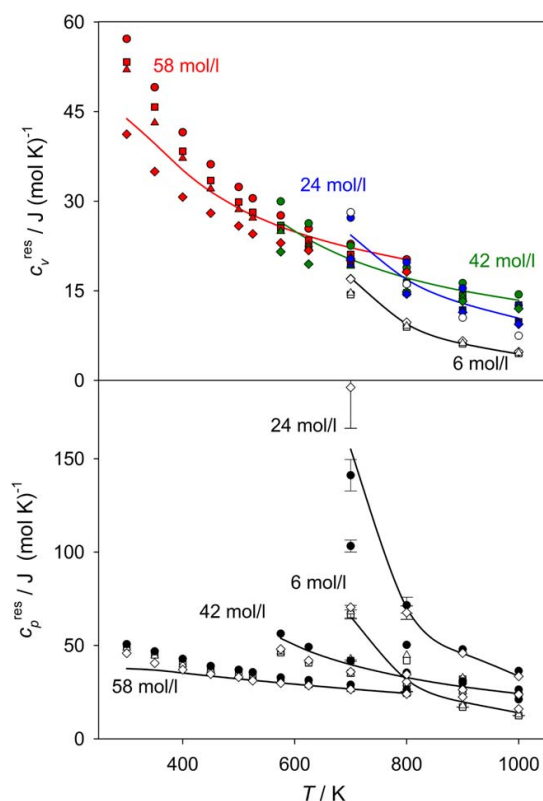


**Figure 7.** Residual isochoric (top) and residual isobaric heat capacity (bottom) along four isochores in the homogeneous fluid region of water: (—) Reference fundamental equation of state by Wagner and Pruß.<sup>[99]</sup> Computational data: (•) TIP4P/2005; (◊) Huang et al.; (◻) TIP4P-TPSS; (△) TIP4P-TPSS-D3. The statistical uncertainties of the simulations are shown if they exceed symbol size. [Color figure can be viewed in the online issue, which is available at [wileyonlinelibrary.com](http://wileyonlinelibrary.com).]

of Huang et al. exhibits good agreement at lower temperatures with increasing deviations for higher temperatures, leading to AAD = 30%. Yet, the best agreement with the reference EOS can be observed for the TIP4P/2005 force field. This also applies to the isothermal compressibility  $\beta_T$  with AAD = 7.3%. The DFT-derived TIP4P-TPSS and TIP4P-TPSS-D3 water models tend to underestimate the isothermal compressibility, especially at lower densities. However, the largest AAD of 26% is observed for the potential of Huang et al., which is mainly due to larger deviations at higher densities. The rather large statistical uncertainties for the potential of Huang et al. and the TIP4P/2005 force field at 700 K and 24 mol/l indicate the proximity to the critical point.

The results for the residual enthalpy, speed of sound and Joule–Thomson coefficient can be found in Figure 9. Regarding the former, the TIP4P/2005 force field yields the largest deviations from the reference EOS<sup>[99]</sup> and underestimates it throughout. By contrast, both the TIP4P-TPSS and TIP4P-TPSS-D3 water models overestimate the residual enthalpy. The AAD of the DFT-derived TIP4P-TPSS and TIP4P-TPSS-D3 water mod-

els are 20% and 16%, respectively. Good agreement with the reference EOS, especially for higher densities, can be found for the potential of Huang et al. with AAD = 11%. Regarding the speed of sound, the TIP4P/2005 force field yields the best results, that is, AAD = 2.6%. The results of the TIP4P-TPSS and TIP4P-TPSS-D3 water models are again very similar to each other and lead to AAD = 6% to 7%. It has to be noted that the agreement to the reference EOS<sup>[99]</sup> of those potentials at 58 mol/l is even better than the agreement of the TIP4P/2005 force field. The worst agreement with the reference for the speed of sound was found for the potential of Huang et al. The deviations are between 20% and 30% for the two highest isochores.

In case of the Joule–Thomson coefficient, a relative evaluation of the simulation data in comparison to the reference EOS is not applicable because this property changes its sign. Therefore, absolute values were considered. Except for the 6 mol/l isochore, the TIP4P/2005 force field performs quite well, yielding an average deviation of 0.1 K/MPa. It can be seen that the potential of Huang et al.<sup>[87]</sup> shows a good agreement throughout. Here, average deviations of 0.07 K/MPa were found. The DFT-derived TIP4P-TPSS and TIP4P-TPSS-D3 water models

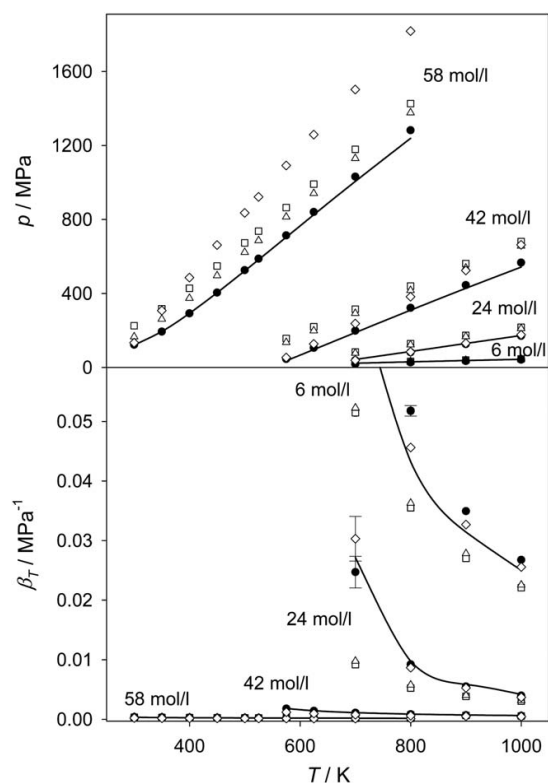


**Figure 8.** Pressure (top) and isothermal compressibility (bottom) along four isochores in the homogeneous fluid region of water: (—) Reference fundamental equation of state by Wagner and Pruß.<sup>[99]</sup> Computational data: (•) TIP4P/2005; (◊) Huang et al.; (◻) TIP4P-TPSS; (△) TIP4P-TPSS-D3. The statistical simulation uncertainties are shown if they exceed symbol size.

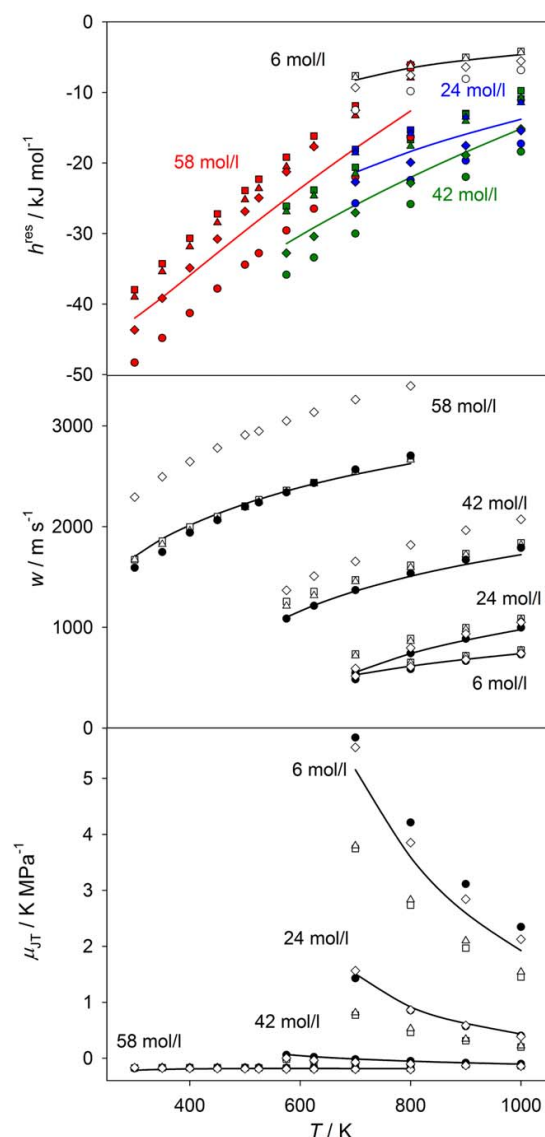


Figure 9. Residual enthalpy (top), speed of sound (center), and Joule–Thomson coefficient (bottom) along four isochores in the homogeneous fluid region of water: (—) Reference fundamental equation of state by Wagner and Pruß;<sup>[99]</sup> Computational data: (•) TIP4P/2005; (◊) Huang et al.; (◻) TIP4P-TPSS; (△) TIP4P-TPSS-D3. The statistical simulation uncertainties are within symbol size. [Color figure can be viewed in the online issue, which is available at [wileyonlinelibrary.com](http://wileyonlinelibrary.com).]

underestimate the Joule–Thomson coefficient throughout, yielding higher average deviations, i.e. 0.2 K/MPa.

#### Transport properties

Transport properties were calculated by MD in the  $NpT$  ensemble with the Green–Kubo formalism.<sup>[89,90]</sup> Simulation results for the translational self-diffusion coefficient and the shear viscosity of the four discussed potentials are presented in Figure 10

at 0.1 MPa for temperatures between 280 K and 340 K, respectively. The results for the translational self-diffusion coefficient were compared to experimental measurements by Harris and Woolf,<sup>[108]</sup> Dullien,<sup>[109]</sup> Holz et al.,<sup>[110]</sup> and Easteal et al.,<sup>[111]</sup> whereas the shear viscosity data were compared to a correlation of experimental data by Huber et al.<sup>[100]</sup> The TIP4P/2005 force field results are in good agreement with the references for both considered properties. The shear viscosity is slightly overestimated, but nonetheless is, within the statistical uncertainties of the MD simulations, in agreement with the correlation of Huber et al.<sup>[100]</sup> However, it can be seen that DFT-derived TIP4P-TPSS and TIP4P-TPSS-D3 water models, as well as the potential of Huang et al., significantly overestimate the translational self-diffusion coefficient. As a consequence, a significant underestimation of the shear viscosity is found for the latter three potentials.

#### Radial distribution function

To determine the liquid water structure, the RDF in the liquid state at 298 K and 0.1 MPa were sampled in the  $NpT$

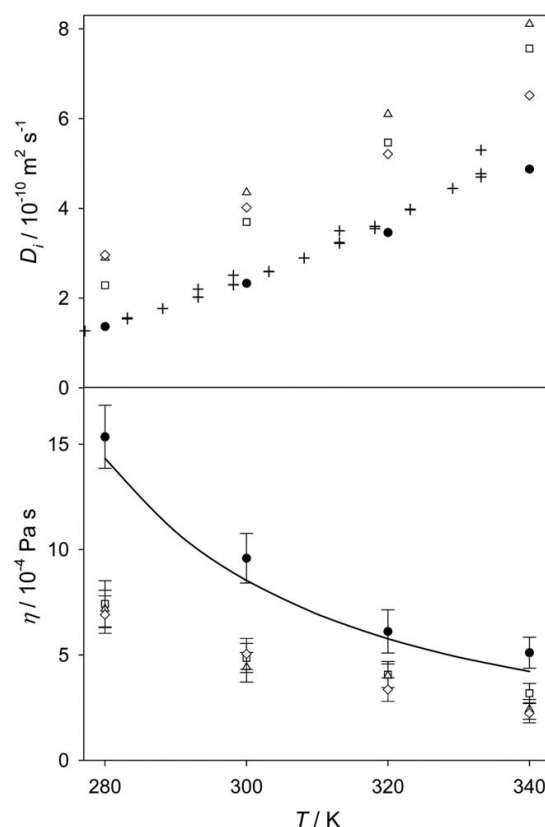
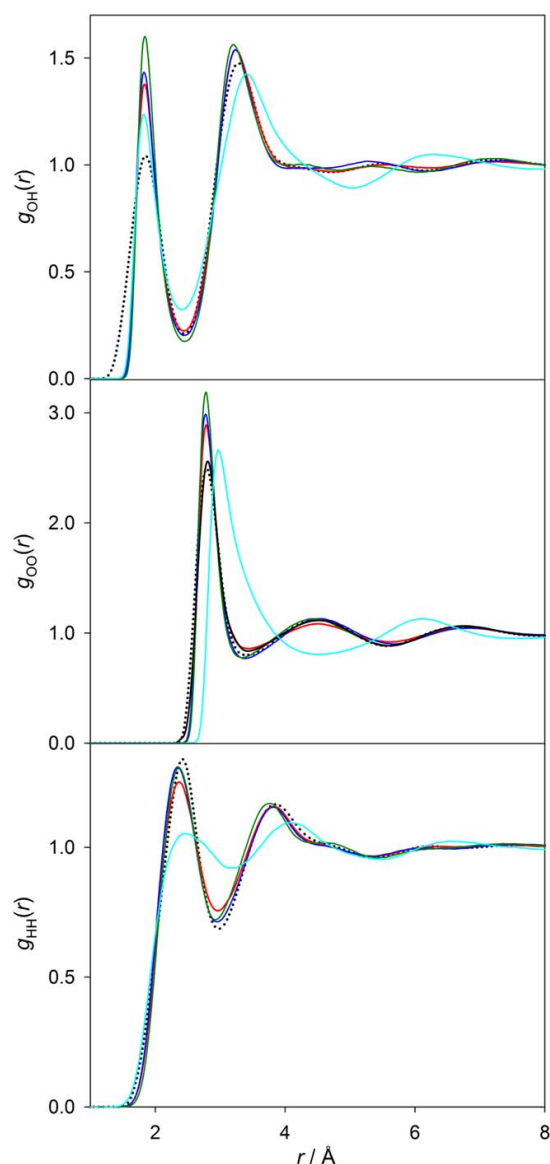


Figure 10. Self-diffusion coefficient (top) and shear viscosity (bottom) of liquid water at 0.1 MPa. (+) Experimental data;<sup>[108–111]</sup> (—) Shear viscosity correlation of experimental data by Huber et al.<sup>[100]</sup> Computational data: (•) TIP4P/2005; (◊) Huang et al.; (◻) TIP4P-TPSS; (△) TIP4P-TPSS-D3. The statistical uncertainties of the MD simulations are shown only if they exceed symbol size.





**Figure 11.** Radial distribution functions in the liquid state at 298 K and 0.1 MPa: (—) Skinner et al.<sup>[83]</sup>; (···) Soper<sup>[84]</sup>; (—) TIP4P-TPSS; (—) TIP4P-TPSS-D3; (—) TIP4P/2005; (—) Huang et al. [Color figure can be viewed in the online issue, which is available at [wileyonlinelibrary.com](http://wileyonlinelibrary.com).]

ensemble. The RDF  $g(r)$  relates the local particle density  $\rho^L(r)$  around a position within a molecule to the overall density  $\rho = N/V$

$$g(r) = \frac{\rho^L(r)}{\rho} = \frac{1}{\rho} \frac{dN(r)}{dV} = \frac{1}{4\pi r^2 \rho} \frac{dN(r)}{dr}, \quad (15)$$

where  $dN(r)$  is the differential number of atoms in a spherical shell volume element  $dV$  with the width  $dr$ , which is located at a distance  $r$  from the regarded position within a molecule.<sup>[112]</sup>

For comparison, very recent experimental measurements from Skinner et al.<sup>[83]</sup> and Soper<sup>[84]</sup> were selected. In Figure 11, the three partial RDF for O—H, O—O, and H—H are shown, which were calculated using the four considered water potentials. It is apparent that the TIP4P/2005 force field as well as the two DFT-derived water models qualitatively reproduce the structure of liquid water. The potential of Huang et al., however, is not able to correctly yield the first maximum of the O—O RDF, failing one of the most crucial experimental tests of water models.<sup>[113]</sup> In addition, it also incapable to reproduce all further solvation shells of liquid water. This is most likely a result of the intramolecular O—H bond length  $r_{OH}$  of this potential, which is roughly 0.4 Å longer than the O—H bond length of the other potentials. In the light of the recent revision of the experimental RDF,<sup>[83,84]</sup> it is particularly impressive that the DFT-derived water models exhibit the best agreement with the experimental reference, despite the fact that they have not been considered during their parametrization. In fact, they are even able to reproduce the correct ordering of the relative O—H peak heights. As such, they even outperform the well-established TIP4P/2005 force field, which is arguably the current benchmark among rigid, nonpolarizable water potentials.<sup>[50]</sup>

## Conclusion

To summarize, in this article we have assessed the accuracy of DFT-derived water models, which were recently developed based on an improved force-matching method.<sup>[62]</sup> To that extent, the resulting water models are compared with the potential of Huang, which was optimized to reproduce the vapor–liquid equilibrium,<sup>[87]</sup> and the well-appreciated TIP4P/2005 force field<sup>[48]</sup> as well as experimental measurements and a reference class equation of state.<sup>[99,100]</sup> Specifically, it is found that the TIP4P/2005 force field exhibits a rather well-balanced accuracy for a large variety of different observables, in particular various thermodynamic properties. The potential of Huang et al. is indeed also an accurate interaction potential for multiple thermodynamic properties, but falls short of qualitatively reproducing the structure of liquid water. As opposed to this, both DFT-derived water models are only able to qualitatively reproduce thermodynamic quantities, but more importantly are in best agreement with the most recent experimental RDF, even superseding the TIP4P/2005 force field. Nevertheless, there are many improvements that could be made to build on this study. In particular, the TIP4P-TPSS-D3 water model developed here is not polarizable; an effect which has the potential to further improve the agreement with experiment and that in the future could be easily incorporated into the current force-matching scheme.

We conclude by noting that the present force-matching scheme will facilitate to routinely parametrize computationally efficient yet predictive potential energy functions based on accurate *ab initio* MD simulations for a large variety of different systems. The development of transferable interaction potentials for more complex liquids, which are in good

qualitative agreement with the experiment, is work in progress and will be reported elsewhere.

### Acknowledgment

We gratefully acknowledge the Paderborn Center for Parallel Computing (PC<sup>2</sup>) for the generous allocation of computer time on the OCuLUS cluster.

**Keywords:** liquid water · force matching · *ab initio* · molecular dynamics · Monte Carlo

How to cite this article: A. Köster. T. Spura. G. Rutkai. J. Kessler. H. Wiebeler. J. Vrabec. T. D. Kühne. *J. Comput. Chem.* **2016**, *37*, 1828–1838. DOI: 10.1002/jcc.24398

- [1] A. Rahman, F. H. Stillinger, *J. Chem. Phys.* **1971**, *55*, 3336.
- [2] D. Eisenberg, W. Kauzmann, *The Structure and Properties of Water*; Oxford University Press: Oxford, **1969**.
- [3] M. Chaplin, *Nat. Rev. Mol. Cell Biol.* **2006**, *7*, 861.
- [4] P. Ball, *Chem. Rev.* **2008**, *108*, 74.
- [5] S. Narayan, V. V. Fokin, K. B. Sharpless, In *Organic Reactions in Water: Principles, Strategies and Applications*; U. M. Lindstrom, Ed.; Blackwell Publishing: Oxford, **2007**.
- [6] S. Narayan, J. Muldoon, M. G. Finn, V. V. Fokin, H. C. Kolb, K. B. Sharpless, *Angew. Chem. Int. Ed.* **2005**, *44*, 3275.
- [7] Y. Jung, R. A. Marcus, *J. Am. Chem. Soc.* **2007**, *129*, 5492.
- [8] K. Karhan, R. Z. Khaliullin, T. D. Kühne, *J. Chem. Phys.* **2014**, *141*, 22D528.
- [9] F. H. Stillinger, *Science* **1980**, *209*, 451.
- [10] R. Ludwig, *Angew. Chem. Int. Ed.* **2001**, *40*, 1808.
- [11] M. Dömer, T. Spura, R. Z. Khaliullin, T. D. Kühne, *Nachr. Chem.* **2013**, *61*, 1203.
- [12] R. Ludwig, D. Paschek, *Chem. Unserer Zeit* **2005**, *39*, 164.
- [13] P. Ball, *Nature* **2008**, *452*, 291.
- [14] T. D. Kühne, R. Z. Khaliullin, *Nat. Commun.* **2013**, *4*, 1450.
- [15] R. Z. Khaliullin, T. D. Kühne, *Phys. Chem. Chem. Phys.* **2013**, *15*, 15746.
- [16] D. Marx, J. Hutter, *Ab Initio Molecular Dynamics - Basic Theory and Advanced Methods*; Cambridge University Press: Cambridge, **2009**.
- [17] T. D. Kühne, *WIREs Comput. Mol. Sci.* **2014**, *4*, 391.
- [18] T. D. Kühne, P. Partovi-Azar, H. Elgabarty, *Nachr. Chem.* **2015**, *63*, 327.
- [19] K. Laasonen, M. Sprik, M. Parrinello, R. Car, *J. Chem. Phys.* **1993**, *99*, 9080.
- [20] M. Sprik, J. Hutter, M. Parrinello, *J. Chem. Phys.* **1996**, *105*, 1142.
- [21] J. C. Grossman, E. Schwegler, E. W. Draeger, F. Gygi, G. Galli, *J. Chem. Phys.* **2004**, *120*, 300.
- [22] I.-F. W. Kuo, C. J. Mundy, M. J. McGrath, J. I. Siepmann, J. VandeVondele, M. Sprik, J. Hutter, B. Chen, M. L. Klein, F. Mohamed, M. Krack, M. Parrinello, *J. Phys. Chem. B* **2004**, *108*, 12990.
- [23] P. H.-L. Sit, N. Marzari, *J. Chem. Phys.* **2005**, *122*, 204510.
- [24] T. Todorova, A. P. Seitsonen, J. Hutter, I. F. W. Kuo, C. J. Mundy, *J. Phys. Chem. B* **2006**, *110*, 3685.
- [25] J. A. Morrone, R. Car, *Phys. Rev. Lett.* **2008**, *101*, 17801.
- [26] J. Schmidt, J. VandeVondele, I.-F. W. Kuo, D. Sebastiani, J. I. Siepmann, J. Hutter, C. J. Mundy, *J. Phys. Chem. B* **2009**, *113*, 11959.
- [27] T. D. Kühne, M. Krack, M. Parrinello, *J. Chem. Theory Comput.* **2009**, *5*, 235.
- [28] J. Wang, G. Roman-Perez, J. M. Soler, E. Artacho, M. V. Fernandez-Serra, *J. Chem. Phys.* **2011**, *134*, 024516.
- [29] C. Zhang, D. Donadio, F. Gygi, G. Galli, *J. Chem. Theory Comput.* **2011**, *7*, 1443.
- [30] I.-C. Lin, A. P. Seitsonen, I. Tavernelli, U. Rothlisberger, *J. Chem. Theory Comput.* **2012**, *8*, 3902.
- [31] T. A. Pascal, D. Schär, Y. Jung, T. D. Kühne, *J. Chem. Phys.* **2012**, *137*, 244507.
- [32] Z. Ma, Y. Zhang, M. E. Tuckerman, *J. Chem. Phys.* **2012**, *137*, 044506.
- [33] C. Zhang, R. Z. Khaliullin, D. Bovi, L. Guidoni, T. D. Kühne, *J. Phys. Chem. Lett.* **2013**, *4*, 3245.
- [34] M. Ceriotti, J. Cuny, M. Parrinello, D. E. Manolopoulos, *Proc. Natl. Acad. Sci. USA* **2013**, *110*, 15591.
- [35] A. A. Hassanali, F. Giberti, J. Cuny, T. D. Kühne, M. Parrinello, *Proc. Natl. Acad. Sci. USA* **2013**, *110*, 13723.
- [36] R. A. DiStasio, Jr., B. Santra, Z. Li, X. Wu, R. Car, *J. Chem. Phys.* **2014**, *141*, 084502.
- [37] T. D. Kühne, R. Z. Khaliullin, *J. Am. Chem. Soc.* **2014**, *136*, 3395.
- [38] K. Forster-Tonigold, A. Groß, *J. Chem. Phys.* **2014**, *141*, 064501.
- [39] H. Elgabarty, R. Z. Khaliullin, T. D. Kühne, *Nat. Commun.* **2015**, *6*, 8318.
- [40] M. Del Ben, J. Hutter, J. VandeVondele, *J. Chem. Phys.* **2015**, *143*, 054506.
- [41] C. Zhang, L. Guidoni, T. D. Kühne, *J. Mol. Liq.* **2015**, *205*, 42.
- [42] S. Y. Willow, M. A. Salim, K. S. Kim, S. Hirata, *Sci. Rep.* **2015**, *5*, 14358.
- [43] T. D. Kühne, M. Krack, F. R. Mohamed, M. Parrinello, *Phys. Rev. Lett.* **2007**, *98*, 66401.
- [44] A. Rahman, F. H. Stillinger, *J. Chem. Phys.* **1974**, *60*, 1545.
- [45] W. L. Jorgensen, J. Chandrasekhar, J. D. Madura, R. W. Impey, M. L. Klein, *J. Chem. Phys.* **1983**, *79*, 926.
- [46] H. J. C. Berendsen, J. R. Grigera, T. P. Straatsma, *J. Phys. Chem.* **1987**, *91*, 6269.
- [47] M. W. Mahoney, W. L. Jorgensen, *J. Chem. Phys.* **2000**, *112*, 8910.
- [48] J. L. F. Abascal, C. Vega, *J. Chem. Phys.* **2005**, *123*, 234505.
- [49] B. Guillot, *J. Mol. Liq.* **2002**, *101*, 219.
- [50] C. Vega, J. L. F. Abascal, *Phys. Chem. Chem. Phys.* **2011**, *13*, 19663.
- [51] G. C. Lie, E. Clementi, *Phys. Rev. A* **1986**, *33*, 2679.
- [52] A. P. Lyubartsev, A. Laaksonen, *Phys. Chem. Lett.* **2000**, *325*, 15.
- [53] S. Izvekov, M. Parrinello, C. J. Burnham, G. A. Voth, *J. Chem. Phys.* **2004**, *120*, 10896.
- [54] R. Bukowski, K. Szalewicz, G. C. Groenenboom, A. van der Avoird, *Science* **2007**, *315*, 1249.
- [55] G. S. Fanourgakis, S. S. Xantheas, *J. Chem. Phys.* **2008**, *128*, 074506.
- [56] V. Babin, G. R. Medders, F. Paesani, *J. Phys. Chem. Lett.* **2012**, *3*, 3765.
- [57] G. R. Medders, A. W. Götz, M. A. Morales, P. Bajaj, F. Paesani, *J. Chem. Phys.* **2015**, *143*, 104102.
- [58] M. Ostheimer, H. Bertagnolli, *Mol. Phys.* **1989**, *3*, 227.
- [59] A. P. Lyubartsev, A. Laaksonen, *Phys. Rev. E* **1995**, *52*, 3730.
- [60] D. Reith, M. Pütz, F. Müller-Plathe, *J. Comput. Chem.* **2003**, *24*, 1624.
- [61] F. Ercolessi, J. B. Adams, *Europhys. Lett.* **1994**, *26*, 583.
- [62] T. Spura, C. John, S. Habershon, T. D. Kühne, *Mol. Phys.* **2014**, *113*, 808.
- [63] R. L. Henderson, *Phys. Lett. A* **1974**, *49*, 197.
- [64] O. Akin-Ojo, Y. Song, F. Wang, *J. Chem. Phys.* **2008**, *129*, 064108.
- [65] J. Sala, E. Guardia, M. Masia, *Comput. Phys. Commun.* **2011**, *182*, 1954.
- [66] J. Sala, E. Guardia, J. Marti, D. Spangberg, M. Masia, *J. Chem. Phys.* **2012**, *136*, 054103.
- [67] D. Kraft, *ACM Trans. Math. Softw.* **1994**, *20*, 262.
- [68] W. H. Press, S. A. Teukolsky, W. T. Vetterling, B. P. Flannery, *Numerical Recipes*; Cambridge University Press: Cambridge, **1992**.
- [69] R. P. Brent, *Algorithms for Minimization without Derivatives*; Prentice-Hall: Englewood Cliffs, **1973**.
- [70] S. Habershon, D. E. Manolopoulos, T. E. Markland, T. F. Miller, *Annu. Rev. Phys. Chem.* **2013**, *64*, 387.
- [71] S. Habershon, T. E. Markland, D. E. Manolopoulos, *J. Chem. Phys.* **2009**, *131*, 024501.
- [72] W. Kohn, *Rev. Mod. Phys.* **1999**, *71*, 1253.
- [73] R. O. Jones, *Rev. Mod. Phys.* **2015**, *87*, 897.
- [74] G. Lippert, J. Hutter, M. Parrinello, *Mol. Phys.* **1997**, *92*, 477.
- [75] J. VandeVondele, M. Krack, F. Mohamed, M. Parrinello, T. Chassaing, J. Hutter, *Comput. Phys. Commun.* **2005**, *167*, 103.
- [76] J. VandeVondele, J. Hutter, *J. Chem. Phys.* **2007**, *127*, 114105.
- [77] J. Tao, J. P. Perdew, V. N. Staroverov, G. E. Scuseria, *Phys. Rev. Lett.* **2003**, *91*, 146401.
- [78] S. Goedecker, M. Teter, J. Hutter, *Phys. Rev. B* **1996**, *54*, 1703.
- [79] M. Krack, *Theor. Chem. Acc.* **2005**, *114*, 145.
- [80] J. Hepburn, G. Scoles, R. Penco, *Chem. Phys. Lett.* **1975**, *36*, 451.
- [81] R. Ahlrichs, R. Penco, G. Scoles, *Chem. Phys.* **1977**, *19*, 119.
- [82] S. Grimme, J. Antony, S. Ehrlich, H. Krieg, *J. Chem. Phys.* **2010**, *132*, 154104.
- [83] L. B. Skinner, C. Huang, D. Schlesinger, L. G. M. Pettersson, A. Nilsson, C. J. Benmore, *J. Chem. Phys.* **2013**, *138*, 074506.

- [84] A. K. Soper, *ISRN Phys. Chem.* **2013**, 2013, 297463.
- [85] M. A. Morales, J. R. Gergely, J. McMinis, J. M. McMahon, J. Kim, D. M. Ceperley, *J. Chem. Theory Comput.* **2014**, 10, 2355.
- [86] M. J. Gillan, D. Alfe, A. Michaelides, *J. Chem. Phys.* **2016**, 144, 130901.
- [87] Y.-L. Huang, T. Merker, M. Heilig, H. Hasse, J. Vrabec, *Ind. Eng. Chem. Res.* **2012**, 51, 7428.
- [88] C. W. Glass, S. Reiser, G. Rutkai, S. Deublein, A. Köster, G. Guevara-Carrion, A. Wafai, M. Horsch, M. Bernreuther, T. Windmann, Colin W. Glass, S. Reiser, G. Rutkai, S. Deublein, A. Köster, G. Guevara-Carrion, A. Wafai, M. Horsch, M. Bernreuther, T. Windmann, H. Hasse, J. Vrabec, *Comput. Phys. Commun.* **2014**, 185, 3302.
- [89] M. S. Green, *J. Chem. Phys.* **1954**, 22, 398.
- [90] R. Kubo, *J. Phys. Soc. Jpn.* **1957**, 12, 570.
- [91] D. Frenkel, B. Smit, *Understanding Molecular Simulation: From Algorithms to Applications*; Academic Press: San Diego, **2002**.
- [92] M. Griebel, S. Knapek, G. Zumbusch, *Numerische Simulation in der Moleküldynamik*; Springer-Verlag: Berlin, **2007**.
- [93] K. Binder, *Rep. Prog. Phys.* **1997**, 60, 487.
- [94] D. Landau, K. Binder, *A Guide to Monte Carlo Simulations in Statistical Physics*; Cambridge University Press: Cambridge, **2013**.
- [95] R. Lustig, *Mol. Phys.* **1988**, 65, 175.
- [96] M. P. Allen, D. J. Tildesley, *Computer Simulation of Liquids*; Oxford University Press: Oxford, **1989**.
- [97] H. C. Andersen, *J. Chem. Phys.* **1980**, 72, 2384.
- [98] R. Span, *Multiparameter Equations of State: An Accurate Source of Thermodynamic Property Data*; Springer-Verlag: Berlin, **2000**.
- [99] W. Wagner, A. Pruß, *J. Phys. Chem. Ref. Data* **2002**, 31, 387.
- [100] M. Huber, R. Perkins, A. Laesecke, D. Friend, J. Sengers, M. Assael, I. Metaxa, E. Vogel, R. Mareš, K. Miyagawa, *J. Phys. Chem. Ref. Data* **2009**, 38, 101.
- [101] B. Eckl, J. Vrabec, H. Hasse, *Mol. Phys.* **2008**, 106, 1039.
- [102] R. L. Rowley, W. V. Wilding, J. L. Oscarson, Y. Yang, N. A. Zundel, T. E. Daubert, R. P. Danner, *DIPPR Data Compilation of Pure Compound Properties: Design Institute for Physical Properties*; AIChE: New York, **2006**.
- [103] J. Vrabec, H. Hasse, *Mol. Phys.* **2002**, 100, 3375.
- [104] I. Nezbeda, J. Kolafa, *Mol. Simul.* **1991**, 5, 391.
- [105] J. Vrabec, M. Kettler, H. Hasse, *Chem. Phys. Lett.* **2002**, 356, 431.
- [106] R. Lustig, *Mol. Simul.* **2011**, 37, 457.
- [107] R. Lustig, *Mol. Phys.* **2012**, 110, 3041.
- [108] K. R. Harris, L. A. Woolf, *J. Chem. Soc. Faraday Trans. 1* **1980**, 76, 377.
- [109] F. A. L. Dullien, *AIChE J.* **1972**, 18, 62.
- [110] M. Holz, S. R. Heil, A. Sacco, *Phys. Chem. Chem. Phys.* **2000**, 2, 4740.
- [111] A. J. Easteal, W. E. Price, L. A. Woolf, *J. Chem. Soc., Faraday Trans. 1* **1989**, 85, 1091.
- [112] K. A. F. Röhrig, T. D. Kühne, *Phys. Rev. E* **2013**, 87, 045301.
- [113] W. L. Jorgensen, J. Tirado-Rives, *Proc. Natl. Acad. Sci. USA* **2005**, 102, 6665.

Received: 5 December 2015  
Revised: 8 April 2016  
Accepted: 14 April 2016  
Published online on 27 May 2016

### 3.6 Comparative study of the Grüneisen parameter for 28 pure fluids

P. Mausbach, A. Köster, G. Rutkai, M. Thol, J. Vrabec, *The Journal of Chemical Physics* 144:244505, 2016.

DOI: [doi.org/10.1063/1.4954282](https://doi.org/10.1063/1.4954282)

Nachgedruckt mit Erlaubnis von AIP Publishing (Copyright 2016).

In Rahmen dieser systematischen Studie wurde der Grüneisen-Parameter für 28 Reinstoffe in einem großen Temperatur- und Dichtebereich ermittelt und mit genauen Zustandsgleichungen, die vom „National Institute of Standards and Technology“ empfohlen werden, verglichen. Dabei wurde ein genereller Trend identifiziert: Der Grüneisen-Parameter steigt mit steigender Dichte und sinkt mit steigender Temperatur. Es konnte gezeigt werden, dass Ausnahmen von diesem Trend nur im Bereich des kritischen Punkts und für Wasser zu finden sind. Weiterhin wurde gezeigt, dass einige Zustandsgleichungen in diesem Zusammenhang ein thermodynamisch inkonsistentes Verhalten zeigten.

Der Autor der vorliegenden Dissertation hat alle für diese Veröffentlichung zugrundeliegenden molekularen Simulationen durchgeführt. Er übernahm die Erstellung aller Abbildungen und die Konsolidierung des Manuskripts. Die Überarbeitung des Manuskripts wurde vom Autor unter Mithilfe von Prof. Peter Mausbach und Prof. Jadran Vrabec durchgeführt. Der Autor wurde während des gesamten Prozesses von Prof. Jadran Vrabec betreut.



## Comparative study of the Grüneisen parameter for 28 pure fluids

Peter Mausbach,<sup>1</sup> Andreas Köster,<sup>2</sup> Gábor Rutkai,<sup>2</sup> Monika Thol,<sup>3</sup> and Jadran Vrabec<sup>2,a)</sup>

<sup>1</sup>Cologne University of Applied Sciences, 50678 Köln, Germany

<sup>2</sup>Thermodynamics and Energy Technology, Universität Paderborn, 33098 Paderborn, Germany

<sup>3</sup>Thermodynamics, Ruhr-Universität Bochum, 44801 Bochum, Germany

(Received 9 May 2016; accepted 8 June 2016; published online 28 June 2016)

The Grüneisen parameter  $\gamma_G$  is widely used for studying thermal properties of solids at high pressure and also has received increasing interest in different applications of non-ideal fluid dynamics. Because there is a lack of systematic studies of the Grüneisen parameter in the entire fluid region, this study aims to fill this gap. Grüneisen parameter data from molecular modelling and simulation are reported for 28 pure fluids and are compared with results calculated from fundamental equations of state that are based on extensive experimental data sets. We show that the Grüneisen parameter follows a general density-temperature trend and characterize the fluid systems by specifying a span of minimum and maximum values of  $\gamma_G$ . Exceptions to this trend can be found for water. *Published by AIP Publishing.* [<http://dx.doi.org/10.1063/1.4954282>]

### I. INTRODUCTION

The dimensionless Grüneisen parameter  $\gamma_G$  is generally used as a thermomechanic property characterizing solids at high pressure. In terms of the lattice vibration spectrum of solids, individual mode Grüneisen parameters are defined by<sup>1</sup>

$$\gamma_i = -\frac{v}{\omega_i} \left( \frac{\partial \omega_i}{\partial v} \right)_T, \quad (1)$$

where  $\omega_i$  is the frequency of each mode,  $v$  the volume, and  $T$  the temperature. A macroscopic Grüneisen parameter can be derived as an average of the  $\gamma_i$  leading to<sup>1</sup>

$$\gamma_G = v \left( \frac{\partial p}{\partial e} \right)_v = \frac{v}{c_v} \left( \frac{\partial p}{\partial T} \right)_v = \frac{\rho}{T} \left( \frac{\partial T}{\partial \rho} \right)_s, \quad (2)$$

in which  $p$  is the pressure,  $e$  the internal energy,  $c_v$  the isochoric heat capacity,  $\rho$  the density, and  $s$  the entropy. For solids,  $\gamma_G$  is often assumed to be independent of the temperature. Incorporating further thermodynamic response functions into Eq. (2) allows for the derivation of additional identities for the Grüneisen parameter

$$\gamma_G = \frac{v \alpha_p}{c_v \beta_T} = \frac{v \gamma_v}{c_v} = \frac{\alpha_p w^2}{c_p}, \quad (3)$$

with the isobaric heat capacity  $c_p$ , the thermal expansion coefficient  $\alpha_p = \frac{1}{v} \left( \frac{\partial v}{\partial T} \right)_p$ , the isothermal compressibility  $\beta_T = -\frac{1}{v} \left( \frac{\partial v}{\partial p} \right)_T$ , the thermal pressure coefficient  $\gamma_v = \left( \frac{\partial p}{\partial T} \right)_v$ , and the speed of sound  $w$ . In addition to its relevance in the solid state, the Grüneisen parameter has received increasing interest in fluid states because  $\gamma_G$  ubiquitously appears in different applications of non-ideal fluid dynamics.

Arp *et al.*<sup>2</sup> published a significant study of this parameter for hydrodynamic processes of compressible fluids. They discussed the Grüneisen parameter in the context of Fanno,

Rayleigh, and isentropic flows and listed a number of variants of equations used for both mass and energy conservation in which  $\gamma_G$  can be expressed. An important outcome of their work is the nature of this parameter near the critical point, where it appears to vanish similar to the speed of sound.

A criterion required for the existence of shock waves in compressible fluid dynamics can be formulated by using the fundamental derivative of gas dynamics<sup>3</sup>

$$\Gamma = 1 + \frac{\rho}{w} \left( \frac{\partial w}{\partial \rho} \right)_s, \quad (4)$$

where the sign of  $\Gamma$  determines the existence and stability of shock waves.  $\Gamma > 0$  is required for classical compressive shock waves. However, some exceptional fluids may have the property of a negative  $\Gamma$  and are called *Bethe-Zel'dovich-Thompson (BZT)* fluids. However, such a behavior still lacks confirmation. They would exhibit a nonclassical gas dynamic behavior in the single-phase vapor region, through the existence of rarefaction shock waves.<sup>4</sup> Menikoff and Plohr<sup>5</sup> showed how properties of shock waves and rarefaction waves are determined solely by the adiabatic exponent  $\kappa = -\frac{v}{p} \left( \frac{\partial p}{\partial v} \right)_s$ , the fundamental derivative  $\Gamma$ , and  $\gamma_G$ , which illustrates the importance of the Grüneisen parameter for this interesting situation.

The Grüneisen parameter was also found to be relevant in density scaling concepts of supercooled liquids.<sup>6</sup> A key quantity in this approach is the density scaling exponent  $\gamma$  that controls relaxation times, depending on density and temperature as a function of  $\rho^\gamma/T$ . It is of great interest to derive the density scaling exponent  $\gamma$  in terms of Grüneisen parameter  $\gamma_G$ . In a recent study,<sup>7</sup> the interrelation between  $\gamma_G$  and  $\gamma$ , as used in the analysis of so-called *Roskilde*—simple liquids,<sup>8</sup> was studied in detail for a Lennard-Jones system in a larger fluid region.

Furthermore, the Grüneisen parameter is found to be a prominent quantity when analyzing geophysical problems in the Earth's core.<sup>9,10</sup> Finally, because the

<sup>a)</sup>Author to whom correspondence should be addressed. Electronic mail: jadran.vrabec@upb.de

Grüneisen parameter establishes a link between thermal and caloric properties, it has become increasingly important for the development of fundamental equations of state (EOS), verifying their qualitatively correct thermodynamic behavior.<sup>11,12</sup>

Despite the fact that the Grüneisen parameter  $\gamma_G$  exhibits a key role in such diverse fields of fluid dynamics, it is surprising that systematic studies of this quantity in the entire fluid region are limited or are quite old.<sup>13–18</sup> Therefore, it is desirable to evaluate this parameter for various atomic and molecular systems for a large region of the fluid phase. It is the aim of this study to investigate the Grüneisen parameter by using a direct molecular simulation method and to compare these theoretical results with those obtained from aggregated experimental data.

This paper is organised as follows. First, a brief overview of the employed molecular simulation method is given. Next, the Grüneisen parameter is analyzed for 28 pure fluids by comparison of the simulation results with EOS recommended by the National Institute of Standards and Technology (NIST). As a measure to characterize the differences between the various fluids, the range of minimum and maximum values of the Grüneisen parameter  $\gamma_G$  are given in a tabulated form. Finally, a conclusion is drawn.

## II. MOLECULAR SIMULATION METHOD

On the basis of a molecular interaction model for a given substance, molecular simulation allows, in principle, for the investigation of any thermodynamic property without any restrictive approximation. The statistical mechanical formalism proposed by Lustig<sup>19,20</sup> constitutes the theoretical framework of the present work and was designed to provide an arbitrary number of Helmholtz energy derivatives from a single molecular simulation run for a given state point. The reduced Helmholtz energy

$$\frac{A}{RT} \equiv \alpha(\tau, \delta) = \alpha^o(\tau, \delta) + \alpha^r(\tau, \delta) \quad (5)$$

is commonly divided into an ideal (superscript “o”) and a residual (superscript “r”) contribution in which  $R$  is the molar gas constant,  $\tau = T_c/T$  is the inverse reduced temperature and  $\delta = \rho/\rho_c$  is the reduced density, where  $T_c$  is the critical temperature, and  $\rho_c$  is the critical density. The ideal contribution  $\alpha^o(\tau, \delta)$  corresponds to the value of  $\alpha(\tau, \delta)$  when no intermolecular interactions are at work. The formalism proposed by Lustig was implemented into the molecular simulation tool *ms2*<sup>21,22</sup> that yields up to eight derivatives of the residual Helmholtz energy

TABLE I. Critical data ( $T_c, p_c, \rho_c$ ), triple point temperature  $T_{tr}$ , molar weight  $M$ , as well as references for equations of state (EOS) and molecular interaction models (IM) applied for the 28 pure fluids. Thermodynamic data are from experiments.

Substance	$T_c$ [K]	$p_c$ [MPa]	$\rho_c$ [mol/l]	$T_{tr}$ [K]	$M$ [g/mol]	EOS	IM
Acetone	508.1	4.7	4.7	178.5	58.079	27	50
Ammonia	405.4	11.33	13.21	195.5	17.03	28	51
Argon	150.69	4.863	13.407	83.806	39.948	29	52
Benzene	562.02	4.907	3.901	278.67	78.112	30	53
Carbon dioxide	304.13	7.377	10.625	216.59	44.01	31	54
Carbon monoxide	132.86	3.494	10.85	68.16	28.01	27	55
Chlorobenzene	632.35	4.521	3.24	227.9	112.557	32	53
Cyclohexane	553.6	4.081	3.224	279.47	84.159	33	56
Dimethylether	400.38	5.337	5.94	131.66	46.068	34	57
Ethane	305.32	4.872	6.857	90.368	30.069	35	52
Ethanol	514.71	6.268	5.93	159.0	46.068	36	58
Ethylene	282.35	5.042	7.637	103.99	28.054	37	52
Ethylene oxide	468.92	3.705	7.17	160.65	44.053	38	59
Fluorine	144.41	5.172	15.603	53.481	37.997	39	52
Hexamethyldisiloxane	518.75	1.939	1.59	204.93	162.38	40	40
Hydrogen chloride	324.55	8.263	11.272	131.4	36.461	41	53
Hydrogen sulfide	373.1	9.0	10.19	187.7	34.081	27	60
Methanol	512.6	8.104	8.6	175.61	32.042	42	61
Nitrogen	126.19	3.396	11.184	63.151	28.013	43	52
Octamethylcyclotetrasiloxane	586.5	1.347	1.043	290.25	296.62	44	44
Oxygen	154.58	5.043	13.63	54.361	31.999	45	52
Phosgene	462.88	6.459	5.592	145.37	98.916	46	53
Propylene	364.21	4.555	5.457	87.953	42.08	11	52
Propyne	402.38	5.626	6.113	170.5	40.06	47	52
Sulfur dioxide	430.64	7.884	8.195	197.7	64.064	27	57
Toluene	591.75	4.126	3.169	178.0	92.138	27	53
Water	647.1	22.064	17.874	273.16	18.015	48	62
1,1,1,2,3,3,3-heptafluoropropane	374.9	2.925	3.495	146.35	170.03	49	63



$$A_{mn}^r = \tau^m \delta^n \frac{\partial^{m+n} \alpha^r(\tau, \delta)}{\partial \tau^m \partial \delta^n} = (1/T)^m \rho^n \frac{\partial^{m+n} \alpha^r(T, \rho)}{\partial (1/T)^m \partial \rho^n}. \quad (6)$$

With this method, the analytical derivatives of Eq. (6) can directly be sampled in order to investigate the Grüneisen parameter. In terms of Helmholtz energy derivatives, the isochoric heat capacity can be expressed by  $c_v = -R(A_{20}^o + A_{20}^r)$  and the pressure derivative with respect to the temperature by<sup>23</sup>  $(\partial p / \partial T)_v = R \rho (1 + A_{01}^r - A_{11}^r)$ . Inserting it in the second expression of Eq. (2) gives

$$\gamma_G = -\frac{1 + A_{01}^r - A_{11}^r}{A_{20}^o + A_{20}^r}. \quad (7)$$

Note that an ideal gas contribution  $A_{20}^o = 1 - c_p^o/R$  is present in the denominator, where  $c_p^o$  is the isobaric heat capacity of the ideal gas. In this study, we apply  $c_p^o$  models corresponding to the most recent and most accurate fundamental equations of state.

For the 28 pure fluids analyzed in this study, each system was sufficiently equilibrated for  $10^5$  cycles at each state point and then sampled for  $10^6$ – $2 \cdot 10^6$  production cycles in canonic (*NVT*) ensemble Monte Carlo simulations (number of particles  $N$ , volume  $V$ , and temperature  $T$  were held constant). The number of particles was set to  $N = 256$ – $864$ . Note that no significant system size effects were encountered. The electrostatic long-range corrections were considered by the reaction field method.<sup>24</sup> Rigid and non-polarizable molecular interaction models were taken from the literature as summarized in Table I. All of these models consist of one or more Lennard-Jones 12-6 potential interaction sites in order to describe the dispersive and repulsive interactions. For the polar interactions, a varying number of point charges, point dipoles, or point quadrupoles was employed. Detailed descriptions of the models are given in the original publications listed in Table I. The statistical uncertainties of the simulation data were estimated by block averaging and the error propagation law.

### III. RESULTS AND DISCUSSION

The Grüneisen parameter of different fluid systems obtained from present simulations was compared with those obtained from accurate EOS. These EOS were carefully correlated to the entire experimental database. Details of the ansatz procedures may be found in the references summarized in Table I. For this study, these EOS were evaluated by the program RefProp 9.1<sup>25</sup> distributed by the NIST. To facilitate the comparison of the results, critical point coordinates  $(T_c, p_c, \rho_c)$ , the triple point temperature  $T_t$ , and the molar weight  $M$  are listed in Table I. For most substances, the temperature dependence of the Grüneisen parameter  $\gamma_G$  along isochores is discussed. In the following figures, symbols represent molecular simulation results and the solid curves the corresponding EOS. Dashed curves represent extrapolations of the EOS. The Grüneisen parameter along vapor-liquid saturation is shown as a dotted line. The statistical uncertainties of the simulation data are typically within symbol size.

For the ideal gas, all derivatives of the residual Helmholtz energy  $A_{mn}^r$  disappear in Eq. (7). With  $c_v^o/R = -A_{20}^o$  and  $R = c_p^o - c_v^o$ , the Grüneisen parameter of the ideal gas is given by the simple relation

$$\gamma_G^o = \frac{c_p^o}{c_v^o} - 1, \quad (8)$$

where  $c_v^o$  denotes the corresponding isochoric heat capacity.  $\gamma_G^o$  isochores were omitted in the figures because they are indistinguishable from the simulation results at the lowest considered density for most investigated substances.

According to their molecular shape, polarity, and hydrogen bonding characteristics, the behavior of  $\gamma_G$  is discussed for the various substances in Subsections III A–III H. However, some general statements about the  $(\rho, T)$  behavior of  $\gamma_G$  should be given up front. The analysis of all 28 fluid systems clearly shows that the Grüneisen parameter  $\gamma_G$  strongly depends on both density *and* temperature, which is contrary to the behavior of most solids. The overall dependence of  $\gamma_G$  in the fluid phase can be discussed in two different state regions. Outside of the vicinity of the critical point and the gas phase at low temperatures, the Grüneisen parameter increases with increasing density and decreases with increasing temperature. This is a general trend for all fluids except for water. Superimposed to this behavior is the critical region. The Grüneisen parameter approaches zero at the critical point<sup>2</sup> in analogy to the speed of sound.

The Grüneisen parameter may be characterized by a span of minimum and maximum values  $(\gamma_{G, \min}^{\text{sim}}, \gamma_{G, \max}^{\text{sim}})$  to allow for a comparison between different substances. Considering a limited number of substances as investigated by Arp *et al.*,<sup>2</sup> it was stated that  $\gamma_G$  lies in a range from the ideal gas value up to about 2 for most homogeneous fluids. In the present simulation study, we find values deviating up to 80%, i.e.,  $\gamma_{G, \max}^{\text{sim}} = 0.387$  for octamethylcyclotetrasiloxane. To allow for more precise statements, the  $(\gamma_{G, \min}^{\text{sim}}, \gamma_{G, \max}^{\text{sim}})$  spans are collected in Table II. Because some of the considered EOS are not valid at higher liquid state densities, the spans were determined on the basis of  $\gamma_G$  simulation data. The largest simulated density  $\rho_{\max}^{\text{sim}}$  is close to the triple point density for all substances.

In order to concentrate on the essential aspects in the present study, 15 fluids are not detailed in the main part of this paper. Instead, they are collected in the supplementary material.<sup>26</sup>

#### A. Spherical non-polar molecules

In Fig. 1, we start with the discussion of  $\gamma_G$  for argon, which is one of the most frequently analyzed fluids. Excluding the critical region, the lowest simulated value of  $\gamma_{G, \min}^{\text{sim}} = 0.671$  occurs at  $(\rho_{\min}^{\text{sim}}, T_{\max}^{\text{sim}}) = (0.21 \text{ mol/l}, 1051 \text{ K})$ , whereas the largest simulated value of  $\gamma_{G, \max}^{\text{sim}} = 2.865$  occurs at  $(\rho_{\max}^{\text{sim}}, T_{\min}^{\text{sim}}) = (35.64 \text{ mol/l}, 81.75 \text{ K})$ . According to this scheme, values for all studied fluids are collected in Table II. Note that  $\gamma_{G, \max}^{\text{sim}} = 2.865$  is almost 45% above the specified range of values indicated by Arp *et al.*<sup>2</sup> At higher densities,

TABLE II. Range of minimum and maximum values of the Grüneisen parameter  $\gamma_G$  obtained from present simulations. No values are included in the table for water because it does not fit into the scheme. Moreover, the results are assigned to different groups (A, B, or C) according to their quality as explained in the text.

Substance	$\rho_{\min}^{\text{sim}}$ mol/l	$T_{\max}^{\text{sim}}$ K	$\gamma_{G, \min}^{\text{sim}}$	$\rho_{\max}^{\text{sim}}$ mol/l	$T_{\min}^{\text{sim}}$ K	$\gamma_{G, \max}^{\text{sim}}$	A	B	C
Acetone	0.1	800	0.062	14	400	0.82	×		
Ammonia	0.1	800	0.183	40	300	1.255			
Argon	0.21	1051	0.671	35.64	81.75	2.865		×	
Benzene	0.1	1000	0.042	11	400	0.93			
Carbon dioxide	0.1	600	0.215	25	275	1.466		×	
Carbon monoxide	0.1	210	0.402	28	100	1.856	×		
Chlorobenzene	0.1	1000	0.041	10.5	275	1.754			
Cyclohexane	1.0	700	0.044	9	340	0.835	×		
Dimethylether	0.1	750	0.075	17	300	1.163			
Ethane	0.1	600	0.104	19	225	1.618	×	×	
Ethanol	0.1	900	0.066	18	375	0.735			×
Ethylene	0.1	600	0.135	22	200	1.826	×		
Ethylene oxide	0.1	1000	0.079	20	350	1.046	×		
Fluorine	0.1	350	0.349	42	100	2.365			×
Hexamethyldisiloxane	0.1	1200	0.018	5	300	0.694	×		
Hydrogen chloride	0.1	400	0.4	33	225	1.532	×		
Hydrogen sulfide	0.2	400	0.309	30	250	1.698			
Methanol	0.1	900	0.11	28	375	0.804			×
Nitrogen	0.1	275	0.402	29	110	1.909	×	×	
Octamethylcyclotetrasiloxane	0.1	1200	0.012	3.2	475	0.387	×		
Oxygen	0.1	300	0.4	36	100	2.127			
Phosgene	0.2	700	0.132	16.2	250	1.985	×		
Propylene	0.1	700	0.076	14	275	1.039	×		
Propyne	0.1	700	0.093	16	300	1.083			×
Sulfur dioxide	0.1	750	0.193	20	350	1.092	×		
Toluene	0.1	950	0.035	9	475	0.65			
Water	...	...	...	...	...	...		×	
1,1,1,2,3,3,3-heptafluoropropane	0.1	750	0.043	10	275	0.925	×		

larger deviations between simulated and EOS values can be observed. The approach of  $\gamma_G$  towards zero near the critical point is nicely indicated by both calculation methods.

## B. Linear quadrupolar molecules

In this section, we discuss the Grüneisen parameter for fluids consisting of linear quadrupolar molecules. Fig. 2 shows  $\gamma_G$  of carbon dioxide as a function of temperature along

different isochores. The agreement of the present simulation results with values from the according EOS is reasonable in the gas phase up to the critical density of 10.625 mol/l, whereas in the liquid phase, the deviations increase with increasing density. In accordance with the considerations of Arp *et al.*,<sup>2</sup>  $\gamma_G$  isochores bend downwards in the critical region. However, because the present simulation data do not cover the vicinity of the critical point, the approach of  $\gamma_G$  to zero cannot be demonstrated.

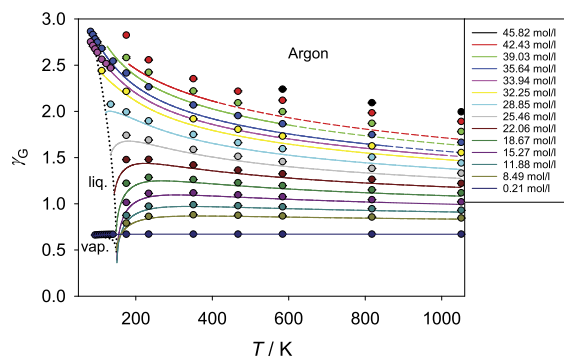


FIG. 1. Grüneisen parameter  $\gamma_G$  of argon as a function of temperature along different isochores ranging from  $\rho = 0.21$  to 45.82 mol/l.

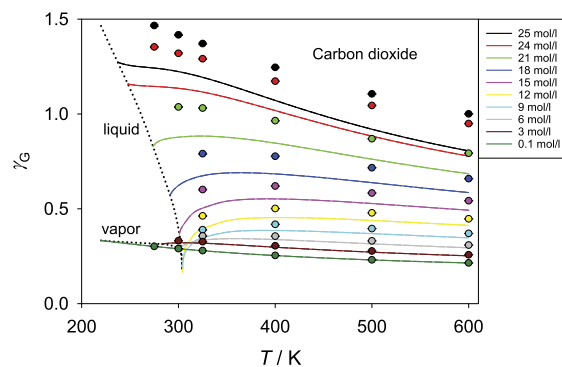


FIG. 2. Grüneisen parameter  $\gamma_G$  of carbon dioxide as a function of temperature along different isochores ranging from  $\rho = 0.1$  to 25 mol/l.



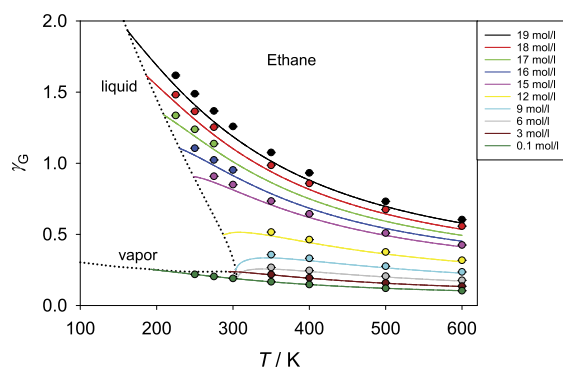


FIG. 3. Gruneisen parameter  $\gamma_G$  of ethane as a function of temperature along different isochores ranging from  $\rho = 0.1$  to 19 mol/l.

The resemblance between simulation results and EOS values, even in the dense liquid phase, is much better for ethane and ethylene as shown in Figs. 3 and 4. Both substances exhibit a strong temperature dependence at higher densities. Increasing the temperature causes a strong decrease of the Gruneisen parameter, which shows that the assumption of temperature independence in solids is not applicable in the liquid phase.

The Gruneisen parameter  $\gamma_G$  of nitrogen (Fig. 5) follows the general trend discussed above. Comparing simulated  $\gamma_G$  values with those calculated from the corresponding EOS shows that larger deviations can be observed at high densities and high temperatures.

Fluorine, oxygen, propyne, and propylene also belong to the class of linear quadrupolar fluids and are discussed in the supplementary material.<sup>26</sup>

### C. Triangular dipolar molecules

As representatives for triangular dipolar molecules, we discuss here the state dependence of the Gruneisen parameter of acetone, ethylene oxide, and phosgene. Dimethylether and sulfur dioxide are discussed in the supplementary material.<sup>26</sup> Fig. 6 presents the  $\gamma_G$  temperature dependence of acetone

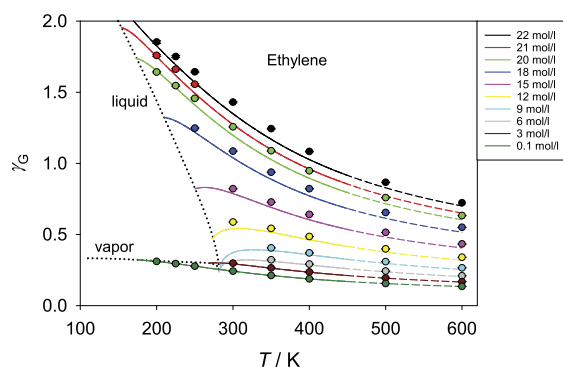


FIG. 4. Gruneisen parameter  $\gamma_G$  of ethylene as a function of temperature along different isochores ranging from  $\rho = 0.1$  to 22 mol/l.

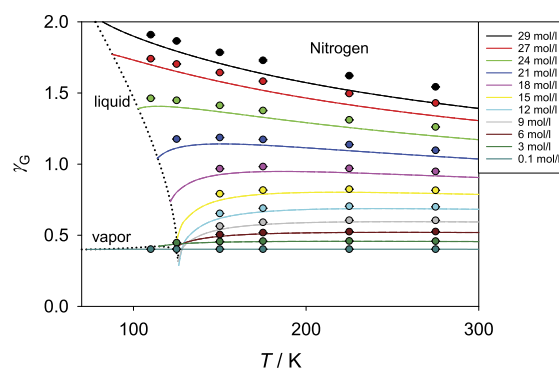


FIG. 5. Gruneisen parameter  $\gamma_G$  of nitrogen as a function of temperature along different isochores ranging from  $\rho = 0.1$  to 29 mol/l.

along isochores with a good agreement between simulated and EOS data.

Figs. 7 and 8 present temperature-dependent results of the Gruneisen parameter for ethylene oxide and phosgene, respectively. For ethylene oxide, the applied EOS<sup>38</sup> belongs to a new generation of EOS because it was correlated to a hybrid data set (experimental and molecular simulation data).<sup>64</sup> The reactive nature of ethylene oxide makes this substance particularly hazardous: it is carcinogenic, mutagenic, and highly flammable at room temperature. It is thus not surprising that the availability of experimental data is very limited. Experimental data cover almost exclusively the gaseous phase. Therefore, molecular simulation data were used to extend the validity of the EOS to the liquid state because elevated temperatures or pressures are not limiting factors for molecular simulation. Fig. 7 shows that up to a density of  $\rho = 16$  mol/l, the correspondence between the EOS and simulation data is good; for  $\rho \geq 18$  mol/l, some deviations can be seen. Near the critical point,  $\gamma_G$  obtained from the EOS suggests an approach to zero, whereas the simulation results do not show this tendency, presumably because the number of particles used in the simulations was not large enough.

For phosgene, the situation is similar as for ethylene oxide. Due to its hazardous and extremely toxic nature, laboratory measurements are hardly available or very old.

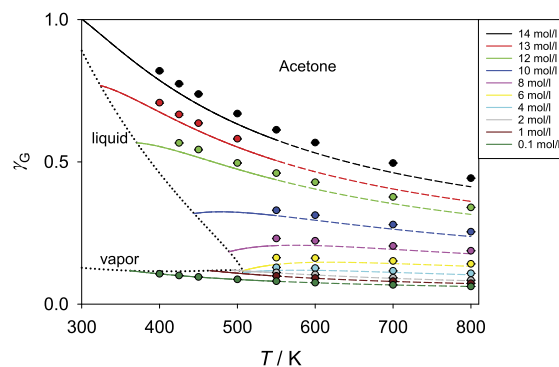


FIG. 6. Gruneisen parameter  $\gamma_G$  of acetone as a function of temperature along different isochores ranging from  $\rho = 0.1$  to 14 mol/l.

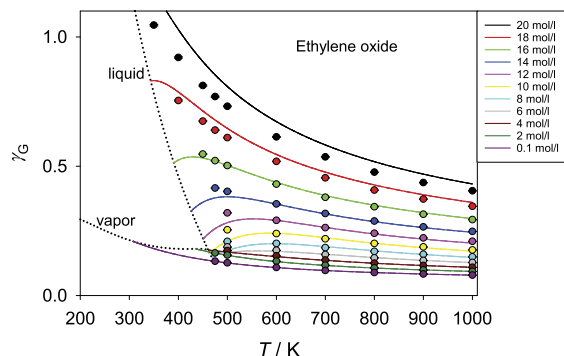


FIG. 7. Gruneisen parameter  $\gamma_G$  of ethylene oxide as a function of temperature along different isochores ranging from  $\rho = 0.1$  to 20 mol/l.

Therefore, a modified Benedict-Webb-Rubin (MBWR) type EOS<sup>65</sup> has been developed for phosgene which is solely based on simulation data.<sup>46</sup> The correlation procedure was improved with respect to the conventional method: based on a purely simulated dataset, usually only pressure and energy values are correlated.<sup>66</sup> For phosgene, also higher order Helmholtz energy derivatives according to Eq. (6) have been applied in the correlation procedure. Fig. 8 shows that the agreement between simulation data and EOS results is excellent throughout and, compared to the conventional method, demonstrates fundamental improvements when using this new fitting technique.

#### D. Hydrogen bonding molecules

Hydrogen bonding fluids are of particular interest in this study because especially water does not follow the general  $(\rho, T)$  trend of  $\gamma_G$ .

Fig. 9 shows the  $(\rho, T)$  behavior of  $\gamma_G$  of hydrogen chloride. From a chemical perspective, real hydrogen chloride is not considered as a hydrogen bonding fluid. Its molecular model, however, is constructed in the same qualitative way as those for hydrogen bonding fluids (like water or methanol), i.e., employing point charges that are eccentrically superimposed to a Lennard-Jones site. Therefore, it is discussed in this section. The agreement between simulated

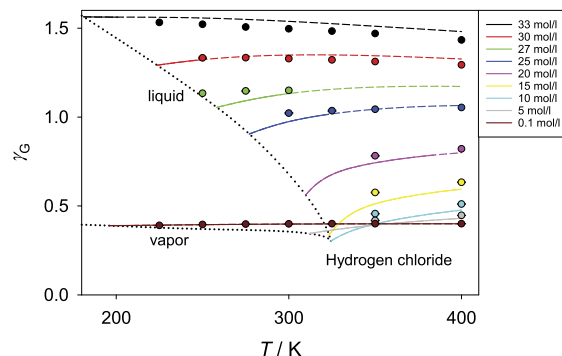


FIG. 9. Gruneisen parameter  $\gamma_G$  of hydrogen chloride as a function of temperature along different isochores ranging from  $\rho = 0.1$  to 33 mol/l.

and EOS data is reasonably well, especially in the high density and high temperature region, where only extrapolations of the EOS (dashed lines) were used. The interesting point in case of hydrogen chloride is that this substance is the only one in the present study, in which the  $\gamma_G$  isochores are roughly independent on temperature at higher densities.

The Gruneisen parameter of water, shown in Fig. 10, behaves very exceptional compared with all other fluids discussed here. The  $\gamma_G$  isochores in stable states from EOS are based on the IAPWS-95 formulation,<sup>48</sup> an equation with a very high level of accuracy, sometimes called reference quality EOS (see the discussion in Sec. III H).  $\gamma_G$  isochores, calculated from this equation, exhibit a maximum in the supercritical region at high densities, e.g., at a density of  $\rho = 58$  mol/l the maximum occurs at  $T = 657$  K slightly above the critical temperature of  $T_c = 647.1$  K. Furthermore,  $\gamma_G$  develops a maximum along the liquid saturation line at a temperature of  $T \approx 480$  K. Decreasing the temperature further causes a crossing of  $\gamma_G$  along the liquid and vapor saturation line at a temperature of  $T \approx 338$  K. In the dense liquid state at low temperatures,  $\gamma_G$  drops sharply and even becomes negative (not shown in Fig. 10), which is contrary to all other fluids in this study. The simulation results, performed with the TIP4P/2005 interaction model,<sup>62</sup> only show a good agreement with the IAPWS-95 EOS at a high density of 58 mol/l and low temperatures as well as on the liquid side of the supercritical

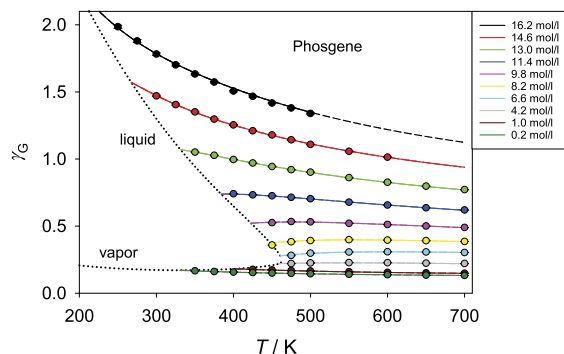


FIG. 8. Gruneisen parameter  $\gamma_G$  of phosgene as a function of temperature along different isochores ranging from  $\rho = 0.2$  to 16.2 mol/l.

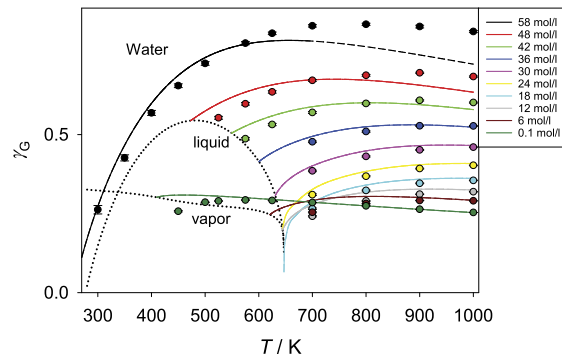


FIG. 10. Gruneisen parameter  $\gamma_G$  of water as a function of temperature along different isochores ranging from  $\rho = 0.1$  to 58 mol/l.

region in a range of  $24 < \rho/\text{mol/l} < 42$ . However, maxima are also present along the simulated isochores at high densities which, compared with the IAPWS-95 EOS, are shifted to higher temperatures, e.g., at  $\rho = 58 \text{ mol/l}$  to a temperature of  $T \approx 800 \text{ K}$ .

Negative values of  $\gamma_G$  can easily be explained by looking at the first expression in Eq. (3). The isothermal compressibility  $\beta_T$  and the isochoric heat capacity  $c_v$  are always positive in the entire single-phase fluid region, whereas the thermal expansion coefficient  $\alpha_p$  shows anomalous behavior when it becomes negative. Therefore, all fluids having a density anomaly show negative values of  $\gamma_G$  which occurs for water at  $T = 277 \text{ K}$  and ambient pressure. An equivalent behavior could be demonstrated, e.g., for the Gaussian core model fluid.<sup>7</sup> As a consequence of a negative thermal expansion coefficient, a strongly decreasing  $\gamma_G$  to negative values can be demonstrated more clearly in the supercooled region (Fig. 11). The Grüneisen parameter of supercooled water was evaluated with a two-state equation of state (TSEOS) correlated to the most recent experimental data. The TSEOS was developed by Holten *et al.*<sup>67</sup> to model the anomalous behavior of several thermodynamic properties of metastable supercooled water. Holten *et al.*<sup>67</sup> assumed that liquid water at low temperatures can be described as a mixture of two interconvertible states of local molecular order, namely, a high-density liquid (HDL) and a low-density liquid (LDL) whose ratio is controlled by thermodynamic equilibrium. It is believed that the competition between these two configurations generates the anomalies of the thermodynamic properties of cold and supercooled water. The model assumes a liquid-liquid (HDL-LDL) critical point at  $p_c = 0 \text{ MPa}$ ,  $\rho_c = 914.84 \text{ g/l}$ , and  $T_c = 228 \text{ K}$  and was fitted to experimental data ranging from the homogeneous ice nucleation temperature up to  $300 \text{ K}$  for pressures below  $400 \text{ MPa}$ . Because it is formulated in terms of Gibbs energy as an implicit function of temperature and pressure, the temperature dependence of the Grüneisen parameter is discussed in Fig. 11 along isobars. The solid lines represent  $\gamma_G$  isobars obtained from the TSEOS covering a range from roughly  $-1$  near the assumed liquid-liquid critical point to  $+1$  at a pressure of  $p = 400 \text{ MPa}$  and

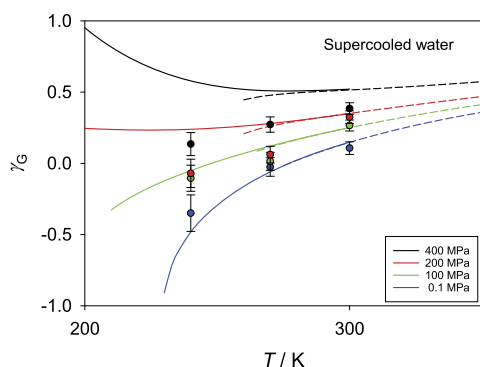


FIG. 11. Grüneisen parameter  $\gamma_G$  of supercooled water as a function of temperature along different isobars ranging from  $p = 0.1$  to  $400 \text{ MPa}$ . Solid lines represent the TSEOS of Holten *et al.*<sup>67</sup> and dashed lines the IAPWS-95 EOS.<sup>48</sup>

low temperatures. The change to negative  $\gamma_G$  values occurs at a pressure of about  $150 \text{ MPa}$  in accordance with the appearance of the expansivity anomaly at this pressure.<sup>68</sup> In the supercooled region, additional simulations were performed with the TIP4P/2005 potential model. Compared with the stable liquid state, larger statistical fluctuations are present in the metastable, supercooled state. However, within the error bars, a reasonable agreement with the TSEOS can be observed up to a pressure of  $p = 100 \text{ MPa}$ . For pressures  $p > 150 \text{ MPa}$  large deviations exist between simulation data and TSEOS results.

It is of some interest to compare the behavior of the Grüneisen parameter obtained from the TSEOS model with the IAPWS-95 formulation<sup>48</sup> close to the melting line.  $\gamma_G$  isobars obtained from the IAPWS-95 EOS are shown as dashed lines in Fig. 11. Both curves exhibit a smooth connection without significant discontinuities at the point of switching. When extrapolating the data from the IAPWS-95 formulation into the supercooled region at  $p = 0.1 \text{ MPa}$ , the Grüneisen parameter follows closely that of the TSEOS. An increase in pressure results in decreasing compliance at low temperatures. This is a result that confirms the findings made in the analysis of the thermodynamic curvature scalar for both EOS.<sup>69,70</sup>

Note that ammonia, methanol, ethanol, and hydrogen sulfide as additional hydrogen bonding fluids are discussed in the supplementary material.<sup>26</sup>

## E. Cyclic molecules

As an example for a cyclic molecule, the Grüneisen parameter of cyclohexane is presented in Fig. 12.  $\gamma_G$  follows the general  $(\rho, T)$  trend and the agreement between simulation and EOS results is satisfactory. Benzene, chlorobenzene, and toluene as additional cyclic molecules are discussed in the supplementary material.<sup>26</sup>

## F. Siloxanes

Siloxanes are considered as an important group of working fluids in heat recovery systems, such as organic Rankine cycles (ORC). They possess an excellent thermal and chemical stability and are not toxic. In addition, siloxanes

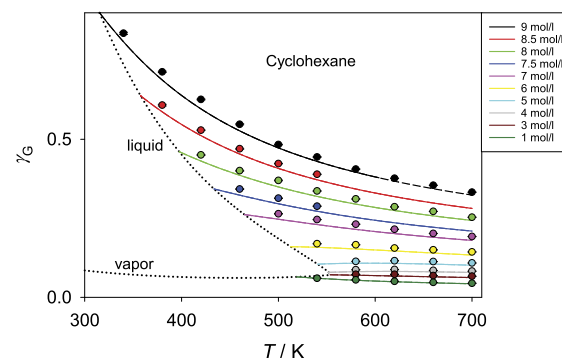


FIG. 12. Grüneisen parameter  $\gamma_G$  of cyclohexane as a function of temperature along different isochors ranging from  $\rho = 1$  to  $9 \text{ mol/l}$ .

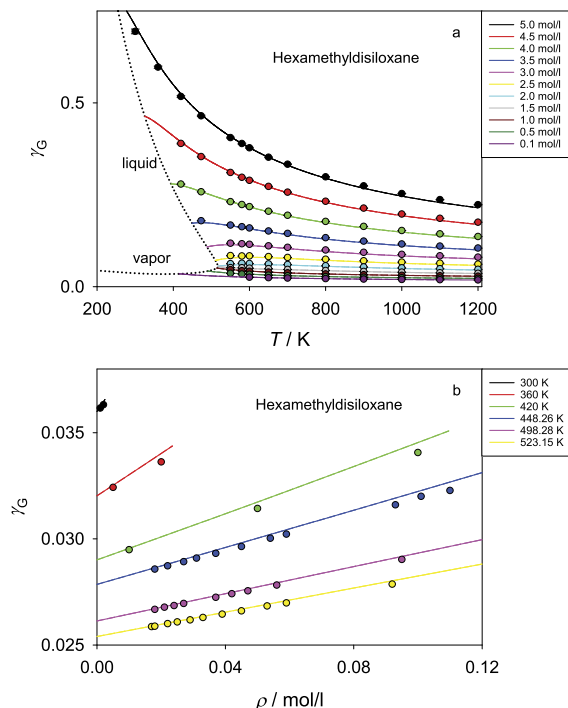


FIG. 13. Grüneisen parameter  $\gamma_G$  of hexamethyldisiloxane as a function of temperature (a) along different isochores ranging from  $\rho = 0.1$  to  $5 \text{ mol/l}$  and as a function of density (b) on the vapor side along different isotherms ranging from  $T = 300$  to  $523.15 \text{ K}$ .

are possible candidates for *BZT* fluids mentioned above.<sup>71</sup> Therefore, two siloxanes are discussed in this paper, namely, hexamethyldisiloxane (Fig. 13) and octamethylcyclotrisiloxane, given in the supplementary material.<sup>26</sup> Particularly hexamethyldisiloxane appears to be a good candidate for becoming a widely employed working fluid for high-temperature ORC processes. In order to extend the existing experimental data of hexamethyldisiloxane particularly to higher temperatures, additional simulations were performed in Ref. 40. A new EOS was developed<sup>40</sup> based on this hybrid data set similar to the method that was used for ethylene oxide. As in the case of ethylene oxide and phosgene, this extended fitting strategy allows for the determination of an EOS with a high accuracy. The temperature-dependent behavior of the Grüneisen parameter is presented in Fig. 13(a). An excellent agreement can be observed between simulated and EOS data.

It is our intention to determine the fundamental derivative of gas dynamics  $\Gamma$ <sup>72</sup> according to Eq. (4) in a future project for the two siloxanes discussed in this study. The region of interest for a *BZT* fluid is the single-phase vapor region. In Fig. 13(b) the density-dependent behavior of  $\gamma_G$  in this region is presented for isotherms up to a temperature of  $T = 523.15 \text{ K}$  slightly above the critical temperature of  $T_c = 518.75 \text{ K}$ . Again, the agreement between simulated and EOS data is good, which should allow for a reliable determination of  $\Gamma$ .

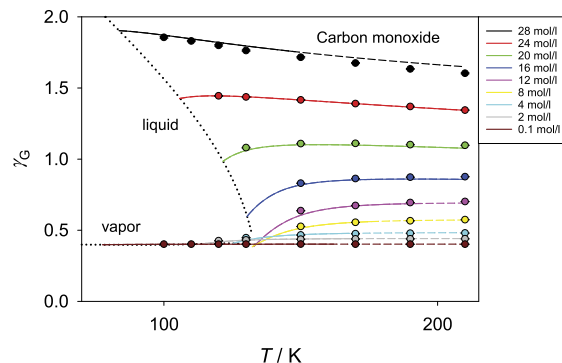


FIG. 14. Grüneisen parameter  $\gamma_G$  of carbon monoxide as a function of temperature along different isochores ranging from  $\rho = 0.1$  to  $28 \text{ mol/l}$ .

### G. Other fluids

In this final group, we discuss the remaining fluids which do not really belong to Secs. III A–III F. The Grüneisen parameter of carbon monoxide is shown in Fig. 14 with a good agreement between simulation and EOS data. The phase behavior of the Grüneisen parameter of 1,1,1,2,3,3,3-Heptafluoropropane ( $\text{C}_3\text{HF}_7$ ) is presented in the supplementary material.<sup>26</sup>

### H. Simulation versus EOS results

For a certain number of fluids, deviations occur between simulation results and the values obtained from the according EOS. For some EOS especially at high densities, only their extrapolated values could be used for comparison because experimental data were limited or not available in this state region. In turn, also the molecular interaction models will not always be optimal in any particular phase region. Therefore, it is of interest to review the simulation results against the EOS data. Proceeding in this direction, the outcomes of the 28 studied fluids are assigned to three groups as summarized in Table II.

Group A contains all fluids with a good or at least satisfactory agreement between simulation and EOS results.

The second, very important, group B collects all fluids which are privileged to have their own reference quality EOS as defined by Span.<sup>23</sup> The construction of this type of EOS requires a large amount of experimental data, months or years of careful data filtering and complex non-linear fitting. Only a very limited number of fluids (less than ten) have a reference quality EOS, such as argon, carbon dioxide, ethane, nitrogen, or water. The simulations for argon (Fig. 1) were performed on the basis of the classical Lennard-Jones potential. One weakness of this potential is the lack of a realistic description of repulsion, which originates from the Pauli exclusion principle. It might be of interest to examine whether the deviations in the Grüneisen parameter at high density and temperature between simulation and EOS data are caused by this issue. Likewise, the molecular interaction model of carbon dioxide (Fig. 2) cannot reproduce results of the corresponding reference quality EOS at high densities.

For water (Fig. 10), the simulation results, based on the TIP4P/2005 interaction model,<sup>62</sup> do not follow the IAPWS-95 reference quality EOS<sup>48</sup> in different regions of the phase space. As it is well known, the development of an interaction model for water that is valid in a large phase space region continues to be a major challenge.<sup>73</sup> The agreement between simulation and EOS values for ethane (Fig. 3) and nitrogen (Fig. 5) is satisfactory.

Recently, the use of the Grüneisen parameter was suggested to verify the correct qualitative behavior of EOS.<sup>11,12</sup> Because of the identities given in Eq. (3), the behavior of the speed of sound as well as the isochoric and isobaric heat capacities can be simultaneously monitored by the Grüneisen parameter. The assumed qualitatively correct behavior of an EOS can be explained in the density-dependent representation of  $\gamma_G$  along isotherms as given, e.g., for argon in Fig. 15. Because of the general  $(\rho, T)$  trend explained above, the isotherms at high temperatures show an increasing Grüneisen parameter with increasing density. Due to the superposition of the critical region with an approach to zero at the critical point, a crossing of isotherms must occur beyond the critical density accompanied with a change to negative curvature as already shown in recent work.<sup>11,12</sup> This behavior is assumed to be correct because it was found for several different fluids. Some of the EOS deviate from this behavior. In Fig. 16, we show two typical examples of deviant behavior of the examined EOS. Fig. 16(a) presents the Grüneisen parameter of fluorine where neither a crossing of the isotherms nor a change to negative curvature at higher densities can be seen. The Grüneisen parameter of propyne (Fig. 16(b)) shows a crossing of the isotherms, whereas a change to a negative curvature does not occur. All fluids for which the EOS differs in such a way from the presumed behavior are collected in group C as summarized in Table II. For these fluids, the simulation results are, at least, more plausible.

Seven fluids (amonia, benzene, chlorobenzene, dimethylether, hydrogen sulfide, oxygen, and toluene) have not been assigned to the three groups. They exhibit the correct assumed behavior of the associated EOS, but still reveal deviations from the simulation results. It is believed that the thermodynamic behavior of benzene and chlorobenzene is

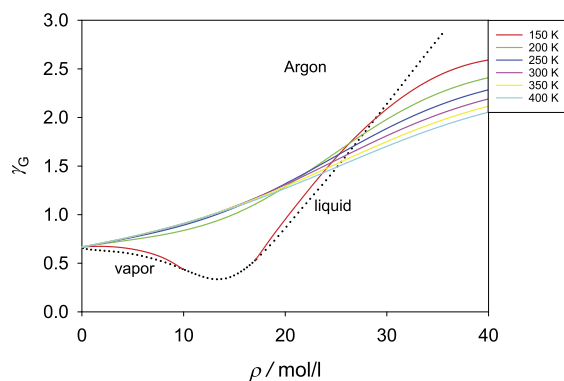


FIG. 15. Grüneisen parameter  $\gamma_G$  of argon as a function of density along different isotherms ranging from  $T = 150$  to  $400$  K obtained from the EOS.<sup>29</sup>

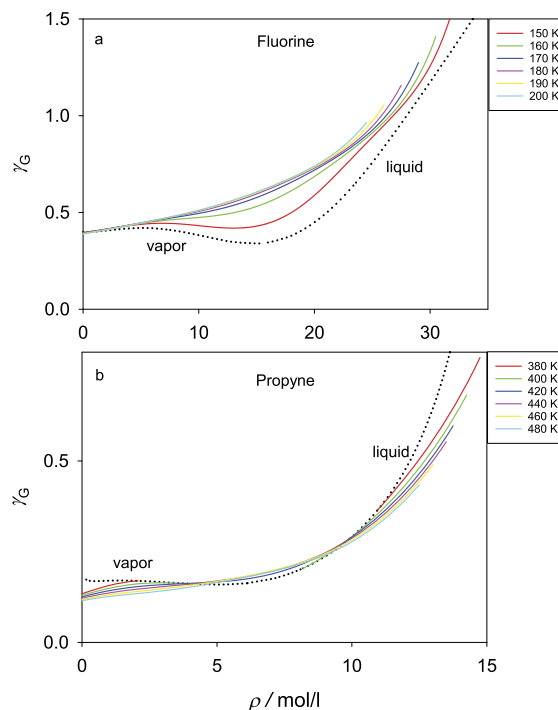


FIG. 16. Grüneisen parameter  $\gamma_G$  as a function of density (a) of fluorine along isotherms ranging from  $T = 150$  to  $200$  K and (b) of propyne along isotherms ranging from  $T = 380$  to  $480$  K. The  $\gamma_G$  isotherms were obtained from the corresponding EOS. They show two typical cases of deviant behavior of the Grüneisen parameter as described in the text.

correctly described by their EOS because not only  $pVT$  data but also accurate speed of sound data were available during the fitting procedure. For the remaining fluids, we have to leave the assessment open.

The maximum values of the simulated Grüneisen parameter  $\gamma_{G, \max}^{\text{sim}}$  vary between 0.387 for octamethylcyclotetrasiloxane and 2.865 for argon. By interpreting the results of Table II, it might be natural to deduce, in some way, a correlation between a decreasing Grüneisen parameter and increasing complexity of the molecules. Because of the absence of a general theory, an attempt was made to find empirical correlations between  $\gamma_G$  and various substance parameters. For this purpose, it is necessary to compare the 28 fluids at equivalent state points. Two state points were chosen for comparison, one close to the respective triple point at  $(\rho_{\text{tr}}, 1.1 T_{\text{tr}})$  and the second one on the liquid saturation line at  $\rho^*(0.7 T_c)$ . A temperature of  $0.7 T_c$  is also widely used for the phase characterization of pure components in terms of the acentric factor  $\omega$ , which is a measure of the non-sphericity of molecules. For both state points, the Grüneisen parameter of all 28 fluids was correlated with different substance parameters (molar weight, molecular degrees of freedom, isochoric heat capacity, compressibility, acentric factor, as well as triple point  $(\rho_{\text{tr}}, T_{\text{tr}})$  and critical data  $(p_c, \rho_c, T_c)$ ) using both simulated and EOS results. For all these parameters, no strong correlation was found. However, a weak correlation between the residual Grüneisen parameter  $\gamma_G^r = \gamma_G - \gamma_G^o$  and the compressibility



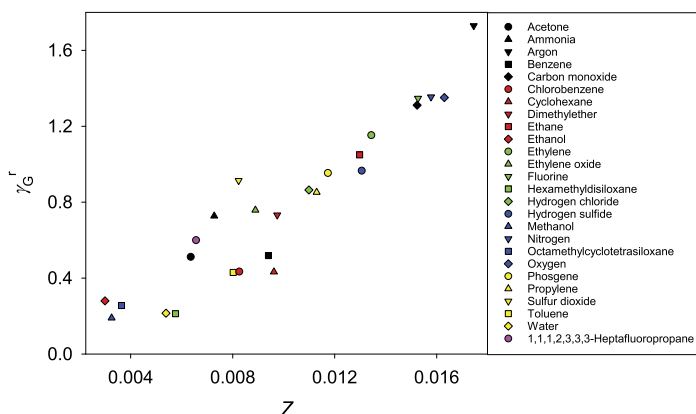


FIG. 17. Residual Grüneisen parameter  $\gamma_G^r = \gamma_G - \gamma_G^0$  as a function of compressibility  $Z = p/(\rho RT)$  on the liquid saturation line at  $\rho'(0.7 T_c)$  for 26 fluids. Carbon dioxide and propyne are not included (see text).

$Z = p/(\rho RT)$  on the liquid saturation line at  $\rho'(0.7 T_c)$  was found, as shown in Fig. 17 for the EOS data. Carbon dioxide and propyne are not included in Fig. 17. For carbon dioxide,  $0.7 T_c < T_{tr}$ . The behavior of  $\gamma_G$  of propyne along the vapor-liquid coexistence line is represented poorly by the according EOS (cf. Fig. 16(b)), causing a larger error in  $\gamma_G^r$ . Fig. 17 suggests an almost linear increase of  $\gamma_G^r$  with increasing compressibility of the fluid components at  $\rho'(0.7 T_c)$ .

#### IV. CONCLUSION

The behavior of the Grüneisen parameter  $\gamma_G$  was analyzed in detail for 28 pure fluids. We establish that the phase space behavior of  $\gamma_G$  for fluids follows a general trend. The Grüneisen parameter increases with increasing density and decreases with increasing temperature, if the critical region is excluded. Therefore, the assumption often used for solids that  $\gamma_G$  is independent of temperature cannot be applied to the fluid state. We find exceptions from this general trend for water. Different spans of  $\gamma_G$  are characterized by a range of minimum and maximum values. Deviations between simulation results and EOS data, especially at high densities, could be assessed by assigning the outcomes to three different quality groups. In group A, all fluids are summarized, providing credible results with respect to EOS and simulation. Group B includes all substances whose EOS is preferable to the simulation results. Group C collects all fluids in which the associated EOS leads to an inconsistent thermodynamic behavior. Here, the simulation results are, at least, more plausible. To the best of our knowledge, this study represents the first detailed analysis of the Grüneisen parameter for a large number of fluids over a very large region of thermodynamic states.

#### ACKNOWLEDGMENTS

The simulations were carried out on the Oculus cluster (PC<sup>2</sup>) at the University of Paderborn and the national supercomputer Hazel Hen at the High Performance Computing Center Stuttgart (HLRS) within Project No. MMHBF2.

- <sup>1</sup>N. W. Ashcroft and N. D. Mermin, *Solid State Physics* (Holt-Saunders International Editions, 1981).
- <sup>2</sup>V. Arp, J. M. Persichetti, and Chen Guo-bang, "The Grüneisen parameter in fluids," *J. Fluids Eng.* **106**, 193–200 (1984).
- <sup>3</sup>P. A. Thompson, "A fundamental derivative in gasdynamics," *Phys. Fluids* **14**, 1843–1849 (1971).
- <sup>4</sup>P. A. Thompson and K. Lambrakis, "Negative shock waves," *J. Fluid Mech.* **60**, 187–208 (1973).
- <sup>5</sup>R. Menikoff and B. J. Plohr, "The Riemann problem for fluid flow of real materials," *Rev. Mod. Phys.* **61**, 75–130 (1989).
- <sup>6</sup>R. Casalini, U. Mohanty, and C. M. Roland, "Thermodynamic interpretation of the scaling of the dynamics of supercooled liquids," *J. Chem. Phys.* **125**, 014505 (2006).
- <sup>7</sup>P. Mausbach and H.-O. May, "Direct molecular simulation of the Grüneisen parameter and density scaling exponent in fluid systems," *Fluid Phase Equilib.* **366**, 108–116 (2014).
- <sup>8</sup>J. C. Dyre, "Hidden scale invariance in condensed matter," *J. Phys. Chem. B* **118**, 10007–10024 (2014).
- <sup>9</sup>O. L. Anderson, "The Grüneisen ratio for the last 30 years," *Geophys. J. Int.* **143**, 279–294 (2000).
- <sup>10</sup>D. J. Stevenson, "Application of liquid state physics to earth's core," *Phys. Earth Planet. Inter.* **2**, 42–62 (1980).
- <sup>11</sup>E. W. Lemmon, U. Overhoff, M. O. McLinden, and W. Wagner, "A reference equation of state for propylene for temperatures from the melting line to 575 K and pressures up to 1000 MPa," *J. Phys. Chem. Ref. Data* (to be published).
- <sup>12</sup>M. Thol, G. Rutkai, A. Köster, R. Lustig, R. Span, and J. Vrabec, "Equation of state for the Lennard-Jones fluid," *J. Phys. Chem. Ref. Data* **45**, 023101 (2016).
- <sup>13</sup>L. Knopoff and J. N. Shapiro, "Pseudo-Grüneisen parameter for liquids," *Phys. Rev. B* **1**, 3893–3895 (1970).
- <sup>14</sup>S. K. Kor, U. S. Tandon, and B. K. Singh, "Pseudo-Grüneisen parameter for liquid argon," *Phys. Lett. A* **38**, 187–188 (1972).
- <sup>15</sup>R. Boehler and G. C. Kennedy, "Pressure dependence of the thermodynamical Grüneisen parameter of fluids," *J. Appl. Phys.* **48**, 4183–4186 (1977).
- <sup>16</sup>R. Boehler, "Melting temperature, adiabats, and Grüneisen parameter of lithium, sodium and potassium versus pressure," *Phys. Rev. B* **27**, 6754–6762 (1983).
- <sup>17</sup>B. K. Sharma, "Volume dependence of thermodynamical Grüneisen parameter of fluorocarbon fluids," *Phys. Lett. A* **99**, 227–229 (1983).
- <sup>18</sup>J. Amoros, J. R. Solana, and E. Villar, "Temperature, pressure and volume dependence of the Grüneisen parameter of dense gaseous and liquid argon," *Mater. Chem. Phys.* **20**, 255–260 (1988).
- <sup>19</sup>R. Lustig, "Direct molecular NVT simulation of the isobaric heat capacity, speed of sound and Joule-Thomson coefficient," *Mol. Simul.* **37**, 457–465 (2011).
- <sup>20</sup>R. Lustig, "Statistical analogues for fundamental equation of state derivatives," *Mol. Phys.* **110**, 3041–3052 (2012).
- <sup>21</sup>S. Deublein, B. Eckl, J. Stoll, S. V. Lishchuk, G. Guevara-Carrion, C. W. Glass, T. Merker, M. Bernreuther, H. Hasse, and J. Vrabec, "ms2: A molecular simulation tool for thermodynamic properties," *Comput. Phys. Commun.* **182**, 2350–2367 (2011).
- <sup>22</sup>C. W. Glass, S. Reiser, G. Rutkai, S. Deublein, A. Köster, G. Guevara-Carrion, A. Wafai, M. Horsch, M. Bernreuther, T. Windmann, H. Hasse, and

- J. Vrabec, "ms2: A molecular simulation tool for thermodynamic properties, new version release," *Comput. Phys. Commun.* **185**, 3302–3306 (2014).
- <sup>23</sup>R. Span, *Multiparameter Equations of State: An Accurate Source of Thermodynamic Property Data* (Springer Verlag, Berlin, 2000).
- <sup>24</sup>J. A. Barker and R. O. Watts, "Monte Carlo studies of the dielectric properties of water-like models," *Mol. Phys.* **26**, 789–792 (1973).
- <sup>25</sup>See <http://www.nist.gov/srd/nist23.cfm> for NIST Reference Fluid Thermodynamic and Transport Properties Database.
- <sup>26</sup>See supplementary material at <http://dx.doi.org/10.1063/1.4954282> for the discussion of the temperature-dependent Grüneisen parameter for 15 additional substances.
- <sup>27</sup>E. W. Lemmon and R. Span, "Short fundamental equations of state for 20 industrial fluids," *J. Chem. Eng. Data* **51**, 785–850 (2006).
- <sup>28</sup>R. Tillner-Roth, F. Harms-Watzenberg, and H. D. Baehr, "Eine neue fundamentalgleichung für ammoniak," *DKV-Tagungsber.* **20**, 167–181 (1993).
- <sup>29</sup>C. Tegeler, R. Span, and W. Wagner, "A new equation of state for argon covering the fluid region for temperatures from the melting line to 700 K at pressures up to 1000 MPa," *J. Phys. Chem. Ref. Data* **28**, 779–850 (1999).
- <sup>30</sup>M. Thol, E. W. Lemmon, and R. Span, "Equation of state for benzene for temperatures from the melting line up to 725 K with pressures up to 500 MPa," *High Temp. - High Pressures* **41**, 81–97 (2012).
- <sup>31</sup>R. Span and W. Wagner, "A new equation of state for carbon dioxide covering the fluid region from the triple-point temperature to 1100 K at pressures up to 800 MPa," *J. Phys. Chem. Ref. Data* **25**, 1509–1596 (1996).
- <sup>32</sup>M. Thol, I. Alexandrov, R. Span, and E. W. Lemmon, "Fundamental equation of state for chlorobenzene," *J. Chem. Eng. Data* (to be published).
- <sup>33</sup>Y. Zhou, J. Lin, S. G. Penoncello, and E. W. Lemmon, "An equation of state for the thermodynamic properties of cyclohexane," *J. Phys. Chem. Ref. Data* **43**, 043105 (2014).
- <sup>34</sup>J. Wu, Y. Zhou, and E. W. Lemmon, "An equation of state for the thermodynamic properties of dimethyl ether," *J. Phys. Chem. Ref. Data* **40**, 023104 (2011).
- <sup>35</sup>D. Bücker and W. Wagner, "A reference equation of state for the thermodynamic properties of ethane for temperatures from the melting line to 675 K and pressures up to 900 MPa," *J. Phys. Chem. Ref. Data* **35**, 205–266 (2006).
- <sup>36</sup>J. A. Schroeder, "A new fundamental equation for ethanol," Master's thesis, University of Idaho, 2011.
- <sup>37</sup>J. Smukala, R. Span, and W. Wagner, "A new equation of state for ethylene covering the fluid region for temperatures from the melting line to 450 K at pressures up to 300 MPa," *J. Phys. Chem. Ref. Data* **29**, 1053–1122 (2000).
- <sup>38</sup>M. Thol, G. Rutkai, A. Köster, M. Kortmann, R. Span, and J. Vrabec, "Fundamental equation of state for ethylene oxide based on a hybrid dataset," *Chem. Eng. Sci.* **121**, 87–99 (2015); Corrigendum, *Chem. Eng. Sci.* **134**, 887–890 (2015).
- <sup>39</sup>K. M. de Reuck, "International thermodynamic tables of the fluid state-11 fluorine," in *International Union of Pure and Applied Chemistry* (Pergamon Press, Oxford, 1990).
- <sup>40</sup>M. Thol, F. H. Dubberke, G. Rutkai, T. Windmann, A. Köster, R. Span, and J. Vrabec, "Fundamental equation of state correlation for hexamethylcyclotrisiloxane based on experimental and molecular simulation data," *Fluid Phase Equilib.* **418**, 133–151 (2016).
- <sup>41</sup>M. Thol, L. Piazza, and R. Span, "A new functional form for equations of state for some polar and weakly associating fluids," *Int. J. Thermophys.* **35**, 783–811 (2014).
- <sup>42</sup>K. M. de Reuck and R. J. B. Craven, *Methanol*, International Thermodynamic Tables of the Fluid State (IUPAC) Vol. 12 (Blackwell Scientific Publications, London, 1993).
- <sup>43</sup>R. Span, E. W. Lemmon, R. T. Jacobsen, W. Wagner, and A. Yokozeki, "A reference equation of state for the thermodynamic properties of nitrogen for temperatures from 63.151 to 1000 K and pressures to 2200 MPa," *J. Phys. Chem. Ref. Data* **29**, 1361–1433 (2000).
- <sup>44</sup>M. Thol, G. Rutkai, A. Köster, F. H. Dubberke, T. Windmann, R. Span, and J. Vrabec, "Thermodynamic properties of octamethylcyclotetrasiloxane," *J. Chem. Eng. Data* (published online).
- <sup>45</sup>R. Schmidt and W. Wagner, "A new form of the equation of state for pure substances and its application to oxygen," *Fluid Phase Equilib.* **19**, 175–200 (1985).
- <sup>46</sup>G. Rutkai and J. Vrabec, "Empirical fundamental equation of state for phosgene based on molecular simulation data," *J. Chem. Eng. Data* **60**, 2895–2905 (2015).
- <sup>47</sup>A. Polt, B. Platzter, and G. Maurer, "Parameter der thermischen Zustandsgleichung von Bender fuer 14 mehratomige reine Stoffe," *Chem. Tech.* **44**, 216–224 (1992).
- <sup>48</sup>W. Wagner and A. Pruss, "The IAPWS formulation 1995 for the thermodynamic properties of ordinary water substance for general and scientific use," *J. Phys. Chem. Ref. Data* **31**, 387–535 (2002).
- <sup>49</sup>E. W. Lemmon and R. Span, "Thermodynamic properties of R-227ea, R-365mfc, R-115, and R-13—1," *J. Chem. Eng. Data* **60**, 3745–3758 (2015).
- <sup>50</sup>T. Windmann, M. Linnemann, and J. Vrabec, "Fluid phase behavior of nitrogen + acetone and oxygen + acetone by molecular simulation, experiment and the Peng-Robinson equation of state," *J. Chem. Eng. Data* **59**, 28–38 (2013).
- <sup>51</sup>B. Eckl, J. Vrabec, and H. Hasse, "An optimised molecular model for ammonia," *Mol. Phys.* **106**, 1039–1046 (2008).
- <sup>52</sup>J. Vrabec, J. Stoll, and H. Hasse, "A set of molecular models for symmetric quadrupolar fluids," *J. Phys. Chem. B* **105**, 12126–12133 (2001).
- <sup>53</sup>Y.-L. Huang, M. Heilig, H. Hasse, and J. Vrabec, "Vapor-liquid equilibria of hydrogen chloride, phosgene, benzene, chlorobenzene, orthodichlorobenzene, and toluene by molecular simulation," *AIChE J.* **57**, 1043–1060 (2011).
- <sup>54</sup>T. Merker, C. Engin, J. Vrabec, and H. Hasse, "Molecular model for carbon dioxide optimized to vapor-liquid equilibria," *J. Chem. Phys.* **132**, 234512 (2010).
- <sup>55</sup>J. Stoll, J. Vrabec, and H. Hasse, "A set of molecular models for carbon monoxide and halogenated hydrocarbons," *J. Chem. Phys.* **119**, 11396–11407 (2003).
- <sup>56</sup>T. Merker, J. Vrabec, and H. Hasse, "Molecular simulation study on the solubility of carbon dioxide in mixtures of cyclohexane + cyclohexanone," *Fluid Phase Equilib.* **315**, 77–83 (2012).
- <sup>57</sup>B. Eckl, J. Vrabec, and H. Hasse, "Set of molecular models based on quantum mechanical *ab initio* calculations and thermodynamic data," *J. Phys. Chem. B* **112**, 12710–12721 (2008).
- <sup>58</sup>T. Schnabel, J. Vrabec, and H. Hasse, "Henry's law constants of methane, nitrogen, oxygen and carbon dioxide in ethanol from 273 to 498 K: Prediction from molecular simulation," *Fluid Phase Equilib.* **233**, 134–143 (2005).
- <sup>59</sup>B. Eckl, J. Vrabec, and H. Hasse, "On the application of force fields for predicting a wide variety of properties: Ethylene oxide as an example," *Fluid Phase Equilib.* **274**, 16–26 (2008).
- <sup>60</sup>T. Kristóf and J. Liszi, "Effective intermolecular potential for fluid hydrogen sulfide," *J. Phys. Chem. B* **101**, 5480–5483 (1997).
- <sup>61</sup>T. Schnabel, A. Srivastava, J. Vrabec, and H. Hasse, "Hydrogen bonding of methanol in supercritical CO<sub>2</sub>: Comparison between 1H NMR spectroscopic data and molecular simulation results," *J. Phys. Chem. B* **111**, 9871–9878 (2007).
- <sup>62</sup>J. L. Abascal and C. Vega, "A general purpose model for the condensed phases of water: TIP4P/2005," *J. Chem. Phys.* **123**, 234505 (2005).
- <sup>63</sup>B. Eckl, Y.-L. Huang, J. Vrabec, and H. Hasse, "Vapor pressure of R227ea+ethanol at 343.13 K by molecular simulation," *Fluid Phase Equilib.* **260**, 177–182 (2007).
- <sup>64</sup>G. Rutkai, M. Thol, R. Lustig, R. Span, and J. Vrabec, "Communication: Fundamental equation of state correlation with hybrid data sets," *J. Chem. Phys.* **139**, 041102 (2013).
- <sup>65</sup>R. T. Jacobsen and R. B. Stewart, "Thermodynamic properties of nitrogen including liquid and vapor phases from 63 K to 2000 K with pressures to 10 000 bar," *J. Phys. Chem. Ref. Data* **2**, 757–922 (1973).
- <sup>66</sup>H.-O. May and P. Mausbach, "Riemannian geometry study of vapor-liquid phase equilibria and supercritical behavior of the Lennard-Jones fluid," *Phys. Rev. E* **85**, 031201 (2012); *Phys. Rev. E* **86**, 059905(E) (2012).
- <sup>67</sup>V. Holten, M. A. Anisimov, and J. V. Sengers, Technical Report prepared for the International Association for the Properties of Water and Steam, 2012, <http://www.iapws.org/minutes/2012/Holten2012-report.pdf>.
- <sup>68</sup>F. Mallamace, C. Corsaro, and H. E. Stanley, "A singular thermodynamically consistent temperature at the origin of the anomalous behavior of liquid water," *Sci. Rep.* **2**, 993 (2012).
- <sup>69</sup>G. Ruppeiner, P. Mausbach, and H.-O. May, "Thermodynamic R-diagrams reveal solid-like fluid states," *Phys. Lett. A* **379**, 646–649 (2015).
- <sup>70</sup>H.-O. May, P. Mausbach, and G. Ruppeiner, "Thermodynamic geometry of supercooled water," *Phys. Rev. E* **91**, 032141 (2015).
- <sup>71</sup>P. Colonna, A. Guardone, and N. R. Nannan, "Siloxanes: A new class of candidate Bethe-Zel'dovich-Thompson fluids," *Phys. Fluids* **19**, 086102 (2007).
- <sup>72</sup>P. Colonna, N. R. Nannan, A. Guardone, and T. P. van der Stelt, "On the computation of the fundamental derivative of gas dynamics using equations of state," *Fluid Phase Equilib.* **286**, 43–54 (2009).
- <sup>73</sup>A. Köster, T. Spura, G. Rutkai, J. Kessler, H. Wiebeler, J. Vrabec, and T. D. Kühne, "Assessing the accuracy of improved force-matched water models derived from *ab initio* molecular dynamics simulations," *J. Comput. Chem.* **37**, 1828–1838 (2016).

### 3.7 Equation of State for the Lennard-Jones Fluid

M. Thol, G. Rutkai, **A. Köster**, R. Lustig, R. Span, J. Vrabec, *Journal of Physical and Chemical Reference Data* 45:023101, 2016.

Nachgedruckt mit Erlaubnis von AIP Publishing (Copyright 2016).

DOI: [doi.org/10.1063/1.4945000](https://doi.org/10.1063/1.4945000)

In dieser Arbeit wurde eine neue Zustandsgleichung für das Lennard-Jones Modellfluid erstellt. Die Besonderheit dieser neuen Zustandsgleichung ist, dass fast ausschließlich partielle Ableitungen der Helmholtzenergie aus dem Lustig-Formalismus [Lus11, Lus12] als Grundlage für die Korrelation genutzt wurden. Neben einem großen Gültigkeitsbereich ( $0.5 < T/T_c < 7$ ,  $p/p_c < 500$ ) hat diese neue Zustandsgleichung ein sehr gutes Extrapolationsverhalten und eine hohe Genauigkeit.

Die im Rahmen dieser Publikation verwendeten molekularen Simulationsdaten wurden vom Autor der vorliegenden Dissertation in Zusammenarbeit mit Dr. Gábor Rutkai berechnet. Die beiden Autoren haben die Beschreibung der zugrundeliegenden Simulationsmethoden durchgeführt. Dr. Monika Thol hat die Anpassung der Zustandsgleichung an die molekularen Simulationsdaten durchgeführt. Der Autor wurde während des gesamten Prozesses von Prof. Jadran Vrabec betreut.





## Equation of State for the Lennard-Jones Fluid

**Monika Thol<sup>a)</sup>**

*Lehrstuhl für Thermodynamik, Ruhr-Universität Bochum, Universitätsstraße 150, 44801 Bochum, Germany*

**Gabor Rutkai and Andreas Köster**

*Lehrstuhl für Thermodynamik und Energietechnik, Universität Paderborn, Warburger Straße 100, 33098 Paderborn, Germany*

**Rolf Lustig**

*Department of Chemical and Biomedical Engineering, Cleveland State University, Cleveland, Ohio 44115, USA*

**Roland Span**

*Lehrstuhl für Thermodynamik, Ruhr-Universität Bochum, Universitätsstraße 150, 44801 Bochum, Germany*

**Jadran Vrabec**

*Lehrstuhl für Thermodynamik und Energietechnik, Universität Paderborn, Warburger Straße 100, 33098 Paderborn, Germany*

(Received 25 January 2016; accepted 16 March 2016; published online 6 May 2016)

An empirical equation of state correlation is proposed for the Lennard-Jones model fluid. The equation in terms of the Helmholtz energy is based on a large molecular simulation data set and thermal virial coefficients. The underlying data set consists of directly simulated residual Helmholtz energy derivatives with respect to temperature and density in the canonical ensemble. Using these data introduces a new methodology for developing equations of state from molecular simulation. The correlation is valid for temperatures  $0.5 < T/T_c < 7$  and pressures up to  $p/p_c = 500$ . Extensive comparisons to simulation data from the literature are made. The accuracy and extrapolation behavior are better than for existing equations of state. © 2016 AIP Publishing LLC for the National Institute of Standards and Technology. [<http://dx.doi.org/10.1063/1.4945000>]

Key words: equation of state; Helmholtz energy; Lennard-Jones model fluid; molecular simulation; thermodynamic properties.

### CONTENTS

1. Introduction .....	2
2. Equation of State .....	3
3. Molecular Simulation .....	3
4. Equations of State from the Literature .....	5
5. New Equation of State .....	8
5.1. Helmholtz energy derivatives .....	8
5.2. Thermal virial coefficients .....	15
5.3. Vapor–liquid equilibrium .....	17
5.4. Density at homogeneous states .....	21
5.5. Critical point .....	26
5.6. Caloric properties .....	27
5.7. Physical behavior and extrapolation .....	31
6. Conclusion .....	34

Acknowledgments .....	35
7. References .....	35

### List of Tables

1. Definitions of common thermodynamic properties and their relation to the Helmholtz energy .....	3
2. Parameters of the residual part of the present equation of state .....	5
3. Equations of state for the Lennard-Jones fluid from the literature .....	5
4. Average absolute relative deviations (AAD) of the data bases of five selected equations of state from the literature .....	6
5. Average absolute relative deviations (AAD) of the present equation of state and the most prominent equations from the literature based on the simulation data of this work. ....	10

<sup>a)</sup>Electronic mail: M.Thol@thermo.ruhr-uni-bochum.de.  
© 2016 AIP Publishing LLC.

023101-2

THOL ET AL.

6.	Selected points on the characteristic ideal curves calculated with the present equation of state . . . . .	16	13.	First derivative of the second and third thermal virial coefficients with respect to temperature. . . . .	16
7.	Parameters of the ancillary equations for vapor pressure, saturated liquid density, and saturated vapor density . . . . .	18	14.	Relative deviation of literature data for vapor pressure, saturated liquid density, and saturated vapor density from the present equation of state. . . . .	17
8.	Average absolute relative deviations of vapor pressure, saturated liquid density, and saturated vapor density from literature data relative to the present equation of state . . . . .	18	15.	Representation of vapor-phase density data. . . . .	21
9.	Average absolute relative deviations of simulation data in homogeneous states from the literature relative to the present equation of state. . . . .	19	16.	Representation of liquid-phase density data. . . . .	22
10.	Critical parameters of the Lennard-Jones fluid from the literature . . . . .	25	17.	Representation of density in the supercritical region. . . . .	23
			18.	Representation of literature data for pressure in the critical region. . . . .	24
			19.	Comparison of metastable gaseous pressure data. . . . .	24
			20.	Selected critical parameters from the literature. . . . .	26
			21.	Relative deviation of literature data for residual internal energy from the present equation of state. . . . .	27
			22.	Relative deviation of literature data for isochoric heat capacity from the present equation of state. . . . .	28
			23.	Isochoric heat capacity versus temperature. . . . .	28
			24.	Relative deviation of literature data for isobaric heat capacity from the present equation of state. . . . .	29
			25.	Isobaric heat capacity versus temperature along isobars. . . . .	29
			26.	Comparison of literature data for the Grüneisen coefficient with the present equation of state. . . . .	30
			27.	Relative deviation of literature data for speed of sound from the present equation of state. . . . .	30
			28.	Comparison of literature data for the Joule–Thomson coefficient with the present equation of state. . . . .	31
			29.	Relative deviation of literature data for thermal expansion coefficient $\alpha$ , isothermal compressibility $\beta_T$ , and thermal pressure coefficient $\gamma$ from the present equation of state. . . . .	32
			30.	Residual isochoric heat capacity and speed of sound versus temperature along isobars. . . . .	33
			31.	Temperature versus density along isobars. . . . .	33
			32.	Characteristic ideal curves as defined by Span and Wagner. <sup>122</sup> . . . . .	33
			33.	Grüneisen coefficient versus density along isotherms (top) and Grüneisen coefficient versus temperature (bottom) along isobars. . . . .	34
			34.	Phase identification parameter versus density along isotherms (top) and versus temperature along isobars (bottom). . . . .	34

### List of Figures

1.	Third virial coefficient versus temperature from the literature. . . . .	5
2.	Extrapolation behavior of five equations of state from the literature along the isotherm $T = 10$ . . . . .	7
3.	Comparison of five equations of state from the literature with the corresponding data sets used for their development. . . . .	8
4.	Data set used to develop the present equation of state. . . . .	9
5.	Relative deviation of simulated residual Helmholtz energy $A_{00}^r$ data (circles) from the present equation of state. . . . .	11
6.	Relative deviation of simulated first derivative of the residual Helmholtz energy with respect to density $A_{01}^r$ data (circles) from the present equation of state. . . . .	12
7.	Relative deviation of simulated first derivative of the residual Helmholtz energy with respect to inverse temperature $A_{10}^r$ data (circles) from the present equation of state. . . . .	12
8.	Relative deviation of simulated second derivative of the residual Helmholtz energy with respect to density $A_{02}^r$ data (circles) from the present equation of state. . . . .	13
9.	Relative deviation of simulated second derivative of the residual Helmholtz energy with respect to inverse temperature $A_{20}^r$ data (circles) from the present equation of state. . . . .	13
10.	Relative deviation of simulated mixed derivative of the residual Helmholtz energy with respect to density and inverse temperature $A_{11}^r$ data (circles) from the present equation of state. . . . .	14
11.	Relative deviation of the simulated third derivatives of the residual Helmholtz energy with respect to density and inverse temperature data (circles) from the present equation of state. . . . .	14
12.	Second, third, and fourth thermal virial coefficients. . . . .	15

## 1. Introduction

The Lennard-Jones 12–6 (LJ) model is the most widely used intermolecular interaction potential in simulation history that is sufficiently realistic to represent small spherical and nonpolar molecules.<sup>1,2</sup> It was studied extensively in the last decades, concluding that it may serve as an important model for studying phase equilibria, phase change processes, clustering behavior, or transport and interface properties of simple fluids. It is commonly expressed as

## EQUATION OF STATE FOR THE LENNARD-JONES FLUID

023101-3

$$u_{\text{LJ}} = 4\varepsilon \left[ \left( \frac{\sigma}{r} \right)^{12} - \left( \frac{\sigma}{r} \right)^6 \right], \quad (1)$$

where  $\sigma$  and  $\varepsilon$  are size and energy parameters, and  $r$  is the distance between two particles.

Although molecular simulation has evolved to a significant contribution in science and engineering, the generation of fluid property data sets is still a challenge. For practical purposes, thermodynamic data must be rationalized in the form of robust correlations. In particular, fundamental equation of state (EOS) correlations allow for the computation of any thermodynamic property given as combinations of derivatives with respect to its natural variables. Here, we use the Massieu–Planck potential  $F(N, V, 1/T)/(k_B T)$  with Helmholtz energy  $F$ , temperature  $T$ , volume  $V$ , number of particles  $N$ , and Boltzmann constant  $k_B$ .

A number of EOS for the LJ fluid exist in the literature. The latest and most accurate ones are Johnson *et al.*,<sup>3</sup> Kolafa and Nezbeda,<sup>4</sup> and Mecke *et al.*,<sup>5</sup> which were set up on the basis of pressure and internal energy data from molecular simulation. As opposed to those previous attempts, the underlying data set for the present EOS consists only of direct derivatives of the residual Helmholtz energy. Preliminary results for such a new approach were presented by Rutkai *et al.*<sup>6</sup> Using residual Helmholtz energy derivatives instead of common thermodynamic properties in thermodynamic correlations was first introduced 20 years ago. Lustig presented a series of statistical thermodynamic developments,<sup>7–13</sup> which were successfully employed by other researchers.<sup>14–16</sup> Recently, the methodology was extended to the canonical ensemble.<sup>17,18</sup> The outline in Ref. 18 is the basis of this work.

## 2. Equation of State

In this section, a new equation of state for the Lennard-Jones model fluid in terms of the reduced Helmholtz energy is presented. All relevant variables together with the mathematical expressions of how to calculate thermodynamic properties are given.

The size and energy parameters  $\sigma$  and  $\varepsilon$  of the potential were used to reduce all properties to dimensionless numbers of order unity, e.g., temperature  $T^* = k_B T / \varepsilon$ , density  $\rho^* = \rho \sigma^3$  (with  $\rho = v^{-1} = N/V$ ), or pressure  $p^* = p \sigma^3 / \varepsilon$ . For brevity, asterisks are omitted in the following, although reduced quantities are used throughout.

The equation of state is written in terms of the reduced Helmholtz energy  $\alpha$  as a function of inverse temperature and density. Separate terms denote ideal-gas behavior (superscript o) and residual contribution (superscript r)

$$\alpha(\tau, \delta) = \frac{a^o(T, \rho) + a^r(T, \rho)}{k_B T} = \alpha^o(\tau, \delta) + \alpha^r(\tau, \delta), \quad (2)$$

with  $a = F/N$  the Helmholtz energy per particle,  $\tau = T_c/T$ , and  $\delta = \rho/\rho_c$ . For the critical properties,  $T_c = 1.32$  and  $\rho_c = 0.31$  are used. Detailed information on the determination of the critical parameters is given in Section 5.5.

$\alpha^o$  relates to a hypothetical ideal gas.  $\alpha^r$  represents the residual Helmholtz energy under full intermolecular interactions in the fluid. All thermodynamic properties can be calculated from

Eq. (2) and its derivatives with respect to  $\tau$  and  $\delta$ . For these derivatives, the following notation is used:

$$A_{mn} = A_{mn}^o + A_{mn}^r = \tau^m \delta^n \frac{\partial^{m+n} (\alpha^o + \alpha^r)}{\partial \tau^m \partial \delta^n}. \quad (3)$$

Thermodynamic properties used in this work are related in Table 1.

As a classical monatomic model, the isobaric heat capacity of the ideal gas is  $c_p^o/k_B = 2.5$ . Integration yields

$$\alpha^o = \ln \delta + 1.5 \ln \tau + c_1 \tau + c_2. \quad (40)$$

The values  $c_1 = -1.515\,151\,515$  and  $c_2 = 6.262\,265\,814$  yield  $h_0^o = 0$  and  $s_0^o = 0$  at  $T_0 = 0.8$ ,  $p_0 = 0.001$ , and the corresponding density of the ideal gas  $\rho_0 = p_0/T_0$ .

The correlation of this work consists of 6 polynomial, 6 exponential, and 11 Gaussian bell-shaped terms

$$\begin{aligned} \alpha^r(\tau, \delta) = & \sum_{i=1}^6 n_i \delta^{d_i} \tau^{t_i} + \sum_{i=7}^{12} n_i \delta^{d_i} \tau^{t_i} \exp(-\delta^{l_i}) \\ & + \sum_{i=13}^{23} n_i \delta^{d_i} \tau^{t_i} \exp(-\eta_i(\delta - \varepsilon_i)^2 - \beta_i(\tau - \gamma_i)^2). \end{aligned} \quad (41)$$

It is valid for temperatures  $0.661 < T < 9$  and for pressures up to  $p = 65$ , corresponding to  $0.5 < T/T_c < 7$  and  $p/p_c = 500$ . The adjustable parameters (coefficients  $n_i$ , temperature exponents  $t_i$ , and Gaussian bell-shaped parameters) as well as the density exponents  $d_i$ , are listed in Table 2.

## 3. Molecular Simulation

In this section, the main information for the molecular simulation of thermodynamic properties is provided. The new approach of direct simulations of reduced Helmholtz derivatives is discussed.

When setting up fundamental equations of state on the basis of experimental data, not every individual derivative with respect to its independent variables can be employed. The development of an EOS explicit in  $F/(k_B T)$  would ideally require the reduced Helmholtz energy itself and its derivatives with respect to the inverse temperature and the density. With experimentally accessible thermodynamic properties, only derivatives  $A_{01}^r$  and  $A_{20}^r$  can be computed individually.  $A_{11}^r$  and  $A_{02}^r$  are nonlinearly related to speed of sound and heat capacities.<sup>6</sup> Fitting Helmholtz energy derivatives directly does not require linearization of any thermodynamic property. Consequently, the fitting procedure allows for an explicit study of all derivatives of the fundamental equation of state.

As molecular simulation allows for the calculation of the residual Helmholtz energy itself, an EOS could be developed considering  $A_{00}^r$  simulation data only, at least in principle. However, an extremely dense and equally distributed grid of state points would have to be sampled across the entire fluid region to capture subtle features of the Helmholtz energy surface. Data sets for fitting EOS should thus contain as much independent thermodynamic information as possible. At present, efficient generation of extensive data sets is cumbersome because most molecular simulation software tools are restricted to

023101-4

THOL ET AL.

TABLE 1. Definitions of common thermodynamic properties and their relation to the Helmholtz energy

Property	Reduced quantity Relation to the reduced Helmholtz energy	
<i>Pressure</i>	$p = -(\partial a / \partial v)_T$ (4)	$p / (\rho RT) = (1 + A_{01}^r)$ (5)
<i>Derivatives of pressure with respect to</i>		
Density	$(\partial p / \partial \rho)_T$ (6)	$(\partial p / \partial \rho)_T = T (1 + 2A_{01}^r + A_{02}^r)$ (7)
Temperature	$(\partial p / \partial T)_\rho$ (8)	$(\partial p / \partial T)_\rho = \rho (1 + A_{01}^r - A_{11}^r)$ (9)
<i>Entropy</i>	$s = -(\partial a / \partial T)_v$ (10)	$s = A_{10}^o + A_{10}^r - A_{00}^o - A_{00}^r$ (11)
<i>Internal energy</i>	$u = a + T s$ (12)	$u / T = A_{10}^o + A_{10}^r$ (13)
<i>Enthalpy</i>	$h = u + p v$ (14)	$h / T = 1 + A_{10}^o + A_{10}^r + A_{01}^r$ (15)
<i>Isochoric heat capacity</i>	$c_v = (\partial u / \partial T)_v$ (16)	$c_v = - (A_{20}^o + A_{20}^r)$ (17)
<i>Isobaric heat capacity</i>	$c_p = (\partial h / \partial T)_p$ (18)	$c_p = - (A_{20}^o + A_{20}^r) + \frac{(1 + A_{01}^r - A_{11}^r)^2}{1 + 2A_{01}^r + A_{02}^r}$ (19)
<i>Gibbs energy</i>	$g = h - T s$ (20)	$g / T = 1 + A_{00}^o + A_{00}^r + A_{01}^r$ (21)
<i>Speed of sound</i>	$w = \sqrt{(\partial p / \partial \rho)_s}$ (22)	$w^2 / T = 1 + 2A_{01}^r + A_{02}^r - \frac{(1 + A_{01}^r - A_{11}^r)^2}{A_{20}^o + A_{20}^r}$ (23)
<i>Grüneisen coefficient</i>	$\Gamma = \frac{(\partial p / \partial T)_\rho}{\rho c_v}$ (24)	$\Gamma = \frac{1 + A_{01}^r - A_{11}^r}{-(A_{20}^o + A_{20}^r)}$ (25)
<i>Phase identification parameter</i>	$\Pi = 2 - \left( \frac{\partial^2 p / \partial \rho \partial T}{(\partial p / \partial T)_\rho} - \frac{(\partial^2 p / \partial \rho^2)_T}{(\partial p / \partial \rho)_T} \right) \rho$ (26)	$\Pi = 2 - \frac{1 + 2A_{01}^r + A_{02}^r - A_{11}^r - A_{12}^r}{1 + A_{01}^r - A_{11}^r} + \frac{2A_{01}^r + 4A_{02}^r + A_{03}^r}{1 + 2A_{01}^r + A_{02}^r}$ (27)
<i>2<sup>nd</sup> thermal virial coefficient</i>	$B = \lim_{\rho \rightarrow 0} (\partial (p / (\rho RT)) / \partial \rho)_T$ (28)	$B\rho = \lim_{\delta \rightarrow 0} (A_{01}^r / \delta)$ (29)
<i>3<sup>rd</sup> thermal virial coefficient</i>	$C = \frac{1}{2} \lim_{\rho \rightarrow 0} (\partial^2 (p / (\rho RT)) / \partial \rho^2)_T$ (30)	$C\rho^2 = \lim_{\delta \rightarrow 0} (A_{02}^r / \delta^2)$ (31)
<i>4<sup>th</sup> thermal virial coefficient</i>	$D = \frac{1}{6} \lim_{\rho \rightarrow 0} (\partial^3 (p / (\rho RT)) / \partial \rho^3)_T$ (32)	$D2\rho^3 = \lim_{\delta \rightarrow 0} (A_{03}^r / \delta^3)$ (33)
<i>Isothermal compressibility</i>	$\beta_T = 1 / (\rho (\partial p / \partial \rho)_T)$ (34)	$\beta_T = \rho^{-1} T (1 + 2A_{01}^r + A_{02}^r)$ (35)
<i>Thermal pressure coefficient</i>	$\gamma = (\partial p / \partial T)_\rho$ (36)	$\gamma = \rho (1 + A_{01}^r - A_{11}^r)$ (37)
<i>Thermal expansion coefficient</i>	$\alpha = \beta_T \gamma = \frac{(\partial p / \partial T)_\rho}{\rho (\partial p / \partial \rho)_T}$ (38)	$\alpha = (1 + A_{01}^r - A_{11}^r) / (T (1 + 2A_{01}^r + A_{02}^r))$ (39)

## EQUATION OF STATE FOR THE LENNARD-JONES FLUID

023101-5

TABLE 2. Parameters of the residual part of the present equation of state according to Eq. (41)

$i$	$n_i$	$t_i$	$d_i$	$l_i$	$\eta_i$	$\beta_i$	$\gamma_i$	$\varepsilon_i$
1	$0.520\,807\,30 \times 10^{-2}$	1.000	4	—				
2	$0.218\,625\,20 \times 10^{+1}$	0.320	1	—				
3	$-0.216\,101\,60 \times 10^{+1}$	0.505	1	—				
4	$0.145\,270\,00 \times 10^{+1}$	0.672	2	—				
5	$-0.204\,179\,20 \times 10^{+1}$	0.843	2	—				
6	$0.186\,952\,86 \times 10^0$	0.898	3	—				
7	$-0.909\,884\,45 \times 10^{-1}$	1.294	5	1				
8	$-0.497\,456\,10 \times 10^0$	2.590	2	2				
9	$0.109\,014\,31 \times 10^0$	1.786	2	1				
10	$-0.800\,559\,22 \times 10^0$	2.770	3	2				
11	$-0.568\,839\,00 \times 10^0$	1.786	1	2				
12	$-0.620\,862\,50 \times 10^0$	1.205	1	1				
13	$-0.146\,671\,77 \times 10^{+1}$	2.830	1	—	2.067	0.625	0.710	0.2053
14	$0.189\,146\,90 \times 10^{+1}$	2.548	1	—	1.522	0.638	0.860	0.4090
15	$-0.138\,370\,10 \times 10^0$	4.650	2	—	8.820	3.910	1.940	0.6000
16	$-0.386\,964\,50 \times 10^0$	1.385	3	—	1.722	0.156	1.480	1.2030
17	$0.126\,570\,20 \times 10^0$	1.460	3	—	0.679	0.157	1.490	1.8290
18	$0.605\,781\,00 \times 10^0$	1.351	2	—	1.883	0.153	1.945	1.3970
19	$0.117\,918\,90 \times 10^{+1}$	0.660	1	—	3.925	1.160	3.020	1.3900
20	$-0.477\,326\,79 \times 10^0$	1.496	2	—	2.461	1.730	1.110	0.5390
21	$-0.992\,185\,75 \times 10^{+1}$	1.830	3	—	28.20	383.0	1.170	0.9340
22	$-0.574\,793\,20 \times 10^0$	1.616	1	—	0.753	0.112	1.330	2.3690
23	$0.377\,292\,30 \times 10^{-2}$	4.970	1	—	0.820	0.119	0.240	2.4300

very few thermodynamic properties, such as internal energy, pressure, isochoric, or isobaric heat capacities. Here, we apply the methodology of Lustig.<sup>17,18</sup> Any  $A_{mn}^r$  is simultaneously available from one single  $NVT$  ensemble simulation for a given state point. The approach was implemented in the molecular simulation tool *ms2* (Ref. 19) up to order  $m = 3$  and  $n = 2$ :  $A_{01}^r$ ,  $A_{10}^r$ ,  $A_{02}^r$ ,  $A_{20}^r$ ,  $A_{11}^r$ ,  $A_{12}^r$ ,  $A_{21}^r$ , and  $A_{30}^r$ . Additionally,  $A_{00}^r$  can be determined using a rigorous test-particle insertion method.<sup>20</sup>

The underlying simulation data set was generated by sampling about 200 state points with the simulation tool *ms2*,<sup>19</sup> covering the homogenous fluid region  $0.7 < T < 9$ ,  $\rho < 1.08$  and pressures up to  $p = 65$ . At each state point, 1372 LJ particles were equilibrated and then sampled for  $10^6$  cycles with Monte Carlo  $NVT$  ensemble simulations,<sup>21</sup> measuring the derivatives mentioned above.

#### 4. Equations of State from the Literature

In this section, the prominent and recent equations for the Lennard-Jones fluid are discussed. The quality of those equations is analyzed by comparing to the underlying simulation data sets and the extrapolation behavior.

TABLE 3. Equations of state for the Lennard-Jones fluid from the literature

Authors	Year	EOS type	Critical parameters		Range of validity	
			$T_c$	$\rho_c$	$T$	$\rho$
Nicolas <i>et al.</i> <sup>25</sup>	1979	MBWR	1.35	0.35	0.55–6	$\leq 1.2$
Johnson <i>et al.</i> <sup>3</sup>	1993	MBWR	1.313	0.31	0.7–6	$\leq 1.25$
Kolafa and Nezbeda <sup>4</sup>	1994	MBWR	1.3396	0.3108	0.7–20	$\leq 1.2$
Mecke <i>et al.</i> <sup>5</sup>	1996	$a$ + HS term	1.328	0.3107	0.7–10 <sup>a</sup>	$\leq 1.2$
May and Mausbach <sup>30</sup>	2012	MBWR	1.3145	0.316	0.5–6	$\leq 1.2$

<sup>a</sup>Reasonable extrapolation behavior up to  $T = 100$  for  $\rho \leq 1$ .

For the Lennard-Jones fluid, many equations of state are available in the literature. Until the early 1990s, there were only semitheoretical, e.g., of Levesque and Verlet,<sup>22</sup> McDonald and Singer,<sup>23</sup> or Song and Mason,<sup>24</sup> and empirical equations using the modified Benedict–Webb–Rubin (MBWR) form, e.g., Nicolas *et al.*,<sup>25</sup> Adachi *et al.*,<sup>26</sup> or Miyano.<sup>27</sup> The semitheoretical equations are mostly restricted to a small range of validity. They have few adjustable parameters so that they are not flexible enough to represent all thermodynamic data within their estimated statistical uncertainty over the entire fluid range. The equations expressed in the MBWR form are more flexible due to the large number of adjustable parameters. Thus, the entire fluid range can be modeled more accurately than with

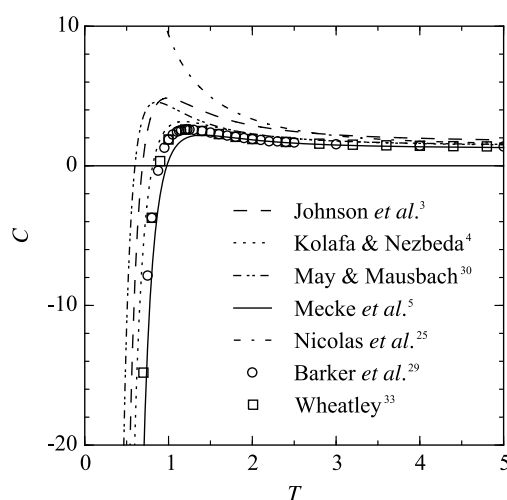


FIG. 1. Third virial coefficient versus temperature from the literature.

023101-6

THOL ET AL.

semithoretical equations. However, lacking physical background, their extrapolation behavior has to be investigated carefully. For the calculation of any thermodynamic property, the pressure-explicit MBWR form must be integrated to yield the Helmholtz energy.<sup>28</sup> The first fundamental equations of state for the Lennard-Jones fluid in terms of the Helmholtz energy were published by Kolafa and Nezbeda<sup>4</sup> and Mecke *et al.*<sup>5</sup>

Table 3 lists prominent and recent equations for the Lennard-Jones fluid. The most cited equation is Johnson *et al.*,<sup>3</sup> so it will be discussed in more detail here. Based on the MBWR equation of Nicolas *et al.*,<sup>25</sup> it consists of 32 linear parameters and one nonlinear parameter. The first five parameters were fitted to

second virial coefficient data of Barker *et al.*,<sup>29</sup> which are exact. All other parameters were established by fitting to pressure and internal energy data sampled with molecular dynamics simulation. No VLE data were used, but a critical point at  $T_c = 1.313$  and  $\rho_c = 0.31$  was applied. Unlike Nicolas *et al.*,<sup>25</sup> the equation of Johnson *et al.*<sup>3</sup> also follows the trend of the third virial coefficient of Barker *et al.*<sup>29</sup> (see Fig. 1). Although they assumed a better representation of the vapor–liquid equilibrium as a consequence, the third virial coefficient was overestimated systematically.

To date, the most accurate equation of state for the Lennard-Jones fluid is the one published by Mecke *et al.*<sup>5</sup> The correla-

TABLE 4. Average absolute relative deviations (AAD) of the data bases of five selected equations of state from the literature. Here, only the data points that are located in the homogenous fluid region are considered. For the determination of the vapor–liquid equilibrium, all equations were applied. Data located in the solid–liquid two-phase region according to Ahmed and Sadus<sup>34</sup> were not considered. The best AAD for each data set among the previous EOS is written in bold face

	No. of pts.	Nicolas <i>et al.</i> <sup>25</sup>	Johnson <i>et al.</i> <sup>3</sup>	Kolafa and Nezbeda <sup>4</sup>	Mecke <i>et al.</i> <sup>5</sup>	May and Mausbach <sup>30</sup>	This work
<b><i>ppT</i> data</b>							
Adams <sup>35 a</sup>	12	2.360	<b>1.970</b>	2.076	2.004	2.024	1.990
Adams <sup>36 a</sup>	15	<b>0.423</b>	0.721	0.731	0.760	0.538	0.740
Hansen <sup>37 a</sup>	6	0.320	0.232	0.208	<b>0.164</b>	0.205	0.167
Hansen and Verlet <sup>38 a</sup>	7	1.252	0.862	0.783	<b>0.766</b>	0.872	0.798
Johnson <i>et al.</i> <sup>3 b,c,d</sup>	149	0.690	0.247	0.151	<b>0.109</b>	0.196	0.129
Kolafa <i>et al.</i> <sup>39 d</sup>	37	0.760	0.458	0.222	<b>0.187</b>	0.375	0.244
Kolafa and Nezbeda <sup>4 b,d</sup>	9	1.560	1.162	0.374	<b>0.236</b>	0.906	0.317
Levesque and Verlet <sup>22 a</sup>	17	52.55	<b>48.20</b>	49.14	49.40	48.41	48.88
McDonald and Singer <sup>23 a</sup>	43	<b>0.362</b>	0.433	0.376	0.406	0.377	0.401
Mecke <i>et al.</i> <sup>5 b</sup>	5	8.205	2.374	<b>0.352</b>	0.522	2.274	1.435
Meier <sup>14 e</sup>	287	0.952	0.353	0.128	<b>0.087</b>	0.206	0.120
Miyano <sup>27 b</sup>	63	1.722	4.236	3.104	<b>1.660</b>	3.687	1.532
Nicolas <i>et al.</i> <sup>25 a,b</sup>	55	0.551	0.709	0.533	<b>0.518</b>	0.661	0.542
Saager and Fischer <sup>40 b</sup>	25	0.568	0.143	0.131	<b>0.120</b>	0.231	0.122
Verlet <sup>41 a</sup>	32	3.896	3.158	2.926	<b>2.908</b>	3.096	2.981
<b><i>u<sup>r</sup></i> data</b>							
Adams <sup>35 a</sup>	12	1.965	2.026	1.932	<b>1.731</b>	1.880	1.710
Adams <sup>36 a</sup>	15	<b>0.398</b>	0.733	0.670	0.648	1.118	0.652
Hansen <sup>37 a</sup>	6	0.637	0.801	0.857	0.620	<b>0.589</b>	0.567
Johnson <i>et al.</i> <sup>3 b,c,d</sup>	149	1.497	1.129	1.333	<b>0.305</b>	0.933	0.392
Kolafa <i>et al.</i> <sup>39 d</sup>	37	1.082	0.459	0.360	<b>0.203</b>	0.696	0.166
Kolafa and Nezbeda <sup>4 d</sup>	9	4.416	10.15	11.05	<b>0.325</b>	8.617	0.549
Levesque and Verlet <sup>22 a</sup>	32	<b>0.862</b>	1.113	1.105	1.031	1.110	0.785
McDonald and Singer <sup>23 a</sup>	43	<b>0.302</b>	0.426	0.417	0.380	0.592	0.377
Mecke <i>et al.</i> <sup>5 b</sup>	5	3.346	<b>0.478</b>	0.521	0.856	1.458	0.752
Meier <sup>14 e</sup>	287	1.860	0.864	0.988	<b>0.198</b>	0.646	0.205
Miyano <sup>27 b</sup>	63	27.07	42.76	43.09	<b>4.469</b>	39.84	3.811
Nicolas <i>et al.</i> <sup>25 a,b</sup>	55	0.857	1.569	1.700	<b>0.684</b>	1.783	0.826
Saager and Fischer <sup>40 b</sup>	25	0.278	0.581	0.619	<b>0.160</b>	0.710	0.221
Verlet <sup>41 a</sup>	32	<b>0.772</b>	0.980	0.933	0.799	1.051	0.730

<sup>a</sup>Used by Nicolas *et al.*,<sup>25</sup> additionally, data of Barker *et al.*<sup>29</sup> (B) were applied to the fit.

<sup>b</sup>Used by Mecke *et al.*,<sup>5</sup> additionally, data of Barker *et al.*<sup>29</sup> (B, C), Kriebel (numerical values not available in the literature), and Lotfi *et al.*<sup>42</sup> (*ppT*) were applied to the fit.

<sup>c</sup>Used by Johnson *et al.*,<sup>3</sup> additionally, data of Barker *et al.*<sup>29</sup> (B, C) were used for comparison.

<sup>d</sup>Used by Kolafa and Nezbeda,<sup>4</sup> additionally, data of Barker *et al.*<sup>29</sup> (B) and Lotfi *et al.*<sup>42</sup> (*ppT*) were applied to the fit.

<sup>e</sup>Used by May and Mausbach.<sup>30</sup>



## EQUATION OF STATE FOR THE LENNARD-JONES FLUID

023101-7

tion is given in the reduced Helmholtz energy  $\alpha$  augmented by a hard-body term. A linear structural optimization algorithm introduced by Setzmann and Wagner<sup>31</sup> was used. The data set consisted of pressure, residual internal energy, virial coefficients, and VLE data, and the equation is valid for  $0.7 \leq T \leq 10$  and  $\rho \leq 1.2$ . The critical temperature  $T_c = 1.328$  was taken from Valleeu<sup>32</sup> as a constraint, and the critical density  $\rho_c = 0.3107$  was obtained from a linear extrapolation of the rectilinear diameter. The authors stated that the extrapolation behavior was correct up to  $T = 100$ . Third virial coefficient data at low temperatures are also best reproduced as illustrated in Fig. 1. The equations of Kolafa and Nezbeda,<sup>4</sup> Johnson *et al.*,<sup>3</sup> and May and Mausbach<sup>30</sup> follow the course of the third virial coefficient, but deviate systematically.

For an assessment of the equation of state correlations listed in Table 3, the data sets that were the basis for the development of these equations are compared to each of them. Based on those results, only the most reliable EOS will be considered for comparison in the following.

Some statistical definitions are used for the evaluation of the equations. The relative deviation of a given property  $X$  is defined as

$$\Delta X = 100 \frac{X_{\text{DATA}} - X_{\text{EOS}}}{X_{\text{DATA}}}, \quad (42)$$

and the average absolute relative deviation AAD is

$$\text{AAD} = \frac{1}{N} \sum_{i=1}^N |\Delta X_i|. \quad (43)$$

In this work, the average absolute relative deviation is separated into different temperature and pressure ranges to avoid misleading results caused by certain regions, e.g., the critical region. The homogeneous fluid range is separated into the gas and liquid phases, and into the critical and supercritical regions. The critical region is defined by  $0.98 \leq T/T_c \leq 1.1$  and  $0.7 \leq \rho/\rho_c \leq 1.4$ . The supercritical region is furthermore divided into three areas: the region of low densities (LD:  $\rho/\rho_c < 0.6$ ), of medium densities (MD:  $0.6 \leq \rho/\rho_c \leq 1.5$ ), and of high densities (HD:  $\rho/\rho_c > 1.5$ ). The vapor-liquid equilibrium data are split into three different temperature ranges: the region of low temperatures (LT:  $T/T_c < 0.6$ ), of medium temperatures (MT:  $0.6 \leq T/T_c \leq 0.98$ ), and of high temperatures (HT:  $T/T_c > 0.98$ ).

In Table 4, the average absolute relative deviation of each publication calculated with the five selected equations of state is listed. In this table, only homogeneous fluid states are considered. It is obvious that the EOS of Mecke *et al.*<sup>5</sup> is the most accurate with respect to the  $p\rho T$  data as well as the residual internal energy. Especially for the most comprehensive data sets, e.g., Meier,<sup>14</sup> Johnson *et al.*,<sup>3</sup> Miyano,<sup>27</sup> Nicolas *et al.*,<sup>25</sup> and Saager and Fischer,<sup>40</sup> the best representation is given by Mecke *et al.*<sup>5</sup> The reason for the large difference between the AAD of the internal energy data of Miyano<sup>27</sup> calculated from the equation of Mecke *et al.*<sup>5</sup> and all other equations is a different extrapolation behavior, which is illustrated in Fig. 2. There, the course of the isotherm  $T = 10$  is presented for very high densities. Although the investigated region is located deeply in the solid phase, a wrong extrapolation behavior also

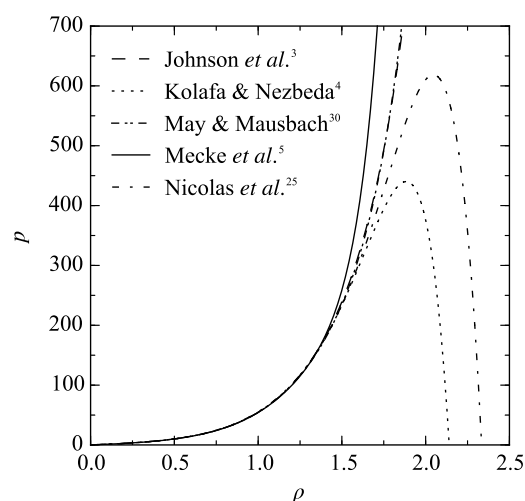


Fig. 2. Extrapolation behavior of five equations of state from the literature along the isotherm  $T = 10$ .

causes a wrong shape of the isotherm in the fluid region.<sup>43</sup> The EOS of Mecke *et al.*<sup>5</sup> is suitable under extreme conditions of temperature, pressure, and density, whereas the other equations exhibit deficiencies. The qualitative behavior of the equations of Johnson *et al.*<sup>3</sup> and May and Mausbach<sup>30</sup> is reasonable because no negative pressures occur. The negative pressures calculated by Nicolas *et al.*<sup>25</sup> and Kolafa and Nezbeda<sup>4</sup> are probably caused by a negative coefficient of a polynomial term or a low-order exponential term that is of leading importance in this region.

In Fig. 3, an overview of the deviations of the data sets investigated in Table 4 is given. Deviations in density are shown on the left side, and deviations in internal energy on the right side. Density deviations in the range of  $0.2 < \rho < 0.7$  exemplify problems for all but the equation of Mecke *et al.*<sup>5</sup> The low-density region is described well by Mecke *et al.*<sup>5</sup> and Kolafa and Nezbeda.<sup>4</sup> The simulation data of Miyano<sup>27</sup> at  $\rho = 1$  detect deficiencies of all equations ( $\text{AAD} = 1.72\% - 4.24\%$ ) whereas Mecke *et al.*<sup>5</sup> yield  $\text{AAD} = 1.66\%$ . For the residual internal energy, it is striking that the data set of Meier<sup>14</sup> is by far better reproduced by Mecke *et al.*<sup>5</sup> ( $\text{AAD} = 0.20\%$ ) than all other correlations ( $\text{AAD} = 0.6\% - 1.8\%$ ). The same follows from the simulation data set of Johnson *et al.*,<sup>3</sup> although their EOS was exclusively fitted to those data. The data set of Nicolas *et al.*<sup>25</sup> is reproduced best with the equation of Mecke *et al.*<sup>5</sup> ( $\text{AAD} = 0.64\%$ ). The corresponding EOS<sup>25</sup> is accurate in this case ( $\text{AAD} = 0.86\%$ ), but reveals significant problems in the low-density region. The equation of May and Mausbach<sup>30</sup> is the most consistent for residual internal energy. Most of the data scatter within  $2\% - 3\%$ , which is still less accurate than the equation of Mecke *et al.*<sup>5</sup> We showed that in the fluid region the equation of state of Mecke *et al.*<sup>5</sup> is significantly superior to any other equation of state in the literature. In the following, we compare our results to that EOS.

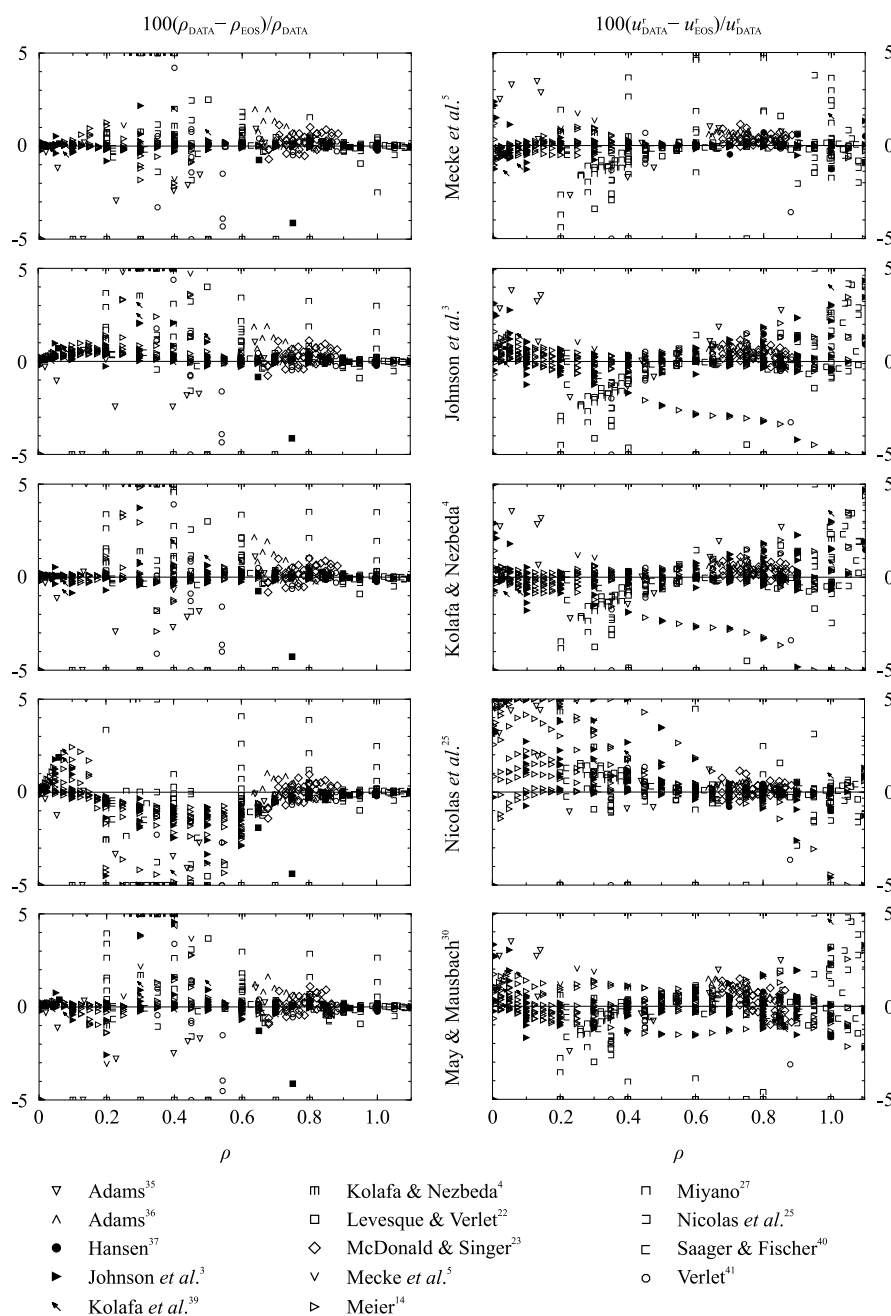


FIG. 3. Comparison of five equations of state from the literature with the corresponding data sets used for their development.

## 5. New Equation of State

In contrast to the equations examined in Section 4, the new equation is based on derivatives of the residual Helmholtz energy with respect to inverse temperature and density. In the following, the new correlation is compared to previous correlations and previous data sets.

### 5.1. Helmholtz energy derivatives

The development of the present equation of state for the Lennard-Jones fluid is exclusively based on the simulated reduced residual Helmholtz energy and its derivatives  $A_{mn}^r$  up to third order, and virial coefficients up to the fourth. No vapor-liquid equilibrium data were considered. The



## EQUATION OF STATE FOR THE LENNARD-JONES FLUID

023101-9

application of this new data type to a fitting procedure is investigated carefully below. Simulation data exhibit statistical uncertainties, different from experimental uncertainties in the case of real fluids. The use of Helmholtz energy derivatives is the first attempt to apply this strategy in developing an EOS. Among many equations of state for this model available in the literature, the EOS of Mecke *et al.*<sup>5</sup> was developed by modern fitting techniques and very accurately represents thermal properties as well as the residual internal energy. The goal of the present fundamental EOS is to represent thermal properties with at least such accuracy while improving the representation of caloric properties, other selected thermody-

namic properties, and extrapolation behavior. The new EOS is analyzed in analogy to modern fundamental equations of state for real fluids and is provided in a form that allows for straightforward implementation in common software tools like TREND,<sup>44</sup> REFPROP,<sup>45</sup> or CoolProp.<sup>46</sup>

Figure 4 shows simulated state points in the  $T - \rho$  plane. The vapor–liquid equilibrium according to the present equation of state and the solid–liquid equilibrium based on the correlations of Ahmed and Sadus<sup>34</sup> and van der Hoef<sup>47</sup> are indicated. At each state point, the residual Helmholtz energy as well as its derivatives with respect to  $1/T$  and  $\rho$  up to third order (without the third density derivative) were sampled. During the fit,

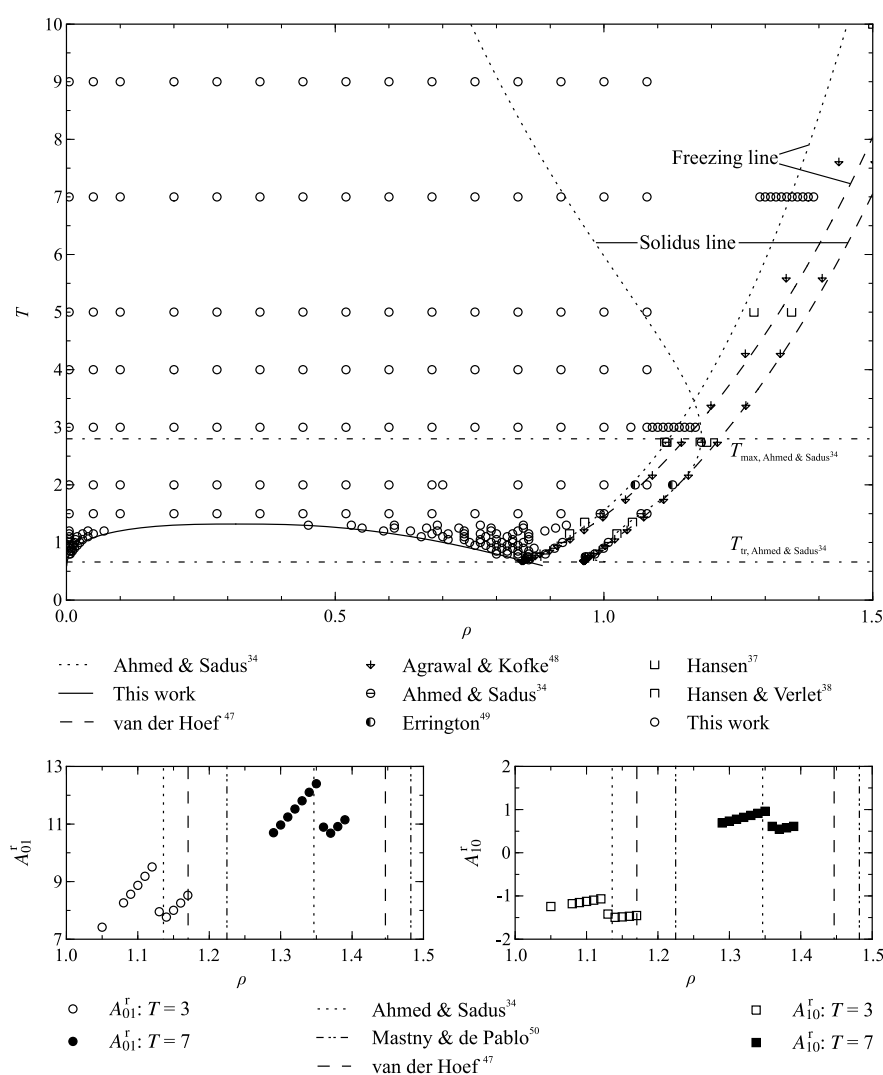


Fig. 4. Top: Data set used to develop the present equation of state. The residual Helmholtz energy and its derivatives up to third order were sampled at each state point. The saturated liquid and vapor lines were calculated with the present equation of state. The solid–liquid equilibrium curves were calculated with the correlations of Ahmed and Sadus<sup>34</sup> and van der Hoef.<sup>47</sup> Selected literature data<sup>34,37,38,48,49</sup> are included for comparison. Bottom: Test simulations of  $A_{01}^r$  and  $A_{10}^r$  along the isotherms  $T=3$  and  $T=7$  are shown to verify the correlation of Ahmed and Sadus.<sup>34</sup> The liquid densities of the solid–liquid equilibrium of Ahmed and Sadus,<sup>34</sup> van der Hoef,<sup>47</sup> and Mastny and de Pablo<sup>50</sup> are plotted for comparison.

statistical uncertainties served as measures for the reliability of the data. Possible unknown systematic errors were ignored. For temperatures  $T > 2.8$ , the freezing line of Ahmed and Sadus<sup>34</sup> is steeper than that of van der Hoef.<sup>47</sup> The data of Agrawal and Kofke<sup>48</sup> and Hansen<sup>37</sup> fall in between both correlations. Therefore, test simulations at  $T = 3$  and 7 were carried out here for assessment (cf. Fig. 4, bottom). Isothermal jumps in  $A_{01}^r$  and  $A_{10}^r$  indicate the onset of freezing. The estimated freezing density of Ahmed and Sadus<sup>34</sup> is closer to the jump than that of van der Hoef.<sup>47</sup> Therefore, the correlation of Ahmed and Sadus<sup>34</sup> is considered here as a boundary of the liquid phase. The solidus line of Ahmed and Sadus<sup>34</sup> is obviously wrong for approximately  $T > 2.5$ . However, in their publication they

state  $T = 2.8$  to be the upper boundary of the range of validity, which is indicated by dashed-dotted lines in Fig. 4, and the unreasonable trend at higher temperatures is an extrapolation effect. Since the present equation of state is explicitly valid in the fluid region only, all available data from the literature beyond that boundary are excluded from the discussion below.

The triple-point temperature  $T_{tr} = 0.661$  published by Ahmed and Sadus<sup>34</sup> is used as the lower temperature limit of the present equation of state. Other reported triple-point temperatures include Agrawal and Kofke<sup>48</sup> ( $T_{tr} = 0.687 \pm 0.004$ ), Hansen and Verlet<sup>38</sup> ( $T_{tr} = 0.68 \pm 0.02$ ), Johnson *et al.*<sup>3</sup> ( $T_{tr} = 0.69$ ), and Ladd and Woodcock<sup>51</sup> ( $T_{tr} = 0.67 \pm 0.01$ ).

TABLE 5. Average absolute relative deviations (AAD) of the present equation of state and the most prominent equations from the literature based on the simulation data of this work (temperature range  $T = 0.7$ –9, pressure range  $p < 65$ ). No simulation data were generated in the critical region ( $0.98 \leq T/T_c \leq 1.1$  and  $0.7 \leq \rho/\rho_c \leq 1.4$ ). Data that are clear outliers for all equations were rejected. The best AAD for each phase and data set is written in bold face

No. of data		Average absolute relative deviations (AAD)/%					
Property		Gas	Liquid	LD <sup>a</sup>	MD <sup>a</sup>	HD <sup>a</sup>	Overall
This work							
A <sub>00</sub> <sup>r</sup>	190	0.10	<b>0.37</b>	<b>0.35</b>	1.40	<b>0.48</b>	<b>0.52</b>
A <sub>01</sub> <sup>r</sup>	190	0.28	<b>0.93</b>	<b>0.52</b>	<b>0.52</b>	<b>0.13</b>	<b>0.53</b>
A <sub>10</sub> <sup>r</sup>	190	<b>0.31</b>	0.02	<b>0.19</b>	<b>0.15</b>	<b>0.12</b>	<b>0.12</b>
A <sub>02</sub> <sup>r</sup>	189	101	<b>5.47</b>	118	3.60	0.70	<b>27.9</b>
A <sub>20</sub> <sup>r</sup>	188	<b>0.43</b>	<b>0.59</b>	<b>0.69</b>	<b>0.84</b>	<b>0.37</b>	<b>0.56</b>
A <sub>11</sub> <sup>r</sup>	187	<b>0.30</b>	<b>0.48</b>	0.29	<b>0.48</b>	<b>1.21</b>	<b>0.63</b>
A <sub>12</sub> <sup>r</sup>	189	<b>105</b>	<b>77.5</b>	<b>126</b>	<b>145</b>	<b>20.4</b>	<b>80.6</b>
A <sub>21</sub> <sup>r</sup>	189	<b>1.78</b>	<b>19.3</b>	<b>3.70</b>	<b>13.9</b>	<b>9.72</b>	<b>12.0</b>
A <sub>30</sub> <sup>r</sup>	183	<b>6.03</b>	<b>3.89</b>	<b>3.63</b>	<b>4.40</b>	<b>2.10</b>	<b>3.70</b>
Mecke <i>et al.</i> <sup>5</sup>							
A <sub>00</sub> <sup>r</sup>	190	<b>0.07</b>	0.37	0.44	2.85	0.56	0.76
A <sub>01</sub> <sup>r</sup>	190	0.41	1.94	0.73	1.00	0.20	1.01
A <sub>10</sub> <sup>r</sup>	190	0.47	<b>0.01</b>	0.25	0.26	0.13	0.16
A <sub>02</sub> <sup>r</sup>	189	101	5.55	118	3.18	<b>0.69</b>	28.0
A <sub>20</sub> <sup>r</sup>	188	1.07	0.88	1.19	1.63	0.44	0.93
A <sub>11</sub> <sup>r</sup>	187	0.53	0.49	<b>0.25</b>	0.73	1.48	0.77
A <sub>12</sub> <sup>r</sup>	189	115	396	>500	>500	467	>500
A <sub>21</sub> <sup>r</sup>	189	4.00	21.3	3.72	37.3	15.4	18.0
A <sub>30</sub> <sup>r</sup>	183	14.6	6.07	3.87	7.17	2.17	5.97
Kolafa and Nezbeda <sup>4</sup>							
A <sub>00</sub> <sup>r</sup>	191	0.36	0.39	1.07	<b>0.81</b>	0.77	0.57
A <sub>01</sub> <sup>r</sup>	191	<b>0.22</b>	3.90	0.87	1.23	1.13	1.82
A <sub>10</sub> <sup>r</sup>	191	19.4	0.09	0.52	1.39	0.36	5.81
A <sub>02</sub> <sup>r</sup>	190	<b>61.4</b>	5.82	<b>113</b>	<b>1.97</b>	1.53	28.0
A <sub>20</sub> <sup>r</sup>	189	11.3	6.73	4.07	13.2	5.79	8.58
A <sub>11</sub> <sup>r</sup>	188	6.55	0.97	0.66	13.7	4.94	5.32
A <sub>12</sub> <sup>r</sup>	189	>500	>500	>500	>500	>500	>500
A <sub>21</sub> <sup>r</sup>	183	14.6	26.4	5.87	29.2	12.5	20.6
A <sub>30</sub> <sup>r</sup>	191	32.6	45.4	14.4	34.0	19.9	33.6
Johnson <i>et al.</i> <sup>3</sup>							
A <sub>00</sub> <sup>r</sup>	191	0.69	0.68	2.26	11.9	2.73	2.66
A <sub>01</sub> <sup>r</sup>	191	0.38	3.85	3.83	2.58	0.83	2.43
A <sub>10</sub> <sup>r</sup>	191	18.4	0.13	0.45	1.32	0.32	5.54
A <sub>02</sub> <sup>r</sup>	190	61.7	5.83	115	2.94	1.22	28.5
A <sub>20</sub> <sup>r</sup>	189	12.4	7.90	4.12	13.2	5.68	9.16
A <sub>11</sub> <sup>r</sup>	188	7.50	1.32	0.62	14.2	5.02	5.73
A <sub>12</sub> <sup>r</sup>	189	>500	>500	>500	>500	>500	>500
A <sub>21</sub> <sup>r</sup>	189	15.6	33.6	6.15	38.5	13.7	25.5
A <sub>30</sub> <sup>r</sup>	183	34.4	53.1	15.7	34.1	18.8	36.5

<sup>a</sup>Supercritical fluid: LD:  $\rho/\rho_c < 0.6$ ; MD:  $0.6 \leq \rho/\rho_c \leq 1.5$ ; HD:  $\rho/\rho_c > 1.5$ .

## EQUATION OF STATE FOR THE LENNARD-JONES FLUID

023101-11

During the fitting procedure, some general aspects of the simulation data must be considered. Temperature derivatives of the Helmholtz energy are usually less uncertain than density derivatives. The equation of state then represents temperature derivatives such as heat capacities better than density derivatives such as compressibilities. The accuracy of all derivatives decreases with increasing order of the derivative. The residual Helmholtz energy itself has to be treated differently because of a possible breakdown of the test-particle method at high density. Furthermore, molecular simulation yields higher relative uncertainties in the gaseous phase than in the liquid phase. Finally, zero crossings occur for some derivatives (e.g.,  $A_{01}^r$ ), which may obscure deviation plots. Here, only selected isotherms are presented for each derivative. A comprehensive overview is given in the supplementary material.<sup>52</sup> For each isotherm, the EOS of Mecke *et al.*<sup>5</sup> is used for comparison. Additionally, average absolute relative deviations (AAD) are presented in Table 5.

Deviations of residual Helmholtz energy  $A_{00}^r$  data are illustrated in Fig. 5.  $A_{00}^r$  is generally reproduced within 0.5% (AAD = 0.46%). However, there are differences depending on temperature and density range. For example,  $A_{00}^r$  in the gaseous phase ( $T = 0.8$ – $1.2$ ) is reproduced within less than 0.2%, whereas the deviations of the low-density data

in the supercritical state increase up to 0.5% (e.g.,  $T = 7$ ). Some isotherms show scatter of the data (e.g.,  $T = 1.5$ – $3$ ), whereas higher temperatures are entirely consistent ( $T = 7$ – $9$ ).

In comparison, modeling the first density derivative  $A_{01}^r$  is more challenging than  $A_{00}^r$ , as shown in Fig. 6. Although the deviation plots show oscillations (e.g.,  $T = 4$ – $9$ ), the accuracy of the equation of state is still within 0.5%. Both the equations of Mecke *et al.*<sup>5</sup> and of this work show similar behavior. The AAD of the present EOS improves over the entire surface: 0.49% vs. 1.01% for Mecke *et al.*<sup>5</sup> The isotherm  $T = 4$  illustrates the difference between low- and high-density simulations. The uncertainty of the data decreases with increasing density. The isotherm  $T = 3$  shows scatter in the data for  $\rho < 0.45$ . Such regions have to be treated carefully to avoid overfitting so that the equation is not forced to follow the scatter of the data.

The first temperature derivative  $A_{10}^r$  shown in Fig. 7 is the most accurate property to determine from molecular simulation. The liquid phase is represented within 0.03% (AAD = 0.02%). The low-density data are more challenging. In the gas phase, they are reproduced within 0.5% (AAD = 0.28%). Since the vapor–liquid equilibrium is located between the gaseous and liquid data, it is difficult to assess

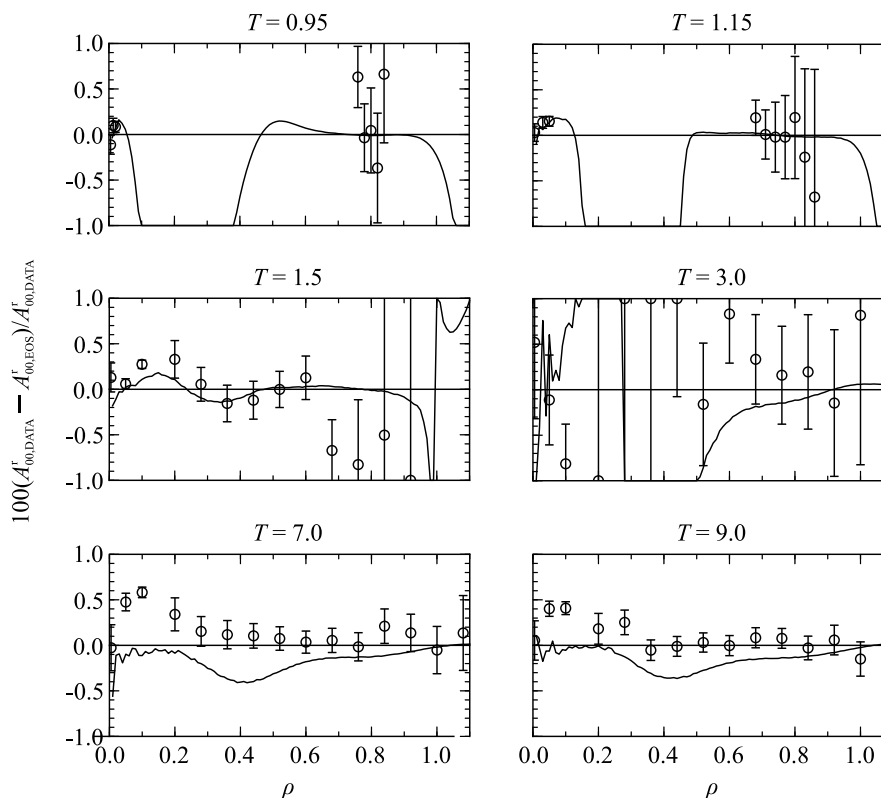


FIG. 5. Relative deviation of simulated residual Helmholtz energy  $A_{00}^r$  data (circles) from the present equation of state. The equation of Mecke *et al.*<sup>5</sup> (solid curve) is plotted for comparison.

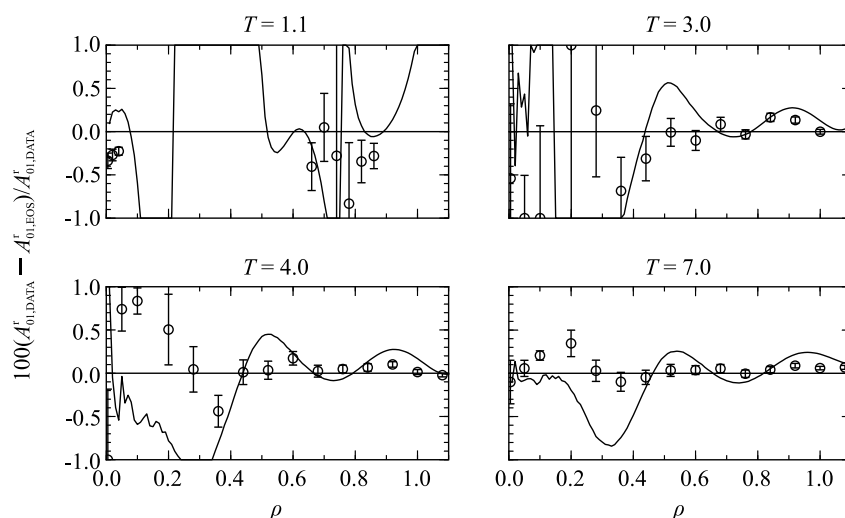


FIG. 6. Relative deviation of simulated first derivative of the residual Helmholtz energy with respect to density  $A_{01}^r$  data (circles) from the present equation of state. The equation of Mecke *et al.*<sup>3</sup> (solid curve) is plotted for comparison.

a correct transition between low- and high-density data. The supercritical state allows for a continuous evaluation of the data over the entire density range. At  $T = 3$  and 5, a consistent trend persists over the entire density range. In contrast,  $T$

$= 1.5$  and 2 show an offset of the relative deviations between low-density and medium-density data. Isotherms  $T = 7$  and 9 were fitted less accurately. During the fit, it was not possible to improve accuracy without compromising lower isotherms.

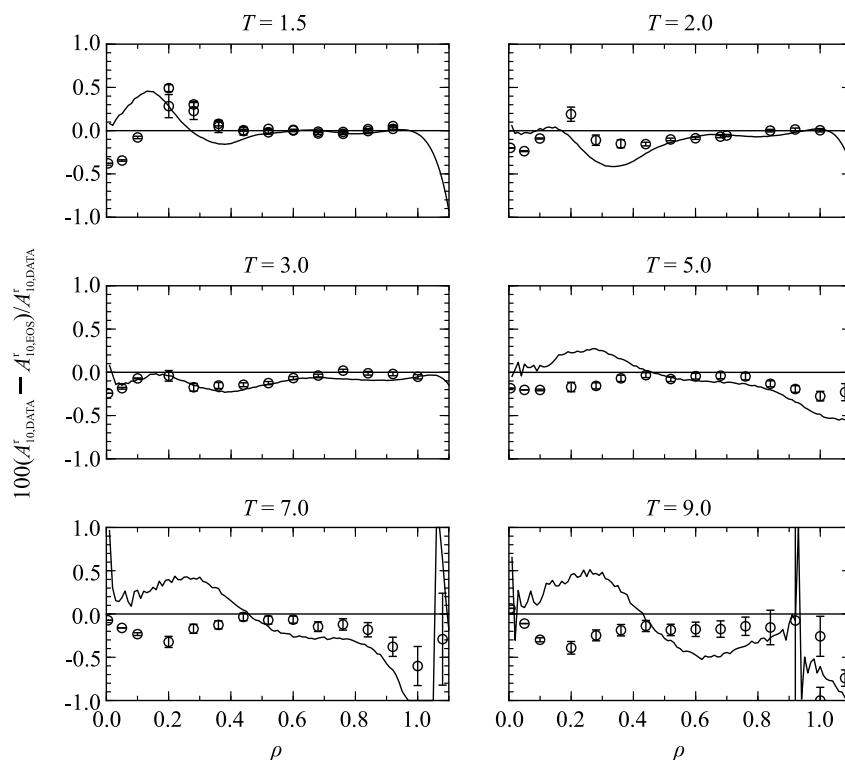


FIG. 7. Relative deviation of simulated first derivative of the residual Helmholtz energy with respect to inverse temperature  $A_{10}^r$  data (circles) from the present equation of state. The equation of Mecke *et al.*<sup>5</sup> (solid curve) is plotted for comparison.

## EQUATION OF STATE FOR THE LENNARD-JONES FLUID

023101-13

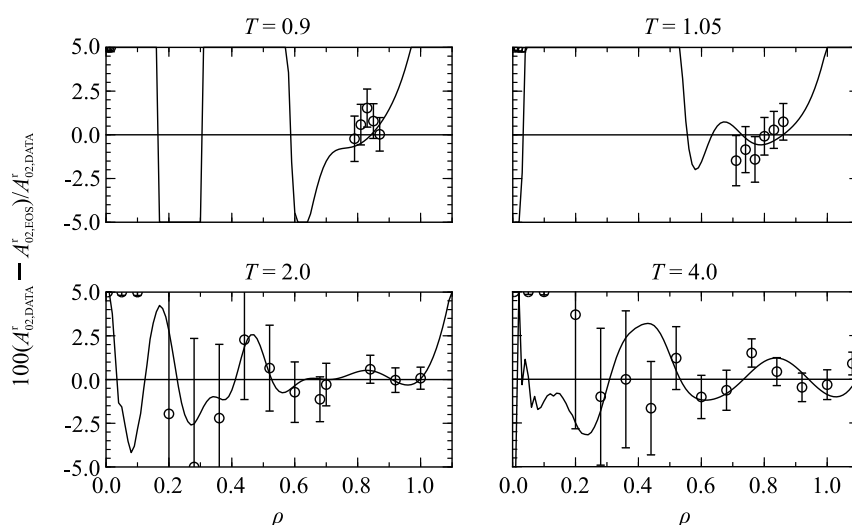


FIG. 8. Relative deviation of simulated second derivative of the residual Helmholtz energy with respect to density  $A_{02}^r$  data (circles) from the present equation of state. The equation of Mecke *et al.*<sup>5</sup> (solid curve) is plotted for comparison.

Therefore, uncertainties in the supercritical state are 0.2% for  $T < 7$  and up to 0.6% for  $T \geq 7$ . The overall AAD of this work and Mecke *et al.*<sup>5</sup> are quite similar: 0.14% vs. 0.16%, respectively.

The second density derivative  $A_{02}^r$  in Fig. 8 is similarly represented with AAD = 28.0% versus 27.8% for Mecke *et al.*<sup>5</sup> High AAD in the low-density region are caused by small numerical values resulting in a high relative deviation. In the liquid region, the data are represented within 1.5%. Both equations show about the same deviations. Similar to  $A_{01}^r$ , deviations in the supercritical region oscillate. Scatter occurs at medium temperatures ( $T = 1.5$ – $5$ ) and  $\rho < 0.45$ . The error of calculated  $A_{02}^r$  data in the supercritical region was estimated

to be 2.5% for  $\rho < 0.45$  ( $AAD_{MD} = 2.66\%$ ) and 1.5% for  $\rho \geq 0.45$  ( $AAD_{HD} = 0.85\%$ ).

Figure 9 shows that  $A_{20}^r$  behaves as smooth as  $A_{10}^r$ . A significant oscillation can be observed for medium temperatures. The gaseous and liquid regions are described with an accuracy of better than 1% ( $AAD_{gas} = 0.47\%$  and  $AAD_{liq} = 0.40\%$ ), which is a large improvement in comparison with the EOS of Mecke *et al.*<sup>5</sup> ( $AAD_{gas} = 1.07\%$  and  $AAD_{liq} = 0.88\%$ ). For  $T \geq 3$ , medium- and high-density data are reproduced within 0.5%. The transition of the low-density into the medium-density range shows an offset. Therefore, the uncertainty is 1%, although the data have lower statistical uncertainties. The supercritical region represents a significant improvement over

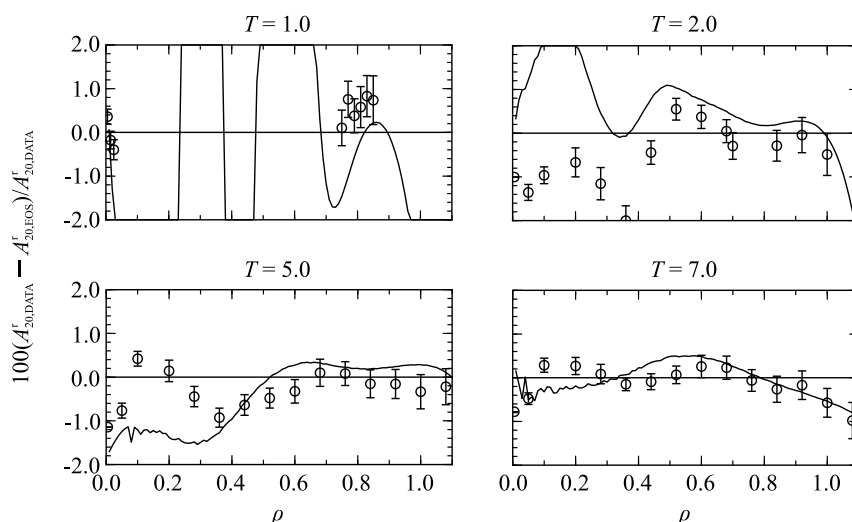


FIG. 9. Relative deviation of simulated second derivative of the residual Helmholtz energy with respect to inverse temperature  $A_{20}^r$  data (circles) from the present equation of state. The equation of Mecke *et al.*<sup>5</sup> (solid curve) is plotted for comparison.

023101-14

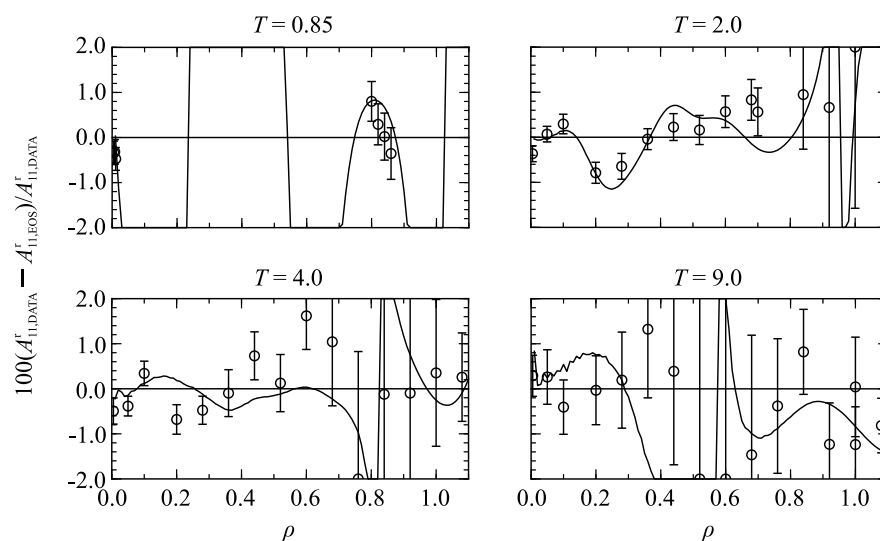
THOL *ET AL.*

FIG. 10. Relative deviation of simulated mixed derivative of the residual Helmholtz energy with respect to density and inverse temperature  $A_{11}^r$  data (circles) from the present equation of state. The equation of Mecke *et al.*<sup>5</sup> (solid curve) is plotted for comparison.

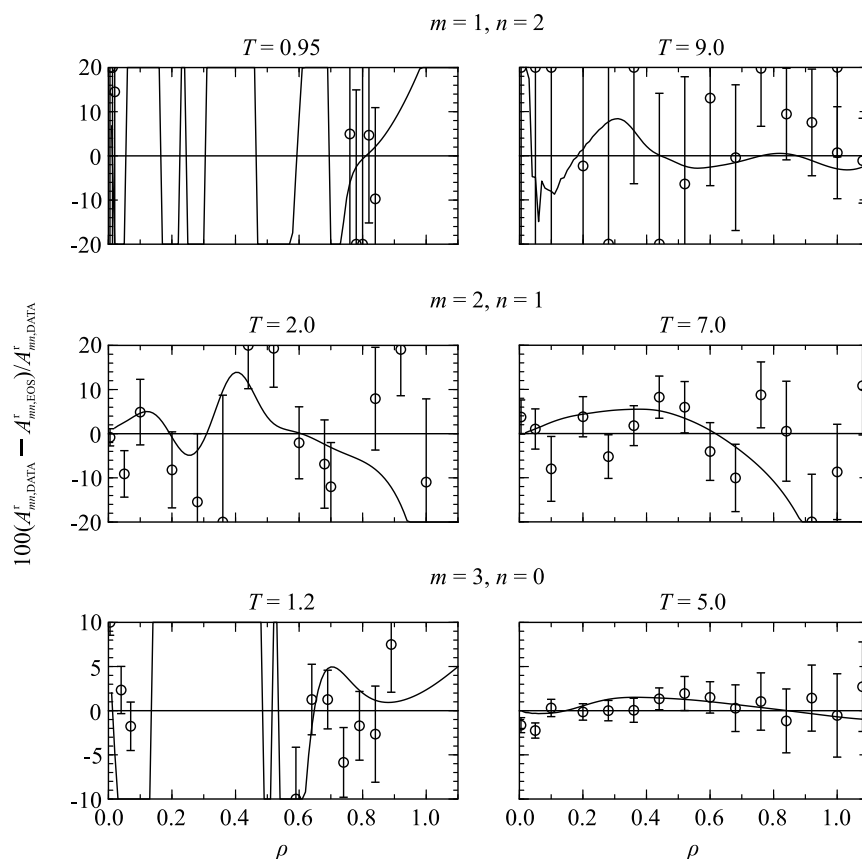


FIG. 11. Relative deviation of the simulated third derivatives of the residual Helmholtz energy with respect to density and inverse temperature data (circles) from the present equation of state: first row  $A_{12}^r$ , second row  $A_{21}^r$ , third row  $A_{30}^r$ . The equation of Mecke *et al.*<sup>5</sup> (solid curve) is plotted for comparison.

Mecke *et al.*<sup>5</sup> The overall AAD is decreased from the previous 0.93% to 0.48% in this work.

Figure 10 shows the mixed derivative  $A_{11}^r$ . The gaseous region is represented within 0.5% (AAD = 0.33%), whereas the deviation in the liquid region increases from 0.5% to 1% toward high densities (AAD = 0.49%). In the supercritical region at densities  $\rho \leq 0.5$ , the accuracy is within 1% (AAD<sub>LD</sub> = 0.28% and AAD<sub>MD</sub> = 0.34%). For  $\rho > 0.5$ , significant scatter occurs with an estimated uncertainty of more than 3%. The overall AAD of both equations is quite similar and no noticeable improvement is achieved.

Third-order derivatives are currently associated with too large statistical uncertainties to be used to parameterize the equation of state and were used for comparison only. At least the third inverse temperature derivative  $A_{30}^r$  shows acceptable deviations with an overall AAD = 4.44% (cf. Fig. 11). Especially in the supercritical region for  $T \geq 4$ , the equation shows agreement with the simulation data within about 3%. Other regions are reproduced within 5%–10%. The deviations of calculated  $A_{12}^r$  data are at least 20% (overall AAD = 88.2%

caused by low-density data).  $A_{21}^r$  data are reproduced within 20% for  $T \leq 2$  and 10% for  $T > 2$  (overall AAD = 12.8%). The deviations with respect to the EOS of Mecke *et al.*<sup>5</sup> are slightly higher for these properties.

## 5.2. Thermal virial coefficients

In addition to the residual Helmholtz derivatives, which are exclusively located in the homogeneous region, the gas phase was modeled with virial coefficients up to the fourth. Second (*B*) and third (*C*) virial coefficients were used to set up previous equations of state (cf. Table 4). Available data from the literature, e.g., Nicolas *et al.*,<sup>25</sup> Barker *et al.*,<sup>29</sup> Shaul *et al.*,<sup>53</sup> Bird *et al.*,<sup>54</sup> Hirschfelder *et al.*,<sup>55</sup> Sun and Teja,<sup>56</sup> and others, are augmented by “exact” calculations provided by Wheatley.<sup>33</sup> Figure 12 displays details. For clarity, only virial coefficient data of Sun and Teja<sup>56</sup> and Wheatley<sup>33</sup> are plotted.

The second virial coefficient from the present EOS represents all available data. The EOS of Mecke *et al.*<sup>5</sup> follows

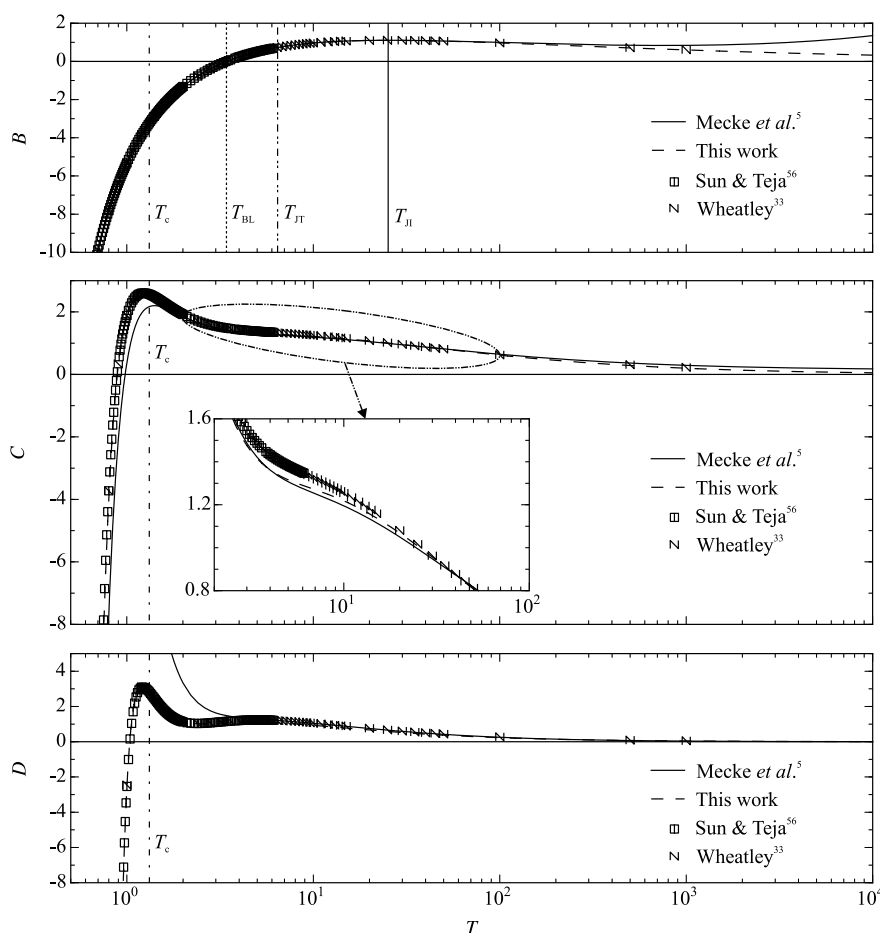


FIG. 12. Second, third, and fourth thermal virial coefficients. The critical temperature  $T_c$ , Boyle temperature  $T_{BL}$ , Joule–Thomson inversion temperature  $T_{JT}$ , and Joule inversion temperature  $T_{JI}$  are indicated.

TABLE 6. Selected points on the characteristic ideal curves calculated with the present equation of state

Property	$T$	$\rho$	$p$
Temperature of Boyle curve in the zero-density limit	3.417		
Joule–Thomson inversion temperature in the zero-density limit	6.425		
Joule inversion temperature in the zero-density limit	25.17		
Maximum of Joule–Thomson inversion curve	2.917	0.387	1.386
Intersection of Joule–Thomson inversion curve and saturated liquid line	1.051	0.673	0.035

the exact second virial coefficient up to  $T = 100$ , which was reported to be the upper range for a reasonable extrapolation behavior.<sup>5</sup> For higher temperatures, the two equations differ from each other. The present EOS follows the calculated second virial coefficient of Wheatley<sup>33</sup> approaching zero, whereas that of Mecke *et al.*<sup>5</sup> does not. The Boyle temperature, Joule–Thomson inversion temperature, and Joule inversion temperature in the zero-density limit are also indicated in Fig. 12. They are in good agreement with values of Hirschfelder *et al.*<sup>55</sup> ( $T_{BL} = 3.42$ ), Friedrich and Lustig<sup>57</sup> ( $T_{BL} = 3.41$ ,  $T_{JT} = 6.47$ ), Breitenstein and Lustig<sup>58</sup> ( $T_{BL} = 3.42$ ,  $T_{JT} = 6.43$ ), and Breitenstein<sup>59</sup> ( $T_{BL} = 3.4179$ ,  $T_{JT} = 6.4308$ ). The exact Joule inversion temperature has not yet been established in the literature. Additional characteristic properties calculated from the present EOS can be found in Table 6.

In addition to the second virial coefficient, its first temperature derivative ( $dB/dT$ ) was reported by Hirschfelder *et al.*<sup>55</sup> As expected, both equations agree with these data for  $T \leq 100$ . For higher temperatures, an unphysical slope for  $B$  of the equation of Mecke *et al.*<sup>5</sup> (cf. Fig. 12) is also visible in Fig. 13 because the temperature derivative is positive. In compar-

ison, the present EOS exhibits a correct negative temperature derivative in that range. However, it is important to keep in mind that the temperature  $T/T_c \approx 75$  is well beyond the range of validity of both equations.

The third virial coefficient is reproduced by the present EOS as accurately as the second virial coefficient, except for the region near the maximum. As the Lennard-Jones fluid is a simple monatomic model, a similar behavior as the equation for argon by Tegeler *et al.*<sup>60</sup> is expected. Their EOS as well as third virial coefficient data determined from highly accurate  $p\rho T$  measurements by Gilgen *et al.*<sup>61</sup> show a maximum slightly below the critical temperature. Figure 12 shows that this is also true for the Lennard-Jones fluid. This behavior is in agreement with the available data. An inflection point in  $C$  is obvious from Fig. 12. Additionally, exact calculations for the first temperature derivative of the third virial coefficient were provided by both Hirschfelder *et al.*<sup>55</sup> and Bird *et al.*<sup>54</sup> In Fig. 13, the inflection point is clearly illustrated by a maximum in the temperature derivative around  $T = 6$ .

On the bottom panel of Fig. 12, the fourth virial coefficient is shown. The available data from exact calculations<sup>33,56</sup> as

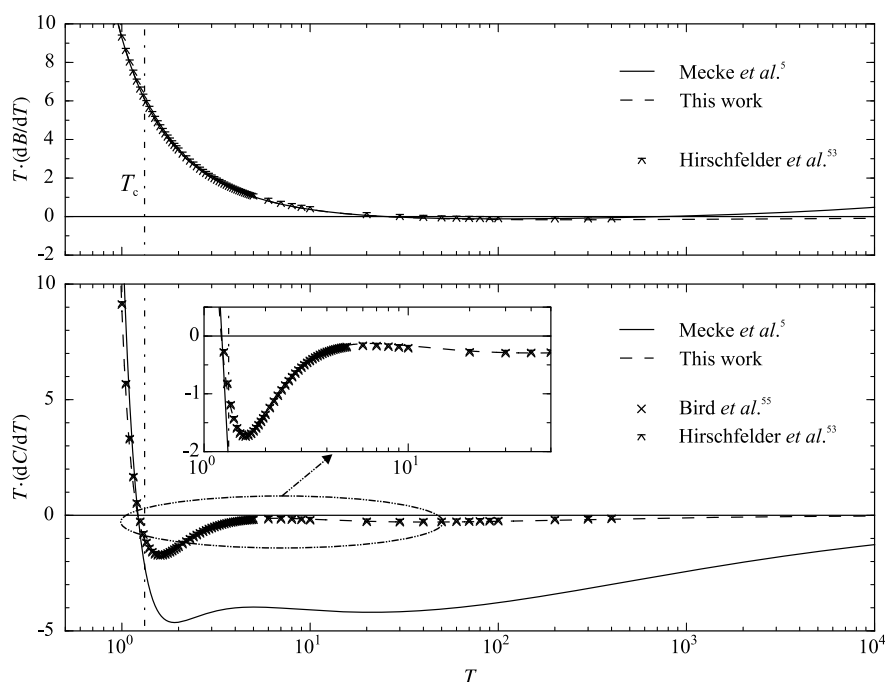


Fig. 13. First derivative of the second and third thermal virial coefficients with respect to temperature.



## EQUATION OF STATE FOR THE LENNARD-JONES FLUID

023101-17

well as the present equation of state show a first maximum around the critical temperature and a second less pronounced maximum at  $T \approx 4.8$ . As discussed by Thol *et al.*,<sup>62</sup> the fourth virial coefficient has rarely been investigated in the context of equations of state and few experimental measurements are available for real fluids. However, no measurements of  $D$  exist in the temperature region where the second maximum occurs ( $T/T_c \approx 3.6$ ).

## 5.3. Vapor–liquid equilibrium

The present equation of state is exclusively based on Helmholtz energy derivatives at homogeneous states and on thermal virial coefficients. Therefore, vapor–liquid equilibrium is output of, and not input to, the fitting procedure. Figure 14 shows relative deviations of available data for vapor pressure  $p_v$ , saturated liquid density  $\rho'$ , and saturated vapor density  $\rho''$ .

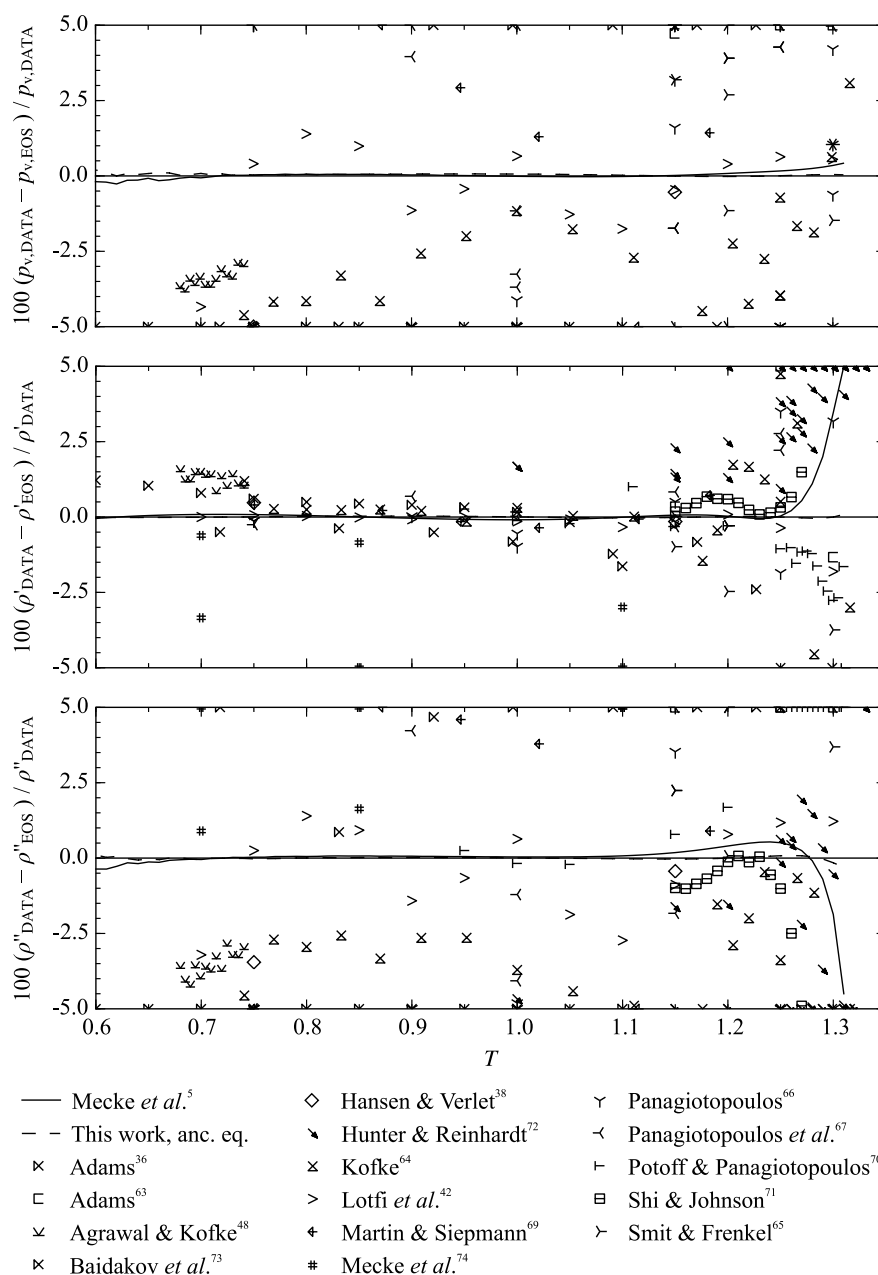


Fig. 14. Relative deviation of literature data for vapor pressure, saturated liquid density, and saturated vapor density from the present equation of state.

023101-18

THOL *ET AL.*

TABLE 7. Parameters of the ancillary equations for vapor pressure, saturated liquid density, and saturated vapor density

<i>i</i>	Vapor pressure, Eq. (44)		Saturated liquid density, Eq. (45)		Saturated vapor density, Eq. (46)	
	$n_i$	$t_i$	$n_i$	$t_i$	$n_i$	$t_i$
1	$-0.540\,00 \times 10^{+1}$	1.00	$0.1362 \times 10^{+1}$	0.313	$-0.696\,55 \times 10^{+1}$	1.320
2	$0.447\,04 \times 10^0$	1.50	$0.2093 \times 10^{+1}$	0.940	$-0.103\,31 \times 10^{+3}$	19.24
3	$-0.185\,30 \times 10^{+1}$	4.70	$-0.2110 \times 10^{+1}$	1.630	$-0.203\,25 \times 10^{+1}$	0.360
4	$0.198\,90 \times 10^0$	2.50	$0.3290 \times 10^0$	17.00	$-0.444\,81 \times 10^{+2}$	8.780
5	$-0.112\,50 \times 10^{+1}$	21.4	$0.1410 \times 10^{+1}$	2.400	$-0.184\,63 \times 10^{+2}$	4.040
6					$-0.260\,70 \times 10^{+3}$	41.60

TABLE 8. Average absolute relative deviations of vapor pressure, saturated liquid density, and saturated vapor density from literature data relative to the present equation of state

Authors	No. of data	Temperature range	Average absolute relative deviations/%			
			LT <sup>a</sup>	MT <sup>a</sup>	HT <sup>a</sup>	overall
Vapor pressure $p_v$						
Adams <sup>36</sup>	11	0.60–1.10	10.2	9.49	–	9.76
Adams <sup>63</sup>	3	1.15–1.30	–	8.81	5.72	7.78
Agrawal and Kofke <sup>48</sup>	13	0.68–0.74	3.35	–	–	3.35
Baidakov <i>et al.</i> <sup>73 b</sup>	7	0.72–1.23	25.0	22.0	–	22.4
Hansen and Verlet <sup>38</sup>	2	0.75–1.15	5.17	0.54	–	2.86
Kofke <sup>64</sup>	22	0.74–1.32	4.39	2.99	1.86	3.01
Lotfi <i>et al.</i> <sup>42</sup>	13	0.70–1.30	2.37	0.91	0.55	1.11
Martin and Siepmann <sup>69</sup>	6	0.75–1.18	17.0	3.85	–	6.03
Panagiotopoulos <sup>66</sup>	22	0.75–1.30	45.5	97.2	2.73	70.6
Panagiotopoulos <i>et al.</i> <sup>67</sup>	18	0.75–1.30	50.2	6.84	3.01	11.2
Smit and Frenkel <sup>65</sup>	12	1.15–1.30	–	9.05	1.26	7.75
Saturated liquid density $\rho'$						
Adams <sup>36</sup>	11	0.60–1.10	0.92	0.52	–	0.67
Adams <sup>63</sup>	3	1.15–1.30	–	2.90	1.33	2.38
Agrawal and Kofke <sup>48</sup>	13	0.68–0.74	1.31	–	–	1.31
Baidakov <i>et al.</i> <sup>73 b</sup>	7	0.72–1.23	0.50	1.02	–	0.95
Hansen and Verlet <sup>38</sup>	2	0.75–1.15	0.48	0.15	–	0.31
Kofke <sup>64</sup>	22	0.74–1.32	0.74	1.69	4.92	1.90
Lotfi <i>et al.</i> <sup>42</sup>	13	0.70–1.30	0.03	0.14	1.81	0.25
Martin and Siepmann <sup>69</sup>	6	0.75–1.18	0.40	0.30	–	0.32
Mecke <i>et al.</i> <sup>74</sup>	6	0.70–1.10	1.98	6.17	–	4.77
Panagiotopoulos <sup>66</sup>	11	0.75–1.30	0.13	1.08	5.23	1.66
Panagiotopoulos <i>et al.</i> <sup>67</sup>	9	0.75–1.30	0.25	1.00	5.28	1.39
Potoff and Panagiotopoulos <sup>70</sup>	19	0.95–1.31	–	0.93	7.24	2.59
Shi and Johnson <sup>71</sup>	13	1.15–1.27	–	0.48	–	0.48
Smit and Frenkel <sup>65</sup>	6	1.15–1.30	–	0.81	3.74	1.30
Saturated vapor density $\rho''$						
Adams <sup>36</sup>	11	0.60–1.10	10.4	12.0	–	11.4
Adams <sup>63</sup>	3	1.15–1.30	–	17.9	12.4	16.1
Agrawal and Kofke <sup>48</sup>	13	0.68–0.74	3.49	–	–	3.49
Baidakov <i>et al.</i> <sup>73 b</sup>	7	0.72–1.23	13.9	6.95	–	7.95
Hansen and Verlet <sup>38</sup>	2	0.75–1.15	3.46	0.44	–	1.95
Kofke <sup>64</sup>	22	0.74–1.32	3.62	5.87	17.5	6.72
Lotfi <i>et al.</i> <sup>42</sup>	13	0.70–1.30	1.73	1.25	1.22	1.32
Martin and Siepmann <sup>69</sup>	6	0.75–1.18	16.8	5.80	–	7.64
Mecke <i>et al.</i> <sup>74</sup>	6	0.70–1.10	29.9	22.7	–	25.1
Panagiotopoulos <sup>66</sup>	11	0.75–1.30	31.7	11.6	16.5	16.2
Panagiotopoulos <i>et al.</i> <sup>67</sup>	9	0.75–1.30	16.8	6.65	8.28	7.96
Potoff and Panagiotopoulos <sup>70</sup>	19	0.95–1.31	–	4.17	13.2	6.54
Shi and Johnson <sup>71</sup>	13	1.15–1.27	–	1.02	–	1.02
Smit and Frenkel <sup>65</sup>	6	1.15–1.30	–	7.76	3.69	7.08

<sup>a</sup>LT:  $T/T_c < 0.6$ ; MT:  $0.6 \leq T/T_c \leq 0.98$ ; HT:  $T/T_c > 0.98$ .<sup>b</sup>Truncated at  $6.78\sigma$ .

## EQUATION OF STATE FOR THE LENNARD-JONES FLUID

023101-19

TABLE 9. Average absolute relative deviations of simulation data in homogeneous states from the literature relative to the present equation of state. For the  $p\rho T$  data in the critical region, pressure deviations are considered instead of density deviations. Critical region:  $0.98 \leq T/T_c \leq 1.1$  and  $0.7 \leq \rho/\rho_c \leq 1.4$ ; Supercritical region: LD:  $\rho/\rho_c < 0.6$ ; MD:  $0.6 \leq \rho/\rho_c \leq 1.5$ ; HD:  $\rho/\rho_c > 1.5$

Authors	No. of data	Temperature and pressure range		Average absolute relative deviations (AAD)/%							Overall
							Supercritical fluid				
		$T$	$p$	Gas	Liq.	Crit. Reg.	LD	MD	HD		
$p\rho T$ data											
Adams <sup>35</sup>	12	2.00–4.00	0.08–15.06	–	–	–	2.77	2.39	0.71	1.99	
Adams <sup>36</sup>	16	1.00–1.20	0.06–1.37	–	0.81	–	–	–	–	0.81	
Adams <sup>63</sup>	28	1.15–1.35	0.04–0.35	3.31	0.72	3.03	2.84	7.11	–	2.40	
Baidakov <i>et al.</i> <sup>73</sup>	99	0.70–2.00	0.00–15.19	1.43	0.06	0.88	0.08	0.65	0.04	0.43	
Carley <sup>76</sup>	11	1.35	0.15–0.75	–	–	1.34	–	5.02	0.75	1.74	
Fickett and Wood <sup>77</sup>	23	1.96–181.14	12.20–1463.83	–	–	–	–	–	2.89	2.89	
Hansen <sup>37</sup>	7	2.74–100.00	1.32–666.4	–	–	–	–	0.23	0.34	0.32	
Hansen and Verlet <sup>38</sup>	7	0.75–1.15	0.00–5.00	0.13	1.07	–	–	–	–	0.80	
Johnson <i>et al.</i> <sup>3</sup>	151	0.80–6.00	0.00–85.71	0.17	0.05	0.94	0.14	0.28	0.08	0.14	
Kolafa and Nezbeda <sup>4</sup>	11	0.81–10.00	0.11–99.18	–	0.19	2.12	–	0.45	0.05	0.70	
Kolafa <i>et al.</i> <sup>39</sup>	45	0.72–4.85	0.03–31.32	0.19	1.88	2.02	–	0.09	0.16	1.25	
Levesque and Verlet <sup>22</sup>	17	1.35	0.14–8.11	–	–	36.8	322	192	13.3	48.9	
Lotfi <i>et al.</i> <sup>42</sup>	4	0.95–1.30	0.00–0.12	–	0.18	1.57	–	–	–	0.53	
Lustig <sup>7</sup>	2	1.18	0.58–0.59	–	0.29	–	–	–	–	0.29	
Lustig <sup>17</sup>	8	1.01–3.00	0.20–8.22	–	0.21	0.68	–	0.03	0.07	0.25	
May and Mausbach <sup>16</sup>	193	0.70–6.17	0.09–99.97	2.48	0.35	2.59	0.63	1.12	0.12	0.53	
McDonald and Singer <sup>78</sup>	21	0.72–1.24	0.00–1.56	–	0.68	–	–	–	–	0.68	
McDonald and Singer <sup>23</sup>	44	0.72–1.24	0.00–1.64	–	0.43	–	–	–	–	0.43	
McDonald and Singer <sup>79</sup>	19	0.72–1.24	0.00–1.34	–	0.68	–	–	–	–	0.68	
McDonald and Singer <sup>80</sup>	48	1.45–3.53	0.15–6.26	–	–	6.74	0.88	1.08	0.88	1.04	
McDonald and Woodcock <sup>81</sup>	3	1.05–2.33	0.01–3.52	–	0.91	–	–	0.40	0.23	0.51	
Mecke <i>et al.</i> <sup>5</sup>	12	1.32–1.33	0.13–0.16	–	–	1.19	–	0.99	–	1.12	
Meier <sup>14</sup>	297	0.70–6.00	0.00–92.95	0.33	0.07	0.63	0.11	0.21	0.05	0.14	
Miyano <sup>27</sup>	71	1.31–100.00	0.00–297.00	–	–	3.83	–	0.59	0.15	1.95	
Morsali <i>et al.</i> <sup>82</sup>	13	5.01	2.58–41.55	–	–	–	–	0.04	0.08	0.08	
Nicolas <i>et al.</i> <sup>25</sup>	55	1.03–6.01	0.20–72.84	–	0.56	8.24	–	1.13	0.23	0.54	
Ree <sup>83</sup>	12	0.81–2.70	0.44–4.37	–	0.46	–	1.20	0.25	0.56	0.51	
Saager and Fischer <sup>40</sup>	26	0.68–4.00	0.00–27.07	–	0.11	–	–	0.28	0.08	0.12	
Schofield <sup>84</sup>	2	0.73	0.14–0.95	–	2.63	–	–	–	–	2.63	
Shaw <sup>85</sup>	240	0.70–136.25	0.12–555.66	–	0.48	–	–	–	0.46	0.47	
Sowers and Sandler <sup>86</sup>	60	1.35–6.00	0.06–25.88	–	–	4.27	0.34	0.43	0.32	0.48	
Streett <i>et al.</i> <sup>87</sup>	76	1.00–3.05	0.00–32.61	–	2.58	–	–	–	1.95	2.37	
Toxvaerd and Praestgaard <sup>88</sup>	8	1.35	0.14–5.56	–	–	5.41	–	–	0.72	2.48	
Verlet and Levesque <sup>89</sup>	5	1.35–2.74	0.15–2.43	–	–	1.98	–	7.54	1.42	2.87	
Verlet <sup>41</sup>	32	0.72–4.62	0.20–10.71	–	0.17	1.53	–	2.96	6.67	2.98	
Weeks <i>et al.</i> <sup>90</sup>	5	0.75–1.35	0.23–5.56	–	0.18	–	–	–	0.33	0.24	
Wood <sup>91</sup>	28	1.06–100.00	0.00–584.94	–	5.63	–	–	–	0.57	1.65	
Wood and Parker <sup>92</sup>	12	2.74	0.00–7.36	–	–	–	–	5.17	16.5	12.7	
Residual internal energy $u^r$											
Adams <sup>35</sup>	12	2.00–4.00	0.08–14.99	–	–	–	2.48	1.48	0.92	1.71	
Adams <sup>36</sup>	16	1.00–1.20	0.09–1.34	–	0.67	–	–	–	–	0.67	
Adams <sup>63</sup>	28	1.15–1.35	0.04–0.34	0.37	0.15	1.31	0.39	0.28	–	0.44	
Baidakov <i>et al.</i> <sup>73</sup>	99	0.70–2.00	0.00–15.21	0.70	0.06	0.74	0.24	0.27	0.05	0.27	
Hansen <sup>37</sup>	7	2.74–100.00	1.32–645.59	–	–	–	–	0.10	0.83	0.73	
Johnson <i>et al.</i> <sup>3</sup>	151	0.80–6.00	0.00–84.90	2.28	0.03	0.32	0.34	0.21	0.29	0.37	
Kolafa <i>et al.</i> <sup>39</sup>	45	0.72–4.85	0.04–31.47	0.58	0.06	2.96	–	0.18	0.19	0.72	
Kolafa and Nezbeda <sup>4</sup>	11	0.81–10.00	0.12–98.73	–	0.08	0.50	–	0.89	0.97	0.51	
Levesque and Verlet <sup>22</sup>	32	0.72–3.67	0.15–28.19	–	0.30	2.54	–	0.36	1.04	1.04	
Lotfi <i>et al.</i> <sup>42</sup>	5	0.75–1.30	0.00–0.12	–	0.07	0.07	–	–	–	0.07	
May and Mausbach <sup>16</sup>	193	0.70–6.17	0.00–98.13	0.48	0.02	0.28	0.13	0.14	0.26	0.20	
McDonald and Singer <sup>78</sup>	23	0.72–1.24	0.00–1.69	–	15.6	–	–	–	–	15.6	
McDonald and Singer <sup>23</sup>	45	0.72–1.24	0.00–1.69	–	0.38	–	–	–	–	0.38	
McDonald and Singer <sup>79</sup>	20	0.72–1.24	0.00–1.10	–	0.69	–	–	–	–	0.69	
McDonald and Singer <sup>80</sup>	48	1.45–3.53	0.15–6.36	–	–	3.85	3.49	1.95	0.74	1.77	
McDonald and Woodcock <sup>81</sup>	5	0.75–2.33	0.04–3.54	–	0.37	–	–	0.28	0.13	0.30	
Mecke <i>et al.</i> <sup>5</sup>	12	1.32–1.33	0.13–0.16	–	–	0.62	–	0.63	–	0.62	
Meier <sup>14</sup>	299	0.70–6.00	0.00–91.66	0.30	0.02	0.53	0.15	0.15	0.27	0.21	
Miyano <sup>27</sup>	71	1.31–100.00	0.00–293.24	–	–	1.80	–	8.42	3.47	3.74	
Nicolas <i>et al.</i> <sup>25</sup>	55	1.03–6.01	0.22–72.61	–	0.17	1.95	–	0.95	0.78	0.78	
Ree <sup>83</sup>	12	0.81–2.70	0.45–4.45	–	0.28	–	3.25	1.86	0.73	0.70	

023101-20

THOL ET AL.

TABLE 9. Average absolute relative deviations of simulation data in homogeneous states from the literature relative to the present equation of state. For the  $p\rho T$  data in the critical region, pressure deviations are considered instead of density deviations. Critical region:  $0.98 \leq T/T_c \leq 1.1$  and  $0.7 \leq \rho/\rho_c \leq 1.4$ ; Supercritical region: LD:  $\rho/\rho_c < 0.6$ ; MD:  $0.6 \leq \rho/\rho_c \leq 1.5$ ; HD:  $\rho/\rho_c > 1.5$ —Continued

Authors	No. of data	Temperature and pressure range		Average absolute relative deviations (AAD)/%							Overall
									Supercritical fluid		
		$T$	$p$	Gas	Liq.	Crit. Reg.	LD	MD	HD		
Saager and Fischer <sup>40</sup>	26	0.68–4.00	0.00–27.04	–	0.06	–	–	0.41	0.23	0.21	
Shaw <sup>85</sup>	243	0.66–136.25	0.02–549.83	–	0.20	–	–	–	1.62	1.20	
Sowers and Sandler <sup>86</sup>	54	1.35–6.00	0.10–25.93	–	–	1.94	0.64	0.73	0.54	0.66	
Streett <i>et al.</i> <sup>87</sup>	76	1.00–3.05	0.00–33.80	–	2.87	–	–	–	9.46	5.13	
Verlet <sup>41</sup>	32	0.72–4.62	0.20–10.69	–	0.68	5.14	–	0.71	0.19	0.81	
Verlet and Levesque <sup>89</sup>	6	1.35–2.74	0.15–2.56	–	–	0.80	–	1.96	1.64	1.41	
Wood <sup>91</sup>	48	1.06–100.00	0.00–3236.83	–	2.92	–	–	–	5.89	5.52	
Wood and Parker <sup>92</sup>	12	2.74	0.00–20.82	–	–	–	–	45.0	31.4	36.0	
Isochoric heat capacity $c_v$											
Adams <sup>35</sup>	12	2.00–4.00	0.08–14.99	–	–	–	0.22	1.17	0.66	0.60	
Adams <sup>63</sup>	27	1.15–1.35	0.04–0.34	1.43	4.35	2.33	0.72	3.09	–	2.96	
Baidakov <i>et al.</i> <sup>73</sup>	97	0.70–2.00	0.00–15.21	1.55	0.42	2.93	0.96	0.96	0.23	0.84	
Boda <i>et al.</i> <sup>93</sup>	8	1.35–2.00	0.15–0.51	–	–	4.72	–	0.47	–	1.53	
May and Mausbach <sup>16</sup>	192	0.70–6.17	0.00–98.13	1.74	0.35	6.89	0.18	0.35	0.13	0.41	
McDonald and Singer <sup>79</sup>	20	0.72–1.24	0.00–1.10	–	7.99	–	–	–	–	7.99	
McDonald and Singer <sup>80</sup>	48	1.45–3.53	0.15–6.36	–	–	9.48	2.39	1.85	1.33	1.88	
Meier <sup>14</sup>	282	0.70–6.00	0.00–91.66	0.40	0.34	5.10	0.15	0.42	0.20	0.48	
Szalai <i>et al.</i> <sup>94</sup>	4	1.10–1.35	0.05–0.14	1.90	–	–	–	1.65	–	1.84	
Wood and Parker <sup>92</sup>	12	2.74	0.00–20.82	–	–	–	–	2.98	25.7	18.5	
Isobaric heat capacity $c_p$											
Boda <i>et al.</i> <sup>93</sup>	39	0.75–1.90	0.00–0.25	0.95	2.98	1.07	1.88	2.41	2.76	2.33	
Lustig <sup>17</sup>	6	1.01–3.00	0.61–8.22	–	–	–	–	0.75	0.88	0.84	
May and Mausbach <sup>16</sup>	185	0.70–6.17	0.09–85.94	2.39	3.97	1.47	1.09	1.15	0.59	0.83	
Grüneisen coefficient $\Gamma$											
Emampour <i>et al.</i> <sup>95</sup>	22	1.20–1.80	0.15–13.82	–	3.37	–	–	5.19	4.36	4.11	
Mausbach and May <sup>96</sup>	191	0.70–6.17	0.09–98.13	1.41	0.53	3.11	0.33	0.43	0.38	0.48	
Speed of sound $w$											
Lustig <sup>17</sup>	8	1.01–3.00	0.20–8.22	–	–	2.89	–	0.21	0.05	0.80	
May and Mausbach <sup>16</sup>	191	0.70–6.17	0.09–85.94	1.47	2.77	2.06	0.17	0.63	0.28	0.45	
Joule–Thomson coefficient $\mu_{JT}$											
Lustig <sup>17</sup>	7	1.01–3.00	0.20–8.22	–	–	3.98	–	5.59	2.15	3.39	
May and Mausbach <sup>16</sup>	170	0.70–6.17	0.09–85.94	3.52	6.73	3.65	2.86	4.02	1.52	2.29	
Thermal expansion coefficient $\alpha$											
Adams <sup>35</sup>	12	2.00–4.00	0.08–14.99	–	–	–	8.63	7.78	11.4	9.32	
McDonald and Singer <sup>79</sup>	13	0.72–1.24	0.00–1.10	–	29.7	–	–	–	–	29.7	
Isothermal compressibility $\beta_T$											
Adams <sup>35</sup>	12	2.00–4.00	0.08–14.99	–	–	–	7.34	7.98	12.1	9.09	
Lotfi <i>et al.</i> <sup>42</sup>	5	0.75–1.30	0.00–0.12	–	2.01	28.6	–	–	–	7.33	
May and Mausbach <sup>16</sup>	188	0.70–6.17	0.09–98.13	2.48	1.19	6.40	1.11	1.49	0.79	1.10	
McDonald and Singer <sup>79</sup>	15	0.72–1.24	0.00–1.10	–	17.1	–	–	–	–	17.1	
Morsali <i>et al.</i> <sup>82</sup>	13	3.76	1.78–34.07	–	–	–	–	0.30	0.68	0.63	
Thermal pressure coefficient $\gamma$											
Adams <sup>35</sup>	12	2.00–4.00	0.08–14.99	–	–	–	8.80	3.30	8.55	7.34	
May and Mausbach <sup>16</sup>	192	0.70–6.17	0.09–98.13	0.42	0.24	0.81	0.18	0.17	0.29	0.26	
Meier <sup>14</sup>	279	0.70–6.00	0.00–91.66	0.26	0.52	1.13	0.14	0.27	0.40	0.36	
Morsali <i>et al.</i> <sup>82</sup>	13	3.76	1.78–34.07	–	–	–	–	0.11	0.20	0.18	

density  $\rho''$ . Ancillary correlations

$$\ln\left(\frac{p_v}{p_c}\right) = \left(\frac{T_c}{T}\right) \sum_{i=1}^5 n_i \left(1 - \frac{T}{T_c}\right)^{t_i}, \quad (44)$$

$$\frac{\rho'}{\rho_c} = 1 + \sum_{i=1}^5 n_i \left(1 - \frac{T}{T_c}\right)^{t_i}, \quad (45)$$

$$\ln\left(\frac{\rho''}{\rho_c}\right) = \sum_{i=1}^6 n_i \left(1 - \frac{T}{T_c}\right)^{t_i} \quad (46)$$

are included in the plots. Parameters are listed in Table 7. Ten different data sets are available for vapor pressure. The AAD are separated into three temperature ranges in Table 8. Molecular simulations were performed with different techniques and mostly low numbers of particles. The data of Adams<sup>36,63</sup> ( $N \approx 200$ ), Hansen and Verlet<sup>38</sup> ( $N \approx 864$ ), Kofke<sup>64</sup> ( $N \approx 108$ –256), Smit and Frenkel<sup>65</sup> ( $N \approx 64$ –512), Panagiotopoulos<sup>66</sup> ( $N \approx 300$ –500), and Panagiotopoulos *et al.*<sup>67</sup> ( $N \approx 300$ –500) are represented with high deviations.

In particular, the vapor pressure data simulated by Panagiotopoulos<sup>66</sup> and Panagiotopoulos *et al.*<sup>67</sup> show a scatter of more than 20% and are not considered in the subsequent discussion. The data set best represented by the present equation of state was published by Lotfi *et al.*<sup>42,68</sup> The  $NpT$  plus test particle method was used with 1372 particles in molecular dynamics mode. The results range from  $T = 0.7$  to 1.3 with a scatter of 1.8% ( $AAD = 1.11\%$ ) relative to the present equation of state. Agrawal and Kofke<sup>48</sup> mainly investigated the solid–liquid and solid–vapor equilibrium. For the determination of the triple point, they simulated the crossing of the vapor–liquid equilibrium curve and the solid–liquid equilibrium curve. Vapor pressure data ( $N \approx 108$ ) at low temperatures show a systematic deviation of  $-3.5\%$ . This trend is in agreement with other data sets for  $T < 0.75$ , e.g., Lotfi *et al.*<sup>42</sup> However, modeling the vapor pressure curve such that it reproduces these data would require an unreasonable course of the saturation line, so they are assumed to be inaccurate. The present EOS is in good agreement with the EOS of Mecke *et al.*<sup>5</sup> at low temperatures. Since the data set of Lotfi *et al.*<sup>42</sup> is the most consistent and accurate one, the corresponding scatter of 1.8% was assumed to be the uncertainty in vapor pressure.

The saturated liquid density was investigated by 14 different authors. The relative deviation with respect to the present equation of state is illustrated in Fig. 14. Most of the data were taken from the same publications as the vapor pressures. Therefore, the underlying molecular simulation conditions are the same. Data scatter less and the representation of the data is much better. For  $T < 1.1$ , the data of Adams<sup>36</sup> ( $AAD = 0.52\%–0.92\%$ ), Hansen and Verlet<sup>38</sup> ( $AAD = 0.15\%–0.48\%$ ), Panagiotopoulos<sup>66</sup> ( $AAD = 0.13\%–1.08\%$ ), Panagiotopoulos *et al.*<sup>67</sup> ( $AAD = 0.25\%–1.00\%$ ), Martin and Siepmann<sup>69</sup> ( $AAD = 0.30\%–0.40\%$ ), Smit and Frenkel<sup>65</sup> ( $AAD = 0.81\%$ ), Potoff and Panagiotopoulos<sup>70</sup> ( $AAD = 0.93\%$ ), and Kofke<sup>64</sup> ( $AAD = 0.74\%$ ) are represented within 1%. The data of Agrawal and Kofke<sup>48</sup> deviate systematically by 1.4% and were not considered further. Again, the most consistent and accurate data set is by Lotfi *et al.*<sup>42</sup> ( $AAD = 0.03\%–0.14\%$ ). For  $T \geq 1.1$ , two different observations are made. The data of Kofke,<sup>64</sup> Shi and Johnson,<sup>71</sup> and Hunter and Reinhardt<sup>72</sup> yield higher densities than the present EOS. The data of Kofke<sup>64</sup> are inaccurate in the lower temperature range. Shi and Johnson<sup>71</sup> published consistent data within a small temperature range ( $T = 1.15–1.27$ ). The present EOS predicts these data within 0.7%, except for the data point at the highest temperature, which is off by 1.5%. The data of Hunter and Reinhardt<sup>72</sup> exhibit significant scatter, which is probably due to varying numbers of particles ( $N = 32–500$ ) used in their simulations. Relative to the present EOS, the data by Potoff and Panagiotopoulos<sup>70</sup> deviate by up to  $-2.7\%$ . These data support the data of Lotfi *et al.*<sup>42</sup> at temperatures close to  $T_c$ . Since no vapor–liquid equilibrium data were used in the fit, the present EOS independently supports that the data of Lotfi *et al.*<sup>42</sup> are accurate over the entire temperature range. The uncertainty of saturated liquid density calculated with the present EOS is assumed to be 0.15% for  $T < 1.1$  and 0.5% for  $T \geq 1.1$  based on the data of Lotfi *et al.*<sup>42</sup>

Finally, the relative deviation of directly simulated saturated vapor density data from the present EOS is plotted in Fig. 14. The available data are from the same sources. The representation of the data is similar to the vapor pressure and is not discussed further. Again, the data set of Lotfi *et al.*<sup>42</sup> as a reference yields a correlation uncertainty of 1.8% over the entire temperature range.

#### 5.4. Density at homogeneous states

It is common for equation of state correlations for real fluids to quote deviations for density at given temperature and pressure. We adopt the tradition, although it was outlined recently that for molecular simulation data the procedure is not necessary.<sup>75</sup> The homogeneous density and the residual internal energy are described equally well by the present EOS and that of Mecke *et al.*<sup>5</sup> The average absolute relative

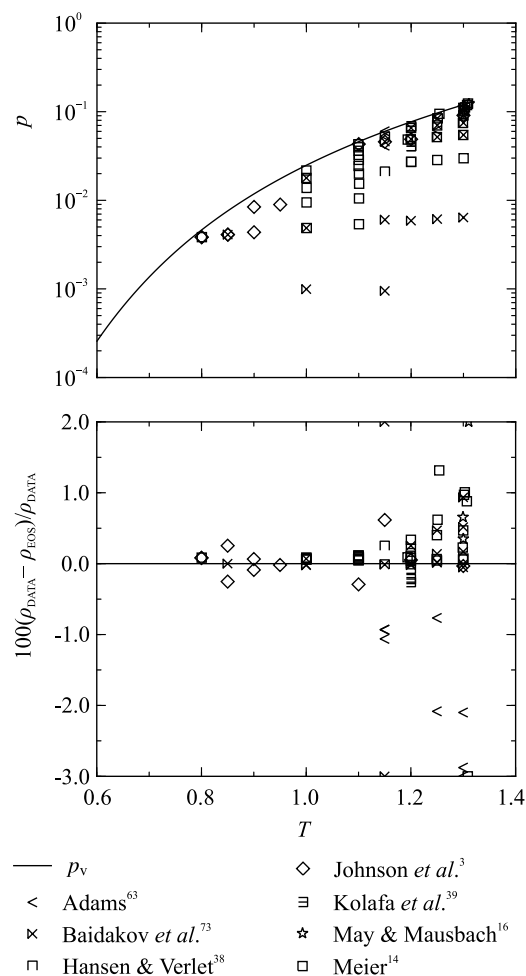


FIG. 15. Representation of vapor-phase density data. Top: Simulated state points relative to the vapor pressure curve. Bottom: Relative deviation of the simulated gas density data from the present equation of state.

023101-22

THOL ET AL.

deviations for literature data are listed in Table 9. The gas phase was studied by seven independent authors. Figure 15 shows comparisons of density data in the gaseous region with the present EOS. Apparently, the most accurate data were published by Johnson *et al.*<sup>3</sup> (AAD = 0.17%), Kolafa *et al.*<sup>39</sup> (AAD = 0.19%), and Meier<sup>14</sup> (AAD = 0.33%). All are

represented by the present EOS within 1%, which validates the description of the vapor phase up to the saturated vapor line. The homogeneous liquid phase was investigated more comprehensively than the gas phase. In total, 26 different data sets are available, which are presented in Fig. 16. In contrast to the gas-phase data, the liquid-phase data are predominantly far

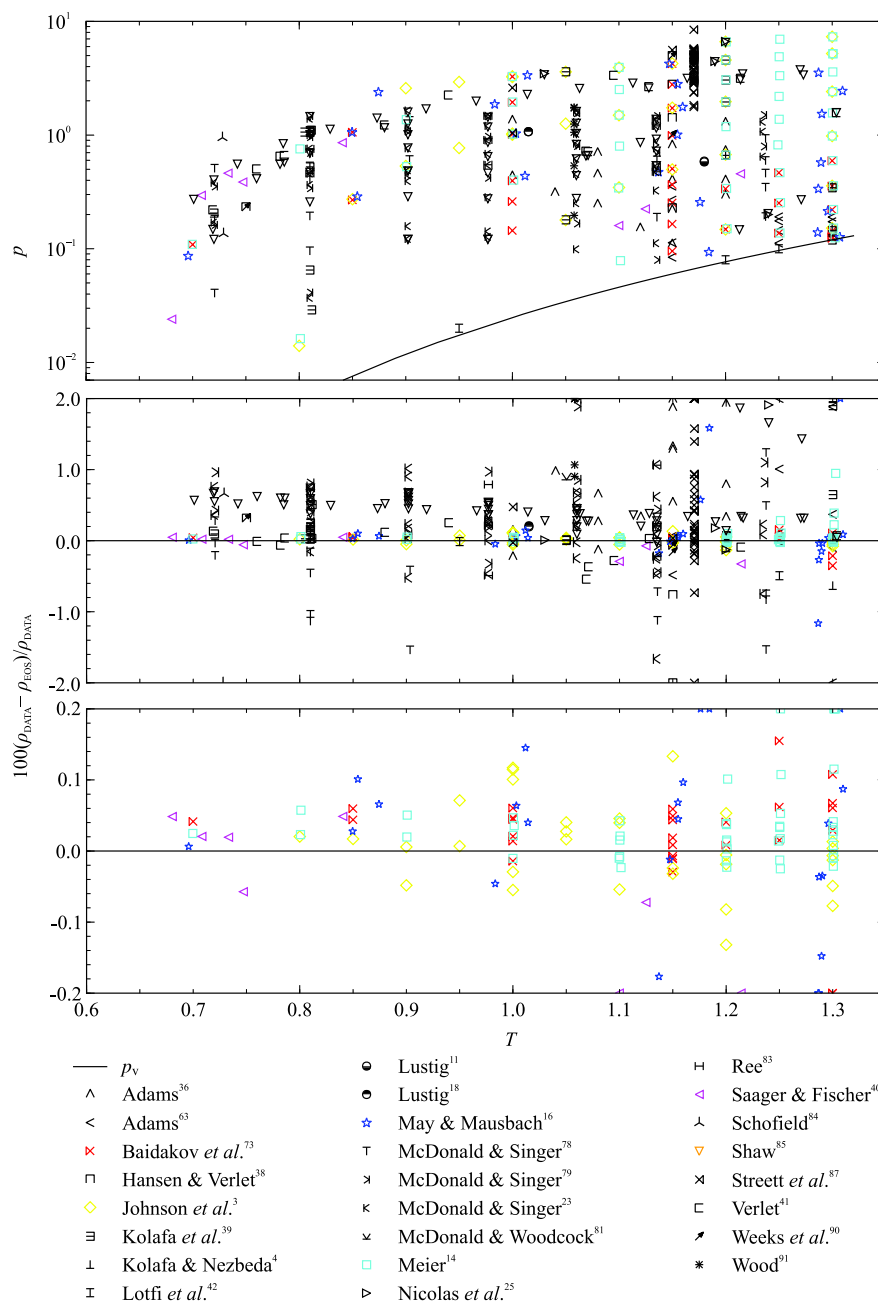


FIG. 16. (Color online) Representation of liquid-phase density data. Top: Simulated state points relative to the vapor pressure curve. Center: Relative deviation of all available simulated data from the present equation of state. Bottom: Relative deviation of selected simulated data from the present equation of state.

## EQUATION OF STATE FOR THE LENNARD-JONES FLUID

023101-23

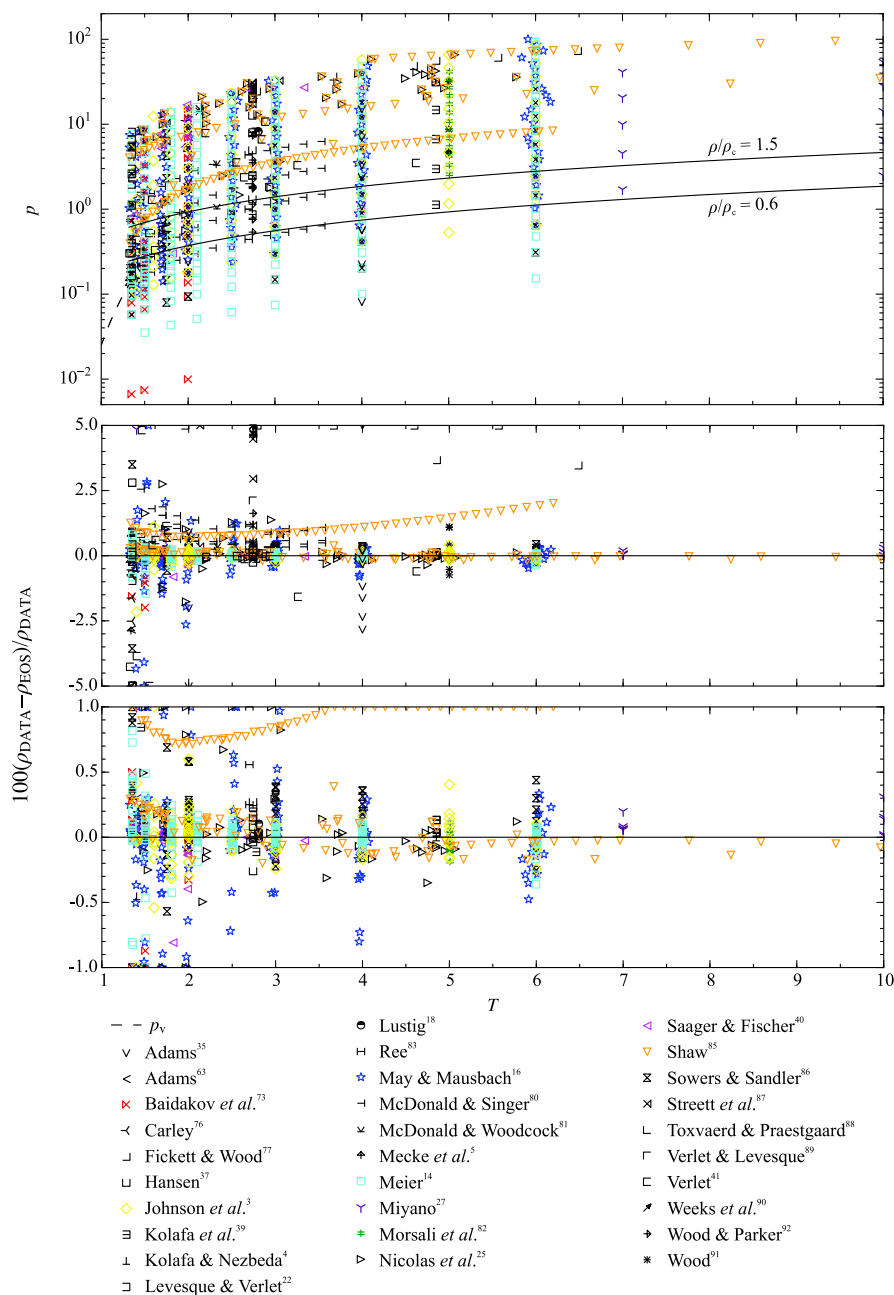


FIG. 17. (Color online) Representation of density in the supercritical region. Top:  $p$ - $T$  diagram of state points. Center: Relative deviation of all available simulation data from the present equation of state. Bottom: Relative deviation of selected simulation data from the present equation of state.

away from the two-phase region. When fitting an equation of state based on such data, as Mecke *et al.*<sup>5</sup> did, saturated liquid density data would be helpful. Thus, Mecke *et al.*<sup>5</sup> applied VLE data to their fit, which was not done here. Keeping in mind that the representation of VLE data is similar for both equations, the strategy of fitting only data at homogeneous states together

with virial coefficients for the gas phase compensates for a lack of VLE data as long as the homogeneous data are close enough to the two-phase region. This is particularly true if derivatives of the Helmholtz energy are considered directly.

Some of the literature data appear to be of poor quality, so only the most accurate and comprehensive data sets<sup>3,14,16,40,73,85</sup>

023101-24

THOL ET AL.

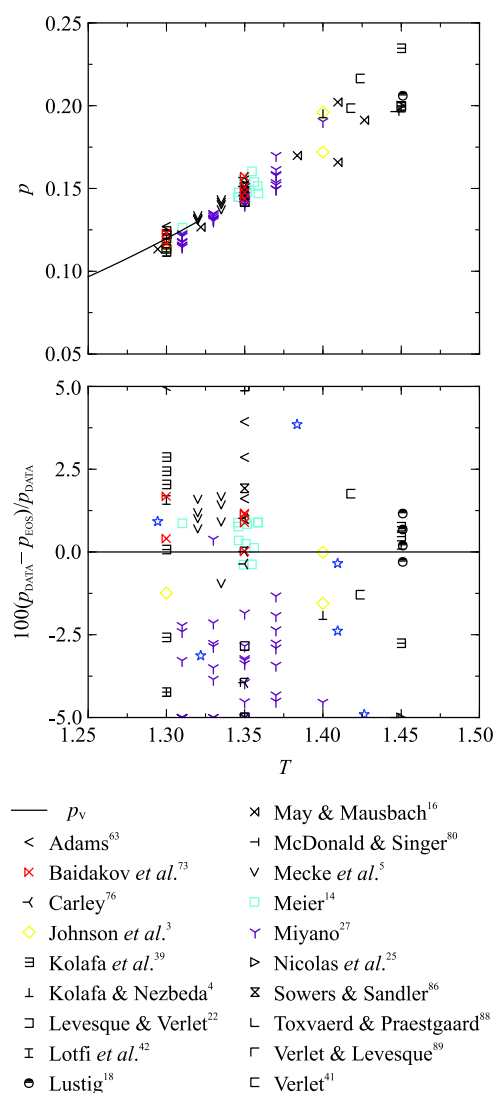


FIG. 18. (Color online) Representation of literature data for pressure in the critical region. Top:  $p$ - $T$  diagram showing the distribution of the state points relative to the vapor pressure curve. Bottom: Relative deviation of the simulated pressure data from the present equation of state in the critical region.

(colored symbols in Fig. 16) are considered for the assessment of uncertainty. The most accurate data are Johnson *et al.*<sup>3</sup> (AAD = 0.05%), Meier<sup>14</sup> (AAD = 0.07%), and Baidakov *et al.*<sup>73</sup> (AAD = 0.06%). The high AAD of 0.35% of May and Mausbach<sup>16</sup> is caused by a few data points near the critical temperature. If those points are excluded, the data set of May and Mausbach<sup>16</sup> is represented as well as the data sets above. For all data, deviations increase with increasing temperature. The lower temperature region ( $T < 1.1$ ) is modeled with an uncertainty of 0.06%. The upper temperature region is reproduced within 0.1%, with slightly higher deviations near the

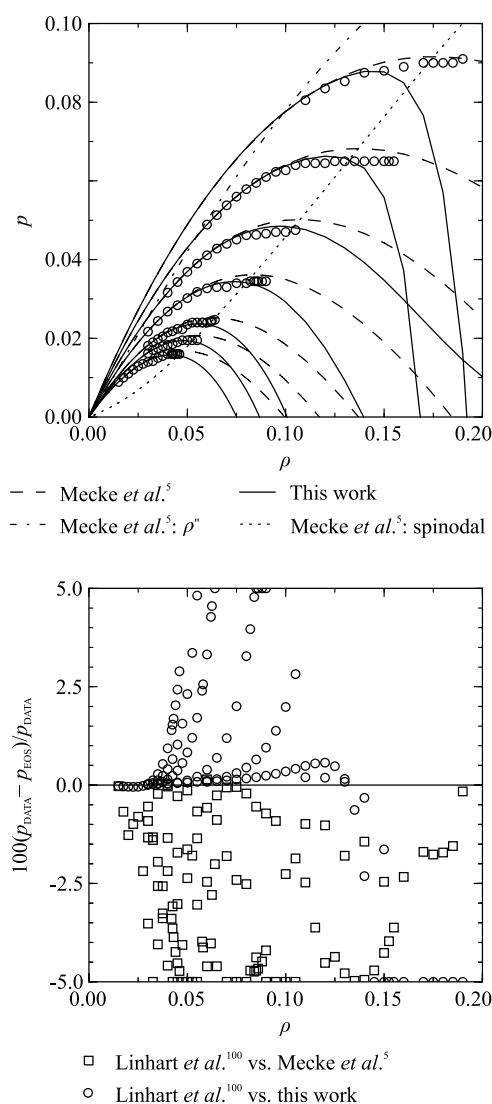


FIG. 19. Comparison of metastable gaseous pressure data of Linhart *et al.*<sup>100</sup>. The EOS of Mecke *et al.*<sup>5</sup> is shown for comparison. Top:  $p$ - $\rho$  diagram with selected isotherms and the spinodal corresponding to the equation of Mecke *et al.*<sup>5</sup>. Bottom: Relative deviation of the metastable pressure data of Linhart *et al.*<sup>100</sup> from the present equation of state (open circles) and that of Mecke *et al.*<sup>5</sup> (open squares).

critical temperature. The uncertainty of the present EOS is estimated to be 0.1% in the entire liquid region.

Similar to Table 5, the average absolute relative deviation for density at supercritical states, as listed in Table 9, is separated into three density ranges and investigated up to  $T = 7$  ( $T/T_c = 5.3$ ). For the HD region, higher temperatures are available ( $T_{\text{max}} = 136$  or  $T_{\text{max}}/T_c \approx 100$ ). In total, 25 data sets with a maximum pressure of approximately  $p_{\text{max}} = 190$  ( $p_{\text{max}}/p_c \approx 1460$ ) are published. For orientation, the range of validity of typical fluid equations of state for real substances



## EQUATION OF STATE FOR THE LENNARD-JONES FLUID

023101-25

is significantly smaller, e.g.,  $T_{\max}/T_c \approx 13$  and  $p_{\max}/p_c \approx 210$  for argon,<sup>60</sup>  $T_{\max}/T_c \approx 6.5$  and  $p_{\max}/p_c \approx 110$  for carbon dioxide,<sup>97</sup> and  $T_{\max}/T_c \approx 15$  and  $p_{\max}/p_c \approx 650$  for nitrogen.<sup>98</sup> The most accurate and comprehensive data sets<sup>3,14,16,40,73,82,85</sup> are plotted as colored symbols and presented at the bottom of Fig. 17. The data of May and Mausbach<sup>16</sup> show relatively large scatter, so they were excluded from the uncertainty analysis. Data in the low-density region ( $\rho < 0.217$ ) by Johnson *et al.*<sup>3</sup> (AAD = 0.14%), Meier<sup>14</sup> (AAD = 0.11%), and Baidakov *et al.*<sup>73</sup> (AAD = 0.08%) are reproduced best. Based on these data sets, the estimated uncertainty in density as a function of temperature and pressure of the present EOS is 0.15%. Data in the medium-density range ( $0.217 \leq \rho \leq 0.434$ ) by Lustig<sup>17</sup> (AAD = 0.03%), Meier<sup>14</sup> (AAD = 0.21%), Kolafa *et al.*<sup>39</sup> (AAD = 0.09%), and Morsali *et al.*<sup>82</sup>

(AAD = 0.04%) agree best with the present equation. The data of Johnson *et al.*<sup>3</sup> are also represented well, with an AAD of 0.28% attributed to two outliers with deviations of 1% and 2%. Based on these five data sets, the estimated uncertainty in density of the present EOS is assumed to be 0.3% in the medium-density range. The high-density range was accurately simulated by Johnson *et al.*<sup>3</sup> (AAD = 0.08%), Lustig<sup>17</sup> (AAD = 0.03%), Meier<sup>14</sup> (AAD = 0.05%), Saager and Fischer<sup>40</sup> (AAD = 0.08%), Baidakov *et al.*<sup>73</sup> (AAD = 0.04%), and Morsali *et al.*<sup>82</sup> (AAD = 0.08%). Based on comparisons with these data, the uncertainty of the present EOS in the high-density region is estimated as 0.2% in density.

Throughout, the uncertainty estimates are higher in the vicinity of the critical point. The critical region was not intended to be modeled as accurately as the remaining fluid region, for

TABLE 10. Critical parameters of the Lennard-Jones fluid from the literature

Authors	Year	$T_c$	$\rho_c$	$p_c$
Adams <sup>63</sup>	1979	1.30(2)	0.33(3)	0.13(2)
Adams <i>et al.</i> <sup>107</sup>	1979	1.30(2)	0.33(3)	—
Amadei <i>et al.</i> <sup>108</sup>	1999	1.350	0.337	0.149
Barker <i>et al.</i> <sup>29</sup>	1966	1.291	0.547	0.249
		1.449	0.771	0.379
		1.300	0.561	0.249
Caillol <sup>102</sup>	1998	1.326(2)	0.316(2)	0.111(2)
Dunikov <i>et al.</i> <sup>101</sup>	2001	1.350(5)	0.310(5)	0.126(8)
Hess <sup>103</sup>	1999	1.28	0.25	0.1056
		1.41	0.29	0.1472
		1.33	0.3	0.1357
Hunter and Reinhardt <sup>72</sup>	1995	1.32	—	—
Johnson <i>et al.</i> <sup>3</sup>	1993	1.313	0.310	—
Kim <i>et al.</i> <sup>109</sup>	1969	1.35	0.30	0.14
		1.28	0.29	0.13
Kofke <sup>64,110</sup>	1993	1.324(12)	0.305(2)	—
		1.321(4)	0.306(1)	—
Kolafa and Nezbeda <sup>4</sup>	1994	1.3396	0.3108	0.1405
Koutras <i>et al.</i> <sup>111</sup>	1992	1.355	0.290	0.147
Levesque and Verlet <sup>22</sup>	1969	1.37	0.31	0.140288
		1.36	0.36	0.151776
		1.36	0.33	0.161568
Lotfi <i>et al.</i> <sup>42</sup>	1992	1.31	0.314	—
Martin and Siepmann <sup>69</sup>	1998	1.2921	0.3117	0.1144
May and Mausbach <sup>30</sup>	2012	1.3145	0.3107	—
Mecke <i>et al.</i> <sup>5</sup>	1996	1.328	0.3107	—
Miyano <sup>27</sup>	1993	1.35	0.32	0.142
Nicolas <i>et al.</i> <sup>25</sup>	1979	1.35	0.35	0.142
Panagiotopoulos <sup>66</sup>	1987	<1.35	0.31(2)	—
Potoff and Panagiotopoulos <sup>104</sup>	1998	1.312(7)	0.316(1)	0.1279(6)
Potoff and Panagiotopoulos <sup>70</sup>	2000	1.312(7)	0.316(2)	—
Rec <sup>83</sup>	1980	1.41	0.33	0.177
Shi and Johnson <sup>71</sup>	2001	1.3241(9)	0.3165(7)	—
		1.3145(2)	0.316(1)	—
		1.316(6)	0.304(6)	—
Smit <sup>105</sup>	1992	1.316(6)	0.304(6)	—
Song and Mason <sup>24</sup>	1989	1.306	0.2625	0.1225
Sowers and Sandler <sup>86</sup>	1991	1.372	0.313	0.156
Sung and Chandler <sup>106</sup>	1974	1.3103	0.318	0.121
		1.31(1)	0.33(3)	—
Sýs and Malijevský <sup>112</sup>	1980	1.35	0.33	0.147
Valleau <sup>32</sup>	1994	1.328(3)	—	—
Verlet and Levesque <sup>89</sup>	1967	1.26	0.297	0.316
Verlet <sup>41</sup>	1967	1.36(4)	0.31(3)	—

several reasons. Natural large-scale fluctuations of a fluid in the critical region make sampling of some thermodynamic properties particularly difficult and uncertain. Molecular simulation results may cause a curvature in the rectilinear diameter<sup>99</sup> at high reduced temperatures when fitting an equation of state to them. That was observed for several different fluids, e.g., benzene, cyclohexane, and hydrogen sulfide, and is presented by Thol *et al.*<sup>62</sup> for the Lennard-Jones fluid truncated and shifted at  $2.5\sigma$ . During fitting iterations of the present EOS for the Lennard-Jones fluid, the nonlinearity of the rectilinear diameter was minimized. Available data are presented in Fig. 18. Some of the simulation data have higher deviations in the critical region than elsewhere. Again, the data of Mecke *et al.*,<sup>5</sup> Lustig,<sup>17</sup> Meier,<sup>14</sup> and Baidakov *et al.*<sup>73</sup> appear to be the most accurate in the critical region. The uncertainty in this region is 2% in pressure.

In Fig. 19, a comparison of the gaseous metastable pressure data published by Linhart *et al.*<sup>100</sup> with the present equation of state is shown. In the top panel, a  $p - \rho$  diagram including the saturated vapor line, the spinodal, and the simulated data along the corresponding isotherms is presented. A reasonable trend of the data is observed for densities  $\rho \leq \rho_{\text{spinodal}}$ . In this region, slopes and curvatures of isotherms of the present EOS are in better agreement with the data than the EOS of Mecke *et al.*,<sup>5</sup> which is confirmed by the deviation plot on the bottom panel of Fig. 19. For  $\rho < 0.15$ , the deviations between the present EOS and the simulation data are much lower than those of

Mecke *et al.*<sup>5</sup> Therefore, the qualitative validity of the present EOS extends into the metastable region up to the gaseous spinodal.

### 5.5. Critical point

The critical point is central for the development of a fluid equation of state. In this work, as in Thol *et al.*<sup>62</sup> and Lustig *et al.*,<sup>75</sup> we did not impose a critical point. The critical temperature and density varied during the fitting procedure. In particular, the modeling of an almost linear rectilinear diameter and the shaping of a distinctive saddle point of the critical isotherm was carefully monitored during the fit to ensure that the critical values did not exceed the uncertainties of the data given in the literature. Table 10 presents critical parameters from the literature, and the most likely critical points are illustrated in Fig. 20. The critical density that was observed during the fit of the present equation of state ( $\rho_c = 0.31$ ) is in line with the average critical density from the literature. It is in good agreement with the critical density of Dunikov *et al.*,<sup>101</sup> Johnson *et al.*,<sup>3</sup> Kolafa and Nezbeda,<sup>4</sup> Martin and Siepmann,<sup>69</sup> Mecke *et al.*,<sup>5</sup> Miyano,<sup>27</sup> and Verlet.<sup>41</sup> For the critical temperature, the main values scatter around  $T_c = 1.35$ . The corresponding critical density data show significant scatter. Therefore, the critical temperature values around  $T_c = 1.32$  seem to be a more adequate basis for comparison. The critical temperature obtained from the present EOS is in good agreement with

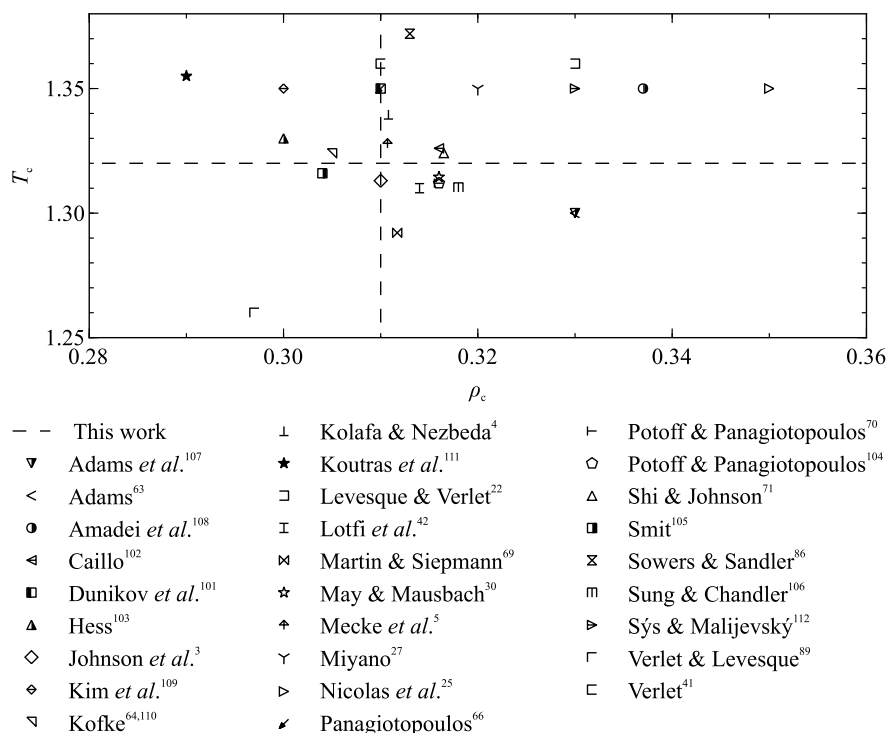


Fig. 20. Selected critical parameters from the literature. The crossing of the two dashed lines denotes the critical point of this work ( $T_c = 1.32$ ,  $\rho_c = 0.31$ ).

## EQUATION OF STATE FOR THE LENNARD-JONES FLUID

023101-27

Caillol,<sup>102</sup> Hess,<sup>103</sup> Johnson *et al.*,<sup>3</sup> Kofke,<sup>64</sup> Lotfi *et al.*,<sup>42</sup> Mecke *et al.*,<sup>5</sup> Potoff and Panagiotopoulos,<sup>70,104</sup> Shi and Johnson,<sup>71</sup> Smit,<sup>105</sup> and Sung and Chandler.<sup>106</sup> Thus, the critical temperature  $T_c = 1.32$  and the critical density  $\rho_c = 0.31$  were applied to the present equation (cf. calculation of  $\tau$  and  $\delta$  in Eq. (2)). The critical pressure  $p_c \approx 0.13006$  is calculated as a function of the critical temperature and density in this work.

## 5.6. Caloric properties

The residual internal energy was investigated to the same extent as the  $p\rho T$  data. The average absolute relative deviations of the data of each author are listed in Table 9. The data sets assumed to be most accurate were pointed out in the density discussion. Since density and residual internal energy

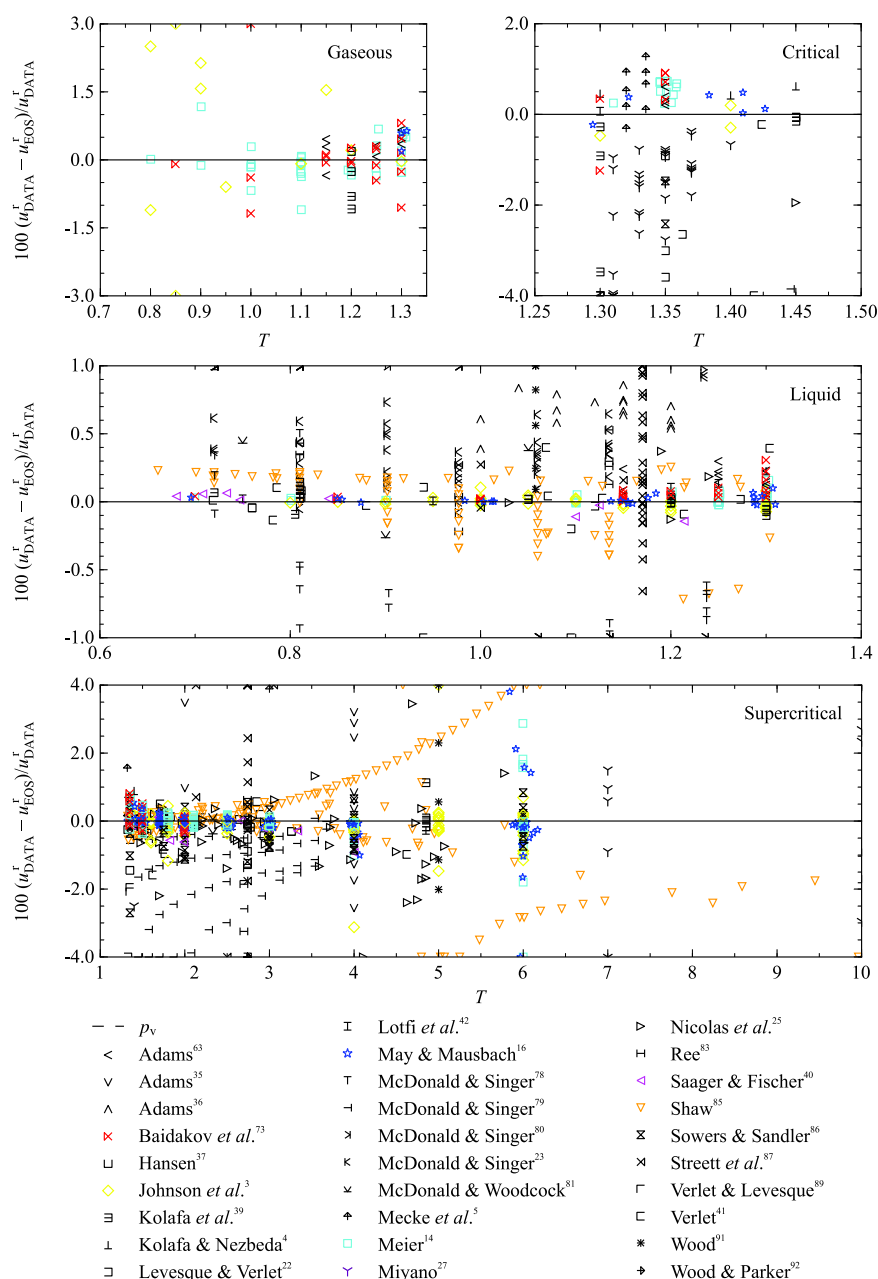


FIG. 21. (Color online) Relative deviation of literature data for residual internal energy from the present equation of state. Separate plots are provided for the gaseous, critical, liquid, and supercritical region.

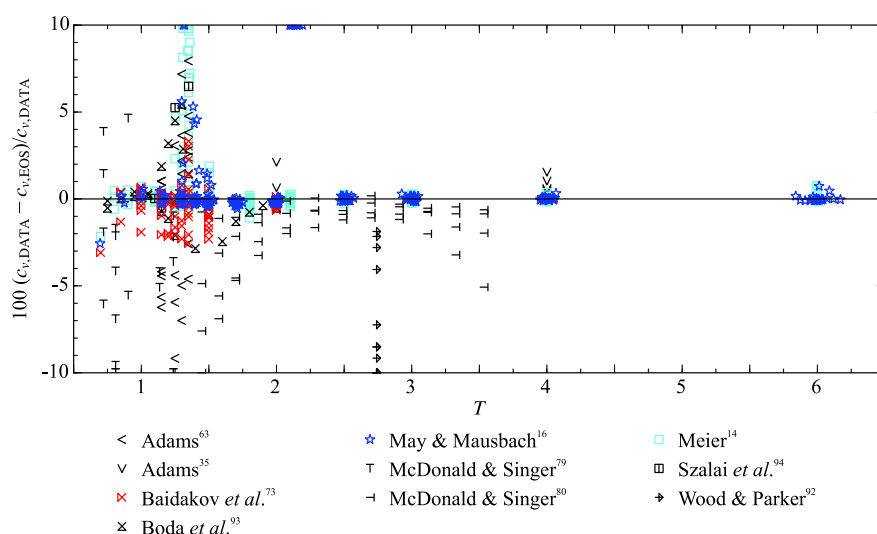


Fig. 22. (Color online) Relative deviation of literature data for isochoric heat capacity from the present equation of state.

are from the same molecular simulation runs, the quality of the data should be similar. Only data colored as for density in Figs. 16 and 17 are discussed.<sup>3,14,16,40,73,85</sup> Figure 21 presents the relative deviation of simulated residual internal energy data from calculated values. In the gaseous region, Meier<sup>14</sup> (AAD = 0.30%) and Baidakov *et al.*<sup>73</sup> (AAD = 0.70%) are represented by the present equation best. Based on these data, the uncertainty of the present EOS is estimated to be 1% in the gaseous region. In the liquid phase, the new equation is in agreement with the data of Johnson *et al.*<sup>3</sup> (AAD = 0.03%), Meier<sup>14</sup> (AAD = 0.02%), May and Mausbach<sup>16</sup> (AAD = 0.02%), and Baidakov *et al.*<sup>73</sup> (AAD = 0.06%). The uncertainty of the residual internal energy calculated with the present EOS is determined to be 0.1% in the liquid region. The uncertainty in the critical region is estimated to be 1%, which is supported by Johnson *et al.*<sup>3</sup> (AAD = 0.32%), May and Mausbach<sup>16</sup> (AAD = 0.28%), Meier<sup>14</sup> (AAD = 0.53%), and Baidakov *et al.*<sup>73</sup> (AAD = 0.74%). The supercritical region is well described up to  $T = 7$  in agreement with the density results. Data of Johnson *et al.*<sup>3</sup> (AAD = 0.21%–0.34%), Meier<sup>14</sup> (AAD = 0.15%–0.27%), May and Mausbach<sup>16</sup> (AAD = 0.13%–0.26%), and Baidakov *et al.*<sup>73</sup> (AAD = 0.05%–0.27%) scatter within 1% of the present EOS, which is assumed to be the uncertainty of the equation.

Only the data set of Lotfi *et al.*<sup>42</sup> is available for the residual enthalpy. The simulations were carried out along the saturation curves (see supplementary material<sup>52</sup>). The saturated liquid line is described within 0.1% for  $T \leq 1$  and 0.5% for  $T > 1$ . The simulations of the saturated vapor phase scatter around the equation by 4%.

In the homogeneous region, isochoric heat capacity data of Meier<sup>14</sup> and May and Mausbach<sup>16</sup> are represented best by the present equation (cf. Fig. 22 and Table 9). Except for the critical region, these data agree within 0.5%. Compared to the equation of Mecke *et al.*,<sup>5</sup> the representation of the data

published by Meier<sup>14</sup> in the vapor phase (AAD = 0.40% vs. AAD<sub>Mecke</sub> = 1.21%) and in the critical region (AAD = 3.09% vs. AAD<sub>Mecke</sub> = 7.49%) are improved significantly. The data of May and Mausbach<sup>16</sup> are reproduced better than those of Meier.<sup>14</sup> Deviations in the critical region increase to 5%. Only one data set<sup>93</sup> was simulated along the saturation lines. For  $T \leq 1.2$ , the data scatter within 0.5% around the present equation, which is within statistical uncertainties. For higher temperatures, the deviations increase significantly. In the low-temperature region of the  $c_v - T$  diagram in Fig. 23, the present EOS and that of Mecke *et al.*<sup>5</sup> show agreement with the data of Boda *et al.*<sup>93</sup> Only at  $T = 0.75$ , the equation of Mecke *et al.*<sup>5</sup> overestimates the saturated liquid isochoric heat capacity, which yields a steeper increase of the saturation line when extrapolated to low temperatures. Therefore, additional simulations were carried out in this work to show that the trend of the present EOS is correct. At  $T = 1.2$ , the saturated liquid and vapor isochoric heat capacities approach the same value and then cross each other. This is perfectly modeled by the

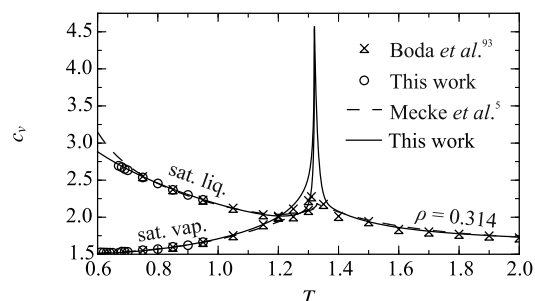


Fig. 23. Isochoric heat capacity versus temperature. The saturated liquid and vapor lines calculated with the equation of Mecke *et al.*<sup>5</sup> are plotted for comparison.

## EQUATION OF STATE FOR THE LENNARD-JONES FLUID

023101-29

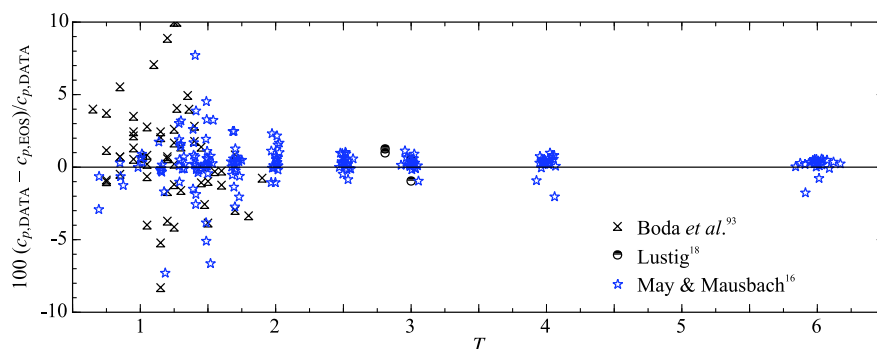


Fig. 24. (Color online) Relative deviation of literature data for isobaric heat capacity from the present equation of state.

present EOS, while the crossing of the equation of Mecke *et al.*<sup>5</sup> is shifted to about  $T = 1.275$ . At  $T > 1.2$ , high deviations of the present EOS from the isochoric heat capacity data of Boda *et al.*<sup>93</sup> are caused by a lower curvature of the simulation data. Large-scale fluctuations in the critical region make sampling of heat capacities difficult. While a classical equation of state cannot reproduce the correct physical behavior for isochoric heat capacity (a weak divergence toward infinity), our EOS at least produces a steep maximum in this property upon approaching the critical point.

The isobaric heat capacity was investigated by three authors. Figure 24 shows relative deviations of the simulation data and the present equation of state. The data of May and Mausbach<sup>16</sup> are represented within 1%, which is estimated to be the uncertainty of the EOS outside of the critical region. In contrast to the isochoric heat capacity, the isobaric heat capacity data of Boda *et al.*<sup>93</sup> show a significant scatter of approximately 5%–10%. These data are investigated in more detail in Fig. 25. Similar to the isochoric heat capacity, the present EOS exhibits a steeper increase of the saturated isobaric heat capacity approaching the critical temperature than that of Mecke *et al.*<sup>5</sup>

Figure 26 presents data for the Grüneisen coefficient  $\Gamma$ . Historically, this property was not utilized in the context of

fluid equations of state. Introduced for fluids by Arp *et al.*,<sup>113</sup> it was found to be valuable for the development of EOS in recent years, e.g., for the truncated and shifted Lennard-Jones fluid,<sup>62</sup> ethylene oxide,<sup>114</sup> hexamethyldisiloxane,<sup>115</sup> R1234ze(E),<sup>116</sup> R245fa,<sup>117</sup> cyclopentane,<sup>118</sup> and cyclohexane.<sup>119</sup> It is defined as the thermal pressure coefficient divided by the density and the isochoric heat capacity (Eq. (24)) and establishes a connection between thermal and caloric thermodynamic properties. The behavior of the speed of sound and the isochoric heat capacity can be monitored simultaneously by the Grüneisen coefficient. Thus, while it is not important for practical tasks, it is useful for verifying correct behavior of equations of state. In Fig. 26, a  $\Gamma$ - $\rho$  diagram and relative deviations of simulated Grüneisen coefficient data from calculated values are depicted. The isotherms show an increasing Grüneisen coefficient with increasing density. Similar to values calculated from many EOS for real fluids (e.g., nitrogen,<sup>98</sup> benzene,<sup>120</sup> argon,<sup>60</sup> and carbon dioxide<sup>97</sup>), a crossing of isotherms occurs near the critical density. This behavior is assumed to be correct because it was found for several different fluids. No direct experimental measurements are available for the Grüneisen coefficient to verify these assumptions. Therefore, Emampour *et al.*<sup>95</sup> and Mausbach and May<sup>96</sup> are important publications providing Grüneisen coefficient data from molecular

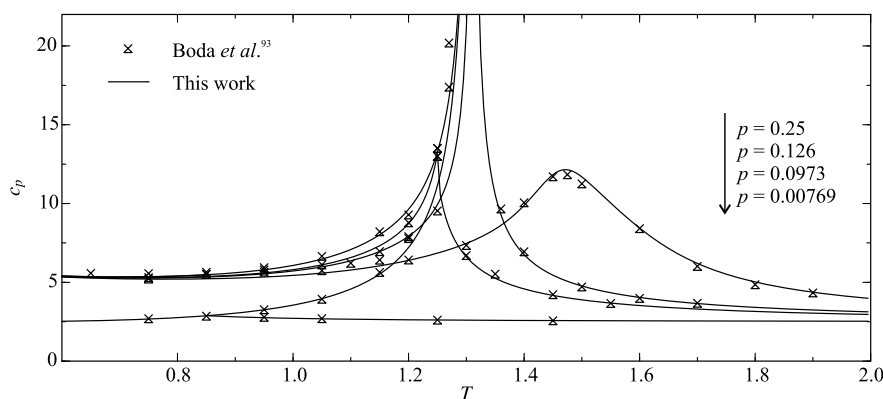


Fig. 25. Isobaric heat capacity versus temperature along isobars.

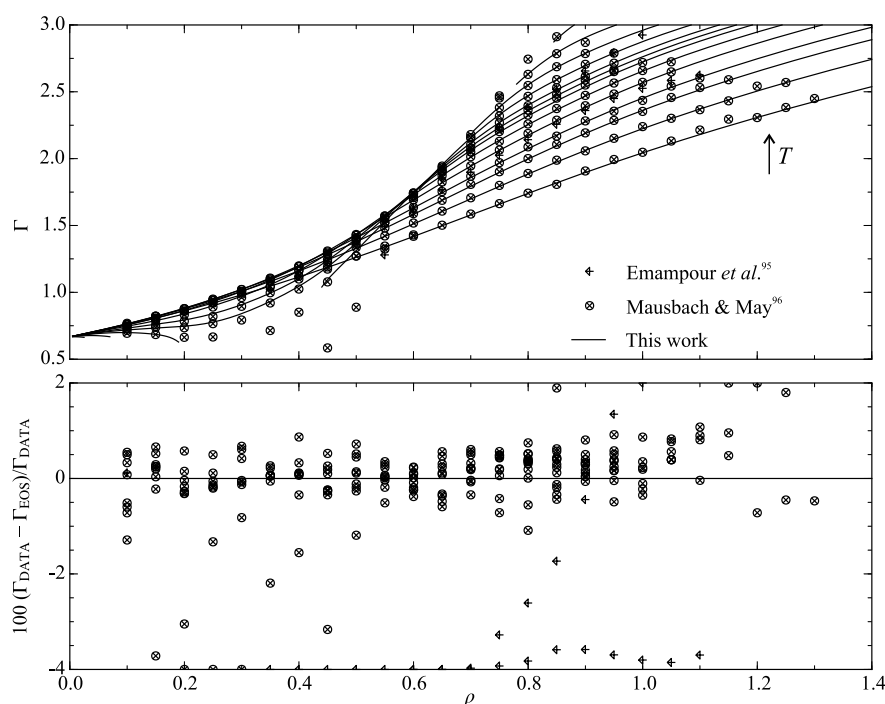


FIG. 26. Comparison of literature data for the Grüneisen coefficient with the present equation of state. Top:  $\Gamma$ - $\rho$  diagram along isotherms. Bottom: Relative deviation of simulated Grüneisen coefficient data from the present equation of state.

simulation. Mausbach and May<sup>96</sup> in particular carried out a comprehensive investigation of the Grüneisen coefficient over a broad range of temperature and density. At least for the Lennard-Jones fluid, they could prove the presumed behavior to be correct. The present EOS follows the trend of the molecular simulation data and the deviation between simulated and calculated data is mostly within 1.5%. The uncertainty increases in the critical region. The simulations of Mausbach and May<sup>96</sup> were carried out in the *NVE* ensemble, where temperature is not an input but measured. Thus, the simulation data slightly scatter around isotherms. However, for the uncertainty

calculation, the measured temperatures of the simulation data were used. The data of Emampour *et al.*<sup>95</sup> were not considered in the uncertainty estimate because they show a systematic negative offset relative to both the data of Mausbach and May<sup>96</sup> and the present EOS.

The speed of sound has not been thoroughly investigated with molecular simulation. Two different data sets are available: May and Mausbach<sup>16</sup> and Lustig.<sup>17</sup> Figure 27 shows relative deviations between the present EOS and the simulation data of about 1%. The uncertainty increases in the vicinity of the critical point.

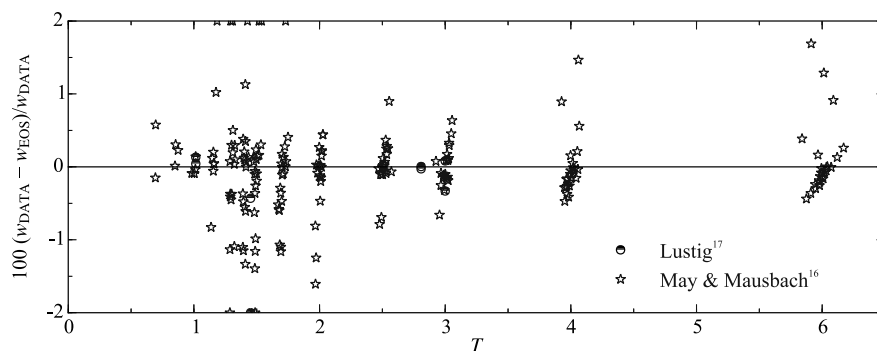


FIG. 27. Relative deviation of literature data for speed of sound from the present equation of state.

## EQUATION OF STATE FOR THE LENNARD-JONES FLUID

023101-31

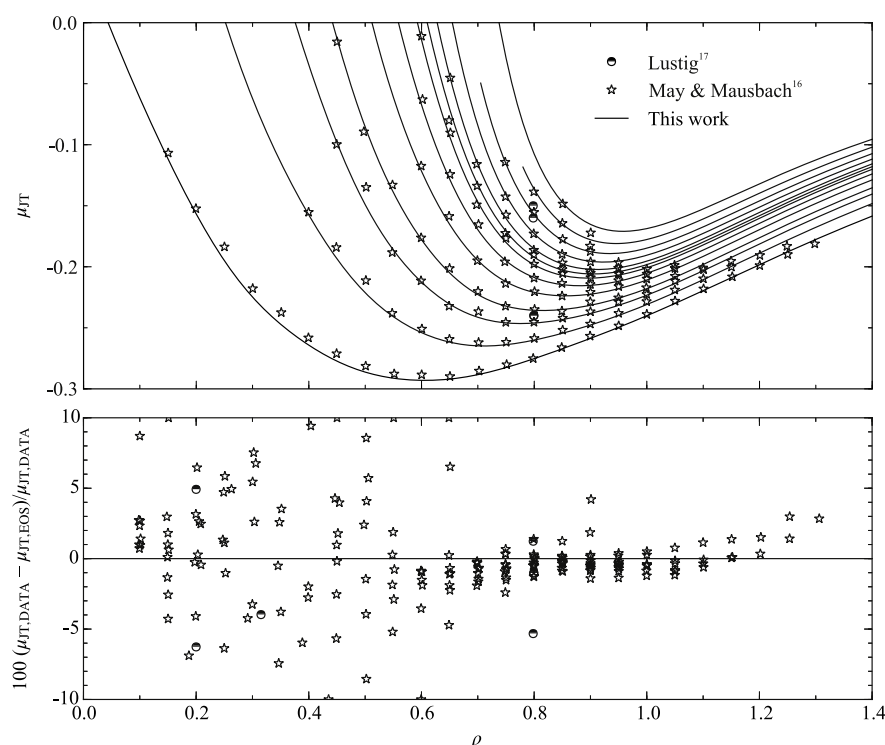


Fig. 28. Comparison of literature data for the Joule–Thomson coefficient with the present equation of state. Top: Joule–Thomson coefficient versus density along isotherms. Bottom: Relative deviation of simulated Joule–Thomson coefficient data from the present equation of state.

The Joule–Thomson coefficient  $\mu_{JT}$  was investigated by Lustig<sup>17</sup> and by May and Mausbach.<sup>16</sup> The top panel of Fig. 28 presents a  $\mu_{JT}$ – $\rho$  diagram with selected isotherms. Over the entire temperature and density range, slopes and curvatures of the present equation of state agree well with the simulation results. The uncertainty for calculated Joule–Thomson coefficient data using the present EOS is estimated to be 2.5% over the entire temperature range and for densities  $\rho \geq 0.6$ . Lower densities go along with larger deviations, which leads to an uncertainty of up to 10%.

The thermal expansion coefficient  $\alpha = 1/v(\partial v/\partial T)_p$ , the isothermal compressibility  $\beta_T = 1/(\rho(\partial \rho/\partial p)_T)$ , and the thermal pressure coefficient  $\gamma = (\partial p/\partial T)_\rho$  are illustrated in Fig. 29. The thermal expansion coefficient was investigated by Adams,<sup>35</sup> McDonald and Singer,<sup>79</sup> and Boda *et al.*<sup>93</sup> Depending on the location on the fluid surface, it is extremely sensitive to the course of isobars in the  $\rho$ – $T$  diagram. Wagner and Thol<sup>121</sup> have shown for water that it is possible to have huge deviations in  $\alpha$  although densities are modeled precisely. Therefore, simulations must be carried out very accurately. New simulations were carried out in this work, which are accurate to within 5% when comparing to the present EOS. The isothermal compressibility and the thermal pressure coefficient are easier to correlate. Reliable data of Meier<sup>14</sup> and May and Mausbach<sup>16</sup> are available for these properties. Calculated data on isothermal compressibility are uncertain by 3% and on pressure coefficient are uncertain by 1%.

### 5.7. Physical behavior and extrapolation

In addition to a comprehensive analysis of thermodynamic properties that are available in the literature, the extrapolation behavior and physical trends of several different properties must be monitored when setting up fundamental equations of state. Figure 30 shows the residual isochoric heat capacity (top) and the speed of sound (bottom), which were monitored during the development of the present EOS. The isochoric heat capacity shows expected behavior, e.g., the increasing heat capacity of the liquid phase extrapolated to low temperatures, the steep increase of the saturated liquid and vapor lines, which meet in a maximum at the critical temperature, and a continuous positive slope and curvature of the saturated vapor line with increasing temperature. The saturated liquid and vapor lines of the speed of sound reach a minimum at the critical temperature, which is related to the maximum of the isochoric heat capacity. Another noticeable trend is a weak positive curvature of the liquid-phase speed of sound extrapolated to low temperatures ( $\partial w/\partial T > 0$ ), which indicates reasonable extrapolation behavior of the EOS.<sup>43</sup> In Fig. 31, temperature as a function of density is shown. Here, it is important that no unreasonable bumps occur in the saturation curves or isobars, and that isobars do not cross each other. Furthermore, the nonlinearity of the rectilinear diameter was minimized as discussed above.

The characteristic ideal curves can be used to assess correct behavior of the equation of state for very high temperatures,

023101-32

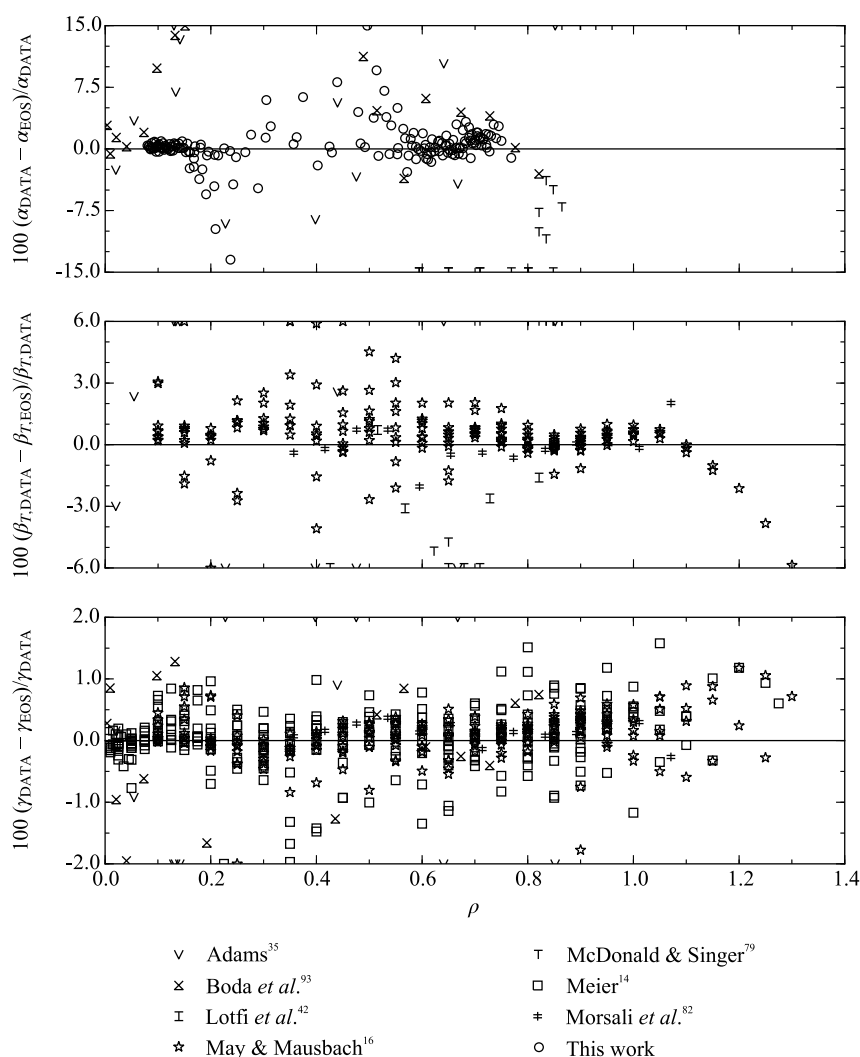
THOL *ET AL.*

FIG. 29. Relative deviation of literature data for thermal expansion coefficient  $\alpha$ , isothermal compressibility  $\beta_T$ , and thermal pressure coefficient  $\gamma$  from the present equation of state.

pressures, and densities.<sup>122</sup> In Fig. 32, the present EOS and that of Mecke *et al.*<sup>5</sup> are shown. Data for the EOS of Mecke *et al.*<sup>5</sup> were compiled with the ThermoC software.<sup>123,124</sup> Additionally, molecular simulation data<sup>125–129</sup> are plotted. The two equations agree at the Boyle, ideal, and Joule–Thomson inversion curves, whereas the Joule inversion curves significantly differ from each other. The molecular simulation data indicate that the course of this curve calculated from the equation of Mecke *et al.*<sup>5</sup> is correct. For all curves, no unphysical bumps or nonmonotonic behavior occurs.

The Grüneisen coefficient as a function of density is shown in Fig. 33. With increasing density, the isotherms should cross each other beyond the critical density. At high temperatures, the Grüneisen coefficient must have a positive slope and negative curvature to ensure correct extrapolation behavior. This is closely related to the bottom plot in Fig. 33, which shows the

Grüneisen coefficient as a function of temperature. This plot looks similar to the speed of sound diagram in Fig. 30. The saturation curves show a steep minimum at the critical temperature. Additionally, isobars for the liquid phase extrapolated to low temperatures are nearly straight lines, with a negative slope. The appropriate course of the Grüneisen coefficient simultaneously ensures correct behavior of the speed of sound, isochoric, and isobaric heat capacity. During the development of the present equation of state, the strategy was found to be much more effective than altering the isochoric heat capacity or the speed of sound directly, which should be taken into consideration in subsequent work.

Another thermodynamic property, established by Venkatarathnam and Oellrich,<sup>130</sup> is the so-called phase identification parameter  $\Pi$ , originally developed to distinguish between vapor and liquid phases without determining the saturation



## EQUATION OF STATE FOR THE LENNARD-JONES FLUID

023101-33

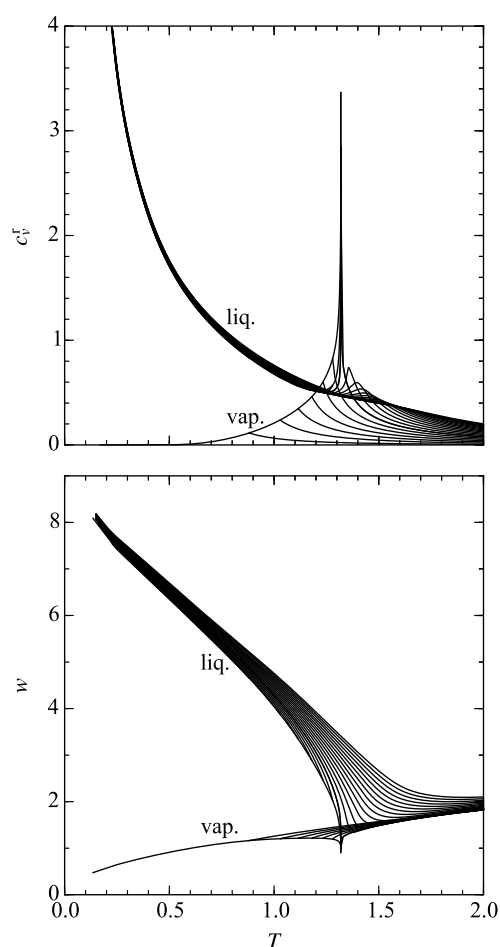


Fig. 30. Top: Residual isochoric heat capacity versus temperature along isobars. Bottom: Speed of sound versus temperature along isobars.

curves. Like the Grüneisen coefficient, this property is not applied for practical purposes. However, in the context of developing equations of state, it may be used to constrain the behavior of EOS correlations. The property is valuable since many different derivatives of the Helmholtz energy are involved (cf. Eq. (26)) and incorrect physical behavior may be detected easily. Figure 34 shows  $\Pi$  along isotherms and isobars. On the top panel, the saturated liquid line shows a negative slope and curvature until the critical density is reached. It exhibits negative slope and positive curvature for increasing density starting at the critical density. Supercritical isotherms form a minimum for  $\rho < \rho_c$ , cross each other at the critical density, and exhibit a maximum in their further course. Any unreasonable behavior of the EOS can easily be detected. Typical problems, which can occur during the fitting procedure, are multiple oscillations of supercritical isotherms and bumps along the saturated liquid line. These problems would also arise in the bottom panel of Fig. 34, where the phase identification parameter is illustrated as a function of

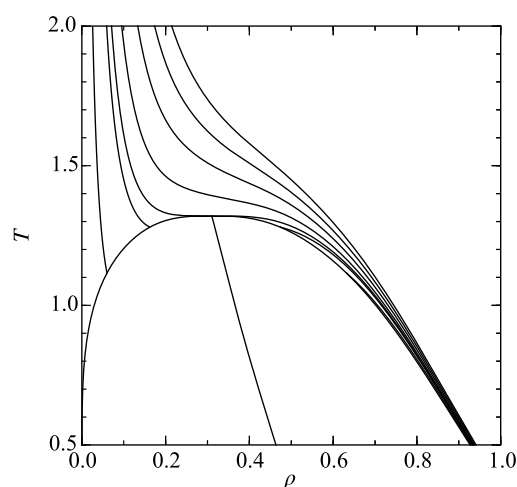


Fig. 31. Temperature versus density along isobars.

temperature along selected isobars. Both saturated liquid and vapor lines have a moderate slope until reaching the vicinity of the critical region. Here, the saturated liquid line increases with distinct positive curvature until it reaches the critical point. In contrast, the saturated vapor line decreases with pronounced negative curvature until reaching the critical point. Supercritical isobars have positive slope and curvature until they reach a maximum at the critical temperature, then they cross each other and converge at high temperatures.

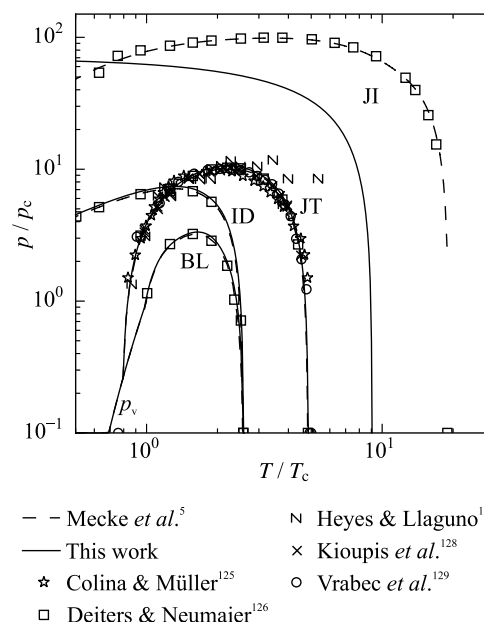


Fig. 32. Characteristic ideal curves as defined by Span and Wagner.<sup>122</sup>  $p_v$ : vapor pressure curve, BL: Boyle curve, ID: ideal curve, JT: Joule-Thomson inversion curve, and JI: Joule inversion curve.

023101-34

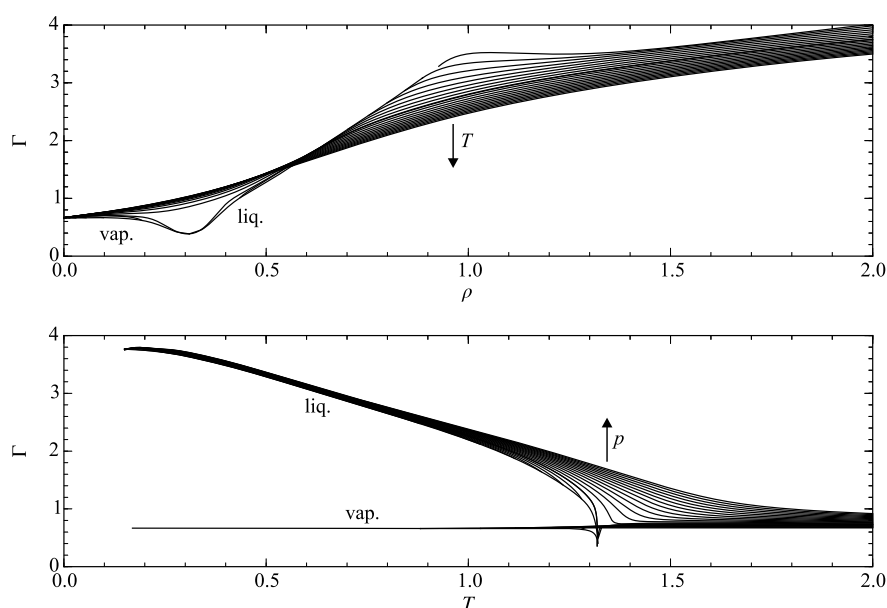
THOL *ET AL.*

Fig. 33. Grüneisen coefficient versus density along isotherms (top) and Grüneisen coefficient versus temperature (bottom) along isobars.

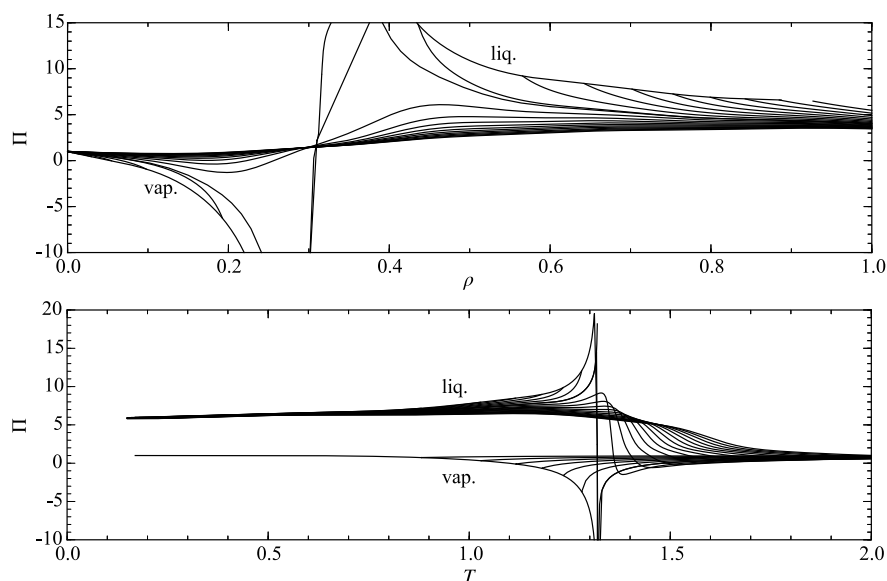


Fig. 34. Phase identification parameter versus density along isotherms (top) and versus temperature along isobars (bottom).

## 6. Conclusion

The fundamental equation of state developed in this work is explicit in the reduced Helmholtz energy and has an exact ideal-gas contribution. The residual part stems from modern fitting techniques and consists of 23 terms. It is valid for reduced temperatures  $0.661 < T < 9$  and for reduced pressures up to  $p = 65$ , corresponding to  $0.5 < T/T_c < 7$  and

$p/p_c = 500$ . For its development, only data for residual Helmholtz energy derivatives and virial coefficients were used. Molecular simulation data from the literature and the equation of state of Mecke *et al.*,<sup>5</sup> which was the best model available in the literature so far, were used to evaluate the present equation comprehensively. The uncertainty of the present EOS is estimated to be 1.8% in vapor pressure and saturated vapor density, and 0.15%–0.5% in saturated liquid density. Uncertainty in

density is 0.1% in the liquid phase, 1% in the gaseous phase, and 0.15%–0.3% in the supercritical region. The uncertainty in pressure amounts to 2% in the critical region. The residual internal energy is reproduced within 1% in the gaseous region, 0.1% in the liquid region, and 1% in the critical and supercritical region. Uncertainty in isochoric heat capacity is 0.5%, whereas the uncertainty in isobaric heat capacity and speed of sound is 1%. The uncertainty of the Grüneisen coefficient is 1.5% and the Joule–Thomson coefficient deviates by 2.5% ( $\rho \leq 0.6$ ) to 10%. The thermal expansion coefficient is reproduced within 15%. The uncertainty of the isothermal compressibility and the thermal pressure coefficient amounts to 3% and 1%, respectively. The overall representation of the simulation data as well as the extrapolation behavior is a significant improvement over existing correlations.

In the supplementary material,<sup>52</sup> molecular simulation data of this work, a fluid file for the application in the software package TREND,<sup>44</sup> and a C++ source code are provided. For the verification of computer implementation, reference values for some properties at different state points are also given.

## Acknowledgments

This work was part of a comprehensive research program supported by the German Research Foundation (DFG). The simulations were carried out on the national supercomputer hazelhen at the High Performance Computing Center Stuttgart (HLRS) within Project No. MMHBF2.

## 7. References

- <sup>1</sup>J. E. Jones, *Proc. R. Soc. A* **106**, 441 (1924).
- <sup>2</sup>J. E. Jones, *Proc. R. Soc. A* **106**, 463 (1924).
- <sup>3</sup>J. K. Johnson, J. A. Zollweg, and K. E. Gubbins, *Mol. Phys.* **78**, 591 (1993).
- <sup>4</sup>J. Kolafa and I. Nezbeda, *Fluid Phase Equilib.* **100**, 1 (1994).
- <sup>5</sup>M. Mecke, A. Müller, J. Winkelmann, J. Vrabec, J. Fischer, R. Span, and W. Wagner, *Int. J. Thermophys.* **17**, 391 (1996); Erratum **19**, 1493 (1998).
- <sup>6</sup>G. Rutkai, M. Thol, R. Lustig, R. Span, and J. Vrabec, *J. Chem. Phys.* **139**, 041102 (2013).
- <sup>7</sup>R. Lustig, *J. Chem. Phys.* **100**, 3060 (1994).
- <sup>8</sup>R. Lustig, *J. Chem. Phys.* **100**, 3068 (1994).
- <sup>9</sup>R. Lustig, *J. Chem. Phys.* **100**, 3048 (1994).
- <sup>10</sup>R. Lustig, *J. Chem. Phys.* **109**, 8816 (1998).
- <sup>11</sup>R. Lustig, *Ber. Bunsen-Ges. Phys. Chem.* **98**, 706 (1994).
- <sup>12</sup>R. Lustig, *Ber. Bunsen-Ges. Phys. Chem.* **99**, 1462 (1995).
- <sup>13</sup>A. Friedrich and R. Lustig, *J. Mol. Liq.* **98–99**, 243 (2002).
- <sup>14</sup>K. Meier, Ph.D. thesis, University of the Federal Armed Forces Hamburg, 2002.
- <sup>15</sup>K. Meier and S. Kabelac, *J. Chem. Phys.* **124**, 064104 (2006).
- <sup>16</sup>H.-O. May and P. Mausbach, *AIP Conf. Proc.* **1501**, 954 (2012).
- <sup>17</sup>R. Lustig, *Mol. Simul.* **37**, 457 (2011).
- <sup>18</sup>R. Lustig, *Mol. Phys.* **110**, 3041 (2012).
- <sup>19</sup>C. W. Glass, S. Reiser, G. Rutkai, S. Deublein, A. Köster, G. Guevara-Carrion, A. Wafai, M. Horsch, M. Bernreuther, and T. Windmann, *Comput. Phys. Commun.* **185**, 3302 (2014).
- <sup>20</sup>B. Widom, *J. Chem. Phys.* **39**, 2808 (1963).
- <sup>21</sup>M. P. Allen and D. J. Tildesley, *Computer Simulation of Liquids* (Clarendon Press, Oxford, 1987).
- <sup>22</sup>D. Levesque and L. Verlet, *Phys. Rev.* **182**, 307 (1969).
- <sup>23</sup>I. R. McDonald and K. Singer, *Mol. Phys.* **23**, 29 (1972).
- <sup>24</sup>Y. Song and E. A. Mason, *J. Chem. Phys.* **91**, 7840 (1989).
- <sup>25</sup>J. J. Nicolas, K. E. Gubbins, W. B. Streett, and D. J. Tildesley, *Mol. Phys.* **37**, 1429 (1979).
- <sup>26</sup>Y. Adachi, I. Fijihara, M. Takamiya, and K. Nakanishi, *Fluid Phase Equilib.* **39**, 1 (1988).
- <sup>27</sup>Y. Miyano, *Fluid Phase Equilib.* **85**, 71 (1993).
- <sup>28</sup>R. Span, *Multiparameter Equations of State: An Accurate Source of Thermodynamic Property Data* (Springer, Berlin, 2000).
- <sup>29</sup>J. A. Barker, P. J. Leonard, and A. Pompe, *J. Chem. Phys.* **44**, 4206 (1966).
- <sup>30</sup>H.-O. May and P. Mausbach, *Phys. Rev. E* **85**, 031201 (2012); Erratum **86**, 059905 (2012).
- <sup>31</sup>U. Setzmann and W. Wagner, *Int. J. Thermophys.* **10**, 1103 (1989).
- <sup>32</sup>J. P. Valleeau (personal communication to Mecke *et al.*, 1996).
- <sup>33</sup>R. J. Wheatley (personal communication, 2013).
- <sup>34</sup>A. Ahmed and R. J. Sadus, *J. Chem. Phys.* **131**, 174504 (2009); Erratum **133**, 229902 (2010).
- <sup>35</sup>D. J. Adams, *Mol. Phys.* **29**, 307 (1975).
- <sup>36</sup>D. J. Adams, *Mol. Phys.* **32**, 647 (1976).
- <sup>37</sup>J.-P. Hansen, *Phys. Rev. A* **2**, 221 (1970).
- <sup>38</sup>J.-P. Hansen and L. Verlet, *Phys. Rev.* **184**, 151 (1969).
- <sup>39</sup>J. Kolafa, H. L. Vörtlér, K. Aim, and I. Nezbeda, *Mol. Simul.* **11**, 305 (1993).
- <sup>40</sup>B. Saager and J. Fischer, *Fluid Phase Equilib.* **57**, 35 (1990).
- <sup>41</sup>L. Verlet, *Phys. Rev.* **159**, 98 (1967).
- <sup>42</sup>A. Lotfi, J. Vrabec, and J. Fischer, *Mol. Phys.* **76**, 1319 (1992).
- <sup>43</sup>E. W. Lemmon, M. O. McLinden, and W. Wagner, *J. Chem. Eng. Data* **54**, 3141 (2009).
- <sup>44</sup>R. Span, T. Eckermann, S. Herrig, S. Hielscher, and M. Thol, *TREND. Thermodynamic Reference and Engineering Data 2.0* (Lehrstuhl für Thermodynamik, Ruhr-Universität Bochum, Bochum, Germany, 2015).
- <sup>45</sup>E. W. Lemmon, M. L. Huber, and M. O. McLinden, *REFPROP. Reference Fluid Thermodynamic and Transport Properties*, Version 9.1 (National Institute of Standards and Technology, Gaithersburg, MD, 2014).
- <sup>46</sup>I. H. Bell, J. Wronski, S. Quoilin, and V. Lemort, *Ind. Eng. Chem. Res.* **53**, 2498 (2014).
- <sup>47</sup>M. A. van der Hoef, *J. Chem. Phys.* **113**, 8142 (2000).
- <sup>48</sup>R. Agrawal and D. A. Kofke, *Mol. Phys.* **85**, 43 (1995).
- <sup>49</sup>J. R. Errington, *J. Chem. Phys.* **120**, 3130 (2004).
- <sup>50</sup>E. A. Mastny and J. J. de Pablo, *J. Chem. Phys.* **127**, 104504 (2007).
- <sup>51</sup>A. Ladd and L. V. Woodcock, *Chem. Phys. Lett.* **51**, 155 (1977).
- <sup>52</sup>See supplementary material at <http://dx.doi.org/10.1063/1.4945000> for numerical test values for the verification of computer implementation, comparisons of the present equation of state with simulated reduced Helmholtz derivatives and residual enthalpies, numerical values of the simulation data generated for this work, the fluid file for the calculation of thermodynamic properties the Lennard-Jones model fluid with Trend,<sup>44</sup> and the C++ source code for the calculation of homogeneous thermodynamic properties of the Lennard-Jones model fluid.
- <sup>53</sup>K. R. S. Shaul, A. J. Schultz, and D. A. Kofke, *Collect. Czech. Chem. Commun.* **75**, 447 (2010).
- <sup>54</sup>R. B. Bird, E. L. Spotz, and J. O. Hirschfelder, *J. Chem. Phys.* **18**, 1395 (1950).
- <sup>55</sup>J. O. Hirschfelder, C. F. Curtiss, and R. B. Bird, *Molecular Theory of Gases and Liquids* (Wiley, New York, 1954).
- <sup>56</sup>T. Sun and A. S. Teja, *J. Phys. Chem.* **100**, 17365 (1996).
- <sup>57</sup>A. Friedrich and R. Lustig, *J. Chem. Phys.* **105**, 9597 (1996).
- <sup>58</sup>T. Breitenstein and R. Lustig, *J. Mol. Liq.* **98–99**, 263 (2002).
- <sup>59</sup>T. Breitenstein, Ph.D. thesis, RWTH Aachen, 2000.
- <sup>60</sup>C. Tegeler, R. Span, and W. Wagner, *J. Phys. Chem. Ref. Data* **28**, 779 (1999).
- <sup>61</sup>R. Gilgen, R. Kleinrahn, and W. Wagner, *J. Chem. Thermodyn.* **26**, 383 (1994).
- <sup>62</sup>M. Thol, G. Rutkai, R. Span, J. Vrabec, and R. Lustig, *Int. J. Thermophys.* **36**, 25 (2015).
- <sup>63</sup>D. J. Adams, *Mol. Phys.* **37**, 211 (1979).
- <sup>64</sup>D. A. Kofke, *J. Chem. Phys.* **98**, 4149 (1993).
- <sup>65</sup>B. Smit and D. Frenkel, *Mol. Phys.* **68**, 951 (1989).
- <sup>66</sup>A. Z. Panagiotopoulos, *Mol. Phys.* **61**, 813 (1987).
- <sup>67</sup>A. Z. Panagiotopoulos, N. Quirke, M. Stapleton, and D. J. Tildesley, *Mol. Phys.* **63**, 527 (1988).
- <sup>68</sup>Because one of the present authors has co-authored Ref. 42, we would like to point out that the employed simulation tool is completely independent of what we have used in the 1990s.
- <sup>69</sup>M. G. Martin and J. I. Siepmann, *J. Phys. Chem. B* **102**, 2569 (1998).
- <sup>70</sup>J. J. Potoff and A. Z. Panagiotopoulos, *J. Chem. Phys.* **112**, 6411 (2000).

023101-36

THOL *ET AL.*

- <sup>71</sup>W. Shi and J. K. Johnson, *Fluid Phase Equilib.* **187–188**, 171 (2001).
- <sup>72</sup>J. E. Hunter and W. P. Reinhardt, *J. Chem. Phys.* **103**, 8627 (1995).
- <sup>73</sup>V. G. Baidakov, G. G. Chernykh, and S. Protsenko, *Chem. Phys. Lett.* **321**, 315 (2000).
- <sup>74</sup>M. Mecke, J. Winkelmann, and J. Fischer, *J. Chem. Phys.* **107**, 9264 (1997).
- <sup>75</sup>R. Lustig, G. Rutkai, and J. Vrabec, *Mol. Phys.* **113**, 910 (2015).
- <sup>76</sup>D. D. Carley, *J. Chem. Phys.* **67**, 4812 (1977).
- <sup>77</sup>W. Fickett and W. W. Wood, *Phys. Fluids* **3**, 204 (1960).
- <sup>78</sup>I. R. McDonald and K. Singer, *J. Chem. Phys.* **50**, 2308 (1969).
- <sup>79</sup>I. R. McDonald and K. Singer, *Discuss. Faraday Soc.* **43**, 40 (1967).
- <sup>80</sup>I. R. McDonald and K. Singer, *J. Chem. Phys.* **47**, 4766 (1967).
- <sup>81</sup>I. R. McDonald and L. V. Woodcock, *J. Phys. C: Solid State Phys.* **3**, 722 (1970).
- <sup>82</sup>A. Morsali, S. A. Beyramabadi, and M. R. Bozorgmehr, *Chem. Phys.* **335**, 194 (2007).
- <sup>83</sup>F. H. Ree, *J. Chem. Phys.* **73**, 5401 (1980).
- <sup>84</sup>P. Schofield, *Comput. Phys. Commun.* **5**, 17 (1973).
- <sup>85</sup>M. S. Shaw, *J. Chem. Phys.* **89**, 2312 (1988).
- <sup>86</sup>G. M. Sowers and S. I. Sandler, *Fluid Phase Equilib.* **67**, 127 (1991).
- <sup>87</sup>W. B. Streett, H. J. Raveché, and R. D. Mountain, *J. Chem. Phys.* **61**, 1960 (1974).
- <sup>88</sup>S. Toxvaerd and E. Praestgaard, *J. Chem. Phys.* **53**, 2389 (1970).
- <sup>89</sup>L. Verlet and D. Levesque, *Physica* **36**, 254 (1967).
- <sup>90</sup>J. D. Weeks, D. Chandler, and H. C. Andersen, *J. Chem. Phys.* **55**, 5422 (1971).
- <sup>91</sup>W. W. Wood, in *Physics of Simple Liquids*, edited by H. N. V. Temperley, J. S. Rowlinson, and G. S. Rushbrooke (North Holland Publishing Company, Amsterdam, 1968), pp. 115–230.
- <sup>92</sup>W. W. Wood and F. R. Parker, *J. Chem. Phys.* **27**, 720 (1957).
- <sup>93</sup>D. Boda, T. Lukács, J. Liszi, and I. Szalai, *Fluid Phase Equilib.* **119**, 1 (1996).
- <sup>94</sup>I. Szalai, J. Liszi, and J. Fischer (private communication to Mecke *et al.*, 1994).
- <sup>95</sup>J. S. Emampour, A. Morsali, S. A. Beyramabadi, M. R. Bozorgmehr, and K. Khakzadan, *Int. J. Phys. Sci.* **6**, 5731 (2011).
- <sup>96</sup>P. Mausbach and H.-O. May, *Fluid Phase Equilib.* **366**, 108 (2014).
- <sup>97</sup>R. Span and W. Wagner, *J. Phys. Chem. Ref. Data* **25**, 1509 (1996).
- <sup>98</sup>R. Span, E. W. Lemmon, R. T. Jacobsen, W. Wagner, and A. Yokozeki, *J. Phys. Chem. Ref. Data* **29**, 1361 (2000).
- <sup>99</sup>J. A. Zollweg and G. W. Mulholland, *J. Chem. Phys.* **57**, 1021 (1972).
- <sup>100</sup>A. Linhart, C.-C. Chen, J. Vrabec, and H. Hasse, *J. Chem. Phys.* **122**, 144506 (2005).
- <sup>101</sup>D. O. Dunikov, S. P. Malysenko, and V. V. Zhakhovskii, *J. Chem. Phys.* **115**, 6623 (2001).
- <sup>102</sup>J. M. Caillol, *J. Chem. Phys.* **109**, 4885 (1998).
- <sup>103</sup>S. Hess, *Physica A* **267**, 58 (1999).
- <sup>104</sup>J. J. Potoff and A. Z. Panagiotopoulos, *J. Chem. Phys.* **109**, 10914 (1998).
- <sup>105</sup>B. Smit, *J. Chem. Phys.* **96**, 8639 (1992).
- <sup>106</sup>S. H. Sung and D. Chandler, *Phys. Rev. A* **9**, 1688 (1974).
- <sup>107</sup>D. J. Adams, E. M. Adams, and G. J. Hills, *Mol. Phys.* **38**, 387 (1979).
- <sup>108</sup>A. Amadei, G. Apol, G. Chillemi, H. J. C. Berendsen, and A. Di Nola, *Mol. Phys.* **96**, 1469 (1999).
- <sup>109</sup>S. Kim, D. Henderson, and J. A. Barker, *Can. J. Phys.* **47**, 99 (1969).
- <sup>110</sup>D. A. Kofke, *Mol. Phys.* **78**, 1331 (1993).
- <sup>111</sup>N. K. Koutras, V. I. Harismiadis, and D. P. Tassios, *Fluid Phase Equilib.* **77**, 13 (1992).
- <sup>112</sup>J. Sýs and A. Malijevský, *Collect. Czech. Chem. Commun.* **45**, 977 (1980).
- <sup>113</sup>V. Arp, J. M. Persichetti, and G.-b. Chen, *J. Fluids Eng.* **106**, 193 (1984).
- <sup>114</sup>M. Thol, G. Rutkai, A. Köster, M. Kortmann, R. Span, and J. Vrabec, *Chem. Eng. Sci.* **121**, 87 (2015); Erratum **134**, 887 (2015).
- <sup>115</sup>M. Thol, F. Dubberke, G. Rutkai, T. Windmann, A. Köster, R. Span, and J. Vrabec, *Fluid Phase Equilib.* **418**, 133 (2016).
- <sup>116</sup>M. Thol and E. W. Lemmon, *Int. J. Thermophys.* **37**, 28 (2016).
- <sup>117</sup>R. Akasaka, Y. Zhou, and E. W. Lemmon, *J. Phys. Chem. Ref. Data* **44**, 013104 (2015).
- <sup>118</sup>H. Gedanitz, M. J. Davila, and E. W. Lemmon, *J. Chem. Eng. Data* **60**, 1331 (2015).
- <sup>119</sup>Y. Zhou, J. Liu, S. G. Penoncello, and E. W. Lemmon, *J. Phys. Chem. Ref. Data* **43**, 043105 (2014).
- <sup>120</sup>M. Thol, E. W. Lemmon, and R. Span, *High Temp. - High Pressures* **41**, 81 (2012).
- <sup>121</sup>W. Wagner and M. Thol, *J. Phys. Chem. Ref. Data* **44**, 043102 (2015).
- <sup>122</sup>R. Span and W. Wagner, *Int. J. Thermophys.* **18**, 1415 (1997).
- <sup>123</sup>U. K. Deiters, ThermoC software, University of Cologne, <http://thermoc.uni-koeln.de/index.html> (accessed March 9, 2016).
- <sup>124</sup>U. K. Deiters, *Chem. Eng. Technol.* **23**, 581 (2000).
- <sup>125</sup>C. M. Colina and E. A. Müller, *Int. J. Thermophys.* **20**, 229 (1999).
- <sup>126</sup>U. K. Deiters and A. Neumaier, "Computer simulation of the characteristic curves of pure fluids," *J. Chem. Eng. Data* (in press).
- <sup>127</sup>D. M. Heyes and C. T. Llaguno, *Chem. Phys.* **168**, 61 (1992).
- <sup>128</sup>L. I. Kioupis, G. Arya, and E. J. Maginn, *Fluid Phase Equilib.* **200**, 93 (2002).
- <sup>129</sup>J. Vrabec, G. K. Kedia, and H. Hasse, *Cryogenics* **45**, 253 (2005).
- <sup>130</sup>G. Venkatarathnam and L. Oellrich, *Fluid Phase Equilib.* **301**, 225 (2011).

### 3.8 Fundamental equation of state for ethylene oxide based on a hybrid dataset

M. Thol, G. Rutkai, **A. Köster**, M. Kortmann, R. Span, J. Vrabec, *Chemical Engineering Science* 121:87-99, 2015 und 134:887-890, 2015.

DOI: [doi.org/10.1016/j.ces.2014.07.051](https://doi.org/10.1016/j.ces.2014.07.051)

Nachgedruckt mit Erlaubnis von Elsevier (Copyright 2015).

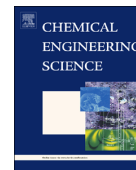
In dieser Arbeit wurde eine neuartige hybride Zustandsgleichung für Ethylenoxid erstellt. Obwohl dieser Stoff ein wichtiges Zwischenprodukt in der Herstellung verschiedener Chemikalien ist, sind zu wenige experimentelle Daten vorhanden, um eine hochwertige empirische Zustandsgleichung daran anzupassen. Hybride Zustandsgleichungen zeichnen sich dadurch aus, dass sowohl Daten aus der molekularen Simulation als auch experimentelle Daten für deren Korrelation verwendet werden. Die mit Hilfe des Lustig-Formalismus [Lus11, Lus12] berechneten partiellen Ableitungen der Helmholtzenergie ermöglichten eine effiziente Nutzung der Simulationsdaten im Anpassungsprozess der Gleichung und tragen insbesondere dazu bei, dass der Gültigkeitsbereich von Gleichungen die nur auf Experimenten beruhen vergrößert wird.

Der Autor der vorliegenden Dissertation hat alle für diese Veröffentlichungen zugrundeliegenden molekularen Simulationen der partiellen Ableitungen der Helmholtzenergie durchgeführt. Diese wurden von Dr. Monika Thol verwendet um eine hybride helmholtzexplizite Zustandsgleichung zu erstellen. Der Autor übernahm die Konsolidierung des Manuskripts. Weiterhin verfasste der Autor in Zusammenarbeit mit Dr. Gábor Rutkai die Beschreibungen über die zugrundeliegenden Simulationsmethoden und -parameter. Die Überarbeitung des Manuskripts wurde in Zusammenarbeit mit Prof. Roland Span und Prof. Jadran Vrabec durchgeführt. Der Autor wurde während des gesamten Prozesses von Prof. Jadran Vrabec betreut.



Contents lists available at ScienceDirect

## Chemical Engineering Science

journal homepage: [www.elsevier.com/locate/ces](http://www.elsevier.com/locate/ces)

## Fundamental equation of state for ethylene oxide based on a hybrid dataset

Monika Thol<sup>a</sup>, Gábor Rutkai<sup>b</sup>, Andreas Köster<sup>b</sup>, Mirco Kortmann<sup>a</sup>,  
Roland Span<sup>a</sup>, Jadran Vrabec<sup>b,\*</sup><sup>a</sup> Lehrstuhl für Thermodynamik, Ruhr-Universität Bochum, Universitätsstr. 100, 44801 Bochum, Germany<sup>b</sup> Lehrstuhl für Thermodynamik und Energietechnik, Universität Paderborn, Warburger Str. 100, 33098 Paderborn, Germany

## HIGHLIGHTS

- An empirical fundamental equation of state (FEOS) is presented for ethylene oxide.
- The FEOS can be used to calculate all thermodynamic properties.
- The underlying dataset consists of experimental and molecular simulation data.

## ARTICLE INFO

## Article history:

Received 26 April 2014

Received in revised form

18 July 2014

Accepted 26 July 2014

Available online 2 August 2014

## Keywords:

Thermodynamic properties  
Fundamental equation of state  
Molecular simulation  
Ethylene oxide

## ABSTRACT

An empirical fundamental equation of state correlation is presented for ethylene oxide. The correlation is explicit in terms of the Helmholtz energy and it can be used to calculate all thermodynamic properties. The underlying dataset consists of experimental and molecular simulation data. The experimental data cover almost exclusively the gaseous phase and are available for temperatures from the triple point up to the critical point. Molecular simulation data are used to extend the validity to the liquid state and up to a maximum temperature of 1000 K and a maximum pressure of 700 MPa.

© 2014 Elsevier Ltd. All rights reserved.

## 1. Introduction

A sufficient amount of reliable thermodynamic data is essential for the design and optimization of almost any process in the chemical industry. Currently, databases alone cannot meet the increasing requirements of process engineering. Mapping the entire thermodynamic property spectrum of a given fluid is often impossible using laboratory experiments due to the associated financial cost, time investment, and potentially extreme measuring conditions. Empirical equations of state (EOS) correlations are one solution for this problem, because they rationalize and summarize experimental data, offering a built-in interpolation and extrapolation scheme for general engineering purposes. Empirical correlations that represent the fundamental equation of state (FEOS) are particularly beneficial (Span, 2000). A FEOS can be expressed in terms of various thermodynamic potentials. However, independent on which representation is chosen, it contains

the complete property information about the system: once a thermodynamic potential is explicitly given as a function of its natural variables, every other thermodynamic property is simply a combination of its derivatives with respect to its natural variables.

The construction of a FEOS that covers the entire fluid region of industrial relevance typically faces the problem of scarce experimental input data. Molecular modeling and simulation have evolved to a point of acceptance in the applied sciences and are a potential solution to satisfy the need for thermodynamic data. Molecular simulation yields macroscopic properties exclusively from microscopic information. Accordingly, its predictive capabilities are, in principle, only limited by the quality of the molecular interaction model that represents the investigated substance. While molecular simulation techniques (Monte Carlo and molecular dynamics) have a huge advantage over experimental measurements when it comes to speed and cost efficiency, the number of molecular interaction models that can really offer an alternative to laboratory measurements, not just on the qualitative, but also on the quantitative level, increased significantly only over the last decade (Industrial fluid properties simulation collective). Extreme temperatures or pressures are not limiting factors for molecular

\* Corresponding author. Tel.: +49 5251 60 2421; fax: +49 5251 60 3522.  
E-mail address: [jadran.vrabec@upb.de](mailto:jadran.vrabec@upb.de) (J. Vrabec).

**Table 1**Parameters for the residual part of the reduced Helmholtz energy  $\alpha^r(\tau, \delta)$  according to Eq. (4).

$k$	$n_k$	$t_k$	$d_k$	$l_k$	$\eta_k$	$\lambda_k$	$\gamma_k$	$\epsilon_k$
1	0.3805675D–01	1.000	4					
2	0.1359482D+01	0.312	1					
3	–0.1833370D+01	0.860	1					
4	–0.5754450D+00	1.114	2					
5	0.1536490D+00	0.500	3					
6	–0.1598130D+01	2.100	1	2				
7	–0.6826090D+00	1.700	3	2				
8	0.6436960D+00	0.754	2	1				
9	–0.5353070D+00	2.500	2	2				
10	–0.1872220D–01	0.900	7	1				
11	0.1238840D+01	2.180	1		1.010	1.12	0.874	0.7202
12	–0.4315460D+00	3.500	1		1.650	2.16	0.617	0.9110
13	–0.2295870D+00	2.340	3		0.896	0.91	0.476	0.6880
14	–0.1931280D+02	4.330	3		22.000	196.00	1.24	0.9100
15	–0.5283590D–01	3.900	2		1.730	0.13	0.562	1.2100

**Table 2**

Experimental data for ethylene oxide from the literature. The original units were converted into SI units and the temperature is given in terms of the international temperature scale of 1990 standard (ITS-90). Data points calculated from an ancillary equation are marked with an asterisk.

Source	Year	Data points	Temperature range (K)	Pressure range (MPa)
<b>Homogeneous density</b>				
Lide (2005) <sup>a</sup>	2005	1	273.15	0.101325
Walters and Smith (1952) <sup>a</sup>	1952	81	294–428	0.006–3.448
Overall <sup>b</sup>		82	273–428	0.006–3.448
<b>Vapor pressure</b>				
Calado et al. (1996)	1996	1	182.33	0.0001
Chao et al. (1986)	1986	1	283.71	0.101325
Coles and Popper (1950)	1950	17	273–305	0.067–0.221
Giauque and Gordon (1949)	1949	14	223–286	0.004–0.108
Giles and Wilson (2006)	2006	2	298–349	0.174–0.767
Gillespie et al. (1985)	1985	2	283–299	0.101–0.174
Hess and Tilton (1950)	1950	1	293.14	0.1462
Kistiakowsky and Rice (1940)	1940	1	283.84	0.101325
Lide (2005)	2005	3	283–284	0.101–0.100
Maass and Boomer (1922)	1922	21	216–286	0.002–0.110
McDonald et al. (1959)	1959	11	284–239	0.103–0.012
Mock and Smith (1950)	1950	10	322–423	0.379–3.827
Olson (1977)	1977	3	273–324	0.065–0.394
Frenkel et al. (2013)*	2013	17	160–469	0.000–7.207
Walters and Smith (1952)	1952	12	294–469	0.151–7.192
Overall <sup>b</sup>		99	182–423	0.000–3.827
<b>Saturated liquid density</b>				
Auwers (1918)	1918	2	279.20	–
Comelli and Francesconi (1991)	1991	11	288–304	–
Comelli and Francesconi (1995)	1995	1	298.15	–
Comelli and Francesconi (1996)	1996	2	298–314	–
Francesconi and Comelli (1994)	1994	1	298.15	–
Francesconi and Comelli (1995)	1995	1	298.15	–
Maass and Boomer (1922)	1922	16	222–294	–
Olson (1977)	1977	3	273–324	–
Perkin (1893)	1893	1	280.15	–
Frenkel et al. (2013)*	2013	17	160–469	–
Walters and Smith (1952)	1952	12	294–469	–
Wurtz (1859)	1859	1	273.15	–
Overall <sup>b</sup>		51	222–469	–
<b>Saturated vapor density</b>				
Olson (1977)	1977	3	273–324	–
Frenkel et al. (2013)	2013	20	377–469	–
Walters and Smith (1952)	1952	12	294–469	–
Overall <sup>b</sup>		15	273–469	–
<b>Speed of sound</b>				
Hurly (2002)	2002	334	285–440	0.049–1.020
Overall <sup>b</sup>		334	285–440	0.049–1.020
<b>Isobaric heat capacity</b>				
Giauque and Gordon (1949)	1949	22	166–284	Vapor pressure
Overall <sup>b</sup>		22	166–284	Vapor pressure



Table 2 (continued)

Source	Year	Data points	Temperature range (K)	Pressure range (MPa)
<b>Enthalpy of vaporization</b>				
Cox and Pilcher (1970)	1970	1	298.10	–
Rowley et al. (2006)* <sup>c</sup>	2006	30	160–423	–
Giauque and Gordon (1949)	1949	1	283.65	–
Lange and Dean (1973)	1973	1	283.75	–
Lide (2005)	2005	2	283–299	–
Company (1980)*	1980	5	233–294	–
Reid et al. (1977)	1977	1	283.66	–
Timmermans (1965)	1965	1	288.10	–
Walters and Smith (1952)*	1952	11	294–461	–
Washburn (1926–1933)	(1926–1933)	1	286.10	–
Yaws (1977)*	1977	15	173–454	–
Overall <sup>b</sup>		8	283–299	–
<b>Ideal isobaric heat capacity</b>				
Chao et al. (1986)	1986	27	100–2999	–
Dorofeeva (1992)	1992	16	100–1501	–
Frenkel et al. (1994)*	1994	291	50–1500	–
Godnev and Morozov (1948)	1948	9	298–1001	–
Guenthard et al. (1950)	1950	3	307–372	–
Guenthard and Heilbronner (1948)	1948	8	298–774	–
Hurly (2002)	2002	12	285–441	–
Kistiakowsky and Rice (1940)	1940	3	307–372	–
Lange and Dean (1973)	1973	5	298–1001	–
Ramasamy and Srinivasacharya (1978)	1978	12	100–1001	–
Sundaram (1963)	1963	8	100–2503	–
Vvedenskii (1969)	1969	14	298–1500	–
Walters and Smith (1952)	1952	12	294–478	–
Overall <sup>b</sup>		129	100–2999	–

<sup>a</sup> One of the data points is located in the two-phase region and was thus neglected in the following.

<sup>b</sup> The overall values do not include any data derived from ancillary equations.

<sup>c</sup> Calculated from the Clausius–Clapeyron equation.

simulation, and any thermodynamic property is obtainable from such calculations, including the derivatives of the chosen thermodynamic potential of the FEOS.

Ethylene oxide is the 14th most produced organic chemical and its global production rate is expected to exceed 27 million tons per year by 2017. Due to its chemical reactivity, it is a vital chemical compound used as an intermediate to produce a wide range of consumer products and other non-consumer chemicals. Its reactive nature also makes the substance itself particularly hazardous: it is carcinogenic, mutagenic, and highly flammable at room temperature. It is not a surprise that the experimental data available in the literature are too few to support FEOS development. Therefore, the approach of combining the available experimental data with straightforwardly obtainable molecular simulation data is one option for constructing a hybrid dataset as a basis for FEOS correlation (Rutkai et al., 2013), which was the target of this work.

## 2. Fundamental equation of state correlation

The present FEOS correlation is explicit in terms of the Helmholtz energy  $a$ , which can be separated into an ideal gas part  $a^0$  and a residual part  $a^r$

$$\alpha(T, \rho) = \frac{a^0(T, \rho) + a^r(T, \rho)}{RT} = \alpha^0(\tau, \delta) + \alpha^r(\tau, \delta), \quad (1)$$

with the inverse reduced temperature  $\tau = T_c/T$ , the reduced density  $\delta = \rho/\rho_c$ , and the molar gas constant  $R = 8.3144621 \text{ J mol}^{-1} \text{ K}^{-1}$  (Mohr et al., 2012) (for specific calculations the molar mass  $M = 44.05256 \text{ g mol}^{-1}$  should be used). The critical temperature  $T_c = 468.92 \text{ K}$  was taken from Walters and Smith (1952) and the critical density  $\rho_c = 7.32 \text{ mol dm}^{-3}$  was determined during the present fit. The ideal contribution  $\alpha^0$  can be calculated from the

isobaric heat capacity of the ideal gas state  $c_p^0$

$$\frac{c_p^0}{R} = 4 + \sum_{k=3}^5 v_k \frac{(u_k/T)^2 \exp(u_k/T)}{[\exp(u_k/T) - 1]^2}, \quad (2)$$

where  $u_3 = 1330 \text{ K}$ ,  $u_4 = 2170 \text{ K}$ ,  $u_5 = 4470 \text{ K}$ ,  $v_3 = 6.79$ ,  $v_4 = 4.53$ ,  $v_5 = 3.68$ . The ideal part of the reduced Helmholtz energy  $\alpha^0$ , integrated from Eq. (2), is

$$\alpha^0 = \ln \delta + 3 \ln \tau + a_1 + a_2 \tau + \sum_{k=3}^5 v_k \ln[1 - \exp(-u_k \tau / T_c)], \quad (3)$$

where  $a_1 = 7.2881975$ ,  $a_2 = -2.782872$ , while  $u_k$  and  $v_k$  are the same as those in Eq. (2). The integration constants  $a_1$  and  $a_2$  were specified such that the enthalpy  $h = 0 \text{ kJ kg}^{-1}$  and the entropy  $s = 0 \text{ kJ kg}^{-1} \text{ K}^{-1}$  at  $T_0 = 298.15 \text{ K}$  and  $p_0 = 1 \text{ atm}$ , and the corresponding ideal gas density is  $\rho_0 = p_0/(RT_0)$ . A comparison of Eq. (2) with the available literature data is shown in Fig. 1. The  $c_p^0$  values used in the fit were published by Chao et al. (1986). The uncertainty of Eq. (2) is  $\pm 0.1\%$  for temperatures above  $T = 350 \text{ K}$ . For lower temperatures, the deviations increase up to  $\pm 0.5\%$ .

The empirical formula that represents the residual part of the reduced Helmholtz energy  $\alpha^r$  consists of five polynomial, five exponential, and five Gaussian bell-shaped terms

$$\begin{aligned} \alpha^r(\tau, \delta) = & \sum_{k=1}^5 n_k \tau^{t_k} \delta^{d_k} + \sum_{k=6}^{10} n_k \tau^{t_k} \delta^{d_k} \exp(-\delta^{l_k}) \\ & + \sum_{k=11}^{15} n_k \tau^{t_k} \delta^{d_k} \exp(-\eta_k(\delta - c_k)^2 - \lambda_k(\tau - \gamma_k)^2). \end{aligned} \quad (4)$$

Table 1 lists the corresponding parameters. Non-analytic terms (Span, 2000) for the critical region of ethylene oxide were not considered in this work due to their complexity and the poor experimental data situation.



### 3. Underlying dataset

#### 3.1. Experimental data

Although ethylene oxide is important for the chemical industry, the corresponding experimental data are very limited. Table 2 summarizes all experimental data that are available in the literature, and Fig. 2 shows the distribution of these data with respect to the homogeneous regions.

For the homogeneous density there is only one comprehensive dataset by Walters and Smith (1952). Additionally, there is only a single data point located in the liquid region (but not at saturation), which was published by Lide (2005). However, during the data preparation it turned out that this data point is actually located within the two-phase region so that it was not considered in the following. Hence, there are only experimental density data available for the gaseous phase. The situation is almost the same for the speed of sound. The only measurements were made by Hurly (2002) for the gaseous phase. All remaining experimental

data are associated with the vapor–liquid equilibrium (VLE). For the vapor pressure, 99 data points are available, but most of them were measured at temperatures below 310 K. For the saturated liquid density, only 51 data points were published, and again, most

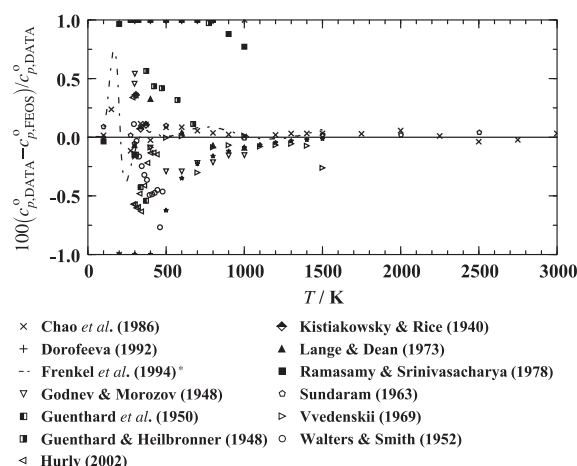


Fig. 1. Comparison of Eq. (2) with experimentally obtained and theoretically derived  $c_p^0$  values. The asterisk marks an ancillary equation.

Table 3

Average absolute relative deviations between experimental or simulation results and the values calculated from the present fundamental equation of state.

Source	AAD/%					
	Vap.	Liq.	Crit.	LD	MD	HD
<b>Simulation data (this work)</b>						
$A_{00}^E$	5.78	0.79	1.30	3.68	9.45	4.01
$A_{01}^E$	7.37	14.0	1.05	2.61	2.26	9.33
$A_{02}^E$	78.6	9.54	4.74	17.4	4.19	10.3
$A_{10}^E$	4.11	0.67	4.06	5.27	1.78	0.82
$A_{11}^E$	5.30	6.10	2.33	3.36	1.38	3.02
$A_{20}^E$	10.7	5.33	13.6	6.54	8.31	6.91
<b>Homogeneous density</b>						
Walters and Smith (1952)	0.28					
<b>Speed of sound</b>						
Hurly (2002)	0.05					
<b>Isobaric heat capacity</b>						
Giauque and Gordon (1949)		0.22				
<b>Enthalpy of vaporization</b>						
Giauque and Gordon (1949)	0.02					
Lange and Dean (1973)	0.11					
Lide (2005)	0.13					
Washburn (1926–1933)	0.54					
Cox and Pilcher (1970)	0.53					
Reid et al. (1977)	0.29					
Timmermans (1965)	0.84					
Eckl et al. (2008)	2.05					
This work	1.01					
<b>Ideal isobaric heat capacity</b>						
Chao et al. (1986)	0.54					
Dorofeeva (1992)	0.49					
Guenthard and Heilbronner (1948)	0.65					
Guenthard et al. (1950)	0.37					
Hurly (2002)	0.40					
Kistiakowsky and Rice (1940)	0.18					
Lange and Dean (1973)	0.12					
Ramasamy and Srinivasacharya (1978)	1.25					
Walters and Smith (1952)	0.36					
Sundaram (1963)	0.04					
Godnev and Morozov (1948)	0.27					
Vvedenskii (1969)	0.10					

(Vap.) homogeneous vapor phase.

(Liq.) homogeneous liquid phase.

(Crit.)  $0.98T_c < T < 1.1T_c$  and  $0.7\rho_c < \rho < 1.4\rho_c$ .

(LD)  $\rho < 0.6\rho_c$  and  $T > T_c$ .

(MD)  $0.6\rho_c \leq \rho \leq 1.5\rho_c$  and  $T > T_c$ .

(HD)  $\rho > 1.5\rho_c$  and  $T > T_c$ .

Table 4

Average absolute relative deviations between experimental or simulated VLE data and the values calculated from the present fundamental equation of state.

Source	AAD/%		
	LT	MT	HT
<b>Vapor pressure</b>			
Olson (1977)	0.41	1.03	
Calado et al. (1996)	1.23		
Chao et al. (1986)		0.13	
Coles and Popper (1950)	1.23	0.31	
Giauque and Gordon (1949)	0.16	0.07	
Giles and Wilson (2006)		0.55	
Hess and Tilton (1950)		0.74	
Kistiakowsky and Rice (1940)		0.67	
Lide (2005)	0.18	0.17	
Maass and Boomer (1922)	0.97	0.70	
McDonald et al. (1959)	0.18	0.31	
Walters and Smith (1952)		0.41	1.74
Mock and Smith (1950)		7.52	
Gillespie et al. (1985)		0.93	
This work	22.80	1.77	
<b>Saturated liquid density</b>			
Olson (1977)	0.21	0.15	
Wurtz (1859)	0.25		
Walters and Smith (1952)		1.36	4.27
Perkin (1893)	0.31		
Maass and Boomer (1922)	0.11	0.78	
Francesconi and Comelli (1995)		1.67	
Francesconi and Comelli (1994)		1.68	
Comelli and Francesconi (1995)		1.47	
Comelli and Francesconi (1996)		2.08	
Comelli and Francesconi (1991)		1.36	
Auwers (1918)	0.22		
This work	0.33	0.34	
<b>Saturated vapor density</b>			
Walters and Smith (1952)		2.58	19.13
Olson (1977)	1.51	4.86	

(LT)  $T < 0.6T_c$ .

(MT)  $0.6T_c \leq T \leq 0.98T_c$ .

(HT)  $T > 0.98T_c$ .

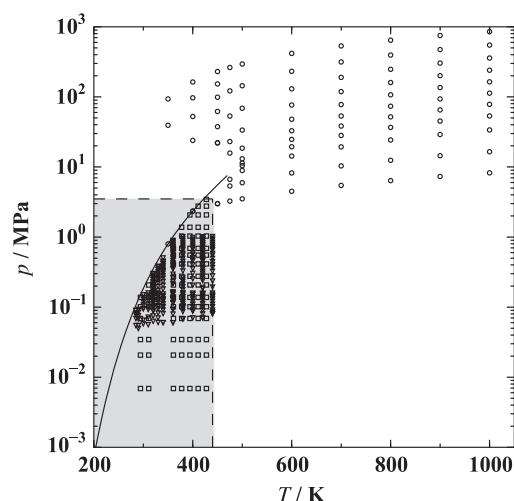


Fig. 2. The gray box indicates the experimental data that are available in the homogeneous gaseous phase, consisting of density (squares) and speed of sound (triangles) values. Molecular simulation data were generated in this work, containing six different Helmholtz energy derivatives at each state point (circles).

of them were measured in the lower temperature region. For the saturated vapor density as well as for the isobaric heat capacity of the saturated liquid, only one dataset is available. Finally, there are eight data points for the enthalpy of vaporization that are in a narrow temperature range from 283 K to 299 K.

### 3.2. Molecular simulation data

The experimental data situation for ethylene oxide shows that it is a suitable fluid to apply the approach of fitting a FEOS on the basis of a hybrid dataset as introduced by Rutkai et al. (2013). This method is supported by the statistical mechanical formalism proposed by Lustig (2011, 2012). The formalism was designed to yield any derivative of the residual Helmholtz energy  $A_{xy}^r = \partial^{x+y} \alpha^r(T, \rho) / \partial (1/T)^x \partial \rho^y \cdot (1/T)^x \rho^y$  (for  $x > 0$  or  $y > 0$ ) from a single molecular simulation run for a given state point, yielding exactly those derivatives that are required by the FEOS to calculate any thermodynamic property as a combination of these derivatives. This approach offers a convenient route to obtain an arbitrary number of truly independent thermodynamic properties, and its capability to support FEOS development was recently tested (Rutkai et al., 2013). In the present work, an extensive dataset was generated containing the six derivatives  $A_{00}^r, A_{10}^r, A_{01}^r,$

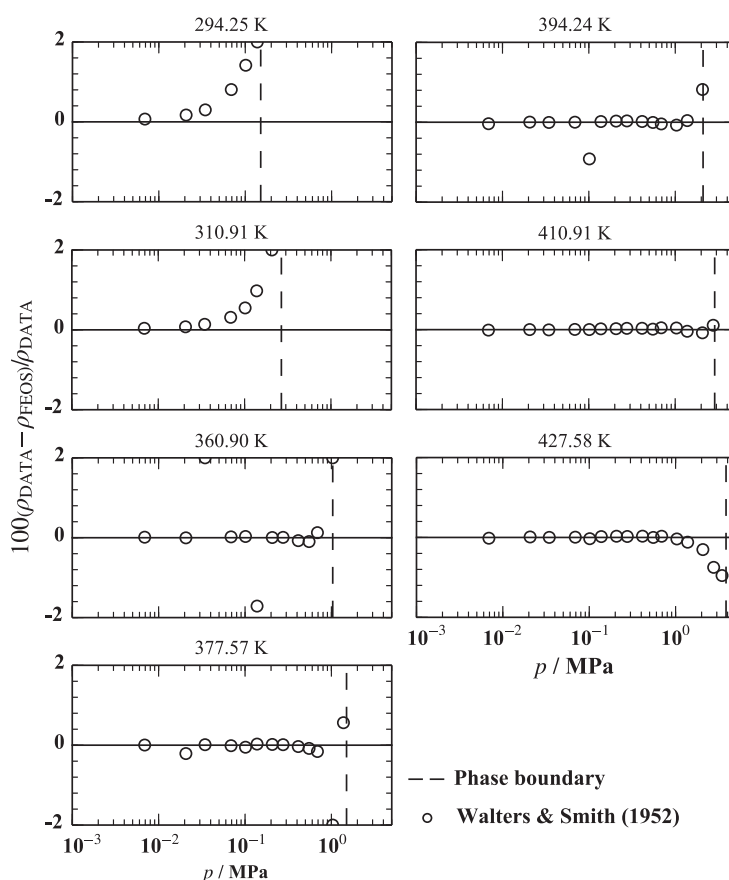


Fig. 3. Comparison of the present fundamental equation of state with homogeneous density measurements by Walters and Smith (1952).

$A_{20}^r$ ,  $A_{11}^r$ , and  $A_{02}^r$  at 92 state points that are well distributed in the homogeneous fluid regions using the molecular simulation tool *ms2* (Deublein et al., 2011; Glass et al., in press). The potential accuracy of the results is, of course, limited by the underlying molecular interaction potential model. However, our previous findings showed that molecular models tend to perform well in the homogeneous fluid regions when comparing  $A_{xy}^r$  simulation results to available FEOS correlations if the molecular model was optimized to experimental VLE data (Rutkai et al., 2013).

#### 4. Simulation details

At each state point 500 particles were sufficiently equilibrated and then sampled for 2 million production cycles with NVT Monte Carlo simulations (Frenkel and Smit, 2002). Electrostatic long-range corrections were approximated by the reaction field method (Barker and Watts, 1973). The residual Helmholtz energy was determined by Widom's test particle insertion (Widom, 1963). The simulations were based on a molecular interaction model by Eckl et al. (2008), which won the Fourth Industrial Fluid Properties Simulation Challenge in 2008 (Case et al., 2008). It consists of three Lennard-Jones (LJ) sites and a point dipole located at the geometric center of the molecule. Two sites were used to represent the methylene groups via the united atom approach, the third one represents the oxygen atom. The internal degrees of freedom were neglected due to the relatively small size of the molecule. The corresponding molecular parameters can be found in Eckl et al. (2008) and in the Appendix. The model was optimized using

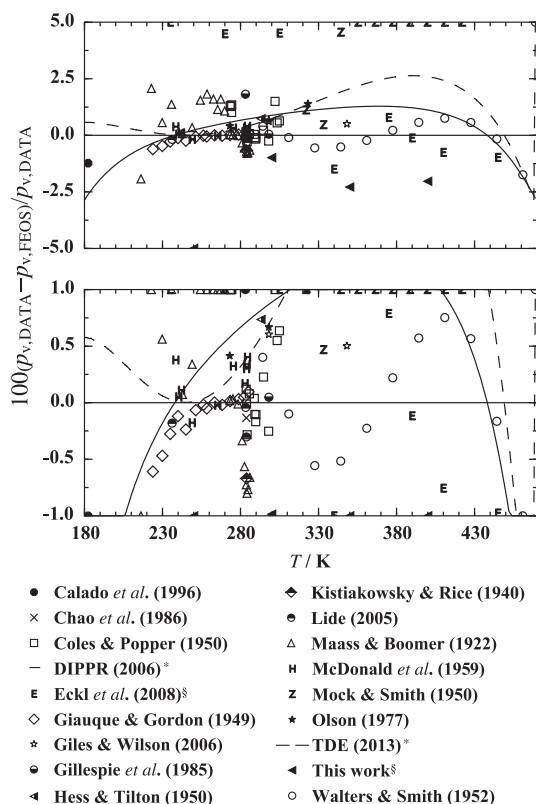


Fig. 4. Comparison of the present fundamental equation of state with vapor pressure data. The asterisk marks ancillary equations and the paragraph symbol stands for molecular simulation data.

the correlations by DIPPR (Rowley et al., 2006) for vapor pressure, saturated liquid density, and heat of vaporization.

#### 5. Evaluation of the fundamental equation of state

The accuracy of the FEOS was determined by comparisons of calculated property values to experimental and simulation data. The present statistical comparisons are based on the relative

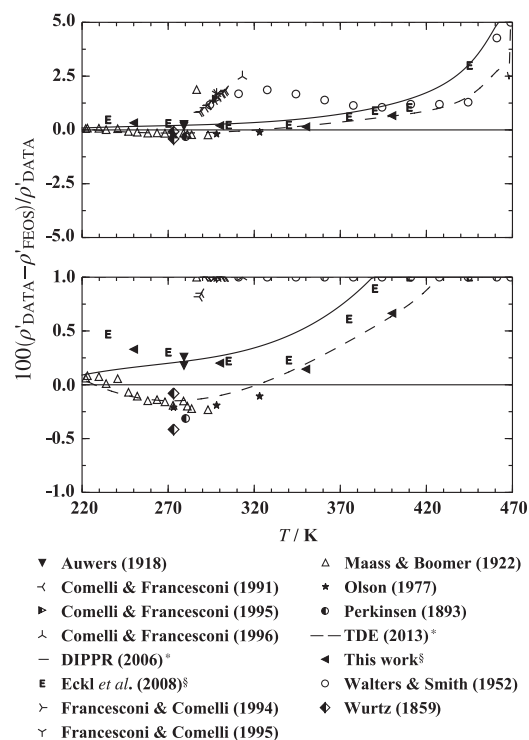


Fig. 5. Comparison of the present fundamental equation of state with saturated liquid density data. The asterisk marks ancillary equations and the paragraph symbol stands for molecular simulation data.

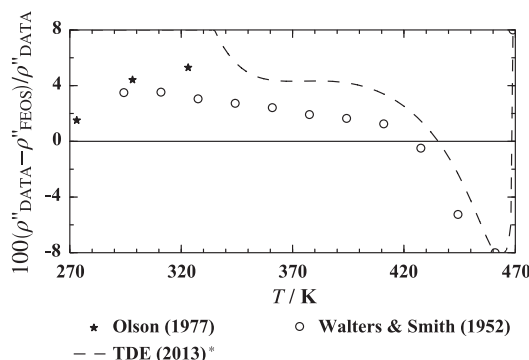


Fig. 6. Comparison of the present fundamental equation of state with saturated vapor density data. The asterisk marks ancillary equations.

deviation of a given property  $X$ , defined as

$$\Delta X = 100 \left( \frac{X_{\text{data}} - X_{\text{FEOS}}}{X_{\text{data}}} \right). \quad (5)$$

With this definition, the average absolute relative deviation is defined as

$$\text{AAD} = \frac{1}{N} \sum_{i=1}^N |\Delta X_i|, \quad (6)$$

where  $N$  is the number of data points. Average absolute relative deviations between experimental data and values calculated from the FEOS are given for different properties in [Tables 3 and 4](#). [Table 3](#) compiles these deviations separately for the vapor phase, the liquid phase, the critical region, and three density ranges of the supercritical region. Saturation properties were also compared with the FEOS, i.e. not with the ancillary equations that are given in Appendix A. The comparisons for vapor pressure and saturated densities were divided

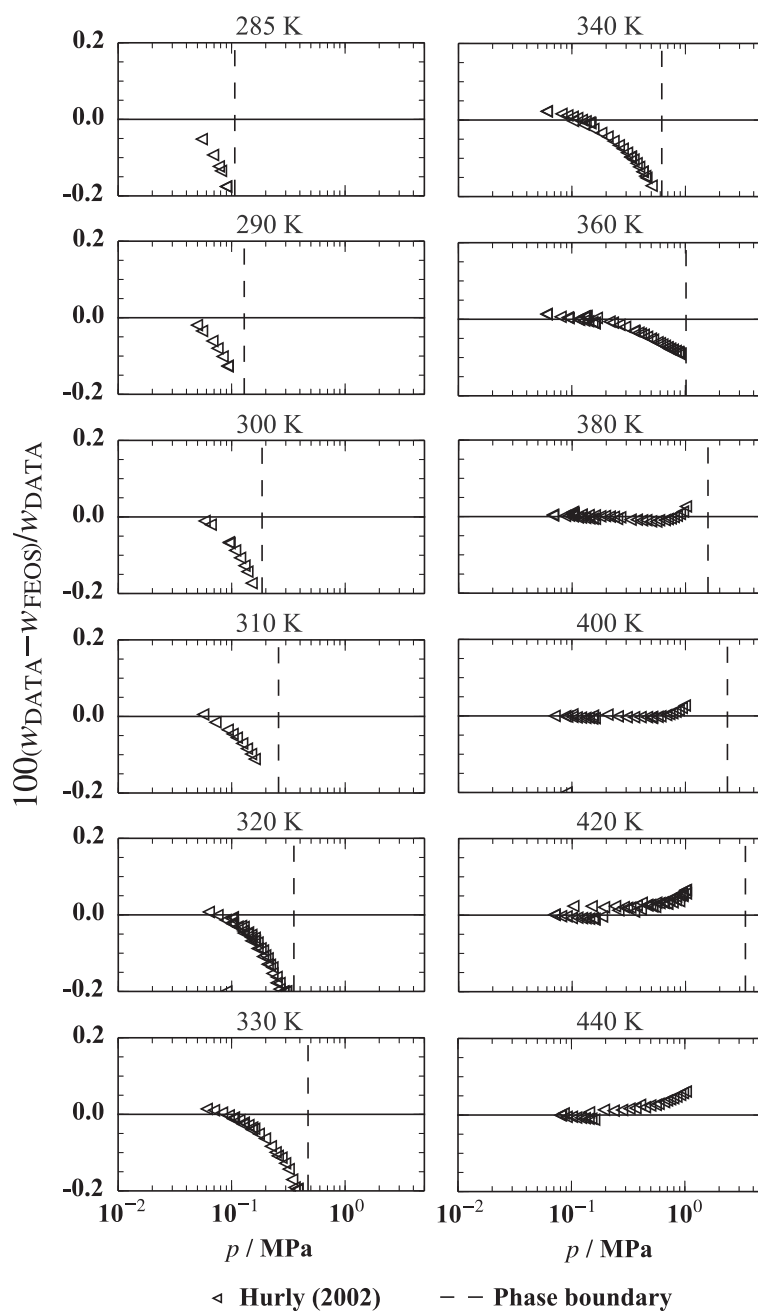


Fig. 7. Comparison of the present fundamental equation of state with experimental speed of sound data by [Hurly \(2002\)](#).

into three different ranges of the reduced temperature  $T/T_c$ , cf. Table 4.

As mentioned above, there are only homogeneous density data available for the gaseous phase. Fig. 3 shows the deviations of the FEOS from the data by Walters and Smith (1952). For temperatures below  $T=360$  K, the deviations were within 0.6%. Higher temperatures were reproduced within 0.1%. Approaching the phase boundary, deviations increase up to 2.5%. As shown in the following, these authors also measured VLE data, which are not consistent with other available data. Thus, the increasing deviations near the phase boundary may be due to a problem within the measurements. Further experimental measurements are needed to verify this assumption.

In Fig. 4, comparisons for the vapor pressure are presented. The first plot shows that most of the data were measured up to  $T=300$  K. For higher temperatures, there are only experimental data by Walters and Smith (1952) that were reproduced within 0.8%. One single data point measured by Giles and Wilson (2006) at  $T=348.15$  K was reproduced within 0.5%. Because it is the only available data point, it can only be treated as a rough guide for the reasonable behavior of the FEOS in that region. Ancillary equations provided by DIPPR (Rowley et al., 2006) and by the Thermo Data Engine (TDE) (Frenkel et al., 2013) were also taken into account. Both equations were developed independently, but they agree within an uncertainty of 2%. Molecular simulation data by Eckl et al. (2008) and simulation results from this work are shown for completeness. In the second plot, the vapor pressure deviations are shown with a higher resolution. For  $220\text{ K} < T < 300\text{ K}$  several datasets are available. Measurements by Giauque and Gordon (1949) ( $\text{AAD}_{\text{LT}} = 0.16\%$ ,  $\text{AAD}_{\text{MT}} = 0.07\%$ ) were reproduced within 0.1% for  $T > 235$  K. Data at lower temperatures were within 0.6%. Data by Coles and Popper (1950) ( $\text{AAD}_{\text{LT}} = 1.23\%$ ,  $\text{AAD}_{\text{MT}} = 0.31\%$ ) were represented within 0.3% for  $T > 280$  K, and those by McDonald et al. (1959) ( $\text{AAD}_{\text{LT}} = 0.18\%$ ) scatter within 0.4%. Below this region ( $T < 220$  K) different trends can be noticed. The ancillary equation from TDE (Frenkel et al., 2013) agrees with the present FEOS within 0.7%. The opposite trend can be seen for the ancillary equation by DIPPR (Rowley et al., 2006). Further measurements are required to definitively determine which source is more correct.

Fig. 5 shows comparisons for the saturated liquid density. Again, two different temperature ranges can be noticed. In the upper temperature range ( $T > 310$  K), only measurements by Walters and Smith (1952) are available. Compared to the data by Maass and Boomer (1922), an offset of about 1.7% at  $T=290$  K can be observed. Between  $288\text{ K} < T < 314\text{ K}$  there are several datasets by Comelli and Francesconi (1991, 1995, 1996); Francesconi and Comelli (1994, 1995) available. These support the trend of the measurements of Walters and Smith (1952). However, fitting these data would lead to an unphysical bend in the phase boundary, and they were thus not included in the present fit. To verify the data by Maass and Boomer (1922) ( $\text{AAD}_{\text{LT}} = 0.11\%$ ,  $\text{AAD}_{\text{MT}} = 0.78\%$ ) that are within 0.2%, measurements between  $273\text{ K} < T < 323\text{ K}$  were provided by Olson (1977) ( $\text{AAD}_{\text{LT}} = 0.21\%$ ). They were also reproduced within 0.3%. Again, ancillary equations by DIPPR (Rowley et al., 2006) and TDE (Frenkel et al., 2013) were used to obtain an impression whether the trend of the present FEOS is reasonable. Up to  $T=385$  K, the DIPPR equation (Rowley et al., 2006) was reproduced within 1%. The TDE (Frenkel et al., 2013) calculations follow the FEOS within 1% up to  $T=425$  K. For both ancillary equations, the deviations are larger in the higher temperature region. This trend could be caused due to fitting the ancillary equations to the data by Walters and Smith (1952), which show the systematic offset discussed before.

For the saturated vapor density, only the two datasets by Walters and Smith (1952) and Olson (1977) were published.

Because of large deviations they were not considered in the present fit. The deviation plot, including the ancillary equation of TDE (Frenkel et al., 2013), can be found in Fig. 6. A DIPPR correlation is not available.

The speed of sound was investigated by Hurly (2002). Hurly (2002) reported a general uncertainty of their apparatus of 0.01%. Because he does not give any information regarding the sample preparation, an overall uncertainty of about 0.1% for these data was assumed. Fig. 7 shows that most of the data were represented within 0.15% for  $T < 360$  K. Approaching the phase boundary, the deviations increase up to 0.2%. Data at higher temperatures were reproduced within the claimed uncertainty of 0.1%.

In Fig. 8, comparisons of the FEOS for the heat of vaporization and the isobaric heat capacity of the saturated liquid are illustrated. A few experimental data points are available for the heat of vaporization. Data by Giauque and Gordon (1949) and Lide (2005) were represented within 0.22%. Other measurements were fitted within 1%. Additionally, several correlations, i.e. TDE (Frenkel et al., 2013), DIPPR (Rowley et al., 2006) and Yaws (1977), were considered. They show different trends, and further experimental measurements are needed to decide which one is correct. For the isobaric heat capacity of the saturated liquid phase, data by Giauque and Gordon (1949) were considered. They were reproduced within 0.7%.

As mentioned above, there are only VLE and gas phase laboratory measurements available. Therefore, molecular simulation data based on the molecular model by Eckl et al. (2008) were applied to the FEOS fit. In this way, the homogeneous liquid phase

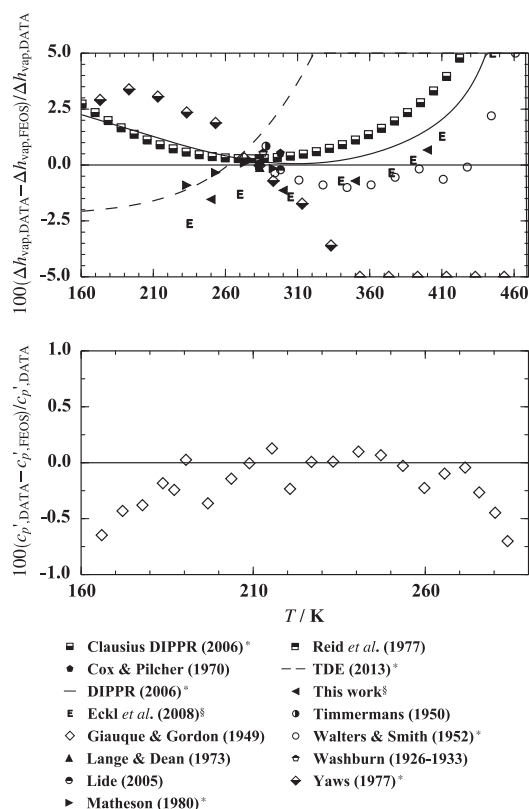
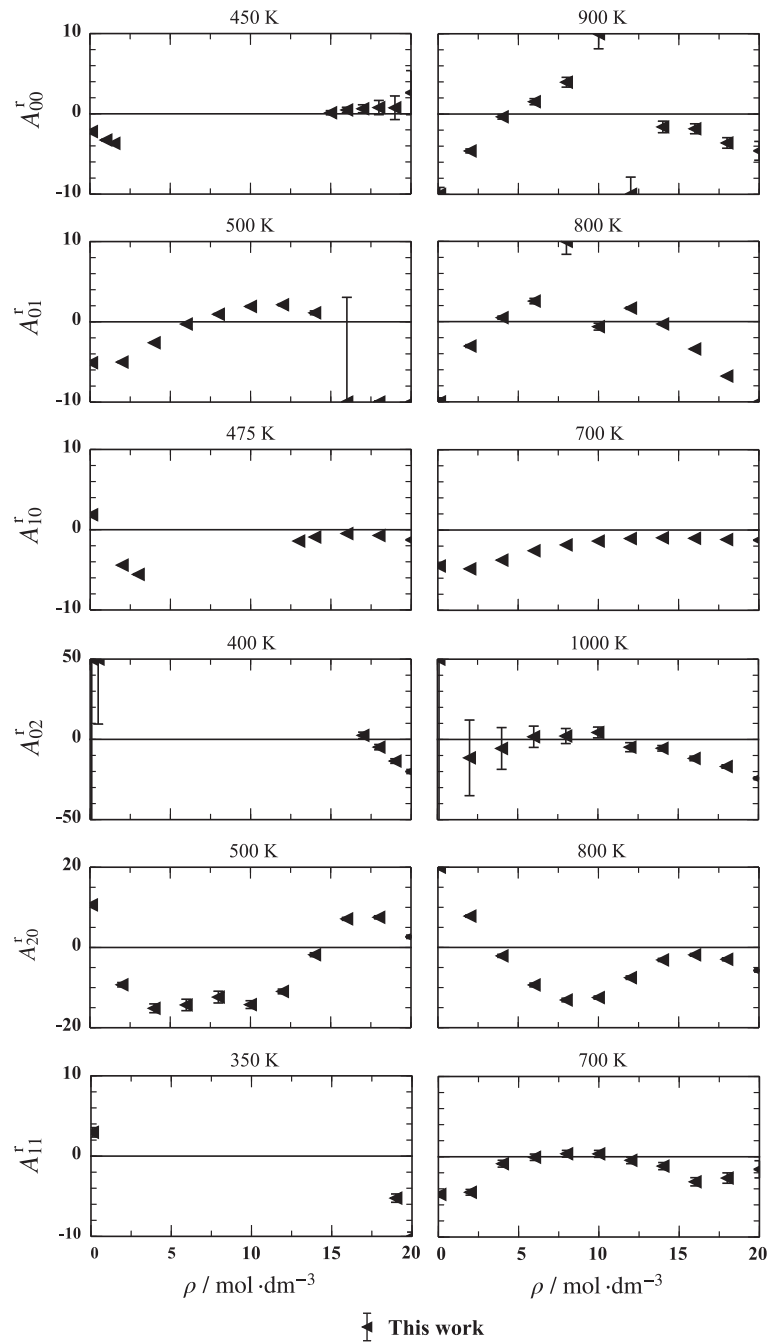


Fig. 8. Comparisons of the present fundamental equation of state for the enthalpy of vaporization (top) and the isobaric heat capacity of the saturated liquid phase (bottom). The asterisk marks ancillary equations and the paragraph symbol denotes molecular simulation data.



**Fig. 9.** Relative deviations between the present fundamental equation of state and simulation data for different  $A_{xy}^r$  along selected isotherms.

as well as the supercritical region can be described. Fig. 9 shows selected deviations of the residual Helmholtz energy  $A_{00}^r$  as well as its derivatives  $A_{xy}^r$  up to the second order. Note that

$$\begin{aligned}
 A_{xy} &= A_{xy}^0 + A_{xy}^r = \tau^x \delta^y \frac{\partial^{x+y} \alpha(\tau, \delta)}{\partial \tau^x \partial \delta^y} \\
 &= (1/T)^x \rho^y \frac{\partial^{x+y} \alpha(1/T, \rho)}{\partial (1/T)^x \partial \rho^y},
 \end{aligned} \quad (7)$$

for  $\tau = T_c/T$  and  $\delta = \rho/\rho_c$ , because the critical values of temperature  $T_c$  and density  $\rho_c$  are constants. Comprehensive comparisons of all simulation data can be found in the supplementary material. Overall, the deviations are as follows:  $A_{00}^r = 5\%$ ,  $A_{01}^r = 6\%$ ,  $A_{10}^r = 5\%$ ,  $A_{02}^r = 20\%$ ,  $A_{20}^r = 15\%$ , and  $A_{11}^r = 5\%$ . For all properties, deviations increase for low densities, where the fluid approaches ideal gas behavior. This is likely caused by two factors: (1) The contribution from the residual Helmholtz energy to the total

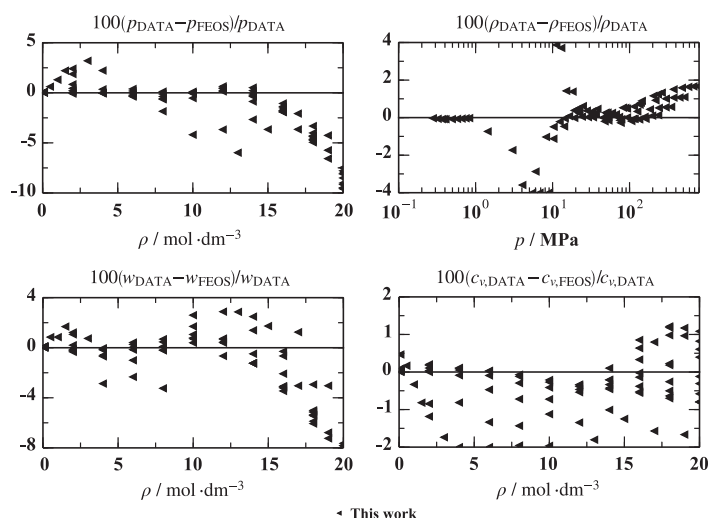


Fig. 10. Comparison of the present fundamental equation of state with thermodynamic properties obtained from molecular simulation data.

property  $A_{xy}^r$  becomes smaller with decreasing density. (2) The numerical values of the derivatives  $A_{xy}^r$  become significantly smaller in absolute terms with decreasing density, thus the error of molecular modeling is more pronounced when deviations with respect to the FEOS are expressed in relative terms. Additionally, isotherms crossing the zero line have to be taken into account. For example at  $T=450$  K, the property  $A_{00}^r$  changes from negative to positive between  $\rho = 10 \text{ mol dm}^{-3}$  and  $\rho = 12 \text{ mol dm}^{-3}$ . This behavior can also be found for  $A_{01}^r$  at  $T=500$  K between  $\rho = 14 \text{ mol dm}^{-3}$  and  $\rho = 16 \text{ mol dm}^{-3}$  and at  $T=800$  K between  $\rho = 8 \text{ mol dm}^{-3}$  and  $\rho = 10 \text{ mol dm}^{-3}$ . Despite the fact that the residual Helmholtz energy and its derivatives are not common fluid properties, the  $A_{xy}^r$  values are related to well known properties like pressure  $p$ , speed of sound  $w$ , isobaric heat capacity  $c_p$ , and isochoric heat capacity  $c_v$

$$\frac{p}{\rho RT} = 1 + A_{01}^r, \quad (8)$$

$$\frac{Mw^2}{RT} = 1 + 2A_{01}^r + A_{02}^r - \frac{(1 + A_{01}^r - A_{11}^r)^2}{A_{20}^0 + A_{20}^r}, \quad (9)$$

$$\frac{c_p}{R} = -(A_{20}^0 + A_{20}^r) + \frac{(1 + A_{01}^r - A_{11}^r)^2}{1 + 2A_{01}^r + A_{02}^r}, \quad (10)$$

$$\frac{c_v}{R} = -(A_{20}^0 + A_{20}^r), \quad (11)$$

where  $M$  is the molar mass. Fig. 10 shows that the overall deviation of 6% in terms of  $A_{01}^r$  causes deviations of about 4% in terms of pressure. Because the speed of sound and the heat capacities are calorific properties, the second derivative of the ideal Helmholtz energy with respect to the temperature  $A_{20}^0$  is needed. It was calculated from Eq. (2). In addition to the ideal part,  $A_{01}^r$ ,  $A_{02}^r$ ,  $A_{11}^r$ , and  $A_{20}^r$  are involved. Although deviations between 5% and 20% occur for these properties, deviations in terms of density, isochoric heat capacity, and speed of sound are 2%, 2%, and 4%, respectively. Deviations increase for higher densities.

Special attention was given to physically reasonable behavior of the FEOS. Therefore, several thermodynamic properties, e.g. speed of sound, isochoric and isobaric heat capacity, VLE, virial coefficients, and the ideal curves, were studied. Fig. 11 shows a summary of the most important diagrams. The extrapolation

behavior of the thermodynamic properties is well-known (Lemmon and Jacobsen, 2005; Lemmon et al., 2009), and all of these plots show physically reasonable properties. In the  $T$  versus  $\rho$  diagram (Fig. 11, top left) the rectilinear diameter is a straight line up to the critical point and the critical isotherm shows a distinctive saddle point at the critical point. In the  $p$  versus  $\rho$  diagram (Fig. 11, top right) the isotherms should converge, but not cross each other at high temperatures, pressures, and densities. The speed of sound (Fig. 11, center left) should show a negative slope and no curvature at low temperatures in the hypothetical liquid phase. As expected, the saturated liquid and vapor lines meet as a minimum at the critical point. For the residual isochoric heat capacity (Fig. 11, center right), the saturated liquid line has a positive curvature and rises towards low temperatures. Related to the minimum at the critical point of the speed of sound, a maximum for the residual isochoric heat capacity can be observed. The second and third thermal virial coefficients  $B$  and  $C$  should be negative for low temperatures, cross the zero line once, and then approach zero after passing through a maximum. For  $B$ , the maximum occurs at the Boyle temperature, and for  $C$ , the maximum occurs at the critical point. The ideal curves should be smooth and show no unusual curvature. Except for small irregularities in the Joule and Joule-inversion curves, the ideal curves (Fig. 11, bottom right) show a reasonable behavior.

## 6. Conclusion

A fundamental equation of state for ethylene oxide was presented. It is given in terms of the Helmholtz energy and can be used to calculate all thermodynamic properties, including density, heat capacities, speed of sound, enthalpy, internal energy, and vapor–liquid equilibria. It is based on a hybrid dataset so that two different classifications for the range of validity have to be made. The experimental data cover temperatures from the triple point up to the critical point. Ethylene oxide was experimentally investigated only little so that the range of validity covered by experimental data includes the homogeneous vapor phase and the vapor–liquid equilibrium. Based on these investigations and a careful analysis of the extrapolation behavior, the range of validity based on experimental data is over a temperature range from the triple point  $T_{tr}$  to 500 K, with a maximum pressure of



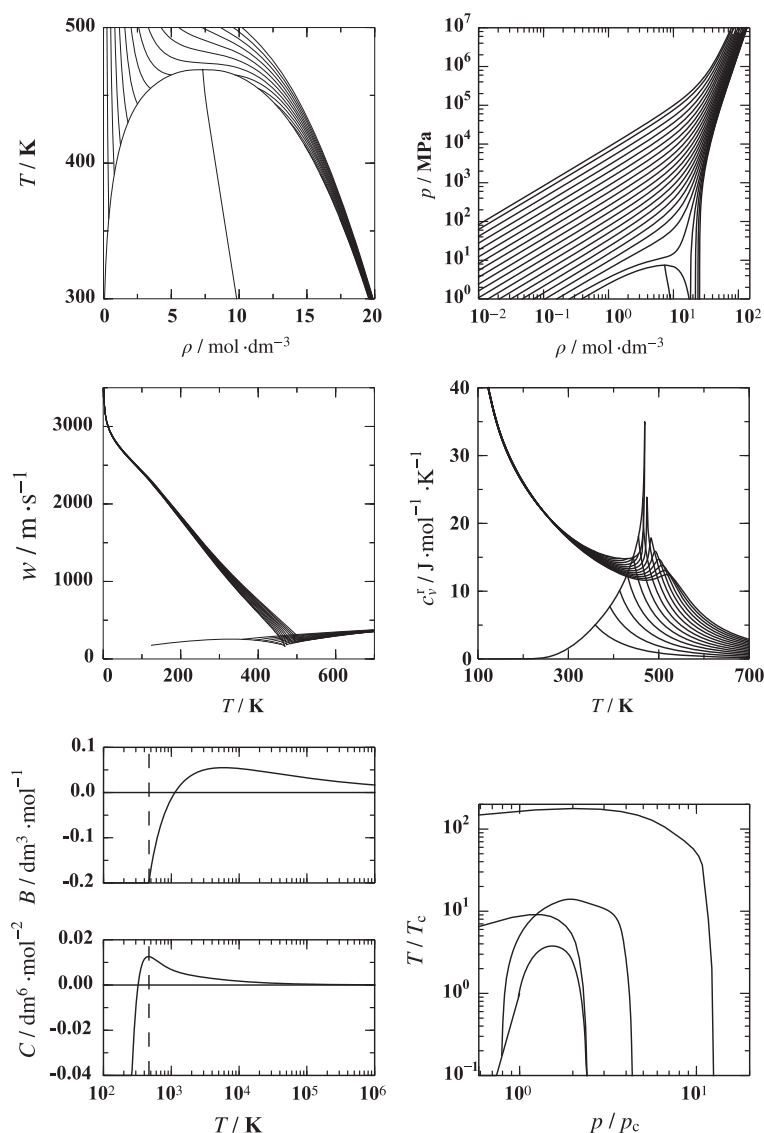


**Fig. 11.** Physical behavior of some thermodynamic properties: VLE curves together with the rectilinear diameter (top left),  $p\rho T$  data at extreme conditions (top right), speed of sound (center left), residual isochoric heat capacity (center right), second and third virial coefficients (bottom left), and ideal curves (bottom right).

**Table 5**

Calculated values of properties for algorithm verification.

$T/K$	$p/\text{MPa}$	$\rho/\text{mol dm}^{-3}$	$h/\text{J mol}^{-1}$	$s/\text{J mol}^{-1} \text{K}^{-1}$	$c_v/\text{J mol}^{-1} \text{K}^{-1}$	$c_p/\text{J mol}^{-1} \text{K}^{-1}$	$w/\text{m s}^{-1}$	$a/\text{J mol}^{-1}$
200 <sup>a</sup>	0.0007171788	22.4762797391	−33442.98983	−122.0751209	54.1084845521	81.5266043374	1794.54046849	−9027.99755819
200 <sup>b</sup>	0.0007171788	0.0004315688	−4103.02312658	24.6247126168	28.276210133	36.6153026833	220.943064557	−10689.7605167
300 <sup>a</sup>	0.1852431635	19.5606827885	−25005.6597986	−88.0098778297	58.0568818562	89.6975069336	1152.98334772	1387.83337153
300 <sup>b</sup>	0.1852431635	0.0776886235	−298.78451672	−5.6536268902	41.4426537002	51.8388241926	254.127483231	−987.127466278
400 <sup>a</sup>	2.3448898851	15.5640200379	−14928.2462422	−59.5392920537	69.0464048677	117.352380776	590.414507618	8736.80963958
400 <sup>b</sup>	2.3448898851	0.9448808588	2699.82561728	−15.4691124051	62.6390709898	93.32073484	238.903280942	6405.79274309
500	1	0.2509683066	11943.4908179	11.6066851136	67.9588531662	78.0665039031	315.413932985	2155.58138999
500	10	5.5466493279	2602.95313485	−22.6269845215	81.9472541876	256.331691752	214.249497553	12113.5551444

<sup>a</sup> Saturated liquid phase.

<sup>b</sup> Saturated vapor phase.



$p_{\max} = 10$  MPa. The uncertainties of the homogeneous density in the gaseous phase are 0.1% for  $T > 360$  K and up to 0.6% for lower temperatures. The uncertainties of the vapor pressure are 0.5% for  $T < 300$  K and up to 0.8% for higher temperatures. For the saturated liquid density, it is difficult to make a statement on the uncertainty because of the poor data situation. It is about 0.25% for  $T < 300$  K, and up to 1.5% for higher temperatures. The speed of sound in the gaseous phase was reproduced within 0.15% for  $T < 360$  K. Higher temperatures were represented within 0.1%. All deviations are larger in the critical region. Using molecular simulation data, the range of validity was extended to the liquid state up to a maximum temperature and pressure of  $T_{\max} = 1000$  K and  $p_{\max} = 700$  MPa. Because of the special data situation, the physical behavior of the FEOS in regions where no experimental data are available was carefully monitored. The extrapolation behavior is reasonable. Reference values are given in Table 5 to verify computer implementation of the FEOS.

## Acknowledgments

The authors gratefully acknowledge financial support by Deutsche Forschungsgemeinschaft under the grants VR6/4-1 and SP507/7-1. The programming effort was funded by BMBF under the project "01IH13005A SkaSim: Skalierbare HPC-Software für molekulare Simulationen in der chemischen Industrie". This work was carried out under the auspices of the Boltzmann-Zuse Society (BZS) of Computational Molecular Engineering. The simulations were carried out on the Cray XE6 (Hermit) at the High Performance Computing Center Stuttgart (HLRS).

## Appendix A. Ancillary equations

For computer calculations it is helpful to use ancillary equations to generate starting values for density iterations. Therefore ancillary equations for vapor pressure, saturated liquid density, and saturated vapor density were developed. The equations and parameters are given below, cf. Table A1. These ancillary equations are not reference equations, thus the FEOS has to be used in order to calculate accurate saturation properties.

Vapor pressure:

$$\ln \frac{p_v}{p_c} = \frac{T_c}{T} \sum_{i=1}^5 n_i \left( 1 - \frac{T}{T_c} \right)^{t_i} \quad (\text{A.1})$$

Saturated liquid density:

$$\ln \frac{\rho'}{\rho_c} = \sum_{i=1}^5 n_i \left( 1 - \frac{T}{T_c} \right)^{t_i} \quad (\text{A.2})$$

Saturated vapor density:

$$\ln \frac{\rho''}{\rho_c} = \sum_{i=1}^6 n_i \left( 1 - \frac{T}{T_c} \right)^{t_i} \quad (\text{A.3})$$

**Table A1**

Parameter values of the present ancillary equations for vapor pressure, saturated liquid density, and saturated vapor density.

i	Eq. (A.1)		Eq. (A.2)		Eq. (A.3)	
	$n_i$	$t_i$	$n_i$	$t_i$	$n_i$	$t_i$
1	−0.74136D+01	1	0.6610D+00	0.25	−0.10592D+01	0.3
2	0.19870D+01	1.5	0.4045D+01	0.7	−0.10712D+02	0.91
3	−0.66330D+01	3.5	−0.4488D+01	1.2	0.16812D+02	1.6
4	0.71500D+01	4.3	0.3445D+01	1.75	−0.27664D+02	2.26
5	−0.47200D+01	5.2	−0.9230D+00	2.4	−0.54968D+02	6.6
6					−0.20428D+03	17

## Appendix B. Molecular model

The coordinates and parameters of the molecular model of ethylene oxide are given in Table B1.

**Table B1**

Sigma ( $\sigma$ ) and epsilon ( $\epsilon$ ) denote the length and energy parameter of the Lennard-Jones (LJ) potential, respectively.  $k_B$  is the Boltzmann constant.  $\mu$  denotes the dipole moment of the point dipole. All coordinates are in principal axes with respect to the center of mass. The orientation of the point dipole is defined with Euler angles:  $\varphi$  is the azimuthal angle with respect to the x–y-plane and  $\theta$  is the inclination angle with respect to the z-axis.

Site	x/Å	y/Å	z/Å	$\sigma/\text{Å}$	$\epsilon/k_B/\text{K}$	$\theta/\text{deg}$	$\varphi/\text{deg}$	$\mu/\text{D}$
CH <sub>2</sub>	0.78	0	−0.48431	3.5266	84.739			
CH <sub>2</sub>	−0.78	0	−0.48431	3.5266	84.739			
O	0	0	0.73569	3.0929	62.126			
Dipole	0	0	0			0	0	2.459

## Appendix C. Supplementary data

Supplementary data associated with this article can be found in the online version at <http://dx.doi.org/10.1016/j.ces.2014.07.051>.

## References

- Auwers, K.V., 1918. Justus Liebig's Annalen der Chemie 415, 98–168.
- Barker, J.A., Watts, R.O., 1973. Mol. Phys. 26, 789–792.
- Calado, J.C.G., Deiters, U.K., Filipe, E.J.M., 1996. J. Chem. Thermodyn. 28, 201–207.
- Case, F.H., Brennan, J., Chaka, A., Dobbs, K.D., Friend, D.G., Gordon, P.A., Moore, J.D., Mountain, R.D., Olson, J.D., Ross, R.B., Schiller, M., Shen, V.K., Stahlberg, E.A., 2008. Fluid Phase Equilib. 274, 2–9.
- Chao, J., Hall, K.R., Marsh, K.N., Wilhoit, R.C., 1986. J. Phys. Chem. Ref. Data 15, 1369.
- Coles, K.F., Popper, F., 1950. Ind. Eng. Chem. 42, 1434–1438.
- Comelli, F., Francesconi, R., 1991. J. Chem. Eng. Data 36, 382–383.
- Comelli, F., Francesconi, R., 1995. J. Chem. Eng. Data 40, 28–30.
- Comelli, F., Francesconi, R., 1996. J. Chem. Eng. Data 41, 101–104.
- Company, M., 1980. Matheson Gas Data Book, 6 ed. Lyndhurst, New Jersey.
- Cox, J.D., Pilcher, G., 1970. Thermochemistry of Organic and Organometallic Compounds. Academic Press, New York.
- Deublein, S., Eckl, B., Stoll, J., Lishchuk, S.V., Guevara-Carrion, G., Glass, C.W., Merker, T., Bernreuther, M., Hasse, H., Vrabec, J., 2011. Comput. Phys. Commun. 182, 2350–2367.
- Dorofeeva, O.V., 1992. Thermochim. Acta 194, 9–46.
- Eckl, B., Vrabec, J., Hasse, H., 2008. Fluid Phase Equilib. 274, 16–26.
- Francesconi, R., Comelli, F., 1994. J. Chem. Eng. Data 39, 106–107.
- Francesconi, R., Comelli, F., 1995. J. Chem. Eng. Data 40, 512–514.
- Frenkel, D., Smit, B., 2002. Understanding Molecular Simulation: From Algorithms to Applications. Academic Press, Elsevier, San Diego.
- Frenkel, M., Chirico, R.D., Diky, V., Kroenlein, K., Muzny, C.D., Kazakov, A.F., Magge, J. W., Abdulgatov, I.M., Lemmon, E.W., 2013. NIST Standard Reference Database 103b: NIST Thermo-Data Engine – Pure Compounds, Binary Mixtures, Reactions, version 8.0. National Institute of Standards and Technology, Standard Reference Data Program, Gaithersburg, MD.
- Frenkel, M., Kabo, G.J., Marsh, K.N., Roganov, G.N., Wilhoit, R.C., 1994. Thermodynamics of Organic Compounds in the Gas State, vols. I and II. Thermodynamics Research Center, College Station, TX.
- Giauque, W.F., Gordon, J., 1949. J. Am. Chem. Soc. 71, 2176–2181.
- Giles, N.F., Wilson, G.M., 2006. J. Chem. Eng. Data 51, 1954–1962.
- Gillespie, P.C., Cunningham, J.R., Wilson, G.M., 1985. AIChE Symp. Ser. 81, 26–40.
- Glass, C.W., Reiser, S., Rutkai, G., Deublein, S., Köster, A., Guevara-Carrion, G., Wafai, A., Horsch, M., Bernreuther, M., Windmann, T., Hasse, H., Vrabec, J., 2014. Computer Physics Communications, in press, <http://dx.doi.org/10.1016/j.cpc.2014.07.012>.
- Godnev, I., Morozov, V., 1948. Zh. Fizicheskoi Khimii 22, 801–803.
- Guenthard, H., Heilbronner, E., 1948. Helv. Chim. Acta 31, 2128–2132.
- Guenthard, H.H., Messikommer, B., Kohler, M., 1950. Helv. Chim. Acta 33, 1809–1823.
- Hess, L.G., Tilton, V.V., 1950. Ind. Eng. Chem. 42, 1251–1258.
- Hurler, J.J., 2002. Int. J. Thermophys. 23, 667–696.
- Industrial fluid properties simulation collective. (<http://fluidproperties.org/>).
- Kistiakowsky, G.B., Rice, W.W., 1940. J. Chem. Phys. 8, 618–622.
- Lange, N.A., Dean, J.A., 1973. Lange's Handbook of Chemistry, 11 ed. McGraw-Hill, New York.
- Lemmon, E.W., Jacobsen, R.T., 2005. J. Phys. Chem. Ref. Data 34, 69–108.
- Lemmon, E.W., McLinden, M.O., Wagner, W., 2009. J. Chem. Eng. Data 54, 3141–3180.

- Lide, D.R., 2005. CRC Handbook of Chemistry and Physics, 86 ed. Taylor and Francis, London.
- Lustig, R., 2011. Mol. Simul. 37, 457–465.
- Lustig, R., 2012. Mol. Phys. 110, 3041–3052.
- Maass, O., Boomer, E.H., 1922. J. Am. Chem. Soc. 44, 1709–1728.
- McDonald, R.A., Shrader, S.A., Stull, D.R., 1959. J. Chem. Eng. Data 4, 311–313.
- Mock, J.E., Smith, J.M., 1950. Ind. Eng. Chem. 42, 2125–2128.
- Mohr, P.J., Taylor, B.N., Newell, D.B., 2012. Rev. Mod. Phys. 84, 1527–1605.
- Olson, J.D., 1977. J. Chem. Eng. Data 22, 326–329.
- Perkin, W.H., 1893. J. Chem. Soc., Trans. 63, 488–491.
- Ramasamy, R., Srinivasacharya, K.G., 1978. Curr. Sci. 47, 668–669.
- Reid, R.C., Prausnitz, J.M., Sherwood, T.K., 1977. The Properties of Gases and Liquids, 3 ed. McGraw-Hill, New York.
- Rowley, R.L., Wilding, W.V., Oscarson, J.L., Yang, Y., Zundel, N.A., Daubert, T.E., Danner, R.P., 2006. DIPPR Data Compilation of Pure Compound Properties: Design Institute for Physical Properties. AIChE, New York.
- Rutkai, G., Thol, M., Lustig, R., Span, R., Vrabec, J., 2013. J. Chem. Phys. 139, 041102.
- Span, R., 2000. Multiparameter Equations of State: An Accurate Source of Thermodynamic Property Data. Springer Verlag, Berlin.
- Sundaram, S., 1963. Z. Phys. Chem. (Muenchen) 36, 376–377.
- Timmermans, J., 1965. Physico-Chemical Constants of Pure Organic Substances, vol II. New York, New York.
- Vvedenskii, A.A., 1969. Z. Fiziceskoj Chim. 40, 1953–1955.
- Walters, C.J., Smith, J.M., 1952. Chem. Eng. Prog. 48, 337.
- Washburn, E.W., 1926–1933. International Critical Tables of Numerical Data, Physics, Chemistry, and Technology, 7 vols + Index. McGraw-Hill, New York.
- Widom, B., 1963. J. Chem. Phys. 39, 2808–2812.
- Wurtz, A., 1859. Ann. Chim. Phys. 55, 433.
- Yaws, C.L., 1977. Physical Properties: A Guide to the Physical, Thermodynamic, and Transport Property Data of Industrially Important Chemical Compounds. McGraw-Hill, New York.

### 3.9 Equation of state for 1,2-dichloroethane based on a hybrid data set

M. Thol, G. Rutkai, **A. Köster**, S. Miroshnichenko, W. Wagner, J. Vrabec, R. Span, *Molecular Physics* 115:1166-1185, 2017.

DOI: [doi.org/10.1080/00268976.2016.1262557](https://doi.org/10.1080/00268976.2016.1262557)

Nachgedruckt mit Erlaubnis von Taylor & Francis (Copyright 2017).

Im Rahmen dieser Arbeit wurde eine hybride Zustandsgleichung für 1,2-Dichlorethan erstellt, eine leichtentzündliche, krebserregende und mutagene Substanz die in der Herstellung von Polyvinylchlorid (PVC) genutzt wird. Für die Bestimmung der dafür verwendeten partiellen Ableitungen der Helmholtzenergie wurde ein neues molekulares Kraftfeld entwickelt. Die mit Hilfe des Lustig-Formalismus [Lus11, Lus12] berechneten partiellen Ableitungen der Helmholtzenergie ermöglichten eine effiziente Nutzung der Simulationsdaten im Anpassungsprozess der Gleichung und tragen insbesondere dazu bei, dass der Gültigkeitsbereich von Gleichungen die nur auf Experimenten beruhen vergrößert wird.

Der Autor der vorliegenden Dissertation hat alle für diese Veröffentlichungen zugrundeliegenden molekularen Simulationen der partiellen Ableitungen der Helmholtzenergie durchgeführt. Das zugrundeliegende Kraftfeld wurde von Dr. Svetlana Miroshnichenko erstellt und optimiert. Die Daten wurden von Dr. Monika Thol verwendet um eine hybride helmholtzexplizite Zustandsgleichung zu erstellen. Der Autor verfasste in Zusammenarbeit mit Dr. Gábor Rutkai die Beschreibungen über die zugrundeliegenden Simulationsmethoden und -parameter. Die Überarbeitung des Manuskripts wurde in Zusammenarbeit mit Prof. Roland Span, Prof. Jadran Vrabec und Prof. Wolfgang Wagner durchgeführt. Der Autor wurde während des gesamten Prozesses von Prof. Jadran Vrabec betreut.

SPECIAL ISSUE IN HONOUR OF JOHANN FISCHER

## Equation of state for 1,2-dichloroethane based on a hybrid data set

Monika Thol<sup>a</sup>, Gábor Rutkai<sup>b</sup>, Andreas Köster<sup>b</sup>, Svetlana Miroshnichenko<sup>b</sup>, Wolfgang Wagner<sup>a</sup>, Jadran Vrabec<sup>b</sup> and Roland Span<sup>a</sup>

<sup>a</sup>Lehrstuhl für Thermodynamik, Ruhr-Universität Bochum, Bochum, Germany; <sup>b</sup>Lehrstuhl für Thermodynamik und Energietechnik, Universität Paderborn, Paderborn, Germany

### ABSTRACT

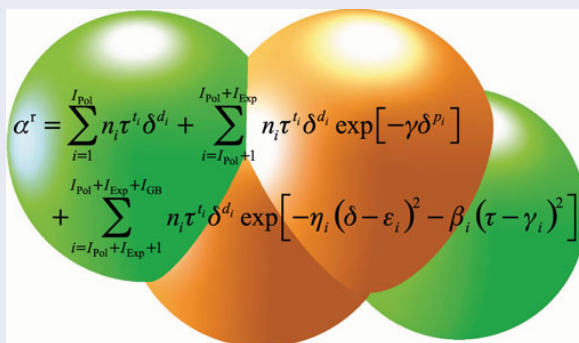
A fundamental equation of state in terms of the Helmholtz energy is presented for 1,2-dichloroethane. Due to a narrow experimental database, not only laboratory measurements but also molecular simulation data are applied to the fitting procedure. The present equation of state is valid from the triple point up to 560 K for pressures of up to 100 MPa. The accuracy of the equation is assessed in detail. Furthermore, a reasonable extrapolation behaviour is verified.

### ARTICLE HISTORY

Received 8 September 2016  
Accepted 14 November 2016

### KEYWORDS

1,2-dichloroethane; equation of state; Helmholtz energy; hybrid data set; thermodynamic properties



$$\alpha^r = \sum_{i=1}^{I_{Pol}} n_i \tau^{t_i} \delta^{d_i} + \sum_{i=I_{Pol}+1}^{I_{Pol}+I_{Exp}} n_i \tau^{t_i} \delta^{d_i} \exp[-\gamma \delta^{p_i}] + \sum_{i=I_{Pol}+I_{Exp}+1}^{I_{Pol}+I_{Exp}+I_{GB}} n_i \tau^{t_i} \delta^{d_i} \exp[-\eta_i (\delta - \varepsilon_i)^2 - \beta_i (\tau - \gamma_i)^2]$$

### 1. Introduction

In modern process engineering, chemical industry, and academy research, there is an increasing demand for accurate thermodynamic properties. Nowadays, such information is provided by equations of state. Due to their fundamental nature, most accurate equations of state are given in terms of the Helmholtz energy with temperature and density as independent variables. Only less than ten substances are modelled in reference quality and an additional 120 substances are described by less accurate industrial equations of state. The thermodynamic properties of all other substances have to be calculated by means of, e.g. cubic equations of state such as those by Peng and Robinson [1] or Redlich and Kwong [2], physically based equations of state according to Statistical Associating Fluid Theory (SAFT) [3], the BACKONE equation of state [4,5], or others like the Lee–Kesler equation of state [6]. The accuracy of correlation equations is

highly dependent on the availability of experimental data, which are used for their fitting. Unfortunately, for many industrial fluids, there are insufficient experimental data available because experiments are time-consuming and expensive. Furthermore, many fluids exhibit challenging properties, such as toxicity, flammability, or corrosiveness, which render experiments in the laboratory particularly difficult. Applying hybrid data sets (from experiments and molecular simulation) to the fitting procedure recently became a promising alternative. In the last years, significant progress was made in the field of molecular modelling and simulation so that the available experimental data sets can now be supplemented by molecular simulation data. An important advantage is that simulations are cheap and fast, and there are no restrictions with respect to challenging fluid properties. Furthermore, limitations of the experimental setup in terms of maximum temperatures or pressures do not apply.

**CONTACT** Monika Thol [m.thol@thermo.rub.de](mailto:m.thol@thermo.rub.de)

Supplemental data for this article can be accessed <http://dx.doi.org/10.1080/00268976.2016.1262557>.

© 2016 Informa UK Limited, trading as Taylor & Francis Group

However, the accuracy of the simulation data are critically dependent on the quality of the underlying molecular model.

In this work, a fundamental equation of state for 1,2-dichloroethane (CAS No. 107-06-2) was developed. It is an oily and colourless fluid under standard conditions, slightly flammable, and toxic. When handling this substance, its narcotic, mutagenic, and carcinogenic properties have to be taken into account. It is used in numerous technical processes, e.g. it serves as an extracting agent for fats and oils as well as a solvent for resin and bitumen. The main application is the manufacturing of vinyl chloride, which is the basic product for polyvinyl chloride [7]. Up to date, there is no Helmholtz energy model for 1,2-dichloroethane available in the literature. Due to the limited database, the equation of state was fitted to experimental data from the literature [8–81] as well as molecular simulation data presented in this work.

## 2. Equation of state

The present equation of state is written in terms of the molar Helmholtz energy  $a$ , which is reduced by the universal gas constant  $R = 8.3144621 \text{ J} \cdot \text{mol}^{-1} \text{ K}^{-1}$  according to Mohr and Taylor [82] and the temperature  $T$

$$\alpha(\tau, \delta) = \frac{a(T, \rho)}{RT}. \quad (1)$$

For the calculation of specific properties, the molar mass  $M = 98.9597 \text{ g} \cdot \text{mol}^{-1}$  [83] has to be applied. The Helmholtz energy is additively composed of an ideal gas (superscript o) and a residual (superscript r) contribution

$$\alpha(\tau, \delta) = \alpha^o(\tau, \delta) + \alpha^r(\tau, \delta), \quad (2)$$

where  $\tau = T_c/T$  and  $\delta = \rho/\rho_c$  with  $T_c$  and  $\rho_c$  being the critical values of temperature and density. The critical temperature  $T_c = 561.6 \text{ K}$  was taken from Garcia-Sanchez and Trejo [16]. The critical density  $\rho_c = 4.33 \text{ mol} \cdot \text{dm}^{-3}$  was determined during the fit so that the best representation of the experimental data was achieved, while a linear trend of the rectilinear diameter in the critical region and a distinct saddle point of the critical isotherm ( $(\partial p/\partial \rho)_{T_c} = 0$  and  $(\partial^2 p/\partial \rho^2)_{T_c} = 0$ ) was ensured.

The Helmholtz energy of the hypothetical ideal gas  $\alpha^o$  can be derived from an equation for the isobaric heat

capacity of the ideal gas

$$\frac{c_p^o}{R} = n_0 + \sum_{i=1}^2 m_i \left( \frac{\theta_i}{T} \right)^2 \frac{\exp(\theta_i/T)}{(\exp(\theta_i/T) - 1)^2}. \quad (3)$$

The constant  $n_0$  refers to the temperature limit  $T \rightarrow 0 \text{ K}$  taking translation and rotation of the molecule into account. This simplified approach presumes that both effects are fully activated so that at least six degrees of freedom exist, leading to a zero temperature contribution  $c_p^o = 4R$ . The Planck-Einstein terms represent the vibrational modes, which have to be considered for every molecule consisting of more than one atom. Since vibration frequencies and the anharmonicities are not known with sufficient precision, a simplified approach according to Span [84] is applied. The parameters  $m_i$  and  $\theta_i$  are treated as adjustable parameters here. In this case, a two-vibration model is sufficient to represent the available data within the required accuracy. For the determination of the parameters, ideal gas heat capacity data of Gwinn and Pitzer [72] were the only data set available for this fluid. Their experimental measurements were carried out with a flow calorimeter described by Pitzer and co-workers [85–87]. No information on sample purity or experimental uncertainty is given. Therefore, comparisons were made to isobaric heat capacity data of cyclohexane and cyclopentane in the ideal gas state, which were measured with the same apparatus. These data sets scatter within approximately 1% around the equations of Zhou *et al.* [88] and Gedantz *et al.* [89], respectively. Therefore, a similar uncertainty is expected for the data for 1,2-dichloroethane. In the paper by Gwinn and Pitzer [72] four different data sets are presented, which were determined by different modifications of the apparatus. Except for one data point at 335 K, all measurements agree with the present equation of state within the expected uncertainty (cf. Figure 1). Additional data of Gwinn and Pitzer [72], which were determined by theory, are reproduced within 1% between 350 and 1000 K (range of validity:  $T > 200 \text{ K}$ ). Outside of this region, deviations increase. During the fitting procedure, it turned out that the representation of these data cannot be improved without compromising the accuracy of other thermodynamic properties like the speed of sound or the isobaric heat capacity. Since these measurements are expected to be more accurate than the  $c_p^o$  data, the main focus was on a reasonable description of the speed of sound or the isobaric heat capacity and the deviations of the isobaric heat capacity of the ideal gas were accepted. Therefore, the uncertainty of the present equation of state is expected to be 1% within the temperature range  $T = 350$  to  $1000 \text{ K}$ . The underlying parameters for Equation (3) are  $m_1 =$

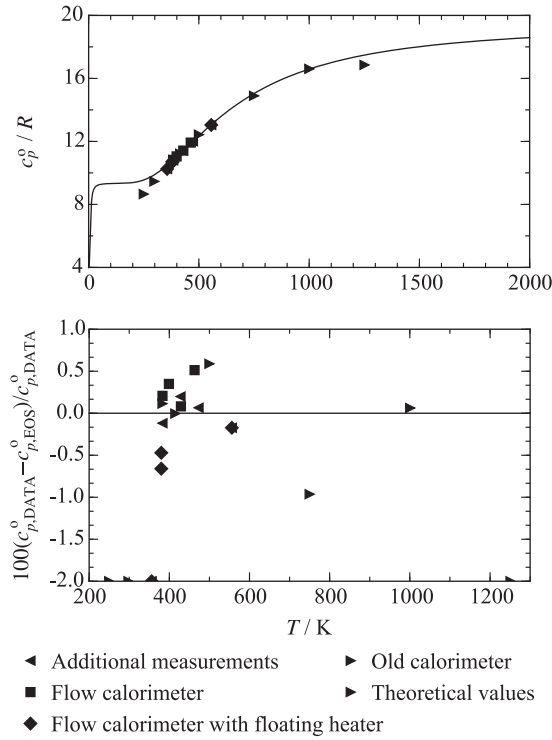


**Figure 1.** Representation of the isobaric heat capacity of the ideal gas of Gwinn and Pitzer [72].

5.35,  $m_2 = 10.05$ ,  $\theta_1 = 22.5$  K, and  $\theta_2 = 2015$  K. For the application in the present Helmholtz energy model, a two-fold integration with respect to the temperature has to be carried out. The resulting reduced Helmholtz energy of the ideal gas is

$$\alpha^o(\tau, \delta) = c^{\text{II}} + c^{\text{I}}\tau + 3 \ln(\tau) + \sum_{i=1}^2 m_i \ln(1 - \exp(-\theta_i/T_c \tau)) + \ln(\delta). \quad (4)$$

The integration constants were determined such that  $h_0 = 0 \text{ J}\cdot\text{kg}^{-1}$  and  $s_0 = 0 \text{ J}\cdot\text{kg}^{-1}\cdot\text{K}^{-1}$  at the normal boiling point temperature  $T_{\text{NBP}}(p_v = 1 \text{ atm})$  and saturated liquid density  $\rho'(p_v = 1 \text{ atm})$ :  $c^{\text{I}} = 0.972870308$  and  $c^{\text{II}} = 15.963798537$ .

The residual contribution to the Helmholtz energy considers the intermolecular interactions in a real fluid. In contrast to the ideal gas, this contribution was described with an empirical expression that contains five polynomial, five exponential, and five Gaussian bell-shaped terms:

$$\begin{aligned} \alpha^r(\tau, \delta) &= \alpha_{\text{Pol}}^r(\tau, \delta) + \alpha_{\text{Exp}}^r(\tau, \delta) + \alpha_{\text{GBS}}^r(\tau, \delta) \\ &= \sum_{i=1}^5 n_i \delta^{d_i} \tau^{t_i} + \sum_{i=6}^{10} n_i \delta^{d_i} \tau^{t_i} \exp(-\delta^{p_i}) \\ &\quad + \sum_{i=11}^{15} n_i \delta^{d_i} \tau^{t_i} \exp(-\eta_i(\delta - \varepsilon_i)^2 - \beta_i(\tau - \gamma_i)^2). \end{aligned} \quad (5)$$

The corresponding parameters are listed in Table 1. For the determination of the required parameters, a non-linear algorithm provided by the National Institute of Standards and Technology was employed [90]. A brief description of the algorithm is outlined in Lemmon and Jacobsen [91]. A non-published 14-terms equation for propane was used as initial solution for the fitting procedure. For a sufficiently accurate description of all available experimental data of 1,2-dichloroethane, one additional term was added here.

### 3. Comparison with experimental literature data

The accuracy of the present equation of state was established by comparison to the available experimental data from the literature. The statistical analysis was carried out

**Table 1.** Parameters of the residual contribution to the present equation of state (cf. Equation (5)).

$i$	$n_i$	$t_i$	$d_i$	$p_i$	$\eta_i$	$\beta_i$	$\gamma_i$	$\varepsilon_i$
1	0.51000000·10 <sup>-1</sup>	1.000	4	-				
2	0.19900000·10 <sup>+1</sup>	0.352	1	-				
3	-0.25950000·10 <sup>+1</sup>	0.890	1	-				
4	-0.66530000·10 <sup>+0</sup>	0.824	2	-				
5	0.23595000·10 <sup>+0</sup>	0.498	3	-				
6	-0.17000000·10 <sup>+1</sup>	1.630	1	2				
7	-0.44530000·10 <sup>+0</sup>	4.070	3	2				
8	0.67247400·10 <sup>+0</sup>	0.679	2	1				
9	-0.21918000·10 <sup>+0</sup>	2.850	2	2				
10	-0.35540000·10 <sup>-1</sup>	1.070	7	1				
11	0.97650000·10 <sup>+0</sup>	1.700	1	-	0.660	0.574	0.995	0.571
12	-0.49517900·10 <sup>+0</sup>	2.090	1	-	1.360	1.800	0.329	0.862
13	-0.23291174·10 <sup>+0</sup>	1.930	3	-	0.711	0.462	0.525	0.597
14	-0.10902450·10 <sup>-1</sup>	3.720	3	-	1.700	3.220	0.850	1.160
15	0.39209000·10 <sup>+0</sup>	1.580	1	-	1.110	2.220	0.585	0.208



by means of relative deviations according to

$$\Delta X = 100 \frac{X_{\text{DATA}} - X_{\text{EOS}}}{X_{\text{DATA}}}, \quad (6)$$

and the average absolute relative deviation

$$AAD = \frac{1}{N} \sum_{i=1}^N |\Delta X_i|. \quad (7)$$

For homogeneous states, the AAD is discussed for gaseous and fluid state regions separately. Measurements in the supercritical state or in the critical region are not available. The thermal vapour-liquid equilibrium is divided into three temperature ranges: low temperature (LT:  $T/T_c < 0.6$ ), medium temperature (MT:  $0.6 \leq T/T_c \leq 0.98$ ), and high temperature (HT:  $T/T_c > 0.98$ ).

### 3.1. Vapour-liquid equilibrium

Comparisons of the vapour pressure data from the literature and calculated values from the present equation of state are presented in Table 2 and Figure 2. Additionally, correlations of the TDE [92] and DIPPR [93] data banks are included in the figure. The table shows that the vapour pressure was extensively investigated, but most of the data are located in a restricted temperature range of 270 to 400 K. An overview on all available vapour pressure data is illustrated in Figure 2 (top) and only the most recent and reliable data sets are depicted in Figure 2 (bottom). The data of Amireche-Ziar *et al.* [8] were measured with a static apparatus as described by Blondel-Telouk *et al.* [94]. The experimental uncertainties as specified by Amireche-Ziar *et al.* [8] yield a combined expanded uncertainty of 0.06%–0.11% and a sample purity of >99% is stated. That agrees very well with the correlation of the data by the present equation of state up to 335 K ( $AAD = 0.080\%$ ). The state points at  $T = 344.8$  K and  $T = 354.9$  K differ by more than 1% from the present equation. Another accurate data set was published by Dohnal *et al.* [15], which is reproduced within 0.05% ( $AAD = 0.021\%$ ). A modified Dvořák-Boublík recirculation still (dynamic method) described by Boublíková and Lu [95] was used and the uncertainty analysis resulted in a temperature and pressure uncertainty of  $\Delta T = 0.02$  K and  $\Delta p = 7$  Pa, respectively. Deviations from the present equation of state and from other vapour pressure data from the literature show that the combined expanded uncertainty of 0.15%–0.2% is probably too conservative. A third experimental data set was measured by Varushchenko *et al.* [37] with an ebulliometer in the same temperature range. The specified experimental uncertainties of  $\Delta T = 0.004$  K

and  $\Delta p = 13$  Pa result in a combined expanded uncertainty of 0.03%–0.35%. This is in good agreement with the present equation of state ( $AAD = 0.083\%$ ). For  $T < 250$  K, the data of Igoudjilene *et al.* [19] ( $AAD = 0.43\%$ ) are underestimated by the present equation of state. During parametrisation, it was not possible to fit these data in a better way without compromising the representation of other properties. The correlation from the TDE [92] shows the same course as these data [19]. However, since other properties, such as density or speed of sound, were considered in addition to the vapour pressure, the course of the present equation of state is more meaningful than results from property-specific vapour pressure equations. The high temperature range ( $T > 400$  K) was investigated by Stull [33] and Garcia-Sanchez and Trejo [16]. The data of Stull [33] were not measured but collected from the literature and exhibit a huge deviation with respect to the present equation of state. Similar results were found for other fluids, e.g. for hexamethyldisiloxane [96] or ethylene oxide [97]. Therefore, these data were not considered in the development of the present equation of state. The measurements of Garcia-Sanchez and Trejo [16] were carried out with a sample purity of 99.7% in a thick-walled Pyrex capillary tube. This technique was originally proposed by Ambrose [98] and used by McLure and Dickinson [99] to carry out vapour pressure measurements of hexamethyldisiloxane. As discussed in detail by Thol *et al.* [96], the experimental arrangement was questionable and the resulting vapour pressure data of hexamethyldisiloxane could only be reproduced within 2%. For 1,2-dichloroethane, the representation is even worse. The investigated temperature range overlaps with other literature data from, e.g. Patel *et al.* [24] ( $AAD = 0.55\%$ ) or Rollet *et al.* [29] ( $AAD = 0.21\%$ ), which allows a closer investigation of the accuracy of these data. Figure 3 shows that the data of Patel *et al.* [24] and Rollet *et al.* [29] are in line with the accurate measurements of Amireche-Ziar *et al.* [8] and Dohnal *et al.* [15]. In the overlapping region, the data of Garcia-Sanchez and Trejo [16] systematically deviate by 4% from other literature data and the present equation of state. Furthermore, a stepwise course of the data in the deviation plot is noticeable, cf. Figure 2 (bottom). This could be a consequence of the chosen calibration procedure: Nine chromel-to-alumel thermocouples, which were installed in the experimental setup, were calibrated to the critical temperatures of seven different alkanes reported by Ambrose [100]. Since these critical points significantly differ from each other, the stepwise course of the data is not surprising. Additionally, the uncertainty of the critical parameters increases with increasing chain length of the alkanes. Finally, the specified uncertainties of 0.2 K and 10 kPa yield a combined expanded uncertainty of 0.5%–13%. Therefore, these data were not used

**Table 2.** Average absolute relative deviations of experimental vapour pressure, saturated liquid, and saturated vapour densities calculated from the present equation of state.

			Average absolute relative deviations (AAD) / %			
Authors	No. of data	Temperature range / K	LT <sup>a</sup>	MT <sup>a</sup>	HT <sup>a</sup>	overall
Vapour pressure $p_v$						
Amireche-Ziar <i>et al.</i> [8]*	20	284–355	0.080	1.14	–	0.50
Barhala <i>et al.</i> [9]	10	292–314	0.62	–	–	0.62
Comelli and Francesconi [10]	3	298–334	0.74	–	–	0.74
Comelli and Francesconi [11]	15	292–356	9.87	2.34	–	5.85
Comtat <i>et al.</i> [12]	14	326–355	2.96	4.24	–	3.78
Davies <i>et al.</i> [13]	4	293–324	0.78	–	–	0.78
Dietrich [14]	58	284–353	0.17	0.19	–	0.17
Dohnal <i>et al.</i> [15]	15	324–355	0.022	0.021	–	0.021
Garcia-Sanchez and Trejo [16]	65	351–547	–	2.15	–	2.15
Giles and Wilson [17]	2	303–354	0.055	0.25	–	0.15
Gutsche and Knapp [18]	15	301–358	0.12	0.099	–	0.12
Igoudjilene <i>et al.</i> [19]	10	263–344	0.43	0.40	–	0.43
Kirschbaum <i>et al.</i> [20]	2	356–362	–	0.46	–	0.46
Kirss <i>et al.</i> [21]	4	319–357	0.19	0.042	–	0.079
McGovern [22]	1	356.62	–	0.084	–	0.084
Miksch <i>et al.</i> [23]	3	286–306	3.36	–	–	3.36
Patel <i>et al.</i> [24]	16	343–382	–	0.55	–	0.55
Pearce and Peters [25]	27	242–373	2.45	1.01	–	2.02
Radulescu and Alexa [26]	6	273–299	1.10	–	–	1.10
Rao and Viswanath [27]*	59	344–404	–	2.01	2.57	2.46
Rivenq [28]	5	318–356	1.55	2.11	–	1.89
Rollet <i>et al.</i> [29]	18	353–385	–	0.21	–	0.21
Sewell and Stock [30]	6	273–324	0.80	–	–	0.80
Sieg <i>et al.</i> [31]	1	356.61	–	0.13	–	0.13
Smith and Matheson [32]	17	352–361	–	0.17	–	0.17
Stull [33]	18	228–559	19.1	4.71	1.61	11.0
Sundaram and Viswanath [34]	20	343–382	–	0.64	–	0.64
Teodorescu <i>et al.</i> [35]	2	323–354	0.15	0.092	–	0.12
Toropov and Nikonovich [36]	3	313–334	0.77	–	–	0.77
Varushchenko <i>et al.</i> [37]	15	298–357	0.083	0.077	–	0.080
Waters <i>et al.</i> [38]	5	263–299	0.82	–	–	0.82
Wilding <i>et al.</i> [39]	2	243–274	4.18	–	–	4.18
Saturated liquid density $\rho'$						
Ali and Tariq [40]	5	298–319	0.19	–	–	0.19
Babak and Udovenko [41]	3	298–349	0.21	0.23	–	0.22
Comelli and Francesconi [10]	1	298.15	0.025	–	–	0.025
Herz and Levi [43]	4	293–324	0.13	–	–	0.13
Joshi <i>et al.</i> [44]	4	298–314	0.015	–	–	0.015
Klofutar <i>et al.</i> [45]	6	293–334	0.066	–	–	0.066
Kumagai and Takahashi [46]	5	298–399	0.073	0.29	–	0.20
Martin <i>et al.</i> [47]	5	303–344	0.46	0.41	–	0.45
Sivaramprasad <i>et al.</i> [48]	5	293–334	0.26	–	–	0.26
Udovenko <i>et al.</i> [49]	4	303–334	0.27	–	–	0.27
Varushchenko <i>et al.</i> [50]	6	293–334	0.036	–	–	0.036
Vogel [51]	5	286–334	0.16	–	–	0.16
Saturated vapour density $\rho''$						
McGovern [22]	1	356.62	–	3.03	–	3.03

<sup>a</sup>LT:  $T/T_c < 0.6$ ; MT:  $0.6 \leq T/T_c \leq 0.98$ ; HT:  $T/T_c > 0.98$ .

Note: All temperatures were adapted to the ITS-90 scale. Data sets, which were applied to the fit, are marked with an asterisk.

to set up the present equation of state. Since these data were the only high temperature measurements, they were monitored during the fit so that they did not exceed a 4% deviation. Therefore, the expected uncertainty of vapour pressure data calculated with the present equation of state is 0.1% for  $T < 400$  K and 4% for higher temperatures.

The relative deviations of experimental saturated liquid density data from the present equation of state are

illustrated in Figure 4. Measurements are only available between 293 and 400 K. Since there are several different data sets of high accuracy available for homogeneous density data at atmospheric pressure, the saturated liquid density data were not applied to the fit. Nonetheless, all of the experimental data are represented within 0.5%. Similar to the vapour pressure measurements, the data of Varushchenko *et al.* [50]



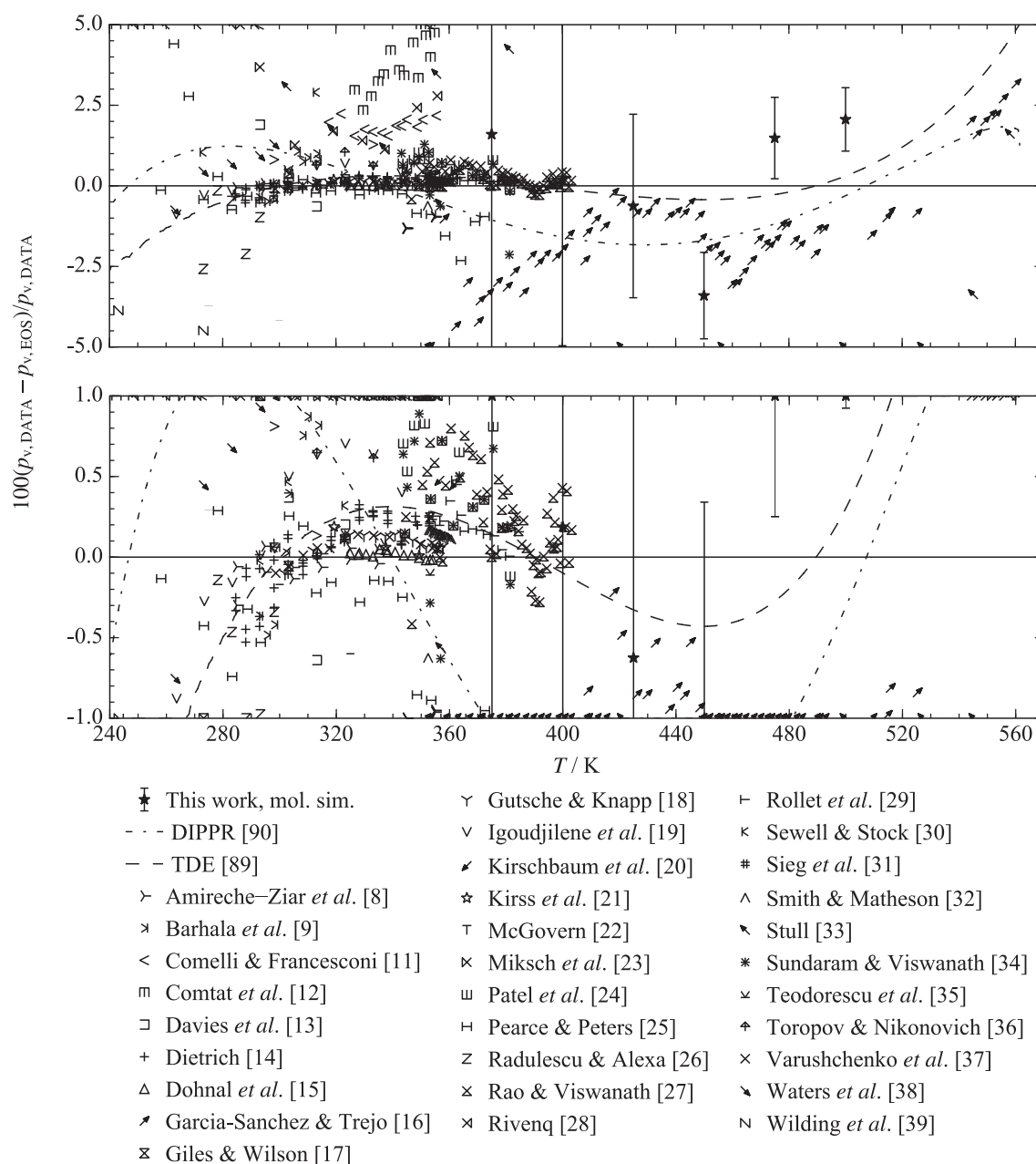
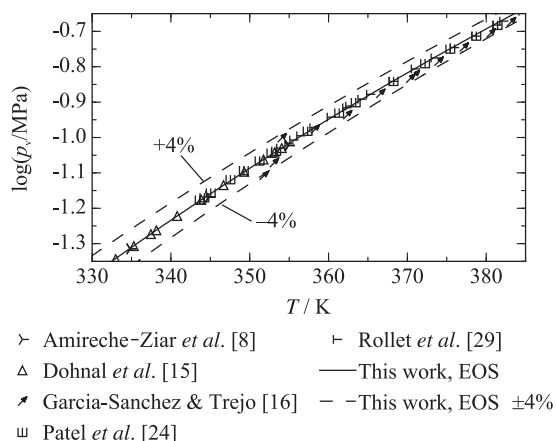


Figure 2. Relative deviations of vapour pressure data from the present equation of state.

(AAD = 0.036%) are of very high accuracy and are reproduced within 0.06%. Joshi *et al.* [44] (AAD = 0.015%) determined their data by means of a pycnometer. Not much information is given on the purification grade or experimental uncertainties. However, their data are reproduced within 0.04%. Considering possible irritations caused by sample impurities, this deviation is in good agreement with the specified overall experimental

uncertainty of  $0.0002 \text{ g}\cdot\text{cm}^{-3}$  as stated by the authors. The experimental data for cyclohexane from the same publication as for 1,2-dichloroethane are reproduced with the equation of Zhou *et al.* [88] within 0.08% (AAD = 0.04%) although they were not considered during the development of the equation. Therefore, it can be assumed that the data are of high accuracy. Another data set was published by Klofutar *et al.* [45] (AAD = 0.066%)



**Figure 3.**  $\log(p_v)$ - $T$  diagram including selected experimental vapour pressure data.

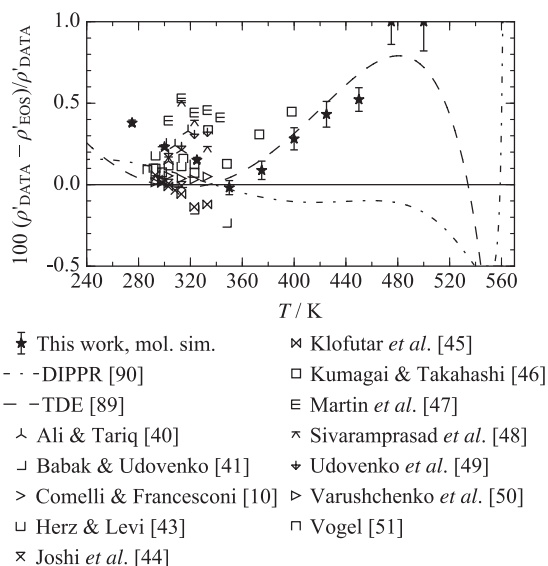


**Figure 4.** Relative deviations of saturated liquid density data from the present equation of state.

and represented within 0.15% by the present equation of state. No information is given on the measurement device or experimental uncertainties. From the calibration fluids mentioned in Ref. [45] it can be concluded that an Anton Paar densimeter was used, which can yield very accurate results. Additionally, comparisons of their benzene measurements were made with the equation of Thol *et al.* [101]. For  $T \leq 313$  K, these data agree with the equation within  $\pm 0.02\%$ . For higher temperatures, the deviations increase up to  $-0.32\%$ . The same trend is observed for 1,2-dichloroethane. For  $T \leq 313$  K, the data are reproduced within  $\pm 0.06\%$ , whereas deviations increase up to  $-0.14\%$  for higher temperatures. An opposing trend was found for the saturated liquid density data of Kumagai

and Takahashi [46] ( $AAD = 0.20\%$ ). For increasing temperatures, the relative deviations from the present equation of state increase up to  $0.45\%$ . Since these data are the only measurements between  $T = 345$  and  $400$  K, they cannot be confirmed.

The temperature range covered by experimental data is restricted so that it is difficult to assess the uncertainty of the present equation for this property. At least within  $T = 285$  and  $400$  K, deviations are  $0.1\%$ – $0.45\%$ .

For the saturated vapour density, only one single-state point is available and no statement on the accuracy of the present equation of state can be made. To ensure at least a correct qualitative behaviour, this line was adjusted by means of the rectilinear diameter  $\rho_{RD} = 0.5(\rho' + \rho'')$  [102].

If a fundamental equation of state is available, the vapour–liquid equilibrium can be calculated by means of the thermal, mechanical, and chemical equilibrium conditions. However, for computer calculations, it is helpful to use ancillary equations to generate initial values for density iterations. In this work, ancillary equations for vapour pressure, saturated liquid density, and saturated vapour density were developed:

$$\ln\left(\frac{p_v}{p_c}\right) = \left(\frac{T_c}{T}\right) \sum_{i=1}^5 n_i \left(1 - \frac{T}{T_c}\right)^{t_i}, \quad (8)$$

$$\frac{\rho'}{\rho_c} = 1 + \sum_{i=1}^4 n_i \left(1 - \frac{T}{T_c}\right)^{t_i}, \quad (9)$$

$$\ln\left(\frac{\rho''}{\rho_c}\right) = \sum_{i=1}^6 n_i \left(1 - \frac{T}{T_c}\right)^{t_i}. \quad (10)$$

The corresponding parameters are given in Table 3.

### 3.2. Density of homogeneous states and thermal virial coefficients

The representation of homogeneous density data with the present equation of state is summarised in Table 4 and illustrated in Figures 5 and 6. Only two data sets of Kumagai and Takahashi [46] and García-Giménez *et al.* [55] could be used to model the pressure dependence of the present equation of state. The measurements of Kumagai and Takahashi [46] are reproduced within  $0.02\%$ – $0.37\%$  ( $AAD = 0.19\%$ ). A systematic increase of the deviations with respect to the present equation of state can be observed for increasing temperatures and pressures. The data were measured with the same apparatus as the corresponding saturated liquid density data. The experiment was operated with a piezometer, which was sealed with mercury enclosed by two stainless-steel membranes.

**Table 3.** Parameters for the ancillary equations (cf. Equations (8)–(10)).

<i>i</i>	$p_v$ : Eq. (8)		$\rho'$ : Eq. (9)		$\rho''$ : Eq. (10)	
	$n_i$	$t_i$	$n_i$	$t_i$	$n_i$	$t_i$
1	$-0.898372 \cdot 10^{+1}$	1.00	$0.170532 \cdot 10^{+1}$	0.30	$-0.293901 \cdot 10^{+1}$	0.37
2	$0.154600 \cdot 10^{+2}$	1.50	$0.178600 \cdot 10^{+0}$	0.70	$-0.645628 \cdot 10^{+1}$	1.20
3	$-0.371100 \cdot 10^{+2}$	1.90	$0.147900 \cdot 10^{+1}$	1.10	$-0.497300 \cdot 10^{+2}$	3.50
4	$0.408520 \cdot 10^{+2}$	2.30	$-0.622480 \cdot 10^{+0}$	1.50	$0.732730 \cdot 10^{+2}$	4.30
5	$-0.200420 \cdot 10^{+2}$	2.80			$-0.837170 \cdot 10^{+2}$	5.40
6					$-0.966800 \cdot 10^{+2}$	13.0

**Table 4.** Average absolute relative deviations of the experimental data of homogeneous states from the present equation of state.

		Temperature and pressure range		Average absolute relative deviation (AAD) / %	
Authors	No. of data	$T$ / K	$p$ / MPa	Gas	Liquid
$p\rho T$ data					
Bhatia <i>et al.</i> [52]	2	293–314	0.101325		0.012
Ciocirlan <i>et al.</i> [53]	4	288–319	0.101325		0.010
Fort and Moore [54]	1	298.14	0.101325		0.020
García-Giménez <i>et al.</i> [55]*	44	288–319	0.1–21		0.010
Hahn <i>et al.</i> [56]	2	293–314	0.101325		0.026
Kumagai and Takahashi [46]*	35	298–399	10–102		0.19
Lagemann <i>et al.</i> [57]	4	293–324	0.101325		0.029
Malhotra <i>et al.</i> [58]	4	278–339	0.101325		0.042
Malhotra and Woolf [59]	6	278–339	0.101325		0.042
Manfredini <i>et al.</i> [60]	17	263–344	0.101325		0.043
Oswal <i>et al.</i> [61]	5	298–334	0.101325		0.028
Ranjbar <i>et al.</i> [62]	6	288–314	0.101325		0.082
Schaaffs [63]	1	293.14	0.101325		0.028
Valtz <i>et al.</i> [64]	51	283–334	0.101325		0.010
Speed of sound $w$					
Ali and Tariq [40]	5	298–319	0.101325		0.65
Bhatia <i>et al.</i> [52]	2	293–314	0.101325		0.074
Fort and Moore [54]	1	298.14	0.101325		0.74
Iloukhani and Samiey [65]	1	303.15	0.101325		0.55
Lagemann <i>et al.</i> [57]*	6	273–324	0.101325		0.067
Nath [66]	1	303.15	0.101325		0.095
Nath and Dixit [67]	2	298–309	0.101325		0.053
Nath and Saini [68]	2	303–314	0.101325		0.19
Nath and Singh [69]	2	303–314	0.101325		0.060
Oswal <i>et al.</i> [61]	5	298–334	0.101325		0.41
Schaaffs [63]	1	293.14	0.101325		17.4
Sekhar <i>et al.</i> [70]	1	303.15	0.101325		0.092
Isobaric heat capacity $c_p$					
Góralski <i>et al.</i> [71]*	30	284–354	0.101325		0.097
Gwinn and Pitzer [72]	6	379–557	0.101325	0.26	
Hallén [73]	1	298.15	0.101325		0.39
Rastorguev and Ganiev [74]	4	293–354	0.101325		0.69
Shehatta [75]	2	298–309	0.101325		0.36
Sieg <i>et al.</i> [31]	1	293.15	0.101325		3.5
Wilhelm <i>et al.</i> [76]	1	298.15	0.101325		0.27
Heat of vapourisation $\Delta h_v$					
Carson <i>et al.</i> [77]	1	298.15	$p_v$	2.0	
Majer <i>et al.</i> [78]	5	298–359	$p_v$	0.21	
McGovern [22]	1	356.62	$p_v$	0.27	
Rao and Viswanath [80]	2	353–357	$p_v$	0.17	
Second virial coefficient $B$					
Bohmhammel and Mannchen [79]	12	364–579		8.97	
Paniego <i>et al.</i> [81]	4	365–414		221	
Sewell and Stock [30]	6	273–324		2.69	

Note: All temperatures were adapted to the ITS-90 scale. Data sets, which were applied to the fit, are marked with an asterisk. The values for the second virial coefficient are calculated as absolute deviations in  $\text{cm}^3 \cdot \text{mol}^{-1}$ .

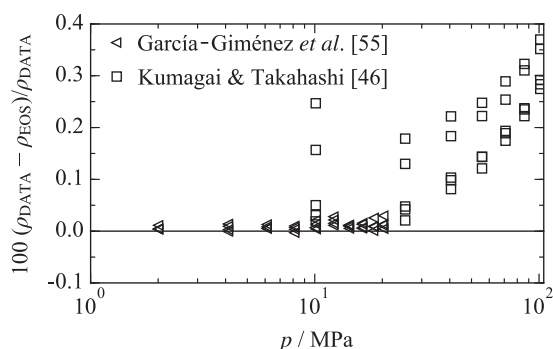


**Figure 5.** Relative deviations of experimental homogeneous density data from the present equation of state for  $285\text{ K} < T < 400\text{ K}$ .

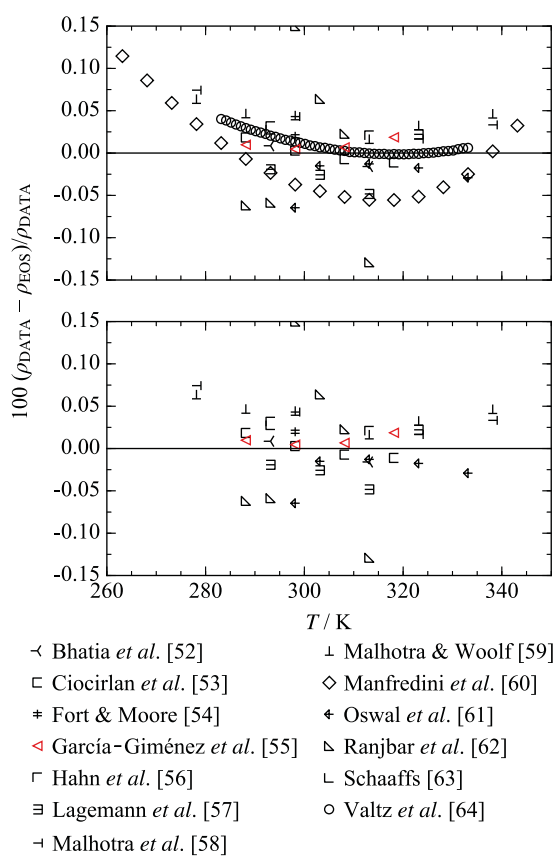


**Figure 6.** Relative deviations of experimental homogeneous density data from the present equation of state at atmospheric pressure.

This movable part was connected to the core of a differential transformer. The sample was filled into a  $4.5\text{ cm}^3$  borosilicate glass bulb, which was calibrated to less than 0.015% in terms of the volume at atmospheric conditions. A mercury thermometer ( $\Delta T = 0.05\text{ K}$ ) was used to monitor the temperature of the thermostat and a Heise

Bourdon gauge with an error of less than 0.1 MPa was used to pressurise the working oil and the sample. The volume change of the sample due to temperature and pressure variation was detected through the displacement of the core. The error in the determination of the displacement was stated to be 0.03 mm, but no mathematical formulation is provided to calculate the influence on the uncertainty of the density. Additionally, no information about the differential transformer is given. Thus, it is not possible to explain the pressure-related increase of the deviations. However, a temperature gradient could be suspected in the apparatus. The upper part was subject to atmospheric conditions, whereas the lower part was heated. With increasing temperature, the temperature gradient rises and the influence is higher. Since there are no other experimental data available in this region, additional investigations are necessary to clarify if this behaviour is caused by the present equation of state or the measurements.

The low temperature and pressure region was explored by Garcia-Gimenez *et al.* [55] ( $AAD = 0.010\%$ ). Data were measured with an Anton Paar vibrating-tube densimeter (DMA 512) with a high pressure cell. The temperature was stable within 0.01 K, whereas the pressure was adjusted with 0.005% of the full scale. With these numbers and a specified uncertainty of  $10^{-4}\text{ g}\cdot\text{cm}^{-3}$  in terms of density, a combined expanded uncertainty of 0.019% follows. Except for five state points, all of these data are reproduced within this uncertainty. Considering the sample purity of 99.7%, these outliers (deviations of up to 0.03%) are still reproduced within their experimental uncertainty. Therefore, it is assumed that the increasing deviation of the data of Kumagai and Takahashi [46] is due to the experimental data. Unfortunately, the measurements of the two author groups only overlap at a single-state point. At  $T = 298.15\text{ K}$  and  $p = 10\text{ MPa}$ , the density of Garcia-Gimenez *et al.* [55] is reproduced within 0.0068%, whereas the one of Kumagai and Takahashi [46] differs by 0.0307% from the present equation. Hence, the data set of Kumagai and Takahashi [46] is assumed to be less accurate. Additional measurements of Kumagai and Takahashi [46] for ammonia carried out with the same apparatus are reproduced within 0.4% with a preliminary equation of state by Lemmon [103]. Thus, the deviations for 1,2-dichloroethane are assumed to be reasonable.

In Figure 6, relative deviations of homogeneous density data measured at atmospheric pressure are presented. Similar to the saturated liquid density, the temperature range is restricted. However, there are several comprehensive data sets available, which are reproduced within 0.12%. In Figure 6 (top), the impression of a wrong curvature of the equation could arise when considering the course of the measurements of Valtz *et al.* [64] ( $AAD =$

0.010%) and Manfredini *et al.* [60] (AAD = 0.043%). Both data sets could not be fitted in a better way without compromising the homogeneous density data of García-Giménez *et al.* [55]. When deleting the data of Valtz *et al.* [64] and Manfredini *et al.* [60] from the plot, cf. Figure 6 (bottom), the eye-catching curvature is not apparent anymore and the remaining data scatter equally distributed around the present equation. Valtz *et al.* [64] carried out their measurements with a vibrating-tube densimeter (Anton Paar, DMA500) and a sample purity of 99.8%. The densimeter was calibrated with dry air and water at  $T = 293.15$  K, but no information is given how the temperature dependence was compensated. Manfredini *et al.* [60] also used a vibrating-tube densimeter (Anton Paar, DMA 60). The same purification grade as for the measurements of Valtz *et al.* [64] is reported. They claim the sample to be contaminated with 0.1% water. When applying a simple linear combination of the mixture 1,2-dichloroethane (99.9%) and water (0.01%), the density of pure 1,2-dichloroethane would be reduced by 0.025%. This is a possible explanation of the systematic shift with respect to the measurements of Valtz *et al.* [64]. However, the data of Valtz *et al.* [64] and Manfredini *et al.* [60] are still reproduced within 0.04% and 0.11%, respectively.

Based on the discussion above, the uncertainty of homogeneous density data calculated with the present equation of state is expected to be 0.05% for  $T < 320$  K and  $p < 20$  MPa, whereas for higher temperatures and pressures the uncertainty increases up to 0.5%.

Three data sets for the second virial coefficient from the literature are shown as absolute deviations from the present equation of state in Figure 7. The data of Sewell and Stock [30] ( $T = 273$  to 323 K) were derived from the Berthelot equation fitted to experimental vapour pressure measurements (AAD<sub>pv</sub> = 0.80%) carried out by the

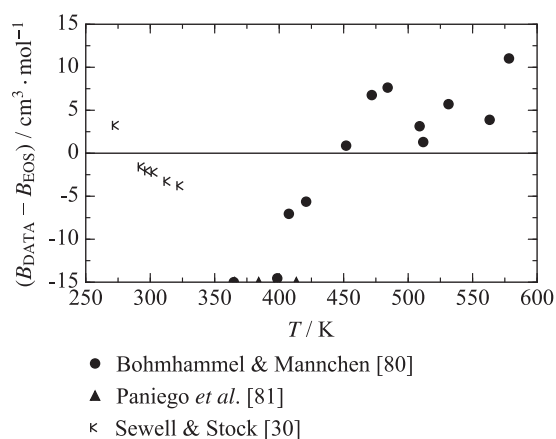


**Figure 7.** Absolute deviations of second virial coefficient data from the present equation of state.

same authors. The absolute deviations of  $3.8 \text{ cm}^3 \cdot \text{mol}^{-1}$  with respect to the present equation of state (corresponding to a relative deviation of 0.4%) without applying the data to the fit proves that this is a reasonable approach. Higher temperatures were investigated by Bohmhammel and Mannchen [79] and their data are reproduced within  $40 \text{ cm}^3 \cdot \text{mol}^{-1}$  (5%), but their information on experimental uncertainties is insufficient to assess the accuracy of these data. Finally, the data of Paniego *et al.* [81] differ by more than  $250 \text{ cm}^3 \cdot \text{mol}^{-1}$  (20%) from the present equation of state. Since the corresponding temperature range is covered by the reasonable data of Bohmhammel and Mannchen [79], the data of Paniego *et al.* [81] were not considered for the validation of the present equation of state.

### 3.3. Caloric properties

In Figure 8, relative deviations of experimental speed of sound data from the present equation of state are depicted. All of them were measured at atmospheric pressure and differ from the present equation of state by less than 1%. Although the publication from 1949 is rather old, data of Lagemann *et al.* [57] were applied to the fit. Their measurements were carried out with a variable-path ultrasonic interferometer as described by McMillan and Lagemann [104]. No information on the experimental uncertainty is given. Therefore, comparisons of their measurements on benzene and heavy water with the corresponding equations of state from the literature [101,105] were made. The calculated deviations

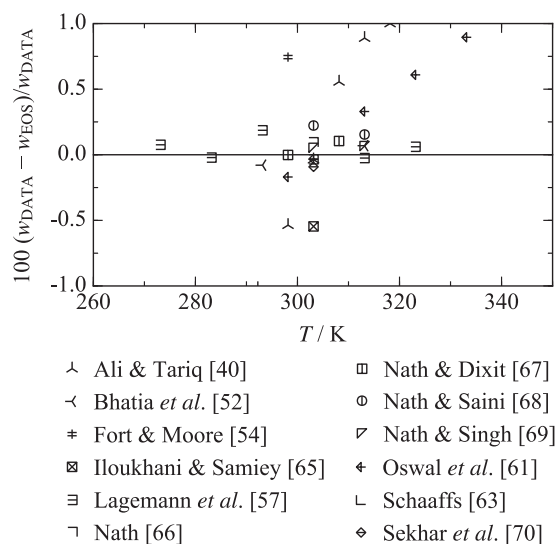


**Figure 8.** Relative deviations of experimental speed of sound data from the present equation of state at atmospheric pressure.

do not exceed 0.5%, without being applied to the fitting procedure of the corresponding equations. Thus, it is assumed to be reasonable to apply the data of Lagemann *et al.* [57] to model the temperature range from 270 to 325 K. Good agreement with measurements by Bhatia *et al.* [52] (AAD = 0.074%), Nath and co-workers [66–69] (AAD = 0.053%–0.019%), and Sekhar *et al.* [70] (AAD = 0.092%) supports this choice. In contrast, two quite recently published data sets of Ali and Tariq [40] and Oswal *et al.* [61] exhibit a different trend. Ali and Tariq [40] (AAD = 0.65%) carried out their measurements with a single crystal variable path ultrasonic interferometer. The specified experimental uncertainty of  $1 \text{ m}\cdot\text{s}^{-1}$  (corresponding to 0.09%) was assessed by comparing their measurements to other literature data. However, their measurements on benzene, which were published in the same paper, differ by up to  $4 \text{ m}\cdot\text{s}^{-1}$  (corresponding to 0.3%) from the respective equation of state of Thol *et al.* [101]. Therefore, the uncertainty statement of Ali and Tariq [40] is questionable. Oswal *et al.* [61] (AAD = 0.41%) state the same experimental uncertainty, but do not give any information how this value was determined. Thus, on the basis of all available data, except for the ones of Ali and Tariq [40], the expected uncertainty of speed of sound values calculated with the present equation of state is estimated to be 0.5% at atmospheric pressure.

An overview about the available experimental isobaric heat capacity data is given in Figure 9. Only three data sets with more than two data points are available. Góralski *et al.* [71] (AAD = 0.097%) measured their data by differential scanning calorimetry as described by Becker *et al.* [106]. The experimental setup as well as the measuring

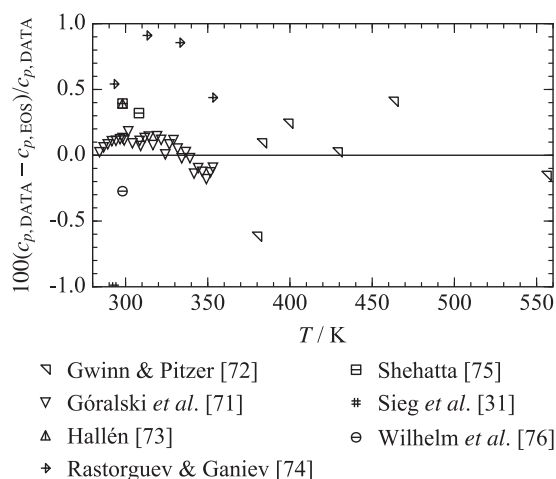


**Figure 9.** Relative deviations of experimental isobaric heat capacity data from the present equation of state at atmospheric pressure.

procedure is described very comprehensively and they claim a combined experimental uncertainty of 0.15%, excluding the effect of sample impurity. Test measurements on water (maximum deviation 0.14% with respect to the IAPWS-95 [107]) verify this specification. Experimental data for toluene differ by up to 0.25%, which is reasonable because the underlying equation of state [108] does not exhibit reference quality. Thus, the present equation of state for 1,2-dichloroethane was modelled so that the experimental uncertainty of 0.15% was maintained. The data set of Rastorguev and Ganiev [74] (AAD = 0.69%) was measured in the same temperature range. It differs by up to 1% from the present equation and the data of Góralski *et al.* [71], and no information on the experimental uncertainties is available. The data set of Gwinn and Pitzer [72] (AAD = 0.26%) is located in the gaseous phase and covers the temperature range between 379 and 557 K. As mentioned in the discussion of the ideal gas heat capacity, no information on sample purity or experimental uncertainties is given. Measurements of the isobaric heat capacity for cyclohexane and cyclopentane [87] carried out with the same apparatus exhibit deviations of up to 1% with respect to the equations of state of Zhou *et al.* [88] and Gedanitz *et al.* [89], which is at the same time the experimental uncertainty of the data. Based on these findings, the experimental uncertainty of the measurements for 1,2-dichloroethane is also expected to be 1% and the representation with the present equation of state is supposed to be reasonable. The expected uncertainty of isobaric heat capacity data calculated with the present equation of state is thus claimed to be 1% in the gaseous region and 0.2% in the liquid state at  $p = 1 \text{ atm}$ .

For the heat of vapourisation, only few measurements are available. Since this property is closely related to the vapour pressure, these data were only used for comparison. The data of Majer *et al.* [78], McGovern [22], and Rao and Viswanath [80] are reproduced within 0.4% and, therefore, verify the behaviour of the vapour pressure curve.

#### 4. Molecular simulation

Based on the available experimental data, the present equation of state for 1,2-dichloroethane is valid for temperatures from the triple point up to 560 K and pressures up to 100 MPa. Similar to the equations of hexamethyldisiloxane [96] and octamethylcyclotetrasiloxane [109], it was extended to a maximum temperature  $T_{\text{max}} = 1000 \text{ K}$  and pressure  $p_{\text{max}} = 1200 \text{ MPa}$  by means of molecular simulation data (cf. Figure 10, where  $A_{\text{mm}}^r$  denote the molecular simulation data). The underlying molecular interaction model that was developed here consists of



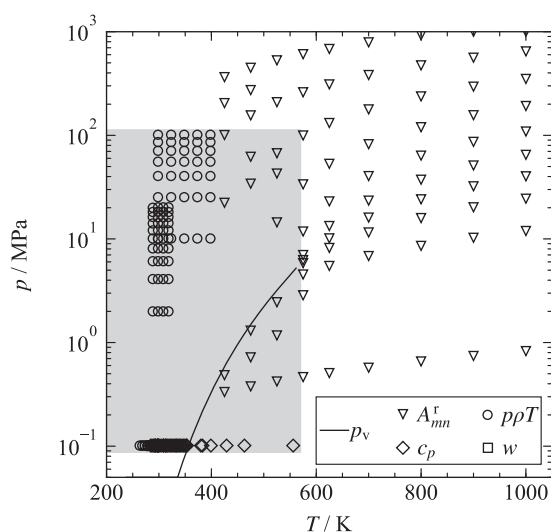


**Figure 10.** Available data for 1,2-dichloroethane in the homogeneous region. The grey area depicts the region where experimental data are available:  $T_{\max} = 560$  K and  $p_{\max} = 100$  MPa. The residual Helmholtz derivatives  $A'_{mn}$  from molecular simulation extend this region up to  $T_{\max} = 1000$  K and  $p_{\max} = 1200$  MPa.

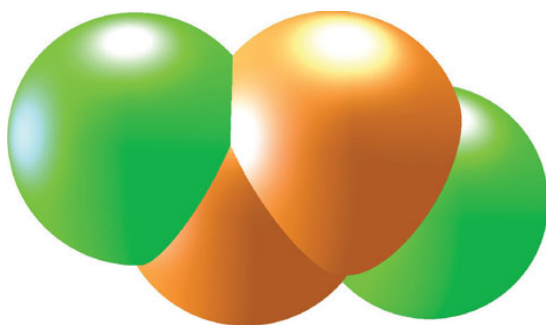


**Figure 11.** (Colour online) Present molecular interaction model for 1,2-dichloroethane. The green spheres represent chlorine atoms, the brown spheres represent methylene groups. Note that the sphere diameters correspond to the Lennard–Jones size parameters, which are depicted according to the molecular geometry scale.

four Lennard–Jones (LJ) sites representing the two chlorine atoms and the two methylene groups ( $\text{CH}_2$ ), and a point quadrupole in the centre of mass, cf. Figure 11. Therefore, the total intermolecular interaction energy in this case writes as

$$U = \sum_{i=1}^{N-1} \sum_{j=i+1}^N \left\{ \sum_{a=1}^{S_i^{\text{LJ}}} \sum_{b=1}^{S_j^{\text{LJ}}} 4\epsilon_{iajb} \left[ \left( \frac{\sigma_{iajb}}{r_{iajb}} \right)^{12} - \left( \frac{\sigma_{iajb}}{r_{iajb}} \right)^6 \right] + \frac{Q_i Q_j}{r_{ij}^5} \cdot f(\omega_i, \omega_j) \right\}, \quad (11)$$

where  $\epsilon_{iajb}$  and  $\sigma_{iajb}$  are the LJ energy and LJ size parameters for the pair-wise interaction between LJ site  $a$  on molecule  $i$  and LJ site  $b$  on molecule  $j$ . The distance between two sites or molecules is denoted by  $r_{iajb}$  or  $r_{ij}$ , respectively. In the case of the electrostatic interaction  $Q$  stands for the quadrupole moment, which is dependent on the orientations  $\omega_i$  and  $\omega_j$  of molecules  $i$  and  $j$  according to [110,111]. Finally, the summation limits  $N$  and  $S_x^{\text{LJ}}$  denote the number of molecules and the number of LJ sites, respectively.

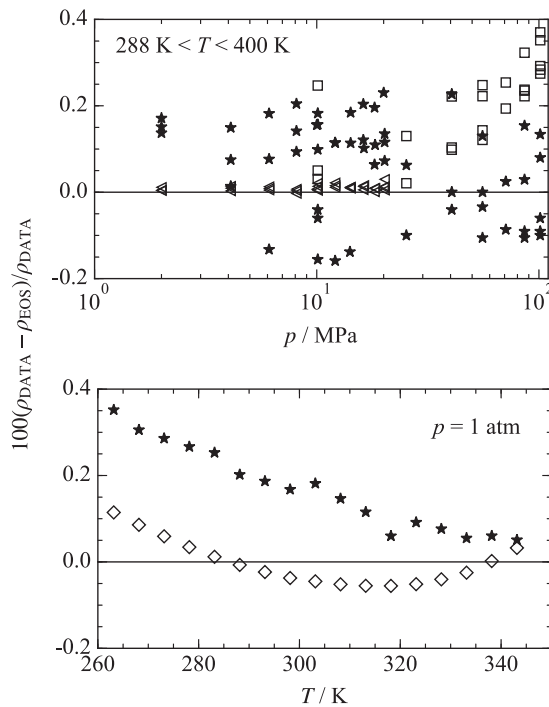
The geometry of the molecule as well as the magnitude and orientation of its quadrupole were initially determined on the basis of quantum chemical calculations. Since 1,2-dichloroethane is a rather compact molecule, its internal degrees of freedom were neglected in the present simulations. However, it has to be noted that the assumption of rigidity is an oversimplification for this molecule, due to the significant influence of other possible conformers on the thermophysical properties. These inherent model limitations are tackled by fitting vapour pressure and saturated liquid density data to experimental values by varying the LJ energy and size parameters of all LJ sites. The resulting parameters are listed in Table 5. Throughout, the simulations were carried out by using cut-off radii equal to half the simulation box sizes using 864 particles. LJ long-range interactions beyond the cut-off radius were corrected as proposed by Lustig [113]. The electrostatic long-range interactions were corrected with the reaction field method [110].

In order to calculate vapour–liquid equilibrium properties, the grand equilibrium method was used [115]. In this two-step procedure, the coexisting phases are simulated independently. In the first step, a Monte Carlo  $NpT$  ensemble simulation in the liquid phase is carried out to obtain the chemical potential as a function of pressure. This was done here with the gradual insertion method [117,118]. After sufficient equilibration, the production is typically carried out for 500000 cycles. In the second step, a pseudo-grand canonical ( $\mu VT$ ) ensemble simulation, which yields the saturated vapour state point, is carried out. Vapour pressure data are reproduced within 3.5% for  $T > 375$  K (cf. Figure 2). For lower temperatures, simulations were not feasible due to sampling problems. The saturated liquid density deviates from the present equation of state by 0.5% for  $T < 400$  K (cf. Figure 4). For higher temperatures, deviations increase. These values are well within the expected accuracy of a molecular model [112]. The representation of the homogeneous state properties by molecular simulation is presented in Figures 12 and 13. The simulated density data scatter around the present equation of state within 0.2%. Keeping in mind that the experimental data are represented within 0.05% for  $T < 320$  K

**Table 5.** Parameters of the present molecular interaction model for 1,2-dichloroethane.

Interaction site	$x / \text{\AA}$	$y / \text{\AA}$	$z / \text{\AA}$	$\sigma / \text{\AA}$	$\varepsilon \cdot k_B^{-1} / \text{K}$	$\varphi / \text{deg}$	$\theta / \text{deg}$	$Q / 10^{-39} \text{ A m}^2 \text{ s}$
Cl	-0.4757	2.1203	0	3.52	135			
CH <sub>2</sub>	0.4757	0.5904	0	3.76	76.95			
CH <sub>2</sub>	-0.4757	-0.5904	0	3.76	76.95			
Cl	0.4757	-2.1203	0	3.52	135			
Quadrupole	0	0	0			60	90	-2.9354

Note: Lennard–Jones interaction sites are denoted by the modelled atoms or atomic groups. The electrostatic interaction site is denoted by quadrupole. Coordinates ( $x, y, z$ ) are given with respect to the centre of mass in a principal axes system. The orientation of the quadrupole is defined in standard Euler angles, where  $\varphi$  is the azimuthal angle with respect to the  $x$ - $z$  plane and  $\theta$  is the inclination angle with respect to the  $z$ -axis.  $k_B$  is the Boltzmann constant.

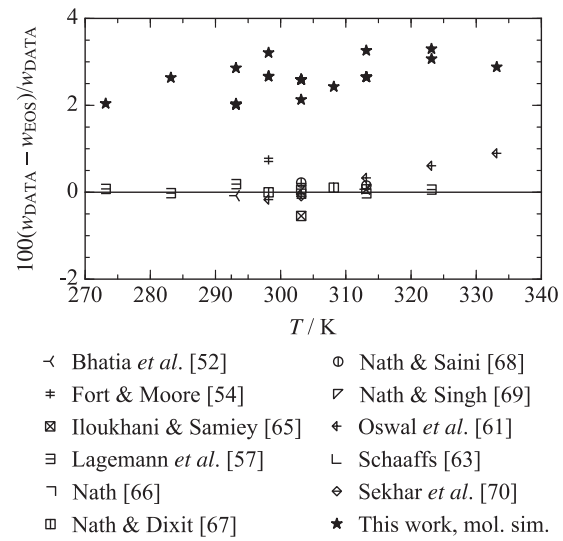


◁ García-Giménez *et al.* [55]    ◇ Manfredini *et al.* [60]  
 □ Kumagai & Takahashi [46]    ★ This work, mol. sim.

**Figure 12.** Relative deviations of experimental homogeneous density data from the present equation of state. At the same  $p$ - $T$  state points, molecular simulation data are presented to verify the accuracy of the present molecular model.

and  $p < 20$  MPa (except for  $p = 1$  atm) as well as 0.5% for higher temperatures and pressures, the density data from molecular simulation are remarkably good. The simulated speed of sound data exhibits a systematic deviation of approximately 3%. For regions where no measurements are available, this uncertainty is acceptable.

After the verification of the molecular model, derivatives of the residual Helmholtz energy were simulated. Based on a methodology by Lustig [114], Thol *et al.*

**Figure 13.** Relative deviations of experimental speed of sound data from the present equation of state at atmospheric pressure. At the same  $p$ - $T$  state points, molecular simulation data are presented to verify the accuracy of the molecular model.

[116] comprehensively presented a new strategy for the development of Helmholtz energy equations of state based on molecular simulation data. In comparison to other literature, the innovation of this strategy is to simulate the residual Helmholtz energy and its derivatives with respect to the natural variables systematically:

$$A_{mn} = A_{mn}^o + A_{mn}^r = \tau^m \delta^n \frac{\partial^{m+n} (\alpha^o + \alpha^r)}{\partial \tau^m \partial \delta^n}. \quad (12)$$

Since the ideal gas contribution is given by the isobaric heat capacity of the ideal gas (cf. Equation (3)), only the residual contribution to the Helmholtz energy is needed. In this work, the simulation data were generated by sampling 83 state points with the simulation tool *ms2* [119]. At each state point, 864 particles were sufficiently equilibrated and then sampled for 2 million cycles with



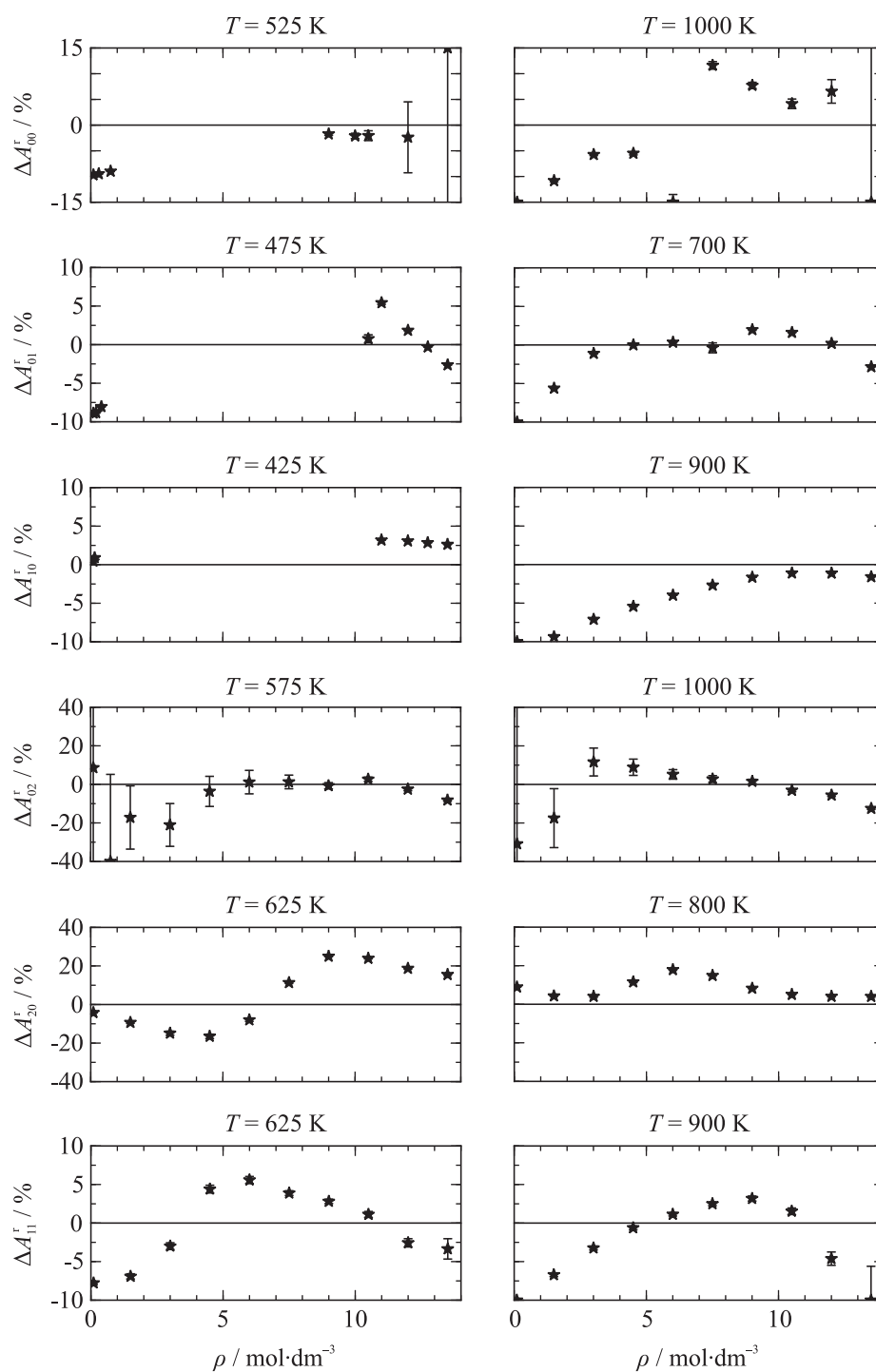


**Figure 14.** Relative deviations of simulated residual Helmholtz derivative data from the present equation of state along selected isotherms. Relative deviations are calculated according to Equation (6).

Monte Carlo  $NVT$  ensemble simulations. From one simulation run, all Helmholtz derivatives up to the third order (except for the third density derivative) were computed. Numerical simulation values along with their statistical uncertainties are given in the supplementary material. These simulation data allow the direct adjustment of the fundamental function and its derivatives with respect to the natural variables during the development of the equation of state. Comparisons of these data with the present equation of state are illustrated in Figure 14. Relative deviations of the residual Helmholtz energy  $A_{00}^r$  are 15%. The first derivatives of the residual Helmholtz energy with respect to the density  $A_{01}^r$  and temperature  $A_{10}^r$  as well as the first mixed derivative  $A_{11}^r$  are reproduced within 10%. The second derivative of the residual Helmholtz energy with respect to the density  $A_{02}^r$  deviates up to 20%, whereas the second derivative of the residual Helmholtz energy with respect to the temperature  $A_{20}^r$  differs by up to 40%. This is most probably the reason for the systematic offset of the simulated speed of sound data depicted in Figure 13. For a better assessment of the quality of the data, the simulated Helmholtz derivatives are transferred to common thermodynamic properties according to the following relations [84]:

$$p/(\rho RT) = 1 + A_{01}^r, \quad (13)$$

$$c_v/R = -(A_{20}^o + A_{20}^r), \quad (14)$$

$$c_p/R = -(A_{20}^o + A_{20}^r) + \frac{(1 + A_{01}^r - A_{11}^r)^2}{1 + 2A_{01}^r + A_{02}^r}, \quad (15)$$

$$wM/(RT) = 1 + 2A_{01}^r + A_{02}^r - \frac{(1 + A_{01}^r - A_{11}^r)^2}{A_{20}^o + A_{20}^r}. \quad (16)$$

These results are compared to the present equation of state in Figure 15. The test simulations of the homogeneous density presented in Figure 12 already indicated a very good accuracy of the data. Here, the molecular simulation data are reproduced within 0.6% for  $\rho \geq 5 \text{ mol} \cdot \text{dm}^{-3}$ . For lower densities, deviations increase up to 4%. The physical behaviour of the present equation of state in this region was carefully monitored during the fitting procedure. Therefore, this effect is most probably caused by the simulation data. However, since no experimental measurements for 1,2-dichloroethane are available in the vapour state, a reliable statement cannot be made here. The simulated isochoric heat capacity scatters around the present equation within 2% for  $\rho \leq 2 \text{ mol} \cdot \text{dm}^{-3}$ .

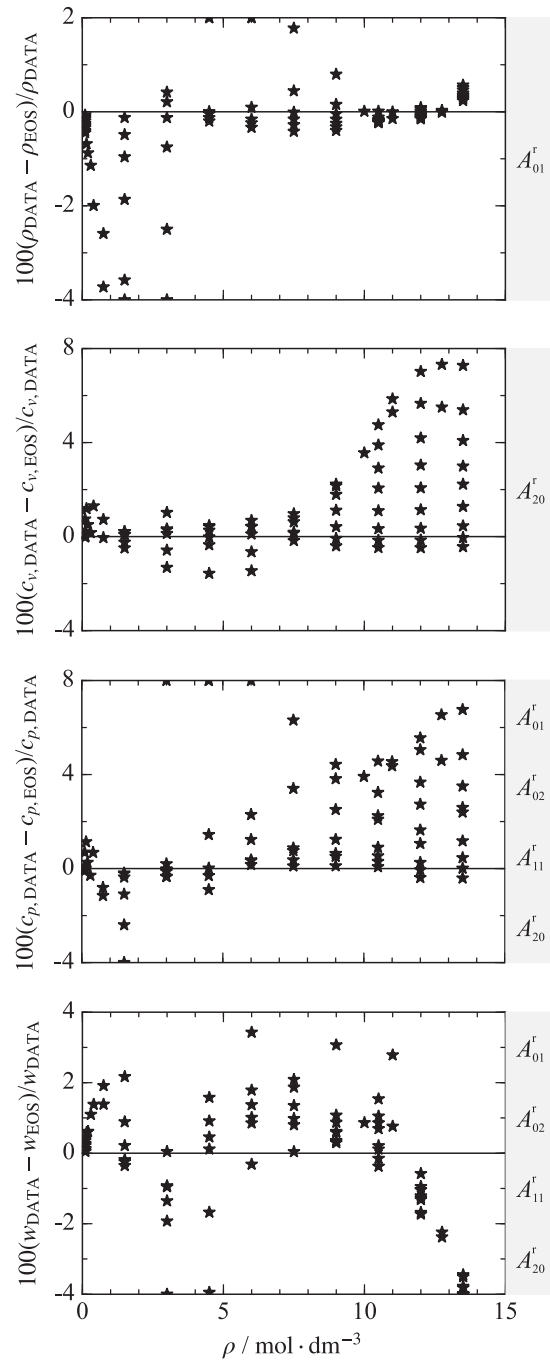


**Figure 15.** Comparison of the present equation of state with thermodynamic properties obtained from molecular simulation data ( $T_{\max} = 1000 \text{ K}$  and  $p_{\max} = 1200 \text{ MPa}$ ). The involved residual Helmholtz energy derivatives are indicated in the grey boxes.

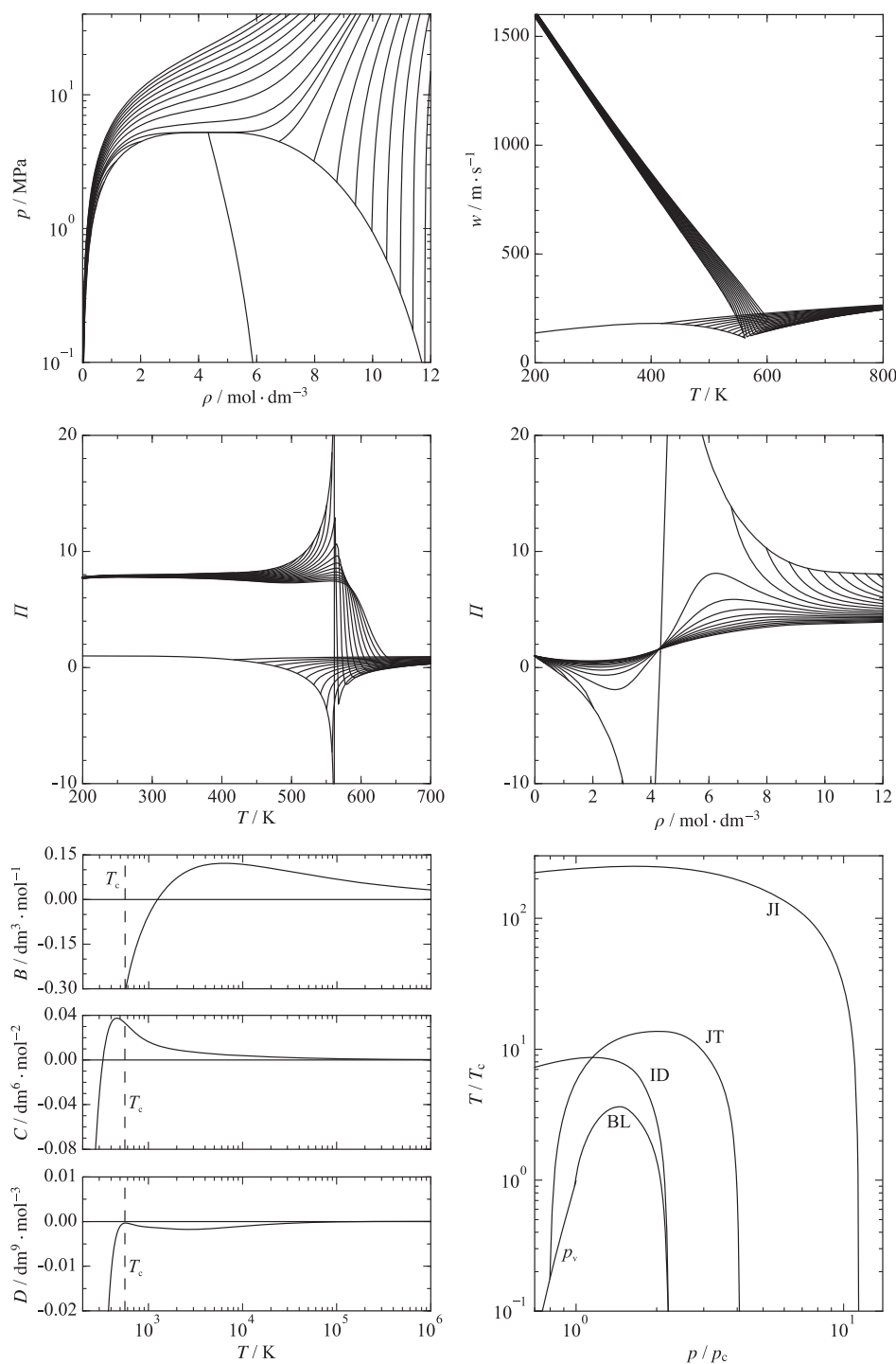


**Figure 16.** Physical behaviour of some thermodynamic properties of 1,2-dichloroethane: vapour-liquid equilibrium curves together with the rectilinear diameter (top left), speed of sound as a function of temperature along selected isobars (top right), phase identification parameter as a function of temperature along selected isobars (centre left), phase identification parameter as a function of density along selected isotherms (centre right), second, third, and fourth virial coefficients (bottom left), and characteristic ideal curves [122] (bottom right).  $p_v$ : vapour pressure curve, BL: Boyle curve, ID: ideal curve, JT: Joule-Thomson inversion curve, JI: Joule inversion curve.

## 5. Physical and extrapolation behaviour

Selected diagrams to verify the physical and extrapolation behaviour of the present equation of state are illustrated in Figure 16. On the top (left), the vapour–liquid equilibrium including the rectilinear diameter is presented and no unreasonable behaviour was detected. The rectilinear diameter ends up as a straight line in the critical region and the critical isotherm exhibits a distinctive saddle point according to the pressure derivatives  $(\partial p / \partial \rho)_{T_c} = 0$  and  $(\partial^2 p^2 / \partial \rho^2)_{T_c} = 0$ . On the top (right), the speed of sound as a function of temperature along selected isobars proves correct physical behaviour. The saturated liquid phase exhibits a straight line with negative slope down to very low temperatures. Additionally, the saturated liquid and vapour lines merge in a minimum at the critical temperature. This is in accordance with a correct course of the isochoric and isobaric heat capacities, where the saturation lines merge in a distinct maximum. The correct behaviour of the phase identification parameter [120] (centre of Figure 16) was discussed in detail by Thol *et al.* [116] and Gao *et al.* [121]. Originally, this property was proposed to discriminate between liquid and vapour states without carrying out time-consuming flash iterations. In the context of developing equations of state, this property is valuable due to the high-order Helmholtz energy derivatives, which are involved. Therefore, wrong shapes of equations of state can easily be detected and revised. For the present equation, no inadequate changes in slope or curvature can be observed. On the bottom of Figure 16, the thermal virial coefficients up to the fourth order (left) and the characteristic ideal curves [122] (right) are presented. The second virial coefficient behaves as expected. The maximum of the third virial coefficient occurs slightly below the critical temperature. 1,2-dichloroethane is slightly associating and, therefore, a shift of the maximum is reasonable. However, this phenomenon is not proven experimentally yet, but only shown for simple potential models, such as the LJ fluid [116,123]. The same applies for the fourth virial coefficient. It approaches negative infinity for  $T \rightarrow 0$  K and a maximum is reached at the critical temperature. The absolute values are negative over the entire temperature range, which should actually remain positive beyond the maximum. However, this behaviour does not affect the calculation of thermodynamic properties for 1,2-dichloroethane within the specified uncertainties. Finally, no unreasonable changes in slope or curvature can be detected in the characteristic ideal curves [122]. Other typical diagrams, e.g. the  $p\rho T$  relation at extreme conditions, the heat capacities, or the Grüneisen coefficient [124] were monitored as well and assessed to be reliable. Therefore, the physical as well as the extrapolation

behaviour of the present equation of state is assumed to be correct.

## 6. Conclusion

The present equation of state for 1,2-dichloroethane is written in terms of the reduced Helmholtz energy, allowing for the calculation of any thermodynamic state property by a combination of its derivatives. The ideal contribution consists of two Planck-Einstein terms, whereas the residual contribution comprises five polynomial, five exponential, and five Gaussian bell-shaped terms. Based on the available experimental data set, it is valid for  $T = 237.52$  to 560 K and pressures of up to  $p = 100$  MPa. The expected uncertainty of vapour pressure data calculated with the present equation of state is 0.1% for  $T < 400$  K and 4% for higher temperatures. Because of the restricted experimental data sets, no statement for the saturated liquid and vapour densities can be made. The uncertainty regarding the homogeneous density was assessed to be 0.05% for  $T < 320$  K and  $p < 20$  MPa, whereas for higher temperatures and pressures uncertainties increase up to 0.5%. The speed of sound can be calculated with an accuracy of 0.5% at atmospheric pressure. The expected uncertainty of the isobaric heat capacity is 1% in the gaseous and 0.2% in the liquid state. The physical and extrapolation behaviour of the equation of state was monitored carefully and found to be reasonable. Finally, the range of validity of the present equation was extended to  $T_{\max} = 1000$  K and  $p_{\max} = 1200$  MPa by means of molecular simulation data. Indications for possible uncertainties in this region are given, but cannot be verified because no experimental measurements are available.

Reference values to verify computer implementation, a fluid file for the application in the software packages REFPROP [125] and TREND [126], and the numerical values of the molecular simulation data are given in the supplementary material.

## Acknowledgments

We would like to thank A. Kasischke for his assistance during the development of the equation of state and Dr E. W. Lemmon for his support. The simulations were carried out on the Cray XC40 (Hazel Hen) computer at the High Performance Computing Center Stuttgart (HLRS) and on the OCULUS cluster of the Paderborn Center for Parallel Computing (PC<sup>2</sup>).

## Disclosure statement

No potential conflict of interest was reported by the authors.

## Funding

This work was supported by Deutsche Forschungsgemeinschaft [grant number VR6/4-2], [grant number SP507/7-2].

## References

- [1] D.-Y. Peng and D.B. Robinson, *Ind. Eng. Chem. Fundam.* **15**, 59 (1976).
- [2] O. Redlich and J.N.S. Kwong, *Chem. Rev.* **44**, 233 (1949).
- [3] S.H. Huang and M. Radosz, *Ind. Eng. Chem. Res.* **29**, 2284 (1990).
- [4] B. Saager, R. Hennenberg, and J. Fischer, *Fluid Phase Equilib.* **72**, 41 (1992).
- [5] B. Saager and J. Fischer, *Fluid Phase Equilib.* **72**, 67 (1992).
- [6] B.I. Lee and M.G. Kesler, *AIChE J.* **21**, 510 (1975).
- [7] Römpp Encyclopedia Online: <http://www.roempp.com> (Thieme Verlag, Stuttgart, 2007, accessed at 10/11/2014).
- [8] F. Amireche-Ziar, G. Boukais-Belaribi, A. Jakob, I. Mokbel, and F.B. Belaribi, *Fluid Phase Equilib.* **268**, 39 (2008).
- [9] A. Barhala, D. Dragoescu, M. Teodorescu, and I. Wichterle, *J. Chem. Thermodyn.* **38**, 617 (2006).
- [10] F. Comelli and R. Francesconi, *J. Chem. Eng. Data* **39**, 560 (1994).
- [11] F. Comelli and R. Francesconi, *J. Chem. Eng. Data* **40**, 21 (1995).
- [12] M. Comtat, M. Enjalbert, and J. Mahenc, *Chim. Ind. Genie Chim.* **102**, 225 (1969).
- [13] W. Davies, J.B. Jaggeh, and H.K. Whalley, *J. Chem. Technol. Biotechnol.* **68**, 26 (1949).
- [14] H.J. Dietrich, *VDI-Forschungsheft* **42**, 1 (1976).
- [15] V. Dohnal, D. Bláhová, and R. Holub, *Fluid Phase Equilib.* **9**, 187 (1982).
- [16] F. Garcia-Sanchez and A. Trejo, *J. Chem. Thermodyn.* **17**, 981 (1985).
- [17] N.F. Giles and G.M. Wilson, *J. Chem. Eng. Data* **51**, 1973 (2006).
- [18] B. Gutsche and H. Knapp, *Fluid Phase Equilib.* **8**, 285 (1982).
- [19] O. Igoudjilene, A. Ait-Kaci, and J. Jose, *Int. Electron J. Phys. Chem. Data* **5**, 135 (1999).
- [20] E. Kirschbaum, H. Fischer, and D. Wolf, *Chem. Ing. Tech.* **34**, 423 (1962).
- [21] H. Kirss, M. Kuus, and E. Siimer, *Proc. Est. Acad. Sci.* **51**, 215 (2002).
- [22] E.W. McGovern, *Ind. Eng. Chem.* **35**, 1230 (1943).
- [23] G. Mijsch, E. Liebermann, and F. Kohler, *Monatsh. Chem.* **100**, 1574 (1969).
- [24] H.R. Patel, S. Sundaram, and D.S. Viswanath, *J. Chem. Eng. Data* **24**, 40 (1979).
- [25] J.N. Pearce and P.E. Peters, *J. Phys. Chem.* **33**, 873 (1928).
- [26] D. Radulescu and M. Alexa, *Rom. J. Chem.* **20**, 89 (1938).
- [27] M.V. Rao and D.S. Viswanath, *J. Chem. Eng. Data* **27**, 41 (1982).
- [28] F. Rivenq, *Bull. Soc. Chim. Fr.* **11**, 2429 (1974).
- [29] A.P. Rollet, P. Toledano, G. Elkai, and M. Sénez, *Publications scientifiques de l'Université d'Alger Sér. B* **2** 403 (1956).
- [30] P.A. Sewell and R. Stock, *Trans. Faraday Soc.* **67**, 1617 (1971).
- [31] L. Sieg, J.L. Cruetzen, and W. Jost, *Z. Phys. Chem. (Leipzig)* **198**, 263 (1951).
- [32] E.R. Smith and H. Matheson, *J. Res. Nat. Bur. Stand.* **20**, 641 (1938).
- [33] D.R. Stull, *Ind. Eng. Chem.* **39**, 517 (1947).
- [34] S. Sundaram and D.S. Viswanath, *J. Chem. Eng. Data* **21**, 448 (1976).
- [35] M. Teodorescu, A. Barhala, and O. Landauer, *Int. Electron J. Phys. Chem. Data* **3**, 101 (1997).
- [36] A.P. Toropov and Nikonovich, *Zh. Fiz. Khim.* **29**, 615 (1955).
- [37] R.M. Varushchenko, S.S. Puchkov, and A.I. Druzhinina, *Russ. J. Phys. Chem.* **56**, 1805 (1982).
- [38] J.A. Waters, G.A. Mortimer, and H.E. Clements, *J. Chem. Eng. Data* **15**, 174 (1970).
- [39] W.V. Wilding, L.C. Wilson, and G.M. Wilson, *Fluid Phase Equilib.* **36**, 67 (1987).
- [40] A. Ali and M. Tariq, *J. Mol. Liq.* **137**, 64 (2008).
- [41] S.F. Babak and V.V. Udovenko, *Russ. J. Gen. Chem. Russian* **20**, 2199 (1950).
- [42] B.H. Billings and D.E. Gray, *American Institute of Physics Handbook. Constants of Polyatomic Molecules*, by G. Herzberg and L. Herzberg, 3rd ed. (McGraw-Hill, New York, 1972).
- [43] W. Herz and M. Levi, *Z. Anorg. Allg. Chem.* **183**, 340 (1929).
- [44] S.S. Joshi, T.M. Aminabhavi, and S.S. Shukla, *J. Chem. Eng. Data* **35**, 247 (1990).
- [45] C. Klotz, Š. Paljk, and S. Golc-Teger, *Thermochim. Acta* **196**, 401 (1992).
- [46] A. Kumagai and S. Takahashi, *J. Chem. Thermodyn.* **17**, 977 (1985).
- [47] A.M. Martin, V.B. Rodríguez, and D.M. Villena, *Afinidad* **40**, 241 (1983).
- [48] G. Sivaramprasad, M.V. Rao, and Prasad, D. H. L., *J. Chem. Eng. Data* **35**, 122 (1990).
- [49] V.V. Udovenko, R.P. Airapetova, and R.I. Filatova, *Russ. J. Gen. Chem. Russian* **21**, 1559 (1951).
- [50] R.M. Varushchenko, O.L. Vikhlakova, N.S. Mirzabekyants, S.S. Puchkov, and V.V. Galkina, *Vestn. Mosk. Univ. Ser. 2 Khim* **22**, 545 (1981).
- [51] A.I. Vogel, *J. Chem. Soc.* **2**, 644 (1948).
- [52] S.C. Bhatia, R. Bhatia, and G.P. Dubey, *J. Chem. Thermodyn.* **42**, 114 (2010).
- [53] O. Ciocirlan, M. Teodorescu, D. Dragoescu, O. Iulian, and A. Barhala, *J. Chem. Eng. Data* **55**, 968 (2010).
- [54] R.J. Fort and W.R. Moore, *Trans. Faraday Soc.* **61**, 2102 (1965).
- [55] P. García-Giménez, J.F. Martínez-López, S.T. Blanco, I. Velasco, and S. Otín, *J. Chem. Eng. Data* **52**, 2368 (2007).
- [56] G. Hahn, P. Svejda, and A. Dallos, *Fluid Phase Equilib.* **86**, 293 (1993).
- [57] R.T. Lagemann, D.R. McMillan, and W.E. Woolf, *J. Chem. Phys.* **17**, 369 (1949).
- [58] R. Malhotra, W.E. Price, L.A. Woolf, and A.J. Eastale, *Int. J. Thermophys.* **11**, 835 (1990).
- [59] R. Malhotra and L.A. Woolf, *Fluid Phase Equilib.* **95**, 227 (1994).
- [60] M. Manfredini, A. Marchetti, S. Sighinolfi, L. Tassi, A. Ulrici, and M. Vignali, *J. Mol. Liq.* **100**, 163 (2002).

- [61] S.L. Oswal, B.M. Patel, A.M. Patel, and N.Y. Ghael, *Fluid Phase Equilib.* **206**, 313 (2003).
- [62] S. Ranjbar, K. Fakhri, and J.B. Ghasemi, *J. Chem. Eng. Data* **54**, 3284 (2009).
- [63] W. Schaaffs, *Z. Phys. Chem.* **194**, 28 (1944).
- [64] A. Valtz, C. Coquelet, G. Boukais-Belaribi, A. Dahmani, and F.B. Belaribi, *J. Chem. Eng. Data* **56**, 1629 (2011).
- [65] H. Iloukhani and B. Samiey, *Phys. Chem. Liq.* **45**, 571 (2007).
- [66] J. Nath, *J. Chem. Thermodyn.* **28**, 481 (1996).
- [67] J. Nath and A.P. Dixit, *J. Chem. Eng. Data* **29**, 313 (1984).
- [68] J. Nath and R. Saini, *J. Chem. Soc. Faraday Trans.* **86**, 645 (1990).
- [69] J. Nath and G. Singh, *J. Chem. Eng. Data* **31**, 327 (1986).
- [70] G.C. Sekhar, P. Venkatesu, and Rao, Murari Venkata Prabhakara, *J. Chem. Eng. Data* **46**, 377 (2001).
- [71] P. Góralski, M. Tkaczyk, and M. Chorażewski, *J. Chem. Eng. Data* **48**, 492 (2003).
- [72] W.D. Gwinn and K.S. Pitzer, *J. Chem. Phys.* **16**, 303 (1948).
- [73] D. Hallén, *J. Chem. Thermodyn.* **25**, 519 (1993).
- [74] Y.L. Rastorguev and Y.A. Ganiev, *Izv. Vyssh. Uchebn. Zaved., Neft Gaz* **10**, 79 (1967).
- [75] I. Shehatta, *Thermochim. Acta* **213**, 1 (1993).
- [76] E. Wilhelm, J.-P. Grolier, and M. Ghassemi, *Thermochim. Acta* **28**, 59 (1979).
- [77] A.S. Carson, P.G. Laye, J.B. Pedley, A.M. Welsby, J.S. Chickos, and S. Hosseini, *J. Chem. Thermodyn.* **26**, 1103 (1994).
- [78] V. Majer, L. Šváb, and V. Svoboda, *J. Chem. Thermodyn.* **12**, 843 (1980).
- [79] K. Bohmhammel and W. Mannchen, *Z. Phys. Chem.* **248**, 230 (1971).
- [80] Y.J. Rao and D.S. Viswanath, *J. Chem. Eng. Data* **18**, 49 (1973).
- [81] A.R. Paniego, Lluna, J. A. Burriel, and J. E. Garcia, *Herero, An. Quim.* **70**, 349 (1975).
- [82] P.J. Mohr, B.N. Taylor, and D.B. Newell, *Rev. Mod. Phys.* **84**, 1527 (2012).
- [83] M.E. Wieser and M. Berglund, *Pure Appl. Chem.* **81**, 2131 (2009).
- [84] R. Span, *Multiparameter Equations of State. An Accurate Source of Thermodynamic Property Data* (Springer, Berlin, 2000).
- [85] K.S. Pitzer, *J. Am. Chem. Soc.* **63**, 2413 (1941).
- [86] K.S. Pitzer and W.D. Gwinn, *J. Am. Chem. Soc.* **63**, 3313 (1941).
- [87] R. Spitzer and K.S. Pitzer, *J. Am. Chem. Soc.* **68**, 2537 (1946).
- [88] Y. Zhou, J. Liu, S.G. Penoncello, and E.W. Lemmon, *J. Phys. Chem. Ref. Data* **43**, 043105 (2014).
- [89] H. Gedanitz, M.J. Dávila, and E.W. Lemmon, *J. Chem. Eng. Data* **60**, 1331 (2015).
- [90] E.W. Lemmon (private communication).
- [91] E.W. Lemmon and R.T. Jacobsen, *J. Phys. Chem. Ref. Data* **34**, 69 (2005).
- [92] M. Frenkel, R.D. Chirico, V. Diky, K. Kroenlein, C.D. Muzny, A.F. Kazakov, J.W. Magee, I.M. Abdulagatov, and E.W. Lemmon, *NIST Standard Reference Database 103b: NIST Thermo-Data-Engine – Pure Components, Binary Mixtures, Reactions, Version 8.0* (National Institute of Standards and Technology, Gaithersburg, 2013).
- [93] R.L. Rowley, W.V. Wilding, J. Oscarson, Y. Yang, N. Zuendel, T. Daubert, and R. Danner, *DIPPR Data Compilation of Pure Chemical Properties* (Taylor & Francis Publishing Company, New York, 2004).
- [94] A. Blondel-Telouk, H. Loiseleur, A. Barreau, E. Behar, and J. Jose, *Fluid Phase Equilib.* **110**, 315 (1995).
- [95] L. Boubliková and B.C.-Y. Lu, *J. Appl. Chem.* **19**, 89 (1969).
- [96] M. Thol, F.H. Dubberke, G. Rutkai, T. Windmann, A. Köster, R. Span, and J. Vrabec, *Fluid Phase Equilib.* **418**, 133 (2016).
- [97] M. Thol, G. Rutkai, A. Köster, M. Kortmann, R. Span, and J. Vrabec, *Chem. Eng. Sci.* **121**, 87 (2015); **134**, 887–890 (2015).
- [98] D. Ambrose, *J. Sci. Instrum.* **40**, 129 (1963).
- [99] I.A. McLure and E. Dickinson, *J. Chem. Thermodyn.* **8**, 93 (1976).
- [100] D. Ambrose, *Vapour-Liquid Critical Properties* (National Physical Laboratory, Teddington, U.K., 1980).
- [101] M. Thol, E.W. Lemmon, and R. Span, *High Temp.-High Press.* **41**, 81 (2012).
- [102] J.A. Zollweg and G.W. Mulholland, *J. Chem. Phys.* **57**, 1021 (1972).
- [103] E.W. Lemmon (private communication).
- [104] D.R. McMillan, *J. Acoust. Soc. Am.* **19**, 956 (1947).
- [105] S. Herrig, Master thesis, Ruhr-Universität Bochum, 2013.
- [106] L. Becker, O. Aufderhaar, and J. Gmehling, *J. Chem. Eng. Data* **45**, 661 (2000).
- [107] W. Wagner and A. Pruss, *J. Phys. Chem. Ref. Data* **31**, 387 (2002).
- [108] E.W. Lemmon and R. Span, *J. Chem. Eng. Data* **51**, 785 (2006).
- [109] M. Thol, G. Rutkai, A. Köster, F.H. Dubberke, T. Windmann, R. Span, and J. Vrabec, *J. Chem. Eng. Data* **61**, 2580 (2016).
- [110] M.P. Allen and D.J. Tildesley, *Computer Simulation of Liquids* (Clarendon Press, Oxford, 1987).
- [111] C.G. Gray and K.E. Gubbins, *Theory of Molecular Fluids* (Clarendon Press, Oxford, 1984).
- [112] J. Vrabec, J. Stoll, and H. Hasse, *J. Phys. Chem. B* **105**, 12126 (2001).
- [113] R. Lustig, *Mol. Phys.* **65**, 175 (1988).
- [114] R. Lustig, *Mol. Phys.* **110**, 3041 (2012).
- [115] J. Vrabec and H. Hasse, *Mol. Phys.* **100**, 3375 (2002).
- [116] M. Thol, G. Rutkai, A. Köster, R. Span, J. Vrabec, and R. Lustig, *J. Phys. Chem. Ref. Data* **45**, 023101 (2016).
- [117] I. Nezbeda and J. Kolafa, *Mol. Sim.* **5**, 391 (1991).
- [118] J. Vrabec, M. Kettler, and H. Hasse, *Chem. Phys. Lett.* **356**, 431 (2002).
- [119] C.W. Glass, S. Reiser, G. Rutkai, S. Deublein, A. Köster, G. Guevara-Carrion, A. Wafai, M. Horsch, M. Bernreuther, T. Windmann, H. Hasse, and J. Vrabec, *Comp. Phys. Commun.* **185**, 3302 (2014).
- [120] G. Venkatarathnam and L.R. Oellrich, *Fluid Phase Equilib.* **301**, 225 (2011).
- [121] K. Gao, J. Wu, P. Zhang, and E.W. Lemmon, *J. Chem. Eng. Data* **61**, 2859 (2016).
- [122] R. Span and W. Wagner, *Int. J. Thermophys.* **18**, 1415 (1997).
- [123] M. Thol, G. Rutkai, R. Span, J. Vrabec, and R. Lustig, *Int. J. Thermophys.* **36**, 25 (2015).

- [124] V. Arp, J.M. Persichetti, and G.-b. Chen, *J. Fluids Eng.* **106**, 193 ([1984](#)).
- [125] E.W. Lemmon, M.L. Huber, and M.O. McLinden, *NIST Standard Reference Database 23: Reference Fluid Thermodynamic and Transport Properties-REFPROP, Version 9.1* (National Institute of Standards and Technology, Gaithersburg, [2013](#)).
- [126] R. Span, T. Eckermann, S. Herrig, S. Hielscher, A. Jäger, and M. Thol, *TREND. Thermodynamic Reference and Engineering Data 2.0* (Lehrstuhl für Thermodynamik, Ruhr-Universität Bochum, Bochum, [2015](#)).

### 3.10 Fundamental equation of state correlation for hexamethyldisiloxane based on experimental and molecular simulation data

M. Thol, F. H. Dubberke, G. Rutkai, T. Windmann, A. Köster, R. Span, J. Vrabec, *Fluid Phase Equilibria* 418:133-151, 2016.

DOI: [doi.org/10.1016/j.fluid.2015.09.047](https://doi.org/10.1016/j.fluid.2015.09.047)

Nachgedruckt mit Erlaubnis von Elsevier (Copyright 2016).

Im Rahmen dieser Arbeit wurde eine hybride Zustandsgleichung für Hexamethyldisiloxan erstellt, eine Substanz die sich hervorragend als Arbeitsmedium in „Organic Rankine Cycles“ eignet. Für die Bestimmung der dafür verwendeten partiellen Ableitungen der Helmholtzenergie wurde ein neues molekulares Kraftfeld entwickelt. Die vorhandenen experimentellen Daten aus der Literatur wurden um Schallgeschwindigkeitsmessungen erweitert. Die mit Hilfe des Lustig-Formalismus [Lus11, Lus12] berechneten partiellen Ableitungen der Helmholtzenergie ermöglichten eine effiziente Nutzung der Simulationsdaten im Anpassungsprozess der Gleichung und tragen insbesondere dazu bei, dass der Gültigkeitsbereich von Gleichungen die nur auf Experimenten beruhen vergrößert wird.

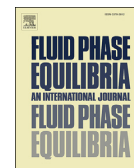
Der Autor der vorliegenden Dissertation hat alle für diese Veröffentlichungen zugrundeliegenden molekularen Simulationen der partiellen Ableitungen der Helmholtzenergie durchgeführt. Das zugrundeliegende Kraftfeld wurde von Dr. Thorsten Windmann erstellt und optimiert. Für die experimentelle Ermittlung der Schallgeschwindigkeit von Hexamethyldisiloxan wurde eine neue Messapparatur von Frithjof Dubberke aufgebaut, der auch die Messungen durchgeführt hat. Alle Daten wurden von Dr. Monika Thol verwendet um eine hybride helmholtzexplizite Zustandsgleichung zu erstellen. Der Autor übernahm die Konsolidierung des Manuskripts. Weiterhin verfasste der Autor in Zusammenarbeit mit Dr. Gábor Rutkai die Beschreibungen über die zugrundeliegenden Simulationsmethoden und -parameter. Die Überarbeitung des Manuskripts wurde in Zusammenarbeit mit Prof. Roland Span und Prof. Jadran Vrabec durchgeführt. Der Autor wurde während des gesamten Prozesses von Prof. Jadran Vrabec betreut.





Contents lists available at ScienceDirect

Fluid Phase Equilibria

journal homepage: [www.elsevier.com/locate/fluid](http://www.elsevier.com/locate/fluid)

## Fundamental equation of state correlation for hexamethyldisiloxane based on experimental and molecular simulation data

M. Thol<sup>a</sup>, F.H. Dubberke<sup>b</sup>, G. Rutkai<sup>b</sup>, T. Windmann<sup>b</sup>, A. Köster<sup>b</sup>, R. Span<sup>a</sup>, J. Vrabec<sup>b,\*</sup><sup>a</sup> Lehrstuhl für Thermodynamik, Ruhr-Universität Bochum, 44801, Bochum, Germany<sup>b</sup> Lehrstuhl für Thermodynamik und Energietechnik, Universität Paderborn, 33098, Paderborn, Germany

### ARTICLE INFO

#### Article history:

Received 31 August 2015  
Received in revised form  
23 September 2015  
Accepted 23 September 2015  
Available online 23 October 2015

#### Keywords:

Thermodynamic properties  
Fundamental equation of state  
Molecular modeling and simulation  
Hexamethyldisiloxane

### ABSTRACT

An empirical fundamental equation of state correlation in terms of the Helmholtz energy is presented for hexamethyldisiloxane. The relatively small amount of thermodynamic data that is available in the literature for this substance is considerably extended by speed of sound measurements and numerical results for Helmholtz energy derivatives from molecular modeling and simulation. The speed of sound apparatus employed in this work is based on the pulse-echo technique and operates up to 150 MPa in the temperature range between 250 K and 600 K. The range of validity of the equation of state, based on laboratory data from literature and speed of sound data of this work, is from 270 K to 580 K and up to 130 MPa. Molecular simulation data are applied to extend the range of validity up to 1200 K and 600 MPa.

© 2015 Elsevier B.V. All rights reserved.

### 1. Introduction

In heat recovery systems, such as organic Rankine cycles (ORC), one important group of working fluids are siloxanes, which belong to the wider class of organo-silicone compounds. Among others, hexamethyldisiloxane (CAS No.: 107-46-0,  $C_6H_{18}OSi_2$ ) appears to be a good candidate for becoming a widely employed working fluid for high temperature ORC processes. However, accurate thermodynamic data for siloxanes are a prerequisite for optimally designed processes.

Traditionally, thermodynamic properties obtained from experiments are summarized in different forms of empirical equations of state. Correlations of the fundamental equation of state (EOS) are particularly useful, because every thermodynamic equilibrium property can be expressed as a combination of derivatives of the thermodynamic potential in terms of which the EOS is explicit. However, a sufficient amount of thermodynamic data is a key factor when it comes to empirical EOS development.

For hexamethyldisiloxane a fundamental EOS was published by Colonna et al. [1] in 2006. Upon commission of our speed of sound measurement apparatus that is briefly described below, it was found that this model yields unreliable data for this property. In

fact, with up to 15%, these deviations were so large that we decided to develop a molecular interaction model to independently corroborate our experimental findings.

Since 2006, the amount of experimental data that is available for hexamethyldisiloxane has expanded, particularly through the work of Abbas [2], but it is still rather poor; additional data sets were generated in the present work by means of speed of sound measurement and molecular modeling and simulation.

In principle, molecular simulation alone could provide any thermodynamic data at any state point and it is more cost and time efficient than laboratory measurements. However, its predictive capability is limited by the quality of the underlying molecular interaction model. Although molecular interaction models are usually adjusted only to a small amount of experimental data, it is generally accepted that they can provide reasonably good predictions for other state points and properties that were not considered during their optimization. However, consistently good inter- and extrapolation ability cannot be guaranteed. Our previous experience with several substances indicated that satisfactory performance still can be expected with respect to predicting various Helmholtz energy derivatives in the homogeneous fluid region, even if the molecular model was optimized exclusively to experimental vapor–liquid equilibrium data [3–7]. Nevertheless, due to the inherent uncertainty of molecular models, experimental data are still essential for EOS development.

Acoustic measurements allow for a fast and convenient access to

\* Corresponding author. Warburger Str. 100, 33098, Paderborn, Germany.  
E-mail address: [jadran.vrabec@upb.de](mailto:jadran.vrabec@upb.de) (J. Vrabec).

the speed of sound. In case of fluids, such measurements contribute substantially to the development and parameterization of EOS [8] because accurate speed of sound data can efficiently be obtained over a large range of temperature and pressure. The common measuring principle for determining the speed of sound of liquids is the pulse-echo technique, which was introduced by Kortbeek et al. [9]. In this method, sound waves, emitted by an excited quartz crystal, propagate through a fluid over a known propagation distance, are reflected and travel back to the quartz crystal. The interference and correlation approaches are common for the pulse-echo technique for determining the propagation time of the wave signal. Here, the correlation approach was employed for the speed of sound measurement.

## 2. Speed of sound measurement

### 2.1. Measurement principle

Speed of sound measurements were carried out with the pulse-echo technique. By emitting a high frequency modulated burst signal with a piezoelectric quartz crystal, which was positioned in the fluid between two reflectors with different path lengths  $l_1$  and  $l_2$ , where  $l_1 < l_2$ , the speed of sound was determined by the time measurement of the signal propagation through the fluid over a known distance [10,11]. The speed of sound, neglecting dispersion and diffraction effects, is given by the ratio of the propagation distance and the propagation time

$$w = \frac{2(l_2 - l_1)}{\Delta t} \quad (1)$$

The measurement of the propagation time difference  $\Delta t$  was based on the correlation method, which was also used by Ball and Trusler [12], combined with a signal enhancement by applying Fast Fourier Transformation (FFT) to the original echo signals [13,14].

The quartz crystal was excited with a burst of 20 cycles, typically with a voltage of 10 V peak-to-peak. Both echoes were sampled, stored to a computer by an oscilloscope (Agilent, DSO1022A) and identified via a threshold. On the basis of the time intervals where the signals exceeded the specified threshold, a significantly extended number of data points in the time interval  $\Delta t_e$  was marked around both echo maxima, starting at  $t_1$  for the first echo and at  $t_2$  for the second echo, cf. Fig. 1 (top).

Because the second echo is affected by greater attenuation due to the longer propagation distance than the first echo, the ratio of the maximum amplitudes of the first echo and the second echo had to be determined. The resulting amplitude factor  $r$ , which depends on the fluid and its thermodynamic state, is required in the correlation approach to consider attenuation [12]. This was done here by multiplying the second echo, i.e. the signal data within  $\Delta t_e$  after  $t_2$ , with the amplitude factor to achieve the same maximum peak magnitude for both echoes, cf. Fig. 1 (center).

The correlation  $z$  overlays the signals of both echoes by

$$z(\Delta t) = \sqrt{\sum_{t_1}^{t_1 + \Delta t_e} [x(t) \cdot r x(t + \Delta t)]^2}, \quad (2)$$

where  $x(t)$  refers to the echo amplitude at the time  $t$ . The time at the maximum of  $z$  is the measured propagation time difference  $\Delta t$ , cf. Fig. 1 (bottom).

### 2.2. Measurement procedure

After filling siloxane into the cell, it was compressed to about

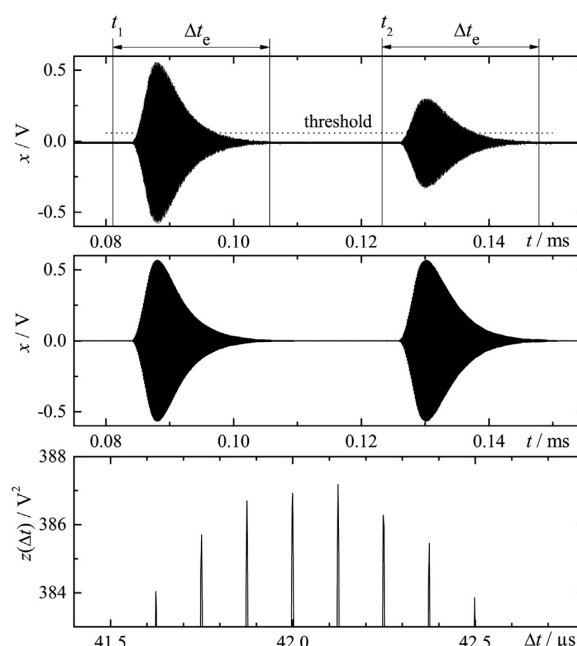


Fig. 1. Steps of the correlation method. Top: First and second echo signals identified via a threshold. Center: Signal reconstructed by Fast Fourier Transformation where the amplitude of the second echo is the same as the amplitude of the first echo. Bottom: Correlation function  $z(\Delta t)$  according to Eq. (2).

20 MPa by a hand-pump and an equilibration time of around 1 h was given to reach a constant pressure level. Each isotherm was studied from high pressure to vapor pressure, where the pressure was measured with a transducer (Honeywell TJE with an operating range up to 70 MPa), which was calibrated with a dead weight tester (Degranges and Hout, 5201-S) and protected by a blowout disc.

The temperature was measured with a Pt100 thermometer (Rössel Messtechnik RM-type), which was mounted in the wall of the pressure cylinder next to the quartz and was calibrated with a standardized 25  $\Omega$  platinum thermometer (Rosemount 162 CE). Hence, the overall uncertainty of the temperature measurement results according to the error propagation law due the individual uncertainty contributions amounts to  $u_T = \pm 15$  mK.

For controlling the cell with a high accuracy over a wide temperature range, the thermostat was constructed with three nested copper shields. Each was monitored with respect to the temperature and equipped with one independently adjustable heater, which was controlled with a combination of a PID controller and an additional proportional (P) controller to quickly specify a constant temperature without overshooting.

The referencing of the path length distance difference  $\Delta l = l_2 - l_1$  was carried out with water, which is available at high purity and for which highly accurate speed of sound measurements are available over a wide range of states, see Ref. [15]. The experimental speed of sound data were corrected by the diffraction correction by Harris [16], where significant dispersion effects are not expected for a resonance frequency of 8 MHz [17].

### 2.3. Results

Speed of sound measurements were carried out for a set of 12

isotherms in the temperature range from 365 K to 573 K up to 20 MPa, cf. Fig. 2. The siloxane was obtained from WACKER with a given purity of  $\geq 99\%$  and was degassed before experimental measurements were carried out.

The uncertainty of the present measurements is larger for lower pressures mainly due to the uncertainty of the pressure sensor. The operating range of the pressure sensor was up to 70 MPa with an accuracy of  $\pm 0.035\%$  of the full scale. Therefore, the absolute uncertainty was 0.025 MPa. This uncertainty had the largest impact at high temperatures and low pressures. The overall speed of sound measurement uncertainty  $u_w$  is composed of the relevant contributions due to uncertainties of temperature and pressure measurements as well as the uncertainty of the referencing procedure.

According to the error propagation law, the total uncertainty was between 0.03% and 0.3%. The higher end of this uncertainty range is mainly caused by the fact that the relative uncertainty of the pressure measurement was significantly higher at low pressures, combined with the high isothermal compressibility of the fluid at such thermodynamic states. Numerical measurement data together with their uncertainties can be found in the [Supplementary Material](#).

### 3. Molecular modeling and simulation

#### 3.1. Molecular model

A molecular interaction model for hexamethyldisiloxane was developed here. It was validated with respect to experimental data or respective correlations from the literature, including saturated liquid density, vapor pressure, enthalpy of vaporization, homogeneous liquid properties (density and speed of sound), second virial coefficient, and transport properties (thermal conductivity and shear viscosity).

The geometry of the model was determined by quantum chemical calculations using the software package GAMESS(US) [18] with the Hartree-Fock method and the 6-31G basis set. Three Lennard-Jones (LJ) sites and three point charges were placed on the silica (Si) and oxygen (O) atoms, while the six methyl groups (CH<sub>3</sub>) were represented with LJ sites only, cf. Fig. 3. Its point charge magnitudes were specified such that they correspond to a dipole

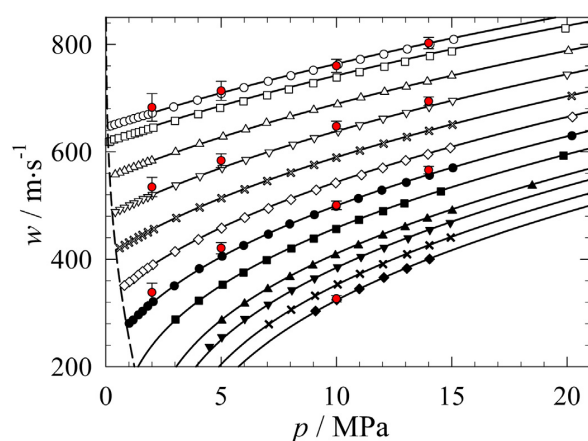


**Fig. 2.** Speed of sound of hexamethyldisiloxane. Present experimental data:  $\circ$  365 K,  $\square$  373 K,  $\triangle$  393 K,  $\times$  413 K,  $\diamond$  433 K,  $\bullet$  453 K,  $\blacksquare$  473 K,  $\blacktriangle$  493 K,  $\blacklozenge$  518 K,  $\blacktriangledown$  533 K,  $\times$  553 K,  $\bullet$  (red) present simulation data; — present equation of state; - - - vapor pressure curve. (For interpretation of the references to color in this figure caption, the reader is referred to the web version of this article.)

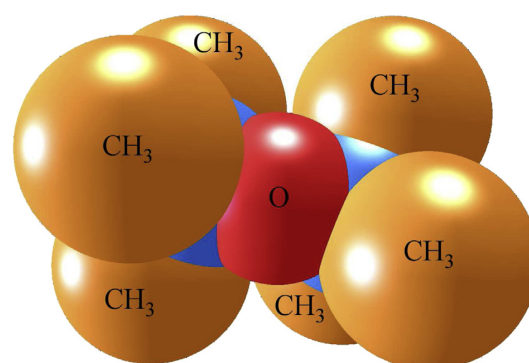


**Fig. 3.** Present molecular interaction model for hexamethyldisiloxane. CH<sub>3</sub>: methyl site, O: oxygen site, not labeled: silica site. Note that the sphere diameters correspond to the Lennard-Jones size parameters, which are depicted according to the molecular geometry scale.

moment of  $2.67 \cdot 10^{-30}$  Cm (a value taken from the DIPPR database [19]). The initial values of the LJ energy ( $\epsilon$ ) and size ( $\sigma$ ) parameters of the CH<sub>3</sub> and O sites were adopted from Schnabel et al. [20] and Vrabec et al. [21], respectively. The LJ parameters of the Si sites were adjusted to experimental saturated liquid density and vapor pressure data. In a last step, all model parameters, including geometric structure and polarity, were fine-tuned with the reduced unit method [22]. The resulting model parameters are listed in Table 1.

#### 3.2. Validation of the molecular model

To validate the present molecular interaction model, simulation results for vapor–liquid equilibria, homogeneous liquid density, speed of sound, second virial coefficient, and transport properties were compared with experimental data from the literature and with correlations from the DIPPR database [19]. All simulation details and numerical data are given in the [Supplementary Material](#). The simulation data for vapor pressure, saturated liquid density, saturated vapor density, and enthalpy of vaporization are presented in absolute plots in the [Supplementary Material](#). As discussed in section 4.3 in detail, for the vapor pressure relative deviations between the molecular simulation data and the present EOS are less than 4% for all simulation points, except for the lowest temperature. Note that the experimental data scatter in this range, too. Experimental data for the saturated liquid density are available between 213 K and 358 K only. The simulation data in this region are well within the scatter of the experimental data and the uncertainty of the DIPPR correlation [19]. The simulation results for the enthalpy of

**Table 1**  
Parameters of the present molecular interaction model for hexamethyldisiloxane. Lennard-Jones sites are denoted by the modeled atoms or atomic groups. Electrostatic sites are denoted by point charge magnitudes  $q$ . Coordinates are given with respect to the center of mass in a principal axes system.

Interaction site	$x$	$y$	$z$	$\sigma$	$\epsilon/k_B$	$q$
	Å	Å	Å	Å	K	e
CH <sub>3</sub>	-2.2796	-0.8698	-0.3545	3.8144	121.3515	
CH <sub>3</sub>	-2.2150	1.2764	1.8825	3.8144	121.3515	
CH <sub>3</sub>	0.5674	0.7717	-2.5502	3.8144	121.3515	
Si	-1.2334	-0.0730	1.0059	3.5133	15.1500	0.1458
O	0.1238	0.6680	0.3350	3.1180	43.6148	-0.2916
Si	1.2923	0.3890	-0.8475	3.5133	15.1500	0.1458
CH <sub>3</sub>	-0.6830	-1.3930	2.2409	3.8144	121.3515	
CH <sub>3</sub>	1.8613	-1.4145	-0.7878	3.8144	121.3515	
CH <sub>3</sub>	2.7335	1.5447	-0.4734	3.8144	121.3515	

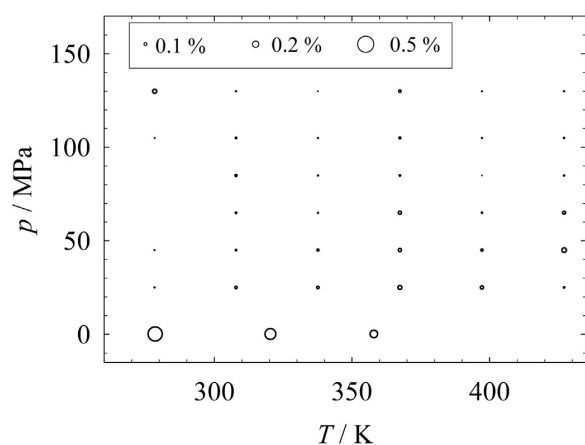


**Fig. 4.** Density in the homogeneous liquid region of hexamethyldisiloxane. Relative deviations between present simulation data and experimental data by Abbas [2] and McLure et al. [23]. ( $\Delta z = (z_{\text{sim}} - z_{\text{exp}})/z_{\text{exp}}$ ). The size of the bubbles indicates the magnitude of the relative deviation.

vaporization agree well with the experimental data over the whole temperature range from 287 K to 500 K. The relative deviations are throughout less than about 1.5%, with the exception of the point at 495 K.

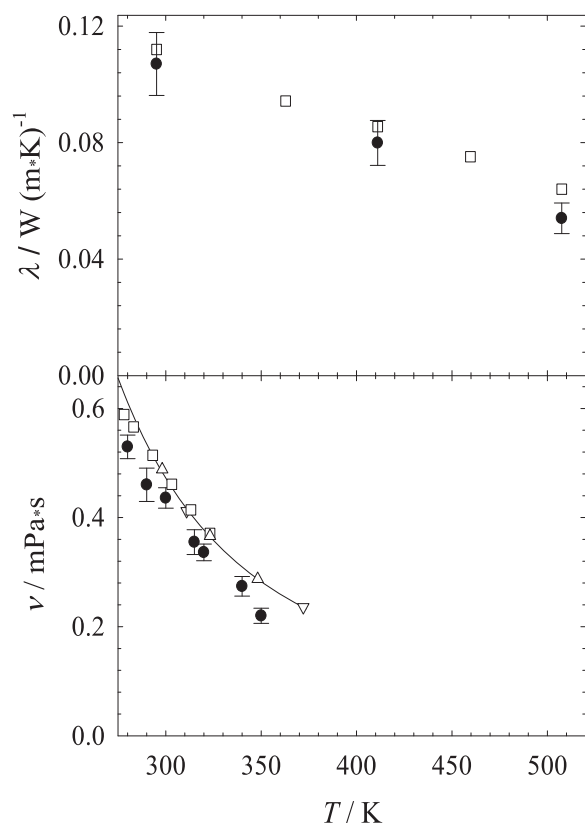


**Fig. 5.** Thermal conductivity at 10 MPa (top) and shear viscosity at 1 atm (bottom) of hexamethyldisiloxane: ● present simulation data; □ experimental data by Abbas [2], △ Hurd [26], and ▽ Wilcock [27]; — correlation of experimental data from the DIPPR database [19].

**Table 2**

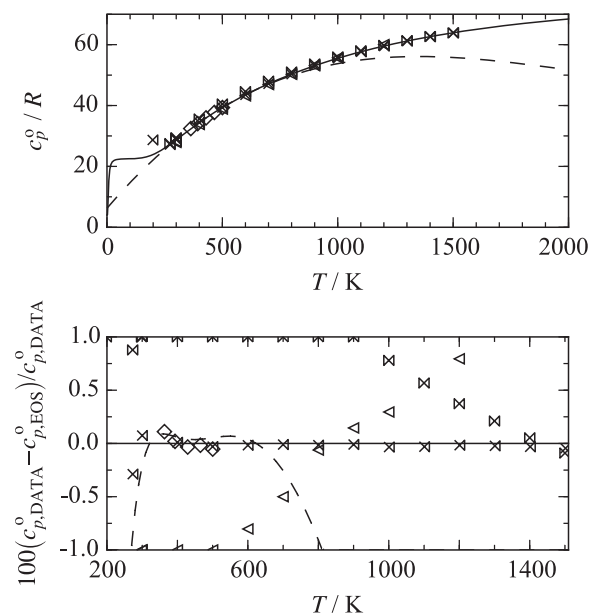
Parameters of the ideal contribution of the present equation of state for hexamethyldisiloxane according to Eq. (10).

$i$	$m_i$	$\theta_i/\text{K}$
1	18.59	20
2	29.58	1400
3	19.74	3600
4	4.87	6300
$c_0$	3.0	
$c^{\text{I}}$	-10.431499	
$c^{\text{II}}$	72.110754	

Simulation results for the homogeneous liquid density were compared to experimental data published by McLure et al. [23] and Abbas [2]. McLure et al. [23] provide data at 1 atm, Abbas [2] performed measurements over a wide temperature and pressure range. Fig. 4 shows the results of the comparison at temperatures from 303 K to 427 K up to a pressure of 130 MPa. It can be seen that the agreement between simulation and experimental data is very satisfying. In general, the relative deviation is less than 0.2%. For the three data points at 1 atm it is slightly higher.

The speed of sound in the liquid state was calculated by simulation, taking the ideal gas contribution of the present EOS into account (see section 4.1). These results were compared with the experimental data generated in the present work. As can be seen in Fig. 2, the simulation results are in line with the experimental data points at the four investigated isotherms 365 K, 413 K, 473 K and 573 K up to a pressure of 14 MPa. Nearly all simulation points agree with the experiment within their statistical uncertainties.

The second virial coefficient was predicted over a temperature range from 220 K to 1500 K by evaluating Mayer's  $f$ -function. This



— — Colonna et al. [1]      △ Nannan et al. [39]  
— This work      ◇ Scott et al. [36]  
× Mosin & Mikhailov [35]      × Scott et al. [36]

**Fig. 6.** Isobaric heat capacity of the ideal gas of hexamethyldisiloxane.

**Table 3**

Parameters of the residual contribution of the present equation of state for hexamethyldisiloxane according to Eq. (11), where  $l_i = 1$ .

$i$	$n_i$	$t_i$	$d_i$	$p_i$	$\eta_i$	$\beta_i$	$\gamma_i$	$\varepsilon_i$
1	$0.5063651 \cdot 10^{-1}$	1.000	4	–				
2	$0.8604724 \cdot 10^{-1}$	0.346	1	–				
3	$-0.9179684 \cdot 10^{-1}$	0.460	1	–				
4	$-0.1146325 \cdot 10^{-1}$	1.010	2	–				
5	$0.4878559 \cdot 10^{-0}$	0.590	3	–				
6	$-0.2434088 \cdot 10^{-1}$	2.600	1	2				
7	$-0.1621326 \cdot 10^{-1}$	3.330	3	2				
8	$0.6239872 \cdot 10^{-0}$	0.750	2	1				
9	$-0.2306057 \cdot 10^{-1}$	2.950	2	2				
10	$-0.5555096 \cdot 10^{-1}$	0.930	7	1				
11	$0.9385015 \cdot 10^{-1}$	1.330	1	–	1.0334	0.4707	1.7754	0.8927
12	$-0.2493508 \cdot 10^{-1}$	1.680	1	–	1.5440	0.3200	0.6920	0.5957
13	$-0.3308032 \cdot 10^{-1}$	1.700	3	–	1.1130	0.4040	1.2420	0.5590
14	$-0.1885803 \cdot 10^{-0}$	3.080	3	–	1.1130	0.5170	0.4210	1.0560
15	$-0.9883865 \cdot 10^{-1}$	5.410	1	–	1.1100	0.4320	0.4060	1.3000
16	$0.1111090 \cdot 10^{-0}$	1.400	2	–	7.2000	7.2000	0.1630	0.1060
17	$0.1061928 \cdot 10^{-0}$	1.100	3	–	1.4500	1.2000	0.7950	0.1810
18	$-0.1452454 \cdot 10^{-1}$	5.300	1	–	4.7300	35.8000	0.8800	0.5250

approach was described e.g. by Eckl et al. [24]. The present results are shown in section 4.5, where the mean absolute deviation over the whole considered temperature range is below  $0.44 \text{ dm}^3 \cdot \text{mol}^{-1}$ .

Thermal conductivity and shear viscosity of liquid hexamethyldisiloxane were obtained by equilibrium molecular dynamics simulations following the Green-Kubo formalism, cf. Guevara-Carrion et al. [25]. Fig. 5 shows the simulation results in comparison with experimental data from the literature and a correlation from the DIPPR database [19]. For the thermal conductivity, simulations were carried out at 10 MPa, cf. Fig. 5 (top). The simulations agree with the experimental data by Abbas [2] mostly within their statistical uncertainties. At 500 K, there is some deviation. The shear viscosity experimental data at 1 atm, published by Abbas [2], Hurd [26], and Wilcock [27], were used for comparison. The shear viscosity from simulation is about 0.1 mPa s below the experimental data in the entire temperature range from 280 K to 350 K, cf. Fig. 5 (bottom). The mean relative deviation of the simulation data with respect to the correlation from the DIPPR database [19] is about 12%.

### 3.3. Large scale thermodynamic data generation

In principle, once a molecular interaction model is available, any thermodynamic information can be obtained from molecular simulation. However, the generation of a data set that contains as much non-redundant thermodynamic information as possible may look cumbersome in practice, because standard textbook approaches in the molecular simulation literature imply that specific statistical mechanical ensembles are required for particular thermodynamic properties. It is true that certain properties have

simpler statistical analogs in certain ensembles and may be difficult to derive in others, but it is nevertheless possible. The statistical mechanical formalism proposed by Lustig [28,29] was designed to provide an arbitrary number of Helmholtz energy derivatives

$$A_{xy}^r = \tau^x \delta^y \frac{\partial^{x+y} \alpha^r(\tau, \delta)}{\partial \tau^x \partial \delta^y} = (1/T)^x \rho^y \frac{\partial^{x+y} \alpha^r(T, \rho)}{\partial (1/T)^x \partial \rho^y}, \quad (3)$$

from a single molecular simulation run for a given state point. In Eq. (3),  $\alpha$  is the reduced Helmholtz energy,  $T$  the temperature,  $\rho$  the density,  $R$  the molar gas constant,  $\tau = T_c/T$  the inverse reduced temperature, and  $\delta = \rho/\rho_c$  the reduced density, in which  $T_c$  is the critical temperature and  $\rho_c$  the critical density.  $\alpha$  is commonly divided into an ideal (superscript “o”) and residual (superscript “r”) contribution

$$\alpha(\tau, \delta) = \frac{a^o(T, \rho) + a^r(T, \rho)}{RT} = \alpha^o(\tau, \delta) + \alpha^r(\tau, \delta), \quad (4)$$

where  $a$  is the molar Helmholtz energy. The ideal contribution  $\alpha^o(T, \rho) = \alpha^o(T) + \alpha^o(\rho)$  corresponds to the value of  $\alpha(T, \rho)$  when no intermolecular interactions are at work [8]. The density dependence of  $\alpha^o(T, \rho)$  is known from the ideal gas law and it is  $\alpha^o(\rho) = \ln(\rho/\rho_{\text{ref}})$ . The exclusively temperature dependent ideal part  $\alpha^o(T)$  has a non-trivial temperature dependence and it is often determined by spectroscopy or *ab initio* calculations. Although molecular interaction models with internal degrees of freedom may describe  $\alpha^o(T)$  accurately, the residual contribution  $\alpha^r(T, \rho) = \alpha(T, \rho) - \alpha^o(T, \rho)$  is typically the target of molecular simulation.

The formalism proposed by Lustig is an implemented feature of our molecular simulation tool *ms2* [30,31] that yields up to eight derivatives of the residual Helmholtz energy. With this method, the analytical derivatives of Eq. (3) can be directly fitted to  $A_{xy}^r$  simulation results, unlike usual thermodynamic properties, such as pressure  $p$ , isochoric heat capacity  $c_v$ , isobaric heat capacity  $c_p$ , and speed of sound  $w$

$$\frac{p}{\rho RT} = 1 + A_{01}^r, \quad (5)$$

$$\frac{c_v}{R} = -(A_{20}^o + A_{20}^r), \quad (6)$$

$$\frac{c_p}{R} = -(A_{20}^o + A_{20}^r) + \frac{(1 + A_{01}^r - A_{11}^r)^2}{1 + 2A_{01}^r + A_{02}^r}, \quad (7)$$

$$\frac{Mw^2}{RT} = 1 + 2A_{01}^r + A_{02}^r - \frac{(1 + A_{01}^r - A_{11}^r)^2}{A_{20}^o + A_{20}^r}, \quad (8)$$

that are linear or non-linear functions of  $A_{xy}^r$ . This approach is a convenient route to obtain an arbitrary number of independent thermodynamic properties, and its contribution to support EOS development was recently shown [3–7]. The large scale molecular simulation data set of the present work contains five derivatives  $A_{10}^r, A_{01}^r, A_{20}^r, A_{11}^r$ , and  $A_{02}^r$  as well as  $A_{00}^r$  at 194 state points that are well distributed in the homogeneous fluid region. At each state point 864 particles were sufficiently equilibrated and then sampled for 2 million production cycles with NVT Monte Carlo simulations [32]. Electrostatic long-range corrections were approximated by the reaction field method [33]. The reduced residual Helmholtz energy  $A_{00}^r$  was determined by Widom’s test particle insertion [34]. A discussion of these data is given in section 4.6, their numerical values can be found in the [Supplementary Material](#).

**Table 4**

Critical parameters from the literature, where the critical density was not measured, but estimated from theoretical models.

Authors	$T_c$ K	$p_c$ MPa	$\rho_c$ mol·dm <sup>−3</sup>
Dickinson et al. [48]	518.8	1.91	1.715
McLure and Dickinson [45]	518.7	1.92	
McLure and Neville [49]			1.589
Nikitin et al. [50]	519	1.92	
Young [51]	516.6	1.91	1.745
Young [52]	516.6	1.91	1.744
This work	518.7	1.93	1.653



#### 4. Fundamental equation of state correlation

In this section, an EOS for hexamethyldisiloxane is presented. Comparisons are made to experimental as well as molecular simulation data, and the physical and extrapolation behavior is analyzed. The present EOS for hexamethyldisiloxane is written in terms of the reduced Helmholtz energy as a function of temperature and density. Because this is a thermodynamic potential, every other equilibrium thermodynamic property can be obtained by differentiating Eqs. (10) and (11) analytically and combining the results. Examples, e.g. for the pressure, are given in Eqs. (5)–(8).

##### 4.1. Ideal gas contribution

The exclusively temperature dependent ideal contribution  $\alpha^0(\tau)$  of the reduced Helmholtz energy  $\alpha(\tau, \delta)$  was derived from a  $c_p^0$  equation

$$\frac{c_p^0}{R} = n_0 + \sum_{i=1}^{I_{\text{pol}}} n_i \tau^{t_i} + \sum_{i=I_{\text{pol}}+1}^{I_{\text{pol}}+I_{\text{pe}}} m_i \left( \frac{\theta_i}{T} \right)^2 \frac{\exp(\theta_i/T)}{(\exp(\theta_i/T) - 1)^2}. \quad (9)$$

For the application to a fundamental EOS in terms of the Helmholtz energy, this equation has to be integrated twice with respect to  $\tau$

$$\alpha^0(\tau, \delta) = c^{\text{II}} + c^{\text{I}} \tau + c_0 \ln(\tau) + \sum_{i=1}^{I_{\text{pol}}} c_i \tau^{t_i} + \sum_{i=I_{\text{pol}}+1}^{I_{\text{pol}}+I_{\text{pe}}} m_i \ln(1 - \exp(-\theta_i/T_c \tau)) + \ln(\delta). \quad (10)$$

The integration constants  $c^{\text{I}}$  and  $c^{\text{II}}$  can be chosen arbitrarily. However, the most common reference state is the normal boiling point (NBP). Here, the temperature and density of the saturated liquid at the reference pressure  $p_0 = 1$  atm have to be determined. At this state point, the default values of the corresponding reference entropy  $s_0(T_{\text{NBP}}, p_0 = 1 \text{ atm})$  and enthalpy  $h_0(T_{\text{NBP}}, p_0 = 1 \text{ atm})$  are set to be zero. Therefore,  $c^{\text{I}}$  and  $c^{\text{II}}$  depend on the residual part of the present equation of state.

In general,  $c_p^0$  equations are correlated to data for the isobaric heat capacity of the ideal gas. These data can be determined from spectroscopy, statistical mechanics, or extrapolation from gaseous speed of sound or isobaric heat capacity measurements. Spectroscopic data are very difficult to analyze for complex molecules. Therefore, they can rarely be used to set up equations of state. When extrapolating ideal gas heat capacities from experimental speed of sound or isobaric heat capacity data, highly accurate measurements are mandatory. Thus, such data are only available for well investigated fluids. Therefore, most data were determined by means of statistical mechanics. Depending on the complexity of the molecule, these data can be associated with high uncertainties so that they have to be treated carefully. When developing a  $c_p^0$  equation, some boundary conditions have to be kept in mind. The functional form of Eq. (9) is physically based and the contributions of molecular translation and rotation are combined in the temperature independent part  $n_0$ . For molecules like hexamethyldisiloxane, it can be assumed that the degrees of freedom of both contributions are fully excited also for very low temperatures. Therefore,  $n_0 = 4$ , corresponding to three degrees of freedom for translation and three degrees of freedom for rotation. The temperature dependent contribution of the molecular vibrations was modeled by

**Table 5**

Average absolute relative deviations of experimental vapor pressure and saturated liquid density data from the present equation of state for hexamethyldisiloxane. All temperatures were adapted to the ITS-90 scale. Datasets, which were applied to the fit, are marked with an asterisk.

Authors	No. of data	Temperature range	Average absolute relative deviations (AAD)/%			
			LT	MT	HT	Overall
<b>Vapor pressure <math>p_v</math></b>						
Abbas [2]	18	284–375	1.894	2.214	—	2.072
Benkeser & Krysiak [54]	1	372.62	—	2.966	—	2.966
Bolotov et al. [55]	1	373.12	—	1.541	—	1.541
Dickinson et al. [48]	3	303–316	0.093	0.041	—	0.076
Flaningham & Williams [56]	1	373.65	—	0.023	—	0.023
Flaningham [57]	15	302–384	0.765	0.318	—	0.437
Guzman et al. [58]	6	333–374	—	0.589	—	0.589
Hunter et al. [59]	1	372.62	—	2.966	—	2.966
Kaczmarek & Radecki [60]	1	374.62	—	2.833	—	2.833
Kaczmarek & Radecki [61]	1	374.02	—	1.066	—	1.066
Kaczmarek & Radecki [62]	1	374.02	—	1.066	—	1.066
Kaczmarek [63]	1	373.62	—	0.099	—	0.099
Kaczmarek [64]	1	373.92	—	0.774	—	0.774
Kaczmarek [65]	1	374.65	—	2.912	—	2.912
Killgore et al. [66]	1	372.98	—	0.663	—	0.663
McLure & Dickinson [45]*	19	491–519	—	1.615	0.380	1.030
Pedersen et al. [67]	1	373.44	—	0.620	—	0.620
Radecki et al. [68]	2	293–375	0.860	1.359	—	1.110
Radecki & Kaczmarek [69]	2	373–374	—	1.541	—	1.541
Radecki & Kaczmarek [70]	1	373.12	—	1.541	—	1.541
Radecki & Kaczmarek [71]	1	373.37	—	0.822	—	0.822
Reuther & Reichel [72]	1	373.62	—	0.099	—	0.099
Sauer [73]	1	373.57	—	0.243	—	0.243
Scott et al. [36]*	21	309–412	0.044	0.030	—	0.031
Speier [74]	1	372.12	—	4.376	—	4.376
Stull [75]	10	244–373	18.34	4.428	—	12.78
Voronkov [76]	1	373.52	—	0.388	—	0.388
Waterman et al. [77]	1	373.82	—	0.043	—	0.043
Zhang et al. [78]	1	373.67	—	0.035	—	0.035
<b>Saturated liquid density <math>\rho'</math></b>						
Gubareva [79]	10	273–354	0.249	0.085	—	0.167
Guzman et al. [58]	5	333–359	—	1.335	—	1.335
Mills & MacKenzie [80]	2	293–303	0.109	—	—	0.109

Planck–Einstein terms. For high temperatures, it has to be ensured that the ideal gas heat capacity approaches a maximum value related to fully excited degrees of freedom considering all contributions, i.e. translation, rotation, and vibration. Since it is too complex to express these contributions on a strictly physical basis, the Planck–Einstein terms were treated empirically. The ideal contribution of the present EOS for hexamethyldisiloxane thus consists of four Planck–Einstein terms and the corresponding parameters are given in Table 2. In Fig. 6, the representation of the isobaric heat capacity of the ideal hexamethyldisiloxane gas is illustrated. The upper part of that figure shows the absolute trend of  $c_p^0/T$  as a function of temperature. The present equation has a correct extrapolation behavior for low temperatures, i.e.  $c_p^0(T \rightarrow 0 \text{ K}) = 4R$ . For high temperatures, an asymptotic behavior of the equation can be observed. Colonna et al. [1] have chosen a simple polynomial approach for fast calculations. This can be helpful when insufficient data are available for the correlation. However, these polynomial terms have to be used carefully because it is easily possible to compromise the extrapolation behavior. As a results of the chosen functional form, the transition of the equation of

Colonna et al. [1] to very low temperatures yields a value of  $6.3R$  and for increasing temperatures the ideal gas heat capacity decreases.

In Fig. 6 (bottom), relative deviations of literature data from the present EOS are shown. Only three different datasets are available. Mosin and Mikhailov [35] derived their data from statistical mechanics. Since no information is given on the accuracy of these data, they were not considered in the development of the present  $c_p^0$  equation. The data of Scott et al. [36] were gained from low temperature calorimetric measurements. Due to limitations of their apparatus, the temperature range was only 360 K to 500 K. Additionally, they used results from investigations on the barrier restricting internal rotation around the Si–O bond to determine the ideal gas heat capacity theoretically, which are in good agreement with their measurements. Therefore, the low temperature region ( $T < 500 \text{ K}$ ) of the present equation was correlated to the experimental results of Scott et al. [36], and higher temperatures were modeled with the help of their theoretical results. For  $T > 300 \text{ K}$ , the ideal gas heat capacity is reproduced within 0.1%, which is also claimed to be the uncertainty of the present equation. For lower temperatures deviations increase.

Table 6

Average absolute relative deviations of the experimental data in the homogeneous region from the present equation of state for hexamethyldisiloxane. All temperatures were adapted to the ITS-90 scale. Datasets, which were applied to the fit, are marked with an asterisk.

Authors	No. of data	Temperature and pressure range		Average absolute relative deviation (AAD)/%					Overall	
				Gas	Liq	Crit. Reg.	Supercritical fluid			
		<i>T</i>	<i>p</i>				LD	MD		HD
<b><i>ppT data</i></b>										
Abbas [2]*	459	278–438	0.9–130	–	0.071	–	–	–	–	0.071
Anderson et al. [88]	1	293.15	0.101325	–	0.120	–	–	–	–	0.120
Bolotov et al. [55]	1	293.15	0.101325	–	0.081	–	–	–	–	0.081
Dickinson [89] <sup>b</sup>	5	303–304	100–501	–	0.476	–	–	–	–	0.476
Fox et al. [90]	1	293.14	0.101325	–	0.174	–	–	–	–	0.174
Gaines [91]	1	297.14	0.101325	–	1.025	–	–	–	–	1.025
Golik and Cholpan [92]	1	303.13	0.101325	–	0.451	–	–	–	–	0.451
Good et al. [93]	1	298.14	0.101325	–	0.168	–	–	–	–	0.168
Hunter et al. [59]	1	298.14	0.101325	–	0.122	–	–	–	–	0.122
Hurd [26] <sup>b</sup>	3	273–314	0.1–1	–	0.275	–	–	–	–	0.275
Kaczmarek [63]	1	293.15	0.101325	–	0.199	–	–	–	–	0.199
Kaczmarek [94]	1	293.15	0.101325	–	0.173	–	–	–	–	0.173
Kaczmarek [64]	1	293.15	0.101325	–	0.199	–	–	–	–	0.199
Kaczmarek [65]	1	293.15	0.101325	–	0.199	–	–	–	–	0.199
Kaczmarek and Radecki [60]	1	293.15	0.101325	–	0.199	–	–	–	–	0.199
Kaczmarek and Radecki [61]	1	293.15	0.101325	–	0.199	–	–	–	–	0.199
Killgore et al. [66]	1	298.14	0.101325	–	0.234	–	–	–	–	0.234
Marcos et al. [95]	61	448–574	0.1–1	0.271	–	–	0.455	–	–	0.365
Matteoli et al. [96]	1	298.15	0.101325	–	0.089	–	–	–	–	0.089
McLure et al. [23]	13	278–358	0.1–1	–	0.328	–	–	–	–	0.328
Radecki et al. [68]	1	293.15	0.101325	–	0.383	–	–	–	–	0.383
Radecki and Kaczmarek [69]	1	293.15	0.101325	–	0.397	–	–	–	–	0.397
Reuther and Reichel [72]	1	293.14	0.101325	–	0.385	–	–	–	–	0.385
Sauer [73]	1	293.14	0.101325	–	0.398	–	–	–	–	0.398
Voronkov [76]	1	293.14	0.101325	–	0.174	–	–	–	–	0.174
Waterman et al. [77]	1	293.14	0.101325	–	0.214	–	–	–	–	0.214
Weast and Astle [97]	1	293.15	0.101325	–	0.147	–	–	–	–	0.147
<b>Speed of sound <i>w</i></b>										
This work*	214	365–573	0.1–30	–	0.174	–	–	–	0.228	0.215
<b>Isobaric heat capacity <i>c<sub>p</sub></i></b>										
Weast and Astle [97]	1	298.14	0.101325	–	0.921	–	–	–	–	0.921
Anderson et al. [88]	1	298.15	0.101325	–	1.310	–	–	–	–	1.310
Abbas [2]*	32	218–374	0.101325	–	0.303	–	–	–	–	0.303
Pedersen et al. [67]	8	301–346	0.101325	–	0.702	–	–	–	–	0.702
Good et al. [93]	1	298.14	0.101325	–	0.881	–	–	–	–	0.881
Scott et al. [36]*	11	363–501	0.0–1	0.042	–	–	–	–	–	0.042
<b>Second virial coefficient <i>B<sup>a</sup></i></b>										
Marcos et al. [95]	6	448–574	–	29.82	–	–	–	–	–	29.82
Scott et al. [36]*	3	332–374	–	35.51	–	–	–	–	–	35.51

<sup>a</sup> AAD of the second virial coefficient  $B$  in  $\text{cm}^3 \text{mol}^{-1}$ .

<sup>b</sup> Calculated values.

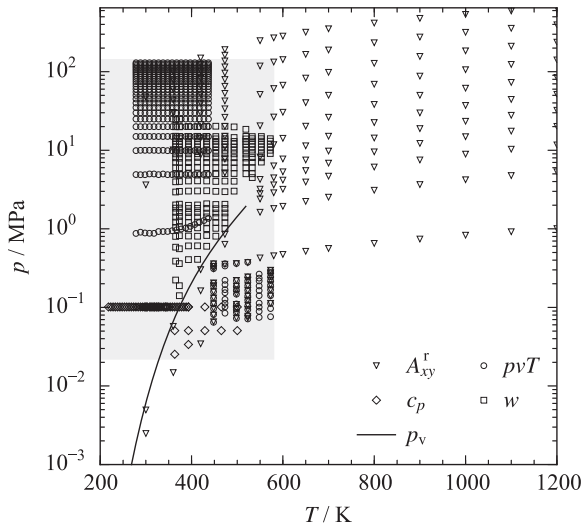


**Fig. 7.** Data in the homogeneous region of hexamethyldisiloxane. The gray area depicts the region where experimental data are available:  $T_{\max} = 580$  K and  $p_{\max} = 130$  MPa. Helmholtz energy derivatives from molecular simulation extend this region up to  $T_{\max} = 1200$  K and  $p_{\max} = 600$  MPa.

When Colonna et al. [1] developed their EOS in 2006, no information on the ideal gas heat capacity was available. Therefore, they applied the Harrison-Seaton zeroth order contribution method [37] to gain information on this property. Unfortunately, the method yields results with 25% uncertainty [19], which is too large for accurate EOS. However, this was the only group contribution method applicable to siloxanes because it is the only one providing information on Si–O bonds. Poling et al. [38] state the same findings, which led to further investigations on the ideal gas heat capacity of siloxanes by Nannan et al. [39]. They made *ab initio* calculations, which were based on information about hexamethyldisiloxane from the literature, and were then transferred to several other siloxanes. Unfortunately, these results were not compared to their experimental results for octamethylcyclotetrasiloxane so that it is not possible to assess the accuracy of their *ab initio* calculations. In a publication that reports a conclusion of their investigations on more accurate ideal gas heat capacities of siloxanes, they claim that the HF/6-31G(d) method is the most accurate one. This method yields an ideal gas isobaric heat capacity of  $c_p^0 = 503 \text{ J} \cdot \text{mol}^{-1} \cdot \text{K}^{-1}$  at  $T = 500$  K, which is the same value as their experiment at  $T = 495$  K. Therefore, these data are assumed to be less accurate than the data of Scott et al. [36] and were only used for comparison here.

#### 4.2. Residual contribution

The residual contribution consists of polynomial, exponential, and Gaussian bell-shaped terms

$$\begin{aligned} \alpha^r(\tau, \delta) &= \alpha_{\text{Pol}}^r(\tau, \delta) + \alpha_{\text{Exp}}^r(\tau, \delta) + \alpha_{\text{GBS}}^r(\tau, \delta) \\ &= \sum_{i=1}^{I_{\text{Pol}}} n_i \delta^{d_i} \tau^{t_i} + \sum_{i=I_{\text{Pol}}+1}^{I_{\text{Pol}}+I_{\text{Exp}}} n_i \delta^{d_i} \tau^{t_i} \exp(-l_i \delta^{p_i}) \\ &\quad + \sum_{i=I_{\text{Pol}}+I_{\text{Exp}}+1}^{I_{\text{Pol}}+I_{\text{Exp}}+I_{\text{GBS}}} n_i \delta^{d_i} \tau^{t_i} \exp\left(-\eta_i(\delta - \varepsilon_i)^2 - \beta_i(\tau - \gamma_i)^2\right). \end{aligned} \quad (11)$$

Polynomial and exponential terms are generally sufficient to accurately describe the whole fluid region, except for critical states. The Gaussian bell-shaped terms [40], which were first applied to Helmholtz EOS by Setzmann and Wagner [41] in 1991, are used for a more accurate description of the critical region. Furthermore, they allow for the development of EOS, which can reproduce data within their experimental uncertainty with a much lower number of terms as before.

The residual contribution of the present EOS consists of five polynomial, five exponential, and eight Gaussian bell-shaped terms. The corresponding parameters are listed in Table 3. These parameters were determined by non-linear fitting techniques, which were also used to set up other modern EOS, e.g. R-125 [42], propane [43], or propylene [44]. Tables 5 and 6 list all data sources, indicating which data were considered in the present fitting routine. Their selection is discussed in detail below. The available dataset is presented in Fig. 7. The shaded area marks the region that is covered by experimental measurements ( $T = 220$  K to 570 K,  $p_{\max} = 130$  MPa). Most are homogeneous liquid density and speed of sound data. The experimental dataset was supplemented here by Helmholtz energy derivatives from molecular simulation. In this way, the range of validity of the present equation of state was extended to a maximum temperature of  $T_{\max} = 1200$  K and a maximum pressure of  $p_{\max} = 600$  MPa. The critical temperature was constrained to the value of McLure and Dickinson [45] ( $T_c = 518.7$  K), which is in close agreement with the other literature values, cf. Table 4. The critical density  $\rho_c = 1.653 \text{ mol dm}^{-3}$  and the critical pressure  $p_c = 1.9311$  MPa were determined during the present fitting procedure. The critical pressure agrees well with the literature values, whereas the critical density differs by up to 5.5%. However, none of the critical density values given in the literature are measurements, they were rather estimated from theoretical models. The triple point temperature  $T_{\text{tp}} = 204.93$  K was taken from Scott et al. [36]. The corresponding liquid triple point density  $\rho_{\text{tp,liq}} = 5.266 \text{ mol dm}^{-3}$  was determined by extrapolating the saturated liquid line to the triple point temperature. Furthermore, the gas constant  $R = 8.3144621 \text{ J mol}^{-1} \text{ K}^{-1}$  [46] and the molecular weight  $M = 162.3768 \text{ g mol}^{-1}$  [47] were applied.

#### 4.3. Assessment of vapor–liquid equilibrium properties

Relative deviations of experimental vapor pressure data from the present equation of state are shown in Fig. 8. Additionally, the corresponding average absolute relative deviations are listed in Table 5. Relative deviations were calculated by

$$\Delta X = 100 \left( \frac{X_{\text{DATA}} - X_{\text{EOS}}}{X_{\text{DATA}}} \right). \quad (12)$$

Based on this definition, the average absolute relative deviation is defined as

$$\text{AAD} = \frac{1}{N} \sum_{i=1}^N |\Delta X_i|. \quad (13)$$

Vapor–liquid equilibrium data were separated into three temperature ranges: low temperature (LT:  $T/T_c \leq 0.6$ ), medium temperature (MT:  $0.6 \leq T/T_c \leq 0.98$ ), and high temperature (HT:  $T/T_c > 0.98$ ). All other properties were classified into gas, liquid, critical region ( $0.98 \leq T/T_c \leq 1.1$  and  $0.7 \leq \rho/\rho_c \leq 1.4$ ), and supercritical region. The latter was further divided into low density (LD:  $\rho/\rho_c \leq 0.6$ ), medium density (MD:  $0.6 \leq \rho/\rho_c \leq 1.5$ ), and high density (HD:  $\rho/\rho_c > 1.5$ ). In the figures, the equation of state of Colonna et al. [1] and the ancillary equations of the DIPPR [19] and TDE [53] databases are plotted for comparison.



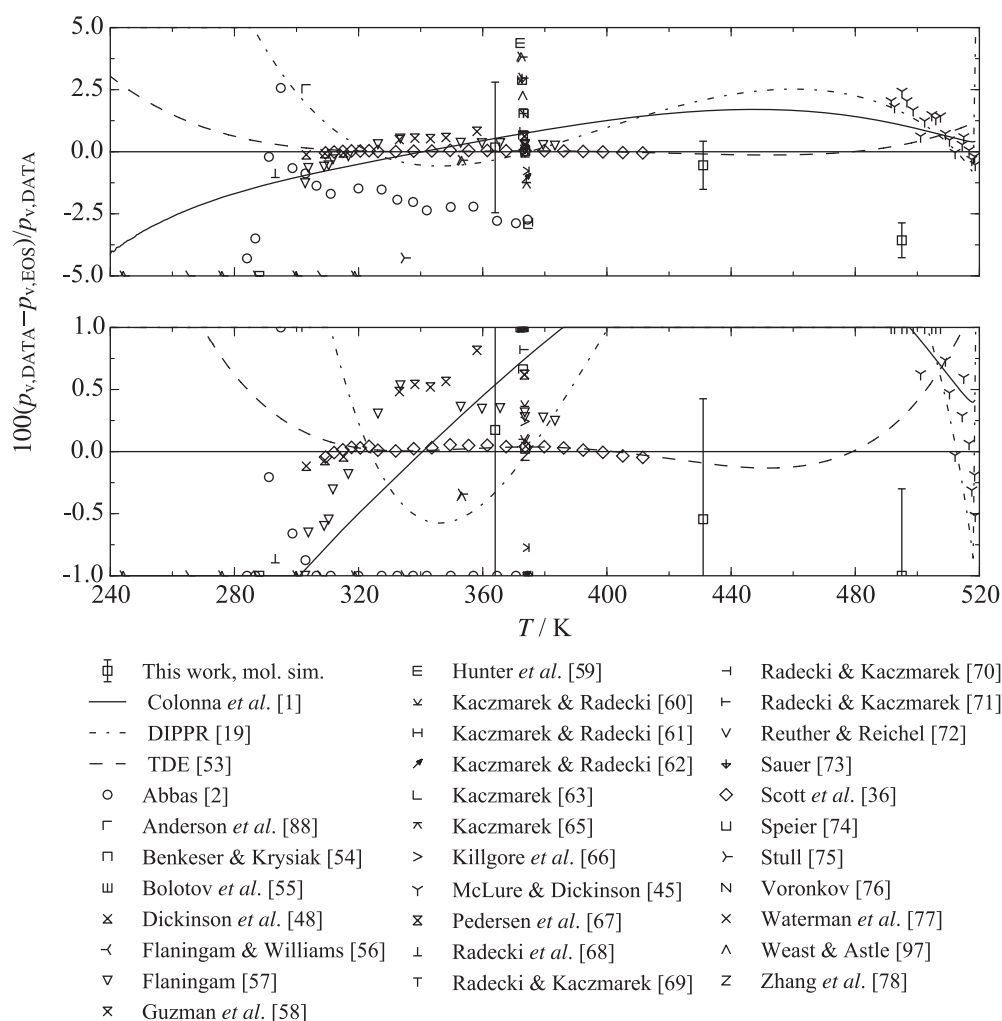


Fig. 8. Relative deviations of experimental vapor pressure data from the present equation of state for hexamethyldisiloxane.

The large number of authors in Table 5 may lead to the impression that the vapor pressure was very well investigated. However, in many references only a single data point is reported. Most of these publications focused on measurements of mixture properties with hexamethyldisiloxane as an involved component. For verification of the sample purity, the normal boiling point was reported. These values differ by more than 1% from each other so that they were not useful for the development of the present EOS. When excluding these data from the dataset, measurements by six different authors remain, which are mostly located between  $T = 300$  K and 400 K.

Abbas [2] reports a comprehensive investigation on thermodynamic properties of hexamethyldisiloxane for a sample purity of 99.7%. The vapor pressure was measured with a comparative ebulliometer, which requires a very well known reference fluid with a high purification grade. No information is given on the reference fluid in her thesis. Since she is calling her apparatus a “Scott-ebulliometer”, it is assumed here that she was using water as a reference fluid as recommended in the original paper describing

the apparatus [81]. This method is known to be very accurate, but Abbas’ [2] data exhibit a systematic negative offset when comparing to the present EOS and other literature data, e.g. Scott *et al.* [36] or Flaningam [57]. For low temperatures the data by Abbas [2] scatter significantly, which could be due the choice of the reference fluid. Because water can easily be superheated for vapor pressures of  $p < 0.003$  MPa, other reference fluids should be chosen for the low temperature region. The specified uncertainties of  $\Delta p = 0.0005 \cdot p_v + 10$  Pa and  $\Delta T = 0.05$  K yield a combined uncertainty of 0.4% to 1.5% for a coverage factor  $k = 2$ . No information is given how these uncertainties were ascertained and the sample purity was not considered.

The vapor pressure measurements of Scott *et al.* [36] and Flaningam [57] agree with each other within approximately 0.5%. Scott *et al.* [36] report a very detailed description of their sample preparation. The sample purity of 99.996% was verified by calorimetric studies of the melting point as a function of fraction melted. Similar to Abbas [2], Scott *et al.* [36] used a comparative ebulliometer for their measurements. As a reference, water was used for

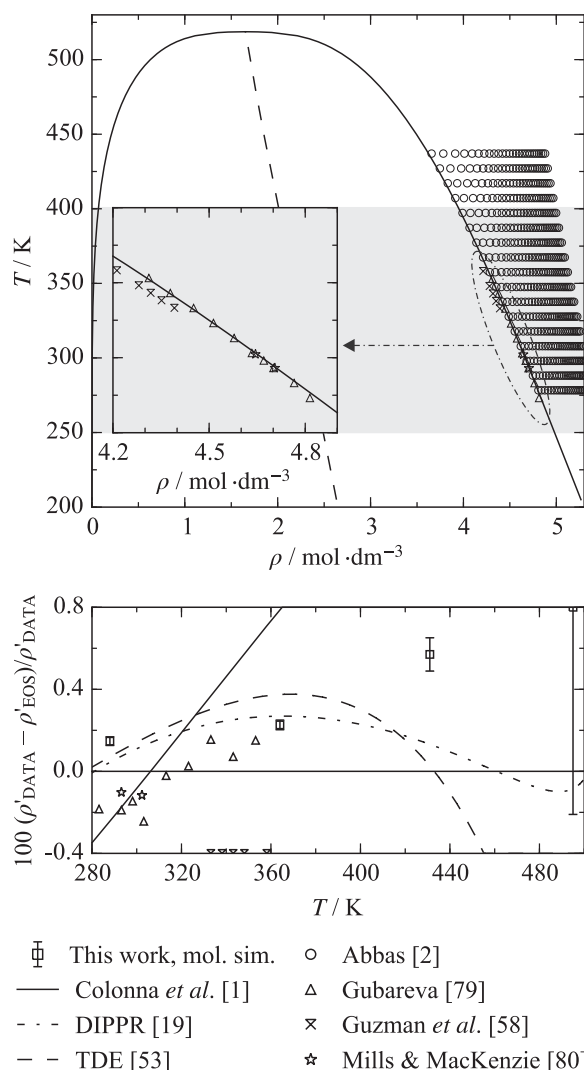


**Fig. 9.** Saturated liquid density of hexamethyldisiloxane. Top:  $T$ - $\rho$  diagram including saturated liquid and homogeneous states near the saturated liquid line. Bottom: Relative deviations of experimental saturated liquid density data from the present equation of state.

high temperatures only, benzene was applied in case of low temperatures. This procedure yields consistent vapor pressure data over the whole temperature range. The measurements of Dickinson et al. [48] confirm the data of Scott et al. [36] at low temperatures. The three state points between  $T = 303$  K and 315 K are reproduced with an AAD = 0.076%. At  $T = 373$  K, the most recent measurement of the normal boiling point by Zhang et al. [78] from 2011 also agrees very well with the data by Scott et al. [36]. Therefore, the present equation was fitted to the data of Scott et al. [36]. These data are reproduced within 0.06% (AAD = 0.031%), which is well within the expected uncertainty. Flaningam [57] carried out his measurements with a sample purity of 99.9% using an ebulliometer as proposed by Stull [82]. In comparison to the comparative ebulliometer, the usage of a capacitive pressure sensor enables for the investigation of the low temperature regime without any

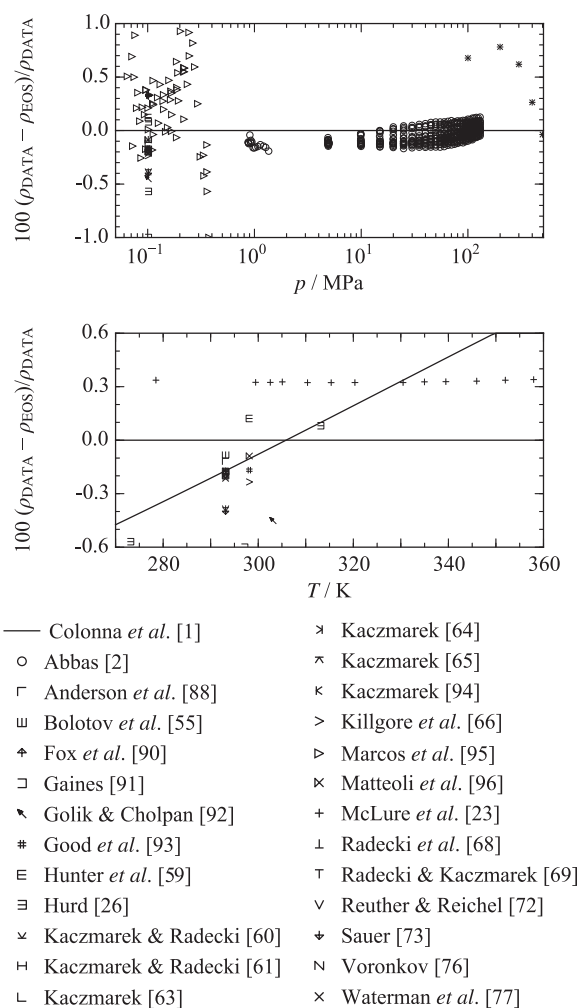


**Fig. 10.** Homogeneous density of hexamethyldisiloxane. Top: Relative deviations of experimental homogeneous density data from the present equation of state. Bottom: Relative deviations of the experimental homogeneous density data at atmospheric pressure from the present equation of state.

modification of the apparatus. In his publication, he verified his apparatus with test measurements on water, methylcyclohexane, and diphenyl ether. However, except for water, these fluids are not practical for test measurements because they are not well investigated. The average pressure error of 0.07% is not expressed in absolute values, which falsifies the results by opposite algebraic signs. Nonetheless, most of the data are reproduced within 0.5% (AAD = 0.437%).

The data by Stull et al. [75] are presented in a paper together with several hundred additional fluids. Thus, they were not measured, but collected from the literature. Compared to the present EOS and other literature sources, these data show huge deviations (AAD = 12.78%) and were thus not taken into account. The vapor pressure measurements of Guzman et al. [58] exhibit a systematic positive offset when comparing to the present EOS or the data of Scott et al. [36]. In their publication, the procedure of sample preparation is described in detail. However, they do not give the value of their sample purity. The only hint is a comparison of the

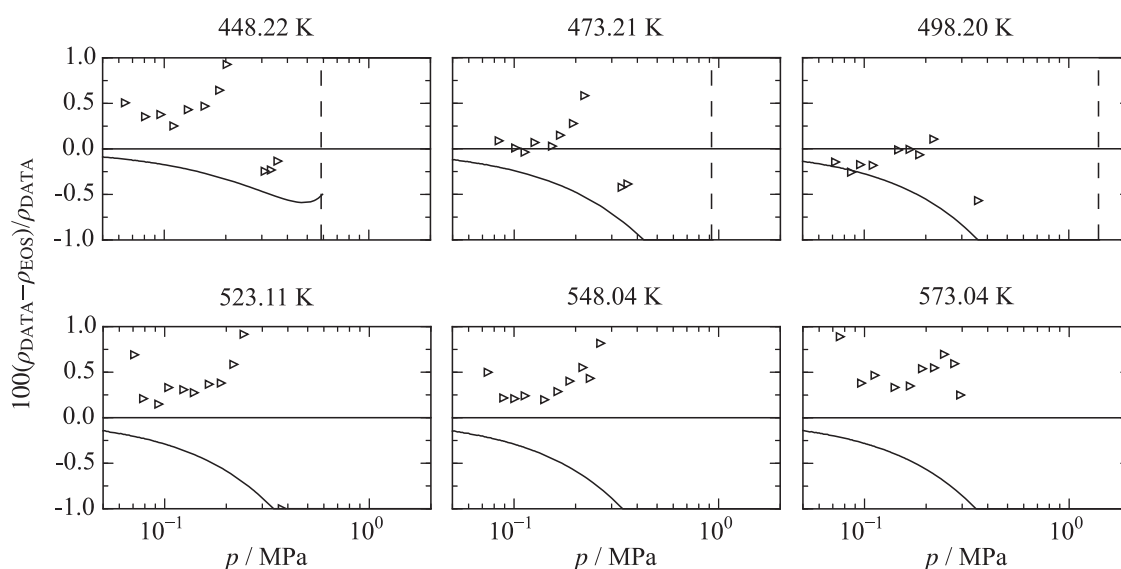


Fig. 11. Relative deviations of gaseous  $p\rho T$  data of Marcos et al. [95] from the present equation of state for hexamethyldisiloxane. — equation of state, Colonna et al. [1]; - - phase boundary.

NBP to the value published by Radecki and Kaczmarek [71]. Because their value already differs by 0.82% from the present EOS, this confirmation is questionable and the positive deviation of the vapor pressure data of Guzman et al. [58] from the present EOS is reasonable.

Finally, there is one dataset of McLure and Dickinson [45] in the high temperature region ( $T = 491$  K to  $519$  K). Because there are no other data available in this region, they cannot be compared to other measurements. Moreover, the lack of data between  $T = 412$  K and  $491$  K prohibits a reliable transition from the low temperature region to the data of McLure and Dickinson [45]. Therefore, the accuracy of these data can only be evaluated with the information given in the corresponding publication and by comparison to the present EOS. They state a sample purity of 99.99%, which was determined with gas chromatography. The experiment was carried out with Pyrex tubes [83] and the temperature was monitored with a thermo couple (type K), which is a quite inaccurate device, if it is not calibrated very carefully. However, the choice of calibrating the

thermo couple to the critical points of hexane, heptane, octane, and nonane is questionable. All of these hydrocarbons are not well investigated and are barely available with a sufficient purity from common manufacturers (e.g. Sigma–Aldrich Co. LLC [84], Merck Millipore Corporation [85], or Alfa Aesar GmbH & Co. KG [86]). This is affirmed by the quite low sample purities of heptane (99.5%) and octane (99%) [83], which were used for calibration. Furthermore, the critical temperatures of hexane ( $T_c = 507.4$  K) and octane ( $T_c = 568.7$  K) [45] differ from those of the EOS of Lemmon and Span [87], which are the most accurate models in the literature for these fluids (hexane:  $T_c = 507.82$  K, octane:  $T_c = 569.32$  K). Additionally, the influence of the sample purity on the critical temperature was investigated in the same paper. A difference of 2.6 K was observed when decreasing the sample purity from 99.99% to 99.7%. Although the hydrocarbons do not behave exactly like hexamethyldisiloxane, these findings show that the purification grade has a large impact on the critical temperature and, therefore, the vapor pressure in the critical region. Thus, the uncertainty of 0.1 MPa (corresponding to

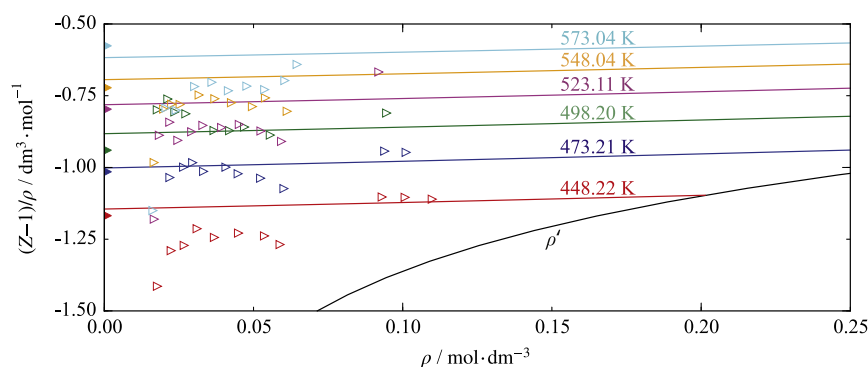


Fig. 12.  $(Z-1)/\rho - \rho$  diagram of hexamethyldisiloxane.  $\triangleright$   $p\rho T$  measurements of Marcos et al. [95];  $\blacktriangleright$  second virial coefficient of Marcos et al. [95]; — present equation of state.

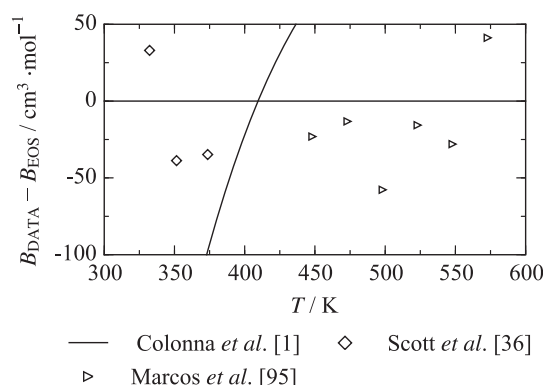


Fig. 13. Absolute deviations of the second virial coefficient of Marcos et al. [95] and Scott et al. [36] from the present equation of state for hexamethyldisiloxane.

0.5% to 0.8%) as specified by the authors [45] has to be questioned. In fact, during the fitting procedure it was not possible to achieve smaller deviations than 2% from the EOS without compromising the representation of other properties. Based on these findings, the expected uncertainty of the present EOS regarding the vapor pressure is 0.2% for  $T \leq 410$  K and 2% for higher temperatures.

Literature shows that the saturated liquid density has been investigated less than the vapor pressure. There are only three different datasets available, which are also very restricted in terms of the temperature range ( $T = 270$  K to 360 K). This is insufficient to model the saturated liquid line of hexamethyldisiloxane. Alternatively, the homogeneous density data of Abbas [2] were used. Since no experimental measurements of the saturated vapor line were published, a straight rectilinear diameter ( $RD = (\rho' + \rho'')/2$ ) was applied as a fitting constraint. In Fig. 9, an overview about the available saturated liquid density and homogeneous density data located near the saturated liquid line is given. The data of Abbas [2] were measured close enough to the phase boundary and cover a broader temperature range than the saturated liquid density data. When correlating the present EOS to the dataset of Abbas [2], the saturated liquid density of Gubareva [79] and Mills and MacKenzie [80], which agree well with each other, are reproduced within 0.2% ( $AAD = 0.167\%$  and  $AAD = 0.109\%$ , respectively). The data of Guzman et al. [58] show a systematic negative offset of about  $-1.3\%$ . Unfortunately, no information on the sample purity or the measurement device is available in Ref. [58] so that it is not possible to discuss the reason for this offset.

For all three vapor–liquid equilibrium properties, ancillary equations were developed, which can be used for initial calculations of starting values of iterative phase equilibrium calculations. The equations and the corresponding parameters can be found in the Supplementary Material.

#### 4.4. Assessment of homogeneous state properties

There are several different datasets available for the homogeneous density. Average absolute relative deviations are given in Table 6 and relative deviations from the present EOS are illustrated in Fig. 10. Similar to the vapor pressure, most of the authors reported only a single value to verify their sample purity.

When leaving out these sources, five datasets of Abbas [2], Dickinson [89], Hurd [26], Marcos et al. [95], and McLure et al. [23] were considered for the development of the present EOS. The data of Dickinson [89] were calculated from a correlation equation based on the available experimental data from the literature. Abbas [2]

published the only pressure dependent dataset in the liquid phase. All other measurements were carried out at atmospheric pressure. Abbas [2] covered a temperature range of 270 K to 440 K with a maximum pressure of 130 MPa. A flexural resonator, which was used for the measurements, was calibrated to water ( $p \leq 30$  MPa) and heptane ( $p > 30$  MPa). For test purposes, liquid densities of water and heptane were compared to the IAPWS-95 [98] (0.04%) and the equation of Lemmon and Span [87] (0.08%). No experimental uncertainty was specified for hexamethyldisiloxane. However, Abbas [2] indicates the uncertainty by referring to the diploma thesis of Schedemann [99], who claimed an uncertainty of  $0.7 \text{ mg} \cdot \text{cm}^{-3}$  to  $0.8 \text{ mg} \cdot \text{cm}^{-3}$ .

For hexamethyldisiloxane, these values correspond to a relative deviation of 0.08% to 0.13%. When considering this statement as a combined uncertainty, including all relevant irritations during the measurement, the calibration has to be carried out extremely carefully. Keeping in mind the sample purity (99.7%) and the test measurements on water and heptane, the deviation of 0.2% from the present equation of state is most probably within the true experimental uncertainty. Therefore, this deviation is also claimed to be the uncertainty of the homogeneous liquid density of the present EOS. Fig. 10, (bottom) presents the deviations of the homogeneous density data measured at atmospheric pressure. The equation of state of Colonna et al. [1] was probably correlated to the data of Hurd [26], because his data point at  $T = 293.15$  K agrees very well with many other data measured at the same temperature. However, these data are not based on real measurements, but were calculated from an equation. For the development of that equation, they measured liquid density data at  $p = 1$  atm. During their measurements they observed a loss of sample, which could be the reason of the different trend in comparison to the dataset of McLure et al. [23]. However, in this work none of the data at  $p = 1$  atm were applied to the fit, which leads to a better representation of the data of McLure et al. [23] at least in terms of the correct slope and curvature. Their measurements were carried out between  $T = 278$  K and 358 K and a systematic offset of 0.33% with respect to the present EOS can be observed. In their publication only little information on the experiment is provided and no experimental uncertainty is given. During the fitting procedure, these data were also applied to the fit to reduce the offset. It turned out that it is not possible to improve the representation of these data without increasing deviations of the liquid density data of Abbas [2]. Since the data of Abbas [2] were chosen to be fitted primarily, the data of McLure et al. [23] were finally rejected from the fit. Therefore, it is assumed that the systematic offset is caused by the comparatively low purity of the sample (99%).

The homogeneous gas phase was exclusively investigated by Marcos et al. [95]. A bore-tube with a varied volume was used for the measurements. The pressure was obtained with a mercury manometer and the temperature was regulated by two thermopiles. The absence of a measurement device to weigh the sample raises the question how they determined the density of their sample. At least one reference value has to be known, which is commonly measured at atmospheric conditions as explained by Singh and Kudchadker [100].

This value can then be used to calculate the density during the experiment when varying the volume with a constant mass. Fig. 10 shows that these values differ by about 0.5% in the literature, but no value for hexamethyldisiloxane was cited by Marcos et al. [95]. Furthermore, they measured a density range of  $2 \text{ kg} \cdot \text{m}^{-3}$  to  $18 \text{ kg} \cdot \text{m}^{-3}$ , which are extremely small values even for state points in the gaseous phase. Therefore, these measurements had to be carried out extremely carefully. Fig. 11 shows that the density data of Marcos et al. [95] are reproduced within 1%, but they are not completely consistent. For a consistency test, the density was

recalculated to the compressibility factor  $Z = pv/(RT)$  and represented in terms of  $(Z-1)/\rho$  as a function of the density in Fig. 12. Six isotherms ranging from 448 K to 573 K are illustrated. For a better assessment, the corresponding isotherms calculated with the present EOS are depicted for orientation. The “high density” data seem to be consistent, at least for the two lowest isotherms. With decreasing density the data start to scatter, which is becoming worse with increasing temperature. The isotherms  $T = 448.22$  K and 473.21 K are slightly shifted to lower values with respect to the present EOS. The other isotherms exhibit a larger scatter and even merge. Therefore, the uncertainty specified by Marcos et al. [95] (0.33 kPa, corresponding to 0.1% to 0.5%) seems to be questionable. Furthermore, a sample purity of 99% is probably insufficient to carry out these sensitive measurements. Thus, the deviation of 1% is assumed to be the uncertainty of both the experimental data and the present EOS in the gaseous region.

Similar to the approach illustrated in Fig. 12, Marcos et al. [95] used their density measurements to extrapolate the second virial coefficient  $B$  of each isotherm. They fitted their data to a virial expansion and extrapolated it to  $\rho \rightarrow 0 \text{ mol dm}^{-3}$ . The resulting virial coefficient is shown in Fig. 12. When comparing their results for the second virial coefficient with their density measurements, it is not clear how they determined it. Except for the two lowest isotherms the extrapolation does not agree with the underlying dataset. Therefore, these results should be treated carefully. In Fig. 13, absolute deviations of the second virial coefficient data from the present EOS are illustrated. Except for one outlier, the data of Marcos et al. [95] and Scott et al. [36] are represented within  $50 \text{ cm}^3 \text{ mol}^{-1}$ , corresponding to 7%.

The reason for setting up a new EOS for hexamethyldisiloxane was the finding that the present measurements of the speed of sound deviate by up to 15% from the equation of Colonna et al. [1].

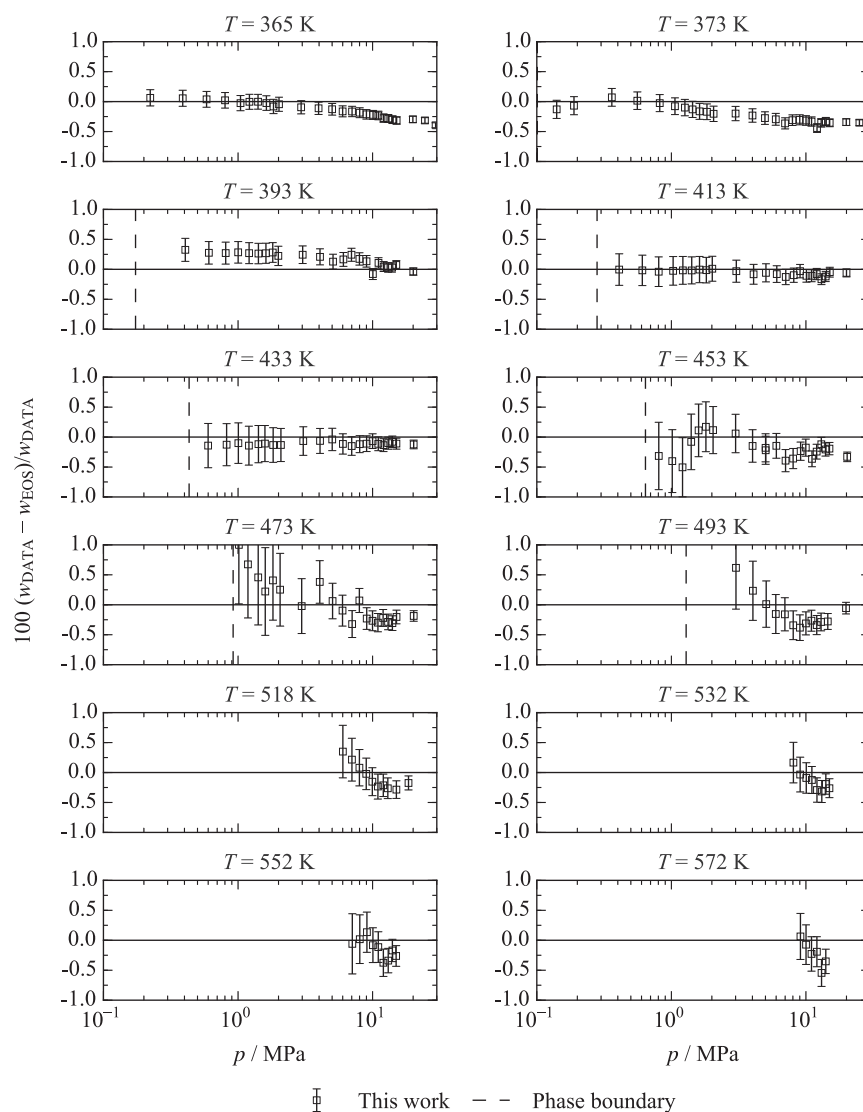
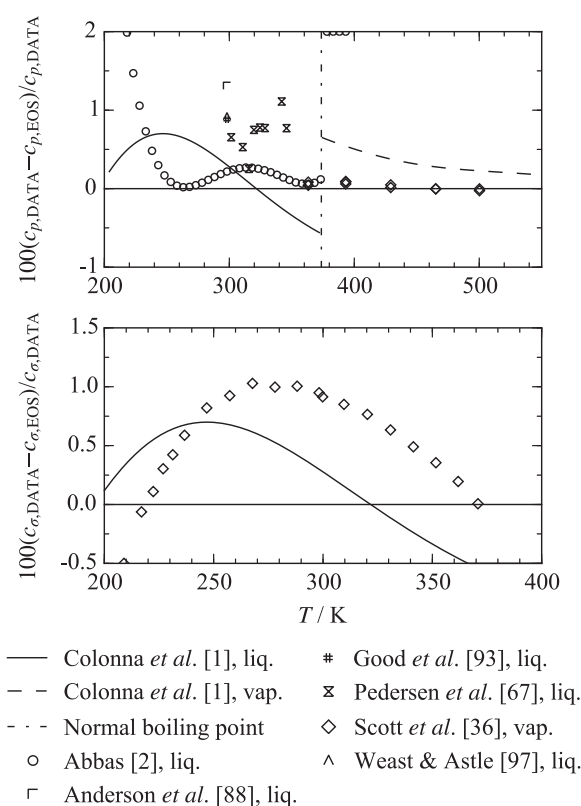


Fig. 14. Relative deviations of experimental speed of sound data of this work from the present equation of state for hexamethyldisiloxane.



**Fig. 15.** Heat capacities of hexamethyldisiloxane. Top: Relative deviations of experimental isobaric heat capacity data from the present equation of state. — Liquid phase of Colonna et al. [1] at  $p = 1$  atm; - - vapor phase of Colonna et al. [1] at  $p = 1$  atm; - - normal boiling point temperature. Bottom: relative deviations of experimental saturated heat capacity data from the present equation of state.

This was caused by the fact that there was no information available on the speed of sound when Colonna et al. [1] developed their equation. In this work, new measurements are reported with a combined expanded uncertainty as indicated in Fig. 14. The sample purity of 99% was not considered for the determination of the experimental uncertainty. These data are reproduced with the present EOS within 0.5% and most of them are represented within the experimental uncertainty. Therefore, the deviation of 0.5% is expected to be the uncertainty of the EOS for liquid state speed of sound data.

The only available caloric data in the gaseous region are the heat capacity measurements of Scott et al. [36]. They were measured with a low temperature calorimeter as explained by Huffman [101] and no statement on the uncertainty was made. However, these data are reproduced here within 0.1%, which is most likely well within the expected experimental uncertainty. Further measurements on the isobaric heat capacity are listed in Table 6 and depicted in Fig. 15. There are four different datasets available in the liquid region at atmospheric pressure. Anderson et al. [88] and Good et al. [93] report only single data points and, therefore, they were only considered for comparison. Thus, the results of Abbas [2] and Pedersen et al. [67] remained for fitting the present EOS.

A nonsteady hot-wire method was used by Abbas [2], where platinum was employed to heat the sample. The pressure was

measured by a diaphragm pressure sensor and the temperature was controlled with a Pt100 thermometer. In this way, results with an experimental uncertainty of 1% were achieved. The same measurement accuracy was stated by Pedersen et al. [67], however, their data are not as consistent as the ones from Abbas [2] and they are restricted to a narrow temperature range. Therefore, the data of Abbas [2] were chosen in the present fitting procedure. These data are represented within 0.5%, excluding four state points at low temperatures  $T < 240$  K. In this way, the data of Pedersen et al. [67] are represented within their experimental uncertainty. Finally, Scott et al. [36] published saturation heat capacity data  $c_g$  (for the thermodynamic definition see Hoge [102]) measured with the same type of apparatus. They state an experimental uncertainty of 0.2%, which is probably too low. During the development of the EOS, it turned out that it was not possible to fit these data within the given uncertainty without compromising the representation of the isobaric heat capacity. Since there are several different datasets available, which agree with each other within the given experimental uncertainty, the homogeneous isobaric heat capacity was chosen to be modeled primarily.

#### 4.5. Assessment of physical and extrapolation behavior

In Fig. 16, typical plots are illustrated to verify the physical and extrapolation behavior of the present EOS. The top, left part of the figure shows the temperature as a function of density along selected isobars ( $p_{\min} = 0.5$  MPa,  $p_{\max} = 5$  MPa). Additionally, the saturated liquid and vapor curves as well as the rectilinear diameter are presented. It is important that there are no bumps in the course of the isobars, the saturation lines have to meet in a flat maximum, and the rectilinear diameter has to be a straight line up to the critical point. The top, right diagram shows the pressure as a function of density along selected isotherms with a maximum temperature of  $T = 10^6$  K. Again, bumps have to be avoided and the isotherms have to approach each other at extremely high temperatures, densities, and pressures in this double logarithmic plot. In the center of Fig. 16, the residual isochoric heat capacity and the speed of sound are presented. For the isochoric heat capacity, the liquid phase has to exhibit a positive curvature over the whole temperature range for non-associating fluids. When extrapolating it to metastable temperatures below the triple point, the residual isochoric heat capacity has to have a negative slope on the hypothetical liquid side, whereas a positive slope has to be observed in the liquid region approaching the critical temperature. The isochoric heat capacity of the vapor phase has to increase monotonously with increasing temperature. Finally, both phases have to merge with a distinctive peak at the critical point. The speed of sound of the saturated liquid and vapor phase have to have a negative slope and curvature in the vicinity of the critical point. Similar to the maximum of the isochoric heat capacity, the saturation curves of the speed of sound have to merge in a minimum at the critical temperature. Furthermore, the extrapolated liquid phase has to exhibit a negative slope and no curvature, or rather a slightly positive curvature. At the bottom of Fig. 16, the second, third, and fourth thermal virial coefficients are shown as well as some characteristic ideal curves. Detailed information on the behavior of the virial coefficients can be taken from the publication of Thol et al. [7]. For the present equation of state, all of the three coefficients show a correct trend. For  $T \rightarrow 0$  K the virial coefficients have to approach negative infinity. With increasing temperature the virial coefficients have to increase and finally vanish at high temperatures after passing a maximum. The maxima of the third and fourth virial coefficient have to be located in the vicinity of



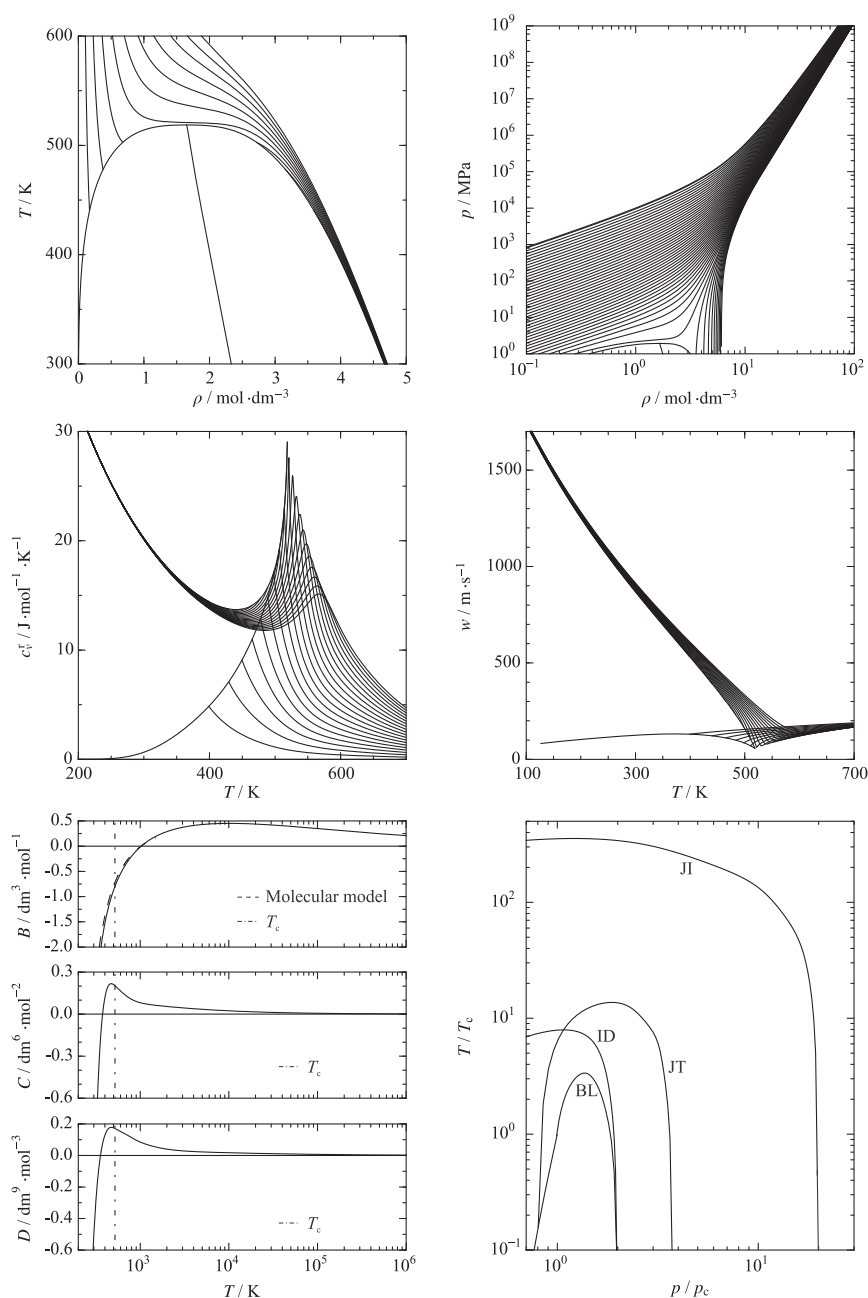


**Fig. 16.** Physical behavior of some thermodynamic properties of hexamethyldisiloxane. Top, left: Isobars and vapor–liquid equilibrium curves together with the rectilinear diameter. Top, right: Pressure as a function of density along isotherms at extreme conditions ( $T_{\max} = 10^6$  K). Center, left: Residual isochoric heat capacity. Center, right: Speed of sound. Bottom, left: Second, third, and fourth virial coefficients, including  $B$  from the molecular interaction model. Bottom, right: Characteristic ideal curves.

the critical temperature. The characteristic ideal curves (for definition see Span and Wagner [103] or Span [8]) have to be smooth without any bumps. All of the plots presented in Fig. 16 exhibit a reasonable behavior with only small changes in the curvature of the Joule-Thomson inversion curve and the Joule inversion curve. Having in mind the restricted dataset available for hexamethyldisiloxane, the plot of the ideal curves still proves

excellent extrapolation behavior.

#### 4.6. Assessment of molecular simulation data

In Fig. 7, the shaded area indicates the region where experimental data are available for hexamethyldisiloxane. On this basis, the range of validity of the present EOS was defined to be

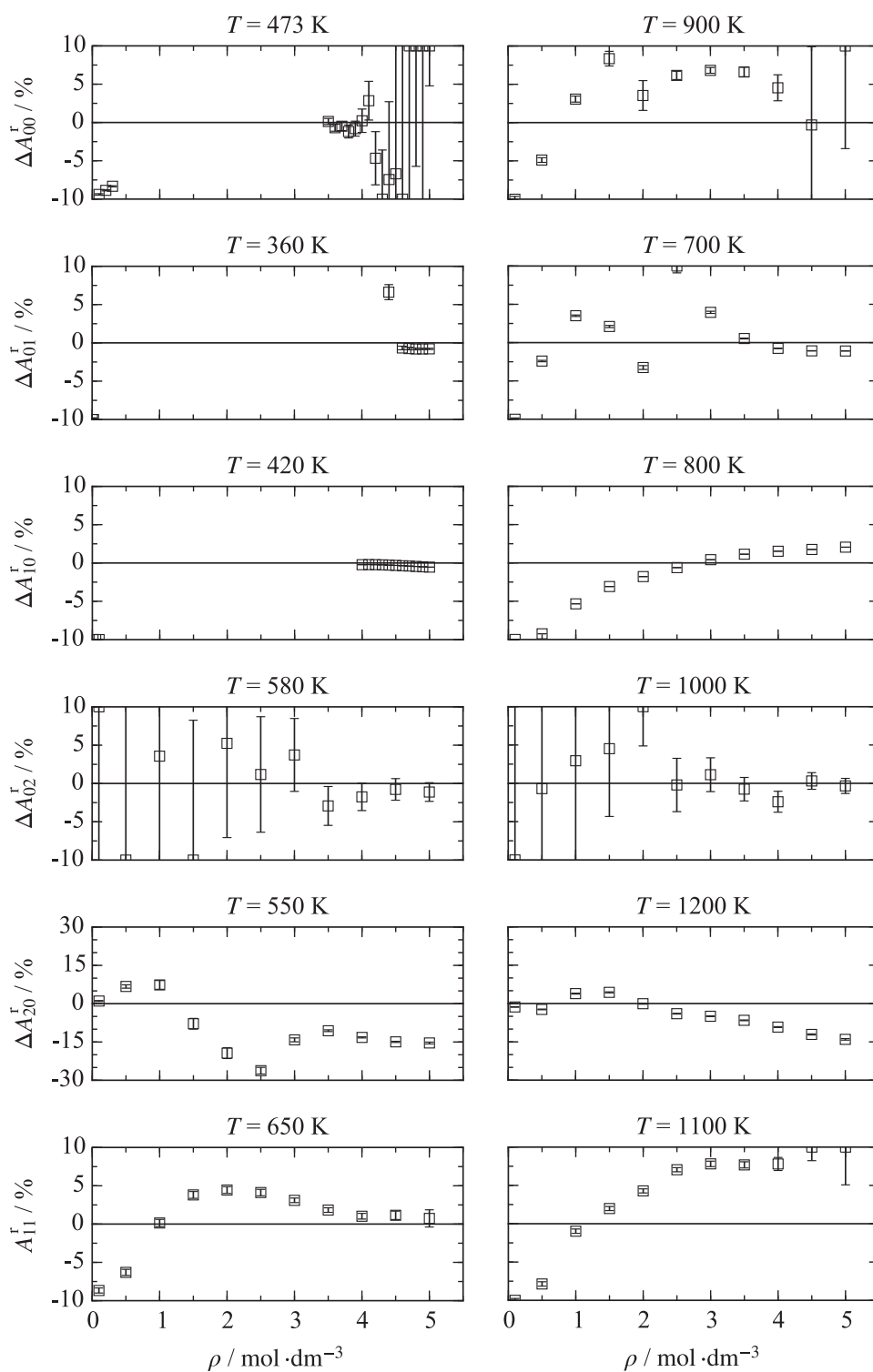


**Fig. 17.** Relative deviations of simulated residual Helmholtz energy derivative data along selected isotherms from the present equation of state for hexamethyldisiloxane. Relative deviations are calculated according to Eq. (12).



$T = 220\text{--}570\text{ K}$  with a maximum pressure of  $p_{\max} = 130\text{ MPa}$ . The large scale molecular simulation data presented in this work were applied to the fit to extend the range of validity to a maximum temperature of  $T_{\max} = 1200\text{ K}$  and a maximum pressure of  $p_{\max} = 600\text{ MPa}$ . During these simulations the thermal stability of the fluid was not considered. Therefore, the extended range of validity has to be comprehended as an extrapolation from the real fluid behavior. The temperature of thermal decomposition, which could not be retrieved from the literature, was considered irrelevant for the development of the EOS and the fluid was treated as if it is stable throughout.

In Fig. 17, relative deviations of the simulated residual Helmholtz energy derivatives from the present EOS are shown along selected isotherms. A comprehensive overview including all simulation data is provided in the [Supplementary Material](#). Generally, the uncertainties of the residual Helmholtz energy  $A_{00}^r$ , the first derivative with respect to the temperature  $A_{01}^r$ , the first derivative with respect to the density  $A_{01}^r$ , the first mixed derivative with respect to the temperature and density  $A_{11}^r$ , and the second derivative with respect to the density  $A_{02}^r$  are 10%. The deviations increase with decreasing density and increasing temperature. The second derivative with respect to the temperature  $A_{20}^r$  was reproduced within 20%. These values may lead to the assumption that it is not reasonable to apply these data to the fit. However, it has to be kept in mind that these data exclusively represent the residual contribution of the EOS. Common thermodynamic properties, which are usually used for the development of EOS, always include the ideal contribution. Therefore, the ideal contribution of the present EOS was used to recalculate the thermodynamic properties pressure, isochoric heat capacity, isobaric heat capacity, and speed of sound from the residual molecular simulation data according to Eqs. (6)–(8).

In Fig. 18, the resulting data are compared to the present EOS. Additionally, the involved residual Helmholtz energy derivatives are indicated in the gray boxes. Although the deviations of the involved derivatives amount to 10% or even 20%, the deviations of the common thermodynamic properties are much smaller. Density data deviate from the present equation of state by no more than 2%, the isochoric heat capacity is reproduced within 1%, the isobaric heat capacity is within 2.5%, and the speed of sound scatters within 4%. Therefore, residual Helmholtz energy derivatives with uncertainties of up to 20% are statistically useful values when an extension of validity ranges is aimed at. Keeping in mind that other simulations for validation predicted the available homogeneous liquid density data within their experimental uncertainties, and the speed of sound data within 4%, the deviations presented in Fig. 18 can be assumed to be a rough estimate of the uncertainty of the present EOS in the extended range of validity. Of course, for a reliable statement further experimental measurements are required in this region.

## 5. Conclusion

The present EOS is written in terms of the reduced Helmholtz energy and can be used to calculate all thermodynamic equilibrium properties. Reference values are given in the [Supplementary Material](#) to verify a computer implementation of the EOS. Moreover, an input file for the equation of state packages REFPROP [104] and Trend [105] as well as a C++ implementation is supplied there. The underlying set of experimental literature data was extended considerably by the speed of sound measurements that were carried out at 210 state points. In addition, five Helmholtz energy derivatives and the Helmholtz energy itself were predicted by molecular simulation at 194 state points, providing 1164 non-

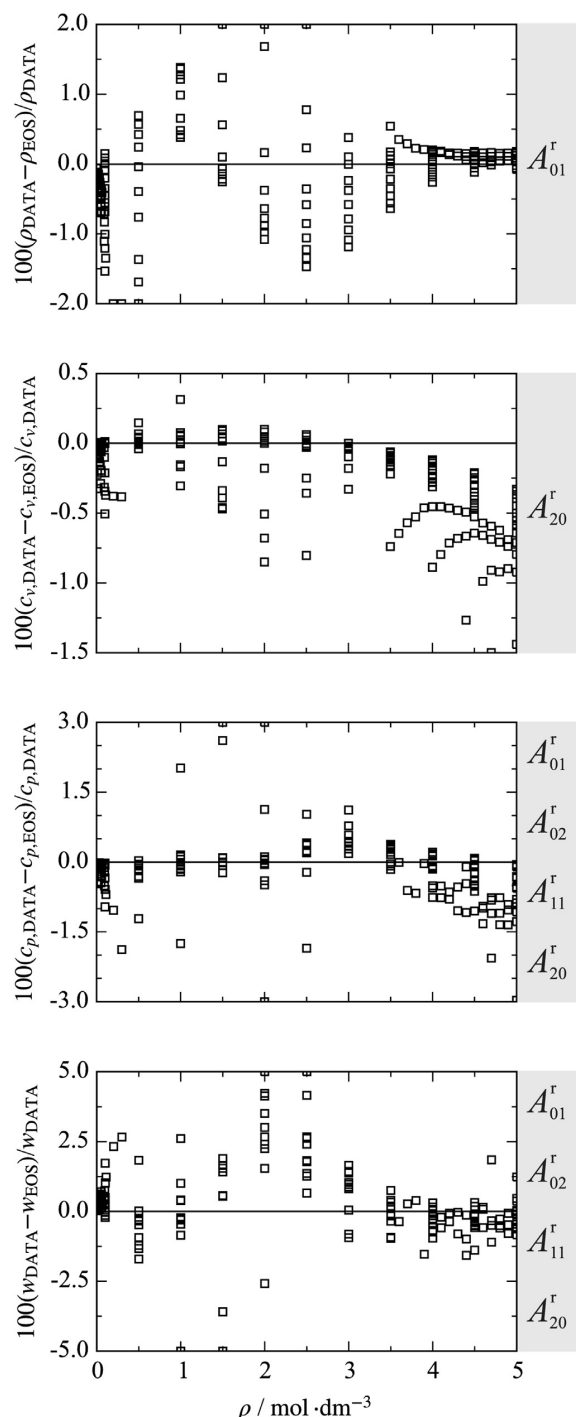


Fig. 18. Comparison of several thermodynamic properties obtained from molecular simulation data with the present equation of state for hexamethyldisiloxane. The involved residual Helmholtz energy derivatives are indicated in the gray boxes.

redundant thermodynamic data points for the EOS fit. The range of validity based on the experimental data covers  $T = 220$  K to 570 K with a maximum pressure of  $p_{\max} = 130$  MPa. By means of molecular simulation data, the temperature and pressure limits were extended to  $T_{\max} = 1200$  K and  $p_{\max} = 600$  MPa. The expected uncertainty in terms of vapor pressure amounts to 0.2% for  $T \leq 410$  K and 2% for higher temperatures. Homogeneous density data can be calculated with an accuracy of 0.2% in the liquid phase and 1% in the gaseous phase. The specified uncertainty for speed of sound data in the liquid phase is 0.5%. The expected uncertainty of the isobaric heat capacity is 0.2% in the gaseous phase and 1% in the liquid phase. The extrapolation behavior was found to be reasonable. For the extended range of validity, only rough estimates on the uncertainty can be made.

### Acknowledgements

The authors gratefully acknowledge financial support by Deutsche Forschungsgemeinschaft under the grants VR6/4-1 and SP507/7-1. This work was carried out under the auspices of the Boltzmann-Zuse Society (BZS) of Computational Molecular Engineering. The simulations were performed on the Cray XC40 (Hor-net) at the High Performance Computing Center Stuttgart (HLRS) under the grant MMHBF2.

### Appendix A. Supplementary data

Supplementary data related to this article can be found at <http://dx.doi.org/10.1016/j.fluid.2015.09.047>.

### References

- [1] P. Colonna, N.R. Nannan, A. Guardone, E.W. Lemmon, *Fluid Phase Equilib.* 244 (2006) 193–211.
- [2] R. Abbas, Anwendung der Gruppenbeitragszustandsgleichung VTPR für die Analyse von reinen Stoffen und Mischungen als Arbeitsmittel in technischen Kreisprozessen (PhD thesis), Technische Universität Berlin, Germany, 2011.
- [3] R. Lustig, G. Rutkai, J. Vrabec, *Mol. Phys.* 113 (2015) 910–931.
- [4] G. Rutkai, M. Thol, R. Lustig, R. Span, J. Vrabec, *J. Chem. Phys.* 139 (2013) 041102.
- [5] G. Rutkai, J. Vrabec, Empirical fundamental equation of state for phosgene based on molecular simulation data, *J. Chem. Eng. Data*, <http://dx.doi.org/10.1021/acs.jced.5b00266>
- [6] M. Thol, G. Rutkai, A. Köster, M. Kortmann, R. Span, J. Vrabec, *Chem. Eng. Sci.* 121 (2015) 87–99, and 134, 887–890 (2015).
- [7] M. Thol, G. Rutkai, R. Span, J. Vrabec, R. Lustig, *Int. J. Thermophys.* 36 (2015) 25–43.
- [8] R. Span, Multiparameter Equations of State: An accurate Source of Thermodynamic Property Data, Springer Verlag, Berlin, 2000.
- [9] P. Kortbeek, M. Muringer, N. Trappeniers, S. Biswas, *Rev. Sci. Instrum.* 56 (1985) 1269–1273.
- [10] F.H. Dubberke, D.B. Rasche, E. Baumhögger, J. Vrabec, *Rev. Sci. Instrum.* 85 (2014) 084901.
- [11] C. Lin, J. Trusler, *J. Chem. Phys.* 136 (2012) 094511.
- [12] S. Ball, J. Trusler, *Int. J. Thermophys.* 22 (2001) 427–443.
- [13] G. Benedetto, R. Gavioso, P.G. Albo, S. Lago, D.M. Ripa, R. Spagnolo, *Int. J. Thermophys.* 26 (2005) 1667–1680.
- [14] F.H. Dubberke, E. Baumhögger, J. Vrabec, *Rev. Sci. Instrum.* 86 (2015) 054903.
- [15] H. Gedanitz, M. Davila, E. Baumhögger, R. Span, *J. Chem. Thermodyn.* 42 (2010) 478–483.
- [16] G.R. Harris, *J. Acoust. Soc. Am.* 70 (1981) 10–20.
- [17] K. Meier, The Pulse-echo Method for High Precision Measurements of the Speed of Sound in Fluids (Habilitation thesis), Bundeswehruniversität, Hamburg, Germany, 2006.
- [18] M.W. Schmidt, K.K. Baldridge, J.A. Boatz, S.T. Elbert, M.S. Gordon, J.H. Jensen, S. Koseki, N. Matsunaga, K.A. Nguyen, S. Su, T.L. Windus, M. Dupuis, J.A. Montgomery, *J. Comput. Chem.* 14 (1993) 1347–1363.
- [19] R. Rowley, W. Wilding, J. Oscarson, Y. Yang, N. Zundel, T. Daubert, R. Danner, The DIPPR Data Compilation of Pure Compound Properties, Design Institute for Physical Properties, AIChE, New York, 2006.
- [20] T. Schnabel, A. Srivastava, J. Vrabec, H. Hasse, *J. Phys. Chem. B* 111 (2007) 9871–9878.
- [21] J. Vrabec, J. Stoll, H. Hasse, *J. Phys. Chem. B* 105 (2001) 12126–12133.
- [22] J. Stoll, Molecular Models for the Prediction of Thermalphysical Properties of Pure Fluids and Mixtures, Fortschritt-berichte VDI, Reihe 3, vol. 836, VDI-Verlag, Düsseldorf, 2005.
- [23] I.A. McLure, A.J. Pretty, P.A. Sadler, *J. Chem. Eng. Data* 22 (1977) 372–376.
- [24] B. Eckl, J. Vrabec, H. Hasse, *Mol. Phys.* 106 (2008) 1039–1046.
- [25] G. Guevara-Carrion, C. Nieto-Draghi, J. Vrabec, H. Hasse, *J. Phys. Chem. B* 112 (2008) 16664–16674.
- [26] C.B. Hurd, *J. Am. Chem. Soc.* 68 (1946) 364–370.
- [27] D.F. Wilcock, *J. Am. Chem. Soc.* 68 (1946) 691–696.
- [28] R. Lustig, *Mol. Sim.* 37 (2011) 457–465.
- [29] R. Lustig, *Mol. Phys.* 110 (2012) 3041–3052.
- [30] S. Deublein, B. Eckl, J. Stoll, S.V. Lishchuk, G. Guevara-Carrion, C.W. Glass, T. Merker, M. Bernreuther, H. Hasse, J. Vrabec, *Comp. Phys. Commun.* 182 (2011) 2350–2367.
- [31] C.W. Glass, S. Reiser, G. Rutkai, S. Deublein, A. Köster, G. Guevara-Carrion, A. Wafai, M. Horsch, M. Bernreuther, T. Windmann, H. Hasse, J. Vrabec, *Comput. Phys. Commun.* 185 (2014) 3302–3306.
- [32] D. Frenkel, B. Smit, *Understanding Molecular Simulation: from Algorithms to Applications*, Academic Press, Elsevier, San Diego, 2002.
- [33] J.A. Barker, R.O. Watts, *Mol. Phys.* 26 (1973) 789–792.
- [34] B. Widom, *J. Chem. Phys.* 39 (1963) 2808–2812.
- [35] A.M. Mosin, A.M. Mikhailov, *Zh. Fiz. Khim* 46 (1972) 537.
- [36] D.W. Scott, J.F. Messerly, S.S. Todd, G.B. Guthrie, I.A. Hosselopp, R.T. Moore, A. Osborn, W.T. Berg, J.P. McCullough, *J. Phys. Chem.* 65 (1961) 1320–1326.
- [37] B.K. Harrison, W.H. Seaton, *Ind. Eng. Chem. Res.* 27 (1988) 1536–1540.
- [38] B.E. Poling, J.M. Prausnitz, J.P. O'Connell, *The Properties of Gases and Liquids*, McGraw-Hill, New York, 2001.
- [39] N.R. Nannan, P. Colonna, C.M. Tracy, R.L. Rowley, J.J. Hurly, *Fluid Phase Equilib.* 257 (2007) 102–113.
- [40] L. Haar, J.S. Gallagher, G.S. Kell, J.V. Sengers (Eds.), *Proc. 8th Symp. Thermophys. Prop.*, ASME, New York, 1982.
- [41] U. Setzmann, W. Wagner, *J. Phys. Chem. Ref. Data* 20 (1991) 1061–1155.
- [42] E.W. Lemmon, R.T. Jacobsen, *J. Phys. Chem. Ref. Data* 34 (2005) 69–108.
- [43] E.W. Lemmon, M.O. McLinden, W. Wagner, *J. Chem. Eng. Data* 54 (2009) 3141–3180.
- [44] E.W. Lemmon, W. Wagner (2015), to be published.
- [45] I.A. McLure, E. Dickinson, *J. Chem. Thermodyn.* 8 (1976) 93–95.
- [46] P.J. Mohr, B.N. Taylor, D.B. Newell, *Rev. Mod. Phys.* 84 (2012) 1527–1605.
- [47] M.E. Wieser, M. Berglund, *Pure Appl. Chem.* 81 (2009) 2131–2156.
- [48] E. Dickinson, I.A. McLure, B.H. Powell, *J. Chem. Soc. Faraday Trans. 1* 70 (1974) 2321–2327.
- [49] I.A. McLure, J.F. Neville, *J. Chem. Thermodyn.* 9 (1977) 957–961.
- [50] E.D. Nikitin, P.A. Pavlov, A.P. Popov, *J. Chem. Thermodyn.* 26 (1994) 1047–1050.
- [51] C. Young, *J. Chem. Thermodyn.* 4 (1972) 65–75.
- [52] C. Young, *J. Chem. Soc. Faraday Trans. 2* (68) (1972) 452–459.
- [53] M. Frenkel, R.D. Chirico, V. Diky, K. Kroenlein, C.D. Muzny, A.F. Kazakov, J.W. Magge, I.M. Abdulagatov, E.W. Lemmon, NIST Standard Reference Database 103b: NIST Thermo-data Engine – Pure Compounds, Binary Mixtures, Reactions, Version 8.0, National Institute of Standards and Technology, Standard Reference Data Program, Gaithersburg, 2013.
- [54] R.A. Benkeser, H.R. Krysiak, *J. Am. Chem. Soc.* 76 (1954) 6353–6357.
- [55] B.A. Bolotov, T.V. Orlova, N.P. Kharitonov, N.N. Shenberg, E.A. Batyaev, N.P. Usacheva, *J. General Chem. (USSR)* 40 (1970) 802–806.
- [56] O.L. Flaningam, D.E. Williams, US-Patent, Pat. No. US 5,478,493 (1995) 1–6.
- [57] O.L. Flaningam, *J. Chem. Eng. Data* 31 (1986) 266–272.
- [58] J. Guzman, A.S. Teja, W.B. Kay, *Fluid Phase Equilib.* 7 (1981) 187–195.
- [59] M.J. Hunter, E.L. Warrick, J.F. Hyde, C.C. Currie, *J. Am. Chem. Soc.* 68 (1946) 2284–2290.
- [60] B. Kaczmarek, A. Radecki, *Pol. J. Chem.* 52 (1978) 431–434.
- [61] B. Kaczmarek, A. Radecki, *Pol. J. Chem.* 61 (1987) 267–271.
- [62] B. Kaczmarek, A. Radecki, *J. Chem. Eng. Data* 34 (1989) 195–197.
- [63] B. Kaczmarek, *Pol. J. Chem.* 57 (1983) 617–619.
- [64] B. Kaczmarek, *J. Chem. Eng. Data* 30 (1985) 249–251.
- [65] B. Kaczmarek, *Pol. J. Chem.* 72 (1998) 1120–1123.
- [66] C.A. Killgore, W.W. Chew, V. Orr, *J. Chem. Eng. Data* 11 (1966) 535–537.
- [67] M.J. Pedersen, W.B. Kay, H.C. Hershey, *J. Chem. Thermodyn.* 7 (1975) 1107–1118.
- [68] A. Radecki, B. Kaczmarek, J. Grzybowski, *J. Chem. Eng. Data* 20 (1975) 163–165.
- [69] A. Radecki, B. Kaczmarek, *J. Chem. Eng. Data* 20 (1975) 378–381.
- [70] A. Radecki, B. Kaczmarek, *J. Chem. Eng. Data* 22 (1977) 168–171.
- [71] A. Radecki, B. Kaczmarek, *J. Chem. Eng. Data* 25 (1980) 230–232.
- [72] H. Reuther, G. Reichel, *Chem. Tech.* 6 (1954) 479–480.
- [73] R.O. Sauer, *J. Am. Chem. Soc.* 66 (1944) 1707–1710.
- [74] J.L. Speier, *J. Am. Chem. Soc.* 70 (1948) 4142–4143.
- [75] D.R. Stull, *Ind. Eng. Chem.* 39 (1947) 517–540.
- [76] M.G. Voronkov, *J. General Chem. (USSR)* 29 (1959) 890–896.
- [77] H.I. Waterman, W.V. Herwijen, H.W. Denhartog, *J. Appl. Chem.* 8 (1958) 625–631.
- [78] W. Zhang, N. Meng, R. Sun, C. Li, *J. Chem. Eng. Data* 56 (2011) 5078–5080.
- [79] A. Gubareva, Onitkehkhim, Code 874 KHP – D83, 1983, pp. 1–6.
- [80] A.P. Mills, C.A. MacKenzie, *J. Am. Chem. Soc.* 76 (1954) 2672–2673.
- [81] G. Waddington, J.W. Knowlton, D.W. Scott, G.D. Oliver, S.S. Todd, W.N. Hubbard, C.J. Smith, H.M. Huffman, *J. Am. Chem. Soc.* 71 (1949) 797–808.
- [82] D.R. Stull, *Ind. Eng. Chem. Anal. Ed.* 18 (1946) 234–242.

- [83] E. Dickinson, I.A. McLure, J. Chem. Soc. Faraday Trans. 1 70 (1974) 2313–2320.
- [84] Sigma–Aldrich Co. LLC (August 2015). [link]. URL <https://www.sigmaaldrich.com>.
- [85] Merck Millipore Corporation (August 2015). [link]. URL <http://www.merckmillipore.com>.
- [86] Alfa Aesar GmbH & Co KG (August 2015). [link]. URL <http://www.alfa.com>.
- [87] E.W. Lemmon, R. Span, J. Chem. Eng. Data 51 (2006) 785–850.
- [88] R. Anderson, B. Arkles, G.L. Larson, Silicon Compounds: Register and Review, Huls America Inc., Piscataway, 1991.
- [89] E. Dickinson, J. Phys. Chem. 81 (1977) 2108–2113.
- [90] H.W. Fox, P.W. Taylor, W.A. Zisman, Ind. Eng. Chem. 39 (1947) 1401–1409.
- [91] G.L. Gaines Jr., J. Phys. Chem. 73 (1969) 3143–3150.
- [92] O.Z. Golik, P.P. Cholpan, Ukr. Fiz. Zh. Ukr. Ed. 5 (1960) 242–251.
- [93] W.D. Good, J.L. Lacina, B.L. DePrater, J.P. McCullough, J. Phys. Chem. 68 (1964) 579–586.
- [94] B. Kaczmarek, Inz. Chem. Proces. 4 (1983) 497–502.
- [95] D.H. Marcos, D.D. Lindley, K.S. Wilson, W.B. Kay, H.C. Hershey, J. Chem. Thermodyn. 15 (1983) 1003–1014.
- [96] E. Matteoli, P. Gianni, L. Lepori, A. Spanedda, J. Chem. Eng. Data 56 (2011) 5019–5027.
- [97] R.C. Weast, M.J. Astle, CRC Handbook of Data on Organic Compounds, CRC Press, Boca Raton, 1985.
- [98] W. Wagner, A. Pruß, J. Phys. Chem. Ref. Data 31 (2002) 387–535.
- [99] A. Schedemann, Aufbau und Inbetriebnahme einer Dichtemessanlage. Messung und Modellierung des PVT-Verhaltens bis zu Drücken von 1400 bar (PhD thesis), Universität Oldenburg, Germany, 2009.
- [100] R.P. Singh, A.P. Kudchadker, J. Chem. Thermodyn. 11 (1979) 205–213.
- [101] H.M. Huffman, Chem. Rev. 40 (1947) 1–14.
- [102] H.J. Hoge, J. Res. Natl. Bur. Stand. (U.S.) 36 (1946) 111–118.
- [103] R. Span, W. Wagner, Int. J. Thermophys. 18 (1997) 1415–1443.
- [104] E.W. Lemmon, M.L. Huber, M.O. McLinden, REFPROP. Reference Fluid Thermodynamic and Transport Properties 9.1, National Institute of Standards and Technology, Boulder (USA), 2014.
- [105] R. Span, T. Eckermann, S. Herrig, S. Hielscher, M. Thol, TREND. Thermodynamic Reference and Engineering Data 2.0, Lehrstuhl für Thermodynamik, Ruhr-Universität Bochum, Germany, 2015.

### 3.11 Thermodynamic Properties of Octamethylcyclotetrasiloxane

M. Thol, G. Rutkai, **A. Köster**, F. H. Dubberke, T. Windmann, R. Span, J. Vrabec, *Journal of Chemical & Engineering Data* 61:2580-2595, 2016.

DOI: [doi.org/10.1021/acs.jced.6b00261](https://doi.org/10.1021/acs.jced.6b00261)

Nachgedruckt mit Erlaubnis der American Chemical Society (Copyright 2016).

Im Rahmen dieser Arbeit wurde eine hybride Zustandsgleichung für Octamethylcyclotetrasiloxan erstellt, eine Substanz die sich hervorragend als Arbeitsmedien in „Organic Rankine Cycles“ eignet. Für die Bestimmung der dafür verwendeten partiellen Ableitungen der Helmholtzenergie wurde ein neues molekulares Kraftfeld entwickelt. Die vorhandenen experimentellen Daten aus der Literatur wurden um Schallgeschwindigkeitsmessungen erweitert. Die mit Hilfe des Lustig-Formalismus [Lus11, Lus12] berechneten partiellen Ableitungen der Helmholtzenergie ermöglichten eine effiziente Nutzung der Simulationsdaten im Anpassungsprozess der Gleichung und tragen insbesondere dazu bei, dass der Gültigkeitsbereich von Gleichungen die nur auf Experimenten beruhen vergrößert wird.

Der Autor der vorliegenden Dissertation hat alle für diese Veröffentlichungen zugrundeliegenden molekularen Simulationen der partiellen Ableitungen der Helmholtzenergie durchgeführt. Das zugrundeliegende Kraftfeld wurde von Dr. Thorsten Windmann erstellt und optimiert. Für die experimentelle Ermittlung der Schallgeschwindigkeit von Octamethylcyclotetrasiloxan wurde eine neue Messapparatur von Frithjof Dubberke aufgebaut, der auch die Messungen durchgeführt hat. Alle Daten wurden von Dr. Monika Thol verwendet um eine hybride helmholtzexplizite Zustandsgleichung zu erstellen. Der Autor verfasste in Zusammenarbeit mit Dr. Gábor Rutkai die Beschreibungen über die zugrundeliegenden Simulationsmethoden und -parameter. Die Überarbeitung des Manuskripts wurde in Zusammenarbeit mit Prof. Roland Span und Prof. Jadran Vrabec durchgeführt. Der Autor wurde während des gesamten Prozesses von Prof. Jadran Vrabec betreut.

## Thermodynamic Properties of Octamethylcyclotetrasiloxane

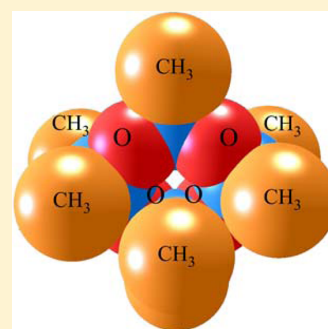
Monika Thol,<sup>†</sup> Gábor Rutkai,<sup>‡</sup> Andreas Köster,<sup>‡</sup> Frithjof H. Dubberke,<sup>‡</sup> Thorsten Windmann,<sup>‡</sup> Roland Span,<sup>†</sup> and Jadran Vrabec<sup>\*,‡</sup>

<sup>†</sup>Thermodynamics, Ruhr-Universität Bochum, Universitätsstraße 150, 44801 Bochum, Germany

<sup>‡</sup>Thermodynamics and Energy Technology, Universität Paderborn, Warburger Straße 100, 33098 Paderborn, Germany

### Supporting Information

**ABSTRACT:** An equation of state for octamethylcyclotetrasiloxane is presented. The available experimental data from the literature are supplemented by new measurements on the speed of sound. Furthermore, a new force field is proposed, allowing the generation of a comprehensive thermodynamic data set by means of molecular simulation. Both the experimental and molecular simulation data are applied to develop a fundamental equation of state in terms of the Helmholtz energy. On the basis of the experimental data, the equation of state is valid from the triple-point temperature to  $T = 590$  K for pressures up to  $p = 180$  MPa and can be used to calculate any thermodynamic equilibrium state property. Its accuracy is assessed by a comprehensive analysis of the underlying experimental data. Finally, the range of validity was extended to  $T_{\max} = 1200$  K and  $p_{\max} = 520$  MPa by means of molecular simulation data.



## 1. INTRODUCTION

Octamethylcyclotetrasiloxane (CAS no. 556-67-2, chemical formula  $C_8H_{24}O_4Si_4$ ) is a cyclic siloxane that is a colorless, oily liquid under standard conditions. In the chemical industry, it is used as an adhesive and sealant, a finishing agent, or a solvent. Furthermore, it is an ingredient of paints, plastics, and rubber products.<sup>1</sup> In the field of energy technology, it is mainly employed as a working fluid in organic Rankine cycles (ORCs) because of some favorable properties, e.g., it is nontoxic, hardly flammable, and chemically stable up to high temperatures.<sup>1</sup> Over the last years, siloxanes were studied comprehensively with the aim to use them in ORC processes. For the design and optimization of such processes, it is essential to have an accurate knowledge of the thermodynamic properties of the fluids involved. The first fundamental equation of state in terms of the Helmholtz energy that provided this information was published in 2006 by Colonna et al.<sup>2</sup> Since the data situation was restricted in terms of quality and quantity at that time, it was challenging to develop a substance-specific equation of state for this fluid. Therefore, the generalized functional form for non- and weakly polar fluids of Span and Wagner<sup>3</sup> was applied, and only the coefficients of the equation of state were fitted to the available experimental database. Recent investigations showed that the available equation of state is disadvantageous with respect to the speed of sound and density in the homogeneous liquid phase as well as its extrapolation behavior.

In the last decades, several approaches have been proposed to overcome the problem of insufficient experimental data for the development of accurate fundamental equations of state, e.g., the construction of generalized functional forms for certain groups of fluids with analogous characteristics.<sup>3–9</sup> A new

approach suggested by Rutkai et al.<sup>10</sup> comprises the implementation of molecular simulation data in the fitting procedure. Significant progress in computational technology and molecular modeling enables time-efficient and comprehensive simulations of thermodynamic properties. Here no restrictions due to challenging fluid characteristics (e.g., toxicity and corrosivity) or apparatus limitations with respect to temperature or pressure have to be taken into account. Therefore, these data provide a potential solution to fill gaps in the experimental database. This new approach was successfully applied to the development of fundamental equations of state for ethylene oxide<sup>11</sup> and hexamethyldisiloxane.<sup>12</sup> Following these lines, a potential model for octamethylcyclotetrasiloxane is presented in this work. The available experimental data are complemented by new measurements of the speed of sound in the liquid state. Both experimental and molecular simulation data sets were utilized for the development of the present equation of state.

## 2. SPEED OF SOUND MEASUREMENT AND MOLECULAR MODELING

The speed of sound of a given fluid can be determined by the time measurement of acoustic signal propagation through the fluid over some known distance. Here the applied measurement principle is based on estimating the time difference  $\Delta t$  between the detection of two distinct echoes of a signal emitted by a modulated high-frequency wave burst with a piezoelectric quartz crystal.<sup>13,14</sup> In the measurement cell, the crystal is placed

Received: March 22, 2016

Accepted: June 1, 2016

Published: June 10, 2016





between two reflectors that are positioned at distances  $l_1$  and  $l_2$  from the crystal such that  $l_1 < l_2$ . The reflectors ensure that the echoes of the original signal are also detected with the crystal. The time shift between the detections,  $\Delta t$ , is caused by the different propagation path lengths  $l_1$  and  $l_2$ . The speed of sound,  $w$ , is then given in terms of the ratio of the difference in the propagation distances  $l_1$  and  $l_2$  to  $\Delta t$  as

$$w = \frac{2(l_2 - l_1)}{\Delta t} \quad (1)$$

assuming that dispersion and diffraction effects can be neglected. The estimation of the time difference  $\Delta t$  was carried out here with the correlation method of Ball and Trusler<sup>15</sup> combined with signal enhancement by fast Fourier transformation. Details of the calculation method and the signal processing are given by Dubberke et al.<sup>16</sup>

The sample was obtained from Wacker with a given purity of  $\geq 99\%$ . Further details can be found in the [Supporting Information](#). Before the measurement, the cell was filled with degassed octamethylcyclotetrasiloxane, and the fluid was compressed to about 20 MPa using a hand pump. A constant pressure level was reached after 1 h of equilibration. The pressure was measured with a transducer (Honeywell TJE with an operating range of up to 70 MPa), calibrated with a dead-weight tester (Degranges and Hout, S201-S), and protected by a blowout disc. The temperature was measured with a Pt100 thermometer (Rössel Messtechnik, RM-type), which was installed on the wall of the pressure cylinder next to the quartz crystal and was calibrated with a standardized 25  $\Omega$  platinum thermometer (Rosemount, 162 CE). The thermostat was constructed with three nested copper shields to allow for fine temperature adjustment of the cell over a wide temperature range. Each shield was equipped with its own independently adjustable heater; each was controlled with a combination of a proportional–integral–derivative (PID) controller and a proportional (P) controller. For the path length difference  $\Delta l$ , calibration measurements were carried out with water. Water at high purity and accurate speed of sound measurement data are available over a wide range of temperature and pressure. Details are described by Gedanitz et al.<sup>17</sup> The obtained speed of sound data were amended by the diffraction correction of Harris,<sup>18</sup> where significant dispersion effects are not expected for a resonance frequency of 8 MHz.<sup>19</sup> The reported uncertainties for the speed of sound were estimated according to the error propagation law, considering the uncertainty of the temperature and pressure measurements as well as the uncertainty of the referencing procedure. The measurements were carried out along six isotherms in the temperature range from 300 to 550 K at pressures of up to 26 MPa (54 data points in total). Numerical results are given in the [Supporting Information](#).

In addition to the speed of sound measurements, molecular simulations were carried out to generate a data set of six Helmholtz energy derivatives at 87 state points, resulting in a set of 522 thermodynamically nonredundant entries. The calculations were performed with the molecular simulation tool ms2<sup>20</sup> through the use of the recently implemented formalism of Lustig.<sup>21,22</sup> This new feature enables the calculation of the residual part  $A_{nm}^r$  of the derivatives

$$\frac{\partial^{n+m} a(T, \rho) / (RT)}{\partial (1/T)^n \partial \rho^m} (1/T)^n \rho^m \equiv A_{nm} = A_{nm}^o + A_{nm}^r \quad (2)$$

for any  $n > 0$  or  $m > 0$  per sampled state point, where  $a$  is the molar Helmholtz energy,  $T$  is the absolute temperature,  $\rho$  is the density, and  $R = 8.3144621 \text{ J} \cdot \text{mol}^{-1} \cdot \text{K}^{-1}$  is the universal gas constant.<sup>23</sup> The ideal part  $A_{nm}^o = A_{nm}^o(T) + \ln(\rho/\rho_{\text{ref}})$ , where  $\rho_{\text{ref}}$  is an arbitrary reference density,<sup>24</sup> corresponds to the value of  $A_{nm}(T, \rho)$  when no intermolecular interactions are present. Consequently,  $A_{nm}^o = 0$  for  $n > 0$  and  $m > 0$ , and  $A_{nm}^o = (-1)^{1+m}$  for  $n = 0$  and  $m > 0$ .  $A_{nm}^o(T)$  has a nontrivial but exclusive temperature dependence and is a sum of contributions due to translational, rotational, and internal molecular degrees of freedom. Since  $a/(RT)$  is a thermodynamic potential, every other equilibrium thermodynamic property can be obtained as a combination of  $A_{nm}$  derivatives. Examples are given later on (eqs 12 to 15). A more complete list is given by Span.<sup>24</sup>

The quality of molecular simulation results is predominantly dependent on the underlying molecular interaction model. The octamethylcyclotetrasiloxane model developed in this work consists of 16 Lennard-Jones (LJ) sites and eight point charges (cf. Figure 1). The geometry of the model was determined by

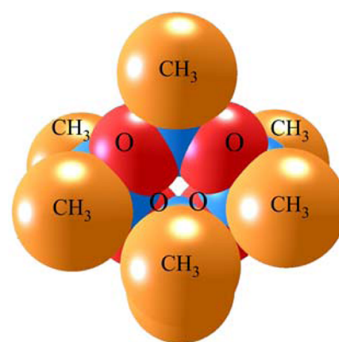


**Figure 1.** Present molecular interaction model for octamethylcyclotetrasiloxane. CH<sub>3</sub>, methyl site; O, oxygen site; not labeled, silica site. The sphere diameters correspond to the Lennard-Jones size parameters, which are depicted according to the molecular geometry scale.

quantum-chemical calculations applying the software package GAMESS(US)<sup>25</sup> with the Hartree–Fock method and the 6-31G basis set. The initial values of the LJ energy ( $\epsilon$ ) and size ( $\sigma$ ) parameters as well as those of the point charges ( $q$ ) were adopted from Thol et al.<sup>12</sup> In the initial phase, the magnitudes of the point charges were adjusted to fit experimental vapor–liquid equilibrium data, namely, saturated liquid density and vapor pressure data. In the last step, all of the model parameters, including the geometric structure, were fine-tuned with the reduced unit method.<sup>26</sup> The resulting model parameters are listed in Table 1. The model itself considers no internal degrees of freedom, which can be justified by the compact structure of the molecule. Therefore, the ideal part  $A_{nm}^o(T)$  was taken from the current equation of state for the calculation of thermodynamic properties for which this contribution is necessary (cf. eqs 12, 14, and 15). Finally, the model was validated by comparing simulation results with experimental vapor–liquid equilibrium data as well as single-phase liquid density, speed of sound, second virial coefficient, and transport property data from the literature. The numerical simulation results and comparisons with the present equation of state are given in the [Supporting Information](#). The molecular force field model by Matsubara et al.<sup>27</sup> is similar in terms of the united-atom approach and rigid-body approximation. Although

Table 1. Parameters of the Present Molecular Interaction Model for Octamethylcyclotetrasiloxane<sup>a</sup>

interaction site	$x/\text{\AA}$	$y/\text{\AA}$	$z/\text{\AA}$	$\sigma/\text{\AA}$	$\epsilon \cdot k_B^{-1}/\text{K}$	$q/e$
CH <sub>3</sub>	4.3198	-0.2718	1.3971	3.8181	122.4689	
CH <sub>3</sub>	3.9847	-1.7562	-1.3286	3.8181	122.4689	
Si	3.1365	-0.7701	0.0267	3.5167	15.2895	0.3036
O	1.9213	-1.6816	0.7475	3.1248	44.0134	-0.3036
CH <sub>3</sub>	1.6735	3.2187	-1.5120	3.8181	122.4689	
CH <sub>3</sub>	1.4331	2.2420	1.4613	3.8181	122.4689	
Si	1.3378	1.7784	-0.3619	3.5167	15.2895	0.3036
O	2.4782	0.5925	-0.7067	3.1248	44.0134	-0.3036
CH <sub>3</sub>	-2.2590	1.2815	1.3636	3.8181	122.4689	
CH <sub>3</sub>	-2.6052	-0.1997	-1.3611	3.8181	122.4689	
Si	-1.4157	0.2953	0.0056	3.5167	15.2895	0.3036
O	-0.2012	1.2041	-0.7199	3.1248	44.0134	-0.3036
CH <sub>3</sub>	0.2869	-2.6955	-1.4467	3.8181	122.4689	
CH <sub>3</sub>	0.0459	-3.7042	1.5158	3.8181	122.4689	
Si	0.3828	-2.2517	0.3814	3.5167	15.2895	0.3036
O	-0.7576	-1.0687	0.7370	3.1248	44.0134	-0.3036

<sup>a</sup>Lennard-Jones sites are denoted by the modeled atoms or atomic groups. Electrostatic sites are denoted by point charge magnitudes  $q$ . Coordinates  $(x, y, z)$  are given with respect to the center of mass in a principal axes system.  $k_B$  is the Boltzmann constant.

it leads to excellent results for transport properties, the representation of the pressure–volume–temperature ( $pVT$ ) relation is inferior. Recently, Xu and Leng<sup>28</sup> published a new model for octamethylcyclotetrasiloxane that is better suited for  $pVT$  data, considering the internal molecular degrees of freedom. The performance of the present molecular model for the speed of sound is shown in Figure 2. As can be seen,

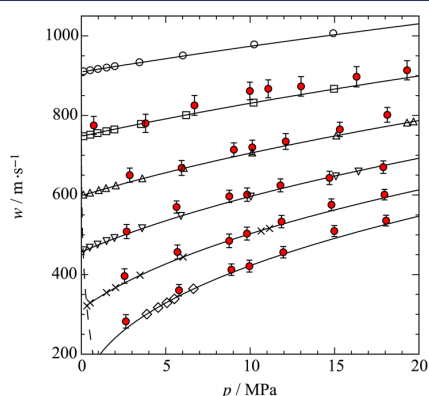


Figure 2. Speed of sound of octamethylcyclotetrasiloxane. Present experimental data: ○, 300 K; □, 350 K; △, 400 K; ▽, 450 K; ×, 500 K; ◇, 550 K. Red ●, present simulation data. Curves: —, present equation of state; - - -, vapor pressure curve.

nearly all of the simulation results agree with the experimental values within their statistical uncertainties. Figure 3 shows the performance for the thermal conductivity and shear viscosity for liquid states. Simulation results were obtained by equilibrium molecular dynamics simulations and the Green–Kubo formalism (cf. Guevara-Carrion et al.<sup>29</sup>). The model slightly underpredicts the literature thermal conductivity data over the whole temperature range. For the shear viscosity, except for the value at 300 K, the simulation results agree with the literature data within their statistical uncertainties.

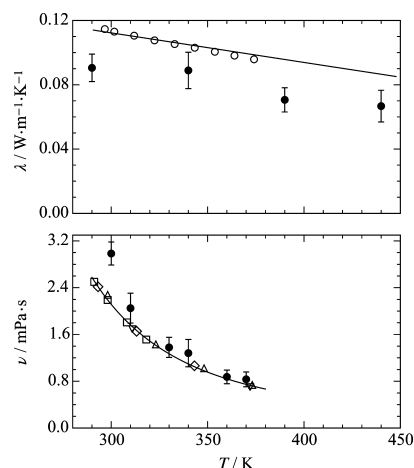


Figure 3. (top) Thermal conductivity and (bottom) shear viscosity of octamethylcyclotetrasiloxane at 0.1 MPa: ●, present simulation data; experimental data of ○, Abbas et al.;<sup>30</sup> □, Marsh;<sup>31</sup> ◇, Waterman et al.;<sup>32</sup> △, Reuther;<sup>33</sup> ▽, Wilcock;<sup>34</sup> —, correlation from the DIPPR database.<sup>35</sup>

### 3. EQUATION OF STATE

The equation of state presented here is expressed in terms of the molar Helmholtz energy  $a$  with the independent variables temperature  $T$  and density  $\rho$ . For a dimensionless description, the Helmholtz energy is reduced by the temperature and the universal gas constant  $R$ :

$$\alpha(\tau, \delta) = \frac{a(T, \rho)}{RT} \quad (3)$$

According to the theorem of corresponding states, the independent variables are reduced by the critical temperature  $T_c$  and critical density  $\rho_c$ . The reduced Helmholtz energy then reads as

$$\alpha(\tau, \delta) = \alpha^\circ(\tau, \delta) + \alpha^r(\tau, \delta) \quad (4)$$

where  $\tau = T_c/T$  and  $\delta = \rho/\rho_c$ . The ideal contribution (superscript "O") is derived from the following equation for the isobaric heat capacity:

$$\frac{c_p^O}{R} = (c_0 + 1) + \sum_{i=1}^3 m_i \left( \frac{\theta_i}{T} \right)^2 \frac{\exp(\theta_i/T)}{(\exp(\theta_i/T) - 1)^2} \quad (5)$$

Polynomial terms were avoided to ensure correct extrapolation behavior. Since the present fundamental equation of state is expressed in terms of the reduced Helmholtz energy, eq 5 has to be integrated twice with respect to  $\tau$ :

$$\alpha^O(\tau, \delta) = c^{II} + c^I \tau + c_0 \ln(\tau) + \sum_{i=1}^3 m_i \ln(1 - \exp(-\theta_i/T_c \tau)) + \ln(\delta) \quad (6)$$

The integration constants  $c^I$  and  $c^{II}$  can be chosen arbitrarily. For fluids that are liquids under standard conditions, the most common reference state is the normal boiling point. At  $p = 1$  atm, the saturation temperature  $T_0$  and the saturated liquid density  $\rho'_0$  are determined. At this state point, the integration constants are chosen such that the enthalpy is  $h_0(T_0, \rho'_0) = 0$  J·mol<sup>-1</sup> and the entropy is  $s_0(T_0, \rho'_0) = 0$  J·mol<sup>-1</sup>·K<sup>-1</sup>. The integration constants and the parameters for the Planck–Einstein terms are listed in Table 2.

**Table 2. Parameters of the Ideal Part of the Present Equation of State (cf. eq 6)**

$m_1$	0.292757
$m_2$	38.2456
$m_3$	58.975
$\theta_1/K$	40
$\theta_2/K$	200
$\theta_3/K$	1800
$c_0$	3.0
$c^I$	-21.674365
$c^{II}$	71.163605

The residual part (superscript "r") comprises polynomial (Pol), exponential (Exp), and Gaussian bell-shaped (GBS) terms:

$$\begin{aligned} \alpha^r(\tau, \delta) &= \alpha_{\text{Pol}}^r(\tau, \delta) + \alpha_{\text{Exp}}^r(\tau, \delta) + \alpha_{\text{GBS}}^r(\tau, \delta) \\ &= \sum_{i=1}^5 n_i \delta^{d_i} \tau^{t_i} + \sum_{i=6}^{10} n_i \delta^{d_i} \tau^{t_i} \exp(-\delta^{\eta_i}) \\ &\quad + \sum_{i=11}^{15} n_i \delta^{d_i} \tau^{t_i} \exp[-\eta_i(\delta - \epsilon_i)^2 - \beta_i(\tau - \gamma_i)^2] \end{aligned} \quad (7)$$

The polynomial and exponential terms are in principle sufficient for the description of the whole fluid surface. The GBS terms, introduced by Haar et al.<sup>36</sup> and applied in a modified form to the fundamental equation of state for methane by Setzmann and Wagner,<sup>37</sup> allow for a more accurate representation of the critical region. Nowadays, these terms are used in all fluid regions, which leads to a reduction in the total number of terms. For a long time, equations with 20 to 50 terms were common practice,<sup>24</sup> whereas recent equations of state consist of 14 to 25 terms<sup>38–41</sup> because of this functional form. The present equation of state consists of five polynomial, five exponential, and five GBS terms. Its parameters are listed in Table 3.

The equation presented here was constrained to the critical temperature  $T_c = 586.5$  K reported by Young.<sup>42</sup> The critical density  $\rho_c = 1.043$  mol·dm<sup>-3</sup> and the critical pressure  $p_c = 1.347$  MPa were determined during the fit. The triple-point temperature  $T_{\text{tr}} = 290.25$  K reported by Mekhtiev and Karasharli<sup>43</sup> was applied as the lower temperature limit. The resulting triple-point density is  $\rho'_{\text{tr}} = 3.24$  mol·dm<sup>-3</sup>. Additionally, the molecular weight  $M = 296.61576$  g·mol<sup>-1</sup> was adopted.<sup>44</sup>

The calculation of any thermodynamic equilibrium state property from the derivatives of the reduced Helmholtz energy with respect to its independent variables can be taken from Span.<sup>24</sup>

#### 4. COMPARISON TO EXPERIMENTAL AND MOLECULAR SIMULATION DATA

In this section, the present equation of state is compared to experimental and molecular simulation data. An overview of the homogeneous data is given in Figure 4. The gray area indicates the region covered by experimental measurements. The triangles depict the state points where molecular simulation data were generated in this work. In addition to these

**Table 3. Parameters of the Residual Part of the Present Equation of State (cf. eq 7)**

$i$	$n_i$	$t_i$	$d_i$	$p_i$	$\eta_i$	$\beta_i$	$\gamma_i$	$\epsilon_i$
1	$5.273743 \cdot 10^{-2}$	1.000	4					
2	$4.176401 \cdot 10^{+0}$	0.270	1					
3	$-4.737070 \cdot 10^{+0}$	0.510	1					
4	$-1.289588 \cdot 10^{+0}$	0.998	2					
5	$5.272749 \cdot 10^{-1}$	0.560	3					
6	$-2.558391 \cdot 10^{+0}$	1.750	1	2				
7	$-9.726737 \cdot 10^{-1}$	3.090	3	2				
8	$7.208209 \cdot 10^{-1}$	0.790	2	1				
9	$-4.789456 \cdot 10^{-1}$	2.710	2	2				
10	$-5.563239 \cdot 10^{-2}$	0.998	7	1				
11	$3.766589 \cdot 10^{+0}$	0.930	1		0.861	0.75	1.124	0.926
12	$8.786997 \cdot 10^{-2}$	3.170	1		1.114	0.55	1.388	1.300
13	$-1.267646 \cdot 10^{-1}$	1.080	3		1.010	1.00	1.148	1.114
14	$-1.004246 \cdot 10^{+0}$	1.410	2		1.110	0.47	1.197	0.996
15	$-1.641887 \cdot 10^{+0}$	0.890	2		1.032	1.36	0.817	0.483



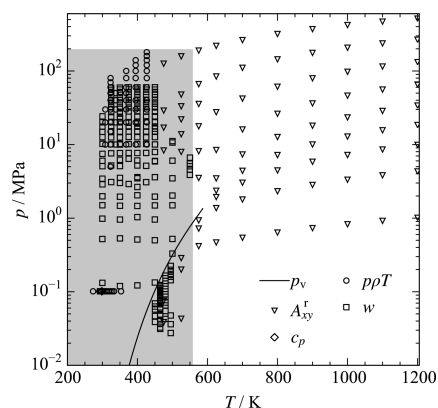


**Figure 4.** Available data for octamethylcyclotetrasiloxane in the homogeneous region. The gray area depicts the region where experimental data are available:  $T < 590$  K and  $p < 180$  MPa. The residual Helmholtz derivatives from molecular simulation extend this region up to  $T_{\max} = 1200$  K and  $p_{\max} = 520$  MPa.

properties, vapor–liquid equilibrium and ideal gas heat capacity data were available.

In the next sections, the data analysis is based on relative deviations  $\Delta X$ , defined as

$$\Delta X = 100 \frac{X_{\text{DATA}} - X_{\text{EOS}}}{X_{\text{DATA}}} \quad (8)$$

Average absolute relative deviations (AADs) were calculated as follows:

$$\text{AAD} = \frac{1}{N} \sum_{i=1}^N |\Delta X_i| \quad (9)$$

For the statistical analysis, vapor pressure, saturated liquid density, and saturated vapor density data are separated into three temperature ranges: low temperature (LT:  $T/T_c \leq 0.6$ ), medium temperature (MT:  $0.6 \leq T/T_c \leq 0.98$ ), and high temperature (HT:  $T/T_c > 0.98$ ). All other properties are categorized as gas, liquid, critical region ( $0.98 \leq T/T_c \leq 1.1$  and  $0.7 \leq \rho/\rho_c \leq 1.4$ ), or supercritical region. The last of these is further divided into low density (LD:  $\rho/\rho_c \leq 0.6$ ), medium density (MD:  $0.6 \leq \rho/\rho_c \leq 1.5$ ), and high density (HD:  $\rho/\rho_c > 1.5$ ). In the diagrams, the equation of Colonna et al.<sup>2</sup> and the correlation equations of the DIPPR<sup>35</sup> and TDE<sup>45</sup> databases are plotted for comparison.

**4.1. Ideal Gas State.** In general, the ideal gas behavior of siloxanes has been only scarcely investigated. This challenge was discussed in detail by Thol et al.<sup>12</sup> and here will only be summarized briefly. When setting up the first set of Helmholtz equations, Colonna et al.<sup>2</sup> applied the Harrison–Seaton zeroth-order contribution method.<sup>46</sup> This was the only method providing information about Si–C bonds. However, the DIPPR database<sup>35</sup> reports a possible uncertainty of up to 25% for data from this method, which is not acceptable for accurate equations of state. Therefore, Nannan et al.<sup>47</sup> investigated the ideal gas behavior of several siloxanes more comprehensively. As a first approach, they measured speed of sound data for gaseous states, which they used to derive  $c_p^\circ$  data. For small molecules, this is an accurate approach. However, with increasing complexity of the molecule, the uncertainty in this

approach increases. A rough estimation can be made with the following relation:<sup>24</sup>

$$\left| \frac{\Delta c_p^\circ}{c_p^\circ} \right| = \left| 2 \left( \frac{c_p^\circ}{R} - 1 \right) \frac{\Delta w^\circ}{w^\circ} \right| \quad (10)$$

Because of the large isobaric heat capacity of octamethylcyclotetrasiloxane, this results in an uncertainty of 3.9% with respect to  $c_p^\circ$  data, although the speed of sound measurements are claimed to be accurate to within 0.02%.<sup>47</sup> Since the measurements were carried out over a restricted temperature range (450 to 495 K), these data are not sufficient to set up the ideal part for an equation of state covering the whole temperature range. Thus, Nannan et al.<sup>47</sup> determined  $c_p^\circ$  data over a broad temperature range by means of ab initio calculations. They found similar results for two methods without giving any information on the accuracy of the data. Because the ab initio calculations were not done at the same temperatures as the measurements, the experiments cannot directly be used to assess the uncertainty of the calculations. The same calculations for hexamethyldisiloxane showed a deviation from the corresponding equation<sup>12</sup> of approximately 3%. Therefore, the  $c_p^\circ$  data were used only as an approximate guide for the present fit. In Figure 5, the representation of the  $c_p^\circ$  data of

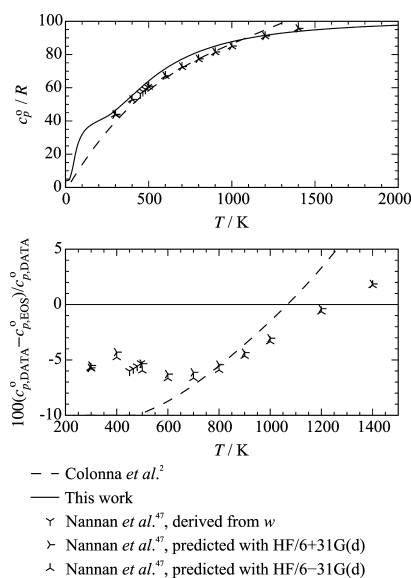


**Figure 5.** Representation of the isobaric heat capacity of the ideal octamethylcyclotetrasiloxane gas with the present equation of state.

Nannan et al.<sup>47</sup> by the present equation of state is depicted. In the top panel, the reduced ideal gas heat capacity is illustrated as a function of temperature. For computational efficiency, Colonna et al.<sup>2</sup> applied a simple polynomial approach for their ideal gas equation of state, which does not extrapolate well. For  $T \rightarrow 0$  K, only translational and rotational molecular degrees of freedom are excited,<sup>12,24</sup> which leads to  $c_p^\circ/R = 4$ . The polynomial approach of Colonna et al.<sup>2</sup> results in an incorrect value of  $c_p^\circ/R \approx -2$ .

For high temperatures, an asymptotic course with a limiting value based on the maximum number of molecular degrees of freedom has to be modeled. Because of the polynomial form, the ideal gas heat capacity of Colonna et al.<sup>2</sup> increases

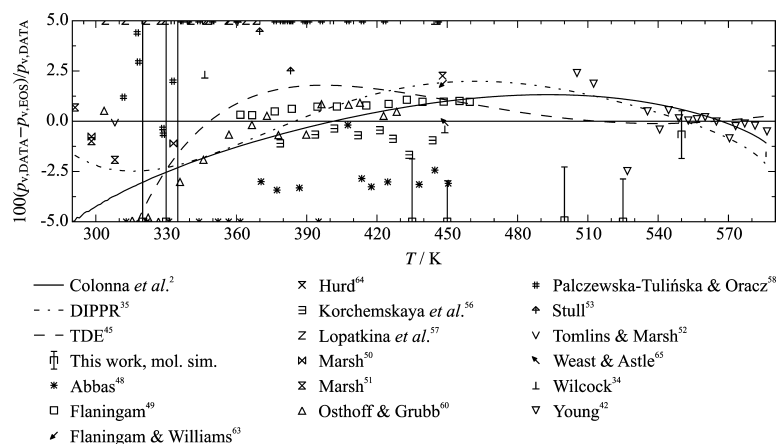


Figure 6. Relative deviations of the vapor pressure data from the present equation of state.

Table 4. Average Absolute Relative Deviations of Experimental Vapor Pressure Data and Saturated Liquid and Vapor Densities from the Present Equation of State<sup>a</sup>

authors	no. of data points	T range/K	AAD/%			
			LT <sup>b</sup>	MT <sup>b</sup>	HT <sup>b</sup>	overall
Vapor pressure $p_v$						
Abbas et al. <sup>48</sup>	18	312–451	7.56	4.00	—	4.79
Flaningham <sup>49*</sup>	13	361–460	—	0.76	—	0.76
Flaningham and Williams <sup>63</sup>	1	448.15	—	1.87	—	1.87
Hurd <sup>64</sup>	1	447.99	—	2.26	—	2.26
Korchemskaya et al. <sup>56</sup>	10	378–446	—	2.44	—	2.44
Lopatkina et al. <sup>57</sup>	12	304–369	26.5	8.14	—	20.4
Marsh <sup>50</sup>	2	298–334	0.94	—	—	0.94
Marsh <sup>51</sup>	3	291–309	1.20	—	—	1.20
Osthoff and Grubb <sup>60</sup>	16	303–429	3.53	0.58	—	1.69
Palczewska-Tulińska and Oracz <sup>58</sup>	24	311–447	3.40	8.04	—	6.10
Stull <sup>53</sup>	10	294–445	12.5	5.97	—	8.60
Tomlins and Marsh <sup>52</sup>	1	308.14	0.063	—	—	0.063
Weast and Astle <sup>65</sup>	1	448.91	—	0.054	—	0.054
Wilcock <sup>34</sup>	2	346–449	2.32	0.40	—	1.36
Young <sup>42*</sup>	16	505–587	—	0.75	0.28	0.67
Saturated liquid density $\rho'$						
Golik and Cholpan <sup>66</sup>	1	303.13	0.29	—	—	0.29
Hurd <sup>64</sup>	5	273–354	4.64	0.017	—	3.72
Korchemskaya et al. <sup>56</sup>	1	293.14	0.035	—	—	0.035
Levien <sup>67</sup>	1	298.14	0.024	—	—	0.024
Marsh <sup>51</sup>	3	291–309	0.044	—	—	0.044
McLure and Barbarin-Castillo <sup>68*</sup>	14	292–409	0.006	0.028	—	0.015
Palczewska-Tulińska and Oracz <sup>58</sup>	22	292–434	0.13	0.17	—	0.15
Patnode and Wilcock <sup>55</sup>	1	293.14	0.066	—	—	0.066
Shinoda and Hildebrand <sup>69</sup>	1	298.14	0.005	—	—	0.005
Tanaka <sup>70</sup>	1	293.14	0.066	—	—	0.066
Tomlins and Marsh <sup>52</sup>	1	308.14	0.043	—	—	0.043
Waterman et al. <sup>32</sup>	1	293.14	0.030	—	—	0.030
Young <sup>42*</sup>	7	503–577	—	0.24	0.44	0.26
Saturated vapor density $\rho''$						
Korchemskaya et al. <sup>56</sup>	9	378–446	—	6.19	—	6.19
Young <sup>42</sup>	8	536–580	—	10.5	18.5	11.5

<sup>a</sup>All temperatures were adapted to the ITS-90 Scale; data sets that were applied to the fit are marked with an asterisk. <sup>b</sup>LT,  $T/T_c \leq 0.6$ ; MT,  $0.6 \leq T/T_c \leq 0.98$ ; HT,  $T/T_c > 0.98$ .

monotonously, whereas the present functional form reaches a limiting value. In the bottom panel of Figure 5, the three different methods used by Nannan et al.<sup>47</sup> to predict  $c_p^o$  data are

compared with the present equation of state. For  $T < 800$  K, the data systematically deviate by approximately 7%. At higher temperatures, the deviations decrease. The parameters of eq 5

were simultaneously adjusted to fit the  $c_p^\circ$  data of Nannan et al.<sup>47</sup> and available data for the speed of sound and isobaric heat capacity (e.g., refs 47 and 48). During the fitting procedure, it turned out that it was not possible to represent the  $c_p^\circ$  data in a more accurate way without compromising the other properties. Since the accuracy of the  $c_p^\circ$  data is questionable, the speed of sound and isobaric heat capacity data were preferentially fitted and the comparably high deviations of the  $c_p^\circ$  data have to be accepted here.

**4.2. Vapor–Liquid Equilibrium.** The available experimental vapor pressure data are summarized in Figure 6 and Table 4. Many authors report vapor pressure data in their publications to point out the purity of their samples. More comprehensive investigations were made by eight research groups, which are discussed in more detail here. As an indication of the quality of the data, the measurements on hexamethyldisiloxane, which were analyzed comprehensively by Thol et al.,<sup>12</sup> were considered where groups published data for both fluids. The lower-temperature region ( $T < 460$  K) was investigated by several different authors, whereas the higher-temperature region was studied only by Young.<sup>42</sup> In the lower-temperature region, the present equation of state was fitted to the vapor pressure data of Flaningam<sup>49</sup> (AAD = 0.76%). He reported these measurements in the same publication as the results for hexamethyldisiloxane. Deviations of 0.5% with respect to the equation for hexamethyldisiloxane were assessed to be reasonable.<sup>12</sup> The experimental uncertainty in the octamethylcyclotetrasiloxane data is assumed to be higher than that in the case of hexamethyldisiloxane because of inferior sample purity (octamethylcyclotetrasiloxane, 99.49%; hexamethyldisiloxane, 99.9%), and the deviations of less than 1.1% with respect to the present equation of state seem to be realistic. In this way, the data of Marsh<sup>50,51</sup> and Tomlins and Marsh<sup>52</sup> scatter around the equation within 1.5% for  $T < 360$  K. Since the vapor pressure of Tomlins and Marsh<sup>52</sup> was measured more recently than the data of Marsh,<sup>50,51</sup> this point was taken as a reference and was reproduced within 0.063% by the present equation of state. Fitting the data of Flaningam<sup>49</sup> in a more accurate way would cause higher deviations in the low-temperature regime. In the temperature region where Flaningam's data<sup>49</sup> are located, recent measurements by Abbas et al.<sup>48</sup> (AAD = 4.79%) are available. In analogy to the results for hexamethyldisiloxane, these data significantly differ from those obtained using the present equation and other literature data. Between 370 and 451 K, a systematic offset of approximately  $-2.7\%$  can be observed. The deviations increase for lower temperatures, which is most probably caused by inappropriate handling of the apparatus (cf. Thol et al.<sup>12</sup>). The data of Stull<sup>53</sup> (AAD = 8.60%) are part of a comprehensive literature study summarizing vapor pressure data for more than 1200 organic substances. In that publication,<sup>53</sup> Hunter et al.,<sup>54</sup> Patnode and Wilcock,<sup>55</sup> and Wilcock<sup>34</sup> are cited to be the primary sources for octamethylcyclotetrasiloxane. In the original publications,<sup>34,54,55</sup> all of them investigated siloxane polymers, and they reported only the normal boiling points of the participating monomers. Since Stull's data<sup>53</sup> exhibit unreasonably high deviations of up to 20%, they were not considered any further. Korchemskaya et al.<sup>56</sup> (AAD = 2.44%) primarily investigated binary mixtures containing siloxanes and reported uncertainties only in terms of composition. No information is given for the uncertainty of the pure fluid data. Except for two state points at  $T \geq 444$  K, the measured vapor pressures are systematically lower than values calculated from

the present equation of state. However, they are still reproduced within 1.1%, which is the same accuracy as for the data of Flaningam.<sup>49</sup>

Lopatkina et al.<sup>57</sup> (AAD = 20.4%) measured the vapor pressure between 304 and 369 K by means of a static method with a quartz Bourdon gauge as a reference. The temperature was controlled with copper–constantan thermocouples. No information on the experimental uncertainties is given. The deviations with respect to the present equation of state increase from 5% to 38% with decreasing temperature. The measurements of Marsh,<sup>50,51</sup> which are located in the same temperature range, indicate that the data of Lopatkina et al.<sup>57</sup> are most likely not correct. Therefore, these data were not considered during the development of the present equation of state. Recent measurements by Palczewska-Tulińska and Oracz<sup>58</sup> were carried out with a comparative ebulliometer applying *n*-dodecane as the reference substance. The specified temperature uncertainty,  $\Delta T = 0.005$  K, and pressure uncertainty,  $\Delta p = 6.7$  Pa, yield a combined expanded uncertainty of 0.03% to 3.8% ( $k = 2$ ). The measurements of Palczewska-Tulińska et al.<sup>59</sup> on cyclohexane were made with the same technique and are reproduced by the equation of Zhou et al.<sup>41</sup> with an AAD of 0.13%. Nonetheless, the measurements on octamethylcyclotetrasiloxane exhibit deviations of up to 8.5% with respect to the present equation of state and other measurements in this region. Data at lower temperatures deviate significantly less than data at high temperatures. These findings agree with their own correlation results presented in ref 58. Similar behavior was found for hexamethylcyclotrisiloxane, and even worse deviations were observed for decamethylcyclopentasiloxane. Therefore, the data were not considered during the development of the present equation of state. Finally, measurements by Osthoff and Grubb<sup>60</sup> (AAD = 1.69%) are available over the same temperature range as the data sets discussed above. The sample purity was estimated to be 99.82% on the basis of a melting point measurement. For the vapor pressure measurements, a modified isoteniscope reported by Smith and Menzies,<sup>61</sup> which is categorized as a static method, was used. No information is given about the experimental uncertainties. For  $T \geq 350$  K, deviations with respect to the present equation of state amount to 1%, which is in accordance with the data of Flaningam<sup>49</sup> and Korchemskaya et al.<sup>56</sup> For lower temperatures ( $T < 350$  K), the percentage deviations increase. This is most likely related to the pressure measurement, which was carried out with a mercury manometer. Since the vapor pressure of octamethylcyclotetrasiloxane is low, only a small column of mercury was observed (1.49 mmHg at the lowest temperature). The percentage deviations from the equation yield systematic absolute deviations of approximately  $-0.3$  mmHg. These differences can easily occur with visual detection of the meniscus. Furthermore, the vapor pressure at the lowest temperature agrees well with the data point of Tomlins and Marsh.<sup>52</sup> Thus, the increasing deviations of the data with respect to the present equation are assumed to be a problem in the data. In their publication, Osthoff and Grubb<sup>60</sup> introduced a correction for all of the vapor pressure data at  $T \geq 353$  K by adding the vapor pressure of mercury. No further explanation for why they did not do the same correction for the low-temperature data was provided. The only experimental data set available for  $T > 460$  K was published by Young<sup>42</sup> (AAD = 0.67%). A modified glass apparatus developed by Ambrose and Townsend<sup>62</sup> was used, and the specified uncertainty amounts to 0.5% to 2%. Except for two data points with deviations of

2.5%, all of their data scatter around the present equation of state within the given experimental uncertainty. On the basis of these results, the expected uncertainty in the vapor pressure data calculated with the present equation of state is 1.5% for  $T \leq 460$  K and 2% for higher temperatures.

The representations of the saturated liquid and vapor densities are depicted in Figure 7, and the average absolute

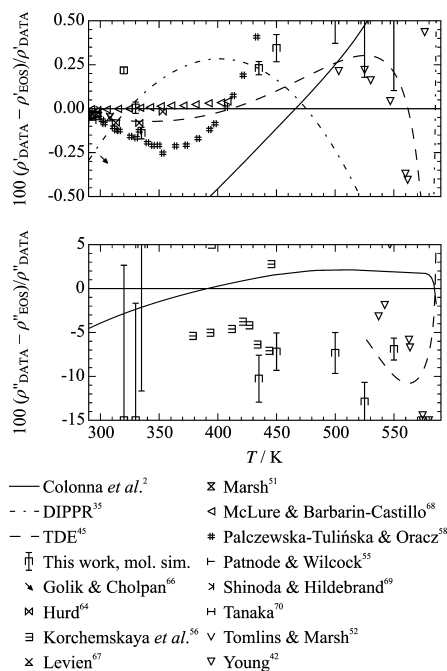


**Figure 7.** Relative deviations of the saturated density data from the present equation of state: (top), saturated liquid density; and (bottom), saturated vapor density.

relative deviations are listed in Table 4. Similar to the vapor pressure, the lower-temperature region was measured by different authors, whereas the high-temperature region was investigated only by Young.<sup>42</sup> The most comprehensive data sets for  $T < 440$  K were published by McLure and Barbarin-Castillo<sup>68</sup> (AAD = 0.015%) and Palczewska-Tulińska and Oracz<sup>58</sup> (AAD = 0.15%). Palczewska-Tulińska and Oracz<sup>58</sup> used an Anton Paar densimeter, and the specified uncertainties yield a combined expanded uncertainty of approximately 0.006% in density. Most probably, the stated uncertainty of the density measurement ( $\Delta\rho = 0.01 \text{ kg}\cdot\text{m}^{-3}$ ) is too optimistic, so the real uncertainty is assumed to be higher. In comparison with the present equation of state and other literature data, the data of Palczewska-Tulińska and Oracz<sup>58</sup> differ by up to 0.4%. The deviations exhibit a parabolic shape, which is the same behavior as for their measurements of decamethylcyclopentasiloxane.<sup>58</sup> This leads to the assumption that either the apparatus or the measurement procedure was incorrect. Thus, the remaining data set of McLure and Barbarin-Castillo<sup>68</sup> was used to develop the present equation of state. The sample was purified up to 99.5%, and the measurements were carried out with a magnetically levitated Archimedian sinker.<sup>68</sup> The specified uncertainties result in a combined expanded uncertainty ( $k = 2$ ) of 0.014%. For  $T < 360$  K, the present equation of state reproduces the data within their experimental

uncertainty. With increasing temperature, the deviations increase to 0.4%. This is caused by the high-temperature data of Young<sup>42</sup> (AAD = 0.26%), which scatter around the present equation of state within 0.45%. For each measurement, Young<sup>42</sup> filled a glass tube with liquid octamethylcyclotetrasiloxane, evacuated the tube while freezing the sample, and sealed the tube after degassing. Subsequently, each tube was heated slowly, and the temperature at which the tube was completely filled with liquid was detected. The mass of the sample was determined from the weight of the sealed tube including the sample and the weight of the opened tube that was purged of the sample. The volume was determined by measuring the weight of the full and cut tube in distilled water. These three steps involve several different sources of uncertainties, which are not discussed in the paper. However, Young<sup>42</sup> states an uncertainty of 0.1% to 0.3%. Since it is not completely clear how the experimental uncertainty was determined, the deviations of 0.45% with respect to the present equation of state seem to be acceptable.

Finally, data sets comprising only few state points were used to verify the representation of the saturated liquid density. The data of Korchemskaya et al.,<sup>56</sup> Levien,<sup>67</sup> Marsh,<sup>51</sup> Patnode and Wilcock,<sup>55</sup> Tanaka,<sup>70</sup> Tomlins and Marsh,<sup>52</sup> and Waterman et al.<sup>32</sup> are reproduced with an AAD < 0.07%. Therefore, the uncertainty in the saturated liquid density data calculated with the present equation of state is assessed to be 0.1% for  $T < 360$  K and 0.5% for higher temperatures.

The saturated vapor density was investigated by Korchemskaya et al.<sup>56</sup> (AAD = 6.19%) and Young<sup>42</sup> (AAD = 11.5%). Korchemskaya et al.<sup>56</sup> focused on mixture measurements and did not provide information on the experimental uncertainties. Young<sup>42</sup> applied the same measuring procedure as for the saturated liquid density. The disappearance of the corresponding phases was detected visually, thus leading to higher uncertainties. For the liquid phase, a remaining gas bubble does not falsify the result too much, whereas a remaining liquid droplet in the gas phase has a large impact. Therefore, the deviations presented in Figure 7 are not surprising. For a reliable uncertainty statement, a more appropriate measuring technique has to be used to carry out new measurements.

**4.3. Homogeneous Region.** Comparisons to homogeneous density data are shown in Figure 8 and summarized in Table 5. At the bottom of Figure 8, relative deviations of experimental data from the present equation of state at atmospheric pressure are illustrated. The temperature range is restricted to 290 to 355 K. Except for the data reported by Schuh and Fischer,<sup>71</sup> all of the data deviate by less than 0.1% from the present equation. The measurements of Marsh<sup>50</sup> (AAD = 0.058%) and Herring and Winnick<sup>72</sup> (AAD = 0.056%) agree perfectly with each other and are reproduced within 0.06%. An even better representation of the data was not possible without compromising the saturated liquid density.

Since the measured saturated liquid density data cover the entire vapor–liquid equilibrium temperature range and the homogeneous density measurements are restricted to a range of 65 K, the saturated liquid density data were primarily correlated. However, reproducing the homogeneous density data at atmospheric pressure in a more accurate way is most probably not required because the deviations can be explained by the claimed experimental uncertainty of the data. The correlation of the high-pressure data was more challenging because contradictory trends were observed (cf. Figure 8, top). Wappman et al.<sup>78</sup> utilized a sample with a purity of 99% for

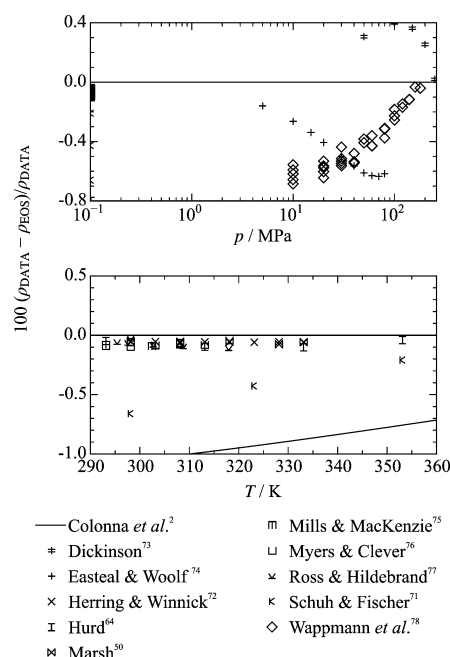


**Figure 8.** Representation of the homogeneous density of octamethylcyclotetrasiloxane. (top) Relative deviations of all available experimental homogeneous density data from the present equation of state. (bottom) Relative deviations of the homogeneous density data from the present equation of state at atmospheric pressure.

their measurements. The employed piston cylinder densimeter was described in detail by Wappmann *et al.*<sup>82</sup> The accuracy of the measurements was assessed with test measurements on methanol, which reproduced Goodwin's data<sup>83</sup> within 0.2%. Without any further explanation, Wappmann *et al.*<sup>78</sup> stated an experimental uncertainty of 0.4% for octamethylcyclotetrasiloxane. The second data set of Eastal and Woolf<sup>74</sup> shows an opposite trend with respect to the present equation of state. They investigated only one isotherm (323.15 K), which was not measured by Wappmann *et al.*<sup>78</sup> Therefore, it is not possible to compare these results directly with each other. Eastal and Woolf<sup>74</sup> measured their density data with an even lower sample purity than Wappmann *et al.*<sup>78</sup> (98%) in a bellows volumeter.<sup>84</sup> The specified uncertainties yield a combined expanded uncertainty of 0.06%, a value that is highly unrealistic considering the sample purity. It was not possible to represent any of the data within the claimed accuracy. Thus, test correlations were established to find out the cause of these problems. Fitting both data sets at the same time was not possible because of their contrary courses. Therefore, only one data set was correlated at a time, and it was still not possible to reach a satisfactory result. Hence, the interaction of different properties was investigated. Next to the homogeneous density data, the speed of sound measurements from this work and the isobaric heat capacity data of Abbas *et al.*<sup>48</sup> recently became available. Both data sets were considered in the fitting procedure. Since the heat capacity measurements by Abbas *et al.*<sup>48</sup> were reasonable for hexamethyldisiloxane,<sup>12</sup> it is unlikely that these data cause problems. As expected, no observable improvement of the density data could be reached when these data were deleted from the fit. Therefore, the present speed of

**Table 5.** Average Absolute Relative Deviations of the Experimental Data in the Homogeneous State from the Present Equation of State<sup>a</sup>

authors	no. of data points	$T$ range/K	$p$ range/MPa	AAD/%						
				gas	liq.	crit. reg.	LD	MD	HD	overall
$p$ $v$ $T$ Data										
Dickinson <sup>73,b</sup>	5	323.19	50.0–251	–	0.27	–	–	–	–	0.27
Eastal and Woolf <sup>74</sup>	10	323.19	5.0–81	–	0.47	–	–	–	–	0.47
Herring and Winnick <sup>72</sup>	8	298–334	0.101325	–	0.056	–	–	–	–	0.056
Hurd <sup>64</sup>	5	273–354	0.101325	–	3.74	–	–	–	–	3.74
Marsh <sup>50</sup>	5	293–334	0.101325	–	0.058	–	–	–	–	0.058
Mills and MacKenzie <sup>75</sup>	2	293–303	0.101325	–	0.087	–	–	–	–	0.087
Myers and Clever <sup>76</sup>	6	293–319	0.101325	–	0.078	–	–	–	–	0.078
Ross and Hildebrand <sup>77</sup>	6	295–318	0.101325	–	0.071	–	–	–	–	0.071
Wappmann et al. <sup>78*</sup>	36	308–427	10.0–181	–	0.42	–	–	–	–	0.42
Schuh and Fischer <sup>71</sup>	3	298–354	0.101325	–	0.43	–	–	–	–	0.43
Speed of sound $w$										
this work*	54	299–550	0.1–27	–	0.12	–	–	–	0.15	0.14
Golik and Cholpan <sup>79</sup>	1	303.13	0.101325	–	0.15	–	–	–	–	0.15
Nannan et al. <sup>47*</sup>	53	450–496	0.0–1.0	0.17	–	–	–	–	–	0.17
Niepmann and Schmidt <sup>80</sup>	117	299–450	2.6–61	–	–	–	–	–	0.47	0.47
Waterman et al. <sup>32</sup>	1	293.14	0.101325	–	0.026	–	–	–	–	0.026
Isobaric heat capacity $c_p$										
Abbas et al. <sup>48*</sup>	28	298–434	0.101325	–	0.18	–	–	–	–	0.18
Marsh and Tomlins <sup>81</sup>	1	298.14	0.101325	–	1.81	–	–	–	–	1.81
Mekhtiev and Karasharli <sup>43</sup>	1	298.14	0.101325	–	2.73	–	–	–	–	2.73
Palczewska-Tulińska and Oracz <sup>58</sup>	24	293–426	$p_v$	–	2.05	–	–	–	–	2.05

<sup>a</sup>All temperatures were adapted to the ITS-90 scale. Data sets that were applied to the fit are marked with an asterisk. For the *pVT* data in the critical region, pressure deviations are considered instead of density deviations. Critical region:  $0.98 \leq T/T_c \leq 1.1$  and  $0.7 \leq \rho/\rho_c \leq 1.4$ . Supercritical region: LD,  $\rho/\rho_c \leq 0.6$ ; MD,  $0.6 \leq \rho/\rho_c \leq 1.5$ ; HD,  $\rho/\rho_c > 1.5$ . <sup>b</sup>Calculated.



sound measurements were tested. After these data were deleted from the fit, the requested result was achieved. The homogeneous density data of Wappmann et al.<sup>78</sup> could be fitted significantly better than before. Hence, the two data sets are not consistent with each other. This effect can be explained on the basis of the definition of the speed of sound:

$$w^2 = \frac{c_p}{c_v} \left( \frac{\partial p}{\partial \rho} \right)_T \quad (11)$$

One of the two data sets comprises a wrong course of the compressibility, so the other data set cannot be correlated within the required accuracy. Since no independent data set for the homogeneous density that could support the data of Wappmann et al.<sup>78</sup> is available, the present speed of sound measurements were chosen to be primarily fitted.

For the present speed of sound measurements, the same apparatus as for hexamethyldisiloxane,<sup>12</sup> ammonia,<sup>14</sup> oxygen,<sup>85</sup> and hydrogen chloride was utilized. In general, the data could be reproduced within 0.5% by the corresponding equations of state, so this accuracy was also the aim in the case of octamethylcyclotetrasiloxane. Figure 9 shows that the speed of sound data are represented by the present equation of state within the specified experimental uncertainties. Additional

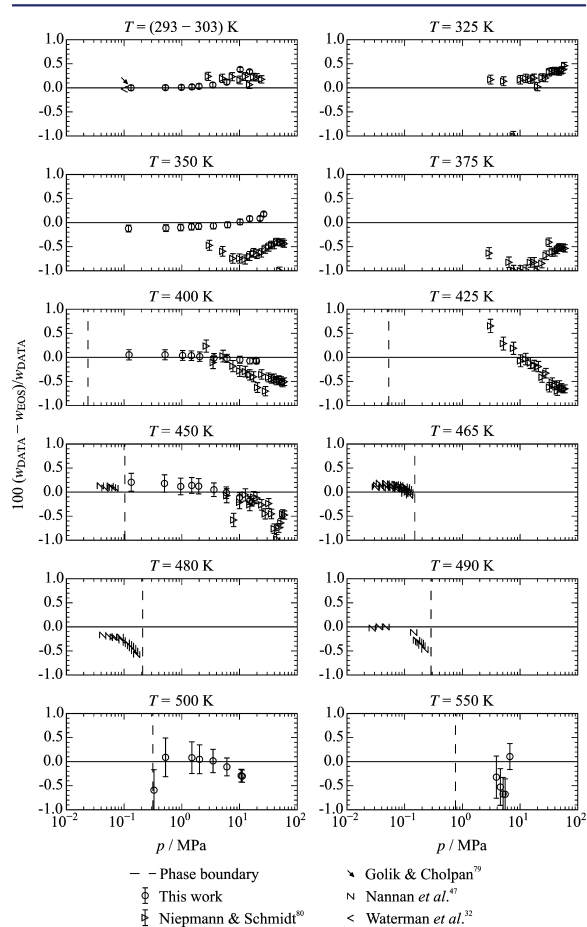


Figure 9. Relative deviations of experimental speed of sound data from the present equation of state.

speed of sound data located in the liquid phase were published by Niepmann and Schmidt.<sup>80</sup> They employed an accurate pulse-echo method, which was also used in the present work. The reported uncertainty of  $0.8 \text{ m}\cdot\text{s}^{-1}$  corresponds to a relative uncertainty of 0.1%. However, with the same apparatus they measured speed of sound data for benzene, which scatter around the corresponding equation of state of Thol et al.<sup>40</sup> within 0.4%. Therefore, relative deviations of approximately 0.5%, except for the isotherms at 350 and 375 K, are plausible. With these deviations in the liquid speed of sound data, a relative deviation of the density data of Wappmann et al.<sup>78</sup> from the present equation of 0.65% could be achieved. The data of Eastal and Woolf<sup>74</sup> deviate in the same range. Finally, the speed of sound data in the gaseous state of Nannan et al.,<sup>47</sup> which were already discussed in section 4.1, are shown in Figure 9. The relative deviation is 0.16% for  $T \leq 465 \text{ K}$  and increases to 0.45% for higher temperatures. The large deviations occur close to the saturated vapor phase, whereas the deviations decrease in the limit of low pressure. This trend proves that the ideal gas contribution  $\alpha^o$  of the present equation of state is reasonable.

To summarize the discussion above, the homogeneous density can be calculated from the present equation of state within 0.1% at atmospheric pressure and 0.7% for higher pressures. Vapor phase measurements are not available, so no statement on the accuracy of the present equation of state can be made. Speed of sound data in the liquid and vapor states can be calculated from the present equation with an expected uncertainty of 0.5%

In Figure 10, comparisons of available experimental isobaric heat capacity data with the present equation of state are

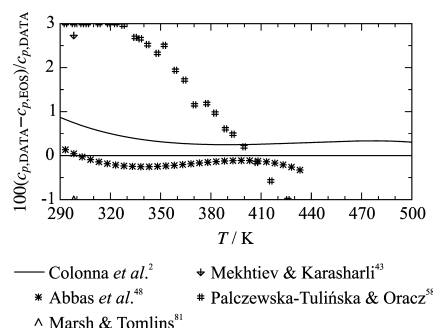


Figure 10. Relative deviations of experimental isobaric heat capacity data from the present equation of state.

depicted. The two main data sets were published by Abbas et al.<sup>48</sup> (AAD = 0.18%) and Palczewska-Tulińska and Oracz<sup>58</sup> (AAD = 2.05%) and exhibit a contrary course. In accordance with the previous discussion on vapor pressure and saturated liquid density, significant deviations of the heat capacity measurements in the saturated liquid state of all substances investigated in the publication of Palczewska-Tulińska and Oracz<sup>58</sup> with respect to other literature data can be observed. Therefore, these data were not considered during the development of the present equation of state. The isobaric heat capacity data for hexamethyldisiloxane measured at atmospheric pressure by Abbas et al.<sup>48</sup> showed good agreement with the corresponding equation and other literature data (cf. Thol et al.<sup>12</sup>). Therefore, the data for octamethylcyclotetrasiloxane were assumed to be reliable and were used in the fit. A

relative deviation of 0.3% could be achieved, which is clearly within the experimental uncertainty of 1% as stated by the authors. Thus, the expected uncertainty in the heat capacity data in the saturated liquid state calculated with the present equation of state is 1% according to the experimental uncertainty of the data of Abbas *et al.*<sup>48</sup>

#### 4.4. Representation of Molecular Simulation Data.

After the present equation of state was fitted exclusively to experimental measurements, molecular simulation data up to 1200 K and 520 MPa were added to the data set used in the fit in order to extend the range of validity. Since the molecular structure of octamethylcyclotetrasiloxane is chemically not stable at such high temperatures and pressures, this extension of the validity range has to be perceived as an extrapolation beyond the stable region. The simulated vapor pressure data differ by up to 10% for  $T \geq 435$  K. Lower temperatures are reproduced even worse. However, the simulated saturated liquid density data differ from the present equation of state within the stated accuracy of 1%, except for the highest temperature ( $T = 550$  K). The accuracy of the molecular model in the homogeneous region was assessed by simulations of the density and speed of sound at selected state points (cf. Figure 11). The homogeneous density is represented within 0.7%,

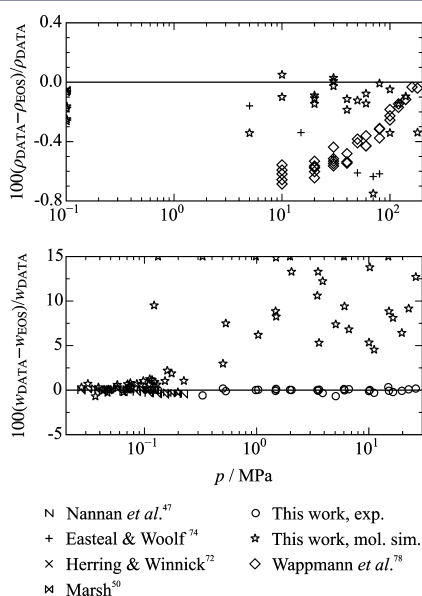


**Figure 11.** Relative deviations of selected (top) density and (bottom) speed of sound data from the present equation of state. At the same  $p$ - $T$  state points, molecular simulation data are presented to verify the accuracy of the present molecular model.

which is the expected uncertainty of the present equation of state. The simulated  $pvT$  data support the course of the density calculated from the equation of state, which resulted primarily from a fit to saturated liquid density and speed of sound data rather than from a fit to the available  $pvT$  data. The gaseous speed of sound data differ by 1.3% from the present equation of state, whereas the liquid state points deviate by up to 15%. The differences become evident from the following equation:

$$\frac{w^2}{RT} = 1 + 2A_{01}^r + A_{02}^r - \frac{(1 + A_{01}^r - A_{11}^r)^2}{A_{20}^o + A_{20}^r} \quad (12)$$

The speed of sound is composed of several residual Helmholtz energy derivatives and the ideal gas heat capacity, which is considered by  $A_{20}^o$ . Because only the residual parts are simulated, the ideal gas part is taken from the present equation of state. In the gas phase, the ideal gas contribution is the dominant part, which compensates for uncertainties of the simulated residual Helmholtz energy derivatives. The liquid state is prevailed by the residual contribution, so the impact of the ideal gas contribution is smaller, which leads to higher deviations.

Comparisons of the simulated residual Helmholtz energy derivatives from the present equation of state along selected isotherms are shown in Figure 12. A comprehensive overview

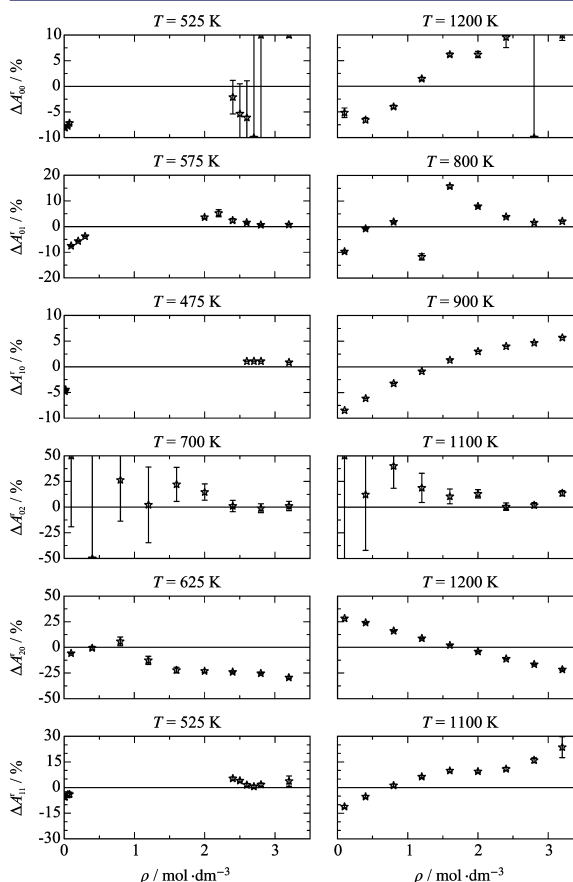


**Figure 12.** Relative deviations of simulated residual Helmholtz energy derivatives data from the present equation of state along selected isotherms. The relative deviations are calculated according to eq 8.

of all of the available simulation data is given in the [Supporting Information](#). Deviations of the residual Helmholtz energy,  $A_{00}^r$ , and the first derivative with respect to the temperature,  $A_{10}^r$ , amount to 10%. Except for a few data points at the zero crossing or at very low densities, the same accuracy can be observed for the first derivative with respect to the density,  $A_{01}^r$ . The first mixed derivative with respect to the temperature and density,  $A_{11}^r$ , is reproduced by the present equation of state within 15%. The second derivative with respect to the temperature,  $A_{20}^r$ , and the second derivative with respect to the density,  $A_{02}^r$ , differ by approximately 30%. For a better

classification of these deviations, the Helmholtz energy derivatives were transferred to common thermodynamic properties (pressure, heat capacities, and speed of sound) according to eq 12 and the following equations:

$$\frac{p}{\rho RT} = 1 + A_{01}^r \quad (13)$$

$$\frac{c_v}{R} = -(A_{20}^o + A_{20}^r) \quad (14)$$

$$\frac{c_p}{R} = -(A_{20}^o + A_{20}^r) + \frac{(1 + A_{01}^r - A_{11}^r)^2}{1 + 2A_{01}^r + A_{02}^r} \quad (15)$$

For the calculation of caloric properties, the ideal contribution of the present equation of state was adopted.

Figure 13 depicts the relative deviations of common thermodynamic properties from the present equation of state.

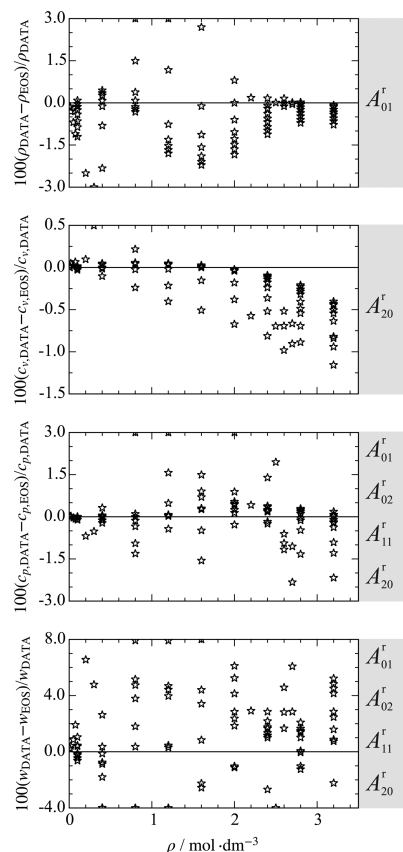


**Figure 13.** Comparison of the present equation of state with thermodynamic properties obtained from molecular simulation data generated in this work. The involved residual Helmholtz energy derivatives are indicated in the gray boxes.

The homogeneous density and the isobaric heat capacity are represented within 2%. The isochoric heat capacity differs from the present equation of state by 1% and for  $\rho \leq 1.2 \text{ mol·dm}^{-3}$  the difference is even 0.5%. Finally, the speed of sound data are reproduced within 7%. Of course, for a reliable statement of the accuracy of the present equation of state, experimental measurements in this range are required.

## 5. PHYSICAL AND EXTRAPOLATION BEHAVIOR

In addition to the accurate representation of experimental and simulation data, the correct physical and extrapolation behavior in regions where no data are available is an essential aspect in the development of equations of state. Especially for the application to mixture models, a reasonable course of thermodynamic properties has to be ensured. Typical diagrams that are analyzed during fitting procedures are shown in Figure 14. On the top left, the vapor–liquid equilibrium is presented in a  $T$ – $\rho$  diagram. The isobars are smooth, and the rectilinear diameter is a straight line up to the critical point. The critical isobar exhibits a saddle point at the critical point. The hypothetical saturated liquid phase of the isochoric heat capacity (top right) increases with decreasing temperature, and the two saturated phases merge at a maximum at the critical point. This diagram is also an indication of the qualitatively correct behavior of the speed of sound, which was observed during the fit as well. In the center of Figure 14, the phase identification parameter<sup>86</sup> is presented as a function of density (left) and temperature (right). Both plots show a correct course as described by Thol et al.<sup>87</sup> and Lemmon et al.<sup>88</sup> No unreasonable changes in slope or curvature were observed. The virial coefficients  $B$ ,  $C$ , and  $D$  are presented at the bottom left. No unreasonable features can be observed for the second virial coefficient. The third virial coefficient exhibits a slight shift of its maximum to lower temperatures than the critical one. It should most likely be located closer to the critical temperature, similar to that of hexamethyldisiloxane.<sup>12</sup> Since this is not a fully investigated phenomenon and it has not been experimentally proven that the maximum occurs approximately at the critical temperature, this slight shift was accepted here. The same holds for the fourth virial coefficient. The qualitative behavior is in very good agreement with the previously analyzed equations of state for Lennard-Jones fluids<sup>87,89</sup> and hexamethyldisiloxane.<sup>12</sup> However, the maximum is also not located at the critical temperature but shifted to a lower value. A noticeable feature can be observed in the further course of the fourth virial coefficient. For Lennard-Jones fluids,<sup>87,89</sup> a second maximum was predicted from the equations of state and statistical mechanics independently. The same effect is observed here for octamethylcyclotetrasiloxane. Without any information on experimental virial coefficients, the present equation of state exhibits this second maximum. Finally, characteristic ideal curves<sup>90</sup> are presented on the bottom right in Figure 14. No unreasonable courses can be observed, ensuring correct extrapolation behavior to very high temperatures, pressures, and densities.

## 6. CONCLUSION

The present equation of state for octamethylcyclotetrasiloxane is written in terms of the reduced Helmholtz energy, so any equilibrium thermodynamic property can be obtained from its derivatives with respect to temperature and density. The ideal contribution contains three Planck–Einstein terms, whereas the residual contribution consists of five polynomial, five exponential, and five Gaussian bell-shaped terms. The range of validity based on experimental data is for temperatures from the triple point to 590 K at pressures up to 180 MPa. The expected uncertainty in the vapor pressure data from the present equation of state is 1.5% for  $T \leq 460 \text{ K}$  and 2% for higher temperatures. Saturated liquid density data are accurate within 0.1% for  $T < 360 \text{ K}$  and 0.5% for higher temperatures.



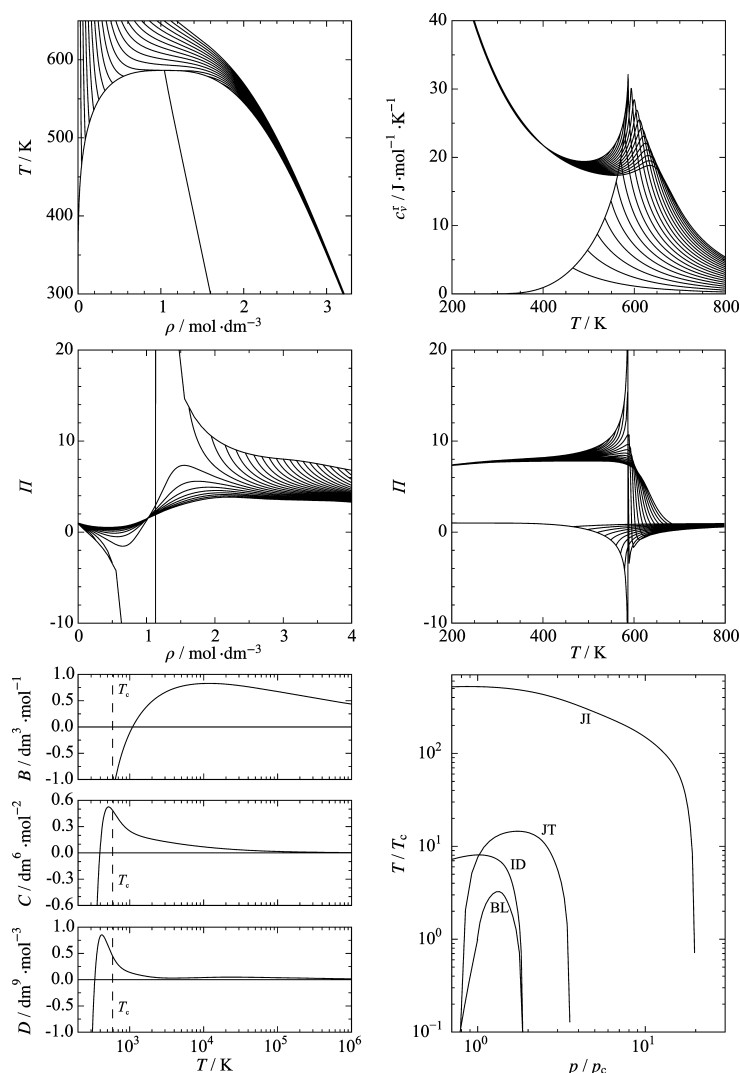


**Figure 14.** Plots of some thermodynamic properties of octamethylcyclotetrasiloxane: (top left) vapor–liquid equilibrium curves together with the rectilinear diameter; (top right) residual isochoric heat capacity; (center) phase identification parameter as a function of (left) temperature and (right) density; (bottom left) second, third, and fourth virial coefficients; (bottom right) characteristic ideal curves<sup>90</sup> (ID, ideal curve; BL, Boyle curve; JT, Joule–Thomson inversion curve; JI, Joule inversion curve).

The uncertainty in the homogeneous density at atmospheric pressure is assessed to be 0.1%. The available experimental data in the high-pressure region are not consistent with the present speed of sound measurements, so the equation is assumed to be accurate within only 0.7%. The expected uncertainty in the speed of sound data calculated with the present equation of state is 0.5%. Next to the analysis of experimental measurements, the extrapolation behavior was investigated comprehensively and found to be reasonable. Finally, the range of validity was extended to  $T_{\max} = 1200$  K and  $p_{\max} = 520$  MPa by means of molecular simulation data. Since no experimental measurements are available in this region, no uncertainty statements can be made, but indications based on the simulation data are given.

Reference values to verify computer implementation are given in the [Supporting Information](#). Additionally, ancillary equations were developed for the vapor pressure as well as

saturated liquid and vapor densities, which can be used for initial calculations of starting values of iterative phase calculations. The corresponding equations and parameters are also listed in the [Supporting Information](#). Furthermore, a parameter file for the software packages TREND<sup>91</sup> and REFPROP<sup>92</sup> and a file containing C++ source code are provided.

## ■ ASSOCIATED CONTENT

### ● Supporting Information

The Supporting Information is available free of charge on the [ACS Publications website](#) at DOI: [10.1021/acs.jced.6b00261](https://doi.org/10.1021/acs.jced.6b00261).

Ancillary equations for vapor pressure, saturated liquid density, and saturated vapor density; simulation details; Tables S6–S9 and S11–S13; and Figures S15–S24 (PDF)

Table S10 (XLSX)

Parameter file for the software packages TREND<sup>91</sup> and REFPROP<sup>92</sup> (TXT)

C++ source code for the calculation of selected thermodynamic properties at homogeneous states (TXT)

Explanatory notes (TXT)

## AUTHOR INFORMATION

### Corresponding Author

\*E-mail: [jadran.vrabec@uni-paderborn.de](mailto:jadran.vrabec@uni-paderborn.de).

### Notes

The authors declare no competing financial interest.

## REFERENCES

- (1) EPA National Center for Biotechnology Information. PubChem Compound Database, CID = 11169. <https://pubchem.ncbi.nlm.nih.gov/compound/11169> (accessed Nov 3, 2015).
- (2) Colonna, P.; Nannan, N. R.; Guardone, A.; Lemmon, E. W. Multiparameter Equations of State for Selected Siloxanes. *Fluid Phase Equilib.* **2006**, *244*, 193–211.
- (3) Span, R.; Wagner, W. Equations of State for Technical Applications. I. Simultaneously Optimized Functional Forms for Nonpolar and Polar Fluids. *Int. J. Thermophys.* **2003**, *24*, 1–39.
- (4) Span, R.; Wagner, W. Equations of State for Technical Applications. II. Results for Nonpolar Fluids. *Int. J. Thermophys.* **2003**, *24*, 41–109.
- (5) Span, R.; Wagner, W. Equations of State for Technical Applications. III. Results for Polar Fluids. *Int. J. Thermophys.* **2003**, *24*, 111–162.
- (6) Thol, M.; Piazza, L.; Span, R. A New Functional Form for Equations of State for Some Weakly Associating Fluids. *Int. J. Thermophys.* **2014**, *35*, 783–811.
- (7) Sun, L.; Ely, J. F. A Corresponding States Model for Generalized Engineering Equations of State. *Int. J. Thermophys.* **2005**, *26*, 705–728.
- (8) Alexandrov, I.; Gerasimov, A.; Grigor'ev, B. Generalized Fundamental Equation of State for the Normal Alkanes (C5–C50). *Int. J. Thermophys.* **2013**, *34*, 1865–1905.
- (9) Grigor'ev, B.; Alexandrov, I.; Gerasimov, A. Generalized Equation of State for the Cyclic Hydrocarbons over a Temperature Range from the Triple Point to 700 K with Pressures up to 100 MPa. *Fluid Phase Equilib.* **2016**, *418*, 15–36.
- (10) Rutkai, G.; Thol, M.; Lustig, R.; Span, R.; Vrabec, J. Communication: Fundamental Equation of State Correlation with Hybrid Data Sets. *J. Chem. Phys.* **2013**, *139*, 041102.
- (11) Thol, M.; Rutkai, G.; Köster, A.; Kortmann, M.; Span, R.; Vrabec, J. Fundamental Equation of State for Ethylene Oxide Based on a Hybrid Dataset. *Chem. Eng. Sci.* **2015**, *121*, 87–99; **2015**, *134*, 887–890.
- (12) Thol, M.; Dubberke, F.; Rutkai, G.; Windmann, T.; Köster, A.; Span, R.; Vrabec, J. Fundamental Equation of State Correlation for Hexamethyldisiloxane Based on Experimental and Molecular Simulation Data. *Fluid Phase Equilib.* **2016**, *418*, 133–151.
- (13) Lin, C.-W.; Trusler, J. P. M. The Speed of Sound and Derived Thermodynamic Properties of Pure Water at Temperatures Between (253 and 473) K and at Pressures up to 400 MPa. *J. Chem. Phys.* **2012**, *136*, 094511.
- (14) Dubberke, F. H.; Rasche, D. B.; Baumhögger, E.; Vrabec, J. Apparatus for the Measurement of the Speed of Sound of Ammonia up to High Temperatures and Pressures. *Rev. Sci. Instrum.* **2014**, *85*, 084901.
- (15) Ball, S. J.; Trusler, J. P. M. Speed of Sound of n-Hexane and n-Hexadecane at Temperatures Between 298 and 373 K and Pressures up to 100 MPa. *Int. J. Thermophys.* **2001**, *22*, 427–443.
- (16) Dubberke, F. H.; Baumhögger, E.; Vrabec, J. Burst Design and Signal Processing for the Speed of Sound Measurement of Fluids with the Pulse-echo Technique. *Rev. Sci. Instrum.* **2015**, *86*, 054903.
- (17) Gedanitz, H.; Davila, M. J.; Baumhögger, E.; Span, R. An Apparatus for the Determination of Speeds of Sound in Fluids. *J. Chem. Thermodyn.* **2010**, *42*, 478–483.
- (18) Harris, G. R. Review of Transient Field Theory for a Baffled Planar Piston. *J. Acoust. Soc. Am.* **1981**, *70*, 10–20.
- (19) Meier, K. The Pulse-Echo Method for High Precision Measurements of the Speed of Sound in Fluids. Habilitation Thesis, University of the Federal Armed Forces, Hamburg, Germany, 2006.
- (20) Glass, C. W.; Reiser, S.; Rutkai, G.; Deublein, S.; Köster, A.; Guevara-Carrion, G.; Wafai, A.; Horsch, M.; Bernreuther, M.; Windmann, T.; Hasse, H.; Vrabec, J. ms2: A Molecular Simulation Tool for Thermodynamic Properties, New Version Release. *Comput. Phys. Commun.* **2014**, *185*, 3302–3306.
- (21) Lustig, R. Direct Molecular NVT Simulation of the Isobaric Heat Capacity, Speed of Sound and Joule–Thomson Coefficient. *Mol. Simul.* **2011**, *37*, 457–465.
- (22) Lustig, R. Statistical Analogues for Fundamental Equation of State Derivatives. *Mol. Phys.* **2012**, *110*, 3041–3052.
- (23) Mohr, P. J.; Taylor, B. N.; Newell, D. B. CODATA Recommended Values of the Fundamental Physical Constants: 2010. *Rev. Mod. Phys.* **2012**, *84*, 1527–1605.
- (24) Span, R. *Multiparameter Equations of State: An Accurate Source of Thermodynamic Property Data*; Springer: Berlin, 2000.
- (25) Schmidt, M. W.; Baldrige, K. K.; Boatz, J. A.; Elbert, S. T.; Gordon, M. S.; Jensen, J. H.; Koseki, S.; Matsunaga, N.; Nguyen, K. A.; Su, S.; Windus, T. L.; Dupuis, M.; Montgomery, J. A. General Atomic and Molecular Electronic Structure System. *J. Comput. Chem.* **1993**, *14*, 1347–1363.
- (26) Merker, T.; Vrabec, J.; Hasse, H. Engineering Molecular Models: Efficient Parameterization Procedure and Cyclohexanol as Case Study. *Soft Mater.* **2012**, *10*, 3–24.
- (27) Matsubara, H.; Pichierr, F.; Kurihara, K. Design of a Versatile Force Field for the Large-Scale Molecular Simulation of Solid and Liquid OMCTS. *J. Chem. Theory Comput.* **2010**, *6*, 1334–1340.
- (28) Xu, R.-G.; Leng, Y. Solvation Force Simulations in Atomic Force Microscopy. *J. Chem. Phys.* **2014**, *140*, 214702.
- (29) Guevara-Carrion, G.; Nieto-Draghi, C.; Vrabec, J.; Hasse, H. Prediction of Transport Properties by Molecular Simulation: Methanol and Ethanol and their Mixture. *J. Phys. Chem. B* **2008**, *112*, 16664–16674.
- (30) Abbas, R.; Ihmels, E. C.; Enders, S.; Gmehling, J. Measurement of Transport Properties for Selected Siloxanes and their Mixtures Used as Working Fluids for Organic Rankine Cycles. *Ind. Eng. Chem. Res.* **2011**, *50*, 8756–8763.
- (31) Marsh, K. N. Mutual Diffusion in Octamethylcyclotetrasiloxane Mixtures. *Trans. Faraday Soc.* **1968**, *64*, 894.
- (32) Waterman, H. I.; Van Herwijnen, W. E. R.; Den Hartog, H. W. Statistical-Graphical Survey of Series of Linear and Cyclic Dimethylsiloxanes. *J. Appl. Chem.* **1958**, *8*, 625–631.
- (33) Reuther, H. Über Silikone XIV: Über das Viskosität-Temperatur-Verhalten von Silikonölen unter besonderer Berücksichtigung des Bereichs unter 0°C. *Chem. Technol.* **1953**, *5*, 268.
- (34) Wilcock, D. F. Vapor Pressure-Viscosity Relations in Methylpolysiloxanes. *J. Am. Chem. Soc.* **1946**, *68*, 691–696.
- (35) Rowley, R. L.; Wilding, W. V.; Oscarson, J.; Yang, Y.; Zuendel, N.; Daubert, T.; Danner, R. *DIPPR Data Compilation of Pure Chemical Properties*; Taylor & Francis: New York, 2004.
- (36) Haar, L.; Gallagher, J. S.; Kell, G. S. The Anatomy of the Thermodynamic Surface of Water: The Formulation and Comparisons with Data. In *Proceedings of the 8th Symposium on Thermophysical Properties*; Sengers, J. V., Ed.; ASME, New York, 1982; pp 298–302.
- (37) Setzmann, U.; Wagner, W. A New Equation of State and Tables of Thermodynamic Properties for Methane Covering the Range from the Melting Line to 625 K at Pressures up to 100 MPa. *J. Phys. Chem. Ref. Data* **1991**, *20*, 1061–1155.
- (38) Lemmon, E. W.; Jacobsen, R. T. A New Functional Form and New Fitting Techniques for Equations of State with Application to Pentafluoroethane (HFC-125). *J. Phys. Chem. Ref. Data* **2005**, *34*, 69–108.

- (39) Lemmon, E. W.; McLinden, M. O.; Wagner, W. Thermodynamic Properties of Propane. III. A Reference Equation of State for Temperatures from the Melting Line to 650 K and Pressures up to 1000 MPa. *J. Chem. Eng. Data* **2009**, *54*, 3141–3180.
- (40) Thol, M.; Lemmon, E. W.; Span, R. Equation of State for Benzene for Temperatures from the Melting Line up to 725 K with Pressures up to 500 MPa. *High Temp. - High Press.* **2012**, *41*, 81–97.
- (41) Zhou, Y.; Liu, J.; Penoncello, S. G.; Lemmon, E. W. An Equation of State for the Thermodynamic Properties of Cyclohexane. *J. Phys. Chem. Ref. Data* **2014**, *43*, 043105.
- (42) Young, C. L. Equilibrium Properties of Octamethylcyclotetrasiloxane near its Critical Point and Applicability of the Principle of Corresponding States. *J. Chem. Thermodyn.* **1972**, *4*, 65–75.
- (43) Mekhtiev, S. A.; Karasharli, K. A. Analysis of the Results of Thermodynamic Studies of a Series of Organosilicon Compounds. *Azerb. Khim. Zhur.* **1981**, *5*, 85–88.
- (44) Wieser, M. E.; Berglund, M. Atomic Weights of the Elements 2007 (IUPAC Technical Report). *Pure Appl. Chem.* **2009**, *81*, 2131–2156.
- (45) Frenkel, M.; Chirico, R. D.; Diky, V.; Kroenlein, K.; Muzny, C. D.; Kazakov, A. F.; Magge, J. W.; Abdulgatov, I. M.; Lemmon, E. W. NIST Standard Reference Database 103b: NIST Thermo-Data-Engine—Pure Components, Binary Mixtures, Reactions, version 8.0; Standard Reference Data Program; National Institute of Standards and Technology: Gaithersburg, MD, 2013.
- (46) Harrison, B. K.; Seaton, W. H. Solution to Missing Group Problem for Estimation of Ideal Gas Heat Capacities. *Ind. Eng. Chem. Res.* **1988**, *27*, 1536–1540.
- (47) Nannan, N. R.; Colonna, P.; Tracy, C. M.; Rowley, R. L.; Hurly, J. J. Ideal-Gas Heat Capacities of Dimethylsiloxanes from Speed-of-Sound Measurements and ab initio Calculations. *Fluid Phase Equilib.* **2007**, *257*, 102–113.
- (48) Abbas, R.; Schedemann, A.; Ihmels, C.; Enders, S.; Gmehling, J. Measurement of Thermophysical Pure Component Properties for a Few Siloxanes Used as Working Fluids for Organic Rankine Cycles. *Ind. Eng. Chem. Res.* **2011**, *50*, 9748–9757.
- (49) Flaningam, O. L. Vapor Pressures of Poly(dimethylsiloxane) Oligomers. *J. Chem. Eng. Data* **1986**, *31*, 266–272.
- (50) Marsh, K. N. Thermodynamics of Octamethylcyclotetrasiloxane Mixtures. *Trans. Faraday Soc.* **1968**, *64*, 883–893.
- (51) Marsh, K. N. Enthalpies of Mixing and Excess Gibbs Free Energies of Mixtures of Octamethylcyclotetrasiloxane+Cyclopentane at 291.15, 298.15, and 308.15 K. *J. Chem. Thermodyn.* **1970**, *2*, 359–365.
- (52) Tomlins, R. P.; Marsh, K. N. A New Apparatus for Measuring the Vapour Pressure of Liquid Mixtures. Excess Gibbs Free Energy of Octamethylcyclotetrasiloxane + Cyclohexane at 308.15 K. *J. Chem. Thermodyn.* **1976**, *8*, 1185–1194.
- (53) Stull, D. R. Vapor Pressure of Pure Substances: Organic Compounds. *Ind. Eng. Chem.* **1947**, *39*, 517–540.
- (54) Hunter, M. J.; Hyde, J. F.; Warrick, E. L.; Fletcher, H. J. Organosilicon Polymers. The Cyclic Dimethyl Siloxanes. *J. Am. Chem. Soc.* **1946**, *68*, 667–672.
- (55) Patnode, W.; Wilcock, D. F. Methylpolysiloxanes. *J. Am. Chem. Soc.* **1946**, *68*, 358–363.
- (56) Korchemskaya, K. M.; Shakhparonov, M. I.; Lelchuk, S. L.; Korablina, T. P.; Baburina, I. I.; Voronina, R. D. Pressure and Density of the Vapors of Binary Solutions of Chlorosilanes: IV. Silane. *Izv. Vyssh. Uchebn. Zaved., Khim. Khim. Tekhnol.* **1962**, *5*, 65–69.
- (57) Lopatkina, I. L.; Kucherskaya, L. A.; Kuznetsova, A. G.; Shaurov, Y. K. Vapour Pressure of Cyclosiloxanes. *Russ. J. Phys. Chem.* **1973**, *47*, 1626–1627.
- (58) Palczewska-Tulińska, M.; Oracz, P. Selected Physicochemical Properties of Hexamethylcyclotrisiloxane, Octamethylcyclotetrasiloxane, and Decamethylcyclopentasiloxane. *J. Chem. Eng. Data* **2005**, *50*, 1711–1719.
- (59) Palczewska-Tulińska, M.; Choliński, J.; Szafranski, A.; Wyrzykowska-Stankiewicz, D. Maximum-Likelihood Evaluation of Antoine Equation Constants for Vapor Pressures of Morpholine, n-Heptane, Cyclohexane and Methylcyclohexane. *Fluid Phase Equilib.* **1983**, *11*, 233–243.
- (60) Osthoff, R. C.; Grubb, W. T. Physical Properties of Organosilicon Compounds: III. Thermodynamic Properties of Octamethylcyclotetrasiloxane. *J. Am. Chem. Soc.* **1954**, *76*, 399–401.
- (61) Smith, A.; Menzies, A. W. C. Studies in Vapor Pressure. III. A Static Method for Determining the Vapor Pressures of Solids and Liquids. *J. Am. Chem. Soc.* **1910**, *32*, 1412–1434.
- (62) Ambrose, D.; Townsend, R. 681. Thermodynamic Properties of Organic Oxygen Compounds. Part IX. The Critical Properties and Vapour Pressures, above Five Atmospheres, of Six Aliphatic Alcohols. *J. Chem. Soc.* **1963**, *37*, 3614–3625.
- (63) Flaningam, O. L.; Williams, D. E. Octamethylcyclotetrasiloxane Azeotropes. U.S. Patent 5,492,647, May 8, 1995.
- (64) Hurd, C. B. Studies on Siloxanes: I. The Specific Volume and Viscosity in Relation to Temperature and Constitution. *J. Am. Chem. Soc.* **1946**, *68*, 364–370.
- (65) Weast, R. C.; Astle, M. J. *CRC Handbook of Data on Organic Compounds*; CRC Press: Boca Raton, FL, 1985.
- (66) Golik, O. Z.; Cholpan, P. P. *Ukr. Fiz. Zh.* **1960**, *5*, 242–251.
- (67) Levien, B. J. Excess Volumes of Mixtures of Globular Molecules. II. *J. Chem. Thermodyn.* **1973**, *5*, 679–687.
- (68) McLure, I. A.; Barbarin-Castillo, J. M. Orthobaric Liquid Densities for Octamethylcyclotetrasiloxane, Decamethylcyclopentasiloxane, Dimethicone 20, and a Cyclic Poly(dimethylsiloxane). *J. Chem. Eng. Data* **1994**, *39*, 12–13.
- (69) Shinoda, K.; Hildebrand, J. H. Compressibilities and Isochores of (C<sub>3</sub>F<sub>7</sub>COOCH<sub>2</sub>)<sub>4</sub>C, c-Si<sub>4</sub>O<sub>4</sub>(CH<sub>3</sub>)<sub>8</sub>, n-C<sub>5</sub>H<sub>12</sub>, n-C<sub>8</sub>H<sub>18</sub>, 2,2,4-C<sub>5</sub>H<sub>9</sub>(CH<sub>3</sub>)<sub>3</sub>, c-C<sub>5</sub>H<sub>10</sub>, c-C<sub>6</sub>H<sub>12</sub>, c-C<sub>6</sub>H<sub>11</sub>CH<sub>3</sub>, C<sub>6</sub>H<sub>5</sub>CH<sub>3</sub>, p-C<sub>6</sub>H<sub>4</sub>(CH<sub>3</sub>)<sub>2</sub>, s-C<sub>6</sub>H<sub>3</sub>(CH<sub>3</sub>)<sub>3</sub>, CH<sub>2</sub>Cl<sub>2</sub>. *J. Phys. Chem.* **1961**, *65*, 183.
- (70) Tanaka, T. Heats of Formation of Lower Members of Dimethyl- and Methylisopropoxy-cyclopolsiloxanes. *Bull. Chem. Soc. Jpn.* **1960**, *33*, 282–286.
- (71) Schuh, H.-H.; Fischer, H. The Kinetics of the Bimolecular Self-Reaction of t-Butyl Radicals in Solution: I. Termination Rates. *Helv. Chim. Acta* **1978**, *61*, 2130–2164.
- (72) Herring, W.; Winnick, J. Excess Volumes of Octamethylcyclotetrasiloxane + Carbon Tetrachloride. *J. Chem. Thermodyn.* **1974**, *6*, 957–964.
- (73) Dickinson, E. Pressure Dependence of Shear Viscosity in n-Alkane + Dimethylsiloxane Mixtures. *J. Phys. Chem.* **1977**, *81*, 2108–2113.
- (74) Easteal, A. J.; Woolf, L. A. Self-diffusion and Volumetric Measurements for Octamethylcyclotetrasiloxane under Pressure at 323 K. *J. Chem. Soc., Faraday Trans. 1* **1984**, *80*, 549–551.
- (75) Mills, A. P.; MacKenzie, C. A. The Application of Bond Parachors to Organosilicon Chemistry. *J. Am. Chem. Soc.* **1954**, *76*, 2672–2673.
- (76) Myers, R. S.; Clever, H. L. Surface Tension of Octamethylcyclotetrasiloxane and Hexamethyldisilazane and their Solutions with Carbon Tetrachloride and n-Hexadecane. *J. Chem. Eng. Data* **1969**, *14*, 161–164.
- (77) Ross, M.; Hildebrand, J. H. Energy Volume Relations of Octamethylcyclotetrasiloxane and its Mixtures with Carbon Tetrachloride. *J. Phys. Chem.* **1963**, *67*, 1301–1303.
- (78) Wappmann, S. J.; Tarassov, I. N.; Lüdemann, H.-D. Densities of Octamethylcyclotetrasiloxane + Methane and 2,2-Dimethylpropane + Methane from 10 to 200 MPa and from 294 to 433 K. *J. Chem. Eng. Data* **1996**, *41*, 84–88.
- (79) Golik, A.; Cholpan, P. F. Investigation of Speed of Sound for Some Polysiloxanes. *Akust. Zh.* **1961**, *7*, 33–39.
- (80) Niepmann, R.; Schmidt, U. Speeds of Sound in Liquid Octamethylcyclotetrasiloxane. *J. Chem. Thermodyn.* **1980**, *12*, 1133–1137.
- (81) Marsh, K. N.; Tomlins, R. P. Excess Enthalpies of Octamethylcyclotetrasiloxane Mixtures. *Trans. Faraday Soc.* **1970**, *66*, 783–790.

- (82) Wappmann, S. J.; Karger, N.; Lüdemann, H.-D. pVT Data of Liquid 1-, 2- and 3-Pentanol from 10 to 200 MPa and from 233 to 433 K. *J. Chem. Eng. Data* **1995**, *40*, 233–236.
- (83) Goodwin, R. D. Methanol Thermodynamic Properties from 176 to 673 K at Pressures to 700 bar. *J. Phys. Chem. Ref. Data* **1987**, *16*, 799–892.
- (84) Back, P. J.; Eastal, A. J.; Hurle, R. L.; Woolf, L. A. High-precision Measurements with a Bellows Volumometer. *J. Phys. E: Sci. Instrum.* **1982**, *15*, 360–363.
- (85) Dubberke, F. H.; Riepold, M.; Baumhögger, E.; Vrabec, J. Speed of Sound of Oxygen in Supercritical States up to 500 K and 100 MPa. *J. Chem. Eng. Data* **2016**, *61*, 1632–1636.
- (86) Venkatarathnam, G.; Oellrich, L. Identification of the Phase of a Fluid Using Partial Derivatives of Pressure, Volume, and Temperature without Reference to Saturation Properties: Applications in Phase Equilibria Calculations. *Fluid Phase Equilib.* **2011**, *301*, 225–233.
- (87) Thol, M.; Rutkai, G.; Köster, A.; Span, R.; Vrabec, J.; Lustig, R. Equation of State for the Lennard-Jones Fluid. *J. Phys. Chem. Ref. Data* **2016**, *45*, 023101.
- (88) Lemmon, E. W.; Overhoff, U.; McLinden, M. O.; Wagner, W. Equation of State for Propylene. *J. Phys. Chem. Ref. Data* **2016**, to be published.
- (89) Thol, M.; Rutkai, G.; Span, R.; Vrabec, J.; Lustig, R. Equation of State for the Lennard-Jones Truncated and Shifted Model Fluid. *Int. J. Thermophys.* **2015**, *36*, 25–43.
- (90) Span, R.; Wagner, W. On the Extrapolation Behavior of Empirical Equations of State. *Int. J. Thermophys.* **1997**, *18*, 1415–1443.
- (91) Span, R.; Eckermann, T.; Herrig, S.; Hielscher, S.; Thol, M. *TREND: Thermodynamic Reference and Engineering Data*, version 2.0; Lehrstuhl für Thermodynamik, Ruhr-Universität Bochum: Bochum, Germany, 2015 (private communication).
- (92) Lemmon, E. W.; Huber, M. L.; McLinden, M. O. *NIST Standard Reference Database 23: Reference Fluid Thermodynamic and Transport Properties—REFPROP*, version 9.1; National Institute of Standards and Technology: Gaithersburg, MD, 2013.

### 3.12 Automatized determination of fundamental equations of state based on molecular simulations in the cloud

A. Köster, T. Jiang, G. Rutkai, C. W. Glass, J. Vrabec, *Fluid Phase Equilibria* 425:84-92, 2016.

DOI: [doi.org/10.1016/j.fluid.2016.05.002](https://doi.org/10.1016/j.fluid.2016.05.002)

Nachgedruckt mit Erlaubnis von Elsevier (Copyright 2016).

In dieser Arbeit wurde die Möglichkeit der vollautomatischen Erstellung von helmholtzexpliziten Zustandsgleichungen auf der Basis von molekularen Simulationen untersucht. Dazu wurde eine Cloud-Umgebung mit grafischer Nutzeroberfläche entwickelt, über die es möglich ist, Simulations- und Zustandsgleichungsparameter zu spezifizieren und die Simulationen sowie die Anpassung der Zustandsgleichung zu starten. Für die Anpassung dieser vollautomatisch generierten Zustandsgleichungen werden die partiellen Ableitungen der Helmholtzenergie aus dem Lustig-Formalismus [Lus11, Lus12] verwendet. Durch die Cloud-Umgebung besteht die Möglichkeit der automatischen Verteilung der Simulationen auf verschiedene Rechner.

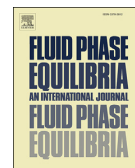
Arbeiten an dieser Publikation wurden vom Autor der vorliegenden Dissertation koordiniert, der gleichzeitig die molekularen Simulationen durchgeführt, die grafischen Nutzeroberflächen entworfen und den zugrundeliegenden Workflow für die automatische Anpassung von Zustandsgleichungen entwickelt hat. Die Ausarbeitung des Manuskripts entstand in Zusammenarbeit von Dr. Gábor Rutkai, Tao Jiang, Dr. Colin W. Glass und des Autors der vorliegenden Dissertation. Die informationstechnische Umsetzung wurde von Tao Jiang und Dr. Colin W. Glass realisiert. Die Überarbeitung des Manuskripts wurde unter Mithilfe von Prof. Jadran Vrabec und Dr. Colin W. Glass durchgeführt. Der Autor wurde während des gesamten Prozesses von Prof. Jadran Vrabec betreut.





Contents lists available at ScienceDirect

## Fluid Phase Equilibria

journal homepage: [www.elsevier.com/locate/fluid](http://www.elsevier.com/locate/fluid)

# Automatized determination of fundamental equations of state based on molecular simulations in the cloud

Andreas Köster <sup>a</sup>, Tao Jiang <sup>b</sup>, Gábor Rutkai <sup>a</sup>, Colin W. Glass <sup>b</sup>, Jadran Vrabec <sup>a,\*</sup><sup>a</sup> Lehrstuhl für Thermodynamik und Energietechnik, Universität Paderborn, Warburger Str. 100, 33098 Paderborn, Germany<sup>b</sup> Höchstleistungsrechenzentrum Stuttgart (HLRS), Universität Stuttgart, 70550 Stuttgart, Germany

## ARTICLE INFO

## Article history:

Received 5 January 2016

Received in revised form

29 April 2016

Accepted 5 May 2016

Available online 9 May 2016

## Keywords:

Thermodynamic properties

Fundamental equation of state

Molecular modelling and simulation

Ethylene oxide

Cloud computing

## ABSTRACT

An automatized procedure for the parameterization of fundamental equations of state (EOS) that are explicit in terms of the Helmholtz energy and are based on molecular simulation data is presented. The simulation runs are carried out via a cloud-based framework that combines multiple, distributed computing resources. A user-friendly graphical user interface ensures that minimal knowledge about the background operations is required. In order to exemplify the capabilities of this approach an EOS for ethylene oxide is created and compared to data from the literature.

© 2016 Elsevier B.V. All rights reserved.

## 1. Introduction

Thermodynamic data are essential for the design and optimization of chemical engineering processes. Typically, the chemical industry is relying on experimental investigations to generate such data. Depending on the type of fluid, this undertaking is difficult to conduct or in the case of hazardous substances, e.g. being explosive, toxic or mutagenic, this might even be practically impossible. As an attractive alternative route, molecular modelling and simulation on the basis of classical force fields has been proven to be an adequate method due to the steady developments of the last decades. Along with its powerful predictive capabilities, large sets of thermophysical data can be rapidly produced with considerably less effort than laboratory measurements.

It has recently been shown that molecular simulation data are useful for the construction of empirical fundamental equation of state (EOS) correlations that are explicit in terms of a thermodynamic potential [1–4], which is most often the Helmholtz energy [5]. Thermodynamic potentials are essential building blocks of thermodynamics, because every other time-independent thermodynamic property can be obtained as a combination of their partial

derivatives with respect to their independent variables. Unfortunately, the exact mathematical expression of a thermodynamic potential, with the exception of very simple systems (e.g. ideal gas or some hard-body fluids), is unknown. The construction of an EOS therefore necessarily means that the mathematical form of such a correlation has to be fitted to thermodynamic data. Once the parameterized correlation is available, it provides thermodynamic data in a consistent manner and can be used to inter- and extrapolate between or beyond the underlying data points. More importantly, EOS have the ability to yield all thermodynamic data, and not just the ones considered in their fitting process. Naturally, the more thermodynamically independent properties are considered during the construction of EOS, the better the representation of other properties. Therefore, in order to create such a correlation, a large number of independent thermodynamic data points has to be available. This scenario is the application field for the statistical mechanical formalism proposed by Lustig [6,7]. With this formalism, the derivatives of the Helmholtz energy up to arbitrary order can be obtained at a given state point by a single canonical (NVT) ensemble molecular simulation run [6,7]. This formalism also exists for the entropy derivatives in the microcanonical (NVE) ensemble [6,7]. Since any thermodynamic property is just a combination of these derivatives, this represents the full set of thermodynamically independent data. Due to this improvement on availability, reliable EOS can very efficiently be fitted on the basis of

\* Corresponding author.

E-mail address: [jadran.vrabec@upb.de](mailto:jadran.vrabec@upb.de) (J. Vrabec).

molecular simulation data only.

However, setting up molecular simulation runs and fitting EOS requires considerable manual effort and expertise. Maginn [8] pointed out that molecular simulation has to overcome some barriers in order to become a mainstream tool in chemical engineering. One of these barriers is the time which is necessary to set up and analyze a molecular simulation run compared to its actual runtime. Furthermore, there are few software packages which are able to yield all properties that are important for the chemical industry (e.g. phase equilibria, gas solubility, heat capacity, density, etc.) [8]. Hence, the goal of this work is to automatize and optimize this workflow by combining the molecular simulation tool *ms2* [9] with an EOS fitting algorithm and embedding this into a cloud-based simulation framework which requires minimal knowledge about the background operations, and has a simple graphical user interface (GUI) for creating the necessary input for simulations. In the background, a job manager efficiently allocates the molecular simulation runs to the available high performance computing (HPC) resources. Once the simulation runs are terminated and the results are ready, the empirical EOS correlation is fitted and its parameters are returned, along with the quality of representation of the simulation data. Thus, the development of EOS is essentially becoming an automatic process. In this work, the capabilities of this approach and the resulting EOS are compared for ethylene oxide with experimental data from the literature and with the recently published EOS by Thol et al. [4] for this fluid, that we consider as a reference here.

## 2. Fundamental equation of state correlation

The present EOS correlation is explicit in terms of the Helmholtz energy  $a$ . It is common to separate  $a$  into an ideal contribution  $a^0$  and a residual contribution  $a^r$

$$\alpha(T, \rho) = \frac{a^0(T, \rho) + a^r(T, \rho)}{RT} = \alpha^0(T, \rho) + \alpha^r(T, \rho) \quad (1)$$

$$= \alpha^0(\tau, \delta) + \alpha^r(\tau, \delta),$$

with the reduced inverse temperature  $\tau = T_c/T$ , the reduced density  $\delta = \rho/\rho_c$  and the molar gas constant  $R = 8.3144621 \text{ J mol}^{-1} \text{ K}^{-1}$  [10], where  $T_c$  is the critical temperature and  $\rho_c$  is the critical density. The ideal contribution  $a^0$ , which only depends on the properties of single molecules, can usually be obtained from spectroscopic data or ab initio calculations, whereas the much more demanding residual contribution is the target of molecular simulation because it depends on the interactions between the molecules. The empirical equation that represents the residual contribution to the reduced Helmholtz energy  $\alpha^r$  consists of polynomial and exponential terms

$$\alpha^r(\tau, \delta) = \sum_{k=1}^{N_{\text{pol}}} n_k \tau^{l_k} \delta^{d_k} + \sum_{k=N_{\text{pol}}+1}^{N_{\text{pol}}+N_{\text{exp}}} n_k \tau^{l_k} \delta^{d_k} \exp(-\delta^{l_k}). \quad (2)$$

In general, the simultaneous optimization of coefficients  $n_k$ , exponents  $t_k$ ,  $d_k$ ,  $l_k$  as well as the number and type of polynomial and exponential terms requires expert use of complex non-linear fitting algorithms [5,11]. Assuming that a sufficient amount of thermodynamic data is available, such an effort usually takes months or years, requiring a high level of human intervention and experience. The recently published EOS of Thol et al. [4] for ethylene oxide is such a model, and was therefore chosen as a reference in the present work. In the fitting process of that EOS [4], both experimental and molecular simulation data were used. Nonetheless, such an approach is currently not feasible in an automatized EOS development process. There are, however,

recommendations in the literature for the functional form and the values of the exponents  $t_k$ ,  $d_k$ ,  $l_k$  of correlations that have proven to be a good choice for a large number of fluids. These are for example the 10- and 12-term EOS by Span and Wagner [5,12], the 14-term EOS by Sun and Ely [13] and the modified Benedict-Webb-Rubin (MBWR) EOS [14], which consists of 40 terms when transformed into the Helmholtz energy representation [5]. In this work, the MBWR EOS [14] was chosen to represent the molecular simulation data set. Such generalized EOS have the advantage that, since the exponents  $t_k$ ,  $d_k$ ,  $l_k$  in Eq. (2) are known, the task at hand reduces to the fitting of the coefficients  $n_k$ . This can be done in a fully automatized manner and has a response time of seconds, e.g., with the algorithm for weighted multiproperty fits of Hust and McCarty [15], in which the weight corresponds to the statistical uncertainty of the underlying molecular simulation data. The values of the coefficients  $t_k$ ,  $d_k$ ,  $l_k$  and  $n_k$  for the present EOS can be found in Table 1.

## 3. Software architecture

Due to the volume of calculations in the field of molecular simulation, researchers typically rely on large computing infrastructure. Here, a single molecular simulation run is relatively time intensive and the database required to parameterize an EOS should

**Table 1**

Parameters for the residual part of the reduced Helmholtz energy  $\alpha^r(\tau, \delta)$  according to Eq. (2). Note that only the coefficients  $n_k$  were fitted in the automatized procedure, the exponents  $t_k$ ,  $d_k$ ,  $l_k$  were taken from the literature [14].

$k$	$n_k$	$t_k$	$d_k$	$l_k$
1	-0.444761941	0	1	0
2	4.295500322	0.5	1	0
3	-6.304073590	1	1	0
4	2.495663889	2	1	0
5	-1.413871625	3	1	0
6	0.122634301	0	2	0
7	-0.403993247	1	2	0
8	0.953802102	2	2	0
9	3.626258062	3	2	0
10	-0.005286229	0	3	0
11	0.167724139	1	3	0
12	-0.261302669	2	3	0
13	0.037473360	1	4	0
14	-0.148085338	2	5	0
15	-0.112161698	3	5	0
16	0.056427170	2	6	0
17	-0.005390223	2	7	0
18	0.010228306	3	7	0
19	-0.001370416	3	8	0
20	-15.487760440	3	0	0
21	-0.079331908	4	0	0
22	0.006185345	5	0	0
23	15.486057470	3	0	2
24	0.081647538	4	0	2
25	-0.007000321	5	0	2
26	10.769184560	3	2	2
27	1.108403574	4	2	2
28	-0.210854465	5	2	2
29	3.440671002	3	4	2
30	0.841327903	4	4	2
31	-0.256828769	5	4	2
32	0.416506137	3	6	2
33	0.492487787	4	6	2
34	-0.007594133	5	6	2
35	0.123791118	3	8	2
36	0.027697626	4	8	2
37	-0.042799502	5	8	2
38	-0.005719867	3	10	2
39	0.022433309	4	10	2
40	0.002604667	5	10	2



contain results from a large number of independent simulation runs at different state points that cover a large part of the fluid region. Thus, the total computational effort is extensive. However, besides the scalability of an individual simulation run, multiple instances for the different state points can be executed in an embarrassingly parallel fashion. Therefore, the simulation can be scaled both in horizontal and vertical direction, i.e. with respect to number of instances and parallel execution of a single instance.

A highly accurate calculation of thermodynamic properties at a given state point with *ms2* currently requires approximately 20 h on 32 cores. For one EOS, between 100 and 1'000 state points need to be evaluated. Thus, even with exclusive access to a small compute cluster, the calculation can take months. At the same time, filling a HPC machine with relatively small computing jobs is not viable because these machines are intended for large scale jobs. Typically, a limited number of small jobs is welcomed, as this facilitates charging HPC machines to capacity. Therefore, distributing the work load across multiple machines is the most sensible approach, cf. Fig. 1.

To enable the execution of such a large scale simulation workflow, a significant amount of heterogeneous compute resources needs to be allocated dynamically. Here, the simulation workflow was concurrently deployed across multiple HPC systems on a cloud infrastructure. This cloud-based molecular simulation framework is aware of the available resources, initiates the simulations automatically and adapts dynamically to the actual execution time of individual simulation runs. A web browser interface allows for straightforward deployment from a regular workstation. The user is guided through the simulation setup with explanations, requiring minimal expertise.

Besides integrating the simulation software *ms2*, the framework introduces an additional user-controlled cloud environment, offering personalized and isolated front-ends with more flexibility in comparison to traditional HPC login nodes. Custom images can be deployed, root access be granted and additional services (e.g. MySQL, license server) as well as infrastructures (virtual machine internal networks, persistent/shared storage, external firewalls,

etc.) can be operated directly. Another advantage is that users can submit their jobs to different HPC systems through a single application programming interface (API), since the ff-Middleware layer provides an abstraction of the actual batch-system. The present system architecture introduces a three-layer structure, i.e. web user interface, web application/service and calculation layer, cf. Fig. 2.

**Web User Interface:** The web-based GUI runs as a part of the web browser on e.g. a desktop computer using advanced HTML5 and JavaScript techniques in order to provide a dynamic user interface, which allows users to configure, execute, monitor and view the results of the molecular simulation instances running in the cloud.

**Job Manager:** On the middle layer, a software component called *ms2* Job Manager was designed to provide a set of services, implementing a Service Oriented Architecture (SOA), which is exploited both from internal and external components and allows for better scalability, maintainability and availability. The provided services allow to:

- Prepare and upload/download input/output files to/from the HPC systems in the background (Data Manager)
- Submit the simulation jobs to the portable batch system (PBS) queue on HPC systems (Execution Manager)
- Monitor the job execution (Job Monitor)
- Store the history data in terms of simulation configurations, input/output data, provenance and tracking information (MySQL database)

Thus, users can perform complex simulation workflows on distributed computing resources by simply clicking a few buttons. Therefore, many of the obstacles that currently confound the delivery, accessibility and usability of traditional, non-service-oriented simulation applications are avoided.

#### 4. Workflow

The procedure of the cloud-based EOS creation is briefly described in the following. In a first step, the molecular force field model and the state points are specified, cf. Fig. 3. This can be done by defining a grid or by clicking into the temperature-density plane. It is important to distribute the state points relatively evenly, covering the entire homogeneous fluid region of interest. In a preceding publication [2], it was shown that at least 100 state points should be specified for that purpose. Although vapor-liquid equilibrium (VLE) data are generally employed in EOS fitting, they are not necessarily required here if the homogeneous region is very well sampled. Additionally, some simulation settings, like the number of simulation steps and the number of compute nodes, have to be supplied. When the start button is activated, the calculations are distributed to the available resources and the status of each simulation is indicated by the color of the particular state point (grey: pending, yellow: queued, blue: running, green: successfully terminated).

When the simulations are completed, the fitting GUI can be opened, cf. Fig. 4. In addition to some basic options, like type of EOS or number of iterations, some fluid specific settings, e.g. a rough estimate of the fluid's critical point for EOS fitting, have to be specified. If the critical point is not known, it is important to initially start fitting with an isotherm which is likely to be higher than the critical temperature. Otherwise, the isotherm could contain state points in the vapor-liquid two-phase region.

As a result of this procedure, the saturated liquid and saturated vapor density curves are displayed, cf. Fig. 5. It is possible to restart the fitting with adjusted parameters or return to the previous GUI to add further state points.

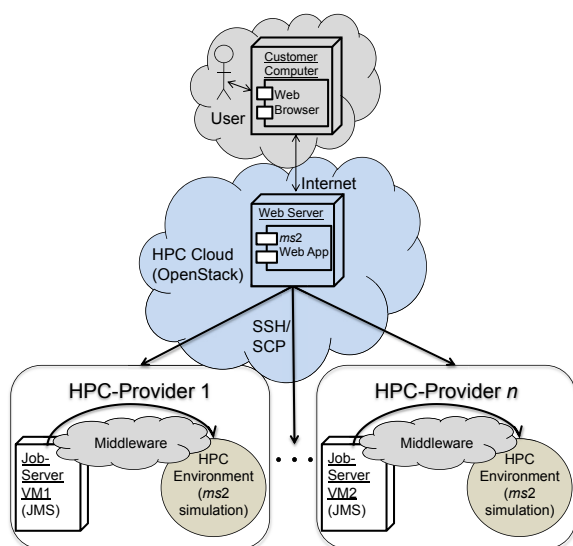


**Fig. 1.** Distributed execution of molecular simulation runs through the High Performance Computing (HPC) cloud. SSH: Secure Shell; SCP: Secure Copy Protocol; JMS: Java Messaging Service.

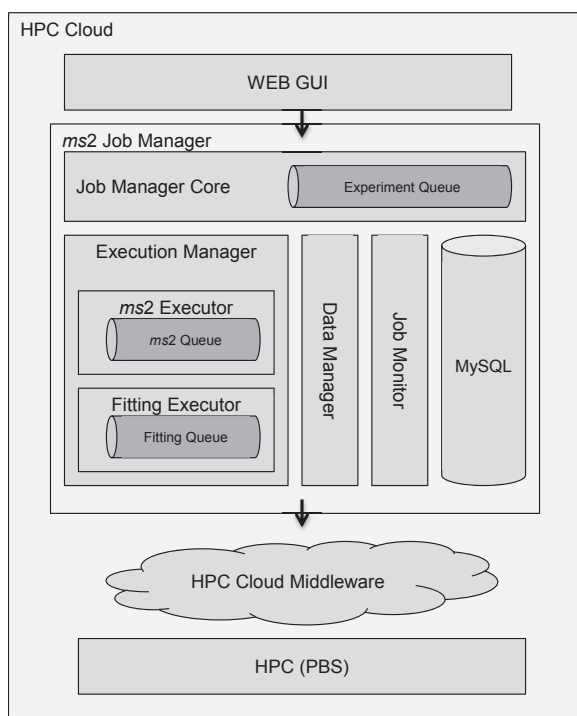


Fig. 2. Components of the ms2 Job Manager.

### 5. Underlying molecular simulation data

The automatized creation of the simulation data set is based on the statistical mechanical formalism proposed by Lustig [6,7] which was used here in its NVT ensemble form. This formalism was designed to yield any residual Helmholtz energy derivative  $A_{mn}^r$  (for  $m > 0$  or  $n > 0$ ) at a given state point, specified by its temperature and density, from a single simulation run per state point. These derivatives are exactly the properties that can be obtained by deriving eq. (2) with respect to its independent variables, i.e. reduced inverse temperature  $\tau$  and reduced density  $\delta$

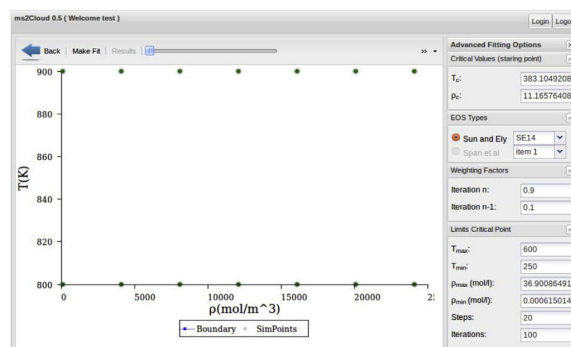


Fig. 4. Web interface of cloud-enabled molecular simulation. Second step: initial settings for EOS fitting.

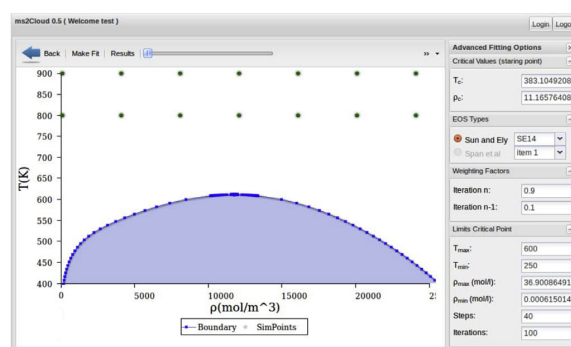


Fig. 5. Web interface of cloud-enabled molecular simulation. Third step: adjustment of the fitting details.

$$A_{mn}^r = \tau^m \delta^n \frac{\partial^{m+n} \alpha^r(\tau, \delta)}{\partial \tau^m \partial \delta^n} = \frac{(1/T)^m \rho^n \partial^{m+n} \alpha^r(1/T, \rho)}{\partial (1/T)^m \partial \rho^n}, \quad (3)$$

because in  $\tau = T_c/T$  and in  $\delta = \rho/\rho_c$  the critical temperature  $T_c$  and the critical density  $\rho_c$  are constants. Consequently, each  $A_{mn}^r$  result from a molecular simulation run represents a new analytical derivative of eq. (2) and stands for a new equation. The complete set of such

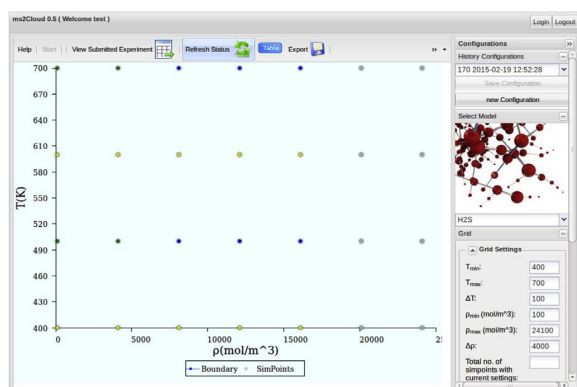


Fig. 3. Web interface of cloud-enabled molecular simulation. First step: specification of simulation conditions.

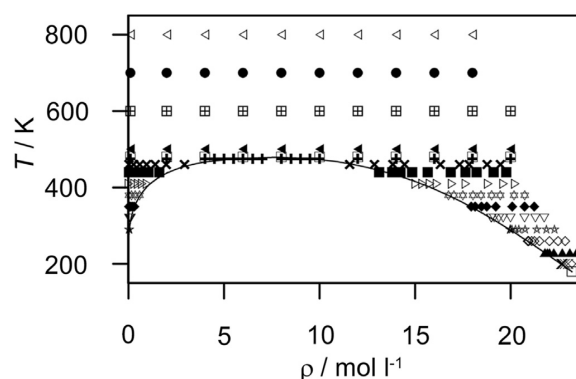


Fig. 6. Distribution of the molecular simulation state points in the homogeneous fluid region. The symbols represent different isotherms and the solid line delimits the vapor-liquid two-phase region.

**Table 2**

Experimental data for ethylene oxide from the literature. The units as given in the sources were converted into SI units and the temperature is given in terms of the international temperature scale of the 1990 standard (ITS-90). Data points calculated from an ancillary equation are marked with an asterisk.

Source	Year	Data points	Temperature range (K)	Pressure range (MPa)
<b>Homogeneous density</b>				
Lide [21] (1)	2005	1	273.15	0.101325
Walters & Smith [22] (1)	1952	81	294–428	0.006–3.448
Overall (3)		82	273–428	0.006–3.448
<b>Vapor pressure</b>				
Calado et al. [23]	1996	1	182.33	0.0001
Chao et al. [24]	1986	1	283.71	0.101325
Coles & Popper [25]	1950	17	273–305	0.067–0.221
Giauque & Gordon [26]	1949	14	223–286	0.004–0.108
Giles & Wilson [27]	2006	2	298–349	0.174–0.767
Gillespie et al. [28]	1985	2	283–299	0.101–0.174
Hess & Tilton [29]	1950	1	293.14	0.1462
Kistiakowsky & Rice [30]	1940	1	283.84	0.101325
Lide [21]	2005	3	283–284	0.100–0.101
Maass & Boomer [31]	1922	21	216–286	0.002–0.110
McDonald et al. [32]	1959	11	239–284	0.012–0.103
Mock & Smith [33]	1950	10	322–423	0.379–3.827
Olson [34]	1977	3	273–324	0.065–0.394
Frenkel et al. [19]*	2013	17	160–469	0.000–7.207
Walters & Smith [22]	1952	12	294–469	0.151–7.192
Overall (3)		99	182–423	0.000–3.827
<b>Saturated liquid density</b>				
Auwers [35]	1918	2	279.20	–
Comelli & Francesconi [36]	1991	11	288–304	–
Comelli & Francesconi [37]	1995	1	298.15	–
Comelli & Francesconi [38]	1996	2	298–314	–
Francesconi & Comelli [39]	1994	1	298.15	–
Francesconi & Comelli [40]	1995	1	298.15	–
Maass & Boomer [31]	1922	16	222–294	–
Olson [34]	1977	3	273–324	–
Perkins [41]	1893	1	280.15	–
Frenkel et al. [19]*	2013	17	160–469	–
Walters & Smith [22]	1952	12	294–469	–
Wurtz [42]	1863	1	273.15	–
Overall (3)		51	222–469	–
<b>Saturated vapor density</b>				
Olson [34]	1977	3	273–324	–
Frenkel et al. [19]*	2013	20	377–469	–
Walters & Smith [22]	1952	12	294–469	–
Overall (3)		15	273–469	–
<b>Speed of sound</b>				
Hurly [43]	2002	334	285–440	0.049–1.020
Overall (3)		334	285–440	0.049–1.020
<b>Enthalpy of vaporization</b>				
Cox & Pilcher [44]	1970	1	298.10	–
Rowley et al. [20]* (2)	2006	30	160–423	–
Giauque & Gordon [26]	1949	1	283.65	–
Lange & Dean [45]	1973	1	283.75	–
Lide [21]	2005	2	283–299	–
Matheson [46]*	1980	5	233–294	–
Reid et al. [47]	1977	1	283.66	–
Timmermans [48]	1965	1	288.10	–
Walters & Smith [22]*	1952	11	294–461	–
Washburn [49]	1926–1933	1	286.10	–
Yaws [50]*	1977	15	173–454	–
Overall (3)		8	283–299	–

(1) One of the data points is located in the two-phase region and was thus neglected.

(2) Calculated from the Clausius-Clapeyron equation.

(3) The overall values do not include any data derived from ancillary equations.

equations forms a system of linear equations that has to be solved for the coefficients  $n_k$ , which can be done with the algorithm of Hust and McCarty [15].

The dataset of the present work was generated using the molecular simulation tool *ms2* [9]. For each sampled state point *ms2* yields every of the following derivatives:  $A_{10}^E, A_{01}^E, A_{20}^E, A_{11}^E, A_{02}^E, A_{30}^E, A_{21}^E, A_{12}^E$ . However, it is not always necessary to include all of them into the EOS fitting in order to have a good representation for all of them. Here, only four derivatives  $A_{10}^E, A_{01}^E, A_{20}^E, A_{11}^E$  at 205 state points in the homogeneous fluid region were used, cf. Fig. 6. Since

all of these derivatives are thermodynamically independent, the database for the EOS fitting process is large (820 independent data points).

A single NVT Monte Carlo simulation [16] was performed at each state point and then sampled according to Lustig's formalism [6,7]. The simulations were based on the molecular interaction model of Eckl et al. [17] that won the Fourth Industrial Fluid Properties Simulation Challenge in 2008 [18]. The model was optimized to experimental vapor pressure, saturated liquid density and heat of vaporization data as functions of temperature, which is a standard

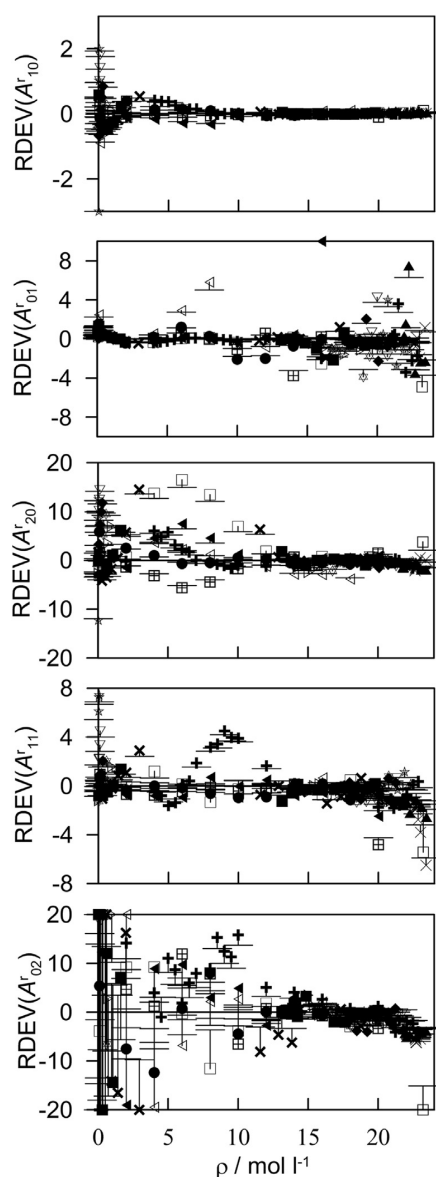


**Fig. 7.** Relative deviation of the residual Helmholtz energy derivatives from molecular simulation to the present fundamental equation of state (baseline). Symbols refer to different isotherms.

practice today. Its parameters and additional simulation details can be found in the appendix.

It should be pointed out that the accuracy of the EOS with respect to experimental data depends in the present context on two factors: (1) The quality of the molecular model that represents ethylene oxide here. (2) The representation quality of the simulation data by the EOS.

The investigation of factor (2) is the subject of this paper. Factor (1), the quality and efficient optimization of molecular models, is crucial when comparing molecular simulation data with experimental results, and this topic is perhaps the most discussed issue in

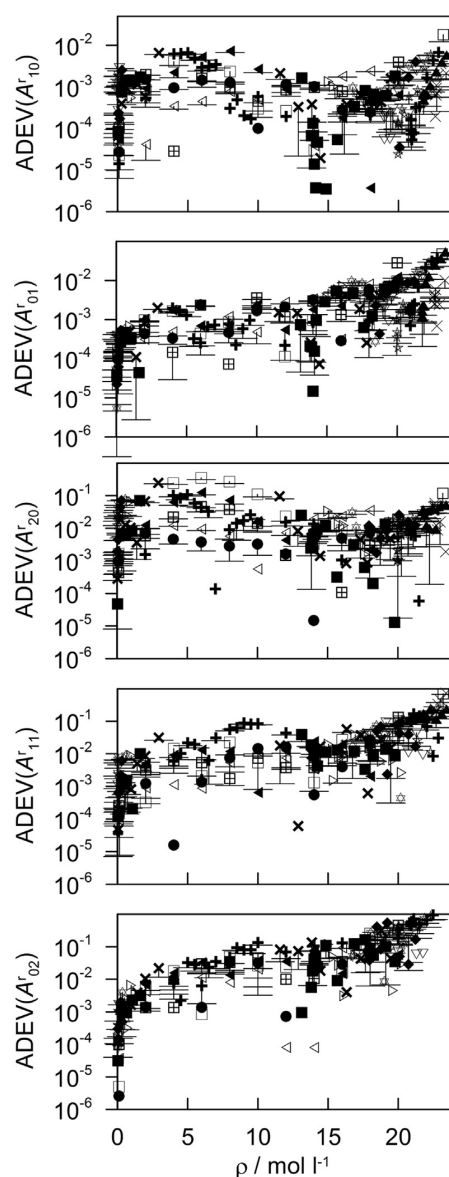


**Fig. 8.** Absolute deviation of the residual Helmholtz energy derivatives from molecular simulation to the present fundamental equation of state. Symbols refer to different isotherms.

the simulation community. It is generally accepted, however, that molecular models can, and often do, perform well for state points, properties and scenarios that were not considered during their optimization. This assumption is supported by our previous findings, in which numerous EOS correlations based on experimental data were compared with  $A_{rm}^r$  simulation results based on molecular models that were optimized exclusively to experimental VLE data [1].

## 6. Results

In order to validate the automatically generated EOS, its representation of the input data from molecular simulation was

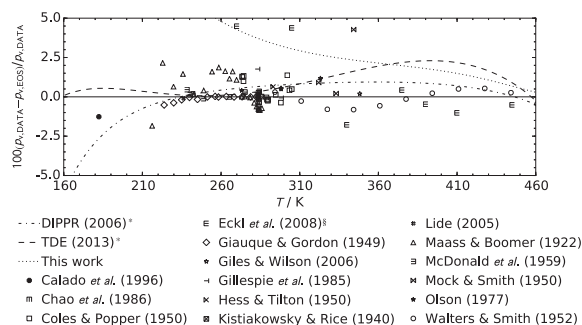


**Fig. 9.** Comparison of the present fundamental equation of state with the one by Thol et al. [4] (baseline) and experimental data for the vapor pressure. The asterisk marks ancillary equations and the paragraph symbol indicates molecular simulation data by Eckl et al. [17]. The statistical uncertainty of the molecular simulation data increases gradually with decreasing temperature (0.6% at 445 K, 1.6% at 340 K and 17% at 270 K).

assessed. Furthermore, it was compared to experimental data from the literature, references can be found in Table 2, and to correlations thereof [19,20]. This comparison was done here on the basis of VLE properties, i.e. vapor pressure, saturated liquid density, saturated vapor density and heat of vaporization.

The agreement of the present EOS with the Helmholtz energy derivatives from molecular simulation can be seen in terms of the relative deviation plots in Fig. 7. The symbols refer to the isotherms introduced in Fig. 6. Fig. 7 shows that for an increasing order of the derivatives the representation of the molecular simulation data gets worse, mostly due to the larger statistical uncertainties of the simulation data.  $A_{10}^r$  and  $A_{01}^r$  agree mainly within  $\pm 2\%$ , whereas  $A_{20}^r$  and  $A_{02}^r$  agree mainly within  $\pm 10\%$ . The mixed Helmholtz energy derivative (i.e.  $A_{11}^r$ ) deviates within  $\pm 4\%$ . Deviation data for  $A_{30}^r$ ,  $A_{21}^r$ ,  $A_{12}^r$  are not shown, since their statistical uncertainties are rather high compared to the other derivatives. Therefore, the EOS always meets  $A_{30}^r$ ,  $A_{21}^r$ ,  $A_{12}^r$  within their uncertainties. Note that the numerical values for the residual reduced Helmholtz energy  $A_{fm}^r$  are rather small, resulting in large relative deviations while the absolute deviations are small too, cf. Fig. 8. It is apparent from the deviation plots that the generalized MBWR EOS performs quite well to fit the entire dataset.

Fig. 9 shows the relative deviations in terms of the vapor pressure. The baseline in all VLE deviation plots represents the reference EOS by Thol et al. [4], which is more advanced and of higher quality than the one automatically generated in this work. It can be seen that the agreement between the present EOS and the

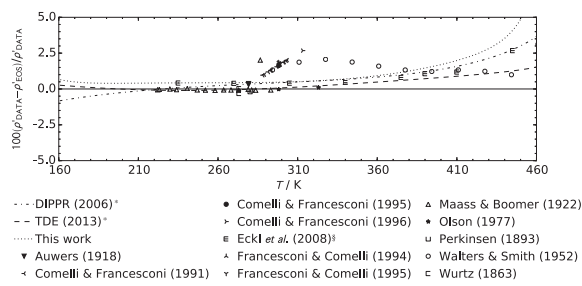


**Fig. 10.** Comparison of the present fundamental equation of state with the one by Thol et al. [4] (baseline) and experimental data for the saturated liquid density. The asterisk marks ancillary equations and the paragraph symbol indicates molecular simulation data by Eckl et al. [17]. The statistical uncertainty of the molecular simulation data decreases gradually with decreasing temperature (0.5% at 445 K, 0.04% at 340 K and 0.02% at 235 K).

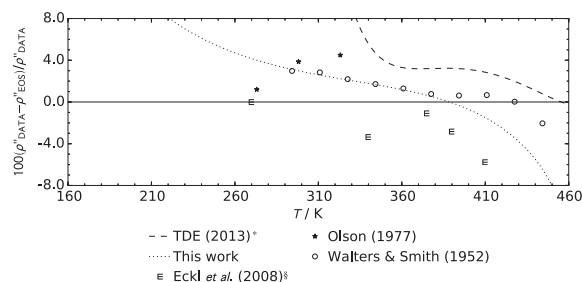


**Fig. 11.** Comparison of the present fundamental equation of state with the one by Thol et al. [4] (baseline) and experimental data for the saturated vapor density. The asterisk marks an ancillary equation and the paragraph symbol indicates molecular simulation data by Eckl et al. [17]. The statistical uncertainty of the molecular simulation data decreases gradually with decreasing temperature (0.5% at 410 K, 0.3% at 340 K and 0.08% at 270 K).

experimental data below 260 K is poor. Between 290 and 470 K, the agreement gets more reasonable with deviations of under 2.5% compared to the EOS by Thol et al. [4]. Since the EOS created in this work is based exclusively on the molecular model by Eckl et al. [17], it coincides well with their simulation data. In Fig. 10, comparisons for the saturated liquid density data are presented. In the range where most experimental data are available, i.e. from 220 to 320 K, the present EOS agrees within 1% to the reference EOS [4] and the experimental data. At higher temperatures, the saturated liquid density is overestimated, yielding deviations of up to +5% at 440 K.

For the saturated vapor density, only very little experimental data are available, cf. Fig. 11. From 270 to 420 K, the deviations of the present EOS compared to the equation of Thol et al. [4] are within  $\pm 4\%$ . In the vicinity of the critical point the agreement is worse. Fig. 12 shows the deviations with respect to the heat of vaporization. At temperatures below 335 K the experimental data and the EOS by Thol et al. [4] are underestimated by the present EOS, above 335 K they are overestimated. Furthermore, the ancillary equation from the DIPPR database is reproduced well at higher temperatures. The agreement between the simulation data by Eckl et al. [17] and the present EOS is consistently good. Deviation plots for density and speed of sound in the homogeneous fluid region can be found in Figs. C.13 and C.14. At lower pressures, the present EOS and the one by Thol et al. [4] agree similarly well with the experimental data for the speed of sound and the homogeneous density.

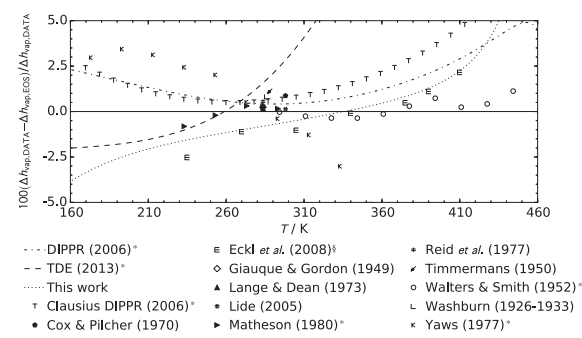


**Fig. 12.** Comparison of the present fundamental equation of state with the one by Thol et al. [4] (baseline) and experimental data for the enthalpy of vaporization. The asterisk marks ancillary equations and the paragraph symbol indicates molecular simulation data by Eckl et al. [17]. The statistical uncertainty of the molecular simulation data decreases gradually with decreasing temperature (0.2% at 410 K, 0.04% at 340 K and 0.04% at 235 K).



At higher pressures the representation of the present EOS gets worse, resulting in a maximum relative deviation of around  $-0.4\%$  for the speed of sound and around  $+3.0\%$  for the homogeneous density.

## 7. Conclusion

The cloud-based molecular simulation framework developed here allows for the automatic execution of large-scale simulation workflows across multiple, distributed computing resources. Simulations were concurrently deployed across two HPC systems, a Cray supercomputer and a large compute cluster. Carrying out a full workflow, i.e. defining the system, preparing and executing simulation runs and fitting the final EOS, is simplified to a few clicks in a user-friendly interface, thus enabling non-expert users to create fundamental EOS in a matter of days. The fully automatized generation of EOS on the basis of molecular modelling and simulation is a valuable process that is well supported by the powerful capabilities of cloud computing. This avoids most of the obstacles that currently confound the delivery, accessibility and usability of this non-service-oriented type of simulation on state of the art computing resources. According to the proposals of Maginn [8] the present work provides a contribution to making molecular simulation more accessible, hopefully encouraging more entities to use such techniques.

## Acknowledgments

The research leading to these results has received funding from the European Union's Seventh Framework Programme [FP7/2007–2013] under grant agreement n° 609029 (FORTISSIMO). The simulations were carried out on the Cray XE6 (Hermit) at the High Performance Computing Center Stuttgart (HLRS) and on the OCULUS cluster of the Paderborn Center for Parallel Computing (PC<sup>2</sup>).

## Appendix A. Simulation details

At each state point 864 particles were sufficiently equilibrated and then sampled for 2 million production cycles with NVT Monte Carlo simulations [16]. The cut-off radius was set to be half the length of the simulation volume. Electrostatic long-range corrections were approximated by the reaction field method [51].

## Appendix B. Molecular model

The coordinates and parameters of the molecular model for ethylene oxide are given in Table B.3. The model consists of three Lennard-Jones sites and one point dipole and was optimized to experimental data for vapor pressure, saturated liquid density and enthalpy of vaporization.

**Table B.3**

Sigma ( $\sigma$ ) and epsilon ( $\epsilon$ ) are the length and energy parameters of the Lennard-Jones (LJ) potential, respectively.  $k_B$  is the Boltzmann constant.  $\mu$  denotes the dipole moment of the point dipole. All coordinates are given in a principal axes system with respect to the center of mass. The orientation of the point dipole is defined with Euler angles:  $\varphi$  is the azimuthal angle with respect to the x-y plane and  $\theta$  is the inclination angle with respect to the z axis.

Site	$x/\text{\AA}$	$y/\text{\AA}$	$z/\text{\AA}$	$\sigma/\text{\AA}$	$\epsilon/k_B/\text{K}$	$\theta/\text{deg}$	$\varphi/\text{deg}$	$\mu/\text{D}$
CH <sub>2</sub>	0.78	0	-0.48431	3.5266	84.739			
CH <sub>2</sub>	-0.78	0	-0.48431	3.5266	84.739			
O	0	0	0.73569	3.0929	62.126			
Dipole	0	0	0			0	0	2.459

## Appendix C. Additional data

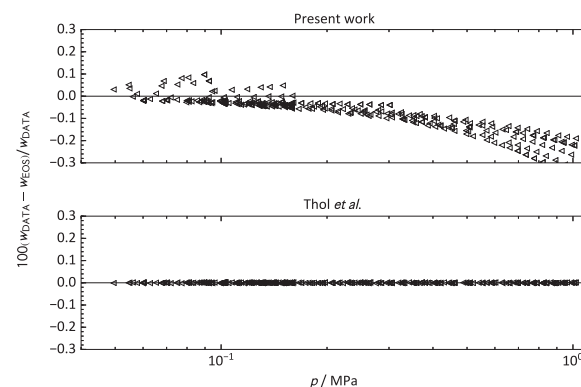


Figure C.13: Comparison of the present fundamental equation of state (top) with the one by Thol et al. [4] (bottom) for the speed of sound  $w$ . Experimental speed of sound data by Hurly [43] ( $\triangleleft$ ) are plotted.

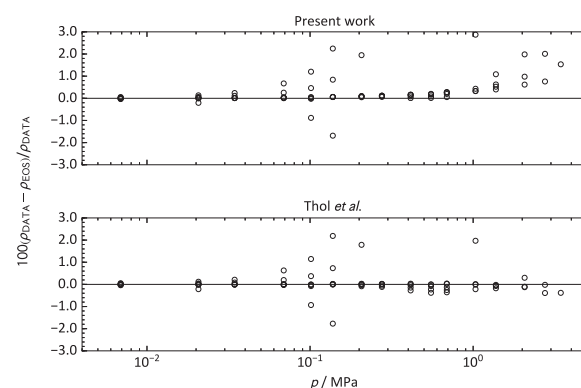


Figure C.14: Comparison of the present fundamental equation of state (top) with the one by Thol et al. [4] (bottom) for density  $\rho$  in homogeneous fluid states. Experimental data by Walters and Smith [22] ( $\diamond$ ) are plotted.

## References

- [1] G. Rutkai, M. Thol, R. Lustig, R. Span, J. Vrabec, J. Chem. Phys. 139 (2013) 041102.
- [2] G. Rutkai, J. Vrabec, J. Chem. Eng. Data 60 (2015) 2895–2905.
- [3] M. Thol, G. Rutkai, R. Span, J. Vrabec, R. Lustig, Int. J. Thermophys. 36 (2015) 25–43.
- [4] M. Thol, G. Rutkai, A. Köster, M. Kortmann, R. Span, J. Vrabec, Chem. Eng. Sci. 121 (2015) 87–99 and 134 (2015) 887–890.
- [5] R. Span, Multiparameter Equations of State: an Accurate Source of Thermodynamic Property Data, Springer Verlag, Berlin, 2000.
- [6] R. Lustig, Mol. Simul. 37 (2011) 457–465.
- [7] R. Lustig, Mol. Phys. 110 (2012) 3041–3052.
- [8] E.J. Maginn, AIChE J. 55 (2009) 1304–1310.
- [9] C.W. Glass, S. Reiser, G. Rutkai, S. Deublein, A. Köster, G. Guevara-Carrion, A. Wafai, M. Horsch, M. Bernreuther, T. Windmann, H. Hasse, J. Vrabec, Comput. Phys. Commun. 185 (2014) 3302–3306.
- [10] P.J. Mohr, B.N. Taylor, D.B. Newell, Rev. Mod. Phys. 84 (2012) 1527–1605.
- [11] E.W. Lemmon, R.T. Jacobsen, J. Phys. Chem. Reference Data 34 (2005) 69–108.
- [12] R. Span, W. Wagner, Int. J. Thermophys. 24 (2003) 1–39.
- [13] L. Sun, J. Ely, Int. J. Thermophys. 26 (2005) 705–728.
- [14] R.T. Jacobsen, R.B. Stewart, J. Phys. Chem. Reference Data 2 (1973) 757–922.
- [15] J. Hust, R. McCarty, Curve-fitting techniques and applications to thermodynamics, Cryogenics 7 (1967) 200–206.
- [16] D. Frenkel, B. Smit, Understanding Molecular Simulation: from Algorithms to Applications, Academic Press, Elsevier, San Diego, 2002.
- [17] B. Eckl, J. Vrabec, H. Hasse, Fluid Phase Equilib. 274 (2008) 16–26.
- [18] F.H. Case, J. Brennan, A. Chaka, K.D. Dobbs, D.G. Friend, P.A. Gordon,

- J.D. Moore, R.D. Mountain, J.D. Olson, R.B. Ross, M. Schiller, V.K. Shen, E.A. Stahlberg, *Fluid Phase Equilib.* 274 (2008) 2–9.
- [19] M. Frenkel, R.D. Chirico, V. Diky, K. Kroenlein, C.D. Muzny, A.F. Kazakov, J.W. Magge, I.M. Abdulagatov, E.W. Lemmon, NIST Standard Reference Database 103b: NIST Thermo–data Engine – Pure Compounds, Binary Mixtures, Reactions, Version 8.0, National Institute of Standards and Technology, Standard Reference Data Program, Gaithersburg, 2013.
- [20] R.L. Rowley, W.V. Wilding, J.L. Oscarson, Y. Yang, N.A. Zundel, T.E. Daubert, R.P. Danner, DIPPR Data Compilation of Pure Compound Properties: Design Institute for Physical Properties, AIChE, New York, 2006.
- [21] D.R. Lide, *CRC Handbook of Chemistry and Physics*, 86 ed., Taylor and Francis, London, 2005.
- [22] C.J. Walters, J.M. Smith, *Chem. Eng. Prog.* 48 (1952) 337–343.
- [23] J.C.G. Calado, U.K. Deiters, E.J.M. Filipe, *J. Chem. Thermodyn.* 28 (1996) 201–207.
- [24] J. Chao, K.R. Hall, K.N. Marsh, R.C. Wilhoit, *J. Phys. Chem. Reference Data* 15 (1986) 1369–1436.
- [25] K.F. Coles, F. Popper, *Industrial Eng. Chem.* 42 (1950) 1434–1438.
- [26] W.F. Giauque, J. Gordon, *J. Am. Chem. Soc.* 71 (1949) 2176–2181.
- [27] N.F. Giles, G.M. Wilson, *J. Chem. Eng. Data* 51 (2006) 1954–1962.
- [28] P.C. Gillespie, J.R. Cunningham, G.M. Wilson, *AIChE Symp. Ser.* 81 (1985) 26–40.
- [29] L.G. Hess, V.V. Tilton, *Industrial Eng. Chem.* 42 (1950) 1251–1258.
- [30] G.B. Kistiakowsky, W.W. Rice, *J. Chem. Phys.* 8 (1940) 618–622.
- [31] O. Maass, E.H. Boomer, *J. Am. Chem. Soc.* 44 (1922) 1709–1728.
- [32] R.A. McDonald, S.A. Shrader, D.R. Stull, *J. Chem. Eng. Data* 4 (1959) 311–313.
- [33] J.E. Mock, J.M. Smith, *Industrial Eng. Chem.* 42 (1950) 2125–2128.
- [34] J.D. Olson, *J. Chem. Eng. Data* 22 (1977) 326–329.
- [35] K.V. Auwers, *Justus Liebig's Ann. Chem.* 415 (1918) 98–168.
- [36] F. Comelli, R. Francesconi, *J. Chem. Eng. Data* 36 (1991) 382–383.
- [37] F. Comelli, R. Francesconi, *J. Chem. Eng. Data* 40 (1995) 28–30.
- [38] F. Comelli, R. Francesconi, *J. Chem. Eng. Data* 41 (1996) 101–104.
- [39] R. Francesconi, F. Comelli, *J. Chem. Eng. Data* 39 (1994) 106–107.
- [40] R. Francesconi, F. Comelli, *J. Chem. Eng. Data* 40 (1995) 512–514.
- [41] W.H. Perkin, *J. Chem. Soc. Trans.* 63 (1893) 488–491.
- [42] A. Wurtz, *Ann. de Chimie de Physique* 55 (1859) 400–432.
- [43] J.J. Hurly, *Int. J. Thermophys.* 23 (2002) 667–696.
- [44] J.D. Cox, G. Pilcher, *Thermochemistry of Organic and Organometallic Compounds*, Academic Press, New York, 1970.
- [45] N.A. Lange, J.A. Dean, *Lange's Handbook of Chemistry*, eleventh ed., McGraw-Hill, New York, 1973.
- [46] Matheson, *Matheson Gas Data Book*, sixth ed., Lyndhurst, New Jersey, 1980.
- [47] R.C. Reid, J.M. Prausnitz, T.K. Sherwood, *The Properties of Gases and Liquids*, third ed., McGraw-Hill, New York, 1977.
- [48] J. Timmermans, *Physico-chemical Constants of Pure Organic Substances II*, Elsevier, New York, 1965.
- [49] E.W. Washburn, *International Critical Tables of Numerical Data, Physics, Chemistry, and Technology*, McGraw-Hill, New York, 2010, pp. 1926–1933.
- [50] C.L. Yaws, *Physical Properties: a Guide to the Physical, Thermodynamic, and Transport Property Data of Industrially Important Chemical Compounds*, McGraw-Hill, New York, 1977.
- [51] J.A. Barker, R.O. Watts, *Mol. Phys.* 26 (1973) 789–792.



### **3.13 Premelting, solid-fluid equilibria, and thermodynamic properties in the high density region based on the Lennard-Jones potential**

**A. Köster**, P. Mausbach, J. Vrabec, *The Journal of Chemical Physics* 147:144502, 2017.

DOI: [doi.org/10.1063/1.4990667](https://doi.org/10.1063/1.4990667)

Nachgedruckt mit Erlaubnis von AIP Publishing (Copyright 2017).

In dieser umfassenden Studie wurden Effekte in der näheren Umgebung des Feststoff-Flüssigkeits-Gleichgewichts für das Lennard-Jones Wechselwirkungspotential untersucht. Dabei wurden sowohl der fluide Bereich bei hohen Dichten als auch der Feststoffbereich analysiert und auf der Basis verschiedener Zustandsgrößen mit genauen Zustandsgleichungen verglichen. Es zeigte sich, dass einige thermodynamische Zustandsgrößen sogenannten „Premelting-Effekten“ unterliegen, die zu einer starken Variation dieser Größen in der Nähe der Feststoff-Flüssigkeits-Phasengrenze führen.

Der Autor der vorliegenden Dissertation hat alle für diese Veröffentlichung zugrundeliegenden molekularen Simulationen durchgeführt. Die Verfassung des Manuskripts entstand in Zusammenarbeit von Prof. Peter Mausbach und dem Autor. Dieser übernahm auch die Erstellung aller Abbildungen und die Konsolidierung des Manuskripts. Die Überarbeitung des Manuskripts wurde durchgeführt vom Autor unter Mithilfe von Prof. Peter Mausbach und Prof. Jadran Vrabec. Der Autor wurde während des gesamten Prozesses betreut von Prof. Jadran Vrabec.



## Premelting, solid-fluid equilibria, and thermodynamic properties in the high density region based on the Lennard-Jones potential

Andreas Köster,<sup>1</sup> Peter Mausbach,<sup>2</sup> and Jadran Vrabec<sup>1,a)</sup>

<sup>1</sup>Thermodynamics and Energy Technology, Universität Paderborn, 33098 Paderborn, Germany

<sup>2</sup>Technical University of Cologne, 50678 Köln, Germany

(Received 16 June 2017; accepted 22 September 2017; published online 10 October 2017)

The Lennard-Jones potential is used to study the high density fluid and face centered cubic solid state region, including solid-fluid equilibria. Numerous thermodynamic properties are considered, elucidating the behavior of matter in this poorly studied region. The present molecular simulation results are extensively compared to the latest and most accurate equation of state models for fluid and solid phases. It is shown that current models do not cover the thermodynamics of the system adequately near the solid-fluid phase transition. Furthermore, thermodynamic stability is analyzed, indicating that published solid-fluid coexistence data may not be correct at high temperatures. Particular attention is paid to the premelting zone, a range of states close to the melting line, which is characterized by strong variations of several thermodynamic properties. Because the underlying microscopic mechanisms are not yet fully understood, it is hoped that these data may contribute to the development of a theoretical framework for describing premelting effects. *Published by AIP Publishing.* <https://doi.org/10.1063/1.4990667>

### I. INTRODUCTION

Thermodynamic states ranging from the high density fluid to the solid have attracted much interest in the past decade, and a number of new theoretical approaches have been developed to discuss the important aspects of this region.<sup>1–5</sup> However, this fact is accompanied by the surprising observation that comprehensive thermodynamic information is available for hardly any real substance in this region. Common approaches to thermodynamic data are empirical equations of state (EOS), but only very few substances were sufficiently measured in the laboratory to correlate high quality reference EOS.<sup>6</sup> A thermodynamic quantity which can serve as a measure for the quality of EOS correlations is the Grüneisen parameter  $\gamma_G$ , which was analyzed in detail in a recent paper on 28 real fluids.<sup>7</sup> That analysis showed that thermodynamic properties in the liquid region beyond the triple point density are poorly described for most substances, mainly due to the lack of experimental data. Nonetheless, extrapolations of EOS beyond their specified limits are frequently applied although their validity in the high density fluid region is not determined in general. It is therefore of some interest to investigate deviations between EOS and experimental or simulation results for a large number of thermodynamic properties, which is a feature of this study for the Lennard-Jones (LJ) fluid state near freezing. It is shown that, at least for some thermodynamic properties, extrapolations of the EOS lead to thermodynamic inconsistencies.

The provision of complete thermodynamic information for a large region of the solid state is even more limited, a fact that should find more attention during the development of

EOS that forms the basis for common thermodynamic software tools.<sup>8–10</sup> The melting process is of particular interest for various practical applications. In contrast to the highly developed theory of melting for two dimensional (2D) systems, the more important premelting phenomena in three dimensional (3D) crystals are only inadequately understood. For these reasons, it is desirable to provide complete thermodynamic information at least for model substances in this region.

The statistical mechanical formalism proposed by Lustig<sup>11,12</sup> allows for such an investigation because it facilitates, in principle, the concurrent calculation of any partial Helmholtz energy derivative in the canonical ( $NVT$ ) ensemble within a single simulation run. In the present study, we employ this idea for the LJ potential. The LJ interaction potential is widely used in molecular simulation studies because it is sufficiently realistic to represent small spherical, nonpolar molecules,<sup>13</sup> and it is an important model for studying phase equilibria,<sup>14</sup> phase change processes,<sup>15,16</sup> clustering behavior,<sup>17</sup> or transport<sup>18</sup> and interface properties<sup>19</sup> of simple fluids. For its fluid state up to moderately high densities, a number of high quality EOS exist in the literature.<sup>20–24</sup> The LJ potential is commonly expressed as

$$u_{\text{LJ}} = 4\epsilon \left[ \left( \frac{\sigma}{r} \right)^{12} - \left( \frac{\sigma}{r} \right)^6 \right], \quad (1)$$

where  $\sigma$  and  $\epsilon$  are size and energy parameters, while  $r$  is the distance between two particles.

In this study, thermodynamic properties were investigated on the basis of Lustig's formalism<sup>11,12</sup> in a very large temperature and density range. Particular attention was paid to a detailed study of the premelting zone close to the melting line. For this purpose, solid-fluid equilibria (SFE) were determined up to high temperatures. Simulation results were compared to the latest and most accurate EOS for the fluid and solid

<sup>a)</sup>Author to whom correspondence should be addressed: jadran.vrabec@upb.de

phases. All numerical simulation data are supplied in the [supplementary material](#). The paper is organized as follows: Secs. II and III introduce the molecular simulation method and the approach to determine SFE. Subsequently, the results are discussed for the high density fluid (Sec. IV) and face centered cubic (fcc) solid state (Sec. V). Conclusion sums up the present findings.

## II. MOLECULAR SIMULATION METHOD

The molecular simulation tool *ms2*<sup>25–27</sup> was recently augmented by the statistical mechanical formalism by Lustig,<sup>11,12</sup> which allows for the concurrent sampling of an arbitrary number of partial Helmholtz energy derivatives in the *NVT* ensemble during a single simulation run. Every time independent thermodynamic property can be calculated from a combination of these partial derivatives.<sup>6</sup> The total molar Helmholtz energy

$$a(T, \rho) = a^o(T, \rho) + a^r(T, \rho) \quad (2)$$

can be separated into an ideal (superscript “o”) and a residual (superscript “r”) contribution. The latter is a consequence of the intermolecular interactions. For complex fluids, the ideal contribution to the Helmholtz energy is non-trivial and has to be determined experimentally (e.g., by spectroscopy) or by *ab initio* calculations. In the present case, the ideal contribution is straightforward because the LJ potential is classical monatomic. The reduced residual Helmholtz energy

derivatives can be written as

$$A_{mn}^r = (1/T)^m \rho^n \frac{\partial^{m+n} a^r(T, \rho)/(RT)}{\partial (1/T)^m \partial \rho^n}, \quad (3)$$

wherein  $T$  denotes the temperature,  $\rho$  the density, and  $R$  the ideal gas constant.  $m$  and  $n$  represent the order of the partial derivative with respect to density and inverse temperature, respectively. Although Lustig’s formalism<sup>11,12</sup> may be used to sample the partial Helmholtz energy derivatives up to arbitrary order, it was implemented in *ms2* only up to the order  $m = 3$  and  $n = 2$ , yielding eight derivatives per simulation run. Table I gives an overview on their conversion into common thermodynamic properties. As usual, for studies based on the LJ potential, all thermodynamic data are reported here in a reduced unit system. This reduction is based on the LJ size  $\sigma$  and energy  $\varepsilon$  parameters, e.g.,  $T^* = Tk_B/\varepsilon$ ,  $\rho^* = \rho\sigma^3$ , and  $p^* = p\sigma^3/\varepsilon$  with Boltzmann’s constant  $k_B$  and pressure  $p$ . The asterisk will be omitted in the following. Most simulations were carried out with  $N = 1372$  particles using Monte Carlo (MC) sampling with an acceptance rate<sup>28</sup> of 0.5. Starting from a fcc lattice, each run was equilibrated for  $10^5$  cycles and then sampled for 2 to  $3 \cdot 10^6$  cycles, where one cycle corresponds to 1372 translational propagation attempts. The cutoff radius was chosen to be half the edge length of the cubic simulation volume to evaluate the interactions explicitly to the largest possible extent. A detailed discussion of this choice is given in the [supplementary material](#). Molecular simulations were conducted in the high density fluid region, in the solid region and close to the SFE, cf. Fig. 1. Statistical uncertainties

TABLE I. Thermodynamic properties in relation to the reduced Helmholtz energy derivatives, where the ideal contributions are  $A_{10}^o = -A_{20}^o = 3/2$ .

Property	Relation to the reduced Helmholtz energy derivatives
Pressure $p = -(\partial a / \partial v)_T$	$\frac{p}{\rho RT} = 1 + A_{01}^r$
Internal energy $u = a - T(\partial a / \partial T)_v$	$\frac{u}{RT} = A_{10}^o + A_{10}^r$
Enthalpy $h = u + pv$	$\frac{h}{RT} = 1 + A_{01}^r + A_{10}^o + A_{10}^r$
Isochoric heat capacity $c_v = (\partial u / \partial T)_v$	$\frac{c_v}{R} = -A_{20}^o - A_{20}^r$
Isobaric heat capacity $c_p = (\partial h / \partial T)_p$	$\frac{c_p}{R} = -A_{20}^o - A_{20}^r + \frac{(1 + A_{01}^r - A_{11}^r)^2}{1 + 2A_{01}^r + A_{02}^r}$
Thermal expansion coefficient $\alpha = \frac{(\partial p / \partial T)_\rho}{\rho(\partial p / \partial \rho)_T}$	$\alpha T = \frac{1 + A_{01}^r - A_{11}^r}{1 + 2A_{01}^r + A_{02}^r}$
Isothermal compressibility $\beta_T = (\rho(\partial p / \partial \rho)_T)^{-1}$	$\beta_T \rho RT = \frac{1}{1 + 2A_{01}^r + A_{02}^r}$
Thermal pressure coefficient $\gamma_v = (\partial p / \partial T)_\rho$	$\frac{\gamma_v}{\rho R} = 1 + A_{01}^r - A_{11}^r$
Entropy gradient $(\partial s / \partial \rho)_T = 1/\rho^2(\partial^2 a / \partial T \partial v)$	$(\partial s / \partial \rho)_T \frac{\rho}{R} = -(1 + A_{01}^r - A_{11}^r)$
Density scaling exponent $\gamma = (\partial \ln T / \partial \ln \rho)_{s,r}$	$\gamma = -\frac{A_{01}^r - A_{11}^r}{A_{20}^r}$
Grüneisen parameter $\gamma_G = (\partial \ln T / \partial \ln \rho)_s$	$\gamma_G = -\frac{1 + A_{01}^r - A_{11}^r}{A_{20}^o + A_{20}^r}$
Speed of sound $w = ((\partial p / \partial \rho)_s)^{1/2}$	$\frac{Mw^2}{RT} = 1 + 2A_{01}^r + A_{02}^r - \frac{(1 + A_{01}^r - A_{11}^r)^2}{A_{20}^o + A_{20}^r}$
Joule-Thomson coefficient $\mu_{JT} = (\partial T / \partial p)_h$	$\mu_{JT} \rho R = \frac{-(A_{01}^r + A_{02}^r + A_{11}^r)}{(1 + A_{01}^r - A_{11}^r)^2 - (A_{20}^o + A_{20}^r)(1 + 2A_{01}^r + A_{02}^r)}$

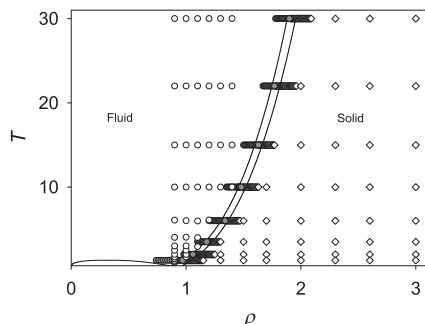


FIG. 1. Locations of the state points used for the present study: (○) molecular simulations in the homogeneous fluid phase; (○, gray) molecular simulations for the determination of the freezing line; (○) molecular simulations in the homogeneous fcc solid phase.

of the simulation data were estimated by block averaging,<sup>29</sup> and the error propagation law was used for all subsequent calculations.

### III. SOLID-FLUID EQUILIBRIA

For a study on the phase behavior of a thermodynamic system in the high density fluid region up to the solid state, solid-fluid coexistence plays a central role. Knowledge of the first-order freezing/melting transition is important in various fields, but it has proven to be difficult to give accurate predictions from experimental or theoretical treatments. Because key aspects of this phenomenon are poorly understood, computer simulation methods are valuable for exploring the freezing and melting behavior.

In this study, the SFE is investigated by initially determining the freezing point (FP) from pressure values sampled throughout the phase transition at constant temperature. Figure 2 shows the result of such a computation for two isotherms,  $T = 1.3$  and  $T = 22$ . An abrupt change of the density dependent pressure reflects the entry into the two-phase solid-fluid region. By means of empirical arguments and using a combination of equilibrium and non-equilibrium molecular dynamics simulations, Ge *et al.*<sup>30</sup> identified this pressure discontinuity as the FP of the SFE, an outcome that is used in

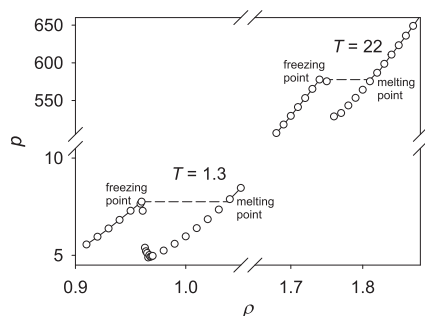


FIG. 2. Pressure as a function of density along the isotherms  $T = 1.3$  and  $T = 22$ : (○) present simulation data; (—) stable phase regions. According to Ge *et al.*,<sup>30</sup> the pressure discontinuity determines the freezing point density  $\rho_{FP}$ , and the isobaric tie line to the solid branch yields the melting point density  $\rho_{MP}$ .

the present study. The method of Ge *et al.*<sup>30</sup> was successfully applied in the literature to investigate the SFE of various simple fluid systems.<sup>31–34</sup> The following considerations rely on these findings.

In a second step, the melting point (MP) is determined by extending an isobaric tie line from the known FP to the solid state branch as shown in Fig. 2. Compared to other methods,<sup>35–39</sup> this approach has the advantage of simplicity and robustness, and it can naturally be combined with the thorough sampling of Helmholtz energy derivatives.

This procedure was applied along eight isotherms  $T = 1.3, 2, 3.5, 6, 10, 15, 22$ , and  $30$  to obtain the respective FP and MP densities  $\rho_{FP}$  and  $\rho_{MP}$  to calculate the course of the freezing line (FL) and the melting line (ML) in  $(\rho, T)$  coordinates. Therefore, the accuracy of the resulting FL and ML in this approach mainly depends on the density increment  $\Delta\rho$  with which the phase transition is scanned. This increment was initially set to  $\Delta\rho = 0.01$  to obtain a first estimate of the FP; subsequently, it was set to  $\Delta\rho = 0.001$  between adjacent simulation runs to increase accuracy. Because of this discretization, slight scatter occurs between the coexistence points at different temperatures, which were, however, averaged out by a fitting procedure. FP and MP coordinates generated in this way were used to adjust an empirical correlation function as employed by Ahmed and Sadus<sup>33</sup> and van der Hoef,<sup>40</sup>

$$\rho_{FP} = T^{1/4} [l_0 + l_1 T^{-1} + l_2 T^{-2} + l_3 T^{-3} + l_4 T^{-4} + l_5 T^{-5}], \quad (4)$$

$$\rho_{MP} = T^{1/4} [s_0 + s_1 T^{-1} + s_2 T^{-2} + s_3 T^{-3} + s_4 T^{-4} + s_5 T^{-5}]. \quad (5)$$

For a proper description of the FL and the ML in the vicinity of the triple point, additional FP and MP data in the temperature range  $0.8 \leq T \leq 2.74$  from the literature<sup>33</sup> were considered for the fits. Parameters  $l_i$  and  $s_i$  are summarized in Table II. The resulting FL and ML, together with the present simulation results and those of Ahmed and Sadus,<sup>33</sup> are shown in Fig. 3 (top). Moreover, an extrapolation of the FL correlation from Ref. 33 is shown. Although only a limited temperature range  $0.8 \leq T \leq 2.74$  was considered by Ahmed and Sadus,<sup>33</sup> the agreement with the present results is satisfactory even at high temperatures. As shown by Thol *et al.*,<sup>24</sup> an extrapolation of the ML based on the parameters given in Ref. 33 fails numerically and is therefore omitted in Fig. 3 (top). Ahmed and Sadus also calculated SFE with the Gibbs-Duhem integration (GDI) algorithm;<sup>34</sup> the associated FL and ML are shown in Fig. 3. In a recent study, Heyes and Braňka<sup>41</sup> recalculated the course of the FL and the ML on the

TABLE II. Empirical parameters of the polynomial correlations (4) and (5) for the coexisting fluid and solid densities of the Lennard-Jones potential.

$i$	$l_i$	$s_i$
0	0.794 326 405 787 077	0.824 314 738 009 423
1	0.287 446 151 493 139	0.345 860 792 558 053
2	−0.405 667 818 555 559	−0.406 050 983 191 368
3	0.417 645 193 659 883	0.391 153 270 627 875
4	−0.211 440 758 862 587	−0.164 344 343 309 084
5	0.040 324 958 732 013	0.018 024 225 929 690

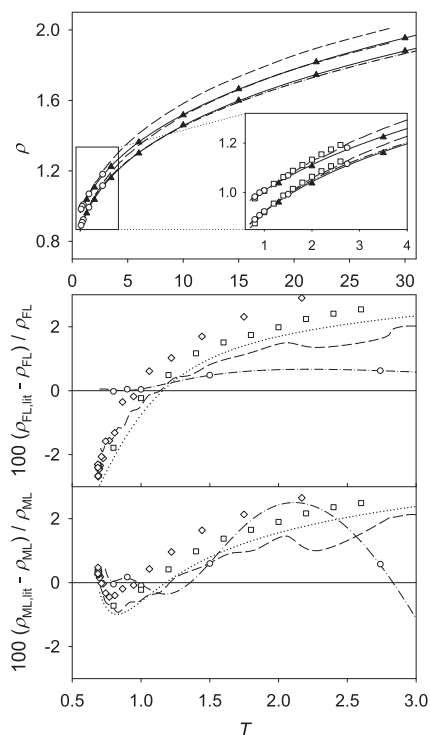


FIG. 3. Density  $\rho$  as a function of temperature along the freezing and the melting line (top), freezing line density  $\rho_{FL}$  deviations (center), and melting line density  $\rho_{MP}$  deviations (bottom) of literature data compared to the present results: ( $\blacktriangle$ ) present simulation data and (—) correlations thereof, cf. Eqs. (4) and (5); ( $\circ$ ) data of Ahmed and Sadus<sup>33</sup> and (— · —) an extrapolation of the freezing line correlation;<sup>33</sup> (—) data of Ahmed and Sadus (GDI algorithm);<sup>34</sup> ( $\square$ ) data of Pedersen;<sup>37</sup> ( $\circ$ ) data of Agrawal and Kofke.<sup>39</sup> Note that the latter data set is omitted in the top part of the figure for visibility reasons.

basis of molecular simulation data from the literature.<sup>34,36,42,43</sup> Their results closely follow the coexistence lines of Ahmed and Sadus<sup>34</sup> and are not shown in Fig. 3 (top) for visibility reasons. The same is true for SLE data of Agrawal and Kofke.<sup>39</sup> However, the majority of published SFE data are limited to a relatively small temperature interval. This region is shown in the inset of Fig. 3 (top), where the results of Pedersen<sup>37</sup> are also depicted.

To allow for a more detailed inspection, the relative deviation between density data from the literature and the present work along the FL and the ML is shown for temperatures  $T < 3$ , cf. Fig. 3. The relative deviation of the FL density of Ahmed and Sadus<sup>33</sup> based on the method of Ge *et al.*<sup>30</sup> from the present data is only 0.5%. FL density data of Pedersen<sup>37</sup> and Heyes and Braňka<sup>41</sup> are similar to those of Ahmed and Sadus<sup>34</sup> and Agrawal and Kofke,<sup>39</sup> which were both calculated with the GDI method. At  $T = 3$ , the relative deviation of the FL density of Ahmed and Sadus<sup>34</sup> compared to the present data is roughly 2%, whereas the density data from Agrawal and Kofke<sup>39</sup> deviate by about 3%. The situation is similar for the ML density shown in Fig. 3 (bottom). An additional comparison of the temperature dependent melting pressure with various results from the literature is given in the [supplementary material](#).

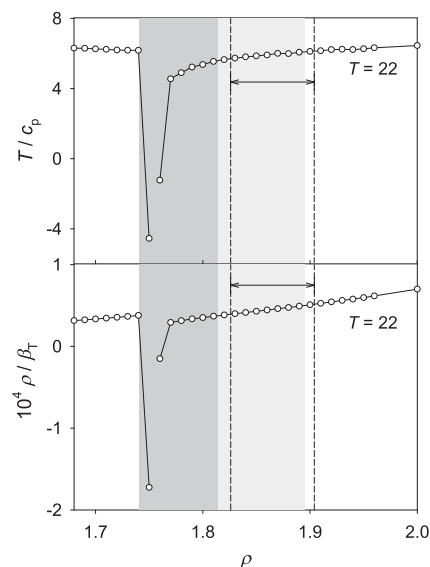


FIG. 4. Thermodynamic stability coefficients  $T/c_p$  (top) and  $\rho/\beta_T$  (bottom) as a function of density at  $T = 22$ : ( $\circ$ ) present simulation data; (dark grey area) present two-phase region; (light grey area) two-phase region of Ahmed and Sadus (GDI algorithm);<sup>34</sup> (area between the dashed lines) two-phase region of Agrawal and Kofke.<sup>39</sup>

It is striking that the coexistence lines obtained from GDI<sup>34,39</sup> deviate systematically from the results of the present study, particularly as the temperature increases, cf. Fig. 3 (top). To elucidate this issue, thermodynamic stability coefficients were calculated. Thermodynamic stability theory postulates stability conditions for a fluid or a solid by the inequalities<sup>44</sup>

$$\frac{T}{c_p} > 0, \quad (6)$$

and

$$\frac{\rho}{\beta_T} > 0. \quad (7)$$

If those conditions are not met, the system is unstable. The quantities  $T/c_p$  and  $\rho/\beta_T$  were calculated along all eight isotherms considered. Figure 4 depicts the results of this calculation for  $T = 22$  in a density region close to solid-fluid coexistence. Clearly, the stability coefficients satisfy inequalities (6) and (7) within the respective coexistence regions predicted by Ahmed and Sadus<sup>34</sup> and Agrawal and Kofke.<sup>39</sup> This means that the system in these regions is in a stable or metastable solid state. In contrast, within the two-phase region of the present study  $T/c_p$  and  $\rho/\beta_T$  become negative, as required for a first order phase transition. Obviously, freezing and melting points obtained from the GDI method<sup>34,39</sup> at higher temperatures appear to be at too high densities, which is an important outcome of the present investigation.

The entropy of fusion at the freezing/melting transition  $\Delta s_{\text{fusion}} = \Delta h/T$ , where  $\Delta h$  is the difference between the enthalpy of fluid and fcc crystal at the coexistence temperature  $T$ , is shown in Fig. 5. The entropy of fusion decreases rapidly with increasing temperature and approaches an almost constant value at higher temperatures. At low temperatures, all simulation results are close to each other, and at high

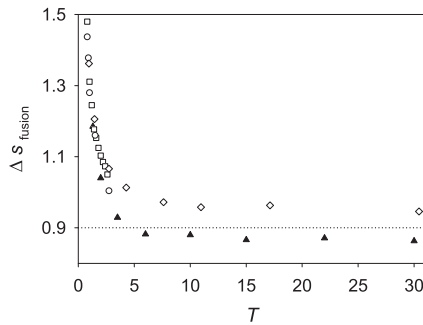


FIG. 5. Entropy of fusion  $\Delta S_{\text{fusion}}$  as a function of temperature: ( $\blacktriangle$ ) present simulation data; ( $\circ$ ) data of Ahmed and Sadus;<sup>33</sup> ( $\square$ ) data of Pedersen;<sup>37</sup> ( $\diamond$ ) data of Agrawal and Kofke;<sup>39</sup> ( $\cdots$ )  $\Delta S_{\text{fusion}} = 0.9$  corresponding to the  $r^{-12}$  potential.<sup>45</sup>

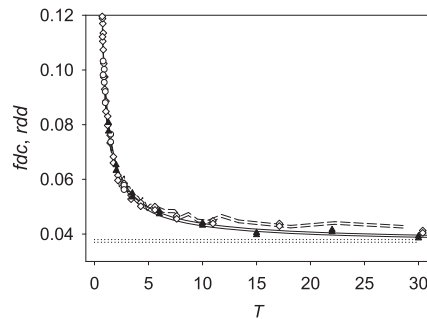


FIG. 6. Fractional density change at freezing  $fdc$  and relative density difference at freezing  $rdd$  as a function of temperature: ( $\blacktriangle$ ) present simulation data and (—) correlations thereof, cf. Eqs. (4) and (5); ( $\circ$ ) data of Ahmed and Sadus;<sup>33</sup> ( $\diamond$ ) data of Agrawal and Kofke;<sup>39</sup> (---) data of Ahmed and Sadus (GDI algorithm);<sup>34</sup> ( $\cdots$ )  $fdc$  and  $rdd$  ratios corresponding to the  $r^{-12}$  potential.<sup>45</sup> The  $rdd$  curve is always below the  $fdc$  curve in this figure.

temperatures, the data of Agrawal and Kofke<sup>39</sup> are 9% above the present data. GDI results from Ahmed and Sadus<sup>34</sup> are not shown in Fig. 5 since necessary data were not published by these authors. At  $T \geq 6$ , present values for  $\Delta S_{\text{fusion}}$  approach those of the solely repulsive  $r^{-12}$  potential for which  $\Delta S_{\text{fusion}} = 0.9$ .<sup>45</sup>

The fractional density change at freezing  $fdc = (\rho_{\text{MP}} - \rho_{\text{FP}})/\rho_{\text{FP}}$ , also known as the miscibility gap, and the relative density difference at freezing  $rdd = 2(\rho_{\text{MP}} - \rho_{\text{FP}})/(\rho_{\text{MP}} + \rho_{\text{FP}})$  are shown in Fig. 6. These two properties can be used to quantify the influence of the interaction potential on solid-fluid coexistence.<sup>32</sup> Both  $fdc$  and  $rdd$  decrease significantly with increasing temperature, indicating that the two-phase region in a  $T, \rho$ -diagram is narrower at high temperatures than at low temperatures. The  $fdc$  and  $rdd$  ratios of the  $r^{-12}$  potential are 0.038 and 0.037, respectively,<sup>45</sup> cf. Fig. 6.

#### IV. THERMODYNAMIC PROPERTIES OF THE HIGH DENSITY FLUID STATE

Molecular simulation results ranging from the FL to the supercritical state of the LJ potential are presented along isochores in temperature dependent plots. The validity of the recently developed reference EOS by Thol *et al.*<sup>24</sup> is assessed

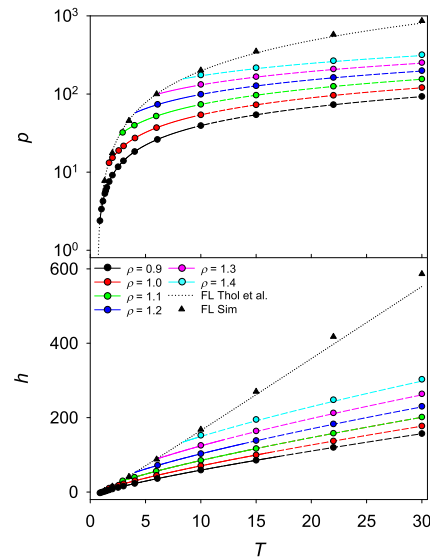


FIG. 7. Pressure  $p$  (top) and enthalpy  $h$  (bottom) along isochores in the high density fluid state: (—) EOS by Thol *et al.*,<sup>24</sup> (---) extrapolated and ( $\cdots$ ) using  $\rho$  and  $T$  coordinates from Eq. (4) to calculate  $p$  and  $h$  values on the freezing line; ( $\bullet$ ) present simulation data in the fluid phase and ( $\blacktriangle$ ) on the freezing line.

by comparing it to the present data. Since the data set used by Thol *et al.*<sup>24</sup> for the parametrization of their EOS included state points in the range  $0.7 < T < 9$  and  $\rho < 1.08$ , a large part of the present simulation data is compared to an extrapolation of that EOS. In the main body of this text, first or second order derivative data of the high density fluid state are presented, whereas other thermodynamic properties can be found in the

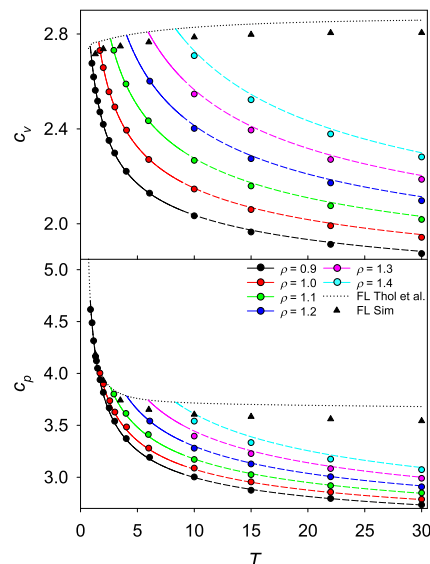


FIG. 8. Isochoric heat capacity  $c_v$  (top) and isobaric heat capacity  $c_p$  (bottom) along isochores in the high density fluid state: (—) EOS by Thol *et al.*,<sup>24</sup> (---) extrapolated and ( $\cdots$ ) using  $\rho$  and  $T$  coordinates from Eq. (4) to calculate  $c_v$  and  $c_p$  values on the freezing line; ( $\bullet$ ) present simulation data in the fluid phase and ( $\blacktriangle$ ) on the freezing line.



supplementary material. Thermodynamic properties on the FL itself cannot be calculated from that EOS directly, instead  $(\rho, T)$  coordinates from the present FL correlation (4) were employed to obtain those values. Note that statistical simulation uncertainties of data discussed in the following are only depicted if they exceed the symbol size.

### A. First order derivative properties

Pressure  $p$  and enthalpy  $h$  are shown in Fig. 7. Both  $p$ , which is displayed on a logarithmic scale, and  $h$  increase almost linearly with increasing temperature. Agreement with the EOS by Thol *et al.*<sup>24</sup> up to its specified limits is almost perfect, with deviations of 0.2% for pressure and 0.3% for enthalpy. At higher temperatures, larger deviations occur, i.e., 2% for pressure and enthalpy at  $\rho = 1.4$  and  $T = 30$  and 6% to 7% for both properties on the FL at  $T = 30$ .

### B. Second order derivative properties

Figure 8 shows molecular simulation results for the isochoric and isobaric heat capacities, which decrease monotonically with increasing temperature in the homogeneous fluid state. Along the FL, however,  $c_v$  increases with temperature and seems to approach a constant value at very high temperatures. Deviations to the EOS by Thol *et al.*,<sup>24</sup> especially for

the four lowest isochores, are negligible. However, the  $c_v$  and  $c_p$  data along the FL from the EOS by Thol *et al.*<sup>24</sup> and the present molecular simulations agree only qualitatively. This discrepancy is most likely caused by the fact that the isochoric heat capacity  $c_v$  is a property which is very sensitive to phase transitions, i.e., very small density variations in the vicinity of a coexistence curve lead to significant changes of  $c_v$ .<sup>46,47</sup> Moreover, the density limit of the reference EOS by Thol *et al.*<sup>24</sup> is substantially exceeded on the FL, which seems to be particularly problematic for these thermodynamic properties.

As shown in Fig. 9 (top and center), the thermal expansion coefficient  $\alpha$  and the isothermal compressibility  $\beta_T$  decrease monotonically with increasing temperature. The density dependence of  $\alpha$  is comparably smaller than that of  $\beta_T$ , whereas the temperature dependence is converse. Very good consistency between the EOS by Thol *et al.*<sup>24</sup> and the present molecular simulation data was found. Again, deviations are larger for very high densities and along the FL. Figure 9 (bottom) shows the thermal pressure coefficient  $\gamma_v$ , which is a combination of  $\alpha$  and  $\beta_T$ . Good agreement between the present molecular simulation data and the EOS by Thol *et al.*<sup>24</sup> holds for  $\rho \leq 1.2$ , whereas deviations are larger for higher density. The molecular simulation results are steeper than the EOS along the FL.

## V. THERMODYNAMIC PROPERTIES OF THE FCC SOLID STATE

Thermodynamic properties of the LJ fcc solid obtained from simulation were compared with two solid state models for the Helmholtz energy, which are rare in the literature. The most accurate EOS for the LJ fcc solid to date was published by van der Hoef.<sup>40,48</sup> It has a rather limited range of validity  $0.1 \leq T \leq 2.0$  and  $\rho_{m,s} \leq \rho \leq 1.2$ , where  $\rho_{m,s}$  is the density at melting or sublimation. A larger range of applicability is provided by a very recent contribution of Lustig.<sup>49</sup> In his entirely theoretical approach with no empirical parameter, the Lennard-Jones and Devonshire (LJD) cell theory was developed to essentially obtain complete thermodynamic information for any cubic lattice, including fcc, and any interaction potential that is part of the Mie class.<sup>50</sup> Within LJD theory, the exact Helmholtz energy of the system is decomposed into several contributions, which are subject to approximations employing cell theory methods.<sup>51</sup>

$$\begin{aligned} \frac{A(NVT)}{Nk_B T} &= \frac{A_{\text{ref}}(NVT)}{Nk_B T} + \frac{A_{\text{com}}(NVT)}{Nk_B T} + \frac{A_{\text{cor}}(NVT)}{Nk_B T} \\ &= -\ln \frac{v_f(NVT)}{\Lambda^3(T)} + \frac{u_0}{k_B T} - \ln \sigma_{\text{com}}(NVT) \\ &\quad - \ln \left[ 1 + \sum_{ij} \langle f_{ij} \rangle + \sum_{ij} \sum_{kl} \langle f_{ij} f_{kl} \rangle + \dots \right]. \end{aligned} \quad (8)$$

The so-called free volume

$$v_f = \int_{\text{cell}_i} \exp \left[ -\frac{\phi(\mathbf{r}_i) - \phi(\mathbf{r}_i = 0)}{k_B T} \right] d\mathbf{r}_i \quad (9)$$

where the cell field  $[\phi(\mathbf{r}_i) - \phi(\mathbf{r}_i = 0)]$  represents the change in potential energy when particle  $i$  is displaced from  $\mathbf{r}_i = 0$  to

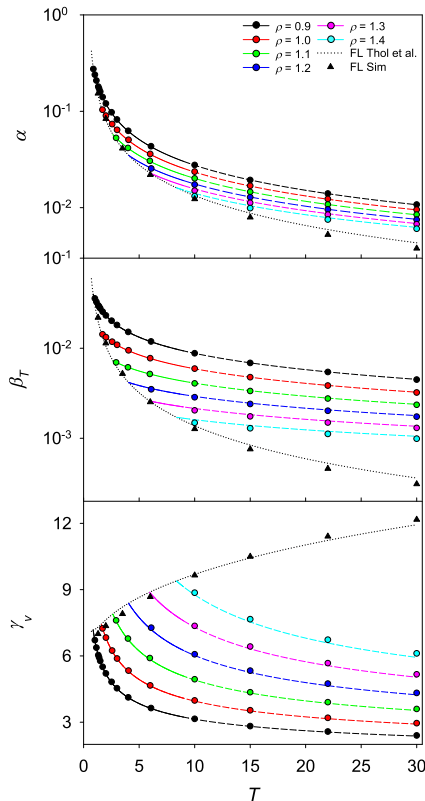


FIG. 9. Thermal expansion coefficient  $\alpha$ , isothermal compressibility  $\beta_T$ , and thermal pressure coefficient  $\gamma_v$  along isochores in the high density fluid state: (—) EOS by Thol *et al.*,<sup>24</sup> (---) extrapolated, and (···) using  $\rho$  and  $T$  coordinates from Eq. (4) to calculate  $\alpha$ ,  $\beta_T$ , and  $\gamma_v$  values on the freezing line; (●) present simulation data in the fluid phase and (▲) on the freezing line.



$\mathbf{r}_i$  with all other particles held fixed. The functions

$$f_{ij} = \exp \left[ -\frac{\Delta_{ij}}{k_B T} \right] - 1, \quad (10)$$

consider that particles in different cells are correlated through  $\Delta_{ij}$ <sup>51</sup> and averages  $\langle f_{ij} f_{kl} \rangle$  are taken over the participating cells  $i \dots l$ .  $\Lambda$  is the thermal de Broglie wavelength and  $u_0$  is the intensive static lattice energy when all particles are at the center of their cells. With these approximations, Helmholtz energy derivatives can eventually be calculated according to Eq. (3) and converted into thermodynamic properties,<sup>49</sup> cf. Table I.

A comparison of these three approaches is presented here in density dependent plots along isotherms. Besides thermodynamic data presented, the isochoric heat capacity at low temperatures is studied in the [supplementary material](#). For clarity, some isotherms are shifted to avoid overlaps. For a given thermodynamic quantity  $X$ , an offset

$$X_{\text{shifted}}(\rho, T_i) = X(\rho, T_i) + i \Delta_X, \quad (11)$$

was specified with  $i = 0, 1, 2, \dots, 7$  and  $T_0 = 1.3$ ,  $T_1 = 2.0$ ,  $T_2 = 3.5, \dots, T_7 = 30$ . In the figures discussed in this section, simulation results from the fluid phase close to the FL are shown for isotherm  $T = 1.3$  only. Presentation of simulation results was extended beyond the ML, covering the metastable solid in the two-phase region because superheated crystals are of significant interest.<sup>52,53</sup> Again, statistical uncertainties of the molecular simulation data are only shown in the plots if they exceed symbol size.

### A. First order derivative properties

Figure 10 presents pressure and enthalpy. Agreement between the EOS by van der Hoef,<sup>40</sup> LJD theory,<sup>49</sup> and present simulation results is very good. Enthalpy from LJD

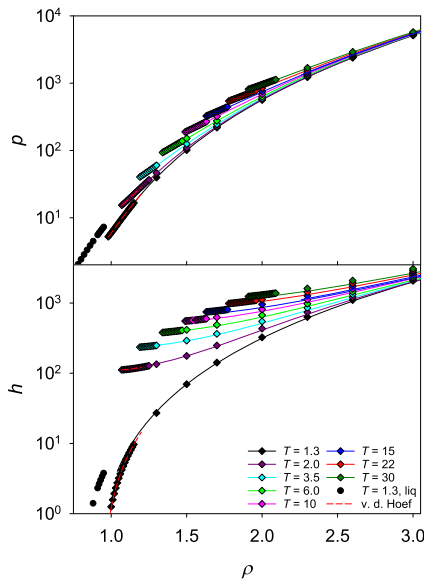


FIG. 10. Pressure  $p$  (top) and enthalpy  $h$  (bottom) of the fcc solid phase along different isotherms: (—) LJD theory,<sup>49</sup> (---) EOS by van der Hoef;<sup>40</sup> (●) present simulation data in the solid phase and (●) in the fluid phase at  $T = 1.3$ . Note the shift of the isotherms  $\Delta_h = 100$  according to Eq. (11).

theory<sup>49</sup> shows slight deviations to molecular simulation with increasing density and temperature.

### B. Heat capacities and premelting

The isochoric heat capacity  $c_v$  is shown in Fig. 11 (top). Agreement between LJD theory<sup>49</sup> and the simulation data is essentially perfect at higher densities, i.e., the relative deviation is only 0.1% at  $\rho = 3$ . Results of both methods approach the well-known Dulong-Petit value of  $c_v = 3$  at high densities. A minimum of  $c_v$  occurs along isotherms, followed by a sharp increase of the isochoric heat capacity approaching the ML. LJD theory<sup>49</sup> fails to reproduce this behavior of  $c_v$ . At least for  $T < 2$ , the EOS by van der Hoef<sup>40</sup> behaves correctly.

Independently generated internal energy data  $u$  allow for an additional approach to calculate the isochoric heat capacity  $c_v$ . Simulation runs were carried out along the isochore  $\rho = 1.05$  to calculate  $c_v$  from the Helmholtz energy derivative  $A_{20}$  as well as from its definition  $c_v = (\partial u / \partial T)_v$ . The derivative  $(\partial u / \partial T)_v$  was approximated by a central difference scheme, filtering magnified noise with Savitzky-Golay smoothing.<sup>54</sup> Figure 12 shows the results of both approaches. The agreement of the two simulation methods is very good. Both data sets show a strong increase of  $c_v$  approaching the ML at higher temperatures and approaching the sublimation line at lower temperatures. Agreement with the EOS by van der Hoef<sup>40</sup> is very good. At higher temperatures, the increase of  $c_v$  is not as pronounced as sampled by simulation. Both methods [using  $A_{20}$  or  $(\partial u / \partial T)_v$ ] were also applied for the fluid phase and compared to the EOS by Thol *et al.*<sup>24</sup> cf. Fig. 12. The results show an excellent consistency. The strong increase of  $c_v$  in the vicinity of the ML reflects a response to bulk premelting effects, a long-standing, but still unresolved phenomenon

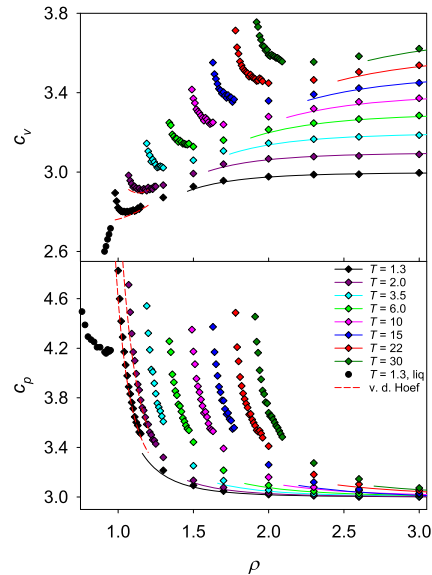


FIG. 11. Isochoric heat capacity  $c_v$  (top) and isobaric heat capacity  $c_p$  (bottom) of the fcc solid phase along different isotherms: (—) LJD theory,<sup>49</sup> (---) EOS by van der Hoef;<sup>40</sup> (●) present simulation data in the solid phase and (●) in the fluid phase at  $T = 1.3$ . Note the shift of the isotherms  $\Delta_{c_v} = 0.1$  according to Eq. (11).

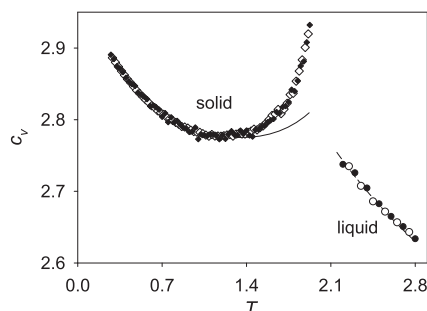


FIG. 12. Isochoric heat capacity  $c_v$  at  $\rho = 1.05$  in the fluid and fcc solid phase: (♦) present molecular simulation data in the fcc solid phase obtained from A20 and (○) numerically obtained from  $(\partial u/\partial T)_v$ ; (●) present simulation data in the fluid phase obtained from A20 and (○) numerically obtained from  $(\partial u/\partial T)_v$ ; (—) EOS by van der Hoef;<sup>40</sup> (---) EOS by Thol *et al.*<sup>24</sup>

in 3D crystals. Premelting can be thought of as a localized loss of crystalline order that can be observed well below the melting transition.<sup>55</sup> Melting normally starts at an interface as a heterogeneous process. In contrast, homogeneous melting occurs in surface-free bulk crystals in which the loss of crystalline order arises due to defects in the equilibrium lattice structure.<sup>56</sup> In molecular simulation, however, surface-free fcc crystals are typically maintained by periodic boundary conditions. It is well known that thermodynamic properties of solids experience strong variation in the vicinity of the ML due to lattice defects.<sup>57–59</sup> It is thus desirable to describe contributions of lattice defects concisely with a strict theoretical approach. However, a comprehensive theoretical framework that has been developed for 2D systems<sup>60–62</sup> could not be extended to 3D crystals so far. In 3D, the most reliable theories suggest that the defects breaking crystalline order are dislocation lines<sup>52,55,56,63–65</sup> that are emerging near the ML. Regardless of the fact that the microscopic mechanism of premelting is not fully understood, it is of interest to obtain quantitative information on the response behavior of thermodynamic properties due to these effects, which was one goal of this study.

The density dependence of the isobaric heat capacity  $c_p$  is presented in Fig. 11 (bottom). A strong increase of  $c_p$  close to the ML is observed. The agreement between LJD theory<sup>49</sup> and simulation is good at high density, where the results again approach the Dulong-Petit value of  $c_p = 3$ . The EOS by van der Hoef<sup>40</sup> agrees almost perfectly with the simulation data when approaching the ML. In contrast to  $c_v$ , the isobaric heat capacity does not exhibit a minimum along isotherms. Including the fluid region into the discussion, both heat capacities  $c_v$  and  $c_p$  exhibit a  $\lambda$ -like shape along isotherms (Fig. 11) as well as isochores (Fig. 12) across the solid-fluid transition.

### C. Other thermodynamic properties

The density dependence of the thermal pressure coefficient  $\gamma_v$  is shown in Fig. 13 (top). Outside the premelting zone,  $\gamma_v$  increases with increasing density. Close to the melting transition, it passes through a minimum and then rises at low temperatures, less pronounced as at higher temperatures.

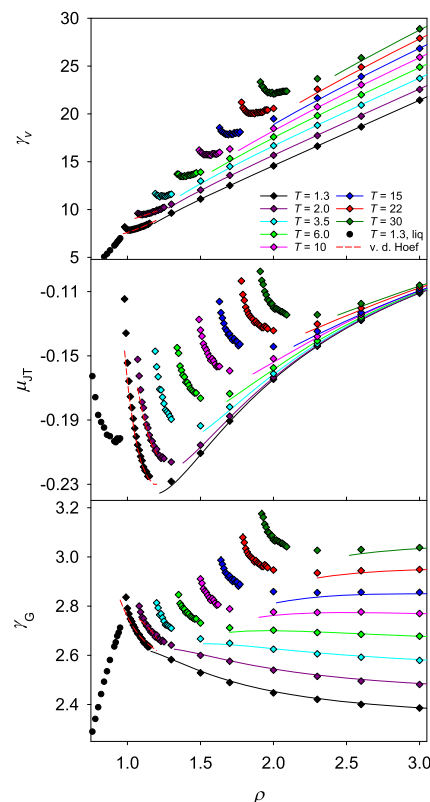


FIG. 13. Thermal pressure coefficient  $\gamma_v$ , Joule-Thomson coefficient  $\mu_{JT}$ , and Grüneisen parameter  $\gamma_G$  of the fcc solid phase along different isotherms: (—) LJD theory;<sup>49</sup> (---) EOS by van der Hoef;<sup>40</sup> (♦) present simulation data in the solid phase and (●) in the fluid phase at  $T = 1.3$ . Note the shift of the isotherms  $\Delta\gamma_v = 1.2$  and  $\Delta\gamma_G = 0.1$  according to Eq. (11).

Figure 13 (center) shows the Joule-Thomson coefficient  $\mu_{JT}$  along isotherms. The results obtained from the EOS by van der Hoef<sup>40</sup> agree very well with the present simulation data at low densities and temperatures, whereas LJD theory<sup>49</sup> agrees well at higher densities. A pronounced minimum occurs along all isotherms.

Isotherms of the Grüneisen parameter  $\gamma_G$  are presented in Fig. 13 (bottom), where simulated values exhibit only a very weak minimum at higher temperatures.  $\gamma_G$  depends strongly on density and temperature in the premelting region, and a weak temperature dependence is present at high densities. Considering also the fluid data at  $T = 1.3$ , again a  $\lambda$ -like shape of  $\gamma_G$  across the solid-fluid transition was observed. Thermodynamic properties discussed so far exhibit excellent agreement at higher densities between simulation data and LJD theory.<sup>49</sup> However, when approaching the ML, the simulation results show a strong variation in some properties, indicating a response to premelting effects. There, LJD theory<sup>49</sup> obviously does not contain the underlying physics. Instead, the EOS by van der Hoef,<sup>40</sup> as an equation correlated to simulation data, does describe the behavior of state properties in this region mostly with acceptable accuracy. However, there are thermodynamic properties for which LJD theory<sup>49</sup> much better predicts the phase behavior, at least qualitatively,

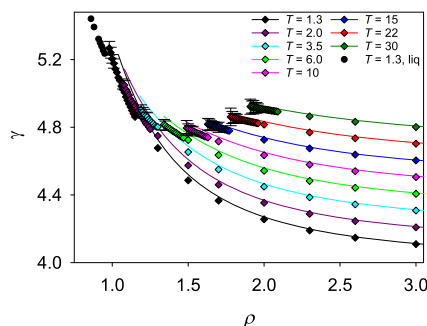


FIG. 14. Density scaling exponent  $\gamma$  of the fcc solid phase along different isotherms: (—) LJD theory;<sup>49</sup> (♦) present simulation data in the solid phase and (•) in the fluid phase at  $T = 1.3$ . Statistical uncertainties are only displayed if they exceed symbol size. Note the shift of the isotherms  $\Delta\gamma = 0.1$  according to Eq. (11).

sometimes up to the ML. These state variables are reported in the remainder of this section and in the [supplementary material](#).

The density scaling exponent  $\gamma$  from LJD theory<sup>49</sup> shows deviations with respect to simulation data close to the ML; however, the qualitative behavior is predicted correctly, cf. Fig. 14. At low temperatures,  $\gamma$  drops strongly with increasing density, approaching the postulated value of  $\gamma \approx 4.0$  at a very high density (and pressure).<sup>66</sup>

Figure 15 (top) shows the thermal expansion coefficient  $\alpha$ . Generally,  $\alpha$  decreases very quickly with increasing density. Simulation data and LJD theory<sup>49</sup> agree very well for all densities and temperatures up to the ML, with only minor deviations. Within its validity range, the EOS by van der Hoef<sup>40</sup> also coincides well with these calculations.

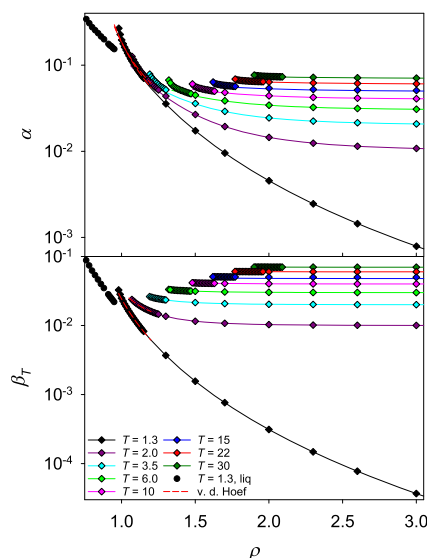


FIG. 15. Thermal expansion coefficient  $\alpha$  and isothermal compressibility  $\beta_T$  of the fcc solid phase along different isotherms: (—) LJD theory;<sup>49</sup> (---) EOS by van der Hoef;<sup>40</sup> (♦) present simulation data in the solid phase and (•) in the fluid phase at  $T = 1.3$ . Note the shift of the isotherms  $\Delta\alpha = 0.01$  and  $\Delta\beta_T = 0.01$  according to Eq. (11).

The isothermal compressibility  $\beta_T$  behaves similarly, as presented in Fig. 15 (bottom). All three calculation methods agree very well. At high temperatures, the density dependence is weak.

## VI. CONCLUSION

Essentially complete thermodynamic information on time independent properties was determined for the LJ potential over a large range of states from the high density fluid up to the fcc solid state. Such comprehensive thermodynamic descriptions of this state region, including the freezing/melting transition, are rare in the literature. Molecular simulation results were compared to the latest and most accurate models for the fluid and solid phases. It was found that these equations lead, at least for some thermodynamic properties, to an inconsistent thermodynamic behavior close to the FL or the ML. Due to the lack of experimental or molecular simulation data in this region, a number of investigations make use of extrapolations of such models. Precise thermodynamic information provided in this study should allow for more accurate statements. This study reports solid-fluid coexistence data at high temperatures that differ from data obtained with the GDI method. Calculations of thermodynamic stability coefficients suggest that the LJ system is in a stable solid state within the SFE range of the GDI method. Particular attention was also paid to the influence of premelting effects on thermodynamic properties near the ML. A theoretical framework describing premelting of 3D crystals has not been developed so far and simulations are a valuable tool for obtaining relevant information to do so. It was shown that a number of properties exhibit strong variations in the premelting zone. The question remains how these findings can be interpreted and how a connection to the underlying microscopic mechanisms can be established. One possible path was recently proposed by Köbler and Bodryakov,<sup>67</sup> describing heat capacity data by means of critical-like power functions.

## SUPPLEMENTARY MATERIAL

See [supplementary material](#) for additional results, a simulation parameter setting analysis, and all the underlying numerical Helmholtz energy derivative data.

## ACKNOWLEDGMENTS

The authors thank Rolf Lustig for providing a computer program to calculate different properties within the framework of his LJD theory<sup>49</sup> as well as for valuable advice and fruitful discussions. Furthermore, the authors gratefully acknowledge the Paderborn Center for Parallel Computing (PC<sup>2</sup>) for the generous allocation of computer time on the OCuLUS cluster and computational support by the High Performance Computing Center Stuttgart (HLRS) under the grant MMHBF2. The present research was conducted under the auspices of the Boltzmann-Zuse Society of Computational Molecular Engineering (BZS).

<sup>1</sup>J. C. Dyre, *J. Phys. Chem. B* **118**, 10007 (2014).

<sup>2</sup>D. Fragiadakis and C. M. Roland, *Phys. Rev. E* **83**, 031504 (2011).

- <sup>3</sup>D. Bolmatov, V. V. Brazhkin, and K. Trachenko, *Nat. Commun.* **4**, 2331 (2013).
- <sup>4</sup>Y. Rosenfeld and P. Tarazona, *Mol. Phys.* **95**, 141 (1998).
- <sup>5</sup>G. Ruppeiner, P. Mausbach, and H.-O. May, *Phys. Lett. A* **379**, 646 (2015).
- <sup>6</sup>R. Span, *Multiparameter Equations of State: An Accurate Source of Thermodynamic Property Data* (Springer Verlag, Berlin, 2000).
- <sup>7</sup>P. Mausbach, A. Köster, G. Rutkai, M. Thol, and J. Vrabec, *J. Chem. Phys.* **144**, 244505 (2016).
- <sup>8</sup>R. Span, T. Eckermann, S. Herrig, S. Hielscher, A. Jäger, and M. Thol, *TREND. Thermodynamic Reference and Engineering Data 3.0* (Lehrstuhl für Thermodynamik, Ruhr-Universität Bochum, Germany, 2016).
- <sup>9</sup>E. W. Lemmon, M. L. Huber, and M. O. McLinden, NIST reference fluid thermodynamic and transport properties-REFPROP, NIST Standard Reference Database 23, v9.1, 2002.
- <sup>10</sup>I. H. Bell, J. Wronski, S. Quoilin, and V. Lemort, *Ind. Eng. Chem. Res.* **53**, 2498 (2014).
- <sup>11</sup>R. Lustig, *Mol. Simul.* **37**, 457 (2011).
- <sup>12</sup>R. Lustig, *Mol. Phys.* **110**, 3041 (2012).
- <sup>13</sup>G. Rutkai, M. Thol, R. Span, and J. Vrabec, *Mol. Phys.* **115**, 1104 (2016).
- <sup>14</sup>A. Lotfi, J. Vrabec, and J. Fischer, *Mol. Phys.* **76**, 1319 (1992).
- <sup>15</sup>M. Heinen, J. Vrabec, and J. Fischer, *J. Chem. Phys.* **145**, 081101 (2016).
- <sup>16</sup>M. Horsch, J. Vrabec, and H. Hasse, *Phys. Rev. E* **78**, 011603 (2008).
- <sup>17</sup>M. Horsch, J. Vrabec, M. Bernreuther, S. Grottel, G. Reina, A. Wix, K. Schaber, and H. Hasse, *J. Chem. Phys.* **128**, 164510 (2008).
- <sup>18</sup>G. A. Fernandez, J. Vrabec, and H. Hasse, *Fluid Phase Equilib.* **221**, 157 (2004).
- <sup>19</sup>J. Vrabec, G. K. Kedia, G. Fuchs, and H. Hasse, *Mol. Phys.* **104**, 1509 (2006).
- <sup>20</sup>J. K. Johnson, J. A. Zollweg, and K. E. Gubbins, *Mol. Phys.* **78**, 591 (1993).
- <sup>21</sup>J. Kolafa and I. Nezbeda, *Fluid Phase Equilib.* **100**, 1 (1994).
- <sup>22</sup>M. Mecke, A. Müller, J. Winkelmann, J. Vrabec, J. Fischer, R. Span, and W. Wagner, *Int. J. Thermophys.* **17**, 391 (1996); Erratum **19**, 1493 (1998).
- <sup>23</sup>H.-O. May and P. Mausbach, *Phys. Rev. E* **85**, 031201 (2012); Erratum **86**, 059905 (2012).
- <sup>24</sup>M. Thol, G. Rutkai, A. Köster, R. Lustig, R. Span, and J. Vrabec, *J. Phys. Chem. Ref. Data* **45**, 023101 (2016).
- <sup>25</sup>S. Deublein, B. Eckl, J. Stoll, S. V. Lishchuk, G. Guevara-Carrion, C. W. Glass, T. Merker, M. Bernreuther, H. Hasse, and J. Vrabec, *Comput. Phys. Commun.* **182**, 2350 (2011).
- <sup>26</sup>C. W. Glass, S. Reiser, G. Rutkai, S. Deublein, A. Köster, G. Guevara-Carrion, A. Wafai, M. Horsch, M. Bernreuther, T. Windmann, H. Hasse, and J. Vrabec, *Comput. Phys. Commun.* **185**, 3302 (2014).
- <sup>27</sup>G. Rutkai, A. Köster, G. Guevara-Carrion, T. Janzen, M. Schappals, C. W. Glass, M. Bernreuther, A. Wafai, S. Stephan, M. Kohns, S. Reiser, S. Deublein, M. Horsch, H. Hasse, and J. Vrabec, "ms2: A molecular simulation tool for thermodynamic properties, release 3.0," *Comput. Phys. Commun.* (to be published).
- <sup>28</sup>D. Frenkel and B. Smit, *Understanding Molecular Simulation: From Algorithms to Applications* (Elsevier, San Diego, 2001).
- <sup>29</sup>H. Flyvbjerg and H. G. Petersen, *J. Chem. Phys.* **91**, 461 (1989).
- <sup>30</sup>J. Ge, G.-W. Wu, B. Todd, and R. J. Sadus, *J. Chem. Phys.* **119**, 11017 (2003).
- <sup>31</sup>P. Mausbach, A. Ahmed, and R. J. Sadus, *J. Chem. Phys.* **131**, 184507 (2009); Erratum **132**, 019901 (2010).
- <sup>32</sup>A. Ahmed and R. J. Sadus, *Phys. Rev. E* **80**, 061101 (2009).
- <sup>33</sup>A. Ahmed and R. J. Sadus, *J. Chem. Phys.* **131**, 174504 (2009); Erratum **133**, 229902 (2010).
- <sup>34</sup>A. Ahmed and R. J. Sadus, *J. Chem. Phys.* **133**, 124515 (2010).
- <sup>35</sup>J. R. Errington, *J. Chem. Phys.* **120**, 3130 (2004).
- <sup>36</sup>G. C. McNeil-Watson and N. B. Wilding, *J. Chem. Phys.* **124**, 064504 (2006).
- <sup>37</sup>U. R. Pedersen, *J. Chem. Phys.* **139**, 104102 (2013).
- <sup>38</sup>G. Grochola, *J. Chem. Phys.* **120**, 2122 (2004).
- <sup>39</sup>R. Agrawal and D. A. Kofke, *Mol. Phys.* **85**, 43 (1995).
- <sup>40</sup>M. A. Van der Hoef, *J. Chem. Phys.* **113**, 8142 (2000).
- <sup>41</sup>D. Heyes and A. Braňka, *J. Chem. Phys.* **143**, 234504 (2015).
- <sup>42</sup>J. Sousa, A. Ferreira, and M. Barroso, *J. Chem. Phys.* **136**, 174502 (2012).
- <sup>43</sup>E. A. Mastny and J. J. de Pablo, *J. Chem. Phys.* **127**, 104504 (2007).
- <sup>44</sup>V. P. Skripov and M. Z. Faizullin, *Crystal-Liquid-Gas Phase Transitions and Thermodynamic Similarity* (Wiley VCH, Weinheim, 2006).
- <sup>45</sup>W. G. Hoover, S. G. Gray, and K. W. Johnson, *J. Chem. Phys.* **55**, 1128 (1971).
- <sup>46</sup>V. Baidakov, S. Protsenko, and Z. Kozlova, *Chem. Phys. Lett.* **447**, 236 (2007).
- <sup>47</sup>V. Baidakov, S. Protsenko, and Z. Kozlova, *Fluid Phase Equilib.* **263**, 55 (2008).
- <sup>48</sup>M. A. van der Hoef, *J. Chem. Phys.* **117**, 5092 (2002).
- <sup>49</sup>R. Lustig, *Mol. Phys.* **115**, 1362 (2017).
- <sup>50</sup>G. Mie, *Ann. Phys.* **316**, 657 (1903).
- <sup>51</sup>J. A. Barker, *Lattice Theories of the Liquid State* (Pergamon Press, Oxford, 1963).
- <sup>52</sup>L. Gómez, C. Gazza, H. Dacharry, L. Peñaranda, and A. Dobry, *Phys. Rev. B* **71**, 134106 (2005).
- <sup>53</sup>A. Belonoshko, S. Davis, N. V. Skorodumova, P.-H. Lundow, A. Rosengren, and B. Johansson, *Phys. Rev. B* **76**, 064121 (2007).
- <sup>54</sup>A. Savitzky and M. J. E. Golay, *Anal. Chem.* **36**, 1627 (1964).
- <sup>55</sup>L. Gómez, A. Dobry, C. Geuting, H. Diep, and L. Burakovsky, *Phys. Rev. Lett.* **90**, 095701 (2003).
- <sup>56</sup>A. M. Alsayed, M. F. Islam, J. Zhang, P. J. Collings, and A. G. Yodh, *Science* **309**, 1207 (2005).
- <sup>57</sup>W. D. Kristensen, E. Jensen, and R. Cotterill, *Philos. Mag.* **30**, 229 (1974).
- <sup>58</sup>R. Crawford, W. Lewis, and W. Daniels, *J. Phys. C: Solid State Phys.* **9**, 1381 (1976).
- <sup>59</sup>V. Y. Bodryakov, *Tech. Phys.* **58**, 722 (2013).
- <sup>60</sup>J. M. Kosterlitz and D. J. Thouless, *J. Phys. C: Solid State Phys.* **6**, 1181 (1973).
- <sup>61</sup>D. R. Nelson and B. Halperin, *Phys. Rev. B* **19**, 2457 (1979).
- <sup>62</sup>A. Young, *Phys. Rev. B* **19**, 1855 (1979).
- <sup>63</sup>H. Kleinert, *Gauge Theory in Condensed Matter* (World Scientific, Singapore, 1989).
- <sup>64</sup>L. Burakovsky, D. L. Preston, and R. R. Silbar, *Phys. Rev. B* **61**, 15011 (2000).
- <sup>65</sup>L. Gómez, A. Dobry, and H. Diep, *Phys. Rev. B* **63**, 224103 (2001).
- <sup>66</sup>U. R. Pedersen, N. P. Bailey, T. B. Schröder, and J. C. Dyre, *Phys. Rev. Lett.* **100**, 015701 (2008).
- <sup>67</sup>U. Köbler and V. Bodryakov, *Int. J. Thermodyn.* **18**, 200 (2015).

### 3.14 Round Robin Study: Molecular Simulation of Thermodynamic Properties from Models with Internal Degrees of Freedom

M. Schappals, A. Mecklenfeld, L. Kröger, V. Botan, A. Köster, S. Stephan, E. J. Garcia, G. Rutkai, G. Raabe, P. Klein, K. Leonhard, C. W. Glass, J. Lenhard, J. Vrabec, H. Hasse, *Journal of Chemical Theory and Computation* 13:4270-4280, 2017.

DOI: [doi.org/10.1021/acs.jctc.7b00489](https://doi.org/10.1021/acs.jctc.7b00489)

Nachgedruckt mit Erlaubnis der American Chemical Society (Copyright 2017).

In dieser Arbeit wurde ein Ringversuch durchgeführt um statistische und systematische Fehler bei der Benutzung verschiedener molekularer Simulationswerkzeuge zu identifizieren. Dazu wurde unabhängigen Arbeitsgruppen der gleiche Simulationsauftrag erteilt um anschließend die Ergebnisse zu vergleichen. Dieser Simulationsauftrag beinhaltete die Berechnung von Dichten und potentiellen Energien für vier Reinstoffe unter der Verwendung von jeweils drei verschiedenen Kraftfeldern. Da alle diese Kraftfelder die inneren Freiheitsgrade der Moleküle berücksichtigten, konnte zusätzlich getestet werden, ob diese neu in *ms2* implementierte Funktion vergleichbare Ergebnisse zeigt. Die Studie kommt zu dem Schluss, dass systematische Abweichungen zwischen verschiedenen Arbeitsgruppen und Werkzeugen bei der hohen zugrundeliegenden Komplexität kaum vermeidbar sind.

Der Autor der vorliegenden Dissertation hat alle molekularen Vergleichssimulationen mit dem Simulationsprogramm *ms2* für die Universität Paderborn durchgeführt. Er wurde während des gesamten Prozesses betreut von Prof. Jadran Vrabec.

## Round Robin Study: Molecular Simulation of Thermodynamic Properties from Models with Internal Degrees of Freedom

Michael Schappals,<sup>†</sup> Andreas Mecklenfeld,<sup>‡</sup> Leif Kröger,<sup>§</sup> Vitalie Botan,<sup>§</sup> Andreas Köster,<sup>||</sup> Simon Stephan,<sup>†</sup> Edder J. García,<sup>†</sup> Gabor Rutkai,<sup>||</sup> Gabriele Raabe,<sup>‡</sup> Peter Klein,<sup>⊥</sup> Kai Leonhard,<sup>§</sup> Colin W. Glass,<sup>#</sup> Johannes Lenhard,<sup>▽</sup> Jadran Vrabec,<sup>||</sup> and Hans Hasse<sup>\*,†</sup>

<sup>†</sup>Laboratory of Engineering Thermodynamics (LTD), University of Kaiserslautern, Kaiserslautern, Germany

<sup>‡</sup>Institut für Thermodynamik (ift), Technische Universität Braunschweig, Braunschweig, Germany

<sup>§</sup>Lehrstuhl für Technische Thermodynamik (LTT), RWTH Aachen University, Aachen, Germany

<sup>||</sup>Thermodynamics and Energy Technology (ThEt), University of Paderborn, Paderborn, Germany

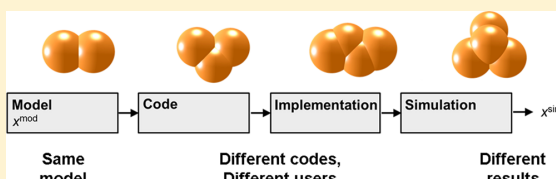
<sup>⊥</sup>Fraunhofer Institute for Industrial Mathematics (ITWM), Kaiserslautern, Germany

<sup>#</sup>High Performance Computing Center (HLRS), Stuttgart, Germany

<sup>▽</sup>Department of Philosophy, Bielefeld University, Bielefeld, Germany

### Supporting Information

**ABSTRACT:** Thermodynamic properties are often modeled by classical force fields which describe the interactions on the atomistic scale. Molecular simulations are used for retrieving thermodynamic data from such models, and many simulation techniques and computer codes are available for that purpose. In the present round robin study, the following fundamental question is addressed: Will different user groups working with different simulation codes obtain coinciding results within the statistical uncertainty of their data? A set of 24 simple simulation tasks is defined and solved by five user groups working with eight molecular simulation codes: DL\_POLY, GROMACS, IMC, LAMMPS, *ms2*, NAMD, Tinker, and TOWHEE. Each task consists of the definition of (1) a pure fluid that is described by a force field and (2) the conditions under which that property is to be determined. The fluids are four simple alkanes: ethane, propane, *n*-butane, and iso-butane. All force fields consider internal degrees of freedom: OPLS, TraPPE, and a modified OPLS version with bond stretching vibrations. Density and potential energy are determined as a function of temperature and pressure on a grid which is specified such that all states are liquid. The user groups worked independently and reported their results to a central instance. The full set of results was disclosed to all user groups only at the end of the study. During the study, the central instance gave only qualitative feedback. The results reveal the challenges of carrying out molecular simulations. Several iterations were needed to eliminate gross errors. For most simulation tasks, the remaining deviations between the results of the different groups are acceptable from a practical standpoint, but they are often outside of the statistical errors of the individual simulation data. However, there are also cases where the deviations are unacceptable. This study highlights similarities between computer experiments and laboratory experiments, which are both subject not only to statistical error but also to systematic error.



## 1. INTRODUCTION

Classical force fields that describe interactions on the atomistic level are widely used to model thermodynamic properties of fluids.<sup>1–6</sup> The theory which relates the force field to the thermodynamic properties is statistical thermodynamics, a well-established branch of science.<sup>7–9</sup> For a long time, the framework of statistical thermodynamics could practically only be applied to simple force fields. However, with the advent of computers and the corresponding development of numerical algorithms and codes, the application range of force fields for modeling thermodynamic properties has expanded drastically. This went along with an increasing number of publicly available codes, an increase in complexity of these codes and algorithms they are based on, an increase in

complexity of the input and output data, and an increasing number of users, many of which are not molecular simulations experts. The present discussion focuses on molecular simulations of thermodynamic properties of fluids, but the results can probably be regarded as typical for many other advanced simulations.

The question of whether a given force field is a good representation of a real fluid is not important for the present work. The sole interest rests on simulation, i.e., the way of retrieving the desired result from a given model. A schematic showing the steps of a simulation process is presented in Figure

**Received:** May 11, 2017

**Published:** July 24, 2017



1. Assume that a molecular model of a certain fluid is given and that a certain property of that fluid is of interest, e.g., its density



**Figure 1.** Schematic for the route from model to simulation result. The property  $x^{\text{mod}}$  described by the model is of interest and to obtain information on it, simulations have to be carried out. Here,  $x^{\text{mod}}$  is not directly accessible, only the simulation result  $x^{\text{sim}}$  is. Errors may occur in every step of the route.

at 300 K and 0.1 MPa, then there is a certain true value of that property  $x^{\text{mod}}$  for the given model. To obtain information on it, the model needs to be studied by simulation. Assume further that everything has to be done from scratch then appropriate algorithms from statistical thermodynamics and numerical mathematics have to be chosen and a corresponding computer code has to be written and implemented on a suitable computer. Only then simulations can be carried out, which will eventually yield a result  $x^{\text{sim}}$  for the property of interest.

It is important to realize that, apart from trivial cases,  $x^{\text{mod}}$  cannot be obtained, only  $x^{\text{sim}}$  can. All steps in the chain depicted in Figure 1 may lead to deviations between  $x^{\text{sim}}$  and  $x^{\text{mod}}$ . This is troublesome in many ways. For example, such differences affect the modeling process itself, which is an iterative procedure in which force field parameters are adjusted by comparing  $x^{\text{sim}}$  to corresponding experimental values  $x^{\text{exp}}$ .<sup>10</sup> Deviations between  $x^{\text{mod}}$  and  $x^{\text{sim}}$ , hence, directly affect parametrization and transferability of model parameters between different simulation codes.

In the discussion below, for brevity, we use terms like “the simulation results for *n*-butane”, acknowledging that this refers not to real *n*-butane but rather to some model of butane.

The situation depicted in Figure 1 is similar to that encountered in laboratory work in which real world objects are studied with experimental equipment. Let a real world quantity  $x^{\text{real}}$  be of interest. In order to get information on it, an experiment has to be carried out, which yields  $x^{\text{exp}}$  as a result. It is fully accepted for laboratory experiments that there are differences between  $x^{\text{real}}$  and  $x^{\text{exp}}$ . These inevitable deviations are usually classified in systematic errors and statistical errors, also called random errors.<sup>11</sup>

The same holds for computer experiments. There are inevitable deviations between  $x^{\text{sim}}$  and  $x^{\text{mod}}$ , and they can be classified in systematic errors and statistical errors. The existence of statistical errors is accepted for computer simulations and they are regularly quantified together with the molecular simulation results. The attitude toward systematic errors in computer simulation is more complicated. Their existence is not put into question, but many scientists consider them as resulting from faults, which can and have to be avoided.<sup>12,13</sup>

With the present study, we try to contribute to shaking this belief. Once some level of complexity is reached, not only statistical but also systematic errors become unavoidable in computer simulation. Measures need to be taken to reduce both statistical and systematic errors to a limit which is acceptable from a practical standpoint. With sufficient effort, this is possible in many cases. However, because there are always limits to the affordable effort, there will always be limits to the error level which can be reached in simulations.

Statistical errors can be assessed by repetition. In computer simulations this is often easier than in laboratory experiments.

Assessing systematic errors is much harder. The present round robin study responds to that challenge. Systematic errors of computer simulations are explicitly addressed by applying a straightforward technique: The same set of simulation tasks was given to different user groups working with different codes, and the results were compared. The question was whether they agree within the statistical uncertainty of the individual data.

Five academic groups participated in the present round robin study, cf. Table 1. During the study, the user groups were

**Table 1.** User Groups Which Participated in the Present Round Robin Study<sup>a</sup>

AA	RWTH Aachen University
BS	Technische Universität Braunschweig
FM	Fraunhofer Institute of Industrial Mathematics
KL	University of Kaiserslautern
PB	University of Paderborn

<sup>a</sup>The central instance was at University of Kaiserslautern.

connected only through a central instance and worked independently. A set of relatively simple molecular simulation tasks was defined; details are given below.

The participating groups worked with different well-established molecular simulation codes, of which the source codes are publicly available, cf. Table 2. In the early stages of

**Table 2.** Molecular Simulation Codes Used in the Present Study and User Groups in Which They Were Applied<sup>a</sup>

Code	Type	Ref	Group
DL_POLY	MD	17	BS
GROMACS	MD	18, 19	BS, KL
IMC	MC		PB
LAMMPS	MD	20	AA, KL
ms2	MD/MC <sup>b</sup>	21	KL, PB
NAMD	MD	22	FM
Tinker	MD	23	AA
TOWHEE	MC	24	BS

<sup>a</sup>MD stands for molecular dynamics and MC for Monte Carlo. <sup>b</sup>ms2 was operated as an MD engine, unless indicated by ms2\*, which refers to its usage as an MC engine.

this round robin study, two commercial molecular simulation tools were considered as well, of which the source codes are confidential. After having obtained very poor initial results and after unsuccessful contacts with the providers of these codes, both were excluded from the study. We do not wish to interfere with commercial interests and will therefore not disclose the names of these codes. The fact is nevertheless mentioned here because it indicates that the question of whether a source code is disclosed to the scrutiny of the scientific community or not is deeply related to their reliability.

Three different force fields with internal degrees of freedom (OPLS,<sup>14,15</sup> TraPPE,<sup>14</sup> and a modified OPLS version with bond stretching potential taken from the AMBER force field,<sup>16</sup> in the following named OPLSAMBER) were applied to model four simple alkanes: ethane, propane, *n*-butane, and iso-butane. The task was to use these force fields to determine the density and potential energy for a given set of liquid states, specified by a grid of temperature–pressure pairs.

The present results can be used as a benchmark for testing new algorithms and software. Such benchmarks are now hardly



available. In fact, the initial motivation of the present work was to obtain such a benchmark for testing a new version of the *ms2* code, which includes the internal degrees of freedom.

Recently, the National Institute of Standards and Technology (NIST) initiated a project to provide simulation reference data.<sup>25</sup> In this endeavor, NIST aims at building a database of well-documented molecular simulation results obtained with well-established simulation techniques. The documentation includes the statistical uncertainty of the data, whereas, up to now, the aspect of systematic errors in the data is not directly addressed in that project.<sup>25</sup>

The issue addressed here is closely related to the reproducibility of scientific results in a broader sense, where the question is this: How reproducible is information on a quantity  $x^{\text{mod}}$  defined by a model, which is only accessible by computer simulation, if different codes are used? This has been studied recently in depth in a round robin study for quantum chemical density functional theory (DFT) simulations, a field in which about 15,000 papers are published each year.<sup>26</sup> The authors did not only evaluate the current situation but also its past evolution and conclude that in their field the level of agreement of the results from different codes has very positively developed over the past decade and is close to reaching a satisfactory level.

The field we are considering here, obtaining precise data for thermodynamic properties from force fields with internal degrees of freedom, is much narrower than the field of quantum chemical DFT. This directly affects the amount of experience with the corresponding simulation codes and the amount of independent testing. It can be expected that this has consequences for the reproducibility of the results obtained with different codes.

The present paper is organized as follows: Initially, general remarks on statistical and systematic errors in molecular simulation are made, showing that systematic errors are the rule, not the exception. Next, the round robin study is explained in detail, including the specification of the simulation tasks. Subsequently, the results are discussed, first for the force fields without bond stretching and then for OPLSAMBER that includes bond stretching. We conclude with a general discussion of the findings and their consequences.

## 2. MOLECULAR SIMULATION ERRORS

**2.1. Statistical and Systematic Errors.** The results obtained in repetitions of a computer simulation usually differ. Hence, a set of more or less scattering results is obtained. The number for  $x^{\text{sim}}$  which is reported based on such a set is an average. Furthermore, some measure  $\sigma_x$  for the scatter of the data set can be obtained, e.g., the standard deviation. The deviation of the simulation result  $x^{\text{sim}}$  from the true value  $x^{\text{mod}}$  is the simulation error, cf. Figure 1. That error is considered to consist of two contributions, the statistical error, which is quantified by  $\sigma_x$ , and the systematic error, which is rarely addressed.

In equilibrium molecular simulations, as they were carried out in the present study, the statistical error is usually determined by the well-known block averaging technique.<sup>27</sup> Its basic idea is to divide the productive period of a simulation run in a number of blocks and to consider each block as a single run. Because the blocks are not truly independent, this is not rigorous, but as long as the blocks are large enough, block averaging is a practically useful approach. The block averages are then subjected to statistical analysis. The numerical results

obtained for  $\sigma_x$  depend not only on the length of the production run but also on the choice of the block size so that it is not straightforward to compare numbers for  $\sigma_x$  obtained differently. Furthermore, also the definition of  $\sigma_x$  may vary for different codes.

In this round robin study, systematic errors were assessed by the execution of the same set of simulation tasks in independent environments. In absence of systematic errors, the results obtained on this meta-level should agree within their statistical errors. However, as shown below, they do not. The scatter of the results on that meta-level obviously contains information on the systematic error that must be expected.

In the following, error sources in molecular simulations are briefly discussed. The list is not exhaustive but illustrates the plethora of error sources, which may be present in all steps of the molecular simulation process, cf. Figure 1.

The impact that a certain error source has on a given simulation result  $x^{\text{sim}}$  depends on various circumstances. The same error source may, e.g., lead to systematic or statistical error (or both), depending on the type of simulation result which is retrieved from the simulation run.

**2.2. Algorithmic Errors.** Statistical thermodynamics provides a solid foundation for molecular simulation. Its core is undisputed and a safe ground. The same holds for many of the algorithms built on that basis. However, when applied in simulations, these algorithms will usually entail errors. For example, in equilibrium simulations it is never possible to sample the entire phase space. Hence, the task is to select and run simulations such that the consequences of the errors are acceptable. Only some well-known aspects are mentioned here; more information on the individual aspects is available in the literature.<sup>8,9,13,28,29</sup>

**Simulation Period.** To rigorously apply statistical thermodynamics, simulations of infinite length would have to be carried out to study equilibrium states, which is obviously impossible. Therefore, the simulation period has to be extensive enough to ensure that the error from incomplete sampling is acceptable. To evaluate how long the run has to be may not be trivial.<sup>30,31</sup>

**Evaluation of Interactions.** For practical reasons, it is generally impossible to evaluate all interactions in the studied system explicitly, even if only pairwise additivity is assumed. The interactions are therefore usually cut off, and long-range corrections are applied. This quickly becomes nontrivial, e.g., for inhomogeneous systems, long-range (electrostatic) interactions, or regarding the application of different cut off schemes (center-of-mass, site-based).

**System Size.** The size of the simulation volume is finite. To avoid undesired boundary effects, techniques like periodic imaging are used. Poor choices may lead to artifacts.

**Equilibration Period.** In equilibrium simulations, the equilibration period which precedes productive sampling must be chosen such that the initial configuration, which is often unphysical, has no influence on the results. It may be nontrivial to decide, when this is the case.

**Choice and Realization of Ensemble.** Although theoretically the choice of the ensemble should not matter, in practice, it does. There are preferences depending on the type of study, and there are also well-known issues with thermostats and barostats.<sup>32,33</sup>

In the discussion above, only physical aspects of simulations were addressed. Additionally, numerical issues have to be considered which may lead to erroneous simulation results. Among these are errors related to time integration in MD

simulations or the construction of Markov chains in MC simulations, which have been extensively discussed in the literature.<sup>8,9</sup>

In many of the cases mentioned above, errors can be avoided or reduced to an acceptable level by carrying out suitable parametric studies. But carrying out such studies for each possible error source for each studied simulation scenario is practically impossible. This is especially true for large, time-consuming simulations. Experienced users will nevertheless generally be able to achieve trustworthy results, but there is no general guarantee that this is the case. The ground may become shaky without anybody noticing it. As illustrated above, many choices have to be made, which cannot be rigorously assessed so that algorithmic errors must be expected and accepted.

**2.3. Software Errors.** Writing complex codes inevitably entails errors. They sometimes lead to very undesirable consequences such as the retraction of scientific papers.<sup>34</sup> There are estimates for the number of errors per 1000 lines of code, which can be obtained from different sources, e.g., by monitoring bug fixes. For large codes, as they are used in molecular simulation, that number is expected to be in the range of 2 to 70 per 1000 lines of code.<sup>35</sup> Numbers at the low end of that range may be expected for comparatively simple codes with a large user community as well as professional development and maintenance. Numbers at the high end can be anticipated for complex codes used by small communities with unsystematic maintenance. For molecular simulation codes, which are generally developed and used in comparatively small academic communities, there should not be too much optimism in this respect. For a typical molecular simulation code of about 100,000 lines, hence, several 100 up to several 1000 errors have to be expected. Fortunately, not all software bugs have an influence on every simulation result. But assuming that there is no influence of software bugs on molecular simulation results would be naive.

The above discussion shows how important professional maintenance of molecular simulation software is, including a feedback system from the user community. Good software requires a continuous effort in debugging. The discussion also highlights the potential advantage of open source over proprietary codes, if a suitable maintenance system and a strong core development team are established.

**2.4. Implementation Bugs.** Molecular simulation is computationally intensive and therefore usually deployed across multiple compute units. However, parallelization renders algorithms more intricate, thereby increasing the likelihood of algorithmic errors and software bugs. For example, a shared memory parallelization of a linked-cell algorithm is prone to suffer from race conditions, which can lead to unexpected behavior.<sup>36</sup>

Molecular simulation codes are usually written in compiled languages, such as C or Fortran to achieve high levels of computational performance. Compilers are extremely complex pieces of software, involving millions of lines of code and a large parameter space defining their behavior. Arguably, the behavior of a compiler cannot be fully predicted, leading to a number of potential pitfalls. When using, e.g., high optimization levels, compilers will aggressively rearrange or even delete instructions, which may have unexpected consequences.

**2.5. Errors in Evaluation of Simulation Results.** The amount of data generated in molecular simulations is extremely large. Most of the primary data are discarded already during the simulation run, and postprocessing of the data is required. This

may include sophisticated steps like identification of events and visualization. For simplicity, these steps are considered here as an integral part of the simulation process itself, cf. Figure 1. But it is acknowledged that errors may also occur in the evaluation of molecular simulation data.

**2.6. User Error.** The input data of the simulation are classified here as follows: (1) specifying the model, (2) specifying the scenario, (3) controlling the algorithms (physical, numerical), (4) controlling the compilation, (5) controlling the actual simulation run, and (6) controlling the evaluation of the simulation results. Any input data are prone to user error.

The importance of user errors has recently been discussed by Wong-ekkabut and Karttunen in a paper entitled: *The good, the bad, and the user in soft matter simulations*,<sup>37</sup> in which they give many nontrivial examples for user errors and conclude that the user is the “most significant error source” and that “one does not become a theorist by buying chalk, experimentalist by buying a microscope, or a computational scientist by downloading software”. On the basis of the experience from the present work, we fully agree and add only that user errors are not a privilege of rookies but regularly happen to experienced users as many examples show.<sup>34</sup>

### 3. ROUND ROBIN STUDY

**3.1. Procedure.** The user groups and simulation codes participating in the present round robin study are summarized in Tables 1 and 2. The procedure is illustrated in Figure 2. The

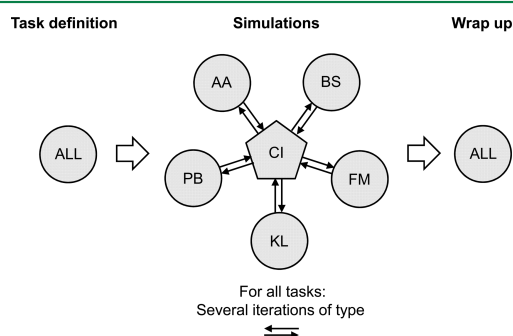


**Figure 2.** Overview of the round robin study. During the simulation phase the five user groups (AA, BS, FM, KL, PB) worked independently, connected only by the central instance (CI).

central instance was at University of Kaiserslautern, and it connected the user groups during the simulation phase of the study, in which the user groups worked independently. Communication between the groups took place only during the preliminary phase, before the simulations were performed, and during the wrap-up phase.

In the preliminary phase of the round robin study, the tasks were defined. Each task is a physical problem to be solved by simulation. More information on the tasks is given in the next section. In addition, simulation settings were specified in the preliminary phase. All production runs were carried out in the isobaric–isothermal (NpT) ensemble with 512 molecules. The cutoff radius was calculated with respect to the center-of-mass and was 14 Å, except for Tinker with 15 Å and IMC with almost half of the edge length of the simulation volume. Statistical errors were estimated by block averaging with a block size of 5000 time steps for MD simulations and at least 1.5 ×

$10^6$  trial displacements for MC simulations. The reported numbers are the standard deviation  $\sigma$  of the block averages. More information is given in the [Supporting Information](#).

Accounting for differences between the codes and the on-site situation of the participating user groups, e.g., regarding computer access, the choices for simulation settings were only recommended and could always be overruled by the general guideline that all groups should work to the best of their knowledge with their codes, while respecting the agreed feedback times of the round robin study. A list of the employed hardware, compilers, and parallelization strategies is given in the [Supporting Information](#).

It turned out to be necessary to carry out several iterations because an inspection of the results submitted to the central instance after the first iteration partially revealed very large differences, cf. [Supporting Information](#) for an example. Most of these differences could later be traced back to different types of input errors or faulty communication. For example, it turned out to be particularly cumbersome that in different codes different types and implementations of intramolecular potentials functions are used. Some of the errors would in the end probably have been eliminated also by a user group working on its own, e.g., by checking internal consistency. But other errors would have remained hidden had the simulations not been carried out in a round robin study. This also illustrates the need for carrying out several iterations in this round robin study. After every iteration, the results were compared by the central instance, and qualitative feedback was given to the participating groups. The feedback consisted only of an indication of those results which deviated strongly from a set of results obtained by other user groups, which showed much better mutual agreement.

Within each iteration step, the reaction to feedback from the central instance was in the sole responsibility of the respective user group. It generally consisted of checking the input parameters and carrying out new simulations with modified parameters. It has to be mentioned that even cryptic feedback, as it was given, may contain valuable information for the search for errors, namely, when only certain results of the respective group were challenged, whereas others were (implicitly) confirmed. This procedure eliminated most gross errors over time.

During every iteration, each user group executed the assigned tasks within several weeks. Subsequently, the results from all groups were reported to the central instance, which evaluated them and gave feedback as described above. On the basis of that feedback, the next iteration was started. The criterion to end the iterations was simply a time-out after about six months. Only the final results are reported below. They would have changed further had the iterations continued.

**3.2. Tasks.** The idea was to select a set of comparatively simple molecular simulation tasks and to focus on the quantitative accuracy of the results. The tasks were exactly the same for all groups, but not all codes could be used for all tasks. They consisted of finding numbers for the specific density  $\rho$  and the molar potential energy  $u$  of different fluid models for a range of liquid state points. The molar potential energy  $u$  was calculated from the contributions of all pair-potentials, i.e., intra- and intermolecular, excluding the kinetic energy. For brevity,  $\rho$  is referred to as density and  $u$  as energy in the following.

Four substances were considered in the study: ethane, propane, *n*-butane, and iso-butane. They have an increasing

complexity with respect to the intramolecular interactions but are similar with respect to the intermolecular interactions. Twelve state points at temperatures of 98, 173, 248, and 298 K and pressures of 5, 41, and 70 MPa were chosen, where all considered substances are liquid. The large number of state points allows for assessing the internal consistency of the corresponding data set.

[Table 3](#) gives an overview of the considered force fields; their parameters are reported in the [Supporting Information](#). All

**Table 3. Studied Force Fields**

Force field	Description	Ref
OPLS	Optimized potentials for liquid simulations	14, 15
TraPPE	Transferable potentials for phase equilibria	14
OPLSAMBER	OPLS with stretching vibrations from AMBER	14–16

force fields describe the alkyl groups on the basis of the united atom approach and account for the internal degrees of freedom. However, OPLS and TraPPE do not account for bond stretching. Therefore, when ethane is described with these force fields, it is a rigid body, which is realized by constraint algorithms.

To also include a force field with high frequency bond stretching vibrations, the OPLS force field was modified by including the bond stretching potential from the AMBER force field, named OPLSAMBER here. Using that simple combination is not critical here as the aim is not the comparison to experimental data. For intermolecular interactions between unlike sites, the Lorentz–Berthelot combining rules were used throughout.

The following restrictions regarding the application of the present simulations codes to the studied force fields were encountered: IMC, *ms2*\*(MC), and NAMD cannot handle fixed bond lengths and were therefore only used for OPLSAMBER. LAMMPS cannot handle models constraining three or more consecutive bond stretching vibrations and was thus not used for *n*-butane with OPLS and TraPPE. The results obtained with Tinker for the energy are not reported here because the energy calculation was erroneous in this study. The source of this deviation could not be identified until the time-out of this work.

## 4. RESULTS AND DISCUSSION

**4.1. Overview.** Systematic errors were investigated by solving identical simulation tasks with different codes, running on different computers, operated by different user groups. In the following, we simply refer to this as “results of different groups”, even though there are cases in which results were produced with different codes by the same user group. The main interest lies on quantitative differences between the results of the different groups, while comparison with experimental data is not of interest.

First, the results for the two force fields without bond stretching (OPLS and TraPPE) and subsequently those for the force field with bond stretching (OPLSAMBER) are discussed because the findings with respect to the systematic errors differ between these groups. As expected, the findings regarding the systematic errors do not differ significantly for data sets obtained for different pressures. Therefore, mainly results at 41 MPa are discussed. The numerical simulation results from the present study including information on the statistical

uncertainties as obtained from the respective programs are reported in the [Supporting Information](#).

**4.2. Force Fields without Bond Stretching. 4.2.1. Density.** Before entering a broader discussion of the results, a typical example is presented and discussed in detail. The results for the density of *n*-butane at 41 MPa obtained with the OPLS force field are chosen for this purpose. Results obtained after the first iteration are shown in the [Supporting Information](#), the final ones in [Figure 3](#). After elimination of the gross errors

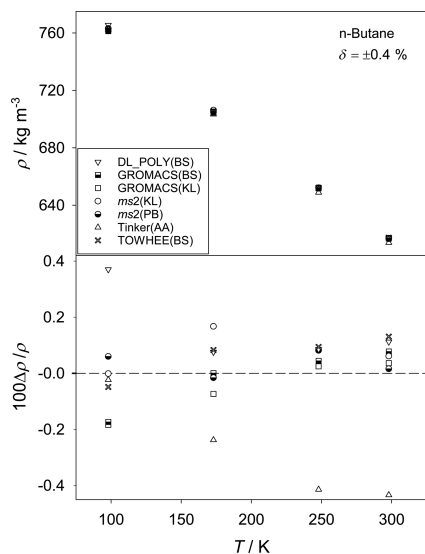


**Figure 3.** Density of *n*-butane at 41 MPa from the OPLS force field as a function of temperature. Symbols: results from different groups working with different codes. Top: absolute numbers. Bottom: relative deviations from the arithmetic mean value (dashed line). Here,  $\delta$  indicates the width of the band in which these relative deviations lie and is taken here as an estimate for the systematic uncertainty of the data.

during the iterations, the results seem to agree very well at a first glance, cf. [Figure 3](#) (top). The scatter of the results is only about  $\pm 3 \text{ kg/m}^3$ , which is acceptable for many applications.

For a detailed discussion of the results, the arithmetic mean of the results from the different groups was calculated and the relative deviation of the individual results from that arithmetic mean determined. Taking the arithmetic mean as a guess for the true model value for the density, the deviation can be interpreted as the uncertainty resulting from systematic error. The result for the above example is included in [Figure 3](#) (bottom). The deviations lie in a band of  $\delta = \pm 0.4\%$  in that case. Two of the programs, GROMACS and *ms2*, were both used by two different groups. The corresponding results agree within  $\pm 0.2\%$ .

We refrain here from entering a detailed discussion of results of individual simulation codes or different algorithms. This would inevitably lead to discussing their strengths and weaknesses and would have to include benchmarking computational performance, which is not in the scope of the present study.

The above results for the deviations have to be compared to the statistical uncertainty of the individual results. The error bars are not included in [Figure 3](#) for clarity. The data obtained

for the case studied here at 98 and 248 K are used to discuss this topic exemplarily in [Figure 4](#). The error bars reported in

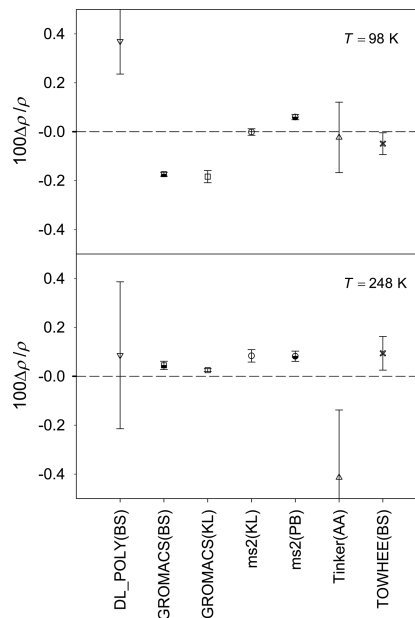


**Figure 4.** Statistical uncertainty of the data obtained for the density of *n*-butane at 41 MPa and 98 K (top) and 248 K (bottom) from the OPLS force field. Symbols: mean values with error bars determined from block averages of the production phase. The large error bars of the DL\_POLY and Tinker data are due to the chosen barostat. Dashed line: arithmetic mean of all results.

[Figure 4](#) were determined from an evaluation of the block averages of the production phase and represent the standard deviation  $\sigma$ . The large error bars obtained from DL\_POLY and Tinker are related to fluctuations in pressure and temperature for these programs, where they were up to  $\pm 5 \text{ MPa}$  and  $\pm 5 \text{ K}$  for DL\_POLY and Tinker and below  $\pm 0.2 \text{ MPa}$  and  $\pm 0.1 \text{ K}$  for the other three programs. At 248 K, all results agree within  $\pm 0.1\%$ , with Tinker being the sole exception. At 98 K, the results agree within  $\pm 0.2\%$ , again with one exception, i.e., DL\_POLY. However, the comparably large deviations of Tinker and DL\_POLY from the average of all results are still within the large error bars for these simulations. But for many of the other results, which have distinctly smaller error bars, the deviation of the results from the mean of all results clearly exceeds the error bar. Not even the results obtained with the same code by different groups agree within their error bars in all cases.

Regarding the data obtained at 248 K, cf. [Figure 4](#) (bottom), it can be argued that after removal of the Tinker result, a more favorable picture would be obtained. The average of all results would be shifted upward, and the deviation of the remaining results from the average would be within the error bars in most cases. However, this statement is biased by arbitrarily disregarding one result. But even if such a bias was accepted, which we do not, and a similar procedure would be repeated for the data obtained at 98 K, the results would still not match within their error bars, cf. [Figure 4](#) (top). The results shown in [Figure 4](#) are typical. In general, the results from the different



simulation codes do not agree within their statistical uncertainty.

It should be noted that we simply report and evaluate the data as they were obtained in the final iteration. Further improvements would have been possible if more time would have been given for the round robin study. For example, in the above case, the groups working with Tinker and DL\_POLY could have revisited the particular simulations and could have worked on the barostat parameters or other settings. But this merely shows that it is fairly easy to adjust simulation settings to obtain a desired value, which is obviously unacceptable.

Furthermore, one could argue that some programs are more reliable than others and therefore should be preferred. While this may be true, we refrain from an assessment of simulation codes, a task which is out of the scope of the present study. We also note that a discussion of the quality of the codes would have to have been led, if the sole aim of the study would have been the determination of reference data. Nevertheless, the unbiased data from the present study can well be used as reference data, although reference values with even smaller error bars could probably be obtained in a dedicated study.

The results obtained for the density of the other three substances with the OPLS force field at 41 MPa are shown in Figures 5, 6, and 7. They basically confirm the results for *n*-

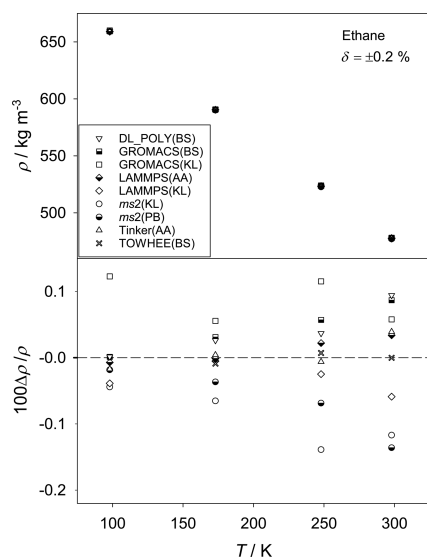


**Figure 5.** Density of ethane at 41 MPa from the OPLS force field as a function of temperature. Symbols: results from different groups working with different codes. Top: absolute numbers. Bottom: relative deviations from the arithmetic mean value (dashed line). Here,  $\delta$  is the width of the band in which the relative deviations of the individual results from their arithmetic mean lie.

butane. Also, values for  $\delta$  are reported, which indicate the width of the band in which the relative deviations of the individual results around their arithmetic mean lie. The value of  $\delta$  is taken here as an estimate for the systematic uncertainty of the simulation data. For the discussed case, the results here are  $\delta = \pm 0.4\%$  for *n*-butane (cf. Figure 3),  $\pm 0.2\%$  for ethane and propane (cf. Figures 5 and 6), and  $\pm 0.6\%$  for iso-butane (cf. Figure 7). Note that even the small value for ethane exceeds the statistical uncertainty of the simulation data in most cases.

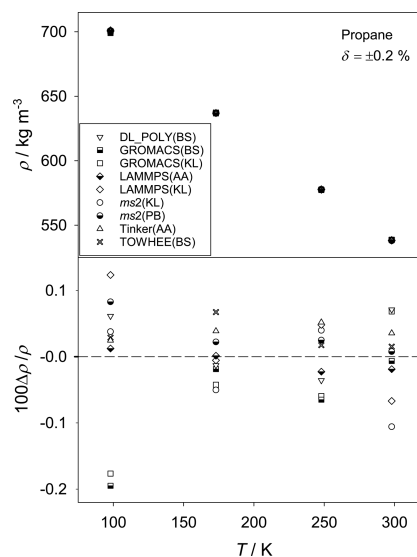


**Figure 6.** Density of propane at 41 MPa from the OPLS force field as a function of temperature. Symbols: results from different groups working with different codes. Top: absolute numbers. Bottom: relative deviations from the arithmetic mean value (dashed line). Here,  $\delta$  is the width of the band in which the relative deviations of the individual results from their arithmetic mean lie.

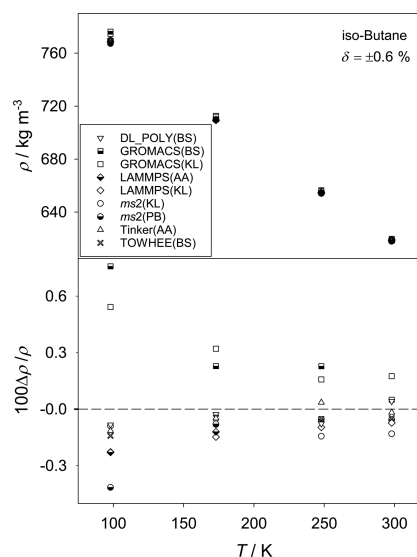


**Figure 7.** Density of iso-butane at 41 MPa from the OPLS force field as a function of temperature. Symbols: results from different groups working with different codes. Top: absolute numbers. Bottom: relative deviations from the arithmetic mean value (dashed line). Here,  $\delta$  is the width of the band in which the relative deviations of the individual results from their arithmetic mean lie.

The corresponding results for the TraPPE force field as well as the data for the other pressure levels obtained with the OPLS and TraPPE force fields are presented in the Supporting Information in numerical form. They all confirm the statements above.

**4.2.2. Energy.** The data obtained for the molar potential energy  $u$  of the studied alkanes as a function of the temperature with the OPLS force field are presented in Figure 8.

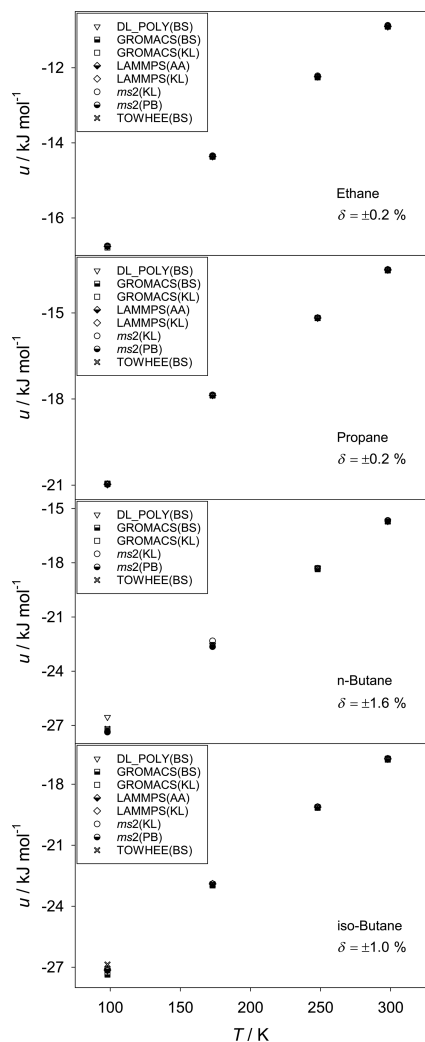


**Figure 8.** Energy of ethane, propane, *n*-butane, and iso-butane (from top to bottom) at 41 MPa from the OPLS force field as a function of temperature. Symbols: results from different groups working with different codes. Here,  $\delta$  is the width of the band in which the relative deviations of the individual results from their arithmetic mean lie.

Figure 8 contains numbers for  $\delta$ , which characterize the scatter of the results from the different groups. They are taken here as a measure for the systematic error, i.e.,  $\delta = \pm 0.2\%$  for ethane and propane,  $\pm 1.0\%$  for iso-butane, and  $\pm 1.6\%$  for *n*-butane. The statistical uncertainties of the individual results are similar to those for the density, i.e., about  $\pm 0.05\%$  for GROMACS and *ms2*,  $\pm 0.1\%$  for TOWHEE, and  $\pm 0.3$  to  $1.2\%$  for DL\_POLY. As for the density, the deviations between the results from the different groups are generally outside of the statistical uncertainty of the individual results. The results from the TraPPE force field are similar and listed numerically in the Supporting Information.

**4.3. Force Fields with Bond Stretching.** **4.3.1. Density.** Figure 9 shows the results for the density of the alkanes

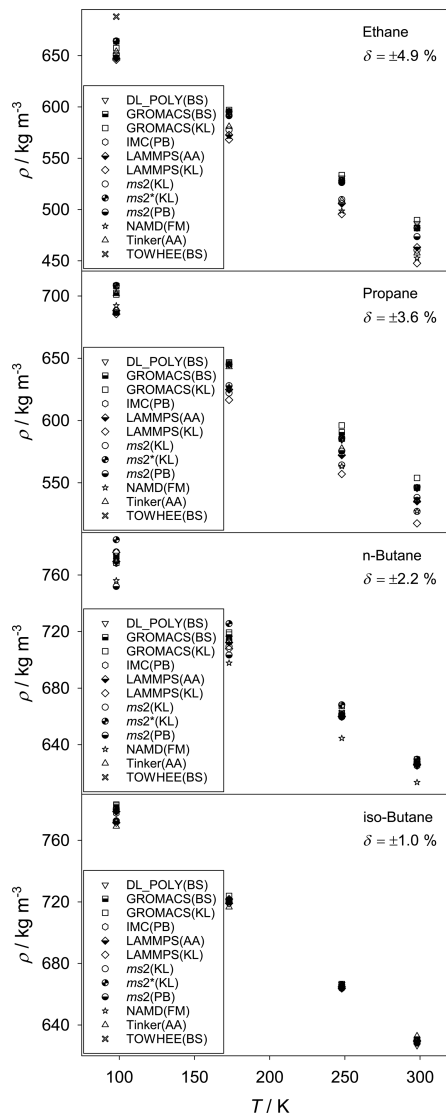


**Figure 9.** Density of ethane, propane, *n*-butane, and iso-butane (from top to bottom) at 41 MPa from the OPLSAMBER force field as a function of temperature. Symbols: results from different groups working with different codes. Here,  $\delta$  is the width of the band in which the relative deviations of the individual results from their arithmetic mean lie.

obtained with the OPLSAMBER force field for which all simulation codes could be used. The scatter of the data obtained by the different groups is much larger than for the force fields without bond stretching, i.e.,  $\delta = \pm 4.9\%$  for ethane,  $\pm 3.6\%$  for propane,  $\pm 2.2\%$  for *n*-butane, and  $\pm 1.0\%$  for iso-butane and, hence, roughly one order of magnitude larger than those found in the studies presented above. The results for the density deviate by up to about  $50 \text{ kg/m}^3$ , which is unacceptable for many applications. It is pointed out that the results

presented in Figure 9 are those at the end of the iterations of the round robin study, i.e., after elimination of gross errors.

The statistical uncertainties are exemplarily shown in Figure 10 for *n*-butane at 41 MPa and 173 and 248 K. The error bars

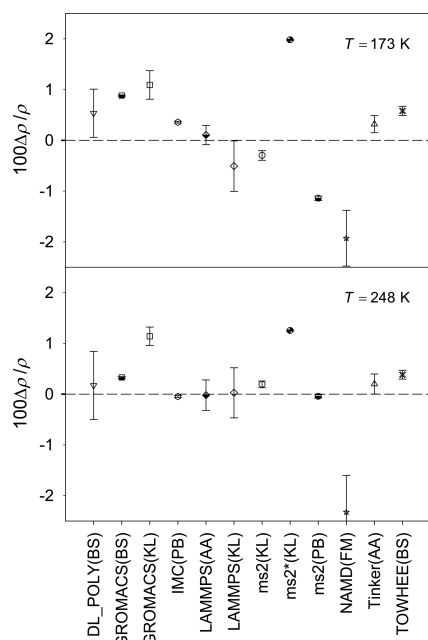


**Figure 10.** Statistical uncertainty of the data obtained for the density of *n*-butane at 41 MPa and 173 (top) and 248 K (bottom) from the OPLSAMBER force field. Symbols: mean values with error bars determined from block averages of the production phase. Dashed line: arithmetic mean of all results.

of the individual results obtained by the different groups have the same order of magnitude as for the force fields considered in Section 4.2 and range between about  $\pm 0.05$  and  $\pm 0.5\%$ . The deviations between the results obtained by the different groups are, hence, much larger than the individual statistical uncertainties. This holds even in cases in which the same program was used by different groups. The results for the other pressure levels are similar.

The only difference between the OPLS and OPLSAMBER force fields is the consideration of bond stretching. It is evident to assume that this is the cause of the large deviations. In the MD simulations shown in Figure 10 different time steps were used. In the range of 0.12–1.2 fs no systematic influence of the time step was observed. For example, the LAMMPS results shown in Figure 10 agree, even though they were obtained with time steps differing by a factor of 10.

Another interesting finding that might shed light on the reasons of the discrepancies is the following: for both OPLS and TraPPE an increase of the deviations between the results from the different groups as measured by  $\delta$  was observed for increasing complexity of the molecule, i.e., going from ethane to the butanes, cf. Section 4.2. The opposite trend was found for OPLSAMBER, cf. Figure 9.

In general, with increasing model complexity also the complexity of the model evaluation increases, which in turn

leads to an increase of the number of potential sources of systematic error of the simulation result.

**4.3.2. Energy.** The results obtained from the OPLSAMBER force field for the energy at 41 MPa are presented in Figure 11.

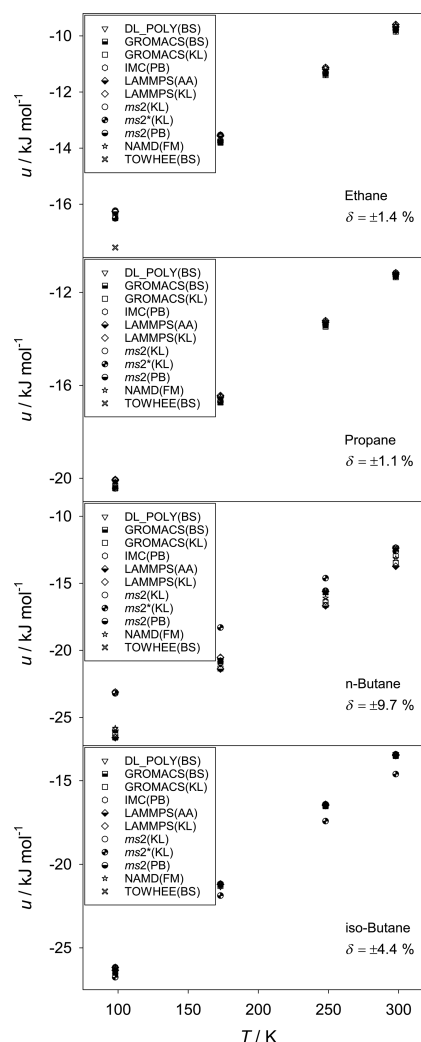


**Figure 11.** Energy of ethane, propane, *n*-butane, and iso-butane (from top to bottom) at 41 MPa from the OPLSAMBER force field as a function of temperature. Symbols: results from different groups working with different codes. Here,  $\delta$  is the width of the band in which the relative deviations of the individual results from their arithmetic mean lie.

Again, the results for the other pressure levels are similar. The results obtained by different groups deviate, generally, by  $\delta = \pm 1.4\%$  for ethane,  $\pm 1.1\%$  for propane,  $\pm 9.7\%$  for *n*-butane, and  $\pm 4.4\%$  for iso-butane. The statistical uncertainties reported by the different codes are typically in the range of  $\pm 0.1\%$  to  $0.6\%$ . Hence the deviations between the results from the different groups exceed the statistical uncertainty of the individual results by far, which underpins the above statements on the importance of systematic errors.



## 5. CONCLUSIONS

The present work addresses the issue of systematic errors in molecular simulation. The quality of the models, i.e., the question whether they are a good description of some real fluid or not, is not addressed.

Statistical and systematic errors were assessed by a round robin study. The same set of simulation tasks was given to independently working user groups, which used different molecular simulation codes for solving the tasks. Under ideal circumstances, i.e., in the absence of systematic errors, the results from the different groups should agree within their statistical uncertainties. The results show that this is not the case in reality. The present study is the first of its kind and addresses the issue on a broad front. There were five participating groups, which worked with eight different molecular simulation codes. The tasks were quite simple: the determination of the density and the potential energy of four pure liquids, i.e., ethane, propane, *n*-butane, and iso-butane, on a given temperature–pressure grid. Three molecular model types were used, all of them with internal degrees of freedom.

The collected data demonstrate that systematic errors are important in molecular simulations. In many cases, the deviations between the results obtained by the different groups far exceed the statistical uncertainty of the individual results. Potential reasons for these errors are plentiful and are briefly discussed. Systematic errors can probably not be completely avoided once a certain degree of simulation complexity is reached. This is highlighted by the fact that the deviations between the results from the different groups were distinctly larger for more complex force fields.

We emphasize that it must be the goal to aim at entirely avoiding systematic errors in molecular simulations. However, there should be no doubt that fully achieving this goal is practically impossible.

## ■ ASSOCIATED CONTENT

### Supporting Information

The Supporting Information is available free of charge on the ACS Publications website at DOI: 10.1021/acs.jctc.7b00489.

Results after the first iteration, detailed information on hardware, parallelization, and compilers, and detailed descriptions of the simulation settings and force field specifications, as well as numerical results of all simulation tasks carried out in this work. (PDF)

## ■ AUTHOR INFORMATION

### Corresponding Author

\*E-mail: [hans.hasse@mv.uni-kl.de](mailto:hans.hasse@mv.uni-kl.de).

### ORCID

Michael Schappals: 0000-0002-8131-2027

Leif Kröger: 0000-0003-0463-1726

Jadran Vrabec: 0000-0002-7947-4051

### Notes

The authors declare no competing financial interest.

## ■ ACKNOWLEDGMENTS

L. Kröger, V. Botan, and K. Leonhard thank the Deutsche Forschungsgemeinschaft (DFG) for support within SFB 985 “Functional microgels and microgel systems”. Simulations were performed with computing resources granted by RWTH Aachen University under project rwth0083. A. Mecklenfeld

acknowledges funding by a Georg-Christoph-Lichtenberg fellowship by the federal state of Lower Saxony, Germany. The GROMACS simulations were performed on a cluster of North-German Supercomputing Alliance (HLRN). A. Mecklenfeld and G. Raabe greatly appreciate their support. A. Köster, G. Rutkai, and J. Vrabec gratefully acknowledge financial support by BMBF under Grant 01IH13005A “SkaSim: Skalierbare HPC-Software für molekulare Simulationen in der chemischen Industrie”. Furthermore, they acknowledge the Paderborn Center for Parallel Computing (PC<sup>2</sup>) for the generous allocation of computer time on the OCULUS cluster. M. Schappals, S. Stephan, E. García, and H. Hasse gratefully acknowledge financial support within the Reinhart Koselleck Program (HA1993/15-1) of the German Research Foundation (DFG). Simulations were performed on *elwe* at the Regional University Computing Center Kaiserslautern (RHRK) under Grant TUKL-TLMV. The groups of the University of Kaiserslautern and the University of Paderborn gratefully acknowledge computational support by the High Performance Computing Center Stuttgart (HLRS) under Grant MMHBF2. Simulations of both groups were conducted under the auspices of the Boltzmann-Zuse Society of Computational Molecular Engineering (BZS).

## ■ REFERENCES

- (1) Jorgensen, W. L.; Madura, J. D.; Swenson, C. J. Optimized intermolecular potential functions for liquid hydrocarbons. *J. Am. Chem. Soc.* **1984**, *106*, 6638–6646.
- (2) Jorgensen, W. L.; Maxwell, D. S.; Tirado-Rives, J. Development and Testing of the OPLS All-Atom Force Field on Conformational Energetics and Properties of Organic Liquids. *J. Am. Chem. Soc.* **1996**, *118*, 11225–11236.
- (3) van Gunsteren, W. F.; Daura, X.; Mark, A. E. GROMOS Force Field. *Encyclopedia Comput. Chem.* **1998**, *2*, 1211–1216.
- (4) Yang, L.; Tan, C.-h.; Hsieh, M.-j.; Wang, J.; Duan, Y.; Cieplak, P.; Caldwell, J.; Kollman, P. A.; Luo, R. New-Generation Amber United-Atom Force Field. *J. Phys. Chem. B* **2006**, *110*, 13166–13176.
- (5) Vrabec, J.; Huang, Y.-L.; Hasse, H. Molecular models for 267 binary mixtures validated by vapor-liquid equilibria: A systematic approach. *Fluid Phase Equilib.* **2009**, *279*, 120–135.
- (6) Eggimann, B. L.; Sunnarborg, A. J.; Stern, H. D.; Bliss, A. P.; Siepmann, J. I. An online parameter and property database for the TraPPE force field. *Mol. Simul.* **2014**, *40*, 101–105.
- (7) Hill, T. L. *An Introduction to Statistical Thermodynamics*; Dover Publications: Mineola, NY, 1960.
- (8) Allen, M. P.; Tildesley, D. J. *Computer Simulation of Liquids*; Oxford University Press: Oxford, U.K., 1989.
- (9) Frenkel, D.; Smit, B. *Understanding Molecular Simulation: From Algorithms to Applications*; Academic Press: San Diego, CA, 2002.
- (10) Hasse, H.; Lenhard, J. Boon and Bane: On the Role of Adjustable Parameters in Simulation Models. In *Mathematics as a Tool, Boston Studies in Philosophy and History of the Sciences*; Lenhard, J., Carrier, M., Eds.; Springer, 2017; pp 93–115.
- (11) Bevington, P. R.; Robinson, D. K. *Data Reduction and Error analysis*; McGraw-Hill: New York, 2003.
- (12) van Gunsteren, W. F.; Mark, A. E. Validation of molecular dynamics simulation. *J. Chem. Phys.* **1998**, *108*, 6109–6116.
- (13) Dubbeldam, D.; Torres-Knoop, A.; Walton, K. S. On the inner workings of Monte Carlo codes. *Mol. Simul.* **2013**, *39*, 1253–1292.
- (14) Martin, M. G.; Siepmann, J. I. Transferable Potentials for Phase Equilibria. I. United-Atom Description of n-Alkanes. *J. Phys. Chem. B* **1998**, *102*, 2569–2577.
- (15) Dysthe, D. K.; Fuchs, A. H.; Rousseau, B. Fluid transport properties by equilibrium molecular dynamics. III. Evaluation of united atom interaction potential models for pure alkanes. *J. Chem. Phys.* **2000**, *112*, 7581–7590.

- (16) Cornell, W. D.; Cieplak, P.; Bayly, C. I.; Gould, I. R.; Merz, K. M.; Ferguson, D. M.; Spellmeyer, D. C.; Fox, T.; Caldwell, J. W.; Kollman, P. A. A second generation force field for the simulation of proteins, nucleic acids, and organic molecules. *J. Am. Chem. Soc.* **1995**, *117*, 5179–5197.
- (17) Todorov, I. T.; Smith, W.; Trachenko, K.; Dove, M. T. DLPOLY 3: new dimensions in molecular dynamics simulations via massive parallelism. *J. Mater. Chem.* **2006**, *16*, 1911–1918.
- (18) Hess, B.; Kutzner, C.; van der Spoel, D.; Lindahl, E. GROMACS 4: Algorithms for Highly Efficient, Load-Balanced, and Scalable Molecular Simulation. *J. Chem. Theory Comput.* **2008**, *4*, 435–447.
- (19) Abraham, M. J.; Murtola, T.; Schulz, R.; Páll, S.; Smith, J. C.; Hess, B.; Lindahl, E. GROMACS: High performance molecular simulations through multi-level parallelism from laptops to supercomputers. *SoftwareX* **2015**, *1*–2, 19–25.
- (20) Plimpton, S. Fast Parallel Algorithms for Short-Range Molecular Dynamics. *J. Comput. Phys.* **1995**, *117*, 1–19.
- (21) Glass, C. W.; Reiser, S.; Rutkai, G.; Deublein, S.; Köster, A.; Guevara-Carrion, G.; Wafai, A.; Horsch, M.; Bernreuther, M.; Windmann, T.; Hasse, H.; Vrabec, J. ms2: A molecular simulation tool for thermodynamic properties, new version release. *Comput. Phys. Commun.* **2014**, *185*, 3302–3306.
- (22) Phillips, J. C.; Braun, R.; Wang, W.; Gumbart, J.; Tajkhorshid, E.; Villa, E.; Chipot, C.; Skeel, R. D.; Kalé, L.; Schulten, K. Scalable molecular dynamics with NAMD. *J. Comput. Chem.* **2005**, *26*, 1781–1802.
- (23) Ponder, J.; Richards, F. TINKER molecular modeling package. *J. Comput. Chem.* **1987**, *8*, 1016–1024.
- (24) Martin, M. G. MCCCIS Towhee: a tool for Monte Carlo molecular simulation. *Mol. Simul.* **2013**, *39*, 1212–1222.
- (25) Shen, V.; Siderius, D.; Krekelberg, W.; Hatch, H. NIST Standard Reference Simulation Website, NIST Standard Reference Database Number 173. <https://www.nist.gov/programs-projects/nist-standard-reference-simulation-website> (accessed August 2017).
- (26) Lejaeghere, K.; Bihlmayer, G.; Björkman, T.; Blaha, P.; Blügel, S.; Blum, V.; Caliste, D.; Castelli, I. E.; Clark, S. J.; Dal Corso, A.; De Gironcoli, S.; Deutsch, T.; Dewhurst, J. K.; di Marco, I.; Draxl, C.; Dulak, M.; Eriksson, O.; Flores-Livas, J. A.; Garrity, K. F.; Genovese, L.; Giannozzi, P.; Giantomassi, M.; Goedecker, S.; Gonze, X.; Grånäs, O.; Gross, E. K. U.; Gulans, A.; Gygi, F.; Hamann, D. R.; Hasnig, P. J.; Holzwarth, N. A. W.; Işın, D.; Jochym, D. B.; Jollet, F.; Jones, D.; Kresse, G.; Koepernik, K.; Küçükbenli, E.; Kvashnin, Y. O.; Loch, I. L. M.; Lubeck, S.; Marsman, M.; Marzari, N.; Nitzsche, U.; Nordström, L.; Ozaki, T.; Paulatto, L.; Pickard, C. J.; Poelmans, W.; Probert, M. I. J.; Refson, K.; Richter, M.; Rignanese, G.-M.; Saha, S.; Scheffler, M.; Schlipf, M.; Schwarz, K.; Sharma, S.; Tavazza, F.; Thunström, P.; Tkatchenko, A.; Torrent, M.; Vanderbilt, D.; Van Setten, M. J.; van Speybroeck, V.; Wills, J. M.; Yates, J. R.; Zhang, G.-X.; Cottenier, S. Reproducibility in density functional theory calculations of solids. *Science* **2016**, *351*, aad3000.
- (27) Petersen, H.; Flyvbjerg, H. Error estimates in molecular dynamics simulations. *J. Chem. Phys.* **1989**, *91*, 461–467.
- (28) Rapaport, D. C. *The Art of Molecular Dynamics Simulation*; Cambridge University Press: Cambridge, U.K., 2004.
- (29) Frenkel, D. Simulations: The dark side. In Proceedings of the International School of Physics “Enrico Fermi”; Bologna, Italy, 2012; pp 195–227.
- (30) Seibert, M. M.; Patriksson, A.; Hess, B.; van der Spoel, D. Reproducible Polypeptide Folding and Structure Prediction using Molecular Dynamics Simulations. *J. Mol. Biol.* **2005**, *354*, 173–183.
- (31) Day, R.; Paschek, D.; Garcia, A. E. Microsecond simulations of the folding/unfolding thermodynamics of the Trp-cage miniprotein. *Proteins: Struct., Funct., Genet.* **2010**, *78*, 1889–1899.
- (32) Hünenberger, P. H. In *Advanced Computer Simulation: Approaches for Soft Matter Sciences I*; Holm, C., Kremer, K., Eds.; 2005; pp 105–149.
- (33) Van Der Spoel, D.; Lindahl, E.; Hess, B.; Groenhof, G.; Mark, A. E.; Berendsen, H. J. C. GROMACS: Fast, flexible, and free. *J. Comput. Chem.* **2005**, *26*, 1701–1718.
- (34) Miller, G. A Scientist’s Nightmare: Software Problem Leads to Five Retractions. *Science* **2006**, *314*, 1856–1857.
- (35) McConnell, S. *Code complete*; Microsoft Press: Redmond, WA, USA, 2004.
- (36) Niethammer, C.; Glass, C.; Gracia, J. Avoiding Serialization Effects in Data/Dependency Aware Task Parallel Algorithms for Spatial Decomposition. In Proceedings of the 10th IEEE International Symposium on Parallel and Distributed Processing with Applications (ISPA); Leganes, Spain, 2012; pp 743–748.
- (37) Wong-ekkabut, J.; Karttunen, M. The good, the bad and the user in soft matter simulations. *Biochim. Biophys. Acta, Biomembr.* **2016**, *1858*, 2529–2538.



## 4 Beiträge zu wissenschaftlichen Konferenzen

1. **A. Köster**, T. Jiang, G. Rutkai, C. W. Glass, J. Vrabec, **Präsentation:** Fully automated determination of fundamental EOS based on molecular simulations in the cloud *CAPE Forum - Computer Aided Process Engineering*, 27.04. bis 29.04.2015 in Paderborn, Deutschland.
2. **A. Köster**, G. Rutkai, M. Thol, R. Lustig, R. Span, J. Vrabec, **Präsentation:** Empirische Fundamentalgleichungen auf der Basis von molekularen Simulationen - Ein Überblick, *Thermodynamik Kolloquium* 05.10. bis 07.10.2015 in Bochum, Deutschland.
3. **J. Vrabec**, G. Guevara-Carrion, T. Janzen, A. Köster, **Präsentation:** Thermodynamic properties of water and aqueous alcohol mixtures by molecular simulation, *The International Association for the Properties of Water and Steam (IAPWS) Meeting*, 11.09. bis 16.09.2016 in Dresden, Deutschland.
4. **A. Köster**, G. Rutkai, M. Thol, R. Lustig, R. Span, J. Vrabec, **Präsentation:** Empirische Fundamentalgleichungen auf der Basis von molekularen Simulationen - Ein Überblick, *ProcessNet-Jahrestagung und 32. DECHEMA-Jahrestagung der Biotechnologen*, 12.09. bis 15.09.2016 in Aachen, Deutschland.
5. **A. Köster**, G. Rutkai, M. Thol, R. Lustig, R. Span, J. Vrabec, **Präsentation:** Fundamental Equations of State on the basis of Molecular Simulations, *Eingeladener Vortrag, Gruppe von Prof. Maginn, University of Notre Dame*, 11.11.2016 Notre Dame, IN, USA.
6. **A. Köster**, T. Jiang, G. Rutkai, C. W. Glass, J. Vrabec, **Präsentation:** Automated determination of fundamental EOS based on molecular simulations in the cloud, *Annual meeting of the American Institute of Chemical Engineers*, 13.11. bis 18.11.2016 in San Francisco, CA, USA.

7. **A. Köster**, M. Thol, G. Rutkai, J. Vrabec, R. Lustig, R. Span, **Poster:** Empirical Fundamental Equations of State Correlations Based on Hybrid Datasets, *Annual meeting of the American Institute of Chemical Engineers*, 13.11. bis 18.11.2016 in San Francisco, CA, USA.
8. G. Rutkai, A. Köster, G. Guevara-Carrion, T. Janzen, M., Schappals, C. W. Glass, M. Bernreuther, A. Wafai, S. Stephan, M. Kohns, S. Reiser, S. Deublein, M. Horsch, H. Hasse, **J. Vrabec**, **Präsentation:** ms2 - Release 3.0 of a molecular simulation tool, *International Workshop Molecular Modeling and Simulation: Science, Engineering and Industrial Applications*, 09.03. bis 10.03.2017 in Frankfurt/Main, Deutschland.
9. **A. Köster**, J. Vrabec, **Präsentation:** Molecular model for the hydrogen economy: Hydrogen, Oxygen, Water, Nitrogen and Argon, *Statistical Association Fluid Theory (SAFT) Conference*, 11.05. bis 13.05.2017 in Heidelberg, Deutschland.